UNIVERSITY OF EXETER

ACME2014

Proceedings of the 22nd UK National Conference of the Association for Computational Mechanics in Engineering

2nd - 4th April 2014

College of Engineering, Mathematics and Physical Sciences,

University of Exeter, UK

Edited by :

Akbar Javadi

Mohammed S. Hussain

ACME Association of Computational Mechanics in Engineering - UK

First published 2014 by
The University of Exeter

Electronic Version Only

British Library Cataloguing-in-Publication Data
A catalogue record for this book is available from the British Library

ISBN 978-0-902746-30-5

UNIVERSITY OF EXETER

ACME2014

Proceedings of the 22nd UK National Conference of the Association for Computational Mechanics in Engineering

2nd - 4th April 2014

College of Engineering, Mathematics and Physical Sciences,

University of Exeter, UK

FULL PAPERS

Edited by:

Akbar Javadi

Mohammed S. Hussain

ISBN 978-0-902746-30-5

University of Exeter, UK

PREFACE

The UK Association for Computational Mechanics in Engineering (ACME) was founded with the aim of promoting research in computational mechanics and various engineering applications and establishing formal links and with similar organisations in Europe and the International Association of Computational Mechanics (IACM). One of the principal activities of ACME involves the organisation of the annual conference. The first such conference took place at the University College of Wales Swansea in 1993. Since then, the conferences have provided a forum for reviewing research activities in many areas of mechanics, with an emphasis on interdisciplinary aspects. The conferences have proved to be particularly useful events for bringing together researchers from different disciplines, and especially for providing young researchers with opportunities to present their work.

These conference proceedings contain more than 80 four-page papers presented at the 22nd ACME Conference that was held in the Department of Engineering at the University of Exeter from 3rd to 4th April 2014, following the 3rd ACME School on 2nd April, where four lectures were delivered on the topics of Isogeometric Analysis and Automatic Meshing by renowned academics.

On behalf of the local organising committee, I would like to thank many people who have contributed to this conference, especially, all the authors who meticulously prepared their papers and presented their original research. I would like to express my gratitude to the three invited keynote speakers, Professor Hywel Thomas, Mr Adrian Gaylard and Professor Bassam Izzuddin for their thought provoking lectures and seminal scholarly contributions. I would also like to thank the speakers of the ACME School, Professor Sven Klinkel, Dr Ido Akkerman, Dr Robert Simpson and Professor Philippe Young, for their excellent lectures on the very important topics covered in the School.

I would like to acknowledge the support received from the College of Engineering, Mathematics and Physical Sciences of the University of Exeter in the organisation of this conference. In particular, I would like to thank Ms Karen Pope, Ms Denise Watts and Mr Chris Snow for providing assistance and advise on financial issues and IT services. Finally, I would like to thank the local organising committee members, with special thanks to Mr Mohammed S. Hussain for his dedication and hard work in the day-to-day organisation of ACME2014 conference.

Akbar Javadi
Vice-Chairman of ACME 2014

INVITED PLENARY LECTURES

Prof. Hywel Thomas

Prof. Hywel Thomas is Pro Vice-Chancellor, Engagement and International, Professor of Civil Engineering, and Founder Director of the Geoenvironmental Research Centre (GRC) at Cardiff University. Prof. Thomas will give a lecture on *Geoenergy Research Applications*.

Mr. Adrian Gaylard

Mr. Adrian Gaylard is Jaguar Land Rover's Aerodynamics Technical Specialist. He is the Chair of the Aerodynamics Activity at the SAE and a member of the European Car Aerodynamics Research Association. Adrian will speak on the *Application of Unsteady Aerodynamic Simulation in Automotive Engineering*.

Prof. Bassam Izzuddin

Prof. Bassam Izzuddin is Head of the Computational Structural Mechanics (CSM) Group at Imperial College London. He will give a lecture on *Partitioned Modelling for Nonlinear Analysis of Large-Scale Structural Systems using High Performance Computing,* presenting applications to realistic structures subject to extreme loading.

CONTENTS

FRACTURE, FAILURE MECHANICS

STRUCTURES

MATERIALS, ELASTICITY

Proceedings of the 22nd UK Conference of the
Association for Computational Mechanics in Engineering
2 - 4 April 2014, University of Exeter, Exeter

A coupled Partition of Unity FEM-collocation BEM for acoustic wave scattering in heterogeneous media in two dimensions

Ganesh C. Diwan*[1], Jon Trevelyan[1] and Graham Coates[1]

[1]School of Engineering and Computing Sciences, Durham University, Durham, DH1 3LE

*g.c.diwan@durham.ac.uk

ABSTRACT

The Finite Element Method (FEM) is known for its versatility to handle complex geometries and heterogeneities in the medium properties, while the Boundary Element Method (BEM) is known for its ability of exact treatment of waves propagating to infinity for wave problems. In this paper, we propose a coupled formulation of partition of unity FEM (PUFEM) and partition of unity BEM (PUBEM) to solve acoustic scattering problems in a heterogeneous medium. Numerical examples are presented to establish the convergence of the proposed method. Two of the well known non-reflecting boundary conditions for wave problems are implemented and their performance is compared against the coupled PUFEM-PUBEM results.

Key Words: *Wave scattering; Partition of unity method; Non-reflecting boundary condition; Boundary integral equation; Heterogeneous media*

1. Introduction

Modelling of waves in a heterogeneous medium can become a difficult task for the element based methods with polynomial basis as i) a heterogeneous medium requires a high resolution of mesh when the degree of heterogeneity is high and ii) high frequency wave problems become increasingly costly due the requirement of at least ten nodes per wavelength. Plane wave based methods have been found to offer a clear advantage over polynomial based methods when modelling wave problems in the medium frequency range, see [1][2]. Cases where the wavenumber is not constant in the computational domain are of practical interest. PU based methods have been used in such cases, see [3][4]. It is known that the Sommerfeld radiation condition is satisfied exactly for BEM (at least for the continuous equations) thus the waves propagating to infinity are modelled exactly. FEM (or PUFEM) on the other hand needs the so called non-reflecting boundary conditions (NRBCs) which are approximate and for an improved accuracy the non-reflecting boundary needs to be kept as far as possible from the scatterer to avoid spurious reflections. The heterogeneity, if limited to a relatively small part of the domain, can be modelled using PUFEM. The rest of the domain, if homogeneous and unbounded, can be modelled using PUBEM. It is therefore natural to couple PUFEM and PUBEM for modelling exterior acoustic problems involving wave scattering in heterogeneous medium which is the focus of this paper. The rest of the paper is organised as follows. Section 2 provides an overview of the governing PDE for wave scattering, its weak form for PUFEM and the boundary integral equation. Section 3 gives the partition of unity concept and coupling of PUFEM and PUBEM through matrix equations. This is followed by numerical examples (Section 4) and conclusions (Section 5).

2. Weak form and boundary integral equation

We consider the case of a time-harmonic ($e^{-i\omega t}$) acoustic wave scattering by a rigid sound hard obstacle Ω_s bounded by Γ_s in $\mathbb{R}^2$ (Fig. 1). We seek the total acoustic pressure p exterior to Γ_s that admits the following BVP:

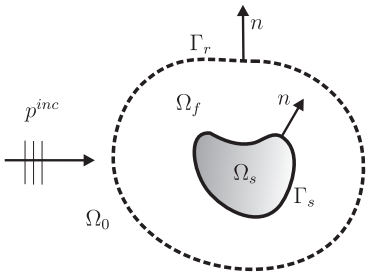

Figure 1: Problem definition

$$\rho\,\nabla\cdot\left(\rho^{-1}\nabla p\right)+k^2p=0\quad\text{in}\quad\mathbb{R}^2\setminus\Omega_s \tag{1}$$

$$\frac{\partial p}{\partial n}=0\quad\text{on}\quad\Gamma_s=\partial\Omega_s \tag{2}$$

$$\lim_{|x|\to\infty}|x|^{1/2}\left(\partial_{|x|}(p-p^{inc})-ik(p-p^{inc})\right)=0 \tag{3}$$

where, ρ is the medium density, p is the total acoustic pressure, $k=\omega/c$, ω is the circular frequency of wave and c is the speed of sound. The parameters ρ and c are allowed to change in space, n is the unit normal on Γ_r (or Γ_s) pointing towards Ω_0, $i=\sqrt{-1}$, p^{inc} is the incident wave and $\Gamma_s\cup\Gamma_r=\emptyset$. The weak form for the Helmholtz equation (1) can be obtained by multiplying with a test function v thus the BVP in (1)-(3) gives,

$$\int_{\Omega_f}\left(\rho^{-1}\nabla v\cdot\nabla p-\rho^{-1}k^2vp\right)d\Omega-\int_{\Gamma_r}\rho^{-1}v\frac{\partial p}{\partial n}d\Gamma=0 \tag{4}$$

The boundary integral equation for p can be written as,

$$c(\mathbf{x})p(\mathbf{x})+\int_{\Gamma_r}\frac{\partial G(\mathbf{x},\mathbf{y})}{\partial n_y}p(\mathbf{y})d\Gamma-\int_{\Gamma_r}G(\mathbf{x},\mathbf{y})\frac{\partial p}{\partial n}d\Gamma+p^{inc}(\mathbf{x}),\quad\mathbf{x},\mathbf{y}\in\Gamma_r \tag{5}$$

where, $\mathbf{x}$ is the collocation point, $\mathbf{y}$ is the field point, $c(\mathbf{x})$ is the jump term and $G(\mathbf{x},\mathbf{y})$ is the Green's function. For a 2D case, $G(\mathbf{x},\mathbf{y})=(i/4)H_0(kr)$, where $H_0(\cdot)$ is the Hankel function of first kind and order zero and $r=|\mathbf{y}-\mathbf{x}|$. We assume Γ_r is smooth and take $c(\mathbf{x})=0.5$. We follow the same PUFEM formulation as used in [5] and implement two of the well known NRBCs viz. the second order Bayliss-Gunzburger-Turkel (BGT-2) and 2nd order Enquist-Majda (EM-2) conditions; for details the readers are referred to [5].

3. Plane wave basis for heterogeneous medium and PUFEM-PUBEM coupling

In this paper, we restrict ourselves to piecewise constant density subdomains. We use 4-noded linear quadrilateral finite elements to discretize Ω_f and we follow the well known partition of unity representation of the pressure field p. The heterogeneity arising on account of density jump in Ω_f results in a corresponding jump in the wavenumber. We therefore use a combined basis which is used globally in the FE domain Ω_f for total pressure p and its normal derivative $\frac{\partial p}{\partial n}$, i.e.,

$$\begin{aligned}p(\mathbf{x})=&\sum_{j=1}^{4}N_j\sum_{m=1}^{M}a_{11}^{k_1}e^{ik_1\mathbf{d}_{jm}\cdot\mathbf{x}}+\cdots+a_{4M}^{k_1}e^{ik_1\mathbf{d}_{jm}\cdot\mathbf{x}}+a_{11}^{k_2}e^{ik_2\mathbf{d}_{jm}\cdot\mathbf{x}}+\cdots+\\&a_{4M}^{k_2}e^{ik_2\mathbf{d}_{jm}\cdot\mathbf{x}}+a_{11}^{k_L}e^{ik_L\mathbf{d}_{jm}\cdot\mathbf{x}}+\cdots+a_{4M}^{k_L}e^{ik_L\mathbf{d}_{jm}\cdot\mathbf{x}},\quad\mathbf{x}\in\Omega_f,\end{aligned} \tag{6}$$

$$\begin{aligned}\frac{\partial p}{\partial n}(\mathbf{x})=&\sum_{j=1}^{4}N_j\sum_{m=1}^{M}b_{11}^{k_1}e^{ik_1\mathbf{d}_{jm}\cdot\mathbf{x}}+\cdots+b_{4M}^{k_1}e^{ik_1\mathbf{d}_{jm}\cdot\mathbf{x}}+b_{11}^{k_2}e^{ik_2\mathbf{d}_{jm}\cdot\mathbf{x}}+\cdots+\\&b_{4M}^{k_2}e^{ik_2\mathbf{d}_{jm}\cdot\mathbf{x}}+b_{11}^{k_L}e^{ik_L\mathbf{d}_{jm}\cdot\mathbf{x}}+\cdots+b_{4M}^{k_L}e^{ik_L\mathbf{d}_{jm}\cdot\mathbf{x}},\quad\mathbf{x}\in\Gamma_r.\end{aligned} \tag{7}$$

where L stands for total number of density jumps in Ω_f. Let the global notation for the pressure and its normal derivative be given as

$$\mathbf{p}=\boldsymbol{Q}\mathbf{a} \tag{8}$$

$$\frac{\partial\mathbf{p}}{\partial\mathbf{n}}=\boldsymbol{Q}\mathbf{b} \tag{9}$$

Here, $\mathbf{a}$ and $\mathbf{b}$ are the vectors of unknown plane wave amplitudes associated with total acoustic pressure p (see (6)) in Ω_f and $\frac{\partial p}{\partial n}$ on Γ_r (see (7)) respectively. Q can be readily formed using either (6) or (7). Using (6)-(7) for the weak form of the Helmholtz equation (4) and the integral equation (5) along with the isoparametric test functions for (4), we obtain following partly symmetric-partly unsymmetric system after combining the discrete forms for (4) and (5).

$$\begin{bmatrix} \mathbf{K_1} & \mathbf{K_2} & \mathbf{R} \\ \mathbf{0} & \mathbf{H} & -\mathbf{G} \end{bmatrix} \begin{Bmatrix} \mathbf{a_1} \\ \mathbf{a_2} \\ \mathbf{b} \end{Bmatrix} = \begin{Bmatrix} \mathbf{0} \\ \mathbf{p^{inc}} \end{Bmatrix} \tag{10}$$

It may be noted from above (see (10)), $\mathbf{a} = [\mathbf{a_1}, \mathbf{a_2}]^T$. It can be readily seen that the coupling between PUFEM and PUBEM is achieved as $\mathbf{K_2}$ and $\mathbf{H}$ multiply the common plane wave amplitudes $\mathbf{a_2}$ associated with Dirichlet data on Γ_r and $\mathbf{R}$ and $\mathbf{G}$ multiply the common plane wave amplitudes $\mathbf{b}$ associated with Neumann data on Γ_r. The block matrices on the left hand side of (10) are given by

$$\mathbf{K_1} = \int\limits_{\Omega_f \setminus \Gamma_r} \rho^{-1} \left[\nabla Q\right]^T \nabla Q \, d\Omega \,, \quad \mathbf{K_2} = \int\limits_{\Omega_f \cap \Gamma_r} \rho^{-1} \left[\nabla Q\right]^T \nabla Q \, d\Omega \,, \quad \mathbf{R} = \int\limits_{\Gamma_r} \rho^{-1} Q^T Q \, d\Omega \,, \tag{11}$$

$$\mathbf{H} = \frac{1}{2}\rho^{-1} Q(\mathbf{x})^T + \int\limits_{\Gamma_r} \rho^{-1} Q(\mathbf{y})^T \frac{\partial G(\mathbf{x}, \mathbf{y})}{\partial n_y} \, d\Omega \,, \quad \mathbf{G} = \int\limits_{\Gamma_r} \rho^{-1} Q(\mathbf{y})^T G(\mathbf{x}, \mathbf{y}) \, d\Omega \tag{12}$$

and $\mathbf{p}^{inc}$ is the vector formed using the usual collocation procedure in BEM with the known incident wave on Γ_r. The BEM equations have to be normalised with the density of homogeneous exterior medium (see (12)). It should be noted that the use of Lagrange multipliers is inevitable if each heterogeneity is modelled with the corresponding wavenumber alone in the basis (see [4]). The use of mixed basis (as in (6) or (7)) eliminates any such need as the continuity of acoustic pressure and normal particle velocity across the interface of two different mediums is satisfied naturally.

4. Numerical examples

We consider a plane wave scattering problem from a sound hard cylinder placed in a medium with a single jump in the density. The problem parameters are listed in Fig.2.

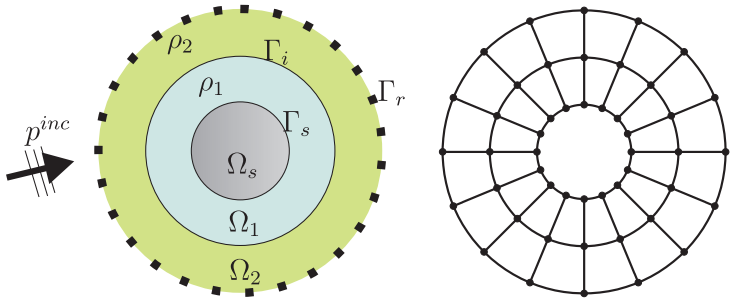

Problem definition Finite Element mesh

Figure 2: Two fluid example: $\rho_1 = 1.2\rho_2, r(\Gamma_s) = 1, r(\Gamma_i) = 2, r(\Gamma_r) = 3, p^{inc} = e^{ik_2 x}, \Omega_f = \Omega_1 \cup \Omega_2$.

Fig.3 shows the contours for real part of normalised total acoustic pressure in the computational domain Ω_f. For this problem, a reference solution based on Bessel function series can be constructed easily. The errors associated with polynomial FEM, PUFEM and coupled PUFEM-PUBEM are also listed in Fig.3. We now present the $Q-$convergence of the proposed coupled algorithm. We take 16 linear elements in the circumferential direction and 2 elements in the radial direction to model the computational domain Ω_f (see Fig. 2). The $Q-$refinement is achieved by increasing the number of plane waves in the basis (see (6)-(7)). The geometry parameters are the same as shown in Fig.2. As seen from Fig. 4, adding more degrees of freedom (dof) to the system improves the accuracy of coupled PUFEM-PUBEM solution unlike for the PUFEM solution which does not improve even after addition of more plane waves. This can be explained by the fact that the NRBCs used for PUFEM, namely BGT-2 and EM-2, are approximate boundary conditions and cannot represent an outgoing wave from Γ_r exactly.

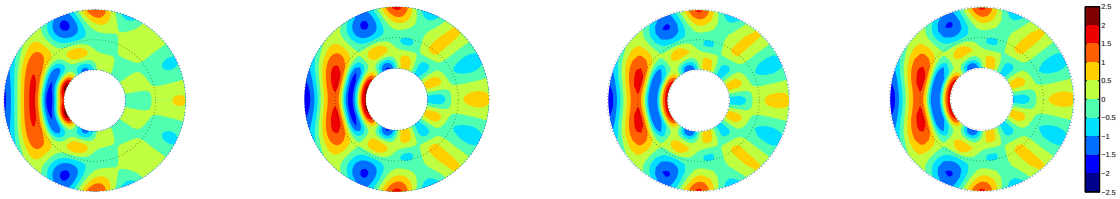

Polynomial FEM, $L^2(\Gamma_s)$ =19.8%, ndof = 2100

PUFEM, $M_1 = M_2 = 16$, $L^2(\Gamma_s) = 1.45\%$, ndof = 1548

Coupled PUFEM-PUBEM, $M_1 = M_2 = 8$, $L^2(\Gamma_s) = 0.4\%$, ndof = 1024

Reference solution

Figure 3: Real part of normalised total acoustic pressure, $k_1 = 2\pi, k_2 = \pi$, M_1:no. of plane waves with k_1 in basis, M_2: no. of plane waves with k_2 in basis.

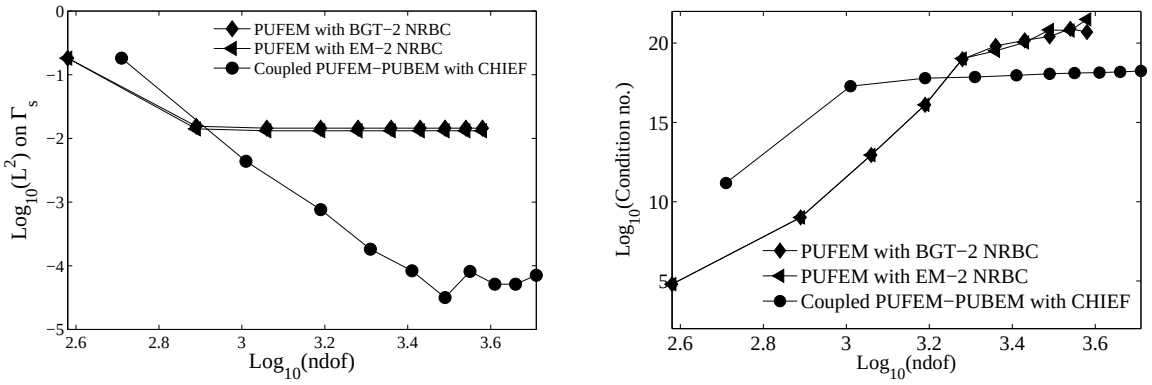

L^2 error on Γ_s

Conditioning of linear system

Figure 4: Q-convergence: PUFEM vs coupled PUFEM-PUBEM- $k_1 = 2\pi, k_2 = \pi$, nodes in radial direction = 3, nodes in circumferential direction = 16, total FE nodes = 48, total FE elements = 32.

5. Conclusions

We have presented a coupled formulation of plane wave enriched FEM and BEM. The error analysis presented shows a uniform convergence for coupled PUFEM-PUBEM algorithm and an improvement over PUFEM. At the same time, the accuracy of PUFEM is limited by the inherent approximations in the NRBCs used. The combined basis is shown to work for a heterogeneous problem without the need to use Lagrange multipliers.

References

[1] T. Huttunen, P. Monk, and J.P. Kaipio. Computational aspects of the ultra-weak variational formulation. *Journal of Computational Physics*, 182(1):27–46, 2002.

[2] C. Gittelson, R. Hiptmair, and I. Perugia. Plane wave discontinuous Galerkin methods: Analysis of the h-version. *ESAIM: Mathematical Modelling and Numerical Analysis*, 43(02):297–331, 2009.

[3] R. Tezaur, I. Kalashnikova, and C. Farhat. The discontinuous enrichment method for medium-frequency Helmholtz problems with a spatially variable wavenumber. *Computer Methods in Applied Mechanics and Engineering*, 268(0):126–140, 2014.

[4] O. Laghrouche, P. Bettess, E. Perrey-Debain, and J. Trevelyan. Wave interpolation finite elements for Helmholtz problems with jumps in the wave speed. *Computer Methods in Applied Mechanics and Engineering*, 194(2):367–381, 2005.

[5] O. Laghrouche, A. El-Kacimi, and J. Trevelyan. A comparison of NRBCs for PUFEM in 2D Helmholtz problems at high wave numbers. *Journal of Computational and Applied Mathematics*, 234(6):1670–1677, 2010.

Proceedings of the 22nd UK Conference of the
Association for Computational Mechanics in Engineering
2 - 4 April 2014, University of Exeter, Exeter

AN ENRICHED QUADTREE/OCTREE IMPLICIT BOUNDARY FINITE ELEMENT METHOD FOR THE SIMULATION OF INCOMPRESSIBLE HYPERELASTIC MATERIALS

Jack S. Hale[1*], Pierre Kerfriden[2], Juan J. Ródenas García[3], and Stéphane P. A. Bordas[1]

[1]Research Unit in Engineering Science, University of Luxembourg, Luxembourg
[2]Cardiff School of Engineering, Cardiff University, Cardiff, Wales, UK
[3]Research Centre for Vehicle Technology (CITV), Universidad Politécnica de Valencia, Spain

[*]jack.hale@uni.lu

ABSTRACT

Octree (and quadtree) representations of computational geometry are particularly well suited to modelling domains that are defined implicitly, such as those generated by image segmentation algorithms applied to medical scans. In this work we consider the simulation of soft-tissue which can be modelled with a hyperelastic constitutive law. We include the effects of both non-linear geometry and material properties.

Similarly to Legrain et al. [1] and Moumnassi et al. [2] we use the implicitly defined level set functions as the basis for a partition of unity enrichment to more accurately represent the domain boundary. Furthermore we use traditional extended finite element (XFEM) ideas to introduce arbitrary cuts and discontinuities in the domain.

We explore the use of a three-field $\mathbf{u}$-p-θ mixed approach to deal with the problem of volumetric-locking in the incompressible limit.

We will discuss the extension of our method towards both traditional parallel and GPU implementation. We aim to solve extremely large problems as well as produce snapshots to feed into model order reduction methods for real-time surgical simulations.

Key Words: *surgery, octree, incompressible, hyperelasticity, XFEM, level sets.*

1. Introduction

A significant amount of research in numerical methods over the past two decades has been dedicated towards alleviating the difficulties associated with accurately and efficiently representing geometrical information about the domain of interest in a numerical simulation.

The traditional path has been to transfer geometrical information from one form, such as a computer aided design (CAD) model, constructive solid geometry (CSG) model or image-based (pixel or voxel) data to a mesh, a conforming partition of the problem domain of interest into simplices or polygonal/polyhedral domains. Particularly in the case of simplex meshes in 2D and 3D there are now relatively robust methods for converting all of the above geometric data sources into meshes, e.g. Simpleware+FE and CGAL [3]. Difficulties still remain particularly with the hexahedral case and often the methods produce meshes with large number of degrees of freedom for complex geometries.

Meshfree methods attempt to help alleviate the difficulty of mesh generation by removing the restriction of having to pre-define connectivity between nodes in the domain; connectivity is a natural consequence of the support domain of each node and to some extent nodes can be placed arbitrarily. However, in the vast majority of cases, meshfree methods still describe the geometry of the domain using an underlying

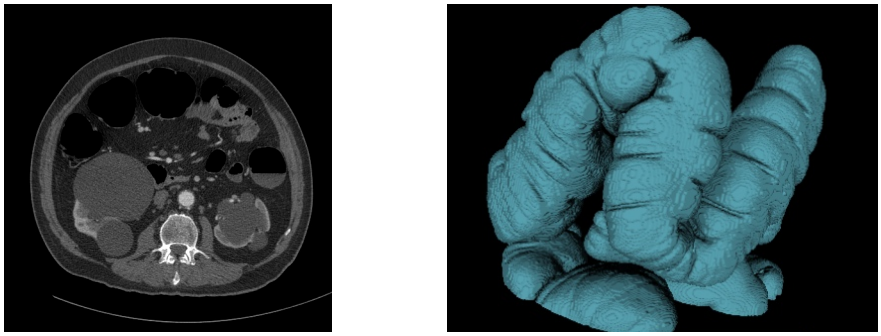

Figure 1: Left: Single image from CAT scan of abdomonen (Source: COLONIX). Right: Isosurface derived from segmentation of part of human colon (black voids in CAT scan left).

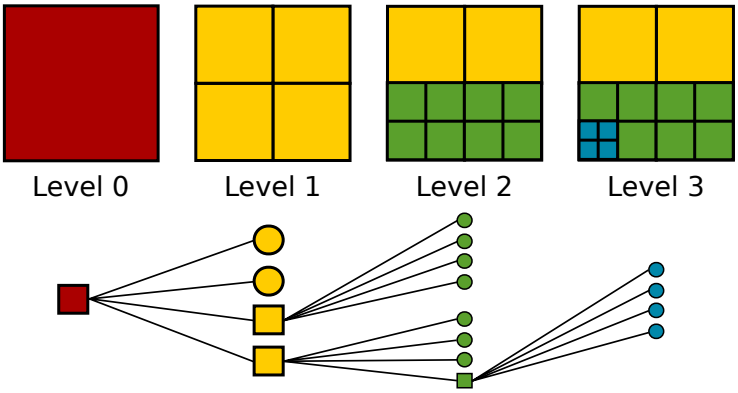

Figure 2: Construction of a quadtree grid and the representative tree. Beginning with level zero (far left) the octree is non-uniformly subdivided to level three (far right). Nodes of the tree with children are shown as squares, and those without children are shown as circles.

mesh or assume that the geometry is formed by the convex hull of the node set. This latter assumption makes describing highly non-convex domains (e.g. cracks) with meshfree methods difficult.

Other methods have attempted to unify the description of the geometrical information and the method of numerical approximation, perhaps most famously the isogeometric analysis method where the same basis functions such as NURBS are used to discretise the geometry and form the basis for solving the PDE.

Partition of Unity Methods (PUM) [4] shift the burden of describing the geometry of the domain from the mesh to the basis functions via suitable enrichment of the discretisation basis. One of the goals of both the generalized finite element method (GFEM) and the eXtended finite element method (XFEM) is to represent the geometry of the problem independently of the discretisation. Methods such as the Finite Cell Method of Parnazian et al. [5] propose the integration of the weak form on sub-cells that approximate the geometry as a stepped surface although they do not use enrichment functions.

We believe that the in the case of image-based analysis, where the geometry is defined implicitly through advanced image segmentation procedures, see fig. 1, that partition of unity methods with seperate representation of discretisation and geometry are particularly well-suited to rapidly producing patient-specific mechanical models of the human body [6]. This paper discusses our first steps in this new project in which we aim to build a parallel distributed-memory solver capable of solving real-world problems in surgical simulation derived directly from patient-specific imagery.

2. Quadtree partition of implicitly defined domain

A quadtree or octree is a tree structure in which each node has four or eight children (respectively) and in this case we use it to recursively subdivide either the 2D or 3D (respectively) bounding box of the problem domain of interest Ω fig. 2. The level of a node in the tree corresponds to the number of subdivisions required to obtain that node.

In this work, in a similar manner to Legrain et al. [1], we construct two trees, one that we call the geometric octree O_g, and one that we call the the discretisation octree O_f. On the geometrical tree we approximate the geometrical information of the problem, derived, for example, from an image-segmentation

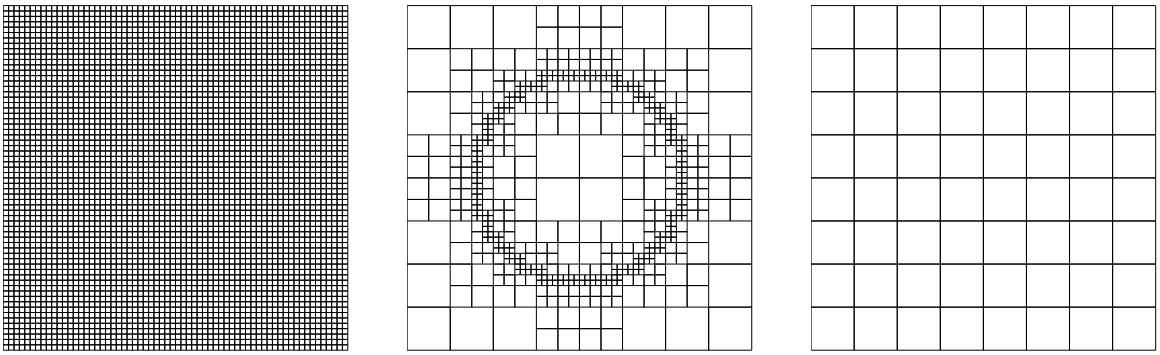

Figure 3: Left: A fine-scale grid O_f is constructed by uniform refinement to level six of the bounding box of the domain and contains information at the smallest geometric level, eg. pixel/voxel data. Middle: The fine-scale grid is coarsened to level three to form the geometric grid O_g based on the implicit information (e.g. level-set) on the fine-scale grid O_f. Right: The geometric grid O_g is coarsened further to form the discretisation grid O_d.

procedure generating a level-set function. On the discretisation tree we construct the numerical method, and we share information between the two via the partition of unity method.

We construct the trees from the highest-level down as shown in fig. 3, although it would be preferable from an efficiency standpoint to construct from the lowest-level up. A point of departure from the work of Legrain et al. is that we do not construct a triangulation from the octree. We believe this approach is superior from a point of view of both efficiency and the ability to use the more robust isoparametric quadrilateral/hexahedral finite element basis functions. We enforce the 2:1 mesh balance, sometimes known as 1-irregular grids to ensure a smooth transition between areas of high and low refinement.

The octree data structure makes handling the relationship between the discretisation and the geometric information very straightforward. By constructing a bi-directional map $\mathcal{M} : O_d \rightarrow O_g$ between the nodes of the two octrees we can easily support fast queries such as asking for the parent of a particular node in the geometric tree or all of the children of a particular node in the discretisation tree. Futhermore we can refine or coarsen both octrees independently of each other and efficiently regenerate the map between the two allowing for future implementation of traditional hp-adaptivity combined with enrichment e adaptivity. The method described in this paper is implemented in the deal.ii finite element framework [7].

3. Incompressible Hyperelastic Material Model

Due to the hydrated nature of soft-tissue it is typically modelled as a nearly-incompressible hyperelastic material. Standard displacement formulations typically suffer from volumetric locking in this regime which occurs because the basis functions are not sufficiently rich to represent the incompressibility constraint enforced by the bulk modulus κ. In this work we minimise the following three-field functional where the pressure p is an independent variational quantity and acts as a Lagrange multiplier to enforce the determinant of the deformation gradient J to an independent representation $\bar{J}$:

$$\Pi(\mathbf{u}, p, \theta) = \int_\Omega \psi(J, \bar{\mathbf{b}})\, d\Omega + \int_\Omega p(J - \bar{J})\, d\Omega - \Pi_{\text{ext}} \tag{1}$$

where $\bar{\mathbf{b}} = J^{-2/3}\mathbf{b}$ is the isochoric part of the left Cauchy-Green strain tensor $\mathbf{b} = \mathbf{F}\mathbf{F}^T$, and the deformation gradient with respect to the reference configuration $\mathbf{X}$ is $\mathbf{F} = I + \frac{\partial \mathbf{u}}{\partial \mathbf{X}}$, and Π_{ext} represents the external loading.

4. XFEM Enrichment

We transfer the geometric information embedded in the geometric octree to the discretisation by means of the Partition of Unity paradigm, or more specifically, the extended finite element method (XFEM). We write the displacement field $\mathbf{u}_h$, pressure field p_h and pressure parameter θ constructed with N standard classical finite element shape functions $\mathbf{N}_i$ enriched with M scalar enrichment functions ψ_j associated with extra degrees of freedom a_i^j as:

$$\mathbf{u}_h(\mathbf{x}) = \sum_{i=1}^{N} \mathbf{N}_i u_i + \sum_{i=1}^{N} \mathbf{N}_i \sum_{j=1}^{M} \psi_j(\mathbf{x}) a_i^j \tag{2}$$

We write similar expressions for p_h and θ_h, noting that we ensure the satisfaction of the LBB stability condition through the higher-order approximation of the displacements $\mathbf{u}_h$ than the auxilliary variables p_h and θ_h. Whilst the definition of the discretisation and the partition of unity enrichment is defined by degrees of freedom seeded from the discretisation octree O_d the integration and construction of the partition of unity enrichments is performed on the geometrical octree O_g.

Currently we only include Heaviside type enrichments (ie. strong discontinuities) to represent material boundaries and we are looking at the best way to include weak discontinuities in our formulation which will be vital for including material discontinuities.

5. Dirichlet Boundary Conditions

Because the boundary of the domain no longer coincides with the positions of the nodes seeded from the discretisation octree we no longer satisfy the basic requirement that our basis functions vanish on the Dirichlet boundary, typically denoted $\mathbf{v} \in H_0^1(\Omega)$. Various methods can be used to enforce the Dirichlet conditions including Nitsche's method, the method of Lagrange multipliers and the penalty method. The application of Nitsche's method to the problem of hyperelasticity is a relatively new field and we are currently investigating the application of methods developed in the Discontinuous Galerkin finite element methods, see e.g. Noels and Radovitzky [8].

Acknowledgements

Jack S. Hale would like to acknowledge the support of the structural position under the chair of Prof. Stéphane P. A. Bordas at the University of Luxembourg. Stéphane P. A. Bordas would like to acknowledge partial support for his time from European Research Council Starting Independent Research Grant (ERC Stg grant agreement No. 279578) entitled 'Towards real time multiscale simulation of cutting in non-linear materials with applications to surgical simulation and computer guided surgery'.

References

[1] G. Legrain, N. Chevaugeon, K. Drau, High order x-FEM and levelsets for complex microstructures: Uncoupling geometry and approximation, Computer Methods in Applied Mechanics and Engineering 241244 (2012) 172–189. doi:10.1016/j.cma.2012.06.001.

[2] M. Moumnassi, S. Belouettar, . Bchet, S. P. Bordas, D. Quoirin, M. Potier-Ferry, Finite element analysis on implicitly defined domains: An accurate representation based on arbitrary parametric surfaces, Computer Methods in Applied Mechanics and Engineering 200 (58) (2011) 774–796. doi:10.1016/j.cma.2010.10.002.

[3] P. Alliez, L. Rineau, S. Tayeb, J. Tournois, M. Yvinec, 3D mesh generation, in: CGAL User and Reference Manual, 4th Edition, CGAL Editorial Board.

[4] J. M. Melenk, I. Babuska, The partition of unity finite element method: Basic theory and applications, Computer Methods in Applied Mechanics and Engineering 139 (1-4) (1996) 289–314. doi:10.1016/S0045-7825(96)01087-0.

[5] J. Parvizian, A. Dster, E. Rank, Finite cell method, Computational Mechanics 41 (1) (2007) 121–133. doi:10.1007/s00466-007-0173-y.

[6] A. Horton, A. Wittek, K. Miller, Subject-specific biomechanical simulation of brain indentation using a meshless method, in: N. Ayache, S. Ourselin, A. Maeder (Eds.), Medical Image Computing and Computer-Assisted Intervention MICCAI 2007, Springer Berlin Heidelberg, 2007, pp. 541–548.

[7] W. Bangerth, R. Hartmann, G. Kanschat, Deal.II- a general-purpose object-oriented finite element library, ACM Trans. Math. Softw. 33 (4). doi:10.1145/1268776.1268779.

[8] L. Noels, R. Radovitzky, A general discontinuous galerkin method for finite hyperelasticity. formulation and numerical applications, International Journal for Numerical Methods in Engineering 68 (1) (2006) 6497. doi:10.1002/nme.1699.

Proceedings of the 22nd UK Conference of the
Association for Computational Mechanics in Engineering
2 – 4April 2014, University of Exeter, Exeter

APPLICATION OF A DENSITY-NUMBER (D-N) FRACTAL MODELLING TO CORRELATE MINERALISED ZONES IN KAHANG Cu-Mo PORPHYRY DEPOSIT

***Amir Bijan Yasrebi[1], Andrew Wetherlet[1], Patrick J Foster[1], John Coggan[1], Peyman Afzal[1,2]**

[1]Camborne School of Mines, University of Exeter, Cornwall Campus, Penryn, TR10 9EZ, UK
[2]Department of Mining Engineering, South Tehran branch, Islamic Azad University, Tehran, Iran

*aby203@exeter.ac.uk

ABSTRACT

The cost of mining for each block in an open pit mine is calculated using the dimension and specific weight of that block. It is clear that the tonnage of these blocks located in each zone is determined on the basis of each zones' ore density. As a result, the delineation of rock characterisation in terms of density plays a significant role in mine planning and design. This paper proposes a new practice named Density-Number (D-N) fractal modelling to separate density populations based on 32 density core samples (data) analysed from 11 boreholes in Kahang Cu-Mo porphyry deposit located in the central Iran. The D-N log-log plot indicates that there are three density populations with breakpoints at 2.618 and 2.673 t/m^3. Correlation between result of the fractal and the geological 3D models illustrates that the rocks with high values of density are associated with chalcopyrite and hypogene units.

Keywords: *Density-Number (D-N) fractal modelling; Kahang Cu-Mo porphyry; chalcopyrite; hypogene*

1. Introduction

Delineation of rock mass characterisation with respect to density is important in mineral exploration, resource evaluation and mine planning especially in optimisation of an ultimate pit limit since the cost and income of mining are related to the variation of density populations (societies) within an ore deposit [1, 2]. Host rocks of porphyry deposits consist of sub-volcanic massive ore bodies such as porphyric quartz diorite (PQD), granite, monzonite and quartz monzonite which are lithological units with high hardness [3, 4]. Variations of mineralogy and lithology units are other useful factors for separation of rock mass characterisation in the porphyry deposits [5].

The mathematical applications in geosciences have been massively created and consequently utilised to identify various phenomena for better interpretation of geological features such as lithology, zonation, alteration and mineralogy or for better understanding of different attributes like density, rock mass characterisation and RQD analysis [6, 7]. A number of models have been intended for purpose of modelling based on statistical, geostatistical. However, the classical statistics methods for delineation of populations from background such as histogram analysis, box plot, summation of mean and standard deviation coefficients and median are not accurate due to the fact that the statistical methods consider only the frequency distribution of information (such as density data) while have no attention to spatial variability since the information about the spatial correlation is not always available [8, 9]. In recent years, models based on fractal geometry as a nonlinear mathematical science proposed by Mandelbrot [10], have been hugely used in different branches of earth sciences since various geological processes and even mining-based issues like rock mass characterisation can be categorised by changes in fractal dimensions resulting from analysis of relevant data and desirable attributes (density in this scenario) [11, 12, 13]. As a result, Fractal analysis has the abilities to justify the differences within the ore deposits especially in hydrothermal occurrences such as porphyry Cu deposits [14]. However, proper knowledge of the rock mass characterisation is crucial to identify rock types and density populations. In other words, differences of fractal dimensions in density data can certify applicable criteria to identify rock mass characterisation by Density-Number (D-N) fractal modelling in the Kahang Cu-Mo porphyry deposit, Central Iran. Then, the obtained result via D-N fractal model is correlated and subsequently validated with chalcopyrite and hypogene as the major mineralisation and zonation unites in the studied area.

2. Methodology

Initially, a database was generated based on density values analysed from 11 boreholes of the total 48 drillcores carried out in the Kahang deposit. The project dimensions are 600×660×780m in X, Y and Z direction and each voxel has a dimension of 4×4×10m respectively. Secondly, the dataset was entered into the RockWorks [TM] v. 15 software package to build up 3D density block model (Fig. 1) utilising Inverse Distance Weighted (IDW) anisotropy as the estimator. The next step was to suggest the Density-Number (D-N) fractal model for delineation of different populations in terms of density within the deposit. Consequently, a mathematical facility of the software called "Multiple of Model & Model" as a tool to manipulate the voxels in a solid model by the corresponding voxels in another equally-dimensioned solid model file has been used for combination between the density 3D block model interpreted via D-N and the most frequent mineralisation and zonation units namely; Chalcopyrite and hypogene respectively (Fig. 2 and 3).

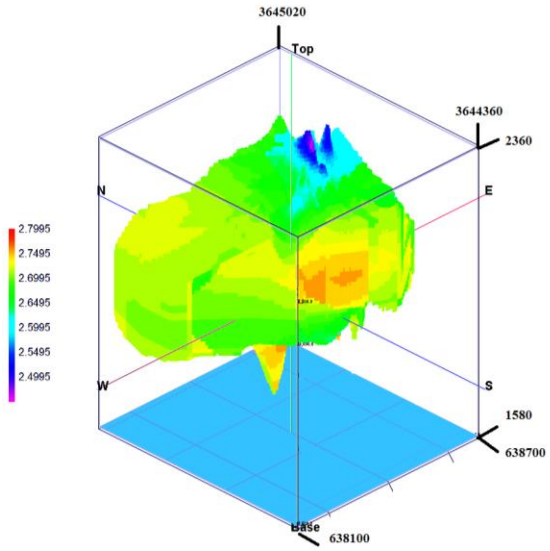

Fig.1. Density (t/m^3) block model

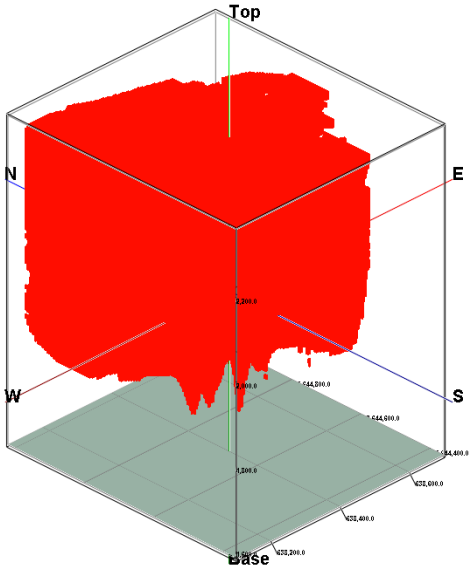

Fig.2. Chalcopyrite unit (m^3) within the deposit

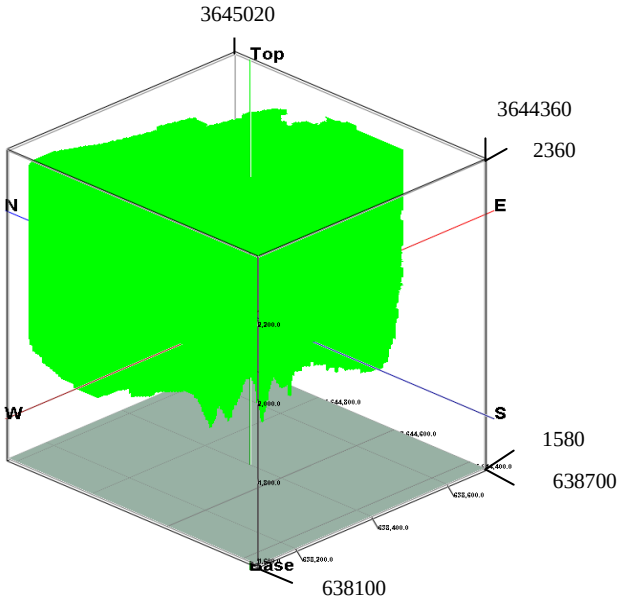

Fig.3. Hypogene model in the Kahang deposit (Scale is in m^3)

3. Fractal Model

The model is expressed by the following equation [10, 11]:

$$N(\geq \rho) = F\rho - D \qquad (1)$$

Where ρ denotes density values, *N(≥ρ)* denotes cumulative number of samples with density values greater than or equal to ρ, F is a constant and D is the scaling exponent or fractal dimension of the distribution of density values. Log–log plot of *N(≥ρ)* versus ρ shows straight line segments with different slopes −D corresponding to different density intervals.

The D-N method was applied to the density data (values). The selection of breakpoints as the threshold values appears to be an objective decision due to the density populations which are recognised by different segments in the D-N log-log plot (Fig. 4). Accordingly, the D-N log-log plot reveals that there are three populations with respect to density thresholds (breakpoints) of 2.618 and 2.673 t/m^3. As a result, the rocks with correspondingly high density commence from density > 2.673 t/m^3, the slope of the straight line fitted in the log-log plot is near to 90°.

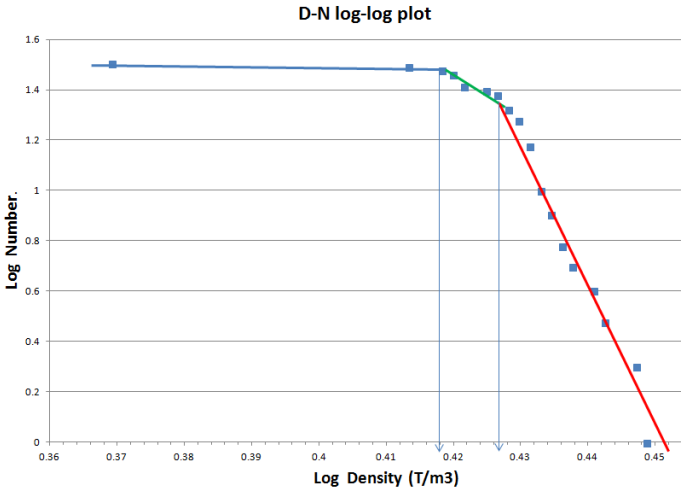

Fig.4. D-N log-log plot in the Kahang deposit

4. Correlation of D-N with the Major Mineralogical and Zonation Units

The result of the D-N model was correlated to the major mineralogical and zonation units of the deposit consisting of chalcopyrite and hypogene constructed by using RockWorks™ v. 15 software and drillcore data (Fig. 5). Rocks with density >2.673 t/m^3 defined by means of the D-N fractal model are well-correlated with chalcopyrite mineralogical unit and hypogene zone defined by the 3D modelling of lithological drillcores data. As a result, there is spatial coincidence between rock mass characterisation in terms of high density driven via means of the D-N model in the most parts of the deposit. Therefore, it can be concluded that chalcopyrite mineralogical unit and hypogene zone host the excellent values for density within the Kahang deposit.

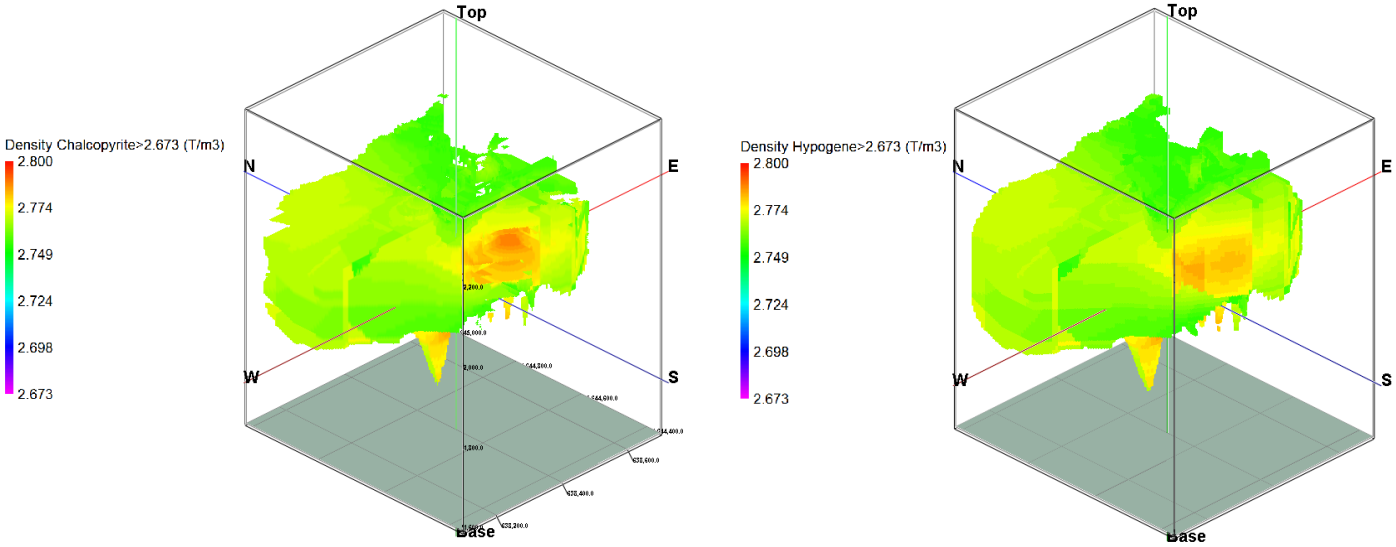

(a) (b)

Fig.5. Correlation of D–N fractal with major geological models: a) Chalcopyrite; b) hypogene

5. Conclusions

In this paper, the D-Number (D-N) fractal model was used to investigate and delineate various density populations in the Kahang Cu-Mo porphyry deposit (Central Iran). The D-N log-log plot illustrates three density populations delineated by two threshold values of 2.618 and 2.673 t/m^3. According to the correlation between result driven by fractal modelling and major mineralogical and zonation units resulted by the 3D geological model in the Kahang deposit, Chalcopyrite and hypogene are associated with density values > 2.673.

Acknowledgements

The authors also are hugely thankful to the Institute of Materials, Minerals and Mining (IOM^3) for its financial support in order to conduct this research.

References

[1] W.A. Hustrulid and M. Kuchta, *Open Pit Mine Planning and Design*, 2nd Edition, Taylor & Francis, London, 2006.

[2] A.B. Yasrebi, A. Wetherelt, P. Foster, P. Afzal, Determination and Analysis of Final Pit Limit of Esfordi Phosphate Open Pit Mine, in: Eskikaya. Ş (Eds.), 22nd World Mining Congress and Expo, Istanbul, pp. 513–522, 2011.

[3] P. Laznicka, *Giant Metallic Deposits Future Sources of Industrial Metals*, Springer- Verlag, Berlin, 2010.

[4] A.B. Yasrebi, P. Afzal, A. Wetherelt, P. Foster, R. Esfahanipour, D. Parvaz, 3D Lithology, Alteration and Zonation Modelling of the Eastern Part of Kahang Cu-Mo-Au Porphyry Deposit in Central Iran, in: A. Sabotinov, M. Mazhdrakov, I. Yilmaz, M. Marschalko (Eds.), *12th International Multidisciplinary Scientific Geo-Conference and Expo (SGEM)*, Albena, pp.417–423, 2012.

[5] A.B. Yasrebi, A. Wetherelt, P. Foster, P. Afzal, J. Coggan and D. Kaveh Ahangaran. Application of RQD-number and RQD-Volume multifractal modelling to delineate rock mass characterisation in Kahang Cu-Mo porphyry deposit, central Iran. *Arch. Min. Sci*, 58, 1023–1035, 2013.

[6] A. Rafiee and M. Vinches. Application of geostatistical characteristics of rock mass fracture systems in 3D model generation. *International Journal of Rock Mechanics and Mining Sciences*, 45, 644-652, 2008.

[7] A.B. Yasrebi, P. Afzal, A. Wetherelt, P. Foster and R. Esfahanipour. Correlation between geology and concentration-volume fractal models: significance for Cu and Mo mineralized zones separation in the Kahang porphyry deposit (Central Iran). *Geologica Carpathica*, 64, 153-163, 2013.

[8] P. Afzal, A. Khakzad, P. Moarefvand, N. Rashidnejad Omran, B. Esfandiari and Y. Fadakar Alghalandis. Geochemical anomaly separation by multifractal modelling in Kahang (Gor Gor) porphyry system, Central Iran. *Journal of Geochemical Exploration*, 104, 34-46, 2010.

[9] P. Afzal, H. Harati, Y. Fadakar Alghalandis and A.B Yasrebi. Application of spectrum–area fractal model to identify of geochemical anomalies based on soil data in Kahang porphyry-type Cu deposit, Iran. *Chemie der Erde*, 73, 533-543, 2013.

[10] B.B. Mandelbrot, *The Fractal Geometry of Nature*, W.H. Freeman, Updated and Augmented Edition, San Francisco, 1983.

[11] F.P. Agterberg, Q. Cheng and D.F. Wright, Fractal modelling of mineral deposits, In: J. Elbrond, X. Tang (Eds.), *24th APCOM symposium proceeding*, Montreal, pp. 43–53, 1993.

[12] Q. Cheng, F.P. Agterberg and S.B. Ballantyne. The separation of geochemical anomalies from background by fractal methods. *Journal of Geochemical Exploration*, 51, 109-130, 1994.

[13] C. Li, T. Ma and J. Shi. Application of a fractal method relating concentrations and distances for separation of geochemical anomalies from background. *Journal of Geochemical Exploration*, 77, 167-175, 2003.

[14] R. Zuo. Identifying geochemical anomalies associated with Cu and Pb–Znskarn mineralization using principal component analysis and spectrum–area fractal modelling in the Gangdese Belt, Tibet (China). *J. Geochem. Explor*. 111, 13-22, 2011.

Proceedings of the 22nd UK Conference of the
Association for Computational Mechanics in Engineering
2 - 4 April 2014, University of Exeter, Exeter

A q-refinement procedure for radiative heat transfer in glass

***M. Shadi Mohamed[1], Mohammed Seaid[2], Jon Trevelyan[2] and Omar Laghrouche[1]**

[1]Institute for Infrastructure & Environment, Heriot Watt University, Edinburgh, EH14 4AS
[2]School of Engineering and Computing Sciences, University of Durham, Durham, DH1 3LE

*m.s.mohamed@hw.ac.uk

ABSTRACT

Numerical simulation of thermal radiation can be highly demanding in terms of computational resources especially when the transient nature of the problem has to be considered. In this work the partition-of-unity finite element method is implemented for solving the transient conduction-radiation problem in glass cooling. A *q*-refinement procedure is used to treat the radiation at different frequency bands. The procedure achieves a significant reduction of the computational costs on top of the reduction already achieved by the partition of unity method.

Key Words: *Finite element method; Partition of unity method; Radiative heat transfer; Glass cooling*

1. Introduction

The computational cost involved in considering thermal radiation is mainly caused by the wide spectrum of electromagnetic waves that are emitted from a thermally radiating material. The optical properties of a material define active frequency bands through which most of the heat energy radiates. The model describing the thermal radiation needs to be solved for each of these frequency bands in order to estimate the cumulative heat energy emitted through radiation. Furthermore, the radiation waves move at the speed of light whereas other heat transfer mechanisms happen at much slower time scales. Thus the radiation scale has an effect on the scale used in the solution of other coupled mechanisms. In this paper, we adopt the simplified P_1 approximation to the RHT problem. We consider glass cooling models with eight frequency bands kindly provided by ITWM [1]. In the current study, a newly developed approach [3] is used to solve the frequency-dependent RHT in glass cooling problems. A refined enrichment approach, to reduce the computational cost especially when a high number of frequency bands is needed, is presented. The performance of the proposed method is compared to the *h*-version FEM.

2. Theory

In the current study we consider the SP_1 approximation for the RHT equations [2]. By discretizating the optical spectrum of the glass into N frequency bands, the SP_1 model consists on solving for the glass temperature T and the radiative energy $\varphi^{(k)}$ for the kth band ($k = 1, 2, \ldots, N$) the following transient conduction-radation equations

$$\begin{aligned}
\frac{\partial T}{\partial t} - \nabla\cdot(k_c\nabla T) &= \sum_{k=1}^{N}\nabla\cdot\Big(\frac{1}{3\kappa_k}\nabla\varphi^{(k)}\Big), && (\mathbf{x},t)\in\Omega\times[0,t_{end}),\\
-\nabla\cdot\Big(\frac{\varepsilon^2}{3\kappa_k}\nabla\varphi^{(k)}\Big)+\kappa_k\varphi^{(k)} &= 4\pi\kappa_k B^{(k)}(T,n_{\mathrm{g}}), && (\mathbf{x},t)\in\Omega\times[0,t_{end}),\\
\varepsilon k_c\mathbf{n}(\hat{\mathbf{x}})\cdot\nabla T + h_c(T-T_b) &= \alpha\pi\Big(B^{(0)}(T_b,n_{\mathrm{b}})-B^{(0)}(T,n_{\mathrm{b}})\Big), && (\hat{\mathbf{x}},t)\in\partial\Omega\times[0,t_{end}),\\
\varphi^{(k)}+\left(\frac{1+3r_2}{1-2r_1}\frac{2\varepsilon}{3\kappa_k}\right)\mathbf{n}(\hat{\mathbf{x}})\cdot\nabla\varphi^{(k)} &= 4\pi B^{(k)}(T_b,n_{\mathrm{g}}), && (\hat{\mathbf{x}},t)\in\partial\Omega\times[0,t_{end}),\\
T(\mathbf{x},0) &= T_0(\mathbf{x}), && \mathbf{x}\in\Omega,
\end{aligned} \tag{1}$$

where $[0, t_{end})$ is the time interval, Ω the spatial domain with boundary $\partial\Omega$, k_c the thermal conductivity, κ_k the absorption coefficient, h_c is the convective heat transfer coefficient, T_b is a given ambient temperature

of the surrounding, $\mathbf{n}(\hat{\mathbf{x}})$ denotes the outward normal at $\hat{\mathbf{x}}$ with respect to $\partial\Omega$, ε is a diffusion scale, α is the mean hemispheric surface emissivity in the opaque spectral region $\nu \in [0, \nu_0]$, where radiation is completely absorbed, and n_{b} and n_{g} are the refractive indices of the surrounding medium and the glass material, respectively. In the above equations, $B^{(k)}(T, n)$ is the spectral intensity of the black-body radiation in the kth band $[\nu_{k-1}, \nu_k)$ given by the Planck function in a medium with refractive index n,

$$B^{(k)}(T, n) = \int_{\nu_{k-1}}^{\nu_k} B(T, \nu, n) d\nu, \qquad B(T, \nu, n) = \frac{2h_P \nu^3}{c_0^2} n^2 (e^{h_P \nu/\kappa_B T} - 1)^{-1}, \tag{2}$$

where h_P, κ_B and c_0 are Planck's constant, Boltzmann's constant and the speed of radiation propagation in the vacuum, respectively [2]. In (1), the integrals r_1 and r_2 are defined by

$$r_1 = \int_0^1 \mu\rho(-\mu) d\mu, \qquad r_2 = \int_0^1 \mu^2 \rho(-\mu) d\mu,$$

where ϱ is the reflectivity obtained according to the Fresnel and Snell laws. Note that the SP_1 approximation (1) consists to solve a system of $(N + 1)$ coupled semi-linear elliptic-parabolic equations.

Using a semi-implicit time stepping scheme, the procedure to advance the solution from the time t_n to the next time t_{n+1} can be carried out in the following two steps:

Step 1. Radiation stage: For $k = 1, 2, \ldots, N$, solve for $\varphi_{n+1}^{(k)}$

$$\begin{aligned} -\nabla \cdot \Big(\frac{\varepsilon^2}{3\kappa_k} \nabla \varphi_{n+1}^{(k)}\Big) + \kappa_k \varphi_{n+1}^{(k)} &= 4\pi\kappa_k B^{(k)}(T_n, n_{\mathrm{g}}), \\ \varphi_{n+1}^{(k)} + \left(\frac{1 + 3r_2}{1 - 2r_1} \frac{2\varepsilon}{3\kappa_k}\right) \mathbf{n}(\hat{\mathbf{x}}) \cdot \nabla \varphi_{n+1}^{(k)} &= 4\pi B^{(k)}(T_b, n_{\mathrm{g}}). \end{aligned} \tag{3}$$

Step 2. Conduction stage: Solve for T_{n+1}

$$\begin{aligned} \frac{T_{n+1} - T_n}{\Delta t} - \nabla \cdot (k_c \nabla T_{n+1}) &= \sum_{k=1}^{N} \nabla \cdot \Big(\frac{1}{3\kappa_k} \nabla \varphi_{n+1}^{(k)}\Big), \\ \varepsilon k_c \mathbf{n}(\hat{\mathbf{x}}) \cdot \nabla T_{n+1} + h_c (T_{n+1} - T_b) &= \alpha\pi \Big(B^{(0)}(T_b, n_{\mathrm{b}}) - B^{(0)}(T_n, n_{\mathrm{b}})\Big), \\ T^0(\mathbf{x}) &= T_0(\mathbf{x}). \end{aligned} \tag{4}$$

For the sake of simplicity we rewrite equations (3) and (4) in a compact form as

$$\begin{aligned} u - \nabla \cdot (\mathcal{E} \nabla u) &= F, \qquad \text{in} \quad \Omega, \\ u + \beta \mathbf{n}(\hat{\mathbf{x}}) \cdot \nabla u &= f, \qquad \text{on} \quad \partial\Omega, \end{aligned} \tag{5}$$

Note that in the solution procedure, only linear systems have to be solved at each time step to update the temperature T_{n+1} and the mean radiative intensities $\varphi_{n+1}^{(k)}$.

A weak variational form for the equations (5) can be reformulated as $\mathbf{a}(u, v) = \mathbf{b}(v), \forall v \in V$ where V is a Sobolev space, v a test function in V, $\mathbf{a}$ and $\mathbf{b}$ are bilinear and linear forms defined respectively, as

$$\mathbf{a}(u, v) = \int_\Omega \Big(\mathcal{E} \nabla v \cdot \nabla u + v\, u\Big) d\mathbf{x} + \oint_{\partial\Omega} \frac{\mathcal{E}}{\beta} v \Big(u - f\Big) d\hat{\mathbf{x}}, \qquad \mathbf{b}(v) = \int_\Omega v F d\mathbf{x}. \tag{6}$$

Let the domain Ω be partitioned into N_e non-overlapping sub-domains Ω^m, $m = 1, \ldots, N_e$. Using a conventional piecewise finite element space, the solution u on Ω^m is approximated as

$$u \simeq u_h^m = \sum_{p=1}^{\#\mathrm{vert}} \mathcal{N}_p u_p^m, \tag{7}$$

where $\mathcal{N}_p$ stands for the (P_1) Lagrangian polynomial and u_p are the nodal values of the used 3−node triangular elements. Approximation (7) requires the mesh size to be small enough to capture the variable field. This limitation is to be alleviated if a set of local enrichment functions are included [3]. In order to achieve better approximation properties than is allowed by the polynomial basis functions $\mathcal{N}_p$ we use the

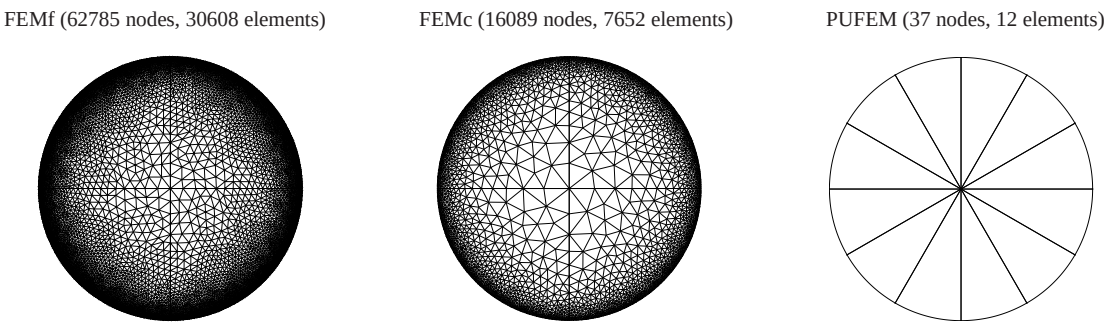

Figure 1: Comparison between FEM and PUFEM mesh grids.

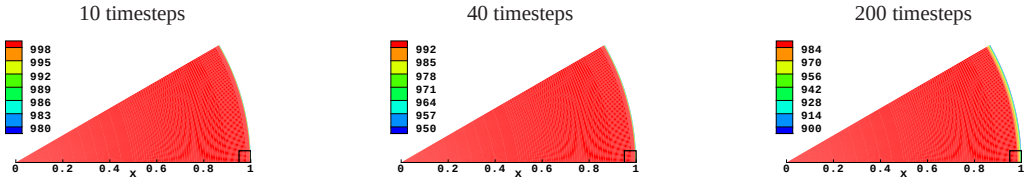

Figure 2: Temperature patterns obtained using the PUFEM at one element after different time steps.

partition of unity method to enrich the solution space with hyperbolic basis functions. It was found that for problems of steep boundary layers using enrichments with steep gradients can significantly improve the approximation of the finite element approach [3]. For example in a polygonal domain and for an edge e, at a position $x = x_e$, the enrichment functions may be written as

$$\overline{G}_{qe} = C_1 + C_2 \tanh\left(\frac{x - x_e}{h_q}\right), \qquad q = 1, 2, \ldots, Q, \tag{8}$$

where C_1 and C_2 are constants defining the amplitude of the enrichment jump while h_q is the parameter to control the steepness of the function $\overline{G}_{qe}$. More details about the choice of the enrichment functions can be found in [3]. The enrichment functions G_q are used within the partition of unity framework to express the nodal values u_p at any time $t = t_n$ and the solution u_h^n identified in expression (7) can be rewritten as

$$u_h^n = \sum_{p=1}^{\#\text{vert}} \sum_{q=1}^{Q} A_p^{q,n} \mathcal{N}_p G_q. \tag{9}$$

Here the element number m is dropped for ease of notation. Thus the new unknowns to be computed by solving the finite element resulting linear system are $A_p^{q,n}$, for $q = 1, 2, \ldots Q$, which may be defined as the contribution of each enrichment function G_q to the nodal value u_p^n at the node p.

3. Numerical results

We check the performance of the proposed PUFEM for glass cooling at ambient temperature 300 K of a disc enclosure with unit radius at initial temperature 1000 K. In all our simulations, eight frequency bands are used for the optical glass spectrum and the diffusion scale $\varepsilon = 1$ is considered. The material properties along with the absorption coefficient can be found in [2]. For the FEM simulations we consider two meshes (a coarse mesh referred to as FEMc and a fine mesh referred to as FEMf) which are presented in Figure 1. In this figure we also include the mesh used in our simulations using the PUFEM. We emphasize the extremely low number of elements and nodes listed in Figure 1 for the PUFEM mesh compared to both the coarse and fine FEM meshes. We present the numerical simulations using the PUFEM with q-refinement. The number of hyperbolic functions used to enrich the PUFEM solution space for solving the energy equation is $Q = 7$. To solve the radiation equations for the mean intensities $\varphi^{(k)}$, with $k = 1, 2, \ldots, 8$, the number of enrichment functions is $Q = 6$ for $\varphi^{(1)}$, $\varphi^{(2)}$ and $\varphi^{(3)}$, whereas $Q = 5$ for $\varphi^{(4)}$ and $\varphi^{(5)}$. This number is reduced to $Q = 4$ for $\varphi^{(6)}$ and $Q = 3$ for $\varphi^{(7)}$ and $\varphi^{(8)}$. Note that due to the global nature of the enrichment, the saving in the computational cost is proportional to the saving in the number of enrichments since the total number of degrees of freedom equals the number of nodes multiplied by the number of enrichments. Thus, almost half of the computational cost

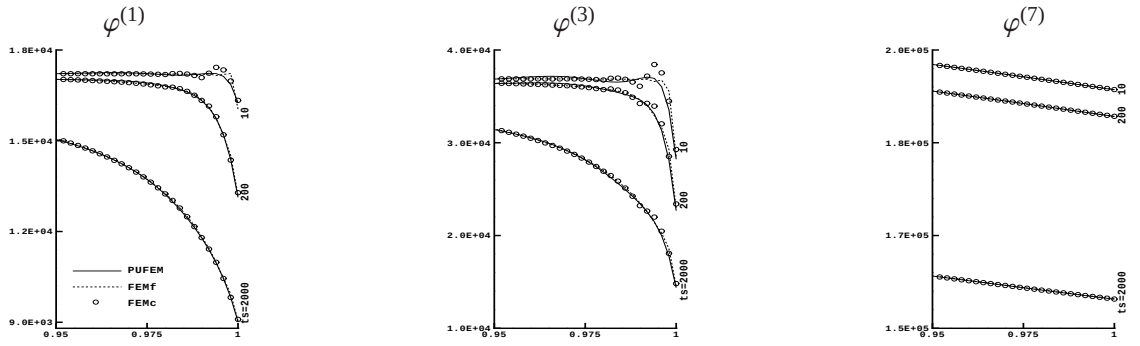

Figure 3: Mean radiative intensities by FEMc, FEMf and PUFEM at 3 instants after 10, 200 and 2000 time steps.

in solving the radiation equation is saved when this refinement strategy is used compared to using a fixed number of enrichments $Q = 7$. In Figure 2 we present snapshots of the temperature as recovered by the PUFEM on one element after 10, 40 and 200 time steps. It can be seen that, at early simulation times, the domain temperature remains uniform except at the boundary layer. The computed results for this test example demonstrate a more stable behavior with the PUFEM compared to FEMc and FEMf. Note that this accuracy in the PUFEM is achieved despite the fact that the total number of degrees of freedom for the PUFEM is only around 1% of that for FEMc. To further examine the performance of the PUFEM we present in Figure 3 the radial cross-sections for the mean radiative intensities for three selected frequency bands after 10, 200 and 2000 time steps where the results obtained for other bands exhibit similar behavior but with different amplitudes. The mean radiative intensities $\varphi^{(2)}$ and $\varphi^{(3)}$ develop steeper gradients than those associated with other frequency bands. Spurious oscillations with different amplitudes are more pronounced in the FEMc results for the first three frequency bands after 10 and 200 time steps than in the PUFEM results. It should also be pointed out that the largest mean radiative intensity is calculated for the frequency band $\varphi^{(7)}$ which dominate the other solutions in the remaining frequency bands. As a consequence, the smooth boundary layers in $\varphi^{(7)}$ may introduce stabilizing effects in the considered radiative heat transfer problem. As mentioned earlier, the pattern described above when refining the enrichment can be seen in Figure 3 in the steeper gradient associated with the temperature as well as the mean radiative intensities $\varphi^{(1)}$, $\varphi^{(2)}$ and $\varphi^{(3)}$. A relatively flat gradient can be seen in the intensities $\varphi^{(7)}$ and $\varphi^{(8)}$. The PUFEM performs very satisfactorily for this frequency-dependent coupled problem since it does not diffuse the moving fronts and no spurious oscillations have been detected near steep gradients of the temperature field and radiative intensities in the computational domain.

4. Conclusions

A *q*-refinement finite element method for radiative heat transfer in glass cooling is presented. Requiring only a small fraction of the number of degrees of freedom required in the conventional FEM, the proposed method shows better stability compared to that observed in the FEM. Indeed, because the main challenge in most glass cooling applications is related to the steep gradients at the boundary layers, it is found that adding steep gradient enrichments circumvent any need to mesh refinement. Other than these steep gradient the solution can be very trivial and can be recovered with a very coarse finite element mesh. Numerical simulations are performed for the glass cooling of a disc enclosure using a eight frequency-dependent media. The presented results demonstrate the capability of the *q*-refinement finite element method that can provide insight into complex radiative heat transfer problems.

References

[1] ITWM. *Fraunhofer-Institut für Techno- und Wirtschaftsmathematik, Kaiserslautern, Germany*. http://www.itwm.de.

[2] E. Larsen, G. Thömmes, A. Klar, M. Seaid, and T. Götz. Simplified P_N approximations to the equations of radiative heat transfer and applications. *J. Comp. Phys.*, 183:652–675, 2002.

[3] M.S. Mohamed, M. Seaid, J. Trevelyan, and O. Laghrouche. Time-independent hybrid enrichment for finite element solution of transient conduction-radiation in diffusive grey media. *J. Comp. Phys.*, 251:81–101, 2013.

Proceedings of the 22nd UK Conference of the
Association for Computational Mechanics in Engineering
2 - 4 April 2014, University of Exeter, Exeter

A REVIEW OF THE MATERIAL POINT METHOD AND ITS LINKS TO OTHER COMPUTATIONAL METHODS

***T.J. Charlton, W.M. Coombs and C.E. Augarde**

Mechanics Research Group, School of Engineering & Computing Sciences, Durham University, South Road, Durham , DH1 3LE, UK

*t.j.charlton@durham.ac.uk

ABSTRACT

There is considerable interest in development of solid mechanics modelling which can cope with both material and geometric nonlinearity, particularly in areas such as computational geotechnics, for applications such as slope failure and foundation installation. One such technique is the Material Point Method (MPM), which appears to provide an efficient way to model these problems. The MPM models a problem domain using particles at which state variables are kept and tracked. The particles have no restriction on movement, unlike in the Finite Element Method (FEM) where element distortion limits the level of mesh deformation. In the MPM, calculations are carried out on a regular background grid to which state variables are mapped from the particles. It is clear, however, that the MPM is actually closely related to existing techniques, such as ALE and in this paper we review the MPM for solid mechanics and demonstrate these links.

Key Words: *Material Point Method; Solid Mechanics; Mesh Free; Finite Deformation Mechanics*

1. Introduction

Most computational methods in solid mechanics can be described as either Eulerian or Lagrangian. Lagrangian methods work by splitting a problem into elements or particles in a mesh, and throughout any deformation this mesh follows the problem domain. The advantage of this is that it is easy to track surfaces and history dependant variables throughout a simulation as the position in relation to other elements is always maintained. A disadvantage of a Lagrangian approach is that problems can begin to occur when a material undergoes large deformations. These large deformations can result in a heavily distorted mesh which, in certain situations, can result in calculations being unable to be completed. Eulerian methods work by having a mesh that is fixed in space and allowing particles to move within it. This is more commonly used in fluid mechanics applications but overcomes any issue of mesh distortion as the mesh remains the same throughout calculations. A disadvantage is that it becomes more difficult to track boundaries and history dependent variables as particles move. Attempts have been made to combine together Eulerian and Lagrangian methods with the aim of keeping the positives without the drawbacks. One method to combine these features is the Material Point Method (MPM) [1]. There are currently many uses of the MPM, often in situations where the FEM struggles due to highly distorted elements. Some uses currently of interest include problems involving impact and collision, penetration, crack propagation, slope stability, soil mechanics and simulation of snow for use in animation. In this paper we will review the MPM and highlight links to other techniques such as the Finite Element (FE) and Arbitrary Lagrangian Eulerian (ALE) methods.

2. Method overview

The Material Point Method (MPM) was first developed by Sulsky et al. [1] as an extension for solid mechanics of the FLuid Implicit Particle (FLIP) [2] method, which itself was an extension to the Particle in Cell (PIC) [3] method used in fluid dynamics. The MPM can be referred to as a meshfree method.

Although a background grid of connected nodes is required to perform calculations, material properties are carried by a series of particles which are free to move independently of each other. In the MPM, material points, known as particles, store state variables and move through a background grid or mesh which can be changed or reset following each time step or load increment. This can be seen in Figure 1 where a material has been deformed and the mesh has been reset with particles in updated positions.

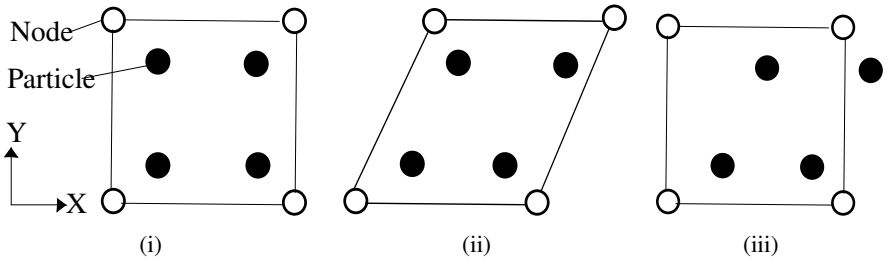

Figure 1: Particle positions as mesh deforms and is reset: (i) original configuration, (ii) deformed mesh and (iii) reset mesh

Initially a material domain is split into a number of elements similar to the FEM. Each of these elements is then populated with a number of material points. Each material point is assigned a weight based on the volume of material that the particle represents. It can be desirable to initially locate particles at Gauss quadrature points to simplify the volume weight calculation. In addition to the mesh covering the material's initial position, the mesh must extend to where the material is expected to deform.

In each element containing particles, the state variables must be mapped from the particles to the grid nodes. This mapping process is carried out within each element using shape functions similar to those used in the FEM. For instance the external force at a grid node is given by

$$\{f_g^{ext}\} = \sum_{i=1}^{n_p} \{N(\xi_i, \eta_i)\} f_{p_i}^{ext} \tag{1}$$

where f_p^{ext} is the particle external force, $\{N(\xi_i, \eta_i)\}$ are the nodal shape functions for the element containing the particle with local coordinates ξ and η and n_p refers to the number of material points in the grid element.

To be able to map to the correct grid nodes it is necessary to know in which element each material point located at a point in time. Although trivial initially, after particles have moved this problem can become more complex, especially if the mesh is not uniform. To simplify this process it is common to reset the background mesh to a uniform grid after each loadstep.

The stiffness of each element is determined from the contributions from each of the particles currently inside. Once the global stiffness matrix is assembled and the grid node displacements determined, the grid node displacements $\{u_g\}$ are then mapped back to particles to get particle displacements $\{u_p\}$ through

$$\{u_p\} = \sum_{i=1}^{n_g} N_i \{u_{g_i}\}, \tag{2}$$

where n_g is the number of element nodes. The particle positions are then updated. The grid node displacements are not used to update the position of nodes in the mesh; the original undeformed mesh is used.

3. Comparison with FEM

The MPM has many similarities with the standard FEM, in fact it is possible to think of the MPM as the same as the FEM but with moving integration points instead of fixed Gauss points in each element. The shape functions used to map between the grid and the particles in the MPM are the same as the shape functions used in the FEM. If material points are located at the positions of Gauss points in the FEM and if the mesh is not reset after each step then the MPM becomes identical to the FEM. In the MPM,

external forces can be applied directly to the grid nodes or can be applied at particles and mapped to the grid, however to do this particles must be placed where forces are applied.

Boundary conditions are applied directly to the background mesh as in the FEM. This works for fixed boundaries with zero displacement conditions however to track boundaries it is necessary for some particle positions to coincide with material boundaries. Currently it is difficult to do this.

As the particles move it is possible that the background element they are in changes. One of the main problems with the MPM is an error which occurs when material points cross element boundaries causing an imbalance of internal forces [4]. In the MPM, if an element becomes void of particles it is turned off so that it no longer contributes to the global stiffness matrix.

Due to the background nodal relationships the MPM is not as computationally expensive as some meshless methods. However, as there is an additional mapping step, it is more expensive than the standard FEM.

4. Comparison with Arbitrary Lagrangian-Eulerian methods

Arbitrary Lagrangian Eulerian (ALE) Methods [5], like the MPM, take advantage of useful aspects of both types of method while trying to avoid disadvantages. In ALE methods a mesh is allowed to move independently of the material moving in an arbitrary manner that can be defined by the user. This is achieved by having a third set of coordinates (the so-called reference coordinates) other than the initial and current configurations, this allows the mesh to be adapted to avoid problems caused by mesh distortions in a purely Lagrangian method. In the MPM the grid can be adapted in a similar manner if desired however it is usual to reset the grid to an undeformed uniform state as this removes the additional expense of particle searching.

5. Comparison with Smoothed Particle Hydrodynamics

Smoothed particle hydrodynamics (SPH) [6] is a Lagrangian meshfree method, where the domain is represented by a set of distributed particles needing no connectivity, rather than split up into a set of nodes in a grid. Like the MPM, each particle possesses a set of material properties and moves according to governing equations. However SPH doesn't have a background grid where calculations take place. Instead, field functions at these points are approximated using a kernel function. These approximations are then smoothed using a weighted average over neighbouring particles. Having no background grid, shape functions cannot be used in the same way as in FEM and MPM. To calculate the support and influence domains of a particle a weighting function is used. This is common to most meshfree methods.

A particular advantage of SPH is its ability to handle large deformations. This is due to the fact that particles aren't restrained to a mesh. However it is not as straightforward to apply boundary conditions when using SPH for solid mechanics. The need to search for a nearest neighbour to define nodal connectivity can also make SPH more computationally expensive than the standard MPM.

6. Numerical example

Due to the similarities between the FEM and the MPM, a compact finite element code has been used as the basis for a MPM code [7]. Material points, which originally were located at Gauss points are freed to move after each load step and then the mesh is reset to its original configuration. Because of these similarities between methods, the constitutive model used in the FEM can also be used in the MPM. A Total Lagrangian FEM code has been modified to facilitate movement of material points, however problems have been noted when material points cross grid element boundaries. As mentioned above, this is a common issue highlighted in the literature.

The code was used for the simple problem of one-dimensional compression of a $1\times1\times1m$ cube, as shown in Figure 2(i). A Young's modulus $E = 1\times10^9 Pa$ and Poissons ratio of $\nu = 0.2$ were used with downward forces totalling $5\times10^9 N$ applied to the four uppermost particles over 10 loadsteps. The particle positions within two elements in the Z direction throughout the simulation are shown in Figure 2(ii). It can be seen that a problem arises when the uppermost particles displace into the lower element. When this happens the internal force calculations result in a displacement back into the previous element for some of the particles. This is repeated over the following loadsteps resulting in a oscillation of particles between two elements.

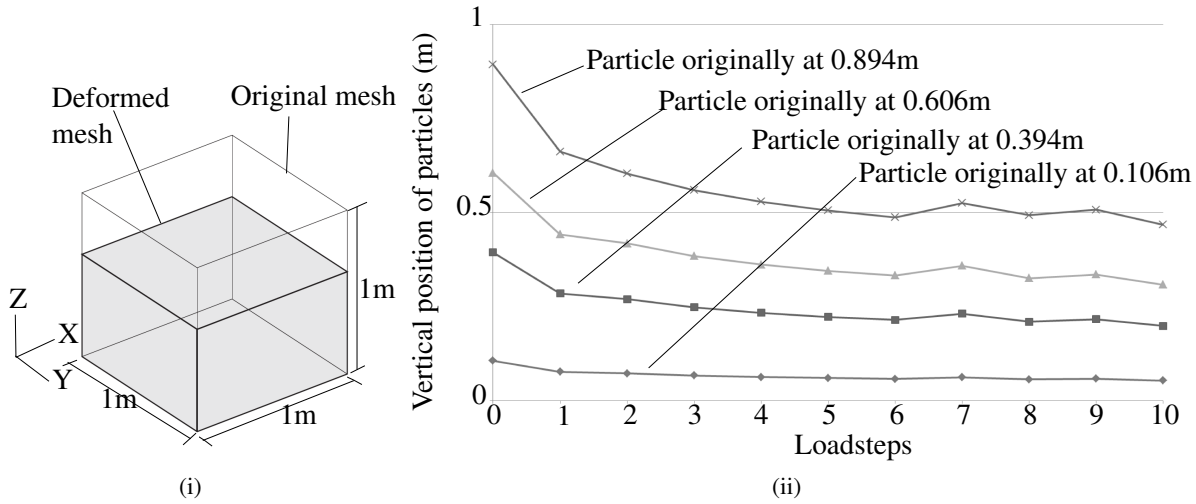

Figure 2: One dimensional compression of a unit cube: (i) Original and deformed mesh. (ii) Position of particles within 2 elements over the period of 10 loadsteps.

One method that addresses the problem that occurs when particles cross element boundaries is the GIMP method where characteristic functions are assigned to particles which give particles a support area so that a particle can affect nodes in cells other than the one where the particle is located. The computational expense of GIMP is larger than that of standard MPM however it provides improved accuracy stability and robustness to simulations [8]. This is the next step in this work.

7. Conclusions and future work

From the work undertaken so far, the MPM appears to a promising technique for dealing with large deformations, that can be simply achieved by altering an existing FE code. A MPM code is being developed using an Updated Lagrangian approach so that calculations are not affected by a stiffness that was calculated when material points were in different positions. It is hoped that in the future a GIMP type method can be implemented to address the boundary crossing problem encountered, and to then use the MPM code for more complex problems involving large deformations.

References

[1] D. Sulsky, Z. Chen, and H. Schreyer, "A particle method for history-dependent materials," *Computer Methods in Applied Mechanics and Engineering*, vol. 118, pp. 179 – 196, 1994.

[2] J. Brackbill and H. Ruppel, "Flip: A method for adaptively zoned, particle-in-cell calculations of fluid flows in two dimensions," *Journal of Computational Physics*, vol. 65, no. 2, pp. 314 – 343, 1986.

[3] M. W. Evans, F. H. Harlow, and E. Bromberg, "The particle-in-cell method for hydrodynamic calculations," DTIC Document, Tech. Rep., 1957.

[4] M. Steffen, R. M. Kirby, and M. Berzins, "Analysis and reduction of quadrature errors in the material point method (mpm)," *International Journal for Numerical Methods in Engineering*, vol. 76, no. 6, pp. 922–948, 2008.

[5] J. Donea, A. Huerta, J.-P. Ponthot, and A. Rodrguez-Ferran, *Arbitrary Lagrangian Eulerian Methods*. John Wiley & Sons, Ltd, 2004.

[6] L. B. Lucy, "A numerical approach to the testing of the fission hypothesis," *The Astronomical Journal*, vol. 82, pp. 1013–1024, 1977.

[7] W. Coombs, R. Crouch, and C. Augarde, "70-line 3d finite deformation elastoplastic finite-element code," in *Numerical Methods in Geotechnical Engineering*. CRC Press, Jun. 2010, pp. 151–156.

[8] S. Bardenhagen and E. Kober, "The generalized interpolation material point method," *Computer Modeling in Engineering and Sciences*, vol. 5, no. 6, pp. 477–496, 2004.

Proceedings of the 22nd UK Conference of the
Association for Computational Mechanics in Engineering
2 - 4 April 2014, University of Exeter, Exeter

A three-dimensional implementation of the boundary element and level set based structural optimisation

***B. Ullah, J. Trevelyan and I. Ivrissimtzis**

School of Engineering and Computing Sciences, Durham University, South Road,
Durham, DH1 3LE, UK.

*baseer.ullah@durham.ac.uk

ABSTRACT

This paper presents a three-dimensional evolutionary structural optimisation approach based on the boundary element and level set methods. The level set method (LSM) is used to provide an implicit description of the structural geometry. The boundary movements in 3D LSM allow automatic hole nucleation by the intersection of two surfaces moving towards each other. This eliminates the need of an additional hole nucleation mechanism as required by the 2D LSM based optimisation methods. A complete algorithm is proposed and tested for boundary element method (BEM) and LSM based structural optimisation in three-dimensions. Optimal geometries obtained compare well against those in the literature for a range of benchmark examples.

Key Words: *level set method; boundary element method; structural optimisation*

1. Introduction

Structural optimisation is considered one of the most important and challenging fields in engineering optimisation. Structural optimisation arranges the assembly of structural elements for sustaining the applied load in the most efficient manner. Numerous methods have been developed over the last decades describing various numerical techniques to generate structures that are optimal in terms of quantities such as weight, cost and stiffness. The LSM is an efficient numerical technique developed by Osher and Sethian [1] for the tracking of propagating interfaces. The LSM uses the Eulerian approach to represent an evolving geometry implicitly. In the implicit representation, the connectivity of the discretisation does not need to be determined explicitly. This is one of the most interesting features of the implicit geometric representation, in that merging and breaking of curves in 2D and surfaces in 3D can be handled automatically. Sethian and Wiegmann [2] first presented an LSM based structural optimisation method for the solution of two-dimensional problems. Since this first paper, numerous LSM based topology optimisation techniques have been proposed for different engineering applications.

This paper presents a three-dimensional structural optimisation method based on the boundary element and level set methods. The proposed method uses the 3D version of the BEM analysis software (3D concept analyst [3]) developed at Durham University. In Section 2 of this paper we present the details of the optimisation algorithm and its implementation. The results obtained from the proposed algorithm are presented and discussed in Section 3, and the paper closes with some concluding remarks in Section 4.

2. Optimisation algorithm

The 3D optimisation algorithm proposed in this study is an extension of the 2D approach presented in [4]. During the optimisation process, the structural geometry evolves into an optimal topology through the progressive removal of inefficient material from the low stressed regions and addition to the high stressed regions. The performance of the optimisation process is monitored through the specific strain energy f_U and the target volume fraction is used as a stopping criterion.

$$f_U = UV \tag{1}$$

The expression used for the strain energy calculation is,

$$U = \int_{\Gamma} \frac{1}{2} t_i u_i d\Gamma \tag{2}$$

where t and u represent traction and displacement, respectively. In practice, since the product $t_i u_i$ is non-zero only over elements on which a non zero traction boundary condition has been prescribed (assuming there are no non-zero displacement constraints applied) the integral involved in Equation (2) conveniently reduces to the integral taken only over these elements. The proposed optimisation algorithm is summarised as follows:

1. Define structural geometry with applied loads and constraints.
2. Initialize level set grid with signed distance function to represent structural geometry implicitly.
3. Trace the zero level set contours.
4. Perform mesh postprocessing and improvement.
5. Carry out boundary element analysis.
6. Calculate the von Mises stress σ_V at each node point of the boundary.
7. Convert σ_V into velocity using the relationship developed in [4].
8. Extend boundary velocities to level set grid points in the narrow band.
9. Solve Equation (3) to update the level set function

$$\frac{\partial \phi}{\partial t} + F|\nabla \phi| = 0 \tag{3}$$

10. Repeat the above procedure from step 3 to 9, until the stopping criterion is satisfied.

Most of the above steps are based on the simple extension of the steps followed in the 2D approach which is discussed in detail in [4]. However, the extraction of the zero level set contours is different than that used in the 2D approach. In 3D LSM , the zero level set contours can be extracted from the cubic cell based level set grid with the marching cubes (MC) algorithm. The MC is a popular algorithm for extracting iso-surface from implicit functions in the form of triangular mesh. A 3D structure can be analysed with the BEM by first discretising its boundary into either triangular or quadrilateral elements. This is then followed by the solution of the equilibrium equations and the calculation of the required properties at the nodal points. In the proposed 3D optimisation method, at each iteration the modified structural geometry is extracted in the form of a triangular mesh and this can be directly used for the BE analysis. However, mesh postprocessing may be required to make it consistent with the BE analysis requirements. Moreover, during the optimisation process, the structural geometry is continuously modified and this may result into some low quality triangular elements which can affect the accuracy of the BE solution. Therefore, in the current implementation, a mesh improvement step is used to improve the quality of elements.

3. Numerical Example

In order to validate the proposed optimisation method, a short cantilever beam has been considered with dimensions, $L = 24$, $W = 8$ and $H = 48$. The geometry of the structure shown in Figure 1 is constrained at the top and bottom portions of the left face, and a load $P = 1.2$KN is applied at the middle of the right face. The level set design domain is discretised into $12 \times 4 \times 24$ cubic cells with edge length $d = 2$. The target volume fraction used in this example is $0.30V_0$. The material properties used are: Poisson's ratio = 0.3, Young's modulus = 210 GPa, Yield stress = 280 MPa.

In this example, the maximum von Mises stress in the initial design, i.e. $\sigma_{Vmax} = 178$ MPa, is used as reference stress for the solution of the optimisation problem. The evolution of the structural geometry during the optimisation process is depicted in Figure 2. It can be seen that during the initial iterations the structural geometry evolves through boundary movements caused by the incremental removal of inefficient material from the low stressed regions of the structure. The optimal design obtained closely resembles that obtained in [5].

Figure 3 shows the von Mises stress distribution in the initial and optimal designs. There are 1724 six-noded triangular elements in the initial and 1200 in the optimal design. Comparison of these plots shows that the stress contours are more uniform in the optimal design than the initial design. This indicates that the optimisation method efficiently redistributes material within the design domain and results in an optimal which is approaching towards a fully stressed design. Figure 4 shows the evolution of f_U during the optimisation process.

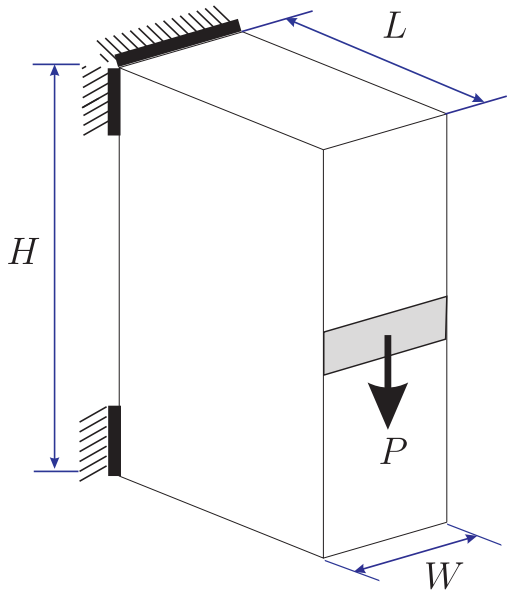

Figure 1: Design domain, loading and boundary conditions

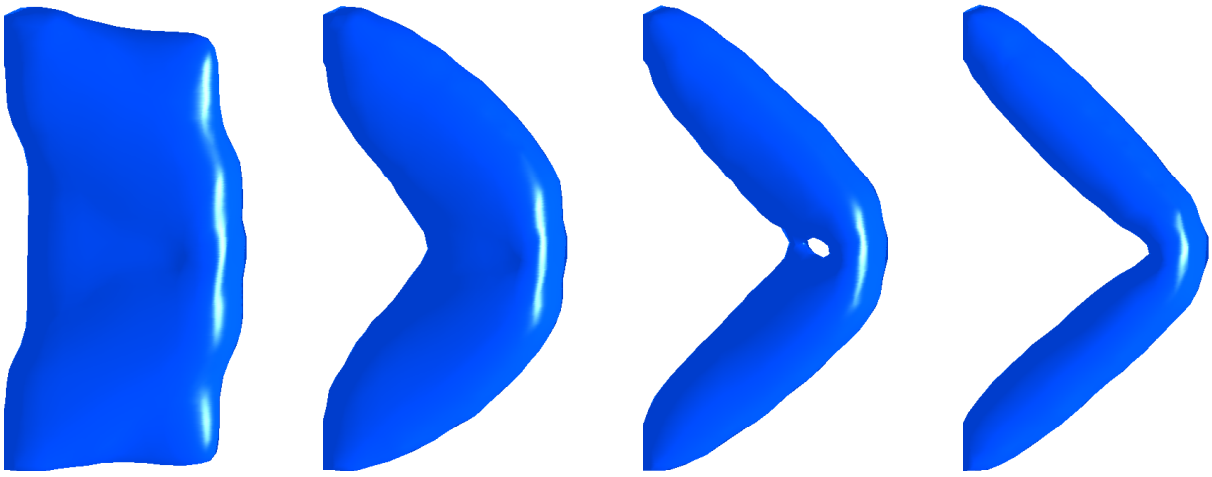

(a) Iteration 2 ($0.77V_0$) (b) Iteration 10 ($0.52V_0$) (c) Iteration 24 ($0.39V_0$) (d) Iteration 37 ($0.30V_0$)

Figure 2: Evolution of structural geometry

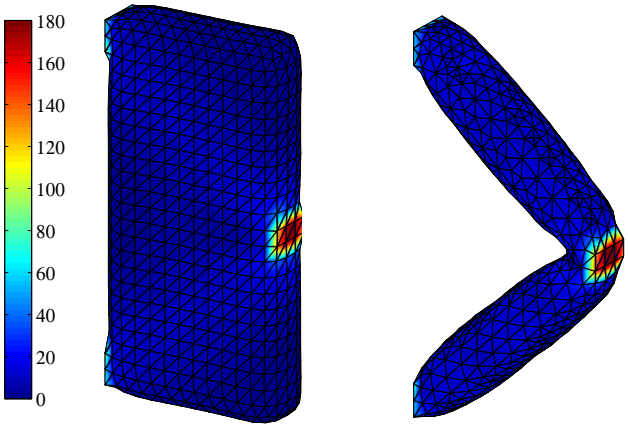

(a) Initial design (b) Optimal design

Figure 3: von Mises stress contours of initial and final optimal geometry

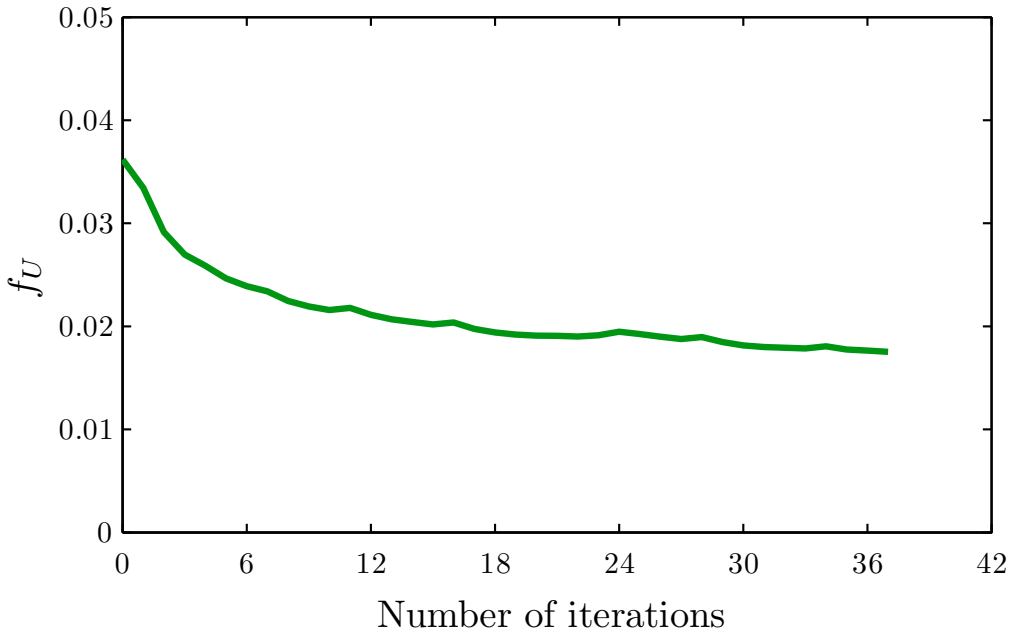

Figure 4: Evolution of f_U

4. Conclusions

A 3D LSM based structural optimisation method has been successfully implemented for this study. During the optimisation process, the structural geometry evolves into an optimal design through the progressive removal of inefficient material from the low stressed regions and addition to the high stressed regions of the structure. This evolutionary approach is integrated with the boundary element and level set methods. The BEM is used to analyze the modified structural geometry at each iteration. During the optimisation iterations, the MC algorithm extracts the new zero level set contours in the form of a triangular mesh. As the BEM is based on a boundary discretisation approach; the extracted geometry can be directly used to analyse the modified geometry. In order to validate the proposed optimisation method, different benchmark examples are considered in this study. Each example is solved with different stress criteria, and similar optimal designs are obtained for each case. The optimal designs obtained for each example closely resemble the optima published within the field of structural optimisation.

Acknowledgements

The first author acknowledges with thanks the financial support through the Durham Doctoral Studentship scheme of Durham University.

References

[1] S. Osher and J. Sethian, Front propagating with curvature-dependent speed: algorithms based on Hamilton-Jacobi formulations, *Journal of Computational Physics*, 79(1), (1988), 12–49.

[2] J. Sethian and A. Wiegmann, Structural boundary design via level set and immersed interface methods, *Journal of Computational Physics*, 163(2), (2000), 489–528.

[3] T.M. Foster, M.S. Mohamed, J. Trevelyan, and G. Coates. Rapid re-meshing and re-solution of three-dimensional boundary element problems for interactive stress analysis. *Engineering Analysis with Boundary Elements*, 36(9), 1331–1343, 2012.

[4] B. Ullah and J. Trevelyan. Correlation between hole insertion criteria in a boundary element and level set based topology optimisation method. *Engineering Analysis with Boundary Elements*, 37(11),1457–1470, 2013.

[5] J. Céa, S. Garreau, P. Guillaume, and M. Masmoudi. The shape and topological optimizations connection. *Computer Methods in Applied Mechanics and Engineering*, 188(4), 713–726, 2000.

Proceedings of the 22nd UK Conference of the
Association for Computational Mechanics in Engineering
2 - 4 April 2014, University of Exeter, Exeter

Energy-momentum Method for Beam Dynamics

***Tien Long Nguyen[1], Carlo Sansour[2] and Mohammed Hjaij[1]**

[1]Department of Civil Engineering, Insitut National des Sciences Appliquees de Rennes, France
[2]Faculty of Engineering, University of Nottingham, UK

*tien-long.nguyen@insa-rennes.fr

ABSTRACT

Non-linear rod dynamics is of great interest in many areas of engineering. It is relevant in structural engineering but also in the aerospace industry, flexible robot dynamics, impact modelling etc. In recent years the focus of research was directed towards Timoshenko-type rod theories were shearing is of importance. Rod degrees of freedom are then the displacement field as well as a rotational field which describes the independent rotation of the cross section. However, the algorithmic and numerical treatment of rotations is not a straightforward task. Specifically for a general model of mechanisms and spatial deformations it is desirable to have a displacement-only formulation which brings us back to the classical Bernoulli beam. While it is well established in linear analysis, the Bernoulli beam is not as common in geometrically exact models of dynamics, especially when it comes to incorporate the rotational inertia into the model. Also the development of stable energy-momentum integration schemes for the same has been considered as rather difficult in comparison to a Timoshenko-type model. This paper is about the development of an energy-momentum integration scheme for the geometrically exact Bernoulli method. We will show that the task is achievable and device a general framework to do so. Further important feature of the model is the full incorporation of the rotational inertia term. Different applications stretching from applications in structural rod dynamics to flexible multibody dynamics and finally impact modelling, will demonstrate the strength of the approach and the excellent performance of the new integration scheme.

Key Words: *non-linear dynamics; finite strain; energy-momentum method; multi-body dynamics*

1. Kinematics, dynamics equation and finite discretisation

Let $\mathcal{B} \subset \mathbb{R}^3$, with $\mathbb{R}$ denoting the real numbers, define a reference configuration of the body. Without loss of generality we want to identify the reference configuration with the body itself. The actual configuration is denoted by $\mathcal{B}_t \subset \mathbb{R}^3$. We assume that our body is thin in two dimensions such that it is rod-like with a cross section A at the reference configuration. The material particles are identified by their position vectors $\boldsymbol{X} \in \mathcal{B}$, the corresponding placement at the actual configuration by $\boldsymbol{x} \in \mathcal{B}_t$. A deformation is a map $\boldsymbol{x} = \boldsymbol{\varphi}(\boldsymbol{X})$, the gradient of which defines the deformation gradient $\boldsymbol{F} = \partial \boldsymbol{x}/\partial \boldsymbol{X}$.We want to restrict ourselves to plane deformations and assume that the deformation lies in the $\boldsymbol{e}_1 - \boldsymbol{e}_2$ plane. For any material point in the cross section a suitable curvilinear coordinate system which we consider to be convected, is then given by the triple s, z, x_3. z is the coordinate in the direction of the normal vector in the cross section. To derive the rod theory we adopt the Bernoulli hypothesis which assumes rigid cross sections and that the deformation can be completely characterized by the assumption

$$\boldsymbol{x} = \boldsymbol{X}(s) - z\boldsymbol{N}(s) + \boldsymbol{u}(s) + z\boldsymbol{n}(s) = \boldsymbol{X}_0(s) + \boldsymbol{u}(s) + z\boldsymbol{n}(s), \tag{1}$$

where $\boldsymbol{X}_0 = \boldsymbol{X}_0(s) + z\boldsymbol{N}(s)$ is the the placement of the centre line at the reference configuration, $\boldsymbol{N}$ and $\boldsymbol{n}$ are the normal vectors in the reference configuration and deformed configuration respectively, $\boldsymbol{u}(s)$ is the displacement at the curvilinear coordinate s. In the context of a in-plane Bernouilli beam, the right Cauchy deformation tensor has only one single non-trivial component which is C_{11} which reads

$$C_{11} = (\boldsymbol{X}_{,s} - z\boldsymbol{N}_{,s} + \boldsymbol{u}_{,s} + z\boldsymbol{n}_{,s}) \cdot (\boldsymbol{X}_{,s} - z\boldsymbol{N}_{,s} + \boldsymbol{u}_{,s} + z\boldsymbol{n}_{,s}), \tag{2}$$

where $(\cdot)$ denotes the scalar product of vectors, a comma denotes a derivative. The expression of $\boldsymbol{n}$ holds $\boldsymbol{n} = \boldsymbol{e}_3 \times \frac{\boldsymbol{X}_{0,s}+\boldsymbol{u}_{,s}}{|\boldsymbol{X}_{0,s}+\boldsymbol{u}_{,s}|}$, where $\times$ denotes the cross product of vectors. With $\boldsymbol{E} = \frac{1}{2}(\boldsymbol{C} - \boldsymbol{1})$ as the Green strain tensor, one is then left with one sigle non-trivial component E_{11} which is given by (the term in z^2 can be neglected since our thickness of the beam is small compared to its length)

$$E_{11} = \boldsymbol{u}_{,s} \cdot \boldsymbol{X}_{0,s} + \frac{1}{2}\boldsymbol{u}_{,s} \cdot \boldsymbol{u}_{,s} + z\left(\boldsymbol{n}_{,s} \cdot (\boldsymbol{X}_{0,s} + \boldsymbol{u}_{,s}) - \boldsymbol{N}_{,s} \cdot \boldsymbol{X}_{0,s}\right). \tag{3}$$

By defining ε_{11} as the axial strain, κ as the change of curvature, their expressions reads

$$\varepsilon_{11} = \boldsymbol{u}_{,s} \cdot \boldsymbol{X}_{0,s} + \frac{1}{2}\boldsymbol{u}_{,s} \cdot \boldsymbol{u}_{,s}, \tag{4}$$

$$\kappa = \boldsymbol{n}_{,s} \cdot (\boldsymbol{X}_{0,s} + \boldsymbol{u}_{,s}) - \boldsymbol{N}_{,s} \cdot \boldsymbol{X}_{0,s}. \tag{5}$$

Starting from Hamilton Principle for our conservative mechanical system, the dynamics equation for our beam is written down as follows

$$\begin{aligned} &\int_L \rho A\ddot{\boldsymbol{u}} \cdot \delta\boldsymbol{u}\, ds\, dt + \int_L \rho I\ddot{\boldsymbol{n}} \cdot \delta\boldsymbol{n}\, ds + \int_L (EA\varepsilon_{11}\delta\varepsilon_{11} + EI\kappa\delta\kappa)\, ds \\ &- \int_L \boldsymbol{q}(s) \cdot \delta\boldsymbol{u}(s)\, ds - \sum_{i=1}^{N} \boldsymbol{P}_i \cdot \delta\boldsymbol{u}_i - \sum_{j=1}^{M} M_{3j}\delta\theta_j = 0, \end{aligned} \tag{6}$$

where E is Young's Modulus of the material, V is the volume of the system, $\boldsymbol{q}(s)$ is distributed external force, $\boldsymbol{P}_i, i = 1, N$ and $\boldsymbol{u}_i$ are the concentrated force and the corresponding displacement respectively, $M_{3j}, j = 1, M$ and θ_j are concentrated external moments and the corresponding rotation angle respectively, I is the moment of inertia of the section and L is the length of the beam, ρ is the material density. In this present paper cubic Hermite polynomials are used as interpolation functions because it ensures the continuity of the first derivative. A 2D beam element having two nodes is considered and each node has four degrees of freedom which correspond to the displacements ($\boldsymbol{u}_1$,$\boldsymbol{u}_2$) and its derivatives ($\boldsymbol{u}'_1$,$\boldsymbol{u}'_2$) in two directions $\boldsymbol{e}_1$ and $\boldsymbol{e}_2$.

2. Energy-momentum time integration scheme

After the spatial discretisation via the finite element method, the numerical approach is completed by devising a step-by-step time integration scheme for the time dependent equations. Classical implicite schemes like the Midpoint rule or Newmark method have been very popular in the structural dynamics community. However while these are stable integration methods in the linear regime, they proved less so in the highly non-linear one, especially in long-term dynamics. They suffer from numerical instabilities like blow-ups as well documented in the literature [1, 2, 3, 5]. Energy-momentum methods proved to provide here the necessary stability. In what follows we will develop such a method tailored to our rod formulation. However, so far no such formulation was attempted for the Bernoulli beam because of the complexities involved in the kinematic assumptions. In the following we want to develop for the first time such an Energy-momentum method. In doing so, we resort to an idea developed in [2, 3]. The method described there is attractive because it is independent of the involved non-linearity, the source of problem in the presently considered beam. The starting point, however is the standard midpoint rule. From step n, where all kinematical fields and velocities are known, we need to find these quantities at time step $n + 1$. Consider ξ to be a scalar which defines any position within the time interval ΔT, with $0 \leq \xi \leq 1$. We start with the following expressions:

$$\boldsymbol{x}_{n+\xi} = \xi\boldsymbol{x}_{n+1} + (1 - \xi)\boldsymbol{x}_n, \tag{7}$$

$$\dot{\boldsymbol{x}}_{n+\xi} = \frac{\boldsymbol{x}_{n+1} - \boldsymbol{x}_n}{\Delta T}, \tag{8}$$

$$\ddot{\boldsymbol{x}}_{n+\xi} = \frac{\dot{\boldsymbol{x}}_{n+1} - \dot{\boldsymbol{x}}_n}{\Delta T}. \tag{9}$$

The first defines a convex set, the following two are true for some value of ξ. The midpoint rule corresponding to $\xi = 0.5$. The key step is to employ strain velocity fields to define the strain fields in replacement of Eq.(4) and (5). Let us consider the following velocity fields:

First from (4), we also have:

$$\dot{\varepsilon} = \dot{\boldsymbol{u}}_{,s} \cdot \boldsymbol{X}_{0,s} + \boldsymbol{u}_{,s} \cdot \dot{\boldsymbol{u}}_{,s} \text{ and} \tag{10}$$

$$\dot{\kappa} = \left(\frac{\partial \kappa}{\partial \boldsymbol{u}_{,s}} . \dot{\boldsymbol{u}}_{,s} + \frac{\partial \kappa}{\partial \boldsymbol{u}_{,ss}} . \dot{\boldsymbol{u}}_{,ss} \right). \tag{11}$$

Using (10) and (11), given the strain field defined at time n, the strain field at step $n+1$ then defined as following:

$$\varepsilon_{n+\xi} = \varepsilon_n + \xi \Delta T \dot{\varepsilon}_{n+\frac{1}{2}}, \tag{12}$$

$$\kappa_{n+\xi} = \kappa_n + \xi \Delta T \dot{\kappa}_{n+\frac{1}{2}}. \tag{13}$$

Specifically for $\xi = 1$, the relations hold

$$\varepsilon_{n+1} = \varepsilon_n + \Delta T \dot{\varepsilon}_{n+\frac{1}{2}} = \varepsilon_n + \Delta T \left(\dot{\boldsymbol{u}}_{,s} \cdot \boldsymbol{X}_{0,s} + \boldsymbol{u}_{,s} \cdot \dot{\boldsymbol{u}}_{,s} \right), \tag{14}$$

$$\kappa_{n+1} = \kappa_n + \Delta T \dot{\kappa}_{n+\frac{1}{2}} = \kappa_n + \Delta T \left(\frac{\partial \kappa}{\partial \boldsymbol{u}_{,s}} . \dot{\boldsymbol{u}}_{,s} + \frac{\partial \kappa}{\partial \boldsymbol{u}_{,ss}} . \dot{\boldsymbol{u}}_{,ss} \right). \tag{15}$$

The midpoint rule together with the strain fields defined in (14) and (15) is proved formally and numerically to conserve the linear momentum, angular momentum and the total energy.

3. Numerical example

To investigate conservation of momentum, angular momentum and energy, we consider a beam without support. The beam is given in Fig. 1, the loading increases linearly to a peak and decreases with the same velocity to zero, Fig. 2. We will run the calculation for one million time steps with $\Delta T = 1e-3s$.
The Energy history is depicted in Fig. 3, Fig. 4 and Fig. 5 reflect the linear momentum and angular momentum respectively. In both figures not only the absolute value but also the components of the mentioned quantities go without saying that conservation is valid for momentum and angular momentum vector.

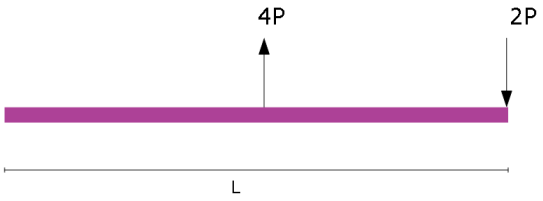

Figure 1: Beam figure

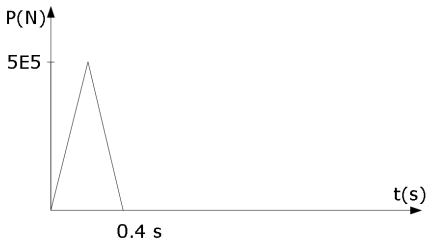

Figure 2: Loading History

Parameters

Beam length $L = 3m$
Cross section area $A = 0.12m^2$
Cross section inertia $I = 1.44E-4m^4$
Young's Modulus $E = 200000Mpa$
Density $\rho = 48831kg/m^3$

Number of element = 4
Time increment $\Delta T = 1e-3s$
Number of steps = 1.000.000

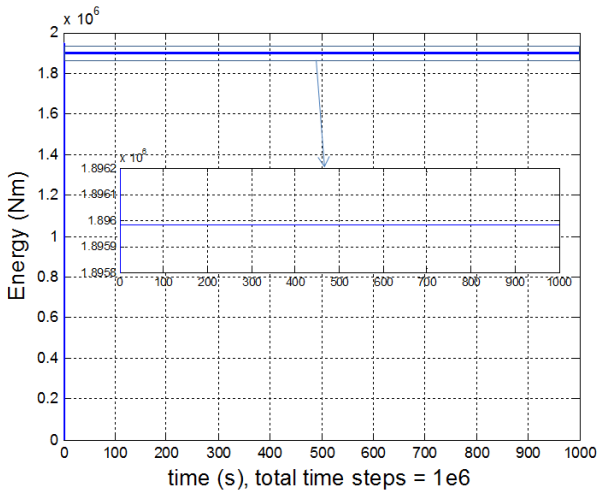

Figure 3: Energy history

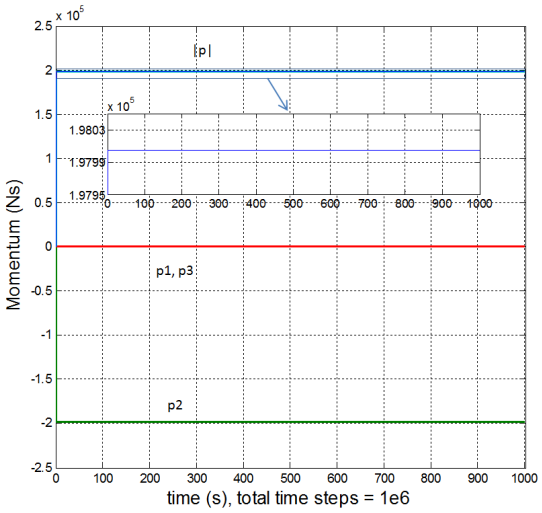

Figure 4: Momentum history

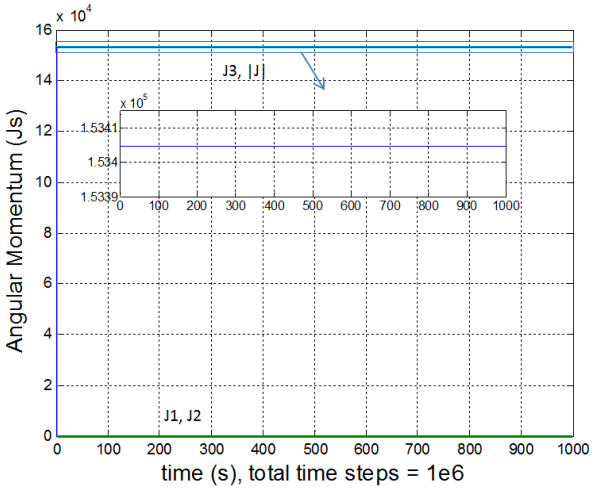

Figure 5: Angular momentum history

References

[1] Klaus-Jurgen Bathe, *Conserving energy and momentum in nonlinear dynamics: A simple implicit time integration scheme*, Computers and Structures 85, 437-445 (2007).

[2] C. Sansour, P. Wriggers, J. Sansour, *On the design of energymomentum integration schemes for arbitrary continuum formulations. Applications to classical and chaotic motion of shells*, Int. J. Numer. Meth. Engng 2004;60:2419-2440.

[3] C. Sansour, P. Wriggers, J. Sansour, *Nonlinear dynamics of shells: theory, finite element formulation, and intergration scheme*, Nonlinear Dyn. 13 (1997),279-305

[4] J.C. Simo, L. Vu-Quoc, *On the dynamics of flexible beam under large overall motion–the plane case: part I and part II*, ASME J. Appl. Mech. 53 (1986),849-854.

[5] J.C. Simo, L. Vu-Quoc, *Non-linear dynamics of threedimensional rods: exact energy and momentum conserving algorithms*, Int. J. Numer. Methods Engrg. 38 (1995),1431-1473.

Proceedings of the 22nd UK Conference of the
Association for Computational Mechanics in Engineering
2 - 4 April 2014, University of Exeter, Exeter

MESHFREE VOLUME-AVERAGED NODAL PRESSURE METHODS FOR INCOMPRESSIBLE ELASTICITY

Jack S. Hale[1*], Christian J. Cyron[2] and Alejandro Ortiz[3]

[1]Research Unit in Engineering Science, University of Luxembourg, Luxembourg
[2]Department of Biomedical Engineering, Yale University, New Haven, Connecticut, United States
[3]Department of Mechanical Engineering, Universidad de Chile, Santiago, Chile

[*]jack.hale@uni.lu, http://orcid.org/0000-0001-7216-861X

ABSTRACT

In this work we present a novel local patch projection technique for alleviating volumetric locking that extends to general order and types of meshfree basis functions. We begin with the classical u-p mixed formulation of incompressible elasticity before eliminating the pressure using a volume-averaged nodal projection technique. This results in a family of projection methods of the type Q_p/Q_{p-1} where Q_p is an approximation space of polynomial order p. These methods are particularly robust on low-quality tetrahedral meshes. Our framework is generic with respects to the type of meshfree basis function used and includes various types of existing finite element methods such as B-bar and nodal-pressure techniques.

As a particular example, we use maximum-entropy basis functions to build a scheme Q_{1+}/Q_1 with the displacement field being enriched with bubble-like functions for stability. The flexibility of the nodal placement in meshfree methods allows us to demonstrate the importance of this bubble-like enrichment for stability; with no bubbles the pressure field is liable to oscillations, whilst with bubbles the oscillation is eliminated. Interestingly however with half the bubbles removed, a scheme we call Q_{1*}/Q_1, certain undesirable tendencies of the full bubble scheme are also eliminated. This has important applications in non-linear hyperelasticity. We also discuss some difficulties associated with moving to second-order maximum entropy shape functions associated with numerical integration errors.

Key Words: *meshless, incompressible, volume-averaged, maximum-entropy.*

1. Mathematical development

By standard arguments it is well known that the problem of linear elasticity can be expressed as the following weak form:

Problem 1. *Find the displacement $\boldsymbol{u} \in \mathcal{U}$ such that $\boldsymbol{u}|_{\Gamma_d} = \boldsymbol{u}_d$ and:*

$$\int_\Omega \boldsymbol{\sigma}(\boldsymbol{\epsilon}(\boldsymbol{u})) : \delta_{\boldsymbol{u}}\boldsymbol{\epsilon}(\boldsymbol{u})\, d\Omega = \int_\Omega \delta_{\boldsymbol{u}}\boldsymbol{u} \cdot \boldsymbol{f}\, d\Omega + \int_{\Gamma_t} \delta_{\boldsymbol{u}}\boldsymbol{u} \cdot \boldsymbol{t}\, d\Gamma \quad \forall\, \delta_u\boldsymbol{u} \in \mathcal{U} \tag{1}$$

where $\boldsymbol{\sigma}$ is the Cauchy stress, $\boldsymbol{\epsilon}$ is the usual small-strain operator, $\boldsymbol{u}$ is the displacement of the solid, Ω is the domain occupied by the solid body with boundary Γ, $\boldsymbol{t}$ are the external tractions applied on Γ_t, $\boldsymbol{f}$ are body forces acting in the domain, and δ_u is the variation with respect to the variable u.

Standard numerical formulations of the displacement formulation of the elasticity problem above lead to the problem of volumetric locking as $\nu \to 1/2$. This results in the following constraint on the hydrostatic pressure $p : \Omega \to L^2(\Omega)/\mathbb{R}$ being enforced exactly:

$$p = -\lambda \operatorname{div} \boldsymbol{u} = -\lambda \operatorname{tr} \boldsymbol{\epsilon} = -\lambda \epsilon_{kk} = 0 \tag{2}$$

The canonical method for alleviating the problem of volumetric locking in numerical formulations of the nearly-incompressible elasticity problem is to treat the pressure as independent variational or weak quantity, resulting in the following variational problem:

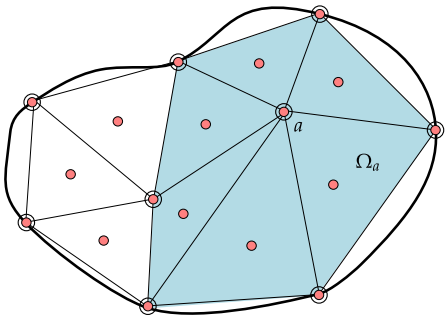

Figure 1: Subset of cells attached to vertex a associated with pressure degree of freedom p_a forming integration domain Ω_a shown by the shaded region.

Problem 2. *Find* $(\boldsymbol{u}, p) \in \mathcal{U} \times \mathcal{P}$ *such that* $\boldsymbol{u} = \boldsymbol{u}_d$ *and:*

$$\begin{aligned}\int_\Omega 2\mu\boldsymbol{\epsilon}(\boldsymbol{u}) : \delta_{\boldsymbol{u}}\boldsymbol{\epsilon}(\boldsymbol{u})\, d\Omega - \int_\Omega p\boldsymbol{I} : \delta_{\boldsymbol{u}}\boldsymbol{\epsilon}(\boldsymbol{u})\, d\Omega \\ = \int_\Omega \delta_{\boldsymbol{u}}\boldsymbol{u} \cdot \boldsymbol{f}\, d\Omega + \int_{\Gamma_t} \delta_{\boldsymbol{u}}\boldsymbol{u} \cdot \boldsymbol{t}\, d\Gamma \quad \forall\ \delta_u\boldsymbol{u} \in \mathcal{U}\end{aligned} \tag{3a}$$

$$\int_\Omega \operatorname{div}\boldsymbol{u}\ \delta_p p\, d\Omega + \int_\Omega \frac{1}{\lambda} p\ \delta_p p\, d\Omega = 0 \quad \forall\ \delta_p p \in \mathcal{P} \tag{3b}$$

In a general sense, by re-arranging the discrete equivalent of eq. (3b) we can express the pressure variable p_h in terms of the displacements $\boldsymbol{u}_h$ by the relation:

$$p_h = -\lambda\Pi_h(\operatorname{div}\boldsymbol{u}_h) \tag{4}$$

where the projection operator $\Pi_h : \mathcal{U}_h \to \mathcal{P}_h$ is a projection from the displacement space $\mathcal{U}_h$ to the pressure space $\mathcal{P}_h$. This projection operator approach derived from the $\boldsymbol{u}$-p mixed formulation constitutes a discrete modification of the energy bilinear form associated with the volumetric or dilational energy of the elastic body which results in the suppression of volumetric locking [1].

We now derive a specific form of Π_h which we refer to as the volume-averaged nodal pressure operator. This operator was introduced originally in the paper of Ortiz et al. [2] and in this work we extend its application to meshfree basis functions of arbitary type and order. We denote N_i as the linear finite element shape functions associated with degrees of freedom i located at the vertices $\mathcal{V}$ of the triangulation $\mathcal{T}$ allowing us to write the discrete pressure variable p_h and associated variation $\delta_p p$ as:

$$p_h = \sum_i N_i(x) p_i \tag{5a}$$

$$\delta_p p = \sum_i N_i(x)\ \delta_p p_i \tag{5b}$$

We denote in a general sense the space $Q_p(\mathcal{N}, \rho)$ as the span of a set of meshless basis functions ϕ_i associated with degree of freedom i located at the nodes $\mathcal{N}$ with polynomial consistency of order p and support sizes ρ. We can then write the discrete displacement variable $\boldsymbol{u}_h$ and associated variation $\delta_{\boldsymbol{u}}\boldsymbol{u}$ as:

$$\boldsymbol{u}_h = \sum_i \phi_i(x)\boldsymbol{u}_i \tag{6a}$$

$$\delta\boldsymbol{u}_h = \sum_i \phi_i(x)\ \delta_{\boldsymbol{u}}\boldsymbol{u}_i \tag{6b}$$

Then by substituting eqs. (5) and (6) into eq. (3) yields for every degree of freedom c in the construction of $\delta_p p$:

$$\int_\Omega N_c \delta p_c \left(\boldsymbol{m}^T \sum_b \boldsymbol{B}_b \boldsymbol{u}_b + \frac{1}{\lambda} \sum_b N_b\ p_b \right) d\Omega = 0 \tag{7}$$

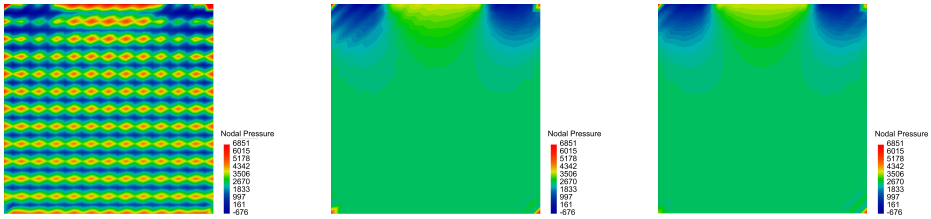

Figure 2: Pressure field p of highly-constrained rigid punch problem. Left: RPIM Q_2/Q_1, Middle: RPIM Q_{2*}/Q_1, Right: RPIM Q_{2+}/Q_1. The solution with no bubbles (left) fails the inf-sup condition, leading to a highly oscillatory pressure field. The half-bubble formulation (middle) retains the stability properties of the full-bubble solution (right).

where the vector $\boldsymbol{m}^T$ takes the trace (tr) of the strain field $\boldsymbol{\epsilon}$:

$$\boldsymbol{m}^T = \begin{Bmatrix} 1 & 1 & 0 \end{Bmatrix} \tag{8}$$

On relying on the arbitrariness of nodal variations we arrive at the following equation:

$$\sum_b \left\{ \int_\Omega N_c \boldsymbol{m}^T \boldsymbol{B}_b \, d\Omega \right\} \boldsymbol{u}_b + \sum_b \left\{ \frac{1}{\lambda} \int_\Omega N_c N_b \, d\Omega \, p_b \right\} = 0 \tag{9}$$

The second term on the left hand-side of eq. (9) can be used to eliminate the pressure from the formulation. An approximate way to acheive this is by lumping the mass-type matrix formed by the second term on the left hand-side of eq. (9), ie. $\sum_b N_c N_b = N_c$. Solving for p_c in eq. (10) gives:

$$p_c = -\lambda \sum_b \left\{ \frac{\int_{\Omega_c} N_c \boldsymbol{m}^T \boldsymbol{B}_b \, d\Omega}{\int_{\Omega_c} N_c \, d\Omega} \right\} \boldsymbol{u}_b \tag{10}$$

where Ω has been replaced by Ω_c to indicate that due to the mass-lumping procedure the volume for integration is now formed by a subset of the cells $\mathcal{K}$ attached to the vertex associated with pressure degree of freedom p_c, see fig. 1.

Finally, based on eq. (10) we can define the volume-averaged nodal projection operator θ_c^q as:

$$\theta_c^q [\cdot] = \frac{\int_{\Omega_c} N_c [\cdot] \, d\Omega}{\int_{\Omega_c} N_c \, d\Omega} \tag{11a}$$

and the volume-averaged projection approximation operator θ_h^q as:

$$\Pi_h := \theta_h^q [\cdot] = \sum_c N_c(x) \theta_c^q [\cdot] \tag{11b}$$

These two expressions are used to eliminate the pressure from eq. (3), and result in a locking-free formulation for incompressible elasticity.

2. Results

In this section we particularly want to show the effect of the quantity of bubble degrees of freedom on the quality of the pressure field solution and convergence. The 'bubbles' are the extra meshfree degrees of freedom inserted at the barycenters of the triangulation in a similar manner to the MINI element which are required for stability. We consider three function spaces for the displacement, the first with no bubbles which we denote Q_p, the second with full-bubbles denoted Q_{p+} and the third with half-bubbles Q_{p*}, ie. 50% of the bubbles removed from the full-bubble solution. This idea of using only half the number of bubbles was introduced in the finite element context by Kim and Lee [3].

We show the pressure field for the highly constrained indented block problem in fig. 2. In this problem a displacement is applied to one third of the top surface and all other surfaces are fully constrained. We use Radial Point Interpolation Method (RPIM) basis functions in this example. The solution with no bubbles fails the inf-sup condition (left), leading to a highly oscillatory pressure field. The half-bubble formulation (middle) retains the stability properties of the full-bubble solution (right).

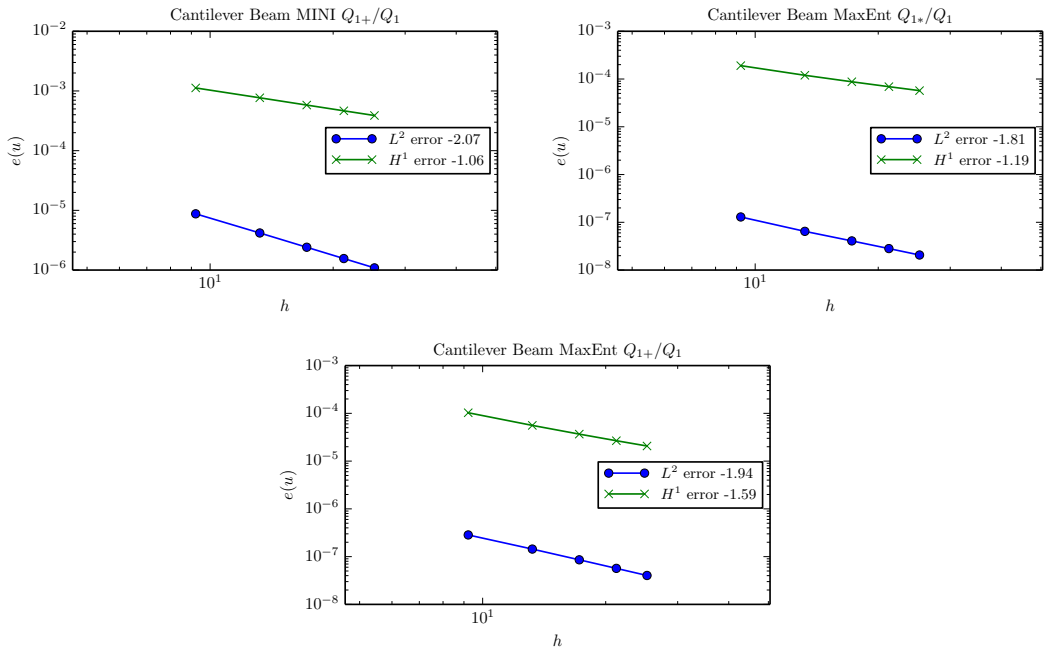

Figure 3: Convergence of Timoshenko beam problem. Top left: MaxEnt Q_2/Q_1, Top right: MaxEnt Q_{2*}/Q_1, Bottom: MaxEnt Q_{2+}/Q_1. With half-bubbles we still acheive the optimal convergence rate in both the H^1 and L^2 norm.

We now consider the classic Timoshenko beam problem, where a parabolic traction is applied on one end and the opposing end is fixed. In this example we use MaxEnt basis functions to demonstate the generality of our approach between different meshless basis functions. In fig. 3 we show the convergence for the displacement variable in the usual displacement norm L^2 and energy-equivalent norm H^1. Even with the half-bubble formulation we obtain optimal-order convergence in both norms and significantly better performance than the classical MINI element of Arnold et al. [4] owing to the superior approximation properties of meshless basis functions. Additionally, upon moving to second-order RPIM functions (results not shown) we find that accurate integration of the weak form is critical to acheive full convergence. We use the modified integration rule of Duan et al. [5] in all of the results shown in this paper.

Acknowledgements

Jack S. Hale would like to acknowledge the financial support of Imperial College London/EPSRC and the structural position under the chair of Prof. Stéphane P. A. Bordas at the University of Luxembourg. Alejandro Ortiz would like to acknowledge the financial support of Fondecyt Grant No. 11110389 'Development and Assessment of An Efficient Numerical Method for Simulation of Nearly Incompressible Large Deformations Problems in Solid Mechanics'. Jack S. Hale and Christian J. Cyron are grateful for the foreign scholar grants funded by Fondecyt Grant No. 11110389 to visit the Universidad de Chile.

References

[1] M. Fortin, F. Brezzi, Mixed and Hybrid Finite Element Methods, Springer-Verlag Berlin and Heidelberg GmbH & Co. K, 1991.

[2] A. Ortiz, M. Puso, N. Sukumar, Maximum-entropy meshfree method for compressible and near-incompressible elasticity, Computer Methods in Applied Mechanics and Engineering 199 (25-28) (2010) 1859–1871. doi:10.1016/j.cma.2010.02.013.

[3] Y. Kim, S. Lee, Modified mini finite element for the stokes problem in 2 or 3, Advances in Computational Mathematics 12 (2-3) (2000) 261–272. doi:10.1023/A:1018973303935.

[4] D. Arnold, F. Brezzi, M. Fortin, A stable finite element for the stokes equations, Calcolo 21 (4) (1984) 337–344. doi:10.1007/BF02576171.

[5] Q. Duan, X. Li, H. Zhang, T. Belytschko, Second-order accurate derivatives and integration schemes for meshfree methods, International Journal for Numerical Methods in Engineering 92 (4) (2012) 399424. doi:10.1002/nme.4359.

Proceedings of the 22nd UK Conference of the
Association for Computational Mechanics in Engineering
2 – 4April 2014, University of Exeter, Exeter

Nonlinear Analysis of Masonry Arches and Bridges Using Mesoscale Partitioned Modelling

Yanyang Zhang[1], Lorenzo Macorini[1]* and Bassam A. Izzuddin[1]
[1]Department of Civil and Environmental Engineering, Imperial College London, London, SW7 2AZ
* l.macorini@imperial.ac.uk

ABSTRACT

This paper presents the results of detailed numerical analyses simulating the response of masonry arches and bridges up to collapse. Past research has shown that detailed numerical descriptions, where bricks and brick-mortar joints are modelled separately can offer a sound representation of the behaviour of masonry components up to collapse. However, because of the significant computational effort, to date the use of this approach has been mainly restricted to 2D analysis. This does not allow the investigation of the inherent 3D response especially in the case of arches with complex geometry and masonry bridges. The modelling approach used in this work benefits from pioneering work undertaken previously at Imperial College, where an accurate 3D mesoscale model for masonry and a partitioning approach for parallel processing have been developed and used for detailed nonlinear analysis of masonry components. The results of numerical studies, which also include comparisons against experimental results, are presented to show the potential and the accuracy of the proposed method for masonry arches and bridges.

Keywords: *nonlinear analysis; masonry arches; masonry bridges; 3D mesoscale description; domain partitioning approach.*

1. Introduction

Masonry arches are critical components of masonry bridges which represent a significant portion of existing bridges in the UK and Europe. Most of these old structures, which were built following rules of thumb or using simple design approaches, need to be assessed considering current safety requirements. In this respect, detailed numerical modelling represents an important vehicle for safety and residual life assessment. Thus in recent years, different numerical strategies for analysing masonry arches and bridges have been developed. These are mainly based upon the use of limit analysis concepts [1], the finite element method (FEM) or discontinuous modelling techniques [2].
When utilising rigid plastic approaches, only the arch ultimate capacity can be evaluated. On the other hand, FEM enables an accurate response prediction at different loading levels up to collapse only when an accurate material description is used for masonry. This is a heterogeneous and strongly nonlinear material whose behaviour is determined not only by the mechanical characteristics of units and mortar joints but also by the specific unit-mortar arrangement considered to build the arch (e.g. multi-ring arches, skew arches etc.). Moreover, the use of detailed FE modelling for masonry arch bridges, which are relatively large structures, is computationally demanding, thus so far it has been mainly employed in 2D plane stain analysis. In many cases, this is a too crude kinematic assumption, as the response of masonry arch bridges is intrinsically three-dimensional also under simple loading conditions. Recently, a few modelling approaches have been proposed for 3D nonlinear analysis of masonry arch bridges using either the continuous approach with a simple nonlinear description for masonry assumed as a uniform and isotropic material [3] or a more advanced nonlinear macro scale homogenised model [4]. In this work, an alternative modelling strategy is presented and used for the analysis of a masonry arch with complex geometry and a masonry arch interacting with backfill material.

2. Mesoscale Partitioned Modelling Approach

A partitioned mesoscale approach is adopted to analyse masonry arches and bridges. This enables the use of a detailed model for describing material nonlinearity [5] in masonry at structural scales, as it is combined with a partitioned approach allowing for parallel computation [6] which guarantees computational efficiency. In the 3D mesoscale description [5], 3D elastic continuum solid elements are used to model masonry blocks, while mortar and brick-mortar interfaces are modelled by means of 2D nonlinear interface elements (Fig. 1a) . Furthermore, zero-thickness interface elements are also arranged in the vertical mid-plane of all blocks so as to account for possible unit failure in tension and shear. This mesoscale approach enables the representation of any 3D arrangement for masonry including the complex arrangement used in multi-ring and skew arches. Concerning the constitutive model for the interface element, it accounts for the actual elastic deformations of mortar and brick-mortar interfaces using specific elastic stiffness values [5], which are functions of the component elastic properties and the joints dimensions. The inelastic response at the interfaces is simulated by means of a cohesive fracture model based on a multi-surface plasticity criterion. The response in tension and shear is described by an elasto-plastic contact law which follows a Coulomb slip criterion. On the other hand, a formulation that considers energy dissipation, de-cohesion and residual frictional behaviour is employed to describe cracks formation and propagation, where plastic work is used to determine the evolution of material parameters.

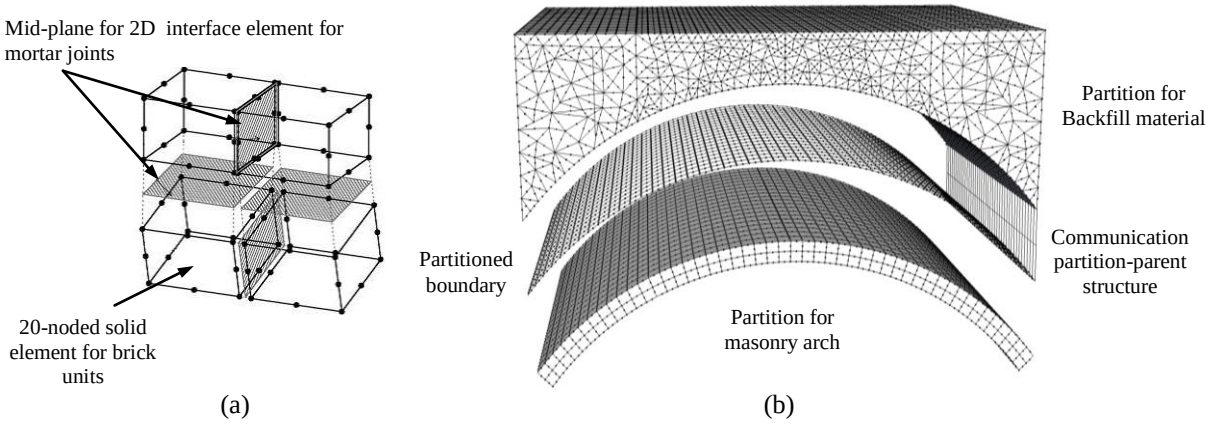

Figure 1 (a) 3D masonry mesoscale modelling for brick-masonry, (b) partitioned approach for modelling masonry arch bridges

To achieve computational efficiency, the analysed structure with masonry is described by a parent structure which consists of super-elements representing the partitioned subdomains. Dual super-elements are used for modelling the partitions as separate processes, where two-way communication between each pair of dual parent/child super-elements allows effective parallelisation of the nonlinear structural analysis simulation [6]. The proposed partitioned approach applied to a simple masonry bridge is illustrated in Figure 1b, where two partitions are used to model the backfill and masonry arch. The two partitions communicate through the parent structure which corresponds to the nodes at the partition boundary between the two subdomains. Evidently, in the case of large structures and to achieve significant speed-up in the numerical simulation, a larger number of partitions can be used for modelling the two subdomains. In the case of masonry bridges, which are heterogeneous systems, the backfill material is modelled through a continuous plastic approach, while the physical interface between the continuous and the discrete mesoscale domain for masonry is represented by nonlinear zero-thickness interface elements allowing separation and plastic sliding.

3. Numerical Examples

The mescale partitioned model was implemented into ADAPTIC [7], a general finite element code for nonlinear analysis of structures, which is used here to analyse masonry arches and bridges. Two numerical examples are presented considering the analysis of a skew masonry arch and the interaction between a masonry arch and backfill.

The analysed skew arch is a two-ring arch with a 45° skew angle. The structure has 3 m direct span, 670 mm width and 215 mm thickness, and was previously tested by applying a concentrated force P at 3/4 span up to failure [8]. In the proposed FE modelling, the arch is modelled with four partitions. To represent the complex 3D geometry typical of skew brick-masonry arches, each half brick is represented by a 20-noded solid element. Nodal coordinates for each element are obtained following the rules of descriptive geometry as suggested in [9], which were adopted to define skew arch geometry in real old masonry bridges. The FE mesh of the arch is displayed in Figure 2a. A tensile strength σ_{t0} = 0.07 N/mm^2 is considered for mortar joints, while an elastic modulus E = 4000 N/mm^2 and Poisson's ratio ν =0.15 are assumed for the brick units.

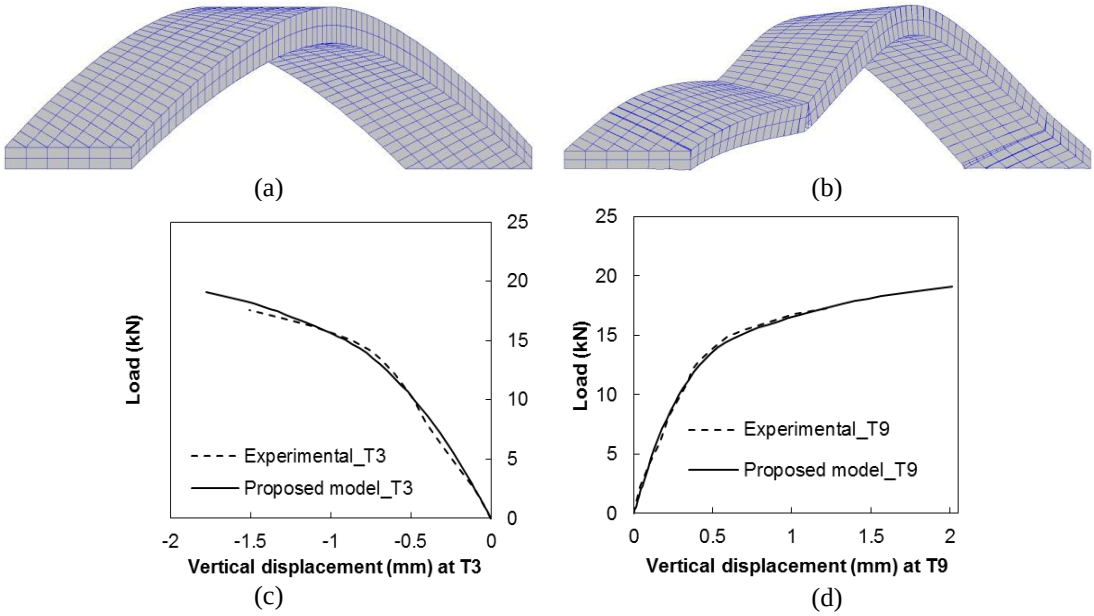

Figure 3 Skew arch: (a) undeformed FE mesh, (b) deformed shape showing failure mechanism, (c) and (d) load-displacement curves for vertical displacement at points T3 and T9.

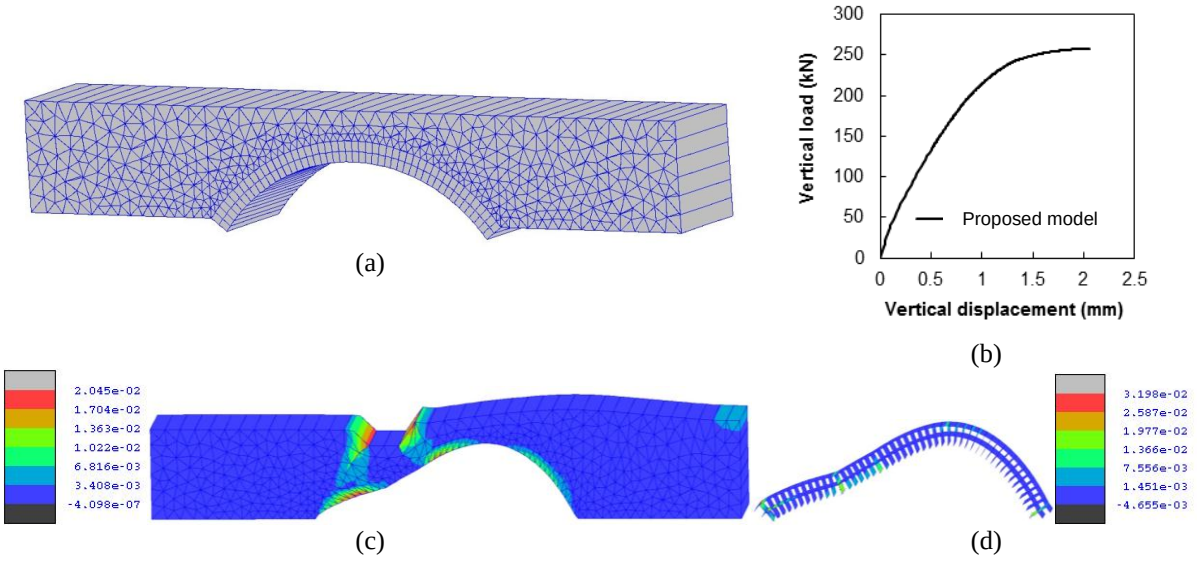

Figure 3 Arch-backfill: (a) Undeformed FE mesh, (b) load-displacement response, (c) deformed shape and plastic deformation contour of backfill partition, (d) deformed shape and plastic work contour (Nmm) at interface elements for masonry arch partition.

Figure 2b shows the deformed shape of the skewed arch barrel at failure, where four large cracks are noted. This is the typical 3D failure mode of masonry skew arches as observed in experimental tests [8] which cannot be represented using simplified 2D models. Figures 2c,d shows numerical-experimental comparisons in term of vertical displacements at 1/4 and 3/4 span. The numerical predictions are very close to the experimental results at different loading levels confirming the accuracy provided by the proposed modelling approach.
The second numerical example investigates the response of an arch strip interacting with backfill material. This is a typical interaction mode in old masonry bridges where loads are transferred through the backfill to the arch, and the backfill offers partial restraint to the arch deformations. Two partitions are used for the arch and the backfill material, where the physical interface between the two domains is modelled with nonlinear frictional interface elements. On the other hand, a continuous plastic model utilising a smooth Mohr-Coulomb yield function is used for modelling the fill material. The elastic modulus, frictional angle, cohesion and Poisson's ratio of the backfill are taken as 1000 N/mm^2, 46.4°, 0.0224 N/mm^2 and 0.2, respectively. Mortar cohesion and tensile strength for mortar joints are taken as 0.35 N/mm^2 and 0.15 N/mm^2, respectively. Figures 3a,b show the FE mesh and the load-displacement response. The displacement are obtained at 1/4 span where the load is applied at the top of the backfill. Figures 3c,d display the deformed shape and plastic deformation contours for fill material and plastic work contour at nonlinear interfaces. The latter shows the development of damage in the arch at maximum load, where it can be seen that large cracks developed in four regions of the arch forming a collapse mechanism.

4. Conclusions

This paper presents an advanced numerical modelling strategy for nonlinear analysis of brick-masonry arch bridges, which combines a mesoscale model for masonry and a partitioning approach allowing parallel computation. Two numerical examples are presented which include comparisons against experimental results. These show the accuracy of the proposed numerical approach in describing the initial stiffness, maximum capacity and failure mechanisms of 3D multi-ring skew arches under static loading as well as the interaction between masonry arches and backfill material. This confirms the significant potential of the proposed modelling approach in the analysis of large heterogeneous systems with masonry components, where the response is determined by the interaction among different structural and non-structural components which can be modelled using continuous or discrete nonlinear models.

References

[1] M. Gilbert, Limit analysis applied to masonry arch bridges: state-of-the-art and recent developments, *ARCH'07-5th International Conference on Arch Bridges*, pp.13-28, 2007.

[2] A. Thavalingam, N. Bicanic, J.I. Robinson, D. A. Ponniah, Computational framework for discontinuous modelling of masonry arch bridges, *Computers and Structures*, 79, 1821-1830, 2001.

[3] P.J. Fanning and T. E. Boothby, Three-dimensional modelling and full scale testing of stone arch bridges, *Computer and Structures*, 79, 2645-2662, 2001.

[4] G. Milani, P.B. Lourenço, 3D nonlinear behaviour of masonry arch bridges, *Computer and Structures*, 110-111, 133-150, 2012.

[5] L. Macorini and B.A. Izzuddin, A non-linear interface element for 3D mesoscale analysis of brick-masonry structures, *Int. J. Numer. Meth. Engng.*, 85, 1584-1608, 2011.

[6] G.A. Jokhio and B.A. Izzuddin, Parallelisation of nonlinear structural analysis using dual partition super-elements, *Advances in Engineering Software*, 60-61, 81-88, 2013.

[7] B.A. Izzuddin, *Nonlinear dynamic analysis of framed structures*, PhD Thesis, Imperial College, *University of London*, 1991.

[8] J. Wang, *The three dimensional behaviour of masonry arches*, PhD Thesis, University of Salford, 2004.

[9] G.W. Buck, *A practical and theoretical essay on oblique bridges*, ICE Publishing, London, 1895.

Proceedings of the 22nd UK Conference of the
Association for Computational Mechanics in Engineering
2-4 April 2014, University of Exeter, Exeter

Numerical Methods For Subsurface Reservoir Simulation: Boundary Aligned Grid Generation and Flux Approximation Schemes

***Shahid Manzoor Toor[1], Michael G. Edwards[1], Ali H. Dogru[2] and Tareq M Al-Shaalan[2]**

[1]College of Engineering, Swansea University, Singleton park, Swansea, SA2 8PP
[2] EXPEC Advanced Research Center, Saudi Aramco, Saudi Arabia

*642969@swansea.ac.uk

ABSTRACT

Reservoir simulation involves computation of subsurface flow fields, reservoirs often comprised of complex geometric objects, which requires feature based and boundary aligned grids. These constraints are satisfied by employing unstructured grid generation methods. Control-volume distributed multi-point flux approximation schemes are used for solving the Darcy pressure equation, both cell centred and cell vertex approximations are used and compared. A technique involving advancing front point placement is devised to generate boundary aligned meshes. A concise description of boundary aligned mesh generation together with applications are presented.

Key Words: *Reservoir simulation; Boundary aligned grid generation; Flux approximation; Unstructured meshing*

1. Introduction

Petroleum reservoir simulation involves computation of subsurface flow fields and fluid flow processes, in order to optimize the recovery of hydrocarbons. Subsurface reservoirs are often comprised of complex geometric and geologic objects and features. In addition to robust numerical methods for solving the flow equations, methods of grid generation are required which can handle geometric complexity. Grid generation for large scale porous media such as oil and gas reservoirs has been a challenging problem for decades. This is due to involvement of complex geometries and random distribution of spatial heterogeneities in the domain[1].

Conventionally, reservoir simulators are based on simple grid blocks i.e. squares and cubes (structured grids). Another class of grid generation methods which generally employs triangles and tetrahedrons as grid elements, often termed unstructured grids[1, 2]. Compared with structured grids, unstructured grids are more flexible and can adapt grid cells to various flow and geometric constraints such as faults, fractures and wells and perform local refinement with smooth transition[2, 3]. However, unstructured grids require special data treatment, so computationally are more involved. The use of unstructured grids in reservoir simulation dated back to the early nineties. Despite unstructured grid generation methods having been successfully employed in modelling complex giant reservoirs, in field applications there is still increased inclination toward the use of structured grids. Fung et al. [2] have reported that this might be the result of novelty of these methods in the field compared with structured grids for which well established simulation tools exist. They are of opinion that more research work is required to carry out simulation on unstructured grids.

2. Methods for Geological Feature Based Grids:

The subsurface flow of hydrocarbons is a very complex phenomenon and is direction dependent, where permeability across the layers can jump by several orders of magnitude. In order to minimize the effect of grid orientation and discretization errors, unstructured grids should conform as closely as possible to geological features such as faults, fractures, pinchouts and wells , e.g. Merland et al.[3]. The unstructured grids used in reservoir modelling, commonly employ Delaunay-Voronoi grids for spatial discretization of domain. Voronoi grids can be made to conform to geologies by special treatment such that their cells become aligned to geological features. Some of the techniques used to construct feature based grids are outlined in [3].

In general feature based grids generated are a result of constrained Delaunay triangulation. However in this work feature based grids are generated with unconstrained Delaunay triangulation. Advancing Front Local Reconnection(AFLR) method is selected, detail and development of which can be found

elsewhere[4, 5], here only a concise description is presented. A method which exploits the concept of advancing front technique in conjunction with Delaunay triangulation is presented in [6]. AFLR is a quite general triangulation method in that, it can be devised to use advancing front point placement in combination with any local connection optimization criterion. However, in this text to construct Delaunay triangulation it is designed to work with Delaunay as a quality criterion.

AFLR starts with valid initial triangulation of boundary points as background mesh. AFLR works in an iterative fashion, wherein during every level it involves three major steps: for every active element define candidate points; filter candidate points thereby rejecting those points which could deteriorate mesh quality; finally the insertion phase, where the set of filtered points are triangulated. Grid generation process is completely controlled by point distribution function(PDF), which in its simplest form can be thought of representative of boundary point spacing. Figure 1 highlights different steps involved in carrying out Delaunay triangulation by employing AFLR.

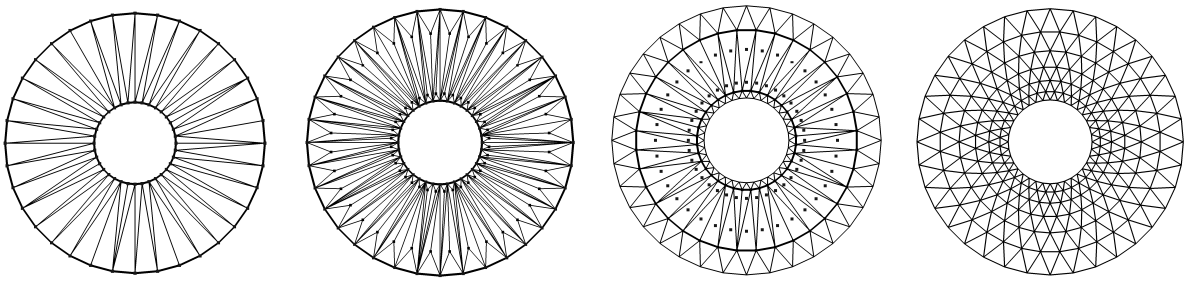

(a) Empty Mesh

(b) Adancing front point placement followed by direct subdivion of containing elements

(c) Connection optimization subject to Delaunay Criterion and Level-1 points

(d) Final Delaunay Triangulation

Figure 1: : Pictorial representation of AFLR meshing technique; highlighting different stages involve in triangulating a domain

3. Boundary Aligned Grid(BAG) Generation

In general reservoir geometries are comprised of features such as faults/fractures, complex spatial distribution of the wells and a wide range of variations in porosity and permeability across different layers[1]. In order to minimize discretization error, it is common practice to generate meshes which are aligned with these features, thereby leading to feature based triangulations, usually termed as boundary aligned grids(BAGs).The grids generated have to provide control-volume boundary alignment consistent with spatial discritization required in flux approximation schemes. These schemes demand control volume aligned grids and can be designed to work either with primal (cell centred schemes) or dual cells (cell-vertex schemes) as their control volumes. Primal cell control volumes are the grid elements in terms of which reservoir domain is directly subdivided, it consists of triangles and/or quadrilaterals. Dual cells are obtained by connecting circumcentres surrounding a primal cell vertex.

Primal Cell BAG: AFLR method can be used to obtain meshes where primal cells are aligned with faults and/or fractures. The key idea in this regard is to embed a discretized curve characterising some geological feature, and then as the front initiates a layer of cells is placed on either side of it thereby providing with permanent protection around it. This method is fully generalizable, some examples of primal cell BAGs generated in a manner similar to one described above are shown in figure 2.

Dual Cell BAG: AFLR method when employed to construct dual(voronoi) cell aligned grid involves embedding a discretized channel(halo) with actual interior boundary as its median line. The channel used is designed to comprise of quadrilateral elements, where each element is allowed to have only four co-circular points. This is because later in construction of the dual, for channel elements it becomes feasible to work with circumcenter, so as to obtain dual which still enjoys the property of being an integral part of a perpendicular bisector(PEBI) grid. Some examples of dual cell boundary aligned grids illustrating the strength of the method are depicted in figure 3.

4. Flux Approximation Schemes:

Flux approximation schemes in reservoir simulation are generally control volume distributed(CVD)[7]. A piecewise constant representation of flow properties is assigned to the control volumes, where field variables are computed at their centres(control points). As described earlier in selecting a control volume normally there are two choices i.e. primal or dual cells. The resulting scheme from each of these two settings is called cell centred and vertex centred approximation respectively. With respect to type of

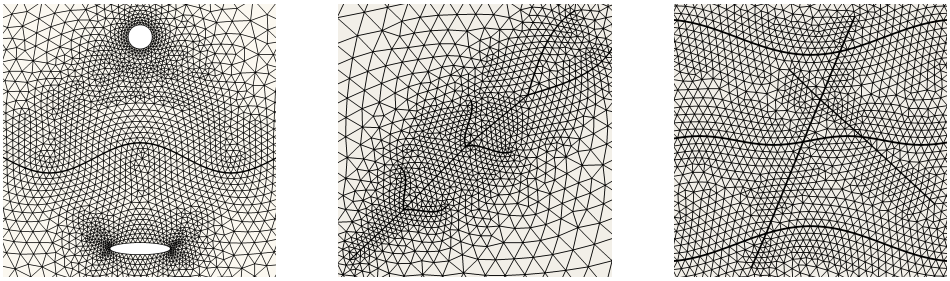

(a) Primal cell BAG with respect to a layer, with two holes postioned on either side of it

(b) Primal cell BAG with respect to a complex frcature

(c) Primal cell BAG of a layered system, embeded with some fratures

Figure 2: : Examples illustrating usefulness of AFLR in generating primal cell BAGs

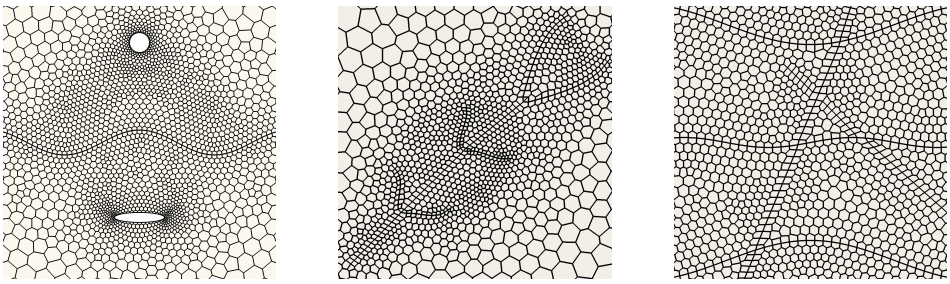

(a) Dual cell BAG with respect to a layer, with two holes postioned on either side of it

(b) Dual cell BAG with respect to a complex frcature

(c) Dual cell BAG of a layered system, embeded with some fratures

Figure 3: : Examples illustrating usefulness of AFLR in generating dual cell BAGs

formulation flux approximation schemes are broadly subdivided into two classes namely: two point flux approximation(TPFA) scheme; and control-volume distributed multipoint flux approximation(CVD-MPFA) schemes. The detailed description, along with their formulation and numerical analysis can be found in[7, 8, 9, 10]. Formulation of these schemes in cell centre and cell vertex modes is analogous and involves switching control volume from primal to dual or vice versa.

Test Case: This problem is taken from[10], where flow field governed by *pressure equation* is simulated in a unit square domain, with permeability tensor whose degree of anisotropy is controlled by parameter $0 < \epsilon \leq 1$. Grid generated by employing AFLR technique along with contour plot of exact solution are shown in figure 4. An anisotropic flow field with $\epsilon = 0.1$ is simulated and solution obtained with TPFA, TPS and FPS formulations both in cell centre and cell vertex mode are shown in figure 5, where L_2 norm indicates deviation from the exact solution.

Numerical studies carried out reveal that in case grid employed is PEBI, and permeability constitute an isotropic field then grid is K-orthogonal by default, for which TPFA provides consistent solutions both in cell centre and cell vertex settings. For an anisotropic field the L_2 error comparison between cell centre and cell vertex results indicates that cell centre formulations capture the effect of anisotropy better than cell vertex, however neither of the formulations yields consistent approximation[7]. The main idea behind CVD-MPFA schemes is to develop a consistent formulation, satisfying local pres-

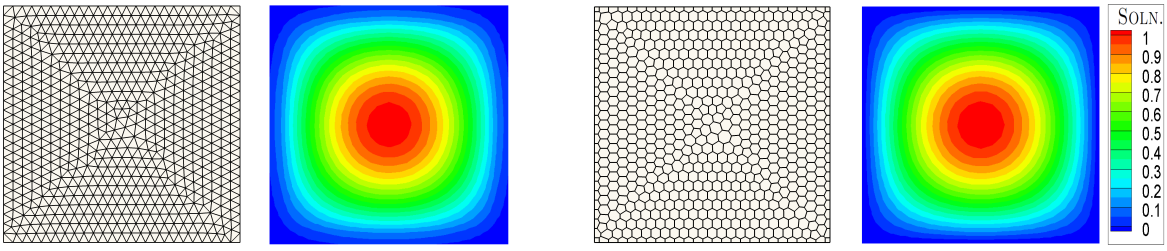

(a) Grid with primal cells as control volumes(cell centre formulation)

(b) Cell center exact solution; contour plot of pressure field

(c) Grid with dual cells as control volumes(cell vertex simulation)

(d) Cell vertex exact solution; contour plot of pressure field

Figure 4: : Problem Definition: Grids generated to simulate pressure field and exact solution plot

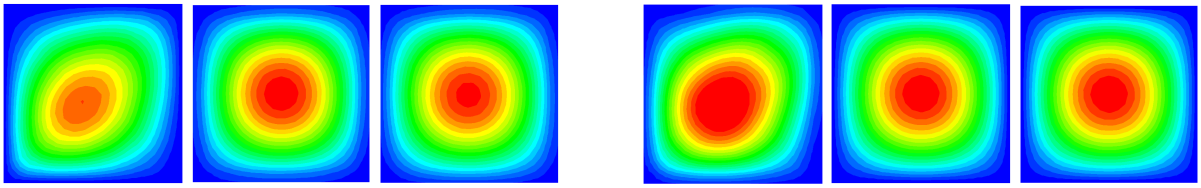

(a) Cell centre TPFA $L_2 = 8.13 \times 10^{-2}$ (b) Cell centre TPS $L_2 = 2.99 \times 10^{-3}$ (c) Cell centre FPS $L_2 = 2.83 \times 10^{-2}$

(d) Cell vertex TPFA $L_2 = 1.04 \times 10^{-1}$ (e) Cell vertex TPS $L_2 = 2.35 \times 10^{-3}$ (f) Cell vertex FPS $L_2 = 3.02 \times 10^{-3}$

Figure 5: : Comparison of TPFA, TPS and FPS formulation both in cell centre and cell vertex settings

sure and flux continuity conditions. The continuity conditions leads to an increased pressure support with wider stencil compared to the standard TPFA scheme, however the number of degrees of freedom remains unchanged[10]. Two commonly employed schemes are triangular pressure support(TPS) and full pressure support(FPS) schemes. FPS schemes involve additional auxiliary pressure support, thus have a wider range of quadrature compared to TPS. While general M-matrix conditions must be satisfied to prevent spurious oscillations, FPS has been shown to be far more robust than the earlier TPS methods[8, 9, 10].

5. Conclusions:

The AFLR is a quite general triangulation technique in that it can be devised to work with any connection optimization criterion. The AFLR has been found to yield quality meshes. In order to generate meshes aligned with geological features, AFLR requires initial embedded discretized curves defining these features. As the front initiates from such a curve, it generates a halo(protection zone) around it, thereby ensuring boundary integrity. The AFLR method has been successfully employed in generating boundary aligned meshes both with respect to primal and dual cells. In flux approximation schemes two point flux approximation yields consistent solutions if grids employed are K-Orthogonal. For non-isotropic permeability tensor, in general CVD-MPFA schemes are found to yield consistent results. The Cell vertex formulation is computationally more efficient and robust compared to cell centred formulation, however it demands dual cell aligned grids.

Acknowledgements:

We thank Saudi Aramco for supporting this work.

References

[1] M. Sahimi, R. Darvishi, M. Haghighi and M.R. Rasaei. Upscaled Unstructured Computational Grids for Efficient Simulation of Flow in Fractured Porous Media. *Transport in Porous Media*, 83, 195–218, 2010.

[2] L.S.K. Fung, X.Y. Ding and A.H. Dogru. An Unstructured Gridding Method for Densely-Spaced Complex Wells in Full-Field Reservoir Simulation, in: *SPE Reservoir Simulation Symposium (The Woodlands, Texas, USA)*, pp.995-1007, 2013.

[3] R. Merland, B. Lévy and G. Caumon. Building PEBI Grids Conforming To 3D Geological Features Using Centroidal Voronoi Tessellations, in: R. Marschallinger and R. Zolb (Eds.), *Mathematical Geosciences at the Crossroads of Theory and Practice (IAMG)*, pp.254-265, 2011.

[4] D.L. Marcum and N.P. Weatherill. Unstructured grid generation using iterative point insertion and local reconnection. *AIAA Journal*, 33, 1619–1625, 1995.

[5] D.J. Mavriplis. An Advancing Front Delaunay Triangulation Algorithm Designed for Robustness. *Journal of Computational Physics*, 117, 90-101, 1995.

[6] I. Sazonov, D. Wang, O. Hassan, K. Morgan and N. Weatherill. A stitching method for the generation of unstructured meshes for use with co-volume solution techniques. *Computer Methods in Applied Mechanics and Engineering*, 195, 1826–1845, 2006.

[7] M.G. Edwards and C.F. Rogers. Finite volume discretization with imposed flux continuity for the general tensor pressure equation. *Computational Geosciences*, 2, 259–290,1998.

[8] M.G. Edwards and H. Zheng. A quasi-positive family of continuous Darcy-flux finite-volume schemes with full pressure support. *Journal of Computational Physics*, 227, 9333–9364, 2008.

[9] M.G. Edwards and H. Zheng. Double-families of quasi-positive Darcy-flux approximations with highly anisotropic tensors on structured and unstructured grids. *Journal of Computational Physics*, 229, 594–625, 2010.

[10] H.A. Friis, M.G. Edwards and J. Mykkeltveit. Symmetric Positive Definite Flux-Continuous Full-Tensor Finite-Volume Schemes on Unstructured Cell-Centered Triangular Grids. *SIAM Journal on Scientific Computing*, 31, 1192–1220, 2009.

Proceedings of the 22nd UK Conference of the
Association for Computational Mechanics in Engineering
2 - 4 April 2014, University of Exeter, Exeter

SUMMATION RULES FOR HIGHER ORDER QUASI-CONTINUUM METHODS

***Claire E. Heaney, Lars A. A. Beex and Pierre Kerfriden**

Institute of Mechanics and Advanced Materials, Cardiff School of Engineering
Cardiff University, Queen's Buildings, The Parade, CARDIFF CF24 3AA Wales, UK.

*claire.e.heaney@gmail.com

ABSTRACT

This paper investigates two summation rules for the Quasi-Continuum (QC) method using higher order interpolation. Summation rules are the discrete equivalent of numerical quadrature used for continuous media. Summation plays a key role in the QC method by reducing the computational expense of assembling the discretised governing equations. A comparison is made between a pre-existing rule and a new rule. Results are shown for a planar beam lattice under uniaxial deformation.

Key Words: *the quasi-continuum method; structural lattice models; summation rules*

1. Introduction

Lattice models are frequently used to represent directly a material's discrete meso-, micro- or nano-structure. A broad range of materials has been modelled in this way, including textiles, paper, collagen networks and concrete. A review of micromechanical applications for lattice models can be found in [7]. Such models do not rely on phenomenologically derived continuum models to relate stresses to strains, but instead, use the small-scale lattice interactions to assemble the discretised governing equations. Atoms, bonds or fibres represented by the lattice models exist on such a small scale that the modelling of realistically sized domains is precluded. The Quasi-Continuum (QC) method was introduced by Tadmor *et. al.* [8] to alleviate this problem for (conservative) atomistic lattices. The QC method has been applied mainly to atomistic crystals, for example, investigating edge disolcations and fracture [8, 6]. However, Beex *et. al.* [4] have recently extended the QC method to apply to non-conservative structural lattice models, and have studied electronic textiles, and also bond failure in paper and textiles [3].

2. Structural lattice models and the Quasi-Continuum method

2.1. Lattice models

In this paper a planar lattice is used consisting of Euler-Bernoulli beams, hence there are both displacement and rotational degrees of freedom. For given boundary conditions, a solution for the lattice is found by minimising the total potential energy of the system. For a lattice of n points or nodes, there are $6n$ degrees of freedom, as the displacements and rotations can be three-dimensional. The assembly of the governing equations involves contributions from all the beams of the lattice. This computational expense, in addition to the large number of degrees of freedom, makes solving problems at an engineering scale impractical. The QC method was introduced to relieve the computational burden associated with lattice calculations.

2.2. The Quasi-Continuum method

The QC method retains the above lattice description for 'fully resolved regions' where the solution is of particular interest, for instance, in the vicinity of a crack. However, an approximation to the above description is introduced throughout the remainder of the domain. The approximation is built on two concepts: interpolation, which aims to reduce the number of degrees of freedom; and summation, which

aims to reduce the cost of assembling the governing equations. A subset of lattice points is chosen, which forms the vertices of a triangulation. Interpolation functions from finite element methodology are used to interpolate the displacements and rotations. Any lattice points inside triangles can then be condensed out of the system, thus reducing the $6n$ degrees of freedom. In the full lattice model, each beam contributes to the energy of the system and so must be visited in order to construct the governing equations. The QC method reduces this computational cost by selecting a subset of the beams, referred to as sampling beams, and assigning a weight to them so that they are able to represent other beams. The locations and weights of the sampling beams are determined by a summation rule. See Figure 1 for a typical QC triangulation. In the interpolated region of Figure 1, the beams from the underlying lattice are now entirely represented by the sampling beams (+). A detailed description of application of the QC method to structural lattices can be found in [1].

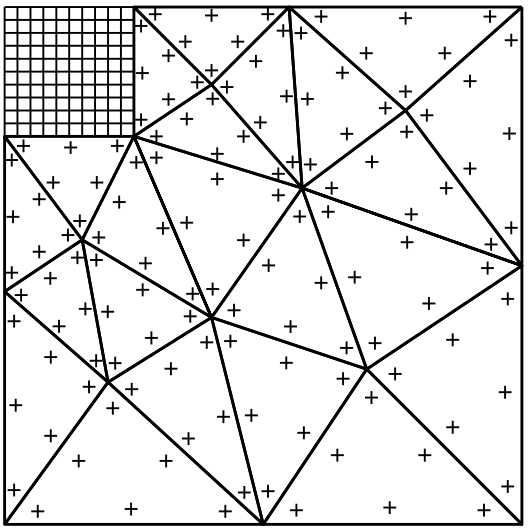

Figure 1: An example of a typical QC triangulation, with a fully resolved region (top left) where all the beams are used, and an interpolated region where only the sampling beams (+) are used.

3. Summation rules

The summation rule determines which beams are selected in the approximation of the governing equations and how many beams each sampling beam represents in the construction of the governing equations. In the literature most summation rules have been designed for atomistic lattices where linear interpolation is used. For structural lattices with linear interpolation, Beex *et. al.* [2] were able to relate the potential energy of the lattice to the interpolation and were therefore able to determine suitable locations for the sampling beams representing a structural lattice. However, Beex *et. al.* [1] observe that, for higher order interpolation functions, it is not clear how the interpolation relates to the potential energy of the interpolated lattice. Inspired by Gunzburger and Zhang [5] who used Gaussian quadrature for one-dimensional chains of atoms, Beex *et. al.* [1] based their summation rule on Gaussian quadrature and we follow this approach here. Given the cubic displacements and quadratic rotations of Bernoulli-Euler beams, four quadrature points should be sufficient, however Beex *et. al.* [1] reported that six quadrature points per triangle gave better results than four, so we use six points here.

3.1. Closest summation rule

First used in [1], the closest summation rule selects as a sampling beam, the beam that is closest to the Gauss point in the either the x or the y direction, as illustrated in Figure 2(a). The weight depends on the weight associated with the Gauss point and the number of beams that the sampling beams represent. For each triangle, beams that are parallel to the $x-$axis and are entirely or partly inside the triangle are located. Beams within a triangle interior are fully represented and contribute a weight of 1 and those aligned with a triangle edge or that cross a triangle edge are given a weight of 0.5. The weights of the beams in the x direction are then totalled and multiplied by the weight from Gaussian quadrature. The same is done for the beams orientated in the y direction.

When modelling a problem with the QC method, the triangles surrounding the fully resolved region are likely to be smaller than elsewhere in the interpolated region. This fact exposes two weaknesses of the closest summation rule. First, as the triangle size approaches the lattice spacing, the closest beam to one Gauss point may also be the closest beam to other Gauss points. In this case the stiffness matrix is not accurately integrated and can become ill-conditioned. The second problem encountered as the triangle size approaches the lattice spacing, is that sampling beams are more likely to straddle two triangles. Consequently the energy in a triangle is dependent not only on the nodal values of that triangle, but also on the nodal values of a neighbouring triangle, which could be described as a ‘non-local’ effect. To attempt to tackle these issues we introduce the mid-beam summation rule.

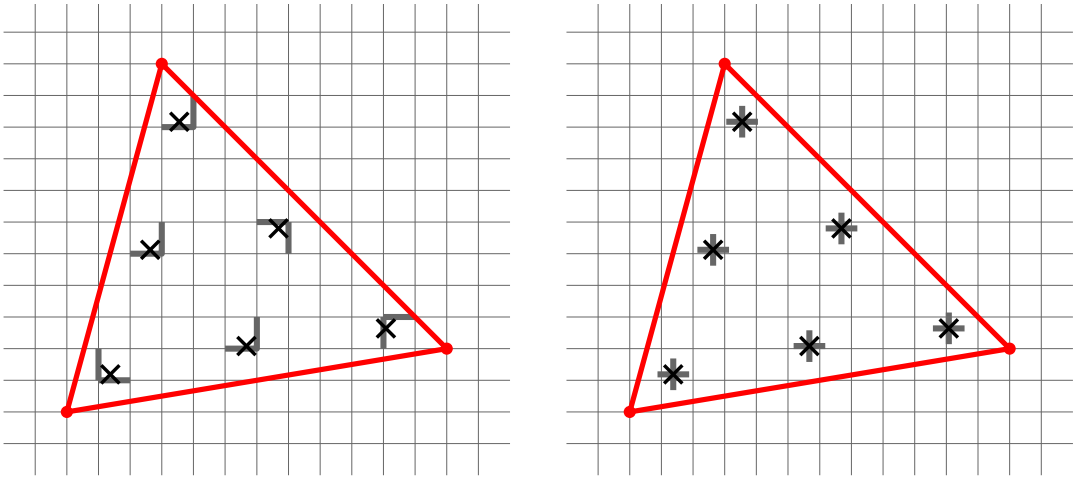

(a) The closest summation rule

(b) The mid-beam summation rule

Figure 2: Shown here is part of the entire beam lattice and one element from the triangulation. Horizontal beams are aligned with the $x-$axis and vertical beams are aligned with the $y-$axis. Gaussian quadrature points are indicated by crosses, and those beams designated as sampling beams are indicated by thicker lines.

3.2. Mid-beam summation rule

This rule is also based on Gaussian quadrature. A horizontal and vertical beam are centred at each Gauss point as shown in Figure 2(b). These beams do not necessarily coincide with beams of the underlying lattice. This is more akin in philosophy to homogenisation techniques, where a unique microstructural unit cell problem is associated with all the integration points of a macro-scale (discretised) problem. The weight of each beam is calculated by multiplying the area of a triangle by the Gauss point weight. In fact, this gives the same weight as for the closest rule, but is a more straightforward and efficient calculation as we do not have to consider all the beams. Unlike for the closest rule, the mid-beam summation rule will result in 12 unique sampling beams, so the ill-conditioning of the stiffness matrix will be avoided. The onset of the non-local effect is also delayed by this summation rule.

In this paper we investigate the error introduced by the use of these two summation rules. In the fully resolved region the lattice is modelled exactly by taking into account all the beams, so no summation rule is required. To focus on the error introduced by summation, the example in this paper uses a domain that has only an interpolated region and no fully resolved region.

4. Results

Results are presented for a beam lattice under uniaxial deformation. Vertical displacements are prevented along the upper and lower boundaries, but are free on the left and right boundaries. Horizontal displacements are zero and one on the left and right edges respectively, and are free along the upper and lower surfaces. Rotations in the x-y plane are free apart from the left edge where they are zero. Other rotations and displacements in the z direction are zero on the boundary. The domain size, given in millimetres, is $[0, 80] \times [0, 40]$; the Young's modulus is 1 kPa; and Poisson's ratio is 0.3. The beam spacing is 1 mm, the beam height and width are 1 mm and 0.1 mm respectively. Seven triangulations were used with the following numbers of triangles: 12, 36, 60, 132, 296, 398 and 470. Three simulations were run for each mesh. The first simulation uses all the beams when constructing the governing equations so no approximation is made in the summation. These results are used as a standard against which the other results are compared. The second simulation uses the closest rule and the third simulation uses the mid-beam summation rule. The energy stored in the beams is calculated for all three simulations; E_{all}, $E_{closest}$ and E_{mid} respectively. The following formula is used to evaluate the error introduced by the summation rules in the integration of the governing equations:

$$\text{error} = \frac{|\,E_{all} - E\,|}{E_{all}}\,, \tag{1}$$

where E is the energy stored by the beams using either the closest or the mid-beam summation rule. In Figure 3 the error given by equation (1) is plotted against the number of triangles for both sampling rules.

For the finest mesh, the closest summation rule resulted in such a high condition number that no solution was obtained. As the number of triangles increases the error also increases. This is due to sampling beams straddling two triangles thereby introducing a non-local effect, and, for the closest rule, as the triangles decrease in size relative to the lattice, the sampling beams may be non-unique and may also be further away from the Gauss point. The results clearly show that the error for the mid-beam summation rule is much less than that of the closest rule.

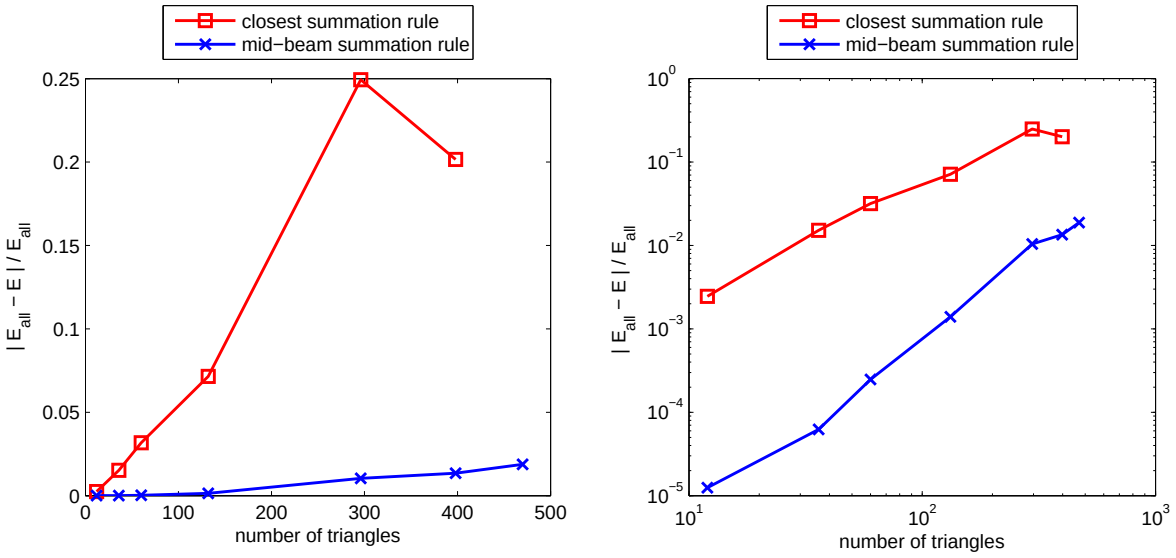

Figure 3: Error in energy for the closest and the mid-beam summation rules in a uniaxial test for several triangulations (with a log-log scale on the right).

5. Conclusions

A new summation rule for the QC method has been introduced. In a uniaxial deformation test, the new mid-beam summation rule performs much better than the previously existing closest summation rule. Future work will involve a more rigorous investigation of the new rule on problems with defects and with more demanding loading conditions in order to assess whether its early promise is fulfilled.

Acknowledgements

Pierre Kerfriden and Claire Heaney would like to acknowledge the financial support of the EPSRC grant "Towards rationalised computational expense for simulating fracture over multiple scales" (EP/J01947X/1). The authors would like to thank the reviewer for his/her useful comments.

References

[1] L.A.A. Beex, P. Kerfriden, T. Rabczuk and S.P.A. Bordas. Multiscale quasicontinuum methods for plate-like beam lattices. Submitted to *Computer Methods in Applied Mechanics and Engineering*, 2014.

[2] L.A.A. Beex, R.H.J. Peerlings and M.G.D. Geers. A quasicontinuum methodology for multiscale analyses of discrete microstructural models. *International Journal for Numerical Methods in Engineering*, 87, 701–718, 2011.

[3] L.A.A. Beex, R.H.J. Peerlings and M.G.D. Geers. A multiscale quasicontinuum method for lattice models with bond failure and fiber sliding. *Computer Methods in Applied Mechanics and Engineering*, 269, 108–122, 2014.

[4] L.A.A. Beex, R.H.J. Peerlings and M.G.D. Geers. A multiscale quasicontinuum method for dissipative lattice models and discrete networks, *Journal of the Mechanics and Physics of Solids*, 64, 154–169, 2014.

[5] M. Gunzburger and Y. Zhang. A quadrature-type approximation to the quasi-continuum method. *Multiscale Modeling & Simulation*, 8, 571–590, 2010.

[6] R. Miller, M. Ortiz, R. Phillips, V. Shenoy and E.B. Tadmor. Quasicontinuum models of fracture and plasticity. *Engineering Fracture Mechanics*, 61, 427–444, 1998.

[7] M. Ostoja-Starzewski. Lattice models in micromechanics. *Applied Mechanics Reviews*, 55, 35–60, 2002.

[8] E.B. Tadmor, M. Ortiz and R. Phillips. Quasicontinuum analysis of defects in solids. *Philosophical Magazine A*, 73, 1529–1563, 1996.

Proceedings of the 22nd UK Conference of the
Association for Computational Mechanics in Engineering
2 – 4April 2014, University of Exeter, Exeter

3D leap-frog scheme for electromagnetic scattering by dielectric media using unstructured meshes

A.Gansen[1]*, M. El Hachemi[2], S. Belouettar[2], O.Hassan[3] and K.Morgan[3],

[1,3]Civil and Computational Engineering Centre, Swansea University, Singleton Park, Swansea,SA2 8PP, U.K
[1,2]Modelling and Simulation Unit, Advanced Materials and Structures, Public Research Centre Henri Tudor, 29,avenue John F.Kennedy , L-1855 Luxembourg
*alex.gansen@tudor.lu

ABSTRACT

Despite many advantages, such as simplicity and low computational cost, the standard Yee algorithm [1] still needs to be improved in order to model objects of complex geometrical shape. In this work, we adapt three dimensional unstructured meshes to meet the necessary requirements and preserve second order accuracy, even close to objects of arbitrary shape. We present the requirements needed for a high quality primal Delaunay and dual Voronoi mesh. The performance of the leapfrog scheme, previously elaborated in [2], will be demonstrated for modelling the scattering of electromagnetic waves by a 3D lossy dielectric object in free space. The results of the simulation will be presented and compared with benchmark tests.

Keywords: *Unstructured, FDTD, Dielectric, lossy media*

1. Introduction

For industrial electromagnetic simulations, the standard Yee algorithm is often the favoured computational solution technique because of its simplicity, its low operation count and its low storage requirements. The main drawback of the classical Yee scheme is the loss of accuracy for objects of complex geometrical shape, due to the orthogonal Cartesian grid that is usually employed. To circumvent this problem, an equivalent unstructured mesh process is implemented on a primal Delaunay mesh and its orthogonal Voronoi dual graph. The difficulty with this method is the generation of meshes with the necessary quality conditions for both the Delaunay and the Voronoi graphs. The second order accuracy of the leapfrog algorithm is only fulfilled if each Voronoi face is a perpendicular bisector of the corresponding Delaunay edge and if each Delaunay face is a perpendicular bisector of the corresponding Voronoi edge. Furthermore, in the primal Delaunay graph, two or more adjacent tetrahedral elements should not share the same circumsphere, otherwise this mesh will be degenerate and the leapfrog algorithm will fail.
To guarantee a high quality mesh, an unstructured tetrahedral mesh is generated by using an iterative constrained centroidal Voronoi tessellation (CVT) [3]. The CVT relocates the generated nodes to the mass centroids of the corresponding Voronoi cells and a new Voronoi tessellation of the relocated nodes is produced.

2. Problem formulation

The formulation employs the integral form of Maxwell's equations [2]. For a three dimensional lossy dielectric medium, of permittivity ε, permeability μ, electric conductivity σ and magnetic conductivity σ_m. Ampère's and Faraday's law in the scattered field formulation are expressed as:

$$\frac{\partial}{\partial t}\int_A \boldsymbol{E}_{scat}d\boldsymbol{A} = \frac{1}{\varepsilon_{av}}\oint_{\partial A}\boldsymbol{H}_{scat}d\boldsymbol{l} - \frac{\varepsilon_{av}-\varepsilon_0}{\varepsilon_{av}}\frac{\partial}{\partial t}\int_A \boldsymbol{E}_{inc}d\boldsymbol{A} - \frac{\sigma_{av}}{\varepsilon_{av}}\int_A \boldsymbol{E}_{scat}d\boldsymbol{A} - \frac{\sigma_{av}}{\varepsilon_{av}}\int_A \boldsymbol{E}_{inc}d\boldsymbol{A} \quad (1)$$

$$\frac{\partial}{\partial t}\int_A \boldsymbol{H}_{scat}d\boldsymbol{A} = -\frac{1}{\mu_{av}}\oint_{\partial A}\boldsymbol{E}_{scat}d\boldsymbol{l} - \frac{\mu_{av}-\mu_0}{\mu_{av}}\frac{\partial}{\partial t}\int_A \boldsymbol{H}_{inc}d\boldsymbol{A} - \frac{\sigma_{m\,av}}{\mu_{av}}\int_A \boldsymbol{H}_{scat}d\boldsymbol{A} - \frac{\sigma_{m\,av}}{\mu_{av}}\int_A \boldsymbol{H}_{inc}d\boldsymbol{A} \quad (2)$$

and
Here, ∂A denotes the closed curve bounding of a surface A, d$\boldsymbol{A}$ is an element of surface area directed normal to the surface and d$\boldsymbol{l}$ is an element of curve length in the direction of the tangent to the curve. In addition, $\boldsymbol{E}_{inc}, \boldsymbol{H}_{inc}$ and $\boldsymbol{E}_{scat}, \boldsymbol{H}_{scat}$ represent the incident electric and magnetic fields and scattered electric and

magnetic fields respectively. The total fields are the sum of the corresponding incident and scattered fields. The material properties $\varepsilon, \mu, \sigma, \sigma_m$ are not constant and their values in free space differ from those in the dielectric. To take the boundary conditions into account we have to average these quantities at the dielectric interface leading to $\varepsilon_{av}, \mu_{av}, \sigma_{av}, \sigma_{m_{av}}$. The incident field represents a monochromatic plane wave illumination from the far field which has the form $E_{inc} = \boldsymbol{E}_0 \cos(\boldsymbol{k} \cdot \boldsymbol{r} - \boldsymbol{\omega t})$, where $\boldsymbol{E}_0$ is the electric field vector, $\boldsymbol{k}$ is the wavevector, $\boldsymbol{r}$ the position vector , $\boldsymbol{\omega}$ the angular frequency and $\boldsymbol{t}$ the time. From the known electric field the magnetic field may be determined using Faraday's law leading to the relation

$$\boldsymbol{H}_{inc} = \frac{1}{\eta} \hat{\boldsymbol{k}} \times \boldsymbol{E} \tag{3}$$

where $\hat{\boldsymbol{k}}$ is the unit wavevector and $\eta = \sqrt{\frac{\mu}{\varepsilon}}$ the impedance.

3. Discrete equations

The Yee algorithm is a low operation count solution method for Ampère's and Faraday's law that is implemented on two mutually orthogonal meshes. A primal tetrahedral mesh is generated using a Delaunay method [4]. The Voronoi diagram associated with this primal mesh is used to define a dual mesh. Each Voronoi face is a perpendicular bisector of the corresponding Delaunay edge and each Delaunay face is a perpendicular bisector of the corresponding Voronoi edge. N_e^D and N_e^V edges form the primal Delaunay and the dual Voronoi mesh respectively. For the scheme to be second order, the unknowns are located at the midpoints of these edges. The unknown at the node on the *i*th Delauany edge corresponds to the projection, $E_{scat,i}$, of the scattered electric field onto the direction of the edge. The unknown at the node on the *j*th Voronoi edge corresponds to the projection, $H_{scat,j}$, of the scattered magnetic field onto the direction of the edge. The discretization of Ampère's and Faraday's law leads to the equations

$$E^n_{scat,i} = \left(\frac{2\varepsilon - \sigma\Delta t}{2\varepsilon + \sigma\Delta t}\right) E^{n-1}_{scat,i} + \left(\frac{2\Delta t}{(2\varepsilon + \sigma\Delta t) A_i^V}\right) \left[\sum_{k=1}^{M_i^V} H^{n+0.5}_{scat,j_{i,k}} l^V_{j_{i,k}} - \sigma A_i^V E_{inc} - (\varepsilon - \varepsilon_0) A_i^V \frac{\partial}{\partial t} E_{inc,i}\right] \tag{4}$$

$$H^{n+0.5}_{scat,j} = \left(\frac{2\mu - \sigma_m\Delta t}{2\mu + \sigma_m\Delta t}\right) H^{n-0.5}_{scat,j} + \left(\frac{2\Delta t}{(2\mu + \sigma_m\Delta t) A_j^D}\right) \left[-\sum_{k=1}^{M_i^D} E^n_{scat,i_{j,k}} l^D_{i_{j,k}} - \sigma_m A_j^D H_{inc} - (\mu - \mu_0) A_j^D \frac{\partial}{\partial t} H_{inc,j}\right] \tag{5}$$

where Δt is the time step, the superscript *n* denotes an evaluation at time level $n\Delta t$, l_i^D represents the length of the *i*th Delaunay edge and A_i^V corresponds to the Voronoi face spanned by the Voronoi edges surrounding Delaunay edge i. Similarly, l_j^V represents the length of the *j*th Delaunay edge and A_j^D corresponds to the Delaunay face spanned by the Delaunay edges surrounding Voronoi edge *j*. The numbers $j_{i,k}, k = 1, \ldots, M_i^V$ refers to the M_i^V edges of the Voronoi face corresponding to the *i*th Delaunay edge, as illustrated in Figure 1. Similarly, the numbers $i_{j,k}, k = 1, \ldots, M_j^D$, refers to the the M_j^D edges of the Delaunay face corresponding to the *j*th Voronoi edge, as illustrated in Figure 2.

Figure 1
The *i*th Delaunay Edge , connecting Delaunay vertices $\boldsymbol{p_1}$ and $\boldsymbol{p_2}$, and the corresponding Voronoi face, formed by the Voronoi edges $\boldsymbol{j_{i,1}, \ldots, j_{i,6}}$

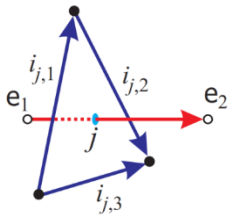

Figure 2
The *j*th Voronoi Edge , connecting Voronoi vertices $\boldsymbol{e_1}$ and $\boldsymbol{e_2}$, and the corresponding Delaunay face, formed by the Delaunay edges $\boldsymbol{i_{j,1}, \ldots, i_{j,3}}$. The 3 Delauany edges may represent on face of a

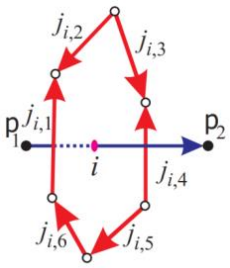

4. Unstructured mesh strategy

All Voronoi and Delaunay edge lengths should be bounded from below, as the update equations are not valid if some edges have length zero. Furthermore, the centre of the circumsphere should lie inside each Delaunay tetrahedron. All Delaunay and Voronoi edges should be bounded from above by a value that is not significantly greater than $\boldsymbol{\delta}$ (the length of cubes forming the Cartesian mesh). If possible, any deviation in the location of the

midpoint of a Voronoi edge from the actual point of intersection with the corresponding Delaunay face should be minimized. Finally, any deviation in the location of the circumcentre of a tetrahedron from its centroid should be minimized. The first two criteria are the more important and the last often cannot be exactly satisfied.

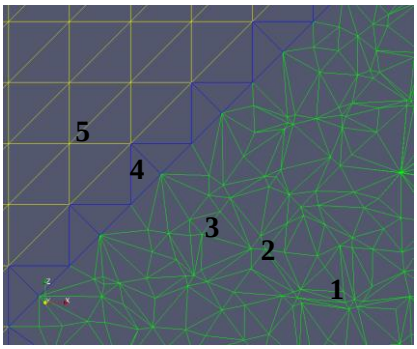

Figure 3 The surface of an arbitrary object, in this case a sphere is approximated by tetrahedral. (1) tetrahedra inside sphere, (2) boundary of sphere (3) tetrahedra outside sphere. After several layers of tetrahedra one layer of pyramids (4) links the tetrahedra to the hexahedra (5). This procedure reduces the computational costs compared to a purely tetrahedral mesh

Traditional automatic unstructured mesh generation methods, such as the advancing front technique [5] and the Delaunay triangulation [4], or their combination [6], are not designed to guarantee the requirements set out above. The corresponding Voronoi diagram is often highly irregular and can include some very short Voronoi edges. This means that regularity of the edge lengths of the dual mesh and the absence of bad elements cannot be guaranteed. Methods based on swapping, reconnection and smoothing [7] used for improving the mesh quality cannot guarantee a suitable mesh [8]. To circumvent these problems, the approach adopted is to construct the unstructured mesh around the object surface by employing a combination of a CVT (Central Voronoi tessellation) [3] with information provided from the ideal mesh. A CVT is a Voronoi tessellation whose generating points are the centroids (centres of mass) of the corresponding Voronoi regions. For the mesh optimization, the requirement that a dual edge must be a bisector of the corresponding Delaunay edge is relaxed. This allows the displacement of the corresponding dual mesh vertex to a point which still ensures orthogonality between two grids and which lies inside the corresponding primal element.

4. Simulation Results

The algorithm is applied for the simulation of scattering of an incident plane wave by a dielectric sphere of diameter 2λ and characterised by material properties $\varepsilon_r = 2$ and $\mu_r = 2$. The mesh is formed out of 478,772 cells in total, 249,968 tetrahedra, 5,804 pyramids and 223,000 hexahedra. The surface of the sphere is formed by 6,674 triangles and the PML is made out of 10 layers of hexahedra. Steady state was reached after 30 cycles. The total time for the calculations on a single core was 22 min. Figure 4 and Figure 5 show the computed the electric and magnetic field distributions respectively.

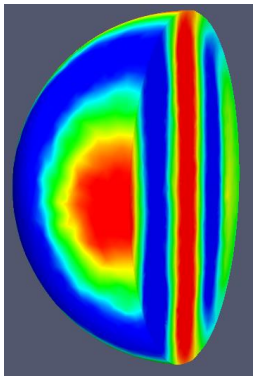

Figure 4

Scattering by a Dielectric Sphere of electric length 2λ with an electric permittivity of 2, view of the E_2 component of the electric field vector.

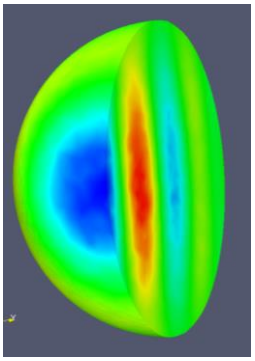

Figure 5

Scattering by a Dielectric Sphere of electric length 2λ with an electric permittivity of 2, view of the H_1 component of the magnetic field vector.

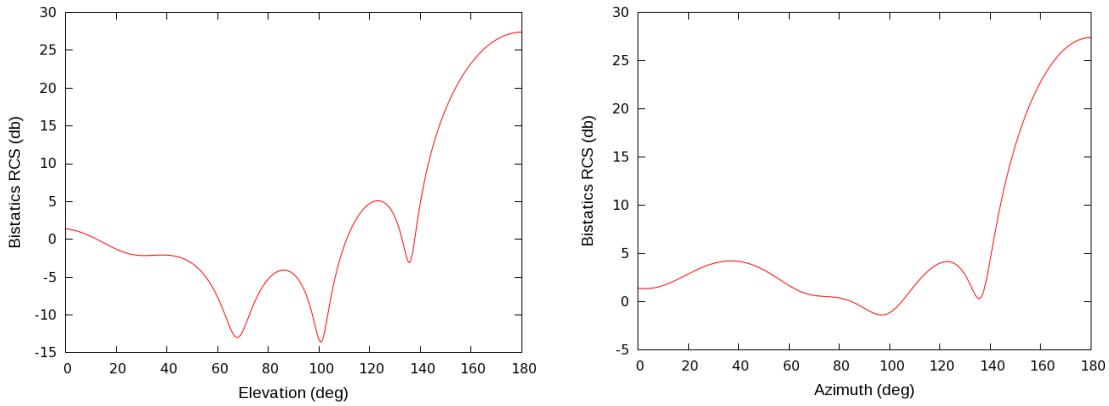

(a) (b)

Figure 6. Scattering by a dielectric sphere of electric length 2λ: (a) RCS distribution in the plane $\theta = 0$ and (b) in the plane $\phi = \pi/2$

5. Conclusion

A time domain solution procedure for electromagnetic scattering simulations has been developed in which a Yee algorithm is used on appropriately generated unstructured tetrahedral meshes, within the scatterer and in a region of free space immediately adjacent to the scatterer, and the free space is filled with hexahedral elements. The example that has been solved indicates that the accurate simulation of electromagnetic scattering problems may be achieved, with an appropriate mesh. The advantages of using this method are (a) the reduction in the storage requirements over the conventional finite element approach; (b) the fast computation that results from the use of the leap frog Yee scheme; (c) the fact that the method allows straightforward modelling of multi-material and complex geometries. A full assessment of the accuracy of the approach, for more challenging examples, is currently underway.

References

[1] K. Yee, "Numerical solution of initial boundary value problems involving Maxwell's equations in isotropic media," *IEEE Transactions on Antennas and Propagation*, no. 14, pp. 302-307, 1966.

[2] Z. Xie, O. Hassan and K. Morgan, "Tailoring unstructured meshes for use with a 3D time domain co-volume algorithm for computational electromagnetics," *International Journal for Numerical Methods in Engineering*, no. 87, pp. 48-65, 2011.

[3] Q. Du, V. Faber and M. Gunzberger, "Centroidal Voronoi tessellations: applications and algorithms," *SIAM Review*, no. 41, pp. 637-676, 1999.

[4] N. Weatherill and O. Hassan, "Efficient three-dimensional Delaunay triangulation with automatic point creation and imposed boundary constraints," *International Journal for Numerical Methods in Engineering* , no. 37, pp. 2005-2040, 1994.

[5] J. Peraire, M. Vahdati, K. Morgan and O. Zienkiewicz, "Adaptive remeshing for compressible flow computation," *Journal of Computational Physics*, no. 72, pp. 449-466, 1987.

[6] P. Frey, H. Borouchaki and P.-L. George, "3D Delaunay mesh generation coupled with an advancing-front approach," *Computer Methods in applied Mechanics and Engineering*, no. 157, pp. 115-131, 1998.

[7] O. Hassan and E. Probert, "Grid control and adaptation," *Handbook of Grid Generation*, pp. 35.1-35.29, 1999.

[8] I. Sazanov, D. Wang, O. Hassan, K. Morgan and N. Weatherill, "A stitching method for the generation of unstructured meshes for use with co-volume solution techniques," *Comput.Methods appl. Mech. Engrg 195*, pp. 1826-1845, 2006.

[9] R. Holland, "Pitfalls of staricase meshing," *IEEE Transactions on Electromagnetic Compatibility*, no. 35, pp. 434-439, 1993.

Proceedings of the 22nd UK Conference of the
Association for Computational Mechanics in Engineering
2 - 4 April 2014, University of Exeter, Exeter

WAVE MODELING USING ENRICHED FINITE ELEMENTS

***K. Christodoulou[1], M.S. Mohamed[1] and O. Laghrouche[1]**

[1]Institute for Infrastructure and Environment, Heriot-Watt University, Edinburgh EH14 4AS, UK

*KC328@hw.ac.uk

ABSTRACT

An enriched finite element method is presented to solve wave scattering problems governed by the Helmholtz equation. The basis functions are constructed by multiplying the polynomial interpolation functions by either plane waves or radial waves. Alternatively, a combination of both plane and radial waves is used. This approach is used to solve two practical problems including the diffraction of an incident plane wave by a circular cylinder or by a square obstacle. In the first case, the obtained results are compared with the analytical solution whereas in the second case a classical finite element solution is used for comparison. It is shown that both plane wave and radial wave enriched elements lead to good quality solutions with significant reduction of the required number of degrees of freedom, in comparison to polynomial based finite elements.

Key Words: *Helmholtz equation; finite elements; plane waves; radial waves; diffraction problem*

1. Introduction

This paper deals with efficient numerical modeling of 2D Helmholtz problems using the Partition of Unity Finite Element Method (PUFEM). The feature of this idea is that analytical solutions to the Helmholtz equation are used to enrich the solution space. These are usually in the form of plane waves. This technique has been very successful in achieving good accuracy results and reducing the number of degrees of freedom in comparison to the standard finite elements.

The partition of unity finite element method was first proposed by Melenk and Babuška [3] and used to solve the Helmholtz equation in the case of a progressive plane wave. Later, the method has been applied to a range of diffraction problems in two and three dimensions [6, 2]. It has also been extended to elastic wave problems [1]. The use of radial waves as enriching functions was investigated in [5] and were found to be more effective than plane waves in the far field. The use of radial waves in the form of Bessel functions was also tried in the framework of the Ultra Weak Variational Formulation (UWVF)[4] in which a singular Helmholtz problem was efficiently solved using combinations of plane waves and Bessel functions.

This work aims at long term to effectively model wave scattering by corners. Such problems present singularities and usually need fine mesh refinements to capture the solution. The use of radial wave enrichment, rather plane waves, seem to be effective in modelling these singularities. However, element assembling remains a burden because of the intensive numerical integration. In this paper, the use of both plane wave and radial wave enrichments is used for modelling the diffracted potential by a smooth circular scatterer. Then wave enriched finite elements are used to model the diffraction of a plane wave by a rigid square. In the first case, the accuracy of the solution is assessed by computing the L_2-norm error via the use of the available analytical solution. For the second case, the solution is compared with the standard FEM results on the boundary of the square.

2. Plane wave diffracted by circular cylinder

Figure 1 (left) shows an incident horizontal plane wave encounters a rigid object is modified and then radiates away to infinity. The scattered wave potential $\phi(x, y)$, which satisfies the two dimensional Helmholtz equation

$$\nabla^2\phi + k^2\phi = 0, \tag{1}$$

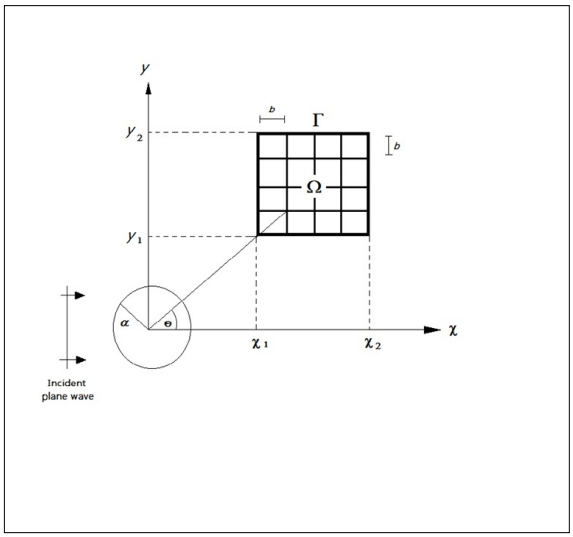

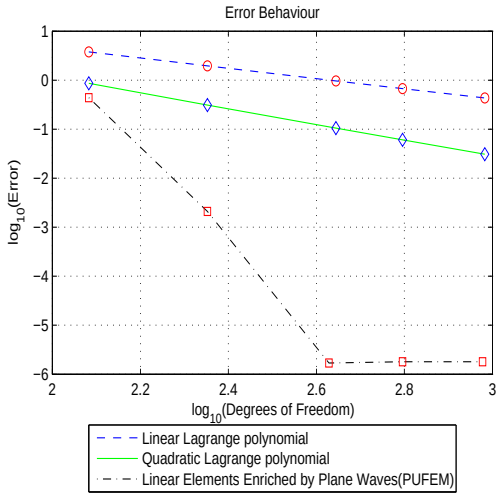

Figure 1: Schematic diagram of the problem (left). Behaviour of the L_2-norm error for linear, quadratic and enriched finite elements (right).

is studied in the domain Ω. Note that ∇^2 is the Laplacian operator, $k = \omega/c$ is the wave number of the considered problem and c is the wave speed. We assume also that the potential satisfies the following Robin boundary condition

$$\frac{\partial \phi}{\partial n} + \mathrm{i}k\phi = g \qquad \text{on} \quad \Gamma, \tag{2}$$

where g is the boundary condition and $\underline{\mathbf{n}}$ is the outward normal to the line boundary Γ. This problem has an analytical solution expressed as a series of Hankel functions and it is imposed on the boundary Γ through the Robin boundary condition given in expression (2). We use the weighted residual scheme by multiplying equation (1) by the weighting function $W(x, y)$ and integrate over the domain Ω such that

$$\int_\Omega W(\nabla^2\phi + k^2\phi)\, d\Omega = 0. \tag{3}$$

Integrating by part the above equation and replacing the normal derivative of the function ϕ by its expression deduced from expression (2), the system of equations to solve is then

$$\int_\Omega (\underline{\nabla W} \cdot \underline{\nabla \phi} - k^2 W\phi) d\Omega + \mathrm{i}k \int_\Gamma W\phi d\Gamma = \int_\Gamma W g d\Gamma. \tag{4}$$

The domain Ω is meshed into n-node finite elements. Within each element the potential is interpolated using the usual Legendre polynomials and enriched by both plane waves and radial waves in the following form

$$\phi = \sum_{i=1}^{n} N_i \left(\sum_{j=1}^{m_p} A_i^j e^{\mathrm{i}k\boldsymbol{r}\cdot\boldsymbol{d}_j} + \sum_{l=1}^{m_r} B_i^l J_l(kr) e^{\mathrm{i}l\theta} \right), \tag{5}$$

where (r, θ) are the polar coordinates, $\boldsymbol{d}_j$ is a given direction in the plane, N_i is the Legendre polynomial at node i and $J_l(kr)$ is the Bessel function of first kind and of order l. The unknowns of the problem are no more the nodal potentials but the coefficients A_i^j and B_i^l of the enriching functions.

We solve the problem stated above by the standard polynomial based finite elements and wave enriched finite elements. In the case of polynomial based finite elements, linear and quadratic elements are considered. To ensure accurate simulation each wavelength must be discretized into around 10 nodal points (*rule of thumb*). In general, this approach leads to huge numbers of nodes for problems with increasing wave number k and because of pollution error the mesh grid must be even finer. Various approaches have been developed to get around the requirement cited above. One of them is to use higher order polynomial basis functions for the solution space.

For this specific example, the wave number $k = 2\pi$. Figure 1 (right) shows the L_2-norm error for the cases of linear and quadratic elements. It is clear that increasing the number of degrees of freedom, by refining the mesh grid, leads to exponential decrease of the error. Moreover, for the same number of degrees of freedom, using quadratic elements leads to better quality results in comparison to the results of the linear

elements.
Using enriched elements, with only plane waves ($m_p \neq 0$ and $m_r = 0$), leads to even better quality results. In this case, the mesh grid remains very coarse while the number of enriching plane waves is increased. A very sharp decrease of the error is noticed, in comparison to the polynomial finite elements, up to a certain level and then the error stagnates. This was shown in past work [1] to be caused by the ill conditioning of the plane wave enrichment approach.
In the next series of numerical results the considered computational domain Ω is placed in three differ-

Table 1: L_2-norm errors for different combinations of plane waves and radial waves

m_p	m_r	$1 \leq x, y \leq 5$	$6 \leq x, y \leq 10$	$11 \leq x, y \leq 15$
16	0	0.00733	0.00672	0.00460
14	2	0.01566	0.00132	0.06246
12	4	0.00619	0.00027	0.00010
10	6	0.03327	0.00922	0.00180
8	8	0.00646	0.02083	0.12690
6	10	0.03771	0.00109	0.00065
4	12	0.68439	0.00022	0.00027
2	14	0.37392	0.00112	0.00028
0	16	0.53989	0.01083	0.00066

ent locations which represent the near field $1 \leq x, y \leq 5$ intermediate field $6 \leq x, y \leq 10$ and far field $11 \leq x, y \leq 15$. It is meshed into linear finite elements enriched by a combination of m_p plane waves and m_r radial waves such that the total number $m = m_p + m_r$ of basis functions is chosen to be 16. The L_2-norm errors for all cases of enrichments are shown in Table 1 for the case of wave number $k = 4\pi$.
First, for the near field location, it is obvious from Table 1 that the plane wave enrichment performs better than the radial wave enrichment. In deed, as the number of plane wave decreases to add radial waves instead, the L_2 error increases. This is noticed again in the case of intermediate field in spite of the better quality results, in comparison to near field case. For the far field case, however, the results are of very good quality and the radial wave enrichment is shown to perform better than the plane wave enrichment. This is probably due to the fact that the diffracted potential propagates away to infinity radially and hence radial waves are more suitable as enrichment functions.

3. Plane wave diffracted by square object

The second example deals with the diffraction of a plane wave by a rigid square object of boundary Γ_1. Applying the finite element procedure of expression (3) to this problem leads to

$$\int_\Omega (-\underline{\nabla W} \cdot \underline{\nabla \phi} + k^2 W \phi) d\Omega - \int_{\Gamma_1} W \underline{\nabla \phi} \cdot \underline{n} \, d\Gamma + \int_{\Gamma_2} W \underline{\nabla \phi} \cdot \underline{n} \, d\Gamma = 0, \tag{6}$$

where the computational domain is Ω is bounded by the internal boundary Γ_1 and the external boundary Γ_2. In this the incident wave is totally reflected and so the Neumann boundary condition is applied

$$\frac{\partial \phi}{\partial n} = -\frac{\partial \phi^i}{\partial n}, \tag{7}$$

applies on Γ_1. Here, ϕ^i and ϕ are the incident and scattered waves, respectively. The boundary Γ_2 is assumed to be placed far enough from the diffracting object to consider that the scattered wave is propagating radially. A simple radiation condition is then used

$$\frac{\partial \phi}{\partial n} + \frac{1}{2r}\phi - \mathrm{i}k\phi = 0. \tag{8}$$

Introducing the boundary conditions (7) and (8) into equation (6), the problem to solve is then

$$\int_\Omega (\underline{\nabla W} \cdot \underline{\nabla \phi} - k^2 W \phi) d\Omega + \int_{\Gamma_2} W (\frac{1}{2r} - \mathrm{i}k)\phi d\Gamma = \int_{\Gamma_1} W (\frac{\partial \phi^i}{\partial n}) \, d\Gamma \tag{9}$$

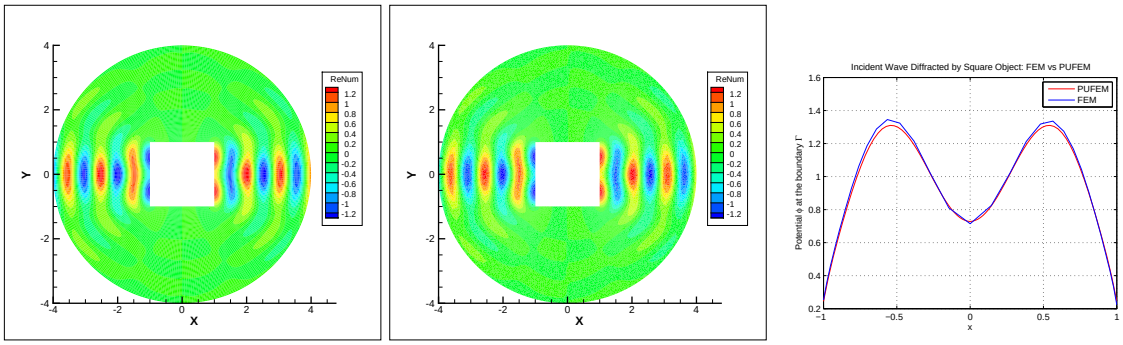

Figure 2: Real part of the diffracted potential: FEM results (left), PUFEM results (middle), PUFEM and FEM results around the scattering square 9right).

This problem does have an analytical solution and so the PUFEM results are compared to those obtained using the polynomial based FEM for $k = 2\pi$. In the case of PUFEM, 16 quadratic elements are taken around the square scatterer and to approximate the wave potential 18 plane waves are used as enrichment functions. For the case of FEM, 9568 triangular linear elements are used. Figure 2 (left and middle) shows contour plots of the real part of the scattered potential which look very similar and Figure 2 (right) shows the real part of the scattered potential around the scatterer obtained by PUFEM and FEM and, overall, the results look very similar. It is worth noting that 4926 degrees of freedom were used in the FEM results while for the PUFEM only 1440 degrees of freedom were used.
In this case of scattering problem with a square body, it is known that they present singularities at the corners. Usually, in the case of FEM, the mesh is over refined around the corners to capture the solution. It is planned to investigate the performance of the PUFEM using either plane waves or radial waves or even a combination of both to deal with such problems.

4. Conclusions

In this work, solutions to wave problems governed by the Helmholtz equation are approximated either by the standard polynomial based finite element method or by enriched finite elements. For the latter case, field enrichment is carried out by using either plane waves, radial waves or a combination of both. For the problems dealt with above, it is clear that the PUFEM leads to better quality results in comparison to low order FEM elements. Regarding the enriched version and for a scattering problem, it was concluded that plane wave enrichment performs better in the near field while radial wave enrichment leads to better quality results in the far field.
An attempt is made here to solve a scattering problem with a rigid square. This problem's solution presents singularities at the corners. The aim is compare the performance of the PUFEM against the FEM which usually requires further mesh refinement around the corners.

References

[1] A. El-Kacimi and O. Laghrouche. Numerical modelling of elastic wave scattering in frequency domain by the Partition of Unity Finite Element Method. *Int. J. Numer. Methods Engrg.*,77, 1646–1669, 2009.

[2] E. Perrey-Debain, O. Laghrouche, P. Bettess, J.Trevelyan. Plane wave basis finite elements and boundary elements for three dimensional wave scattering. *Phil. Trans. R. Soc. Lond. A.*, 362, 561–577, 2004.

[3] J.M. Melenk and I. Babuška. The Partition of Unity Finite Element Method: Basic Theory and Applications, *Comput. Meths. Appl. Mech. Engrg.*, 139, 289–314, 1996.

[4] L. Luostari, T. Huttunen, P. Monk. The ultra weak variational formulation using Bessel basis functions. *Commun. Compu. Phys.*, 11(2), 400–414, 2012.

[5] O. Laghrouche and MS. Mohamed. Locally enriched finite elements for the Helmholtz equation in two dimensions. *Computers and Structures*, 88, 1469-1473, 2010;

[6] O. Laghrouche and P. Bettess. Short wave modelling using special finite elements. *Journal of Computational Acoustics*, 8(1), 189–210, 2000.

Proceedings of the 22nd UK Conference of the
Association for Computational Mechanics in Engineering
2 – 4April 2014, University of Exeter, Exeter

A COUPLED HYDRO-MECHANICAL ANALYSIS OF SLOPE INSTABILITY PROCESSES IN SAN LEO (RN, ITALY)

***L. Nguyen-Tuan [(a)], *M.C. Spreafico [(b)], M. Datcheva [(c)], L. Borgatti[(b)] and T. Schanz [(a)]**
[(a)] Chair for Foundation Engineering, Soil and Rock Mechanics, Ruhr-Universität Bochum, Germany
[(b)] Department of Civil, Chemical, Environmental and Materials Engineering DICAM, Alma Mater Studiorum Università di Bologna, Italy
[(c)] Institute of Mechanics, Bulgarian Academy of Sciences, Sofia,Bulgaria

*long.nguyentuan@rub.de and margherita.spreafic2@unibo.it

ABSTRACT

The calcarenite rock slab, on which the medieval town of San Leo is situated, is severely tectonized and crossed by a number of joint sets and faults. It is affected by lateral spreading instability processes associated with rock falls and topples. The underlying clayey substratum is involved in movements, like earth flows and slides. In the present work these phenomena are analysed within the framework of unsaturated soil mechanics. A coupled hydro-mechanical model employing viscoplasticity (BBM-VP) is adopted herein to numerically simulate the landslide processes in San Leo region. The model allows simulating the hardening and softening processes in the rock material due to hydraulic loading and unloading, and the shear strength change with degree of saturation. The results are then compared with those obtained for the same problem but employing different constitutive model for explaining the viscoplastic behaviour that is independent on suction and based on Drucker-Prager plasticity. The differences of the two conceptual model approaches are analysed.

Keywords: *landslides, BBM, suction, unsaturated soil, San Leo, Italy*

1. Introduction

Rock spreading in brittle formations overlying ductile terrains is a well-known process of instability in the clay-rich hillslopes of the northern Apennines of Italy. It mainly consists of creep and slow movements of the clayey materials, which induce progressive dismembering of the overlying rock slabs [8]. The town of San Leo rises on a rock slab, affected by widespread instability phenomena. Within this study a cross-section in the north side of this slab was analyzed. It was chosen for a number of reasons: i) the last important landslide event occurred in this area; ii) data from field observations are available; iii) at this stage of the research it can be acknowledged that in the local geological and geomorphological context is representative for the whole rock slab.
In the literature many examples of slow moving landslides have been modelled using a viscous component in the formulation of the strain rate. However, in this type of analysis, it is difficult to distinguish between movements related to water infiltration and displacements related to a viscous component in the strain rate, as both processes occur simultaneously. Moreover, other mechanisms may lead to a dissipation of energy during the moving of the earth mass, which are not related to a viscosity component in the strain rate. This paper focuses on the analysis of slow movement initiation in the clayey substratum under rainfall infiltration as a precursor of earthflows. The phenomenon is analysed in the framework of unsaturated soil mechanics, applying coupled hydro-mechanical analysis. Two constitutive models are used in competitive way. The first model is the BBM-VP whose feature is the dependence of the viscoplastic constitutive functions on suction. The second viscoplastic model is based on Drucker-Prager plasticity model with viscoplastic criterion and potential considered not dependent on suction. The results after the application of the two models are then compared and the differences in the predictions of the two models are analysed.

2. Typical Slope Instability Phenomena

The town of San Leo was built on a calcarenite and sandstone slab, which is crossed by several joint sets and faults. It is affected by lateral spreading with associated rock falls and topples, partly

developing along pre-existing discontinuities. Moreover, the underlying clay-shales and loose deposits are involved in earthflows.
The high deformability contrast between the slab and the underlying clay-shale drives the instability of the whole area [3,5]. Together with the structural setting of the slab, a further instability predisposing factor is the groundwater flow path developing inside the plate (Fig. 1). The groundwater flow is driven by discontinuity networks, which induce a rather high secondary permeability within the calcarenite slab. This leads to the formation of ephemeral springs at the base of the cliffs, near the contact with the almost impermeable substratum. The springs promote the remoulding of the basal clay-shale, leading, together with creep and subsequent flows, to the undermining of the foot of the rock slab. These processes can cause the progressive opening and widening of fractures in the rock masses which, in turn lead to higher discharge rates in the springs.
During the most recent and notable landslide event, occurred on 11th May 2006, a rock fall affected the northern side of the slab, suddenly detaching from the vertical cliff. The undrained loading at the top of the clay-shale slope triggered an earthflow which reached velocities in the order of 4.2 cm/h.

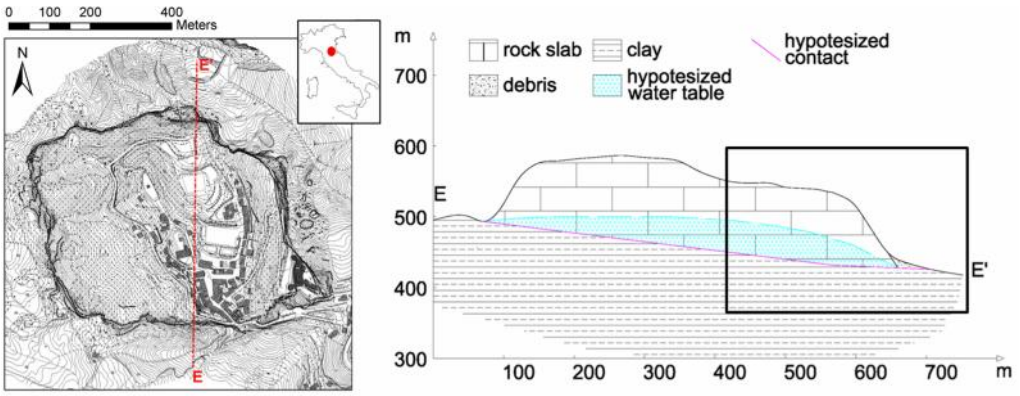

(a) (b)

Fig.1 (a) location of the study area (red point) and trace of the EE' section. (b) South-North EE' section of San Leo slab; the contact between the slab and the substratum under the plate and the water table are sketched; in the black box the location of analyzed sector is reported.

3. Modelling Analysis and Results

Mechanical constitutive model: The mechanical models considered here are elasto-viscoplastic models for unsaturated soil based on the Perzyna viscoplasticity concept [9]. Following the Perzyna viscoplastic concept, the total strain rate is assumed to be a sum of the elastic ($\dot{\boldsymbol{\varepsilon}}^{e}$) and viscoplastic ($\dot{\boldsymbol{\varepsilon}}^{vp}$) strain rates. The formulation for the constitutive modelling is based on the use of pair stress state variables, namely the net stress and the suction (s). Suction is zero when the soil pore system is filled with only fluid. Therefore, the stress variables are suction and net stress for unsaturated condition and effective stress in saturated state. The elastic part is related to the net stress $\boldsymbol{\sigma}'$ through the generalized Hooke's law.
The two viscoplastic models considered here are implemented in the FE program CODE_BRIGHT [4,6,7]. The first one is a linear elastic viscoplastic model for unsaturated soil based on the Barcelona Basic Model [2], named BBM-VP model. The second model is a linear elastic viscoplastic model based on the Drucker-Prager failure criterion, named DP-VP model.
In BBM-VP model yield surfaces F is given according to [1].

$$F(q,p,s) = a\frac{1}{3}q^2 - M^2\gamma\left(p'+p_s\right)\left(p_o - p'\right) \qquad (1)$$

where M determines the slope of the critical state line and it depends on suction according to [2], p_s and p_o are the tensile stress limit and pre-consolidation pressure, p' is the net (effective) stress, q is the deviatoric stress, a and γ are model parameters.

In DP-VP, the yield surface F and the plastic potential G are given by:

$$G = F = q - Mp' - c'\beta_c \tag{2}$$

In this case M and β_c are calculated by providing the best fit to the Mohr-Coulomb hexagon and φ' and c' are the effective angle of friction and the cohesion defining the Mohr-Coulomb failure envelope at saturated condition.

Hydraulic flow law: The advective flow of the water phase is described via the generalized Darcy's law:

$$\mathbf{q}_l = -\frac{\mathbf{k}k_{rl}}{\mu_l}\left(\nabla P_l - \rho_l \mathbf{g}\right) \tag{3}$$

where μ_l is the dynamic viscosity of the pore liquid, g is the gravity acceleration, ρ_l is the liquid density. The tensor of intrinsic permeability **k** is a tensor defined depending on porosity via the Kozeny's model. The relative permeability (k_{rl}) is derived employing the Mualem-van Genuchten model [10].

Numerical model of San Leo landslide:

The slope instability phenomena in San Leo are simplified and the geometry of the adopted model is shown in Fig. 2. The model in Fig 2 is based on the description of the test site given in section 2. The problem is analysed in two phases. In the first phase, the infiltration is analysed considering water flow through non-deformable porous media – the unsaturated rock and the clay-shale material. In the second phase the coupled hydro-mechanical approach is used to analyse the stress-strain behaviour during the infiltration process. For the second phase, the hydraulic boundary conditions correspond to the water pressure obtained in the first phase. The whole slope is subjected to consolidation in order to simulate closely the current conditions of the clay-shale formation in the first stage. Afterwards the infiltration step is simulated in the second stage.

In the first phase the analysis shows that the rain falling on the top of the rock slab permeates into the rock slab due to its weight and the capillary force. Due to the large difference in the permeability of the rock and the clay-shale formation, the groundwater table develops in the rock slab (Fig. 3). This way the water is then drained throughout the foot of the rock wall.

When analysed by BBM-VP model, during water infiltration in the second phase, the model shows differential displacements between the area beneath the rock slab (point A) and the region on the clay-shale slope close to the rock slab (point B). On the contrary, there is no significant change of vertical displacements during water infiltration when analysed by DP-VP model. The displacements are due to the increase of water content that causes an increase of the soil weight. Stress distribution obtained by BBM-VP model demonstrates that the distribution of vertical pressure is influenced by infiltration processes (Fig. 4b). The rather high vertical stress values which are observed close to the boundary of the slab indicate the danger of high shear force which may trigger earthflow beside the other factors.

From the above discussion it can be concluded that the instability phenomena in San Leo should be analysed via a coupled problem formulation. It is also demonstrated that the coupled hydro-mechanical viscoplastic model allows better explaining the mechanical behaviour of the considered clay-shale slope.

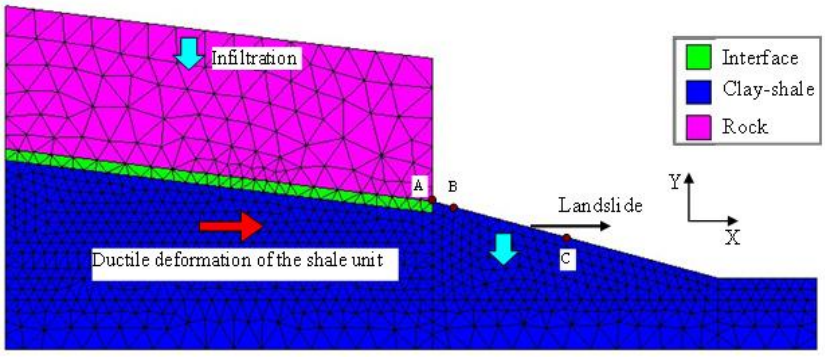

Fig. 2: A conceptual model of instability problems in San Leo slope

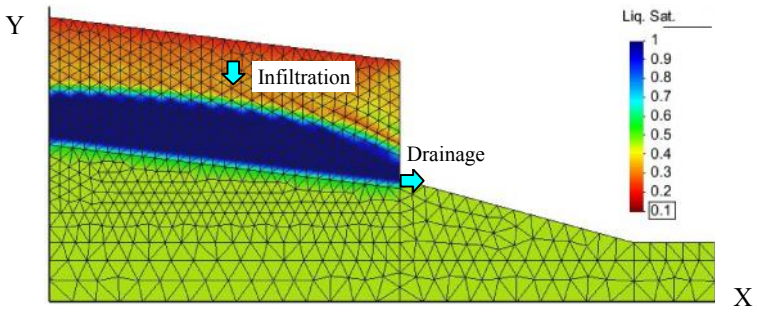

Fig. 2: Phase 1 - Degree of saturation after 4 days of rainfall

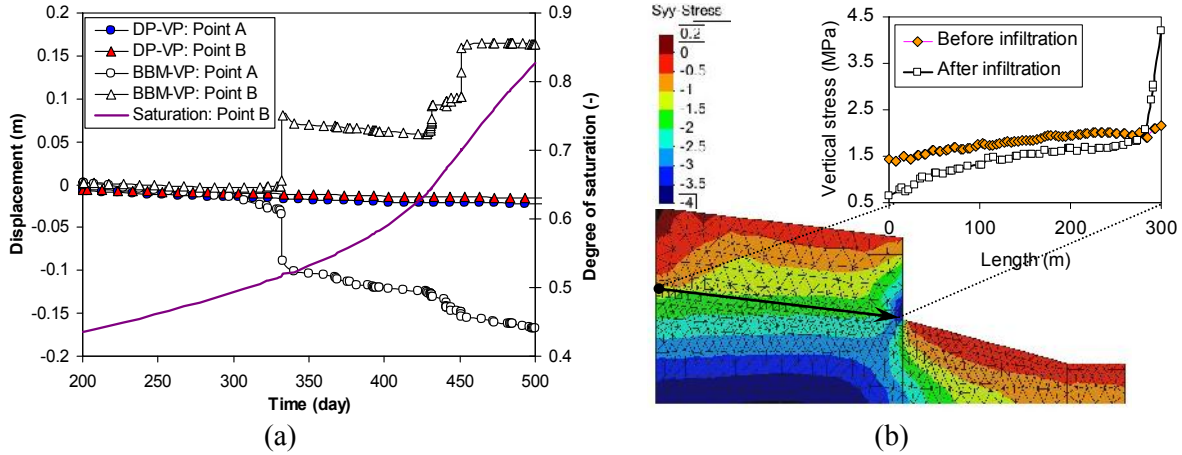

(a) (b)

Fig. 4: Phase 2 - (a) displacement along Y axis and water saturation, (b) Vertical stress at the interface.

References

[1] Alonso, E.; Gens, A. & Josa, A. A constitutive model for partially saturated soils. *Géotechnique*, 40(3), pp. 405-430, 1990.

[2] Alonso, E. E., Olivella, S. and Pinyol, N. M. A review of Beliche Dam, *Géotechnique*, 55(4), pp. 267–285, 2005.

[3] Casagli N. Fenomeni di instabilità in ammassi rocciosi sovrastanti un substrato deformabile: analisi di alcuni esempi nell'Appennino settentrionale, *II Convegno Nazionale dei Giovani ricercatori di Geologia Applicata, Viterbo*, 1994.

[4] CODE_BRIGHT user's guide, Universitat Politècnica de Catalunya, Barcelona, Spain, 2009.

[5] D'Ambra S., Giglio G., Lembo-Fazio A. Interventi di sistemazione e stabilizzazione della Rupe di San Leo. *10° Congress INTERPRAEVENT 2004, Riva del Garda*, 2004.

[6] Olivella S, Gens A, Carrera J, Alonso EE. Numerical formulation for a simulator (CODE_BRIGHT) for the coupled analysis of saline media. *Engineering Computations*, 13(7), pp. 87–112, 1996.

[7] Olivella S. and Gens A. Vapour Transport in Low Permeability Unsaturated Soils with Capillary Effects. *Transport in Porous Media*, 40, pp. 219–241, 2000.

[8] Pasuto A. and Soldati M., 7.25 Lateral Spreading, *In Treatise on Geomorphology*, edited by John F. Shroder, Academic Press, San Diego, pp. 239-248, 2013.

[9] Perzyna, P. Fundamental problems in viscoplasticity. *Advances in Applied Mechanics*, Academic Press, New York, 9, pp. 244-368, 1966.

[10] van Genuchten, M. T. A closed-form equation for predicting the hydraulic conductivity of unsaturated soils. *Soil Sci. Soc. Am. J.*, 44, pp. 892-898, 1980.

Proceedings of the 22nd UK Conference of the
Association for Computational Mechanics in Engineering
2 – 4April 2014, University of Exeter, Exeter

AN ANISOTROPIC CONSTITUTIVE MODEL FOR CYCLIC LOADING OF SOFT CLAYS

***Mohammad Rezania[1], Hesam Dejaloud[2], Mohaddeseh Mousavi Nezhad[3], Yaser Jafarian[2]**

[1] Nottingham Centre for Geomechanics, University of Nottingham, Nottingham, NG7 2RD, UK
[2] International Institute of Earthquake Engineering and Seismology, Tehran, 19395-3913, Iran
[3] Computational Mechanics, School of Engineering, University of Warwick, Warwick, CV4 7AL, UK

* mohammad.rezania@nottingham.ac.uk

ABSTRACT

Soft clays are normally consolidated or lightly overconsolidated soils where even small increases of stresses are likely to cause non-linearity and plasticity in their response. In addition, soft clays have a significant degree of anisotropy in their natural state that adds to the complexity of their behaviour. In this paper a new model is proposed by extending the anisotropic critical state-based model S-CLAY1 with a bounding surface formulation. Both isotropic and rotational hardening rules are incorporated into the bounding surface formulation with an associated flow rule. The new model is shown to capture well the important aspects of observed response during cyclic loading of natural clays such as anisotropy, hysteresis, accumulation of permanent strains and loading-unloading cycles.

Keywords: *soft clays; constitutive modelling; anisotropy; bounding surface; cyclic loading*

1. Introduction

One of the important issues in geotechnical engineering is the response of the natural soft clays to cyclic loadings. This type of clays are usually normally consolidated or lightly over consolidated and have a significant degree of anisotropy in their structure that can further evolve during straining. Several constitutive models have been developed to capture the anisotropic response of these soils (e.g. [1-2]), among which S-CLAY1 model [1] has been widely accepted to provide good results in simulating the plastic anisotropy of soft soils. However, the main focus of these models is on large plastic strains at primary loadings and on subsequent unloading-reloading cycles within the yield surface they only produce purely elastic strains. To overcome the limitations of classical elasto-plastic models in simulating the hysteretic behaviour, Dafalias (1986) [3] modified the Bounding Surface plasticity (BS) theory for geomaterials. In this paper, a new constitutive model is proposed for enhanced prediction of the cyclic behaviour in soft soils by capturing non-linearity and plasticity from the early stages of loading. The new model is based on further extension of S-CLAY1 model through incorporation of a Bounding Surface formulation, hence it is referred to as SCLAY1-BS model. The general formulation of the model is presented in this paper and the enhanced model performance is illustrated with a number of simple examples.

2. SCLAY1-BS Model Formulation

In the following the elements of the proposed model are briefly presented and discussed.

2.1. Bounding Surface and Plastic Potential

The yield surface of original S-CLAY1 model is adopted as the bounding surface ($F = 0$) in the SCLAY1-BS model

$$F = \frac{3}{2}(\{\bar{\sigma}_d - \bar{p}'\alpha_d\}^T\{\bar{\sigma}_d - \bar{p}'\alpha_d\}) - \left(M^2 - \frac{3}{2}\{\alpha_d\}^T\{\alpha_d\}\right)(\bar{p}'_m - \bar{p}')\bar{p}' = 0 \quad (1)$$

where $\bar{\sigma}_d$ and α_d are the deviatoric stress tensor and the deviatoric fabric tensor respectively ($\bar{}$ sign represents that the variable is associated with the bounding surface), *M* is the critical state value, $\bar{p'}$ is the mean effective stress, and $\bar{p'}_m$ is the size of the yield surface related to the soil's preconsolidation pressure. An associated flow rule is adopted; therefore, the same function as above is also utilised as plastic potential function, *G*, for the S-CLAY1-BS model.

2.2. Hardening Laws

Every change in the shape of the bounding surface, such as changes in the size and orientation, are assume to be governed by the isotropic hardening and rotational hardening laws of S-CLAY1 model. The isotropic hardening is assumed to be solely related to plastic volumetric strain ($d\epsilon_v^p$)

$$d\bar{p'}_m = \frac{\nu \bar{p'}_m}{\lambda - \kappa}\, d\epsilon_v^p \tag{2}$$

where ν is the specific volume, λ is the gradient of the normal compression line in the compression plane ($\ln p' - \nu$ space), and κ is the slope of the swelling line in the compression plane. And the rotational hardening law, that describes the changes of inclination of the bounding surface caused by plastic volumetric and plastic shear straining, is defined as

$$d\alpha = \mu \left[\left\{ \frac{3\bar{\sigma}_d}{4\bar{p'}} - \alpha_d \right\} < d\epsilon_v^p > + \beta \left\{ \frac{\bar{\sigma}_d}{3\bar{p'}} - \alpha_d \right\} d\epsilon_d^p \right] \tag{3}$$

where $d\epsilon_d^p$ is the increment of plastic deviatoric strain, μ and β are soil constants and $< >$ are Macaulay brackets. The model parameter β defines the relative effectiveness of plastic shear strains and plastic volumetric strains in rotating the bounding surface; and same as in S-CLAY1, we have

$$\beta = \frac{3(4M^2 - 4\eta_{K0}^2 - 3\eta_{K0})}{8(\eta_{K0}^2 - M^2 + 2\eta_{K0})} \tag{4}$$

where η_{K0} is the stress ratio during K_0 consolidation and similar to *M* it is a function of soil's friction angle [1]. The value of parameter μ that controls the absolute rate of the rotation of the bounding surface toward its current target value can be obtained by simulation of experimental data [1]. The initial inclination of the bounding surface is also determined from

$$\alpha_{K0} = \frac{\eta_{K0}^2 + 3\eta_{K0} - M^2}{3} \tag{5}$$

2.3. Mapping Rule

A radial mapping rule [3] is adopted to project the current stress state to an image point, where the origin of the stress space is assumed to be the fix projection centre in the unload-reload conditions

$$\bar{\sigma}_{ij} = \delta\, \sigma_{ij} \tag{6}$$

where δ is a similarity ratio between the bounding surface and the loading surface.

2.4. Plastic Modulus

In the BS plasticity theory, the plastic modulus of an arbitrary stress point on the loading surface is a function of the plastic modulus of the image point on the bounding surface. A hardening function needs to be defined in order to relate these two plastic moduli to each other. Different hardening functions are proposed for loading and unloading conditions

$$H = \bar{H} + S_l \; (or\; S_{ur}) \tag{7}$$

$$\bar{H} = -\frac{\partial F}{\partial \alpha_d} \left(\frac{\partial \alpha_d}{\partial \epsilon_v^p} < \frac{\partial G}{\partial \bar{p'}} > + \frac{\partial \alpha_d}{\partial \epsilon_d^p} \sqrt{\frac{2}{3} \left(\frac{\partial G}{\partial \bar{\sigma}_d} \right) \cdot \left(\frac{\partial G}{\partial \bar{\sigma}_d} \right)} \right) - \frac{\partial F}{\partial \bar{p'}_m} \frac{\nu \bar{p'}_m}{\lambda - \kappa} \frac{\partial G}{\partial \bar{p'}} = 0 \tag{8}$$

$$S_l = \bar{p'}_m^3\, h_l \times \frac{1 - \delta^{\psi_1}}{\delta} \tag{9}$$

$$S_{ur} = \bar{p'}_m^3 \, h_{ur} \times \frac{1 - \left(\delta^{\psi_2} - 1\right)}{1 - \delta} \tag{10}$$

where h_l, h_{ur}, ψ_1 and ψ_2 are additional model parameters in the SCLAY1-BS compared to the original S-CLAY1 model. The values of these new parameters can be obtained by simulating cyclic, or even monotonic, element test results. Sensitivity analysis over the full set of additional model parameters has shown that the model performance varies only within a limited domain when the value of each individual parameter is changed. As a result determination of these parameter values becomes straightforward when experimental data is available. For example Figures 1(a) and 1(b) show the variations of the model prediction, in simulating the stress path of an arbitrary monotonic triaxial compression test with arbitrary set of parameter values, for different values of h_l and ψ_1, respectively.

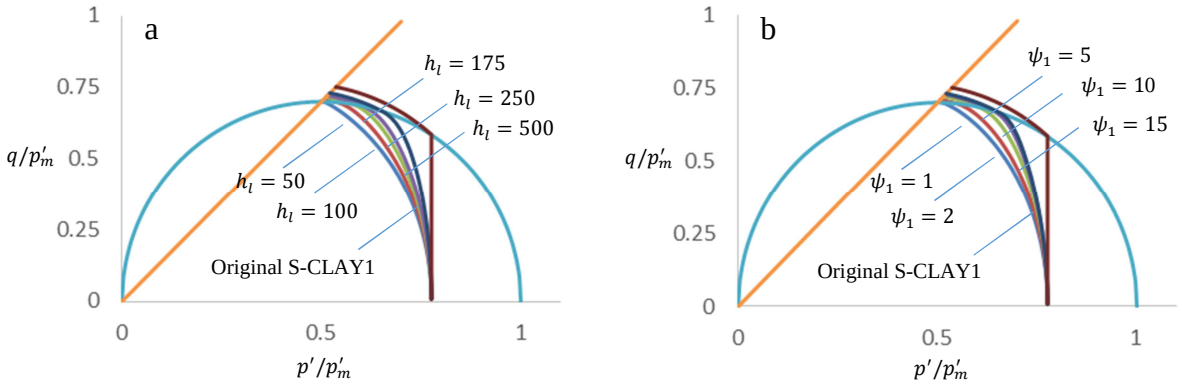

Figure 1: Effect of additional parameters due to bounding surface theory, (a) h_l (b) ψ_1

As it is seen in Figure 1(b), simulation results are converging to a limiting path as ψ_1 value increases.

3. Model Performance

The S-CLAY1-BS model explained in section 2 is used to simulate undrained shearing tests on anisotropically consolidated specimens of two different soft soils, namely Kaolin Clay and San Farncisco Bay Mud [4]. For both soils elasticity and critical state parameter values are those reported in [4], whereas rotational hardening parameters are calculated from Eqs. (4) and (5), and bounding surface parameter values are arbitrarily adjusted simply to illustrate the advantages of incorporating the BS theory into the original anisotropic elasto-plastic model. Parameter values used for the simulations are summarised in Table 1. Figures 2(a) to 2(d) show performances of both S-CLAY1-BS and S-CLAY1 models in simulating undrained cyclic shearing tests on two soils. The simulation results are plotted in $p' - q$ space.

Table 1: Model parameter values

Category	Designation	Kaolin Clay	San Francisco Bay Mud
Elasticity	κ	0.05	0.054
	ν	0.2	0.2
Critical State	λ	0.14	0.37
	M	1.05	1.4
Bounding surface	h_l	100	110
	ψ_1	2	1
	h_u	40	60
	ψ_2	3	3
Rotational hardening	α_0	0.40	0.55
	μ	30	20
	β	0.54	0.87

Figures 2(b) and 2(d) show the results of simulation using the S-CLAY1 model, which does not include the BS feature. It is observed that without the BS feature, the model simulates plastic strains

mainly in the first cycle of loading for the stress states on the yield surface. In the subsequent cycles, the stress moves only inside the yield surface, and no additional plastic strain is produced. In contrast Figures 2(a) and 2(c) show the simulated results of SCLAY1-BS model. Compared with the previous case, here, plastic strains are produced even for the stress states within the bounding surface, accompanied by reduction of p (contractive response) which is due to the distance dependent plastic modulus employed in the bounding surface formulation.

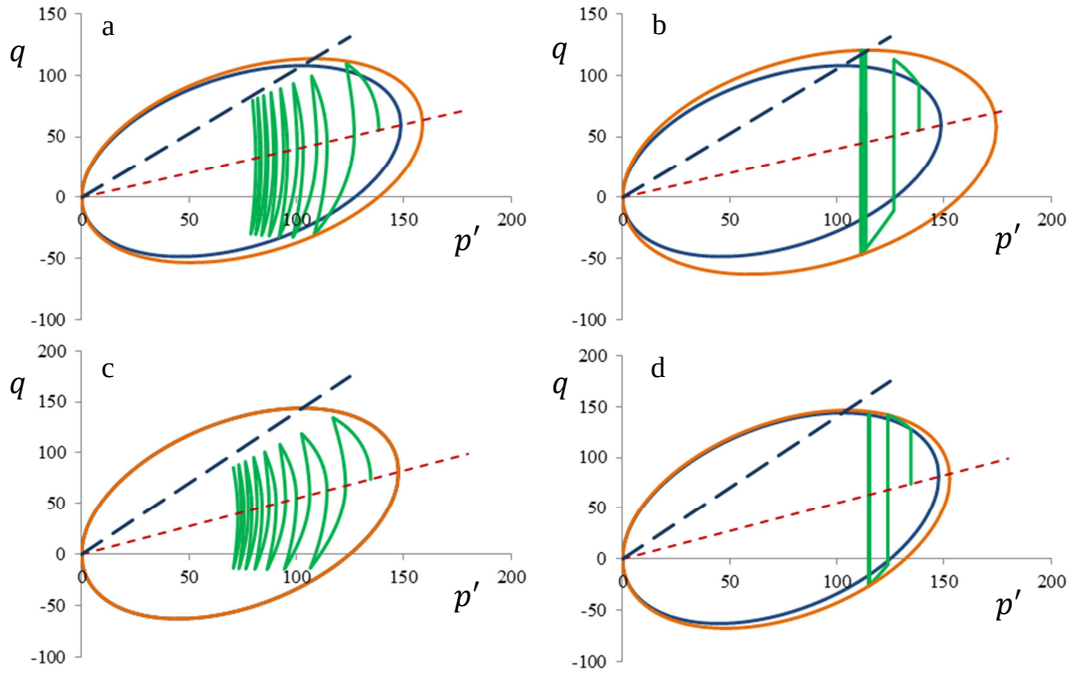

Figure 2: Comparison of S-CLAY1-BS and S-CLAY1 in simuation of cyclic loading in (a),(b) Kaoline clay, (c),(d) San Francisco bay mud

4. Conclusions

A new constitutive model has been developed by further extension of the critical state based model S-CLAY1 and the bounding surface plasticity to simulate inherent and evolving anisotropy in soft clays together with their nonlinear cyclic response. The new model, SCLAY1-BS, has four additional parameters which their values can be readily calibrated through simulations of experimental data. The comparisons of cyclic loadings on two types of clay revealed the much improved capability of the proposed model in simulating the gradual accumulation of permanent strains within the yield surface.

Acknowledgement

The first author appreciates the financial support from the Nottingham University's Dean of Engineering award.

Refrences

[1] S.J. Wheeler, A. Näätänen, M. Karstunen and M. Lojander. An anisotropic elastoplastic model for soft clays. *Canadian Geotechnical Journal*, 40, 403-418, 2003.

[2] Y.F. Dafalias, M.T. Manzari, A.G. Papadimitriou. SANICLAY: simple anisotropic clay plasticity model, *International Journal for Numerical and Analytical Methods in Geomechanics*, 30(12), 1231-1257, 2006.

[3] Y.F. Dafalias. Bounding surface plasticity. I: Mathematical foundation and hypoplasticity. *Journal of Engineering Mechanics*, 112, 966-987, 1986.

[4] H.I. Ling, D.Y. Yue, V.N. Kaliakin, N.J. Themelis. Anisotropic elstoplastic bounding surface model for cohesive soils. *Journal of Engineering Mechanics*, 128, 748-758, 2002.

Proceedings of the 22nd UK Conference of the
Association for Computational Mechanics in Engineering
2 - 4 April 2014, University of Exeter, Exeter

A numerical investigation into the effect of particle form on the strength of granular materials

M. Potticary[1,*], A. Zervos[1] and J. Harkness[1]

[1]Infrastructure Research Group, Faculty of Engineering and the Environment, University of Southampton, University Rd, Southampton SO17 1BJ

*M.Potticary@soton.ac.uk

ABSTRACT

It has long been recognised that the macroscopic mechanical behaviour of a granular material depends, to differing extents, on micro-mechanical properties such as the particle size distribution, the particle shape, the inter-particle friction angle and the particle strength. However, despite the interest this issue has generated over the years, a systematic investigation of some of these effects is still lacking. This paper represents a first attempt to systematically investigate the effect of particle shape. Of the three independent parameters that are generally considered to characterise particle shape in different scales of observation, i.e. form, angularity and roughness, we focus on the effect of form, which describes the overall shape of a particle. We present a new way of quantifying particle form in terms of the axes of an equivalent scalene ellipsoid. To quantify the effect of form on the strength characteristics of a granular assembly we use DEM simulations of triaxial tests on specimens consisting of scalene ellipsoids. The ellipsoids in each specimen have the same form, particle size distribution and interparticle friction, thus eliminating the effects of particle angularity and roughness from the analysis. Some first results for particles of different form are presented systematically and comparisons are made.

Key Words: *Particle Shape; Granular Materials; DEM; Railway Ballast; Triaxial test*

1. Introduction

The shape of its particles is one of the fundamental properties of a granular material. In the case of granular materials, there are three (assumed) independent aspects of shape that are generally considered, each describing geometrical properties of a particle at a different scale of observation. These are particle form, angularity and roughness. Form quantifies the overall shape of a particle, angularity describes the number and sharpness of angles on its perimeter/surface, and roughness relates to the microscopic asperities of the particle surface that are to some extent responsible for interparticle friction.

Particle form in particular is generally quantified using the longest (L), intermediate (I) and shortest (S) dimensions of the particle, although the way these are defined may vary. One possible way is to consider an equivalent scalene ellipsoid with axes equal to $S \leq I \leq L$, as in [2]. Different measures and combinations of measures that can be used to describe form have been proposed, however no consensus exists on whether one has a clear advantage over the others [3]. Also, although particle form is certain to influence the mechanical properties of a particulate, a systematic study of its effect is still lacking.

Here we propose a new way of describing form using the dimensions of an equivalent scalene ellipsoid. We then perform DEM simulations of triaxial compression on granular assemblies of uniform particle form, to investigate how the latter affects the strength of the material. We use the method of potential particles, which allows modelling of particles with (almost) arbitrary shape[4]. Particle size distributions consistent with those of railway ballast are used, while the number of particles in each simulation is consistent with the number of ballast particles present in the specimens of corresponding physical tests.

2. Quantification of particle form

In [3] the authors presented a comprehensive discussion of the different ways in which particle shape, including form, can be quantified. The measures summarised there appear to have been developed heuristically. As a contribution to that discussion, we present a new way of quantifying particle form that is derived mathematically and may be considered more intuitive.

We assume that the form of a particle is characterised by the dimensions $S \leq I \leq L$ of an equivalent scalene ellipsoid. If we consider S, I and L to be coordinates in a three dimensional space, any particle can be represented by a vector $\mathbf{f}$ linking the origin of the axes to point (S, I, L). Clearly, co-linear vectors correspond to particles that share the same form and differ only in size; to quantify form it is thus sufficient to consider only the **direction** of the vector, not its length. A straight-forward way of quantifying direction is by using the elevation and azimuth in spherical coordinates; this will be detailed in a separate publication. Instead, here we quantify form using the deviation of $\mathbf{f}$ from the *spherical axis* $S = I = L$, whose points correspond to particles of perfectly spherical form, in a way analogous to the decomposition of stress into a hydrostatic and a deviatoric component. In particular, we consider the intersection F of $\mathbf{f}$ with the $S + I + L - 1 = 0$ "deviatoric" plane that is normal to the spherical axis, and calculate its in-plane coordinates in a frame of reference centered at the intersection P of the spherical axis (Figure 1.) Taking into account that $0 \leq S \leq I \leq L$, the in-plane coordinates can be derived using standard vector algebra that will not be detailed here. Further, normalisation yields a pair of coordinates (α, ζ) on the "deviatoric" plane that vary between 0 and 1 and are defined as:

$$\alpha = \frac{2(I - S)}{L + I + S}, \qquad \zeta = \frac{L - I}{L + I + S} \tag{1}$$

The two parameters α and ζ suffice to describe all possible forms represented by a scalene ellipsoid, including the degenerate cases of a sphere ($\alpha = \zeta = 0$), a prolate ellipsoid ($\alpha = 0, \zeta > 0$), an oblate ellipsoid ($\alpha > 0, \zeta = 0$), a flat circular ($\alpha = 1, \zeta = 0$) or elliptical ($\alpha + \zeta = 1$) disk, and a needle ($\alpha = 0, \zeta = 1$). Observing the effect that varying each parameter independently has, α can be termed *platyness* and ζ *elongation* of the particle.

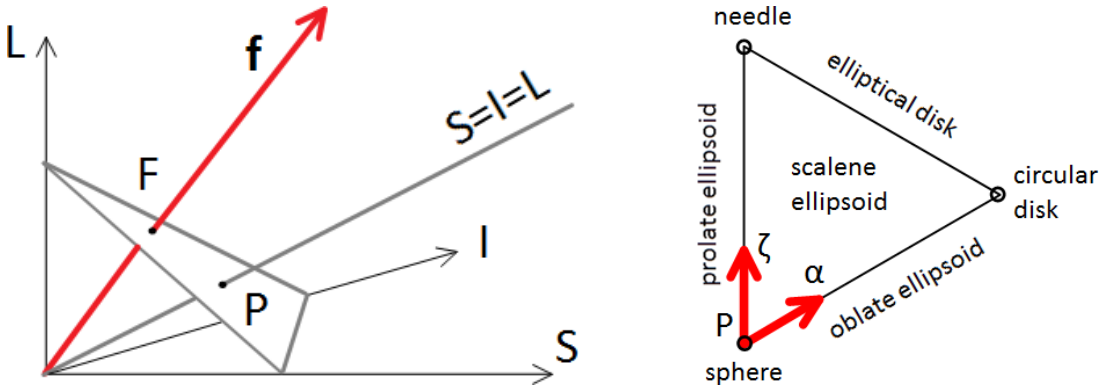

Figure 1: Representation of particle form in (S, I, L) space (left); the α-ζ form parameter space and a description of the corresponding forms (right.)

3. DEM modelling

To quantify the effect of form on the strength characteristics of a granular assembly we use DEM simulations of triaxial tests on specimens consisting of scalene ellipsoids. Attempts to investigate the effect of particle shape more generally by modelling more realistic particle shapes can be found in the literature [5] however these focussed on the effect of angularity and used clumps of spheres to model particles of different shapes. Whether such clumps can adequately reproduce angular particles is debatable, and in any case our focus here is particle form. We therefore decided to use smooth ellipsoid particles, thus removing the effect of particle angularity from the results.

Each DEM specimen used consists of ellipsoid particles that have the same form, i.e. the same (α, ζ) parameters and therefore plot at the same point on the "deviatoric" plane. The different particle forms considered are given in Table 1, in the form $S/I : 1 : L/I$. The corresponding values of the (α, ζ) parameters are also given.

Table 1: The different particle forms considered in the analyses.

Form	Ratio	α	ζ
Form 1	1:1:1	0	0
Form 2	2.25:1:0.45	0.2973	0.3378
Form 3	2.25:1:1	0	0.2941
Form 4	1:1:0.60	0.3077	0

A particle size distribution must also be prescribed for the models. To avoid known issues with monodisperse specimens as well as further constrain the problem to a matter of direct practical interest, we use a particle size distribution consistent with the British Standard for railway ballast [1]. It was assumed that the size of sieve a particle can pass through is determined by its intermediate dimension I. Particles of five different sizes between the maximum and minimum allowable gradation curves for ballast were created and used in each model.

To ensure comparability of the results it was decided that all specimens have the same total volume, as would have been the case with physical tests. The total volume for each model was kept at 0.2m^3, although this caused the number of particles to vary among models. The material most commonly used for railway ballast is granite; typical values for particle density ($2700\ \text{Kg/m}^3$) and interparticle coefficient of friction (30°) are used. In any case, in all models a sufficient number of particles was present, consistent with those of similar physical tests.

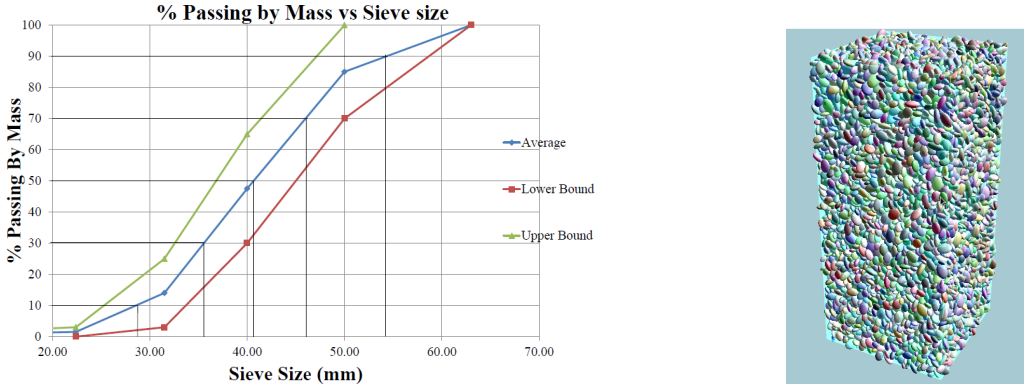

Figure 2: Particle size distribution of DEM models (left) and typical DEM model (right.)

To create a specimen a pre-determined number of particles of different sizes as above are randomly distributed within 3D space to a target void ratio of 2.0. The particles themselves are given random orientation to remove any bias in the initial fabric, which can significantly affect results. The specimen is then subjected to isotropic compression using periodic boundaries, zero gravity forces and no interparticle friction. Once the specimen is compacted to a void ratio of 0.65 and corresponds to a densely packed granular material, isotropic stress of $100kPa$ is applied to the boundaries and, once the specimen has settled interparticle friction is reintroduced. The final pre-test configuration of a typical specimen can be seen in Figure 2. The model is then subjected to triaxial loading, where the lateral pressure is kept constant while the top boundary is moved downwards imposing a constant axial strain rate; all boundaries remain periodic.

Figure 3 shows the mobilised friction angle of all models plotted against shear strain. In all cases a peak is observed, as expected of densely packed granular materials, before a critical state is reached. Peak strengths are not comparable among models because, despite their common initial void ratio, the models are expected to initially be at different relative densities. The friction angle at critical state, however, is unaffected by the initial relative density and thus is comparable. Figure 3 also shows the evolution of volumetric strain for all models; dilatancy consistent with dense initial packings is observed in all cases, and volumetric strain stabilises as a critical state is approached.

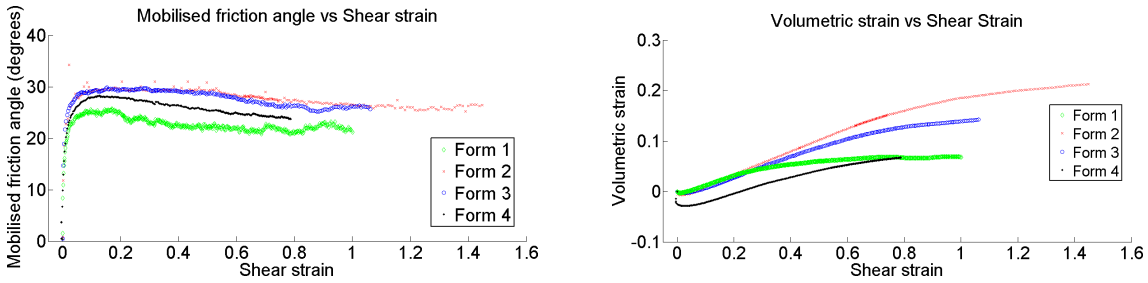

Figure 3: Mobilised friction angle (left) and volumetric strain (right) v.s. shear strain, for different particle forms.

4. Discussion and conclusions

Figure 4 shows the friction angle at critical state for each model, plotted against the (α, ζ) form parameters of its particles. It shows that a departure from spherical form (c.f. Figure 1) increases shear strength and that changes in elongation ζ seem to have a greater effect than changes in platyness α, although further work is needed to fully establish the latter. This work is currently in progress, as the (α, ζ) space is being systematically explored to fully quantify the effect of particle form. Subsequent steps of this work are the investigation of the effects of angularity and roughness, with a long-term goal of predicting shear strength on the basis of particle shape, and designing particulates to a pre-determined standard of strength.

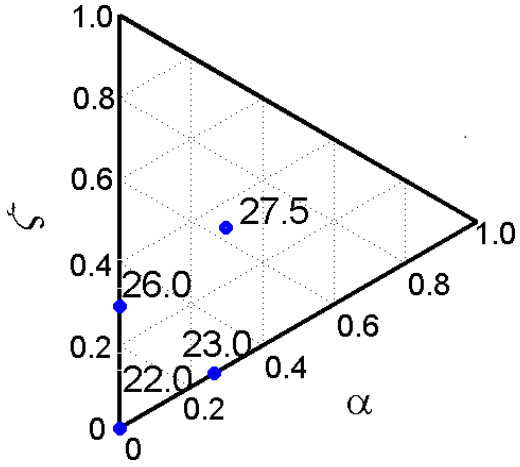

Figure 4: Friction angle at critical state as a function of particle form.

Acknowledgements

We gratefully acknowledge support from EPSRC (Track21 Programme Grant, EP/H044949/1) and Network Rail (Strategic Partnership with the University of Southampton.) Use of the IRIDIS High Performance Computing Facility and associated support services at Southampton are also acknowledged.

References

[1] *BSI Standards Publication Aggregates for railway ballast BS EN 13450:2013 BSI.* BSI Standards Limited 2013, 2013.

[2] C.O.R. Abbireddy, R. Schiebel, and C.R.I. Clayton. A method of estimating the form of coarse particulates. *Géotechnique*, 59(6):493–501, January 2009.

[3] Simon J. Blott and Kenneth Pye. Particle shape: a review and new methods of characterization and classification. *Sedimentology*, September 2007.

[4] J Harkness. Potential particles for the modelling of interlocking media in three dimensions. *International Journal for Numerical Methods in Engineering*, 80:157315(June):1573–1594, 2009.

[5] M.M. Mollanouri Shamsi and a.a. Mirghasemi. Numerical simulation of 3D semi-real-shaped granular particle assembly. *Powder Technology*, 221:431–446, May 2012.

Proceedings of the 22nd UK Conference of the
Association for Computational Mechanics in Engineering
2 – 4April 2014, University of Exeter, Exeter

Coupled discrete element and lattice Boltzmann scheme for simulating soil erosion

***Min Wang, Y.T. Feng and Gyan Pande**

Civil and Computational Engineering Centre, Swansea University, Singleton Park, Swansea, SA2 8PP

* sacewangmin@gmail.com

ABSTRACT

The phenomenon of soil erosion occurs when soil particles are pulled off by seepage forces and transported through the pore channels. This may cause serious damage to hydraulic structures such as earth dams or levees as well as their foundations. In this paper a coupled DEM-LBM technique is employed to investigate this phenomenon at the grain level. The Discrete Element Method and Lattice Boltzmann Method are used for the solid and the fluid, respectively. The Immersed Moving Boundary is adopted for the fluid-solid coupling. It is shown that the coupled DEM-LBM approach is effective for such fluid-particle systems and can capture the evolution of the process of erosion. The commonly used parameter (radius ratio) in 2D simulations is explored in a simple 2-dimentional modelling.

Keywords: *LB Equation; DEM; Immersed Moving Boundary; Fluid-solid Interaction; Soil erosion*

1. Introduction

Fluid-particle interaction plays an important role in geotechnical engineering. Related fluid-particle system covers liquefaction, piping, quick sand conditions in construction and sand production from oil wells in petroleum engineering. Recently, the coupled DEM-LBM technique has been proved to be a promising approach for fluid-particle problems. The coupled DEM-LBM technique was first proposed by Cook at al. [1]. It then attracted great attentions of researchers from different research areas.

2. Lattice Boltzmann Method

The Lattice Boltzmann Method (LBM) is a kind of microscopic or mesoscopic fluid dynamics approach. In the LBM, the fluid domain is divided into regular lattices. The fluid phase is treated as a group of fluid particles which are allowed to move to the adjacent lattice nodes or stay at rest. During each discrete time step of the simulation, fluid particles at each lattice node move to their immediate neighbouring lattice nodes along given directions. At each node, the fluid particles from neighbouring nodes collide, which is controlled by solving the Lattice Boltzmann equation. Finally, the macro fluid behaviour can be obtained through the statistics of the motion of fluid particles [2].
The Lattice Bhatnagar-Gross-Krook (LBGK) Model is one kind of popular Lattice Boltzmann Model. It can be characterised by the following Lattice Boltzmann Equation

$$f_i(\boldsymbol{x} + \boldsymbol{e}_i \Delta t, t + \Delta t) - f_i(\boldsymbol{x}, t) = \Omega \tag{1}$$

Where f_i is the primary variables in the LB formulation (so-called fluid density distribution functions), Ω is the collision operator.
In the LBGK Model, Ω is characterised by a relaxation time τ and the equilibrium distribution function $f_i^{eq}(\boldsymbol{x}, t)$

$$\Omega = -\frac{\Delta t}{\tau}[f_i(\boldsymbol{x}, t) - f_i^{eq}(\boldsymbol{x}, t)] \tag{2}$$

The central issue to LBM is to control the movement of fluid particles via density distribution functions.

3. Discrete Element Method

In the DEM, the Newton's second law (see equation (3) and (4)) is used to determine the translational and rotational motion of each particle arising from the contact forces, applied forces and body forces acting upon it, while the force-displacement law is used to update the contact forces arising from the relative motion at each contact. The dynamic behaviour is represented numerically by a time-stepping algorithm in which the velocities and accelerations are assumed to be constant within each time step. The resultant forces on any particle are determined by the particles with which it is in contact and the hydrodynamic forces.

$$m\boldsymbol{a} + c\boldsymbol{v} = \boldsymbol{F}_c + m\boldsymbol{g} + \boldsymbol{F}_f \tag{3}$$

$$I\ddot{\theta} = T_c \tag{4}$$

where m and I are mass and moment of inertia of the particle, respectively; $\boldsymbol{a}$, $\ddot{\theta}$ and $\boldsymbol{g}$ are, respectively, translational, angular and gravitational accelerations. $\boldsymbol{F}_c$ and T_c denote the contact force and torque between particles; c is a damping coefficient; $\boldsymbol{F}_f$ is the hydrodynamic force.

The normal and tangential contact model used here are based on the Hertz-Mindlin model [3].

4. DEM-LBM Coupling

An accurate fluid-particle interaction scheme is of great importance in DEM-LBM. Since the 1990s, a number of fluid-solid coupling schemes have been proposed for LBM. In this work the commonly used Immersed Moving Boundary is adopted and is extended to incorporate the effect of particle rotation.

In order to resolve the problems in Modified Bounce-back Rule for moving particles, Noble and Torczynski [4] proposed a new boundary scheme. This is accomplished by introducing an additional collision term, Ω_i^s, for nodes covered partially or fully by the solid. Then the collision term in the LB equation including body force becomes

$$\Omega = -\frac{\Delta t}{\tau}(1-B)[f_i(\boldsymbol{x},t) - f_i^{eq}(\boldsymbol{x},t)] + (1-B)\Delta t\boldsymbol{F}_i + B\Omega_i^s \tag{5}$$

Where B is a weighting function that depends on the local solid ratio ε, defined as the fraction of the node area (see Fig. 1).

$$B = \frac{\varepsilon(\tau - 0.5)}{(1-\varepsilon) + (\tau - 0.5)} \tag{6}$$

The additional collision term is based on the bounce-rule for nonequilibrium part and is given by

$$\Omega_i^s = f_{-i}(\boldsymbol{x},t) - f_i(\boldsymbol{x},t) + f_i^{eq}(\rho, \boldsymbol{U}_s) - f_{-i}^{eq}(\rho, \boldsymbol{u}) \tag{7}$$

Where $\boldsymbol{U}_s$ is the velocity of the solid node.

It is well known that particle rotation plays an important role in granular mechanics and in some cases it cannot be neglected. Therefore, the velocity of the solid node should be considered by

$$\boldsymbol{U}_s = \boldsymbol{U}_c + \omega \times \boldsymbol{l}_c \qquad (l_c = \sqrt{(x - x_c)^2 + (y - y_c)^2}) \tag{8}$$

The resultant hydrodynamic force and torque exerted on the solid can be calculated by summing the momentum change of solid nodes:

$$\boldsymbol{F}_f = Ch\Big[\sum_n (B_n \sum_i \Omega_i^s \boldsymbol{e}_i)\Big] \tag{9}$$

$$T_f = Ch\Big\{\sum_n \big[(\boldsymbol{x} - \boldsymbol{x}_c) \times (B_n \sum_i \Omega_i^s \boldsymbol{e}_i)\big]\Big\} \tag{10}$$

Later this method was modified by Holdych [5]. The only difference is that the solid velocity is used to calculate the equilibrium distribution for the last term. The modified version is as follows

$$\Omega_i^s = f_{-i}(\boldsymbol{x},t) - f_i(\boldsymbol{x},t) + f_i^{eq}(\rho, \boldsymbol{U}_s) - f_{-i}^{eq}(\rho, \boldsymbol{U}_s) \tag{11}$$

5. Simulation of Soil Erosion

In this section, the onset and evolution of quicksand which is a typical soil erosion phenomenon will be investigated first. It is followed by exploring the effect of effective radius used in 2-dimentional DEM-LBM simulations.

A two-dimensional numerical simulation of quicksand phenomenon was carried out using the coupled DEM–LBM technique. In this simple simulation there are three large particles (A, B and C) and 93 small particles surrounding large particles. (See Fig. 2). The basic parameters used in the simulations are listed in Table 1. During the tests, a constant fluid pressure was applied to the bottom.

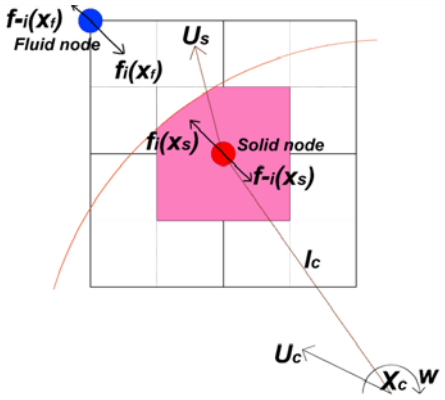

Fig. 1 Immersed moving boundary including rotation

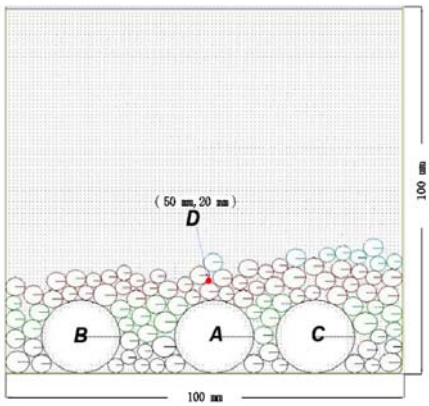

Fig. 2 Quicksand model

Table 1 Parameters used in this study

Parameter	Value	Parameter	Value
Particle density (kg/m3)	2700	Fluid density (kg/m3)	1000
Friction coefficient in the DEM calculation	0.5	Lattice spacing (m)	1.0×10-3
Young's modulus (MPa)	69	LBM time step (s)	1.0×10-4
Poisson's ratio	0.3	Dimensionless relaxation time	0.5003
DEM time step (s)	3.33×10-5	Ratio of hydraulic radius	0.685

Quicksand condition is a special case of soil liquefaction which occurs when a granular deposit is subjected to a large enough upward pore fluid flow. Fig. 3 gives snapshots of the evolution of the quicksand phenomenon from time step 0 to 1500. It can be found that the coupled DEM-LBM technique can easily trace the movement of granular particles and simulate pore water flow. Under the fluid pressure at bottom, the pore water will flow upward and small particles will also move upward under the hydrodynamics from pore water. Finally, the small particles above the large particles are washed away with time. But during the whole process the large particles nearly keep unchanged, as the hydrodynamic forces applied to them are smaller than their weights.

In 2-D simulations combining DEM and other fluid methods, like CFD and LBM, there is a significant issue in the pore water flow path. Because the flow paths are always blocked up by circular particles, it is difficult to obtain realistic flow channels. In order to solve this problem, Boutt at al. [6] proposed a method in which the radius of the particle will be reduced to certain degree (called effective radius) artificially when the fluid flow is implemented. This effective hydraulic radius can be accomplished by introducing a ratio of effective radius to the particle radius. In this study, 6 ratios are chosen for investigation. When the ratio is 1, effective radius is equal to the real particle radius. The movement of large particle A shown in Fig. 4(a) in the vertical direction and the change of pore pressure at the point D during the whole simulation are displayed in Fig. 4(b).

From Fig. 4 we can find that with the decrease of the radius ratio large particle A is gradually fluidised. When the radius ratio is larger than 0.785, there is no movement for particle A in the vertical direction; when the radius ratio is decreased to 0.785, small changes happen and the particle A could move up and down. It can be deemed as a critical state. When the radius ratio is lower than 0.785, complete fluidization can be observed. Meanwhile, it can be also seen the pore water pressure at point D gradually goes up with the decrease of radius ratio.

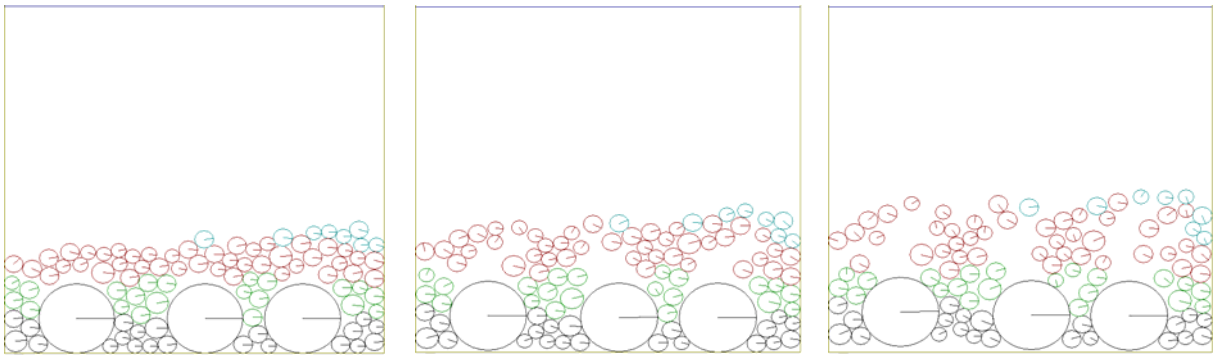

Time step 500 Time step 1000 Time step 1500

Fig. 3 The simulation process of quicksand

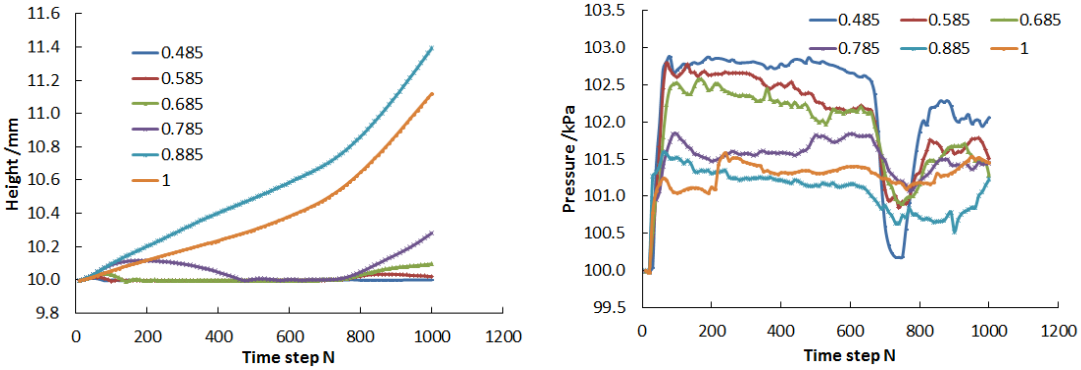

(a) The coordinate of particle A in Y-axis (b) The water pressure at point D

Fig. 4 Impact of effective radius on the 2-D simulation

6. Conclusions

In this paper the implementation of Immersed Moving Boundary including the particle rotation was introduced in the coupled DEM-LBM program and the fluid-solid coupling was illustrated. A simple soil erosion simulation was then performed using the coupled DEM-LBM technique. The impact of effective radius was investigated at the grain level in the quicksand modelling. It is seen that the choosing of effective radius plays a vital role in quicksand simulations. The coupled DEM-LBM scheme seems to be promising and effective for investigating the fluid-particle systems.

References

[1] B.K. Cook, D.R. Noble, et al., Direct simulation of particle-laden fluids. In: J. Girard, M. Liebman, C. Breeds, and T. Doe (Eds), *Pacific Rocks 2000*, Balkema, Rotterdam, pp. 279-286., 2000.

[2] Y.T. Feng, K. Han, and D.R.J. Owen, Coupled lattice Boltzmann method and discrete element modelling of particle transport in turbulent fluid flows: Computational issues. *International Journal for Numerical Methods in Engineering*, 72, pp. 1111-1134., 2007.

[3] C. Thornton and C.W. Randall, Applications of theoretical contact mechanics to solid particle system simulation. In: M. Satake and J.T. Jenkins (eds), *Micromechanics of granular materials*, Amsterdam, Netherlands, pp. 133-142., 1988.

[4] D.R. Noble and J.R. Torczynski. A lattice-Boltzmann method for partially saturated computational cells. *International Journal of Modern Physics*, 9, pp. 1-13., 1998.

[5] D.J. Holdych, Lattice Boltzmann methods for diffuse and mobile interfaces, PhD thesis, University of Illinois at Urbana, 2003.

[6] D.F. Boutt, B.K. Cook, et al., Direct simulation of fluid-solid mechanics in porous media using the discrete element and lattice-Boltzmann methods. *Journal of Geophysical Research*, 112, pp. B10209., 2007.

Proceedings of the 22nd UK Conference of the
Association for Computational Mechanics in Engineering
2 – 4April 2014, University of Exeter, Exeter

Deformation and Safety Control of Buried Pipelines Crossed by Very Large Diameter Slurry Shield Tunneling

***J. Ni, You L. Chen, Hui Z. Zhao and Xue L. Zhou**

Department of Environment and Architecture, University of Shanghai and Technology, No. 516 Jungong Road, 200093Shanghai, China

*wendy_1943@163.com

ABSTRACT

The buried pipelines in urban cities nowadays have a dense distribution and easily get disturbed by tunnelling around. Therefore, ensuring the safety of pipelines during the tunnel construction is important. According to the correlation between ground subsidence and pipeline stress when the pipeline is perpendicular to the tunnel drive, a maximum value of ground subsidence based on the deformation capacity of the pipeline was proposed. A case study of Shanghai South Hong-mei Road Tunnel was carried out, where the deformation of buried pipelines crossed by very large diameter slurry shield tunnelling and its safety control were discussed in order to provide a reference for the prevention of pipeline accidents during construction in practical engineering.

Keywords: *ground subsidence; tunnel construction; buried pipelines; safety control*

1. Introduction

Tunnel projects are often found with a concentrated distribution of all kinds of pipelines in underground space, whose running state is directly related to the quality of people's life. However, no matter how advanced the slurry shield technology, the advance process of large diameter shield will inevitably cause ground subsidence (or swell), and the disturbance on the surrounding soil. Therefore the research on the disturbance of soil around the underground pipelines due to shield driving and its influence on the deformation of the pipelines is valuable.

Researchers have carried out investigation on the soil behaviour under the condition of shield driving [1-3]. A case history of Shanghai South Hong-mei Road Tunnel Project using slurry balance shield at a very large diameter was studied. The theoretical and numerical analyses were carried out and their predictions were compared to the field data. Then the deformation and stress distribution of ethylene gas pipelines during the process of tunnel construction were summarized.

2. Calculation of Soil Subsidence

Currently Peck formula [4] is widely used for calculating the displacement of soils due to tunnel construction. The hypothesis of volume loss proposed by Peck is valid for the soil layer between the ground surface and the plane above the tunnel, i.e., the volume of settlement trough for an arbitrary layer below the ground surface is equal to the soil loss and the shape of the settlement trough can be represented by a normal distribution, as shown in Figure 1. The origin is located at the ground surface directly above the center line of the tunnel, the x axis is perpendicular to the center line of the tunnel, and the z axis is perpendicular to the ground surface and goes down. The maximum vertical displacement ratio of the soil layer at depth z to ground surface can be expressed by:

$$\frac{\delta_{\max}(z)}{\delta_{\max 0}} = (1 - z/z_0)^{-0.3} = \frac{i_0}{i(z)} \tag{1}$$

where i_0 is the width of the settlement trough, $i(z)$ is the width of the settlement trough for the soil layer at depth z, and the depth of the centreline of the tunnel is z_0.

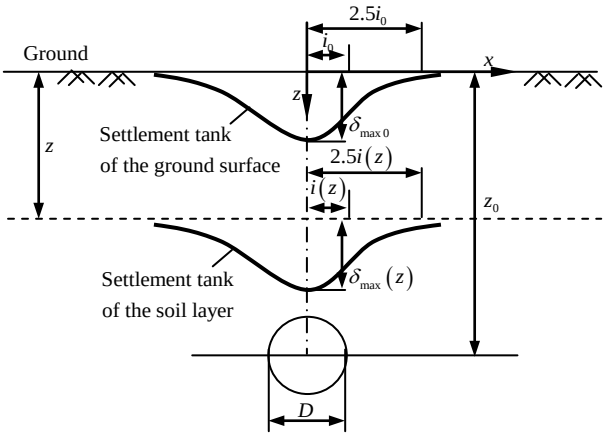

Figure 1: The shape of settlement troughs

3. Accepted Vertical Displacement of Ground Surface

The curvature $1/\rho$ of pipelines rather than the vertical displacement is mostly concerned. According to Attewell [1], the maximum curvature of pipelines occurs at the position $x=0$. When the pipeline is perpendicular to the tunnel, the relationship between the maximum curvature of the pipeline $1/\rho$ and the maximum vertical displacement of the soil layer in which the pipeline is imbedded can be expressed as [5]:

$$\frac{1}{\rho}=\begin{cases}\dfrac{i_{\mathrm{p}}\lambda}{2.3}\left[1-A(2.3i_{\mathrm{p}}\lambda)\right]\dfrac{\delta_{\max}^{\mathrm{p}}}{i_{\mathrm{p}}^{\,2}}, & 1/i_{\mathrm{p}}\,\lambda>0.7\\ \dfrac{i_{\mathrm{p}}\lambda}{2.3}\dfrac{\delta_{\max}^{\mathrm{p}}}{i_{\mathrm{p}}^{\,2}}, & 1/i_{\mathrm{p}}\,\lambda<0.7\end{cases} \tag{2}$$

where i_{p} is the width of the settlement trough at the pipeline and λ is the deformation coefficient of the elastic foundation beam. Practically, the vertical displacement of underground pipelines is usually not easy to measure directly, and therefore the influence of tunnel construction on the underground pipelines can be obtained indirectly by measuring the vertical displacement of the ground. According to the knowledge of mechanics of materials, the strain of the outermost fibres of the pipeline can be expressed by $\varepsilon=(d/2)\times(1/\rho)$, then the normal stress due to bending can be obtained in the form of $\sigma=E_{\mathrm{P}}\cdot\varepsilon=(d/2)\times(1/\rho)E_{\mathrm{P}}$. If the acceptable normal stress of the pipeline is known as $[\sigma]$, then the acceptable curvature of the pipeline can be given as:

$$[\frac{1}{\rho}]=[\sigma]\Big/\left(\frac{d}{2}E_{\mathrm{p}}\right) \tag{3}$$

Substitute Eq. (3) to Eq. (2), the acceptable vertical displacement of the soil layer around the pipeline $[\delta_{\max}^{\mathrm{p}}]$ can be obtained and then the acceptable vertical displacement of the ground surface can be obtained by solving Eq. (1).

4. Case Study

Shanghai Hong-mei Road Tunnel Project was carried out by slurry balance shield at a diameter of 14.93 m. To predict the deformation and stress of an industrial ethylene pipeline above the tunnel in the real project, a steel pipeline with the same material properties was embedded in Feng-xian construction site. The parameters for the numerical analysis are presented in table 1.

The steel pipeline made of three welded steel pipes was totally 30 m long. It was perpendicular to the tunnel and the centre was located at H96. There were 1 reference point and 12 monitoring points and

set every 2.5 m along the steel pipeline (see Figure 2). The vertical displacement of the steel pipeline was monitored by the BGK-4675 type monitoring system. Figure 3 shows the vertical displacement of the steel pipeline. It can be seen that due to the different disturbance of soils caused by shield driving, the differential vertical displacement between the middle and the sides of the steel pipeline gradually increases after the shield tail goes out of ring 10. The maximum vertical displacement of the steel pipeline on 5 November, 2012 is about 14 mm.

Table 1: Parameters for the numerical analysis

	Item	Value	Unit
Steel pipe	Outer diameter d	0.273	m
	Thickness t	7.10×10^{-3}	m
	Elastic modulus E_p	2.10×10^{11}	Pa
	Berried depth z_p	2.0	m
	Acceptable normal stress $[\sigma]$	1.38×10^{8}	Pa
Soil	Soil bed coefficient k	10000	kN/m^3
	Modulus of deformation E_s	5.50×10^{6}	Pa
	Possion's ratio μ	0.30	-
	Internal friction angle φ	16.0	°
Tunnel	Depth of the center line of the tunnel z_0	25.00	m
	Outer diameter D	14.93	m

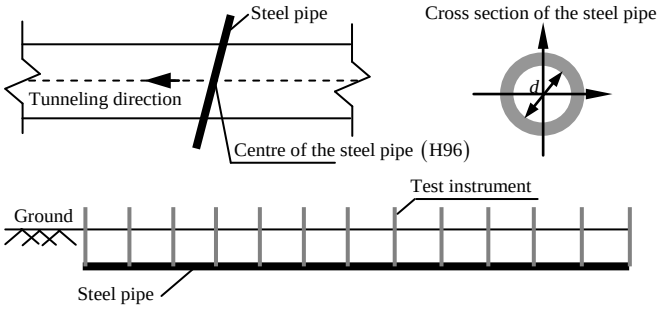

Figure 2: The location of the monitoring points

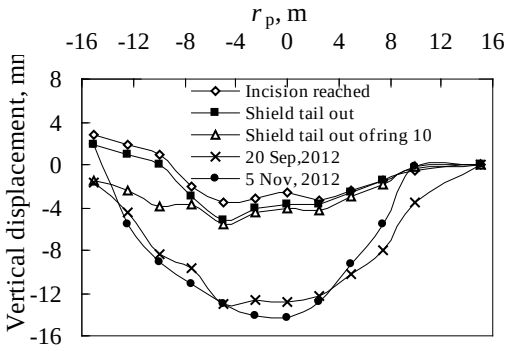

Figure 3: Vertical displacement of the steel pipeline

A two-dimensional model was established for the numerical analysis when a finite element analysis software ABAQUS was used. The Mohr-coulomb law was employed to represent the constitutive model of the soil, and the unit type was set as CPE4. The boundary condition was that there was no horizontal displacement at the side and there were no horizontal and vertical displacements at the bottom. The steel pipeline was simulated as an isotropic and elastic material by using B21 beam element. The steel pipeline and the soil were closely contacted with each other during the whole process. Three cases were considered to investigate the effects of the buried depth and the strength of the steel pipeline on the deformation of the steel pipeline: Pipeline 1 was the real one and had material properties as shown in Table 1; Pipeline 2 had material properties as Pipeline 1 except that it was buried at a depth of 10 m; Pipeline 3 was buried at a depth of 10 m and had a strength smaller than Pipeline 1.

Figure 4 shows the vertical displacements of the ground surface, Pipeline 1, Pipeline 2, and Pipeline 3. It can be seen that the influence zone due to the excavation are roughly the same for different buried depths, about 3.5 times the diameter of the tunnel. The maximum vertical displacement of pipeline 2 is obviously larger than that of pipeline 1, indicating that the maximum value of the settlement trough increases as the buried depth of pipelines increases. In addition, the maximum vertical displacement of Pipeline 3 is larger than that of Pipeline 2, indicating that the maximum value of settlement trough increases as the strength of the pipelines decreases. The bending moment along pipelines is shown in Figure 5. The results show that the pipelines are subjected to negative and positive bending moments for $r_p < D$ and $D \le r_p \le 2D$ respectively, however, the bending moment is small for $r_p > 2D$. The bending moment of Pipeline 1 is larger than that of Pipeline 2, indicating that the bending moment

increases as the buried depth of the pipeline increases. The bending moment of Pipeline 3 is the smallest, indicating that the bending moment decreases as the strength of the pipeline decreases.

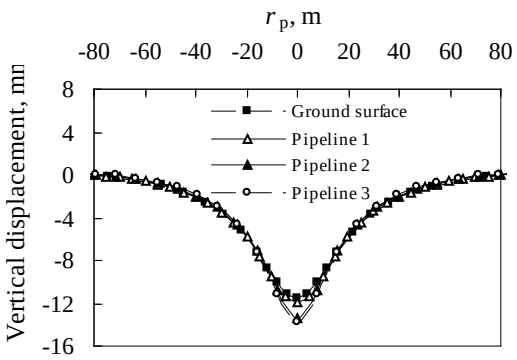

Figure 4: Vertical displacement after excavation

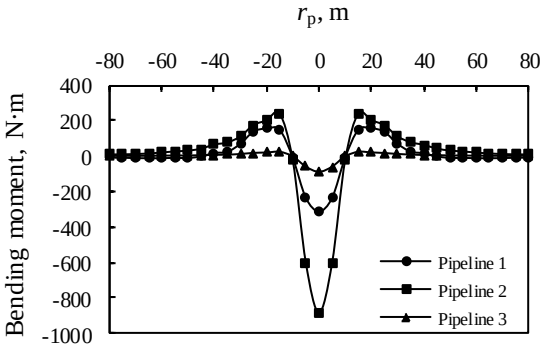

Figure 5: Bending moment after excavation

Figure 6 shows the horizontal displacements of the ground surface, Pipeline 1, Pipeline 2, and Pipeline 3. The horizontal displacement is relatively small compared to the vertical displacement (see Figure 4), and due to the soil loss after excavation, the horizontal displacement is towards the centre. It can be seen that the horizontal displacement decreases as the buried depth and strength of pipelines increase. The measured and numerically predicted vertical displacements for both the ground surface and Pipeline 1 are compared in Figure 7. For the ground surface, the predicted value of 11.5 mm is larger than the measured value of 8.2 mm, however, the shapes of the settlement troughs are almost the same. The difference in measured and predicted values for Pipeline 1 is limited, but the shapes of them are quite different.

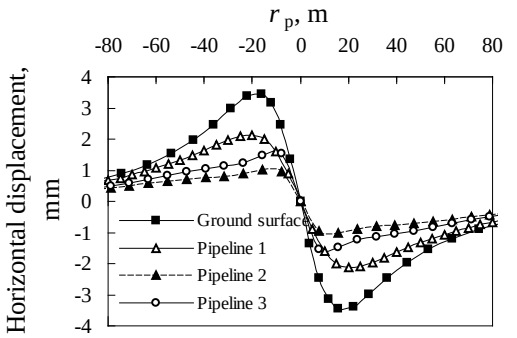

Figure 6: Horizontal displacement after excavation

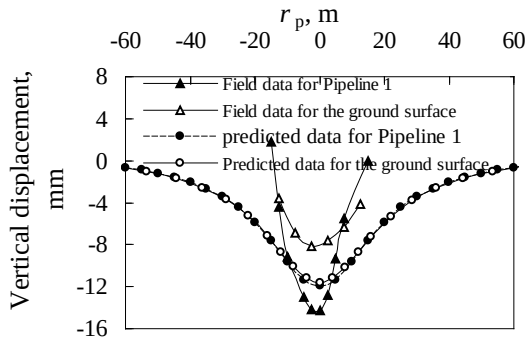

Figure 7: Comparison of predicted and measured data

5. Conclusions

A case study of Shanghai South Hong-mei Road Tunnel Project was carried out, where the vertical displacement, horizontal displacement, and bending moment of the underground pipelines after excavation were discussed. The measured and predicted data were compared and an agreement was achievement to some extent.

References

[1] P.B. Attewell. Soil movements induced by tunneling and their effects on pipelines and structures. London: Blackie & Son Ltd, 1986.

[2] J.H. Hang. Shield tunnel. Beijing: China Railway Press, 1991. (in Chinese)

[3] P.L. Shen and H.B. Zhang. Analysis of land subsidence due to subway tunnel shield construction in Shanghai. Journal of Hohai University (Natural Sciences), 31(5): 556-559, 2003. (in Chinese)

[4] R.B. Peck. Deep excavations and tunneling in soft ground. Proceeding of 7th International Conference on Soil Mechanics and Foundation Engineering. Mexico City: State of the Art Report, 225-290, 1969.

[5] M. Chen. Displacement of pipelines and deformation of surrounding soils subjected to the disturbance of tunnel construction. Beijing: Beijing Jiaotong University, 2008. (in Chinese)

Proceedings of the 22nd UK Conference of the
Association for Computational Mechanics in Engineering
2 – 4April 2014, University of Exeter, Exeter

DIGITAL DATA ACQUISITION FOR EFFECTIVE SLOPE MANAGEMENT

***Matthew L. Eyre[1], Denise Pascoe[1], Patrick J. Foster[1] and John S. Coggan[1]**

[1]Camborne School of Mines, University of Exeter, Cornwall Campus, Cornwall, UK, TR10 9FE

*mle203@exeter.ac.uk

ABSTRACT

Recent improvements in both digital data acquisition and software for subsequent analysis, through use of photogrammetry and both aerial and terrestrial LiDAR (Laser Interferometry Detection And Ranging), have provided improved tools to capture rock mass characteristics, slope geometries and digital terrain models for more effective slope management in the extractive industries. Advantages of using the improved technology (such as safer collection of data – not exposing personnel to dangerous areas; greater areal coverage for data collection – not restricted by man-access/reach; rapid collection of numerous data points; fully geo-referenced x, y, z point cloud data) far out-way the perceived disadvantages (need for correct training to ensure user proficiency of both hardware and software; need for awareness of equipment and software limitations; too much data to analyse effectively in a timely manner). Example use of remotely captured data for subsequent data analysis is presented to demonstrate the wide range of different applications such as providing input for slope stability analyses for subsequent implementation of appropriate mitigation strategies, highlighting unstable regions of a slope, comparative evaluation of point cloud data from repeated scans to monitor movement of material (or placement of materials on tips or stockpiles), providing data for risk-based design and providing capability to undertake real-time monitoring of rock slopes. A key benefit of the detailed point cloud data is the ability to measure and evaluate discontinuity characteristics such as orientation, spacing, persistence and volumetric data which are key factors that dictate the size of any potential failure.

Keywords: *terrestrial LiDAR; slope stability; point cloud data; discontinuity characteristics*

1. Introduction

Remotely captured spatial data, generated from a variety of techniques including both aerial and ground-based laser scanning data (LiDAR) and digital photogrammetry can be used to monitor and track movement or deformation of specific locations or targets on the Earth's surface. Such data can be subsequently used for a range of geological and geomorphological applications including monitoring of both temporal and spatial change of an excavation profile, rock mass characterisation (including determination of orientation and spatial parameters) and generation of hazard maps [1-4]. These techniques are being increasingly used within the mining and minerals industry for more effective management of natural resources; taking advantage of improved, high-resolution monitoring data and reduced exposure of personnel to potentially hazardous working environments [5].

Apart from the obvious improved Health and Safety aspects, remote mapping techniques allow rapid collection of digital data that can be subsequently analysed to provide input parameters for a variety of geomechanical or geotechnical computer-based design models or software. The key advantages of remote techniques are their speed, greater area coverage and ability to map inaccessible areas [6]. The remote data capture systems allow rapid collection of large quantities of data that can be subsequently analysed to provide realistic representations of the slope surface and rock mass fracture network. The data can also be incorporated into slope stability design software to assess potential modes of instability, undertake sensitivity analyses on critical input parameters, carry out back analyses of recent slope failures and provide design-related data for geotechnical investigations (be it for deterministic analysis to calculate a Factor of Safety value or probabilistic analysis to provide probability of failure or evaluation of risk of failure). Advances in technology provide ever increasing opportunities for improved visualisation and a geospatial rich data source for subsequent evaluation.

2. Data capture and acquisition

LiDAR systems can be operated from a static position (terrestrial) or on the move (mobile). Terrestrial systems allow data to be gathered from one set-up location (position) and then the instrument is physically moved to a new position (if required). Mobile (including airborne) based systems incorporate an Inertial Measurement Unit (IMU) that feeds data back into the system of the instruments location and compensate for movement of the equipment when in transit [1]. The terrestrial instrument has to be either set over a known location and subsequently sighted to another in order to obtain an orientation. Alternatively, the surveyor must place a number of targets within the area to be scanned in order to reference them using conventional survey methodologies. This can be achieved by sighting the targets to be scanned using a total station from a known location or using Global Positioning System (GPS) with Real Time Kinematic (RTK) correction to compensate for errors obtained through signals.

Singular point clouds encounter problems with 'blinding'; when the scene is obscured and the point cloud is missing data. In order to overcome this, multiple laser scans are taken to obtain a complete data set for a scene. However, when multiple scans are surveyed, the point clouds have to be joined together. This process is known as registration. Common points are chosen and assigned between the scans. Once enough points (at least 3) are matched between the point clouds, a registration adjustment is processed by the software and an error value is obtained. Once a complete geo-referenced model has been made the data can then be exported for use within many different software applications. However, a clear understanding of the hardware and software requirements are necessary in order to export the data in a useable format for the desired outcome.

3. Applications of digital data for effective slope management

Example use of terrestrial LiDAR data for subsequent data analysis is provided in Fig. 1, which highlights applications for evaluation of both rock mass and slope instability characteristics. This data can also form the basis for development of GIS-based qualitative hazard and risk analysis, provide input for slope instability simulation and be used to undertake real-time monitoring of rock slopes. It can also be used for more effective evaluation of slope management systems, by highlighting kinematically susceptible areas, sheared zones or potentially unstable lithologies, providing data on block size distribution for design of appropriate mitigation measures, analysing trajectory paths and monitoring not only failure source areas but potential run-out distances.

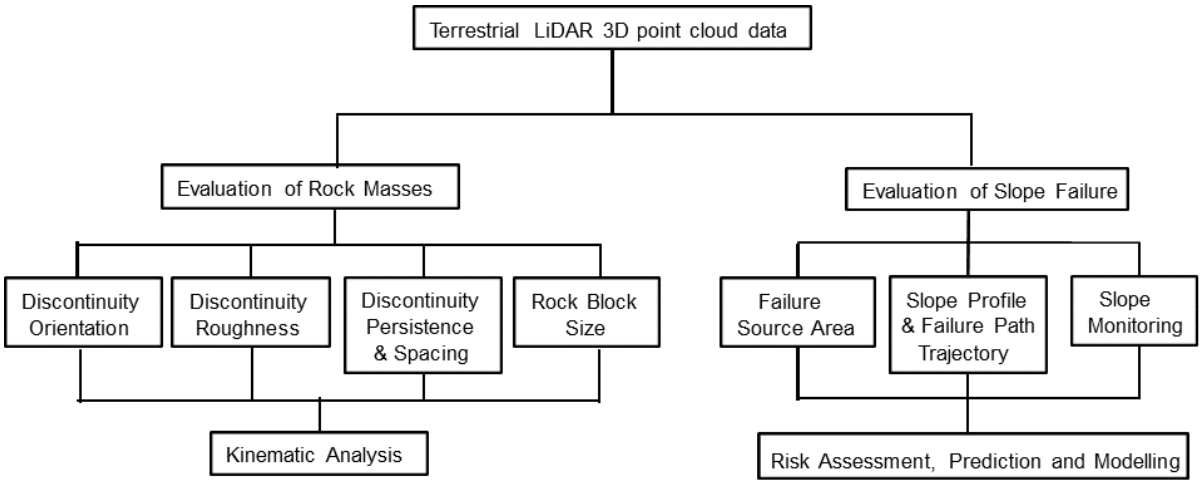

Figure 1: Use and applications of terrestrial LiDAR point cloud data in relation to rock mass characterisation and slope instability evaluation. Adapted from [1].

Example use of terrestrial LiDAR to effectively capture the three-dimensional nature of a rock mass can be seen in Figs. 2 and 3. Evaluation of the fully geo-referenced x, y, z point cloud, using Split-FX

[7], can then be undertaken to determine the orientation of specific discontinuities, which can then be incorporated into stereographic software for kinematic evaluation of discontinuity-controlled failure. Remote characterisation has been applied to different rock types, across a range of varying rock quality. Experience indicates that use of remote data acquisition systems for evaluation of rock fracture network orientations are better suited for geotechnical applications that involve blocky rock masses. Representative scales of mapping should be established, however, to ensure that important features are captured during the mapping exercise, to ensure that critical discontinuities are included within the mapped region.

Figure 2: Photographic image (left) and point cloud representation (right) of a failure scar in a quarry slope face.

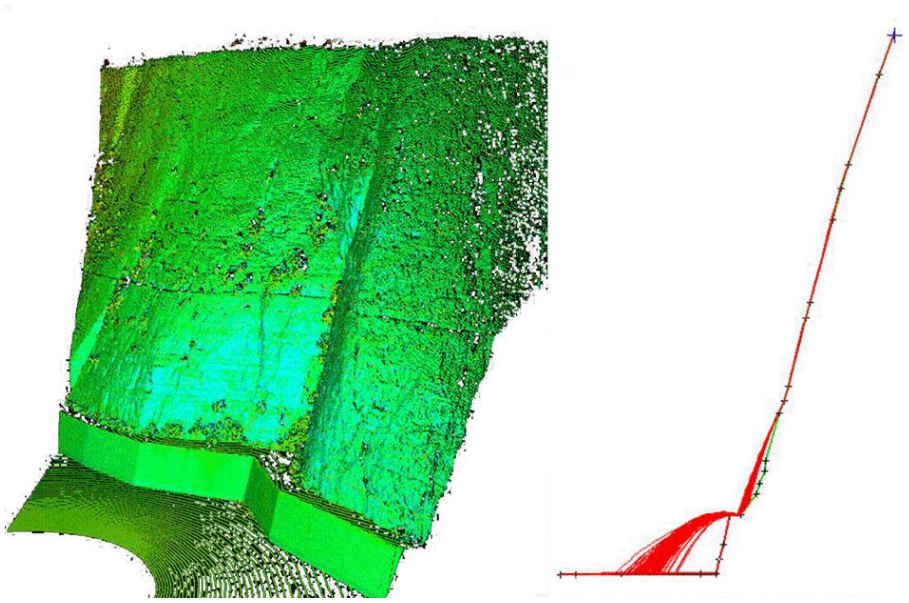

Figure 3: Point cloud representation of a chalk cliff face (left) and subsequent rockfall simulation (right).

A key benefit of the detailed x, y, z point cloud data is the ability to measure and evaluate discontinuity spacing and persistence data which are key factors that dictate the block size and location of strategic key blocks. Block size distribution data/statistics can be used to characterise the rock mass, identify rockfall susceptible lithologies, and indicate the size and potential extent of any likely rockfall. Representative cross-sections taken through point cloud data can been used to undertake two-dimensional rockfall simulations, as depicted in Fig. 3. This type of analysis can be used to assess potential remediation strategies, such as design of catch ditches, stand-off bunds and, if necessary, consideration of catch fences [8]. However, successful use of rockfall simulation software

relies on correct calibration of input parameters [8; 9; 10]. Further software developments are required to incorporate different rock particle shapes within rockfall analysis, together with realistic impact properties to ensure user confidence. Where possible, it is important that any analysis should be validated against historical rockfall records or field trial data [9; 10].

Detrimental effects of blasting may also be quantified (by recognition of the extent and location of any damage induced by blasting). Repeated scans have been used to quantify the volume difference between successive scans (to determine both the location and extent of failure activity between surveys) for a range of application within the extractive industries including monitoring of movement of material.

4. Conclusions

Recent improvements in both digital data acquisition and software for subsequent analysis, through a variety of techniques, have provided improved tools to capture rock mass characteristics, slope geometries and digital terrain models for more effective slope management in the extractive industries.

Research suggests that automated analysis of data using automated routines is not yet recommended, and there is a need for educated users that are familiar with potential limitations/issues with use of both hardware and software. Despite these reservations, when used correctly remote mapping techniques can be extremely useful for not only capturing the geometrical characteristics of the rock mass but also using this information for optimisation of excavation and extraction of resources. The need for effective and efficient management of data collection, data transfer and subsequent analysis and associated interpretation is essential.

References

[1] A.K. Turner, and R.L. Schuster, R.L. (eds.). *Rockfall: characterization and control*. Transportation Research Board, National Academies of Sciences, 658p, 2012.

[2] G.M. Stock, N. Luco, B.D. Collins, E.L. Harp, P. Reichenbach and K.L. Frankel. *Quantitative rock-fall hazard and risk assessment for Yosemite Valley*, Yosemite National Park, California, Division of Resources Management and Science, Yosemite National Park, 92p, 2012.

[3] M. Sturtzenegger and D. Stead. Close range terrestrial digital photogrammetry and terrestrial laser scanning for discontinuity characterization in rock cuts, *Engineering Geology*, 16, 3-4, 163-182, 2009.

[4] A. Volkwein, K. Schellenberg, V. Labiouse, F. Agliardi, F. Berger, F. Bourrier, K.A. Dorren, W. Gerber and M. Jaboyedoff. Rockfall characterisation and structural protection – a review, *Natural Hazards and Earth Systems Sciences*, 11, 2617-2651, 2011.

[5] Guidelines for Open Pit Slope Design. (Eds). J. Read and P. Stacey, CSIRO Publishing, CRC Press, 496p, 2009.

[6] J.S. Coggan, X. Gwynn, Z. Flynn and A. Wetherelt. Comparison of hand-mapping with remote data capture systems for effective rock mass characterisation, In: *Proceedings of 11th Congress of the International Society for Rock Mechanics - the second half century of rock mechanics*, volume 1, 201-205, 2007.

[7] Split Engineering Ltd, Split-FX, http://www.spliteng.com/

[8] Rocscience, RocFall, http://www.rocscience.com/

[9] A. Giacomini, O. Buzzi, B. Renard and G.P. Giani, G.P. Experimental studies on fragmentation of rock falls on impact. *International Journal of Rock Mechanics & Mining Sciences*, 46, 708-715, 2009.

[10] M.E. Robotham, H. Wang and G. Walton. Assessment of risk from rockfall from active and abandoned quarry slopes. *Transactions Institute Mining Metallurgy*, 104, A25-A33, 1995.

Proceedings of the 22nd UK Conference of the
Association for Computational Mechanics in Engineering
2 – 4April 2014, University of Exeter, Exeter

Effect of Permeability Variation with Depth on Soil Resistance to Caisson Penetration

***Moura Mehravar, Ouahid Harireche and Amir M. Alani**

School of Engineering, University of Greenwich, Chatham, Kent, UK

*M.Mehravar@gre.ac.uk

ABSTRACT

Suction-induced seepage is pivotal to the installation of caisson foundations in sand. Indeed, Pressure gradient generated by the imposed suction inside the caisson cavity cause an overall reduction in the lateral soil pressure acting on the caisson wall as well as caisson tip resistance. This transient loosening of soil around the caisson wall helps caisson penetration into the seabed. However, these effects must be controlled to avoid soil failure due to critical condition such as piping which may cause the installation process to fail because of instability of the soil plug trapped inside the caisson cavity. Therefore, in order to have a safe installation process the soil conditions, especially soil resistance and critical condition to piping must be predicted and controlled during entire installation procedure.

In this paper, the effects of excess pore water pressure gradients due to applying suction on soil resistance in homogenous sandy soil and isotropic heterogeneous seabed profile is addressed. For this purpose a simple finite difference model is used to solve the normalised seepage problem. In order to apply the results to any size of the caisson, the problem dimensions are scaled with regard to the caisson radius. The results show that a predication of soil resistance based on constant permeability in the seabed profile with varying permeability by depth is non-conservative, due to an overestimated reduction in effective stress under suction-induced seepage.

Keywords: *Suction Caisson Installation; Varying Permeability with depth; Soil Resistance; Normalised seepage problem*

1. Introduction

A suction caisson consists of a thin-walled upturned 'bucket' of cylindrical shape made of steel [1-2]. This novel type of foundation has been approved to be very successful in oil and gas industry and the current trend is to employ them as foundations for offshore wind turbines. Usually the initial penetration into the seabed takes place under the caisson self-weight, and once the rim of the caisson creates a sufficient seal with seabed due to its dead weight, suction is subsequently applied by pumping out the water trapped inside the internal caisson cavity in order to push the caisson to the desired depth.

In sandy soils, seepage causes an overall reduction in soil resistance and facilitates caisson installation process [3]. The role of the porewater seepage induced by suction has been considered in most of the design procedures of caisson installation in sand [4-6]. The effect of suction during caisson installation in sand has also been considered in centrifuge model testing. A series of experimental tests on suction caisson foundations in a geotechnical centrifuge were conducted to study the variation and distribution of excess pore water pressure generated by suction in homogeneous dense sand [7]. Additionally, numerical modelling such as finite element simulations was employed to model the suction caisson installation process [8]. The existence of low permeability silt layers has been considered by Tran et al [9].

In this paper, the numerical procedure proposed by Harireche et al. [3, 10] is employed to investigate the effect of seepage induced suction on soil resistance during caisson installation in homogenous sand and in a seabed profile with decreasing permeability by depth. The aim of this study is to assess whether a homogenous seabed model is a conservative assumption for caisson installation design or not.

2. Normalised Seepage Problem and Permeability Profiles

In order to draw conclusions that are not related to the problem dimensions, any length measure is scaled with respect to the caisson radius and pressure is normalised by the magnitude of applied suction. Figure 1, shows a vertical section through the meridian plane of the system caisson-soil where a cylindrical system of coordinates r* and z*is used. For the dimensionless counterpart of the caisson penetration depth h*=h/R is adopted.
Meanwhile, to describe the variation of permeability with depth, the following expression is adopted:

$$\bar{k} \equiv \frac{k(z^*)}{k_0} = (1-\beta)e^{-\alpha z^*} + \beta \qquad (1)$$

Where $k \equiv K / n\gamma_w$ and K is the absolute permeability and n denotes the porosity. The coefficient k_0 denotes the permeability at the seabed surface, α and β are two constants, and z*=z/R indicates the normalised depth. Figure 2 shows different permeability profiles and the corresponding values of the parameters α and β. Three cases have been selected, which will be investigated in the following sections. Case A corresponds to a homogeneous seabed profile with constant permeability. In case B, the permeability decreases with depth almost linearly. Finally, in case C, permeability has a non-linear profile and decreases with depth at a much higher rate compared to case B. Additionally, in both cases B and C, the soil is assumed to become impervious at large depth.

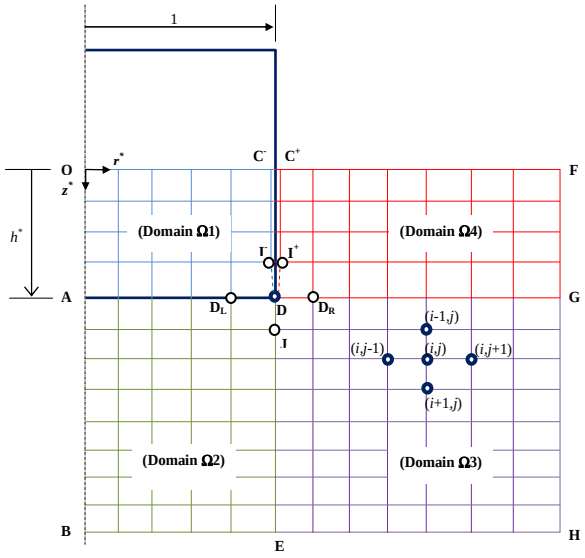

Figure1: Normalised geometry and finite difference mesh

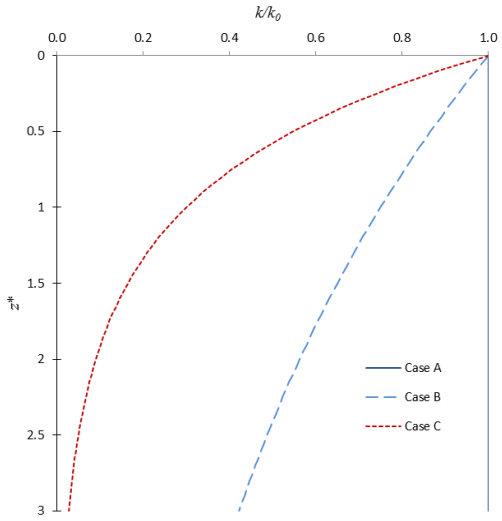

Figure 2: Permeability profile: case A (Constant-permeability), Case B (α=0.288) and Case C (α=1.204)

3. Soil Resistance to Suction Caisson Installation

The suction magnitude imposed over the radial distance OC^- (Fig. 1) is expected to increase during installation. Indeed, as the caisson is pushed into the seabed, suction must be increased to overcome the increasing soil resistance. Water seepage caused by suction produces a hydraulic gradient which, on both faces of the caisson wall, varies with depth. Figures 3a and 3b show the vertical component of the normalised pressure gradient $g^* = \partial p^* / \partial z^*$ on both sides of the caisson wall as a function of scaled depth z^* for the three permeability profiles (cases A, B and C). Values of scaled penetration depth h^* = 0.2 and 1 have been considered. It can be seen that the pressure gradient on each side of the caisson wall is higher at the early stages of the installation process. Maximum values of the gradient occur at the caisson tip.

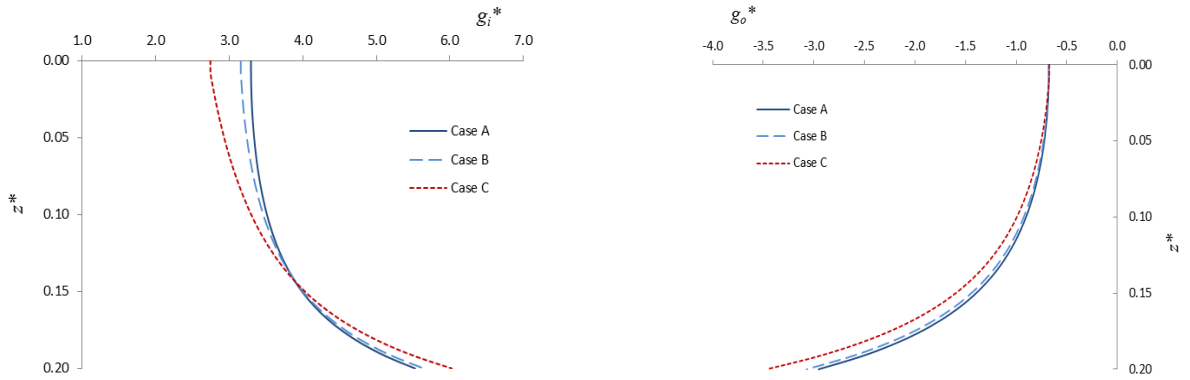

(a)

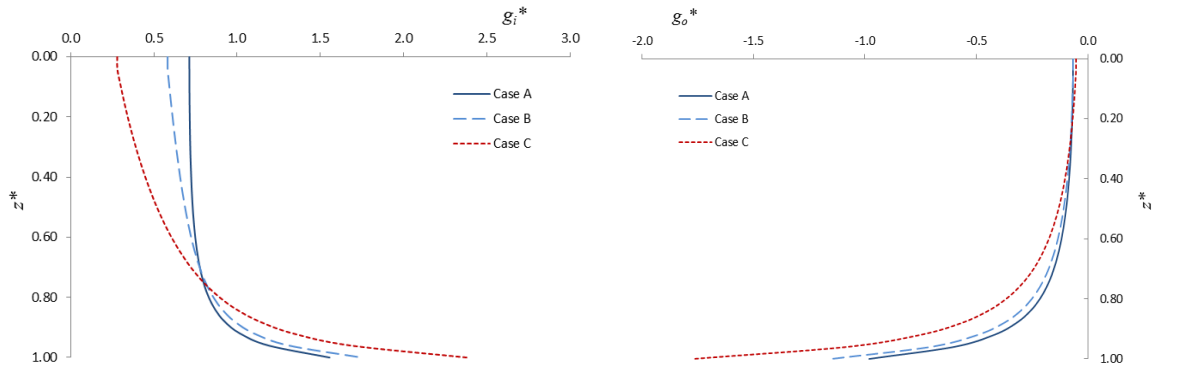

(b)

Figure 3: Dimensionless pressure gradient as a function of normalised depth for different permeability profile (case A, B and C). (a) h^*= 0.2 & (b) h^*=1

4. Lateral Frictional Resistance on Caisson Wall

In the presence of seepage the reduction of lateral effective stress around the caisson wall is expressed by Equation.2 [3, 10].

$$\frac{\Delta\sigma_h^{'}(R,z)}{Ks} = L_i^*(z^*) + L_o^*(z^*) \tag{2}$$

and

$$L_i^*(z^*) \equiv \int_0^{z^*} g_i^*(1,\zeta^*)d\zeta^* > 0 \quad , \quad L_o^*(z^*) \equiv \int_0^{z^*} g_o^*(1,\zeta^*)d\zeta^* < 0 \quad \text{and} \quad \left|L_i^*(z^*)\right| > \left|L_o^*(z^*)\right| \tag{3}$$

Where, g_i (R, ζ) and g_o (R, ζ) denote the vertical component of the pressure gradient on the inner and the outer sides of the caisson wall respectively. Using a numerical calculation of the integrals in Equation 3.0 on the normalised finite difference mesh, the scaled reduction of the lateral effective stress has been obtained for two different scaled penetration depth (Figure 4a, b). It can be observed that a higher rate of variability in the permeability corresponds to a lower reduction in the lateral effective stress. This shows clearly that the assumption of a homogeneous seabed is not in favour of a conservative estimation of soil resistance to caisson penetration as it overestimates the effect of seepage on the reduction of the lateral effective stress.

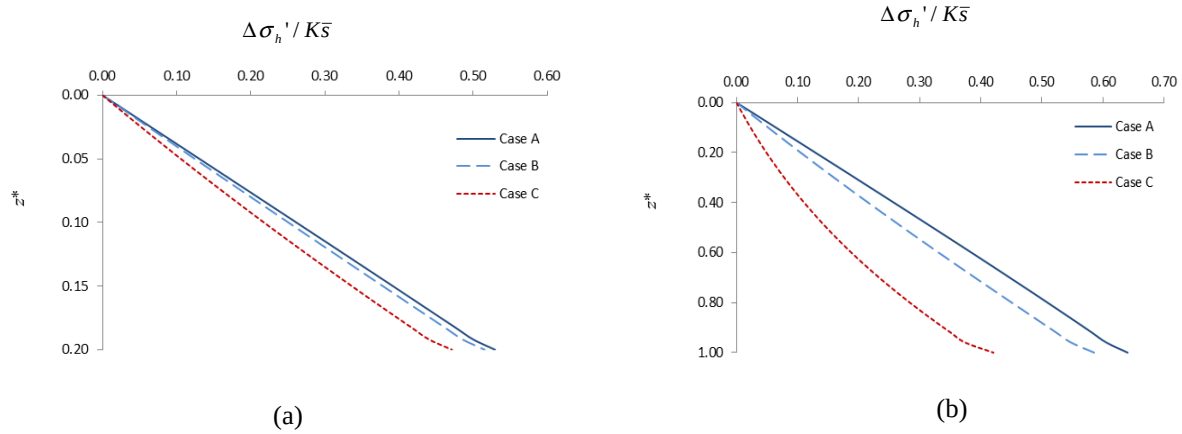

Figure 4: Change in the normalised lateral effective stress on caisson wall due to suction-induced seepage. (a) h^*=0.2 & (b) h^* =1.

5. Conclusion

In this study the effect of a permeability varying with depth on the prediction of shear soil resistance to caisson penetration has been considered. The effect of suction induced seepage on soil resistance to caisson penetration has been investigated using the normalised solution of seepage around the caisson wall. It has been observed that a constant permeability profile leads to an under-estimation of soil resistance to caisson penetration. This highlights the importance of taking into account a permeability profile with certain variability with depth for a more accurate prediction of the required suction throughout the installation process.

Acknowledgements

Funding of a PhD scholarship by the University of Greenwich to support the first author is gratefully acknowledged.

References

[1] B. Byrne, G. Houlsby, C. Martin and P. Fish, “Suction Caisson Foundations for Offshore Wind Turbines,” Wind Engineering, vol. 26, no. 3, pp. 145-155, 2002.

[2] B. W. Byrne and G. T. Houlsby, “Foundation for Offshore Wind Turbines,” Royal Society, pp. 2909-2930, 2003.

[3] O. Harireche, M. Mehravar and A. A. Alani, “Suction caisson installation in sand with isotropic permeability varying with depth,” Applied Ocean Research, vol. 43, pp. 256-263, 2013.

[4] C. Erbrich and T. TI, “Installation of bucket foundations and suction caissons in sand: geotechnical performance,” in Offshore technology conference, Houston, 1999.

[5] M. Senders and M. Randolph, “CPT-based method for the installation of suction caissons in sand,” Journal of Geotechnical and Geoenvironmental Engineering, pp. 14-25, 2009.

[6] M. Tran, R. MF and D. Airey, “Experimental study of suction installation of caissons in dense sand,” in 23rd international conference on offshore mechanics and arctic engineering, Vancouver, Canada, 2004.

[7] M. Tran and M. F. Randolph, “Variation of suction pressure during caisson installation in sand,” *Géotechnique*, vol. 58, no. 1, pp. 1-11, 2008.

[8] S. Zhang, Q. Zheng and X. Liu, “Finite element analysis of suction penetration seepage field of bucket foundation platform with application to offshore oilfield development,” Ocean Engineering, vol. 31, pp. 1591-1599, 2004.

[9] M. Tran, m. F. Randolph and D. Airey, “Installation of suction caissons in sand with silt layers,” Journal of Geotechnical and Geoenvironmental Engineering, vol. 133, no. 10, pp. 1183-1191, 2007.

[10] O. Harireche, M. Mehravar and A. Alani, “Soil conditions and bounds to suction during the installation of caisson foundation in sand,” Ocean Engineering. (under review), 2014.

Proceedings of the 22nd UK Conference of the
Association for Computational Mechanics in Engineering
2 – 4April 2014, University of Exeter, Exeter

FINITE ELEMENT STUDY OF THE BEARING CAPACITY OF SHALLOW FOUNDATIONS WITH NON-ASSOCIATED FLOW RULE

*** M. Hamlaoui[1], A. Oueslati[1] and G. De Saxcé[1]**

[1]Mechanics laboratory of Lille, University of Lille1, Villeneuve d'Ascq, 59650-France

*madani.hamlaoui@ed.unv-lille1.fr

ABSTRACT

This paper is concerned with a numerical study of the vertical bearing capacity of a strip footing foundation. We consider a rough contact between the base of foundation and the substrate which is assumed elastic perfectly plastic follow the Drucker-Prager model. Analyses were performed by incremental finite element simulations. The post-treatment of the numerical results permits one to investigate the effect of the non-associated flow rule on the plastic limit load and the failure mechanism in order to build theoretical solutions.

Keywords: *Bearing capacity; shallow foundation; Drucker-Parger criterion; non associated flow rule; Finite element method*

1. Introduction

The plastic limit load evaluation of soil is of a great importance in theoretical plasticity and civil engineering design. Since the first analytical solutions of the bearing capacity of shallow foundations presented by Prandtl [12] and Reissner [13], a large number of contributions and papers have been published in literature.
The limit analysis [5, 14, 4] considers rigid-perfectly plastic materials under proportional loading. It assume an associated flow rule which means that the dilatancy angle is equal to the friction angle of the material. Nevertheless, it has been recognized that dilatancy angle is lower than the friction one and thus the plasticity is not associated. Some numerical solutions obtained by the finite element method are proposed in the literature [6, 10]. The purpose of this paper is to investigate numerically the influence of the non associativity of the Drucker-Prager model on the plastic limit load. A particular focus is devoted to the failure mechanism which is compared to the Prandtl and Hill mechanisms. The step-by-step elastic plastic computations are derived by the software Cast3m [7].

2. The non associated Drucker-Prager criterion

In their pioneering work [18], Drucker and Prager proposed a generalization of Von Mises criterion by including the effect of the hydrostatic pressure (or the first invariant of the stress field).
The model is known as the Drucker-Prager model for which the yield function is given by:

$$f(\sigma_{ij}) = \sigma_e + \alpha.tr(\sigma_{ij}) + \sigma_0 \leq 0 \text{.....} \text{.....} \text{....} (1)$$

Where: Equivalent stress: $\sigma_e = (\frac{3}{2} s_{ij} s_{ij})^{\frac{1}{2}}$, Deviatoric part of the stress tensor : $s_{ij} = \sigma_{ij} - \delta_{ij}\sigma_m$;

Hydrostatic Stress: $\sigma_m = \frac{1}{3} tr\sigma_{ij}$, Pressure sensitivity factor $\alpha = \frac{\tan\varphi}{3}$, σ_0 :Yield stress

The plastic potential is given by: $g(\sigma_{ij}) = \sigma_e + \beta.tr(\sigma_{ij}) \leq 0 \text{.....} \text{.....} .(2)$

$$\text{Where: } \beta = \frac{\tan\psi}{3}$$

3. Bearing capacity and the collapse mechanism of the strip footing

A rigid strip footing is pressed into an elastic perfectly plastic soil by a vertical loading under the assumption of plane strain conditions. The substratum is considered weightless and obeys the Drucker-Prager model with a non associated flow rule (1) and (2). The interface contact with the punch is assumed rough . The width of the foundation is noted by B and the dimensions of the substrate are LxH

Due to the symmetry, only the half of the sheet is modeled by the finite element method. The substrate is discritized by 6-noded triangular elements as depicted in figure 1. The path loading consists of uniform increments of vertical displacement exerted on the nodes beneath the footing. The two vertical sides of the soil are restrained in horizontal direction while the base is fixed in both directions (see figure 1). The rough condition between the soil and the footing is ensured by preventing the horizontal displacement of the nodes under the footing.

Numerical simulations were carried out with $B = 2m$, $H = 5B$ and $L = 10B$. The following material parameters were used: $E = 30MPa$, $\nu = 0.3$, $\sigma_0 = 0.01MPa$ and $\varphi = 35°$

4. Limit plastic load

Figure 2 represents the load-displacement curves for different dilatancy angles ψ . The footing load is obtained as the sum of the nodal reactions at the nodes below the punch. It is clearly seen that the limit load is well-defined without oscillations in the curves for all values of the dilatancy angle except for very small values of ψ (such as $\psi = 0°$) which are known as difficult cases [3, 9]. It is worth noting that, in many works in literature [10, 15] with Mohr-Coulomb model, oscillations are observed in the load-footing settlement and the intensity of this oscillation increases with increasing mesh refinement and with increasing. As expected, the limit load for non-associated plasticity is lower than the one corresponding to the associated model. More precisely, the limit load decreases with the dilatancy angle. This property has been observed in other published works [9, 1, 2].

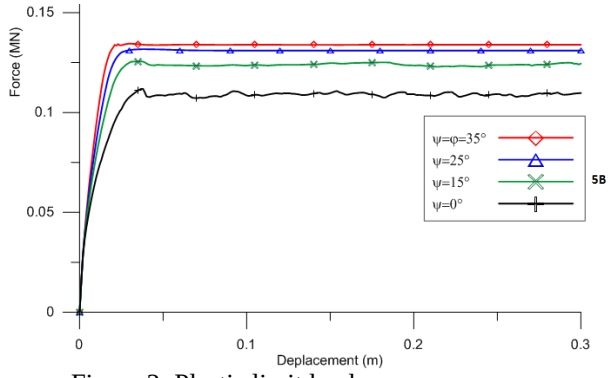

Figure 2: Plastic limit load.

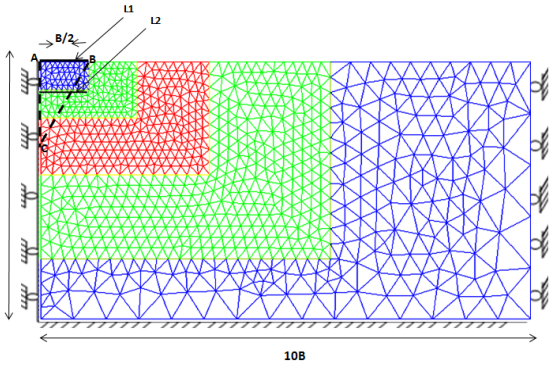

Figure 1: Mesh and boundary conditions

5. Failure mechanism

Figures [5, 6, 7, 8], show the failure patterns depicted by the isovalues of the incremental vertical displacement at the numerical limit load for a friction angle $\varphi = 35°°$ and an angle of dilatancy $.\psi = \{35,25,20,10\}$ .The collapse mechanism is reminiscent of the Prandtl's one [5] and shows three zones of different strains. (See figure 3).

It is important to note that the for associate case $\psi = \varphi = 35°$ in the figure5 the mechanism is identical in shape and size to the mechanism for an associated Mohr-Coulomb model predicted by Method of characteristics, using the computer program ABC [11]) in the figure 4. Moreover, we observe that the extend of rupture area for $\psi = \varphi$ is greater than that for $\psi \prec \varphi$: the deformation is highly localized for the non-associated material while strains seem to be more diffuse inside the mechanism for associated Drucker-Prager model.

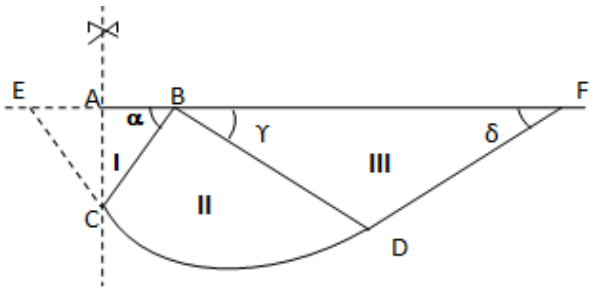

Figure 3: The Prandtl failure mechanism

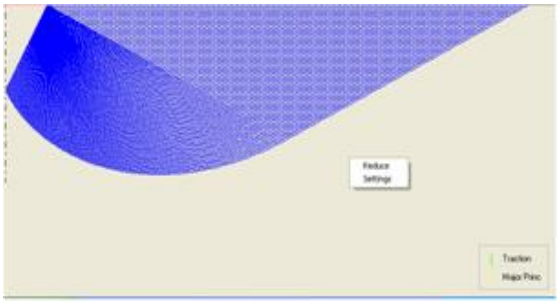

Figure 4: Mechanism with ABC program (ψ=φ=35°)

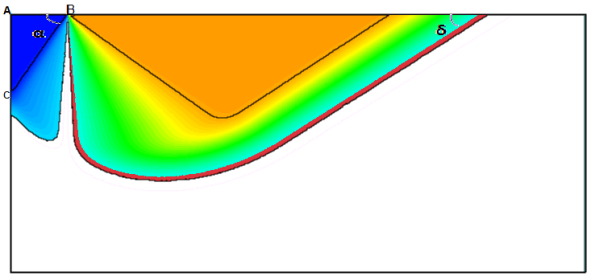

Figure 5: Mechanism for the associated case ψ=φ=35

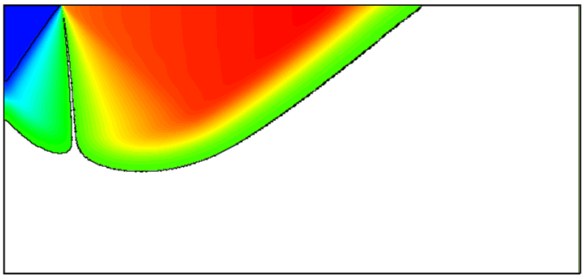

Figure 6: Mechanism for the associated case ψ=25

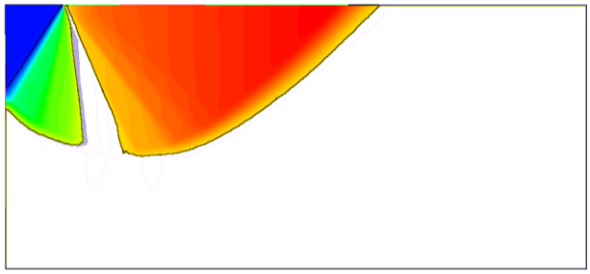

Figure 7: Mechanism for the non associated (ψ=10°)

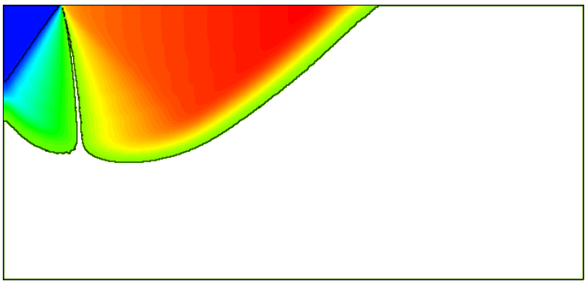

Figure 8: Mechanism for the non associated (ψ=20°)

Moreover, it seems that the triangular wedge (ABC) is independent of the dilatancy angle ψ. To investigate this more detailed analysis by post-treatment of the numerical results has been conducted in order to identify with the maximum of precision the band between the triangular wedge ABC and the Logspiral zone BCD and to measure the base angle α. Recall that for the associated Mohr-Coulomb material $\alpha = \left(\frac{\pi}{4} + \frac{\varphi}{2}\right)$. To capture the transition line, we considered the curves of vertical displacement on two horizontal lines L_1 and L_2 (see figure [1]) and then, by the finite differences method, we computed and plotted the curvature of theses curves, by means of the first derivative, in terms of the horizontal coordinates.

For the associated Drucker-Prager model and for different values of the friction angle φ, the measured values of the angle α obtained by post-processing are in good agreement with the value of $\left(\frac{\pi}{4} + \frac{\varphi}{2}\right)$ as summarized in table 1.Let us now consider the non associated model. For a friction angle ψ=35°, the values of the angle base α obtained by post-treatment are given in table 2 for different values of the dilatancy angle $\psi = \{35,30,25,20,15,10\}$. It is observed that this value is independent of the dilatancy angle and can therefore be estimated by $\left(\frac{\pi}{4} + \frac{\varphi}{2}\right)$ for both associated and non associated

Table 1: the measured angle (α°) for associated case

ψ=φ(°)	Theoretical	Measured	Error %
35	62.5	62.34	0.25
30	60.0	57.60	4.00
25	57.5	55.60	3.20
20	55.0	53.88	2.00
15	52.5	52.05	0.80
10	50	50.33	-0.60

Table 2: the measured angle (α°) for non associated case

ψ (°)	Measured	Error %
35	62.34	0.25
30	62.25	0.40
25	62.25	0.40
20	62.34	0.25
15	62.15	0.56
10	62.25	0.25

6-Conclusions

This paper investigated the effect of the non associativity of the Drucker-Prager model on the plastic limit load and the collapse mechanism of substrate.
The obtained results confirm that the ultimate bearing capacity decreases with the dilatancy angle and provide relevant information on the collapse mechanism:
• For non associated materials, the failure mechanism is a Prandtl-type one for both associates and non associated materials but the extend of failure zone narrows with the dilatancy angle.
• It turns out that α is independent of the dilatancy angle for both associated and non associated materials.
Finally, it should be noted that further research has to be carried out to improve the approach used in this work in order to identify with a maximum of precision the interface lines between different blocs of collapse zones which will help in buliding analytical solution.

7-References

[1] Berga, A., 2012. Mathematical and numerical modeling of the non-associated plasticity of soils —P art2: Finite element analysis. International Journal of Non-Linear Mechanics, 47, 36-45.
[2] Bousshine, L., Chaaba, A., De Saxcé, G., 2001. Softening in stress-strain curve for Drucker-Prager non-associated plasticity. International Journal of Plasticity, 17, 21-46.
[3] de Borst, R., Vermeer, P.A., 1984. Possibilities and limitations of finite elements for limit analysis. Géotechnique. 34, 199–210.
[4] de Buhan, P., 2007. Plasticité et calcul à la rupture. Presses de l'Ecole Nationale des Ponts et Chaussées.
[5] Chen, W.F., 1975. Limit Analysis and Soil Plasticity, Elsevier, New York.
[6] Chen, W.F., 1990. Limit Analysis in Soil Mechanics, Elsevier, Amsterdam
[7] Documentation Cast3M. http://www-cast3m.cea.fr.
[8] Drucker, D.C., Prager, W., Soil mechanics and plastic analysis or limit design, Quart. Appl. Math., 1952, 10, 157-165.
[9] Hjiaj, M., Lyamin, A.V., Sloan, S.W., 2005. Numerical limit analysis solutions for the bearing capacity factor N_γ. International Journal of Solids and Structures, 42, 1681-1704.
[10] Loukidis, D., Salgado, R., 2009. Bearing capacity of strip and circular footings in sand using finite elements. Computers and Geotechnics, 36(5), 871-879.
[11] Martin, C.M. 2003. User guide for ABC Analysis of Bearing Capacity, Version 1.0. OUEL Report No. 2261/03. Department of Engineering Science, University of Oxford.
[12] Prandtl, L., Über die Häete plastischer Körper. Nachr. Ges. Wissensch. Göttingen, Math.-Phys. Klasse, 1920, 74–85.
[13] Reissner, H., Zum Erddruckproblem. Proc., 1st Int. Congr. Appl. Mech., C. B. Biezeno and J. M. Burgers, eds., Delft, 1924, 295–311.
[14] Save, M., Massonnet, C., de Saxcé, G., 1997. Plastic limit analysis of plates, shells and disks. Amsterdam : Elsevier.
[15] Erickson, H.L., Drescher, A., 2002. Bearing capacity of circular footings. J. Geotech. Geoenviron Eng. ASCE, 128, 38–43.
[16] Krabbenhøft, K., Lyamin, A.V., Sloan, S.W., 2007. Formulation and solution of some plasticity problems as conic programs. International Journal of Solids and Structures, 44, 1533-1549.

Proceedings of the 22nd UK Conference of the
Association for Computational Mechanics in Engineering
2 – 4April 2014, University of Exeter, Exeter

NUMERICAL MODELLING OF THE IMPACTS OF SEA LEVEL RISE ON SEAWATER INTRUSION IN UNCONFINED COASTAL AQUIFERS

*** Mohammed S. Hussain[1], Akbar A. Javadi[1] and Victor Robin[1]**

[1]Computational Geomechanics Group, Department of Engineering, University of Exeter, Exeter, EX4 4QF

*msh218@exeter.ac.uk

ABSTRACT

This study presents the application of a density-dependent finite element model to simulate the transient effects of sea level rise (SLR) on seawater intrusion (SWI) in a conceptual case of unconfined aquifer. The model considers both the unsaturated and saturated flow conditions. To model the natural process of SLR, a time-dependent boundary condition is used to define the hydrostatic head imposed by seawater at the coastal boundary where the effect of the gradual rise in the sea level with time is considered. The specified values of SLR are chosen, in the range of that predicted by IPCC (Intergovernmental Panel on Climate Change), for five different periods of time in the current century (from 2014 to 2100). The results indicate that a considerable advance in SWI can be expected in the coastal aquifers until the end of century. The rising of sea level is followed by the lifting of the groundwater table, especially near the shoreline, which gradually declines towards the inland boundary. The effects of spatial variations of the shoreline slope on SWI under SLR condition are also investigated. The results highlight that the flatter slopes of the shoreline intensify the landward process of seawater intrusion.

Keywords: *seawater intrusion; sea level rise; numerical modelling; unsaturated flow; unconfined aquifer*

1. Introduction

Groundwater is a vital component of the global water cycle and it is a valuable resource for water supply. However, the quality of groundwater in the arid and semi-arid coastal areas is one of the environmental issues of the 21st century, which is continuously threatened by the landward intrusion of seawater. Under natural conditions, the replacement of freshwater in coastal aquifers by the seawater due to density-dependent landward movement of saline water body into the freshwater is known as SWI [4]. SWI is considered as the final outcome of this density-dependent interaction between freshwater and seawater and is responsible for dynamic equilibrium of groundwater movement. The hydrodynamic dispersion which is the combination of mechanical dispersion and physio-chemical dispersion (molecular diffusion) controls the spreading out of solute and the mixing process.

A distinct curved zone of saline water, known as the regional "saltwater wedge", is created in the freshwater body and it is the source of contamination that degrades the quality and quantity of freshwater. The negative impacts of SWI would be intensified by the anthropogenic factors such as unplanned exploitation of groundwater and also by the natural factors such as sea level rise (SLR) and tidal effects. The reduction of atmospheric pressure and thermal expansion of oceans are the earliest outcomes of global warming which will in turn lead to the increase of water level in the oceans and seas. However, melting of mountain glaciers, small ice caps, and also melting of polar (Greenland and Antarctic) ice sheets will exacerbate its negative effects in terms of SWI by accelerating the SLR process [2].

Limited research has attempted to study the effects of gradual rise of sea levels on SWI in aquifers. The majority of previous works have focused on simulation of this problem in confined (and even unconfined aquifers) with vertical seaside boundary (without slopes) subjected to constant, time-

independent and unrealistic values of SLR in saturated flow condition. In the present work we study the transient effects of sea level rise on seawater intrusion over a century in a hypothetical unconfined aquifer, considering the effects of the unsaturated (vadose) zone and the shoreline slope.

2. Model Description

In this study, the SUTRA code [1] is used for numerical modelling of 2D case studies of unconfined aquifer. SUTRA implements a hybridization of finite element and integrated finite difference methods to solve the density-dependent flow and transport mass balance equations [1]. A rectangular aquifer with the dimensions 500 m by 30 m is considered as the base model. It is discretized using irregular mesh with 2483 elements and 2594 nodes. The idealized form of the base aquifer and the used boundary conditions are shown in Figure 1. The aquifer is divided vertically in two layers; an unsaturated layer overlying the bottom saturated layer. The hydraulic gradient in the system is 0.0032 corresponding to the defined head boundaries. The modelling parameters used for the groundwater flow, solute transport and porous medium are: D_m, coefficient of water molecular diffusion = $1.0*10^{-9}$ m^2/s; $\partial\rho/\partial C$, change of fluid density with concentration = 700.0 kg^2(seawater)/kg(dissolved solids).m^3; g, gravitational acceleration = 9.8 m/s^2; C_{sea}, solute mass fraction of seawater = 0.0357 kg(dissolved solids)/kg(seawater); ρ_{sea}, density of seawater = 1025 kg/m^3; ρ_o, density of fresh water = 1000 kg/m^3; μ, fluid viscosity = 0.001 kg/(m.s); αL, longitudinal dispersivity = 2.0 m; αT , transverse dispersivity = 0.2 m; permeability of top layer = $1.3*10^{-12}$ m^2; permeability of bottom layer = $1.3*10^{-11}$ m^2; porosity of top layer = 0.37; porosity of bottom layer = 0.35 and thickness of model = 1.0 m. The following unsaturated parameters were considered for Van Genuchten function α=$12.5*10^{-4}$ $(m.s^2)/kg$, n=3.5 and S_{res}=0.01.

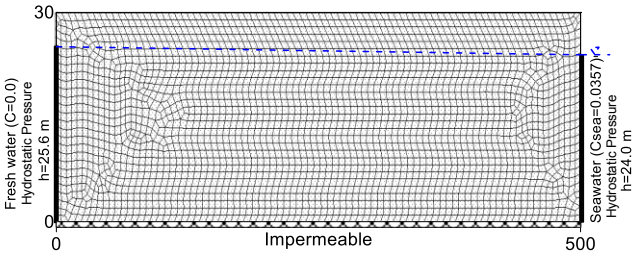

Figure 1: Boundary conditions of base model

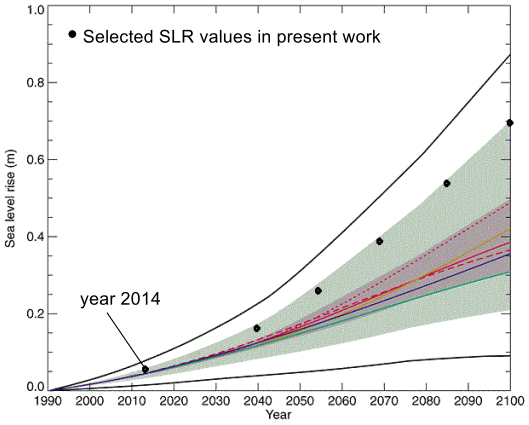

Figure 2: Global average SLR estimated by IPCC [3]

The unsaturated flow simulation in the model requires a fine temporal discretization to limit the instability and oscillatory results of calculated pressure and saturation values which may change sharply during wetting events [1]. To obtain the natural initial values of pressure within the domain, first a steady state solution is obtained through an extra simulation with the head boundary conditions described above at the inland and seaside boundaries of the aquifer. The system essentially reached a steady state after 10000 time steps, with time step of 0.25 days. In order to more closely replicate the behaviour of rising sea levels, the model is subjected to five different increments of rising sea levels starting from current time (year 2014) up to the end of century (year 2100). According to IPCC report [3] future SLR is expected to occur at a rate greatly exceeding that of the recent past. Figure 2 shows the estimated global average SLR between 1990 and 2100 based on different economic and technological development scenarios [3]. By 2100 it is expected that the rise in sea levels would be between 20 cm to 88 cm [3].

The current steady state condition of the model with the sea level located at elevation of 24 m is assumed to represent the hydrological situation for the year 2014 and it is used as the reference level for simulation of the system in the following time periods. The typical values for SLR used in the

present work are marked on Figure 2 for the years 2014, 2040, 2055, 2070, 2085 and 2100 which show the SLR of 0.1m, 0.2m, 0.35m, 0.5m and 0.65m (with respect to 2014 as the base line) in years 2040, 2055, 2070, 2085 and 2100 respectively. The corresponding hydraulic head boundary conditions defined at the seaside boundary in each rising period are increased linearly with time. The simulation outputs (pressure and salinity) of each time period are used as the initial condition for the next period.
Furthermore, the effect of different shoreline slopes (and the corresponding inundated surfaces) on SWI process is investigated under the gradual rise of sea level. The shoreline boundary of the base model is geometrically modified by implementing a different inland slope that starts from elevation of 15 m above the bottom boundary. For the purposes of comparison in this paper, the revised problems are simulated under the same hydraulic gradient (0.0032).

3. Results

An initial steady state simulation is used to estimate the current situation of saltwater wedge profile that exists in the system prior to SLR. The 50% iso-concentration line for this model is shown (by dashed line) in Figure 3. Under the present state (2014) the toe of the saline wedge is advanced by 70 m into the aquifer as a result of natural hydrodynamic dispersion. The results of the gradual rising of sea level at the end of each time period are also presented as 50% isochlor lines. The results show that the salinity wedge continues its inland intrusion to the extent that in year 2100 the toe will be located at 125 m from the coast boundary. The results of variation of groundwater level during the SLR process indicate that there is a significant lifting in water table especially in the vicinity with the sea boundary and it gradually declines towards the inland boundary. This variation of the hydraulic gradient during the SLR increases the thickness of the saturated layer of the system which results in the further inland penetration of saltwater/freshwater interface [5].

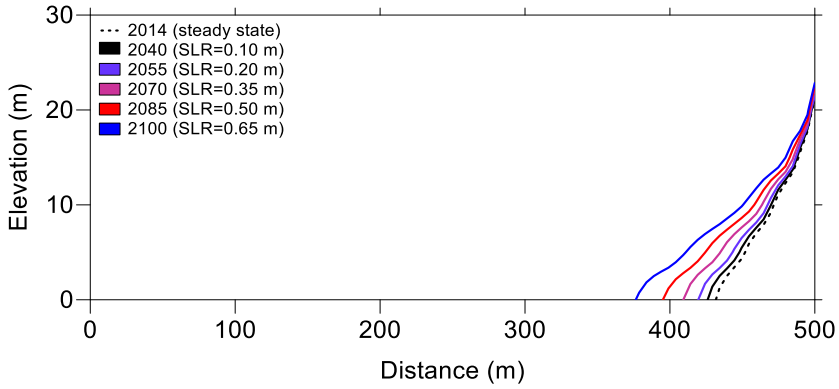

Figure 3: Variations of 50% iso-concentration lines of developed base model with SLR

The 50% iso-concentration profiles of the current steady state condition (year 2014) in aquifers with different shoreline slopes are illustrated in Figure 4a. The inundation surfaces resulting from different shoreline slopes provide the wider contact areas of the models with the seawater. In other word, a wider inundation surface resulting from a flatter slope accelerates the SWI process. These negative patterns of the inclined coastal boundaries also emerge during the rising of the mean sea levels. Figure 4b shows the variations of the same curve of saline/freshwater interface under gradual rising of sea level (up to 0.65 m) at the end of century. In the model with 10% slope the rising of sea level extends the inland location of saline wedge by 70 m compared with its current steady state condition. However, in the aquifer with 5% slope and under the same conditions, the toe location is advancement about 150 m during the same gradual SLR. Therefore the small variations of slopes play an important role in natural periodic progressive of SWI. Generally, the increasing of the inundation surface areas can result in reduction of fresh groundwater resources in the aquifer; lowering the capability of the groundwater discharge of the aquifer to cope with the intruded seawater.

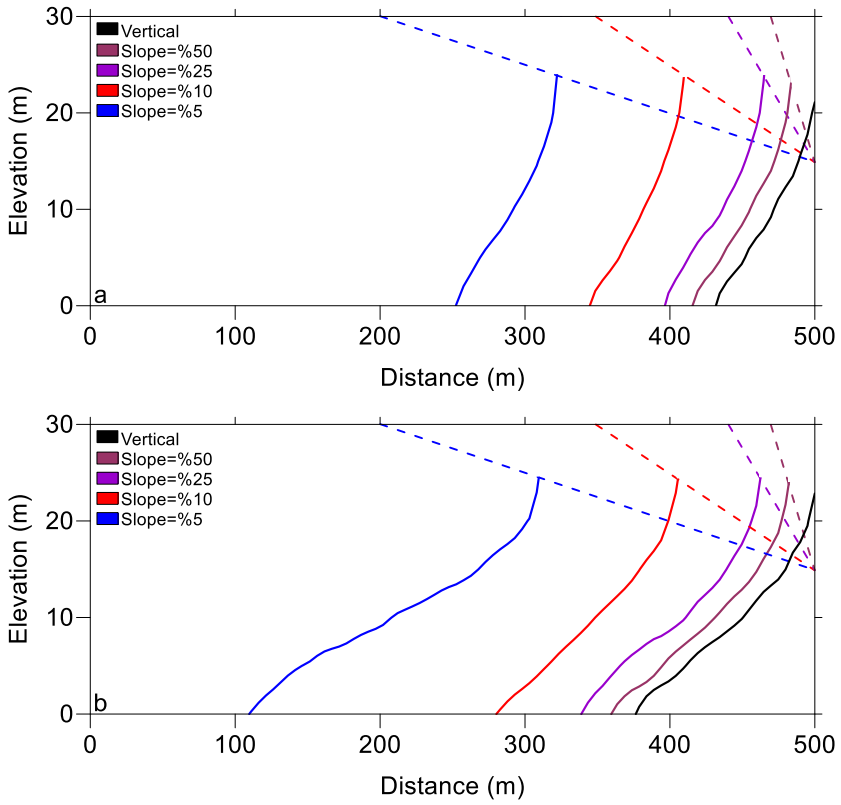

Figure 4: a) Current steady state variations of 50% iso-concentration lines of SWI in the aquifers with different coastal slopes; b) Variations of same isochlors with the SLR at the end of centaury

4. Conclusions

In this study, the transient effects of the gradual rising of sea levels (expected during the current century) on the SWI is investigated through a set of conceptual models of unconfined aquifers with different sloped coastal boundaries. It has been shown that rising of sea level leads to further inland advancement of seawater and the problem is intensified by the flatter slopes of shoreline boundary. An implication of these findings is that the threats and the unexpected outcomes of the SLR (and the global warming) could have serious consequences on the quality and quantity of fresh groundwater resources in real case studies coastal areas, especially in shallow unconfined aquifers.

Acknowledgements

This research was funded and supported by the British Council in the UK.

References

[1] C. I. Voss and A. M., Provost. SUTRA-A model for saturated-unsaturated variable-density ground-water flow with solute or energy transport. *U.S. Geological Survey (USGS), Water Resources Investigations,* Report 02-4231, 2010.

[2] G.H.P., Oude Essink. Density dependent groundwater flow salt water intrusion and heat transport. *Lecture notes: Hydrological Transport Processes/Groundwater Modelling II (KHTP/GWM II)*, Utrecht University Interfaculty Centre of Hydrology Utrecht Institute of Earth Sciences, 2001.

[3] IPCC. Climate Change 2001: Impacts, adaptations, and vulnerability. *Contribution of working group II to the third assessment report of the Intergovernmental Panel on Climate Change.* J. J. McCarthy, O. F., Canziani, N. A., Leary, D. J. Dokken and K. S. White (Eds.),Cambridge University Press,UK, 2001.

[4] L. Adeoti, O. Alile and O. Uchegbulam. Geophysical investigation of saline water intrusion into freshwater aquifers: a case study of Oniru, Lagos State. *Scientific Research and Essays*, 5, 248-259, 2010.

[5] S. W. Chang, T. P. Clement, M. J. Simpson and K.-K Lee. Does sea-level rise have an impact on saltwater intrusion?. *Advances in Water Resources*, 34, 1283-1291, 2011.

Proceedings of the 22nd UK Conference of the
Association for Computational Mechanics in Engineering
2 – 4April 2014, University of Exeter, Exeter

RELIABILITY ASSESSMENT OF COHESIVE VERTICAL CUT STABILITY USING RANDOM FINITE ELEMENT METHOD

***A. Johari[1], A. Gholampour[2] and Z. Abedini[3]**

[1,2]Department of Civil and Environmental Engineering, Shiraz University of Technology, Shiraz, Iran
[3]Department of Civil and Environmental Engineering, Shiraz University, Shiraz, Iran
*johari@sutech.ac.ir

ABSTRACT

The slope stability analysis is one of the fundamental problems in geotechnical analysis and design of earth structures particularly road and embankment. The stability of slope can be analyzed by finite element method as a powerful approach which is accurate, versatile and requires fewer a priori assumptions especially, regarding the failure mechanism. However, the inherent variability of the soil parameters which affect slope stability analysis dictates that the problem is of a probabilistic nature rather than being deterministic. In this research, random finite element method and limit equilibrium stochastic analysis are used for probabilistic analysis and reliability assessment of the stability of cohesive vertical cut. The selected stochastic parameters are cohesion and unit weight, which are modelled using a truncated normal probability distribution function. The height of slope is regarded as constant parameter. The resultant probability distributions of safety factor and reliability index of two methods are compared to each other.

Keywords: *Slope stability analysis; Random finite element method; Cohesive vertical cut.*

1. Introduction

Investigating the stability of slopes and vertical cuts is one of the considerable geotechnical problems and there has been a great deal of research into the stability analysis of slopes and vertical long unsupported cuts corresponding to plane strain problem [8]. In this regard, numerical methods such as elasto-plastic finite element technique have been widely used in different problem conditions. There is a useful literature on using finite element method and its advantages as a discretization tool in slope stability analysis [5].

In recent years, some researchers [7] have been following a more rigorous method of probabilistic geotechnical analysis in which deterministic formulation of the finite element method are combined with random field generation techniques by taking into account mean value, standard deviation, correlation and load design parameters. This numerical methodology is named Random Finite Element Method (RFEM) which was first introduced by Griffiths and Fenton [3] and is employed in many applications. By now many researcher applying this method in geotechnical problem such as slope stability [2], bearing capacity [4] and retaining wall [6]. It is become one of the suggested design approaches.

In this paper, the random finite element method is used for probabilistic analysis and reliability assessment of the stability of cohesive vertical cut. The selected stochastic parameters are cohesion and unit weight, which are modelled using a truncated normal probability distribution function. At the end of the paper, the distribution of stability number is obtained and discussed.

2. Random field technique

Random field are utilized to realistically present the ground, allowing for the ground properties to varying spatially, as they do in nature. The simplest random field's models follow a normal or trenched distribution. This is because the multi-variate normal distribution is relatively simple to use, both analytically and to simulate. A normal random field is characterized by mean (μ), a variance (σ^2) and a correlation structure. The mean could spatially varying, $\mu(\underset{\sim}{x})$, and it is appropriate to do so

when a trend has been identified at the site being modelled. In concept, the variance could also be spatially varying, $\sigma^2(\underset{\sim}{x})$, although this is rarely implemented since a very extensive site investigation would be required in order to even roughly estimate the variance trend. Generally, the variance is assumed to be stationary, in other words the same everywhere.
The most difficult aspect of random field models to both understand and estimate is its correlation structure. The purpose of a correlation structure is to provide some persistence in random field- points close together will have similar properties while widely separated points could have quite different properties. This feature of random fields is what makes it a realistic soil model since, in general, real soils also tend to have similar properties at nearby points and less similar at large separations.

3. Random finite element method

As it is mentioned before, the random finite element method combines elasto-plastic finite element analysis with random field theory. In this technique, a random field of stochastic parameters are generated and mapped onto the finite element mesh. For each random set, the entire elasto-plastic analysis is performed.
In a random field, the value assigned to each element is itself a random variable. These variables can be correlated to each other by controlling the spatial correlation length (θ), which defined for each random parameter. Furthermore, the correlation function is used to represent the field observation that soil samples taken close together are more likely to have similar properties, than samples taken from far apart. The details of methodology could be found in other publications [4].

In random finite element process, for a given set of input (mean, standard deviation and spatial correlation length), Monte Carlo simulations are utilized. This means that the stability analysis of vertical cut is repeated many times until the statistics of the output quantities of stability number become stable.

4. Problem definition

The stability safety factor of cohesion vertical cut stability is determined by limit equilibrium method as:

$$F_S = \frac{4C}{\gamma H} \tag{1}$$

where, H is the height of cut and, γ and c are the soil unit weight and cohesion respectively.
The stochastic stability of this type of slope can be made in several methods. In this research this purely cohesive soil under its own weight is analyzed by elasto-plastic finite element method. The theoretical basis of the method is described in Literature [9].
The soil parameters such as unit weight (γ) and cohesion (c) are considered as input stochastic parameters which are modelled using a truncated normal probability distribution function. The height of slope (H), Young's modulus (E), Poisson's ratio (ν) and friction angle are regarded as constant parameters. The stochastic parameters with truncated normal probability density function are shown in Table 1 and the deterministic parameters are given in Table 2. A computer model was developed by codding in MATLAB. For modelling of the soil behaviour, a specific Moher-Columb elasto-plastic model is used.
The spatial auto-correlation function for normally distributed field's parameters is assumed to be Markovian as:

$$\rho = \exp\left(-\frac{2|\tau|}{\theta}\right) \tag{2}$$

where τ is the distance between any two points and θ is the correlation length beyond which two points in the field are largely uncorrelated. In many studies, the correlation length is considered equal to the smaller model lengths [1,10]. In this study, the correlation length is selected equal to 4.0 m.

Table 1: Stochastic parameters

Parameters	Mean	Standard deviation	Minimum	Maximum
γ	18	0.5	16.50	19.50
C	25	3	16	34

Table 2: Deterministic parameters

Parameters	value
E	3×10^4 MPa
ν	0.30
H	6 m
L	10 m
Φ	0

To solve this stability problem by random finite element technique, a model consists of 56 elements with side length 1.0 m is implemented. These elements have eight nodes and each of the nodes has two degrees of freedom in the horizontal and vertical direction. The boundary conditions are such that the bottom side of the soil layer is fully restrained. The left (A) and the right (B) side of the soil layer are restrained only in the horizontal direction. This two-dimensional plane strain state body analyzed under self-weight. The geometry and mesh details of cohesive vertical cut are shown in Figure 1.

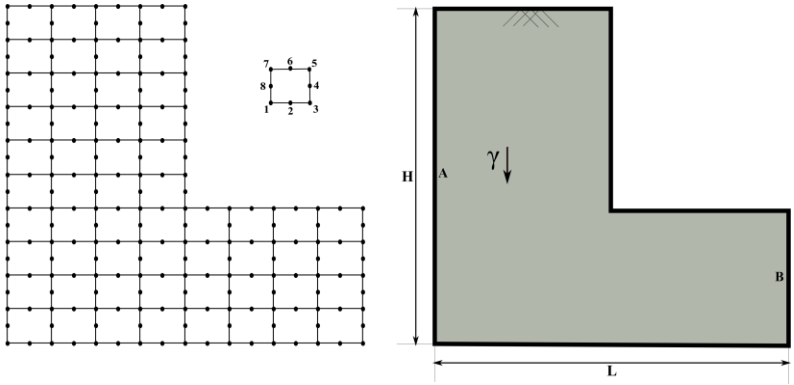

Figure 1: The geometry and mesh details of cohesive vertical cut

It was determined that 10,000 realizations of the Monte-Carlo process for each parametric group, was sufficient to give reliable and reproducible estimates of the probability of pore pressure ratio. Figure 2 show the probability density function and cumulative distribution function of safety factor. It can be seen the probability density function of the safety factor for vertical cut slope has normal distribution and the probability of failure is about 60%.

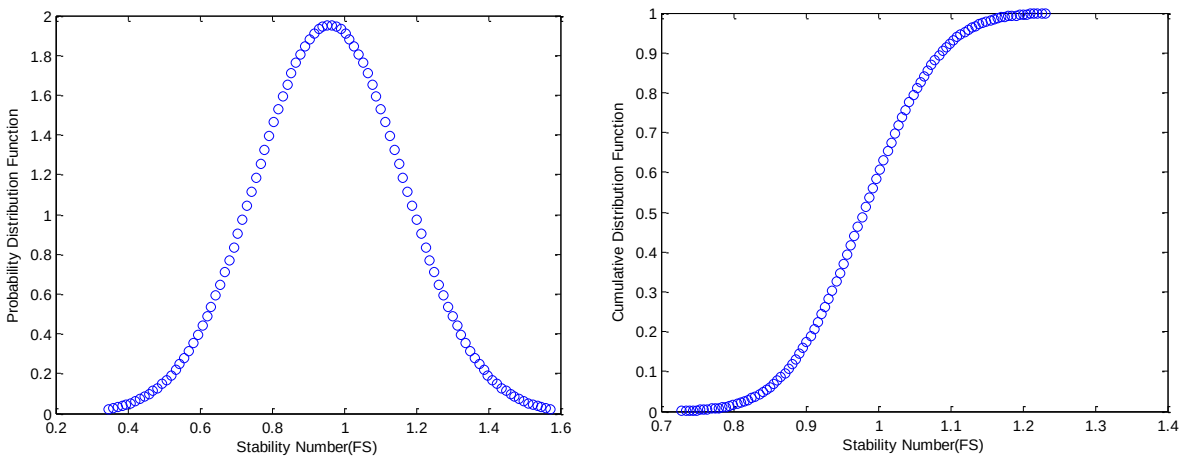

(a) (b)

Figure 2: (a) Probability and (b) Cumulative distribution function of stability number in cohesive vertical cut

5. Conclusions

Slope stability analysis is a probabilistic problem due to the inherent uncertainties in the geotechnical parameters, model performance as well as human uncertainty. In this paper, the random finite element method was used to assess the reliability of vertical cut stability based on the uncertainty in the geotechnical properties. The results showed that the probability distribution of the safety factor also has a nearly normal distribution. The sensitivity analysis also showed that the friction angle is the most influential parameter in stability of vertical cut.

References

[1] A. Der Kiureghian and J.B. Ke. The stochastic finite element method in structural reliability. *Probabilistic Engineering* Mechanics, 3, 83-91, 1998.

[2] D.V. Griffiths and G. A. Fenton. Probabilistic slope stability by finite element. *Journal of Geotechnical and Geoenvironmental Engineering*, 130, 507–518, 2004.

[3] D.V. Griffiths and G.A. Fenton. Seepage beneath water retaining structures founded on spatially random soil. *Geotechnique*, 43, 577−587. 1993.

[4] D.V. Griffiths and G.A. Fenton. Bearing capacity of spatially random soil: the undrained clay Prandtl problem revisited. *Geotechnique*, 51. 351–359, 2001.

[5] D.V. Griffiths and P.A. Lane. Slope stability analysis by finite element. *Geotechnique*, 49, 387-403, 1999.

[6] G. A. Fenton, D. V. Griffiths and M. B. Williams. Reliability of traditional retaining wall design. *Géotechnique*, 55, 55-62, 2005.

[7] G.A. Fenton and D.V. Griffiths. Statistics of flow through a simple bounded stochastic medium. Water Resources, 29, 1825–1830, 1993.

[8] J. Pastor, T.H. Thai and P. Francescato. New bounds for the height limit of a vertical slope. *International Journal of Numerical Analysis Methods Geomechanics*, 24, 165–182, 2000.

[9] M. Smith and D.V. Griffiths. Programming the finite element method, 3rd Ed, John Wiley and Sons, New York.

[10] S. Bruno and A. Der Kiureghian. Stochastic finite element methods and reliability: a state-of-the-art report. *Department of Civil and Environmental Engineering*, University of California, 2000.

Proceedings of the 22nd UK Conference of the
Association for Computational Mechanics in Engineering
2 – 4April 2014, University of Exeter, Exeter

SOIL LIQUEFACTION RELIABILITY ANALYSIS UNDER MONOTONIC LOADING USING RANDOM FINITE ELEMENT METHOD

***A. Johari[1], J. Rezvani pour[2] and A. Fazeli[3]**

[1,2]Department of Civil and Environmental Engineering, Shiraz University of Technology, Shiraz, Iran
[3]Department of Civil Engineering, Persian Gulf University, Bushehr, Iran

*johari@sutech.ac.ir

ABSTRACT

Liquefaction of soils is defined as significant reduction in shear strength and stiffness due to increase in pore pressure. This phenomenon can be assessed in static or dynamic loading types. However, in each type, the inherent variability of the soil parameters dictates that this problem is of a probabilistic nature rather than being deterministic. In this research, a random finite element analysis is used for reliability assessment of static liquefaction potential of loose sand under monotonic loading. The soil behaviour is modelled by an elasto-plastic constitutive model. The selected stochastic parameters are soil parameters such as unit weight, peak friction angle and initial plastic shear modulus. A sensitivity analysis was carried out to evaluate the response of liquefaction potential with respect to changes in input stochastic parameters. It is shown that the unit weight is the most effective parameter within selected stochastic parameters in soil liquefaction potential.

***Keywords**: Reliability analysis, Soil liquefaction, Random finite element method, Monotonic loading*

1. Introduction

Liquefaction resulting from the application of monotonic undrained loading is referred to as static liquefaction. Among the previous research works, limited attempts have been made to stochastic analysis of static liquefaction. However, the inherent uncertainties of the characteristics which affect static liquefaction dictate that the problem is of a stochastic nature rather than being deterministic. In this research, the random finite element method is used to assess the reliability of the static liquefaction potential of sandy soils based on probability density function of modified pore pressure ratio at each depth. The soil parameters such as saturated unit weight, peak friction angle and initial plastic shear modulus are considered as input stochastic parameters. A computer model was developed by coding in MATLAB. For modelling of the soil behaviour, a specific elasto-plastic effective stress constitutive model UBCSAND that was developed by Byrne et al. [1] is used.

2. Constitutive model: UBCSAND

UBCSAND [2] is a 2-dimensional effective stress plasticity model for use in advanced stress-deformation analysis of geotechnical structures. This model predicts the shear stress-strain behaviour of the soil using an assumed hyperbolic relationship and estimates the associated volumetric response of the soil skeleton using a non-associated flow rule. Information on UBCSAND is presented by Beaty and Byrne [3] and Puebla et al. [4].

3. Modified pore pressure ratio

If a soil layer is loaded at surface (e.g., constriction of embankment) the pore pressure ratio must be modified based on increasing in total stress (ΔP) as following:

$$(r_u)_M = \frac{u_{excess}}{P_0' + \Delta P} \tag{1}$$

Where r_u is pore pressure ratio, u_{excess} is excess pore water pressure and P'_0 is initial mean effective stress.

4. Random field modelling

To sake the spatial variability of soil's parameters a two-dimensional (2-D) Gaussian random field modelling is used. In this paper, the exponential correlation function, which is commonly used in random field modelling, is selected [5].

5. Procedure of static liquefaction reliability analysis by RFEM method

For developing the model to reliability analysis of static liquefaction, the finite element method is combined with random field generation techniques. For this purpose a monotonic load is exerted on the surface of saturated loose sand layer and at the end of loading, values of mean total stress, pore water pressure and mean effective stress are determined. Finally for evaluation of liquefaction occurrence, the values of modified pore pressure ratio at each point of field region are obtained.
In each realization after producing the stochastic soil parameter, they are mapped to the elements and the soil mass analyzed by the finite-element method under external load (load incrementally increased) and modified pore pressure ratios are calculated in each point. This analysis over a sequence of realizations (Monte Carlo simulation) yields a sequence of computed responses, allowing the distribution of the modified pore pressure ratio to be estimated.

6. Example

A 10m*30m horizontal saturated loose sand layer is considered and the static loading is exerted to the surface of it. The field region includes 30 by 10 square elements with element size of 1m (Figure 1). A two-dimensional plane strain state body subjected to a monotonic load of 20kN/m.
The stochastic parameters with truncated normal probability density function are shown in Table 1 and the deterministic parameters are given in Table 2. Figure 2 show typical random field realizations of stochastic input parameters. Figure 3 show modified pore pressure ratio variation in soil mass at the end of loading related to one realization. According to this figure, the modified pore pressure ratio and probability of liquefaction occurrence reduced with increase in the soil depth.

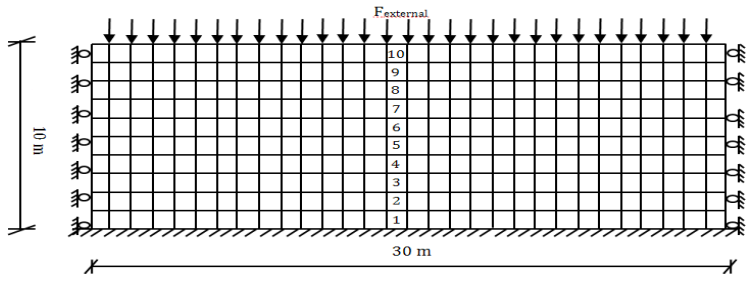

Figure 1: Finite element meshes discretization of problem.

Table 1.Stochastic truncated normal parameters.

Parameter	Mean	Standard deviation	Maximum	Minimum
γ sat	19	0.5	21	17
φ_f	33	1	37	29
G_P^i	30000	5000	50000	10000

Table 2: Deterministic parameters.

Parameter	m_e, n_e	n	k_0	P_a (kPa)	B_f (kPa)	γ_w (kN/m3)	θ (m)	R_f	υ	K_B^e	K_G^e
Value	0.5	0.4	0.5	100	2e5	10	10	0.95	0.35	900	300

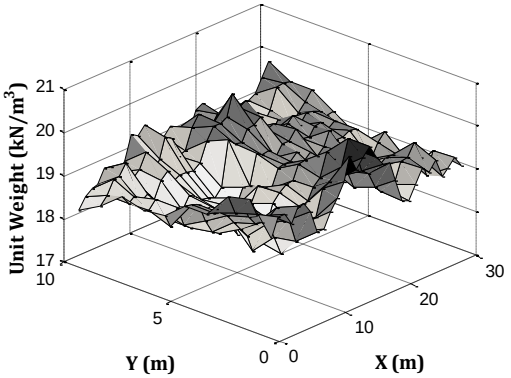

Figure 2: Sample realization of 2D normal random field. Representing spatial variation of saturated unit weight.

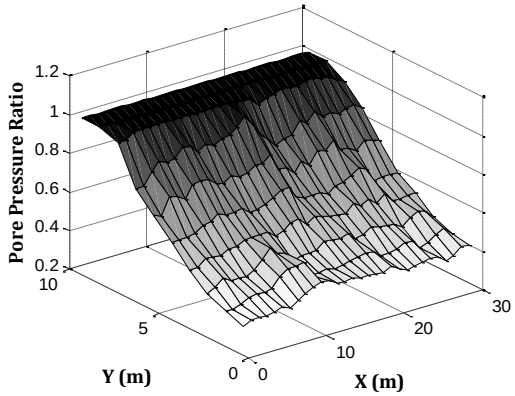

Figure 3: Sample field of modified pore pressure ratio variation.

At the end of analysis a probability distribution curve for the mean total stress, pore water pressure and mean effective stress were achieved in each element. Consequently, the probability distribution function of modified pore pressure ratio in all elements can be determined and probability of liquefaction is obtained at these elements.

Figure 5 shows, the probability of zero mean effective stress in the eighth element is approximately equal to 68% and this probability for the ninth and tenth elements is equal to 100%; that means occurrence of limited liquefaction in eighth element and complete liquefaction in ninth and tenth elements.

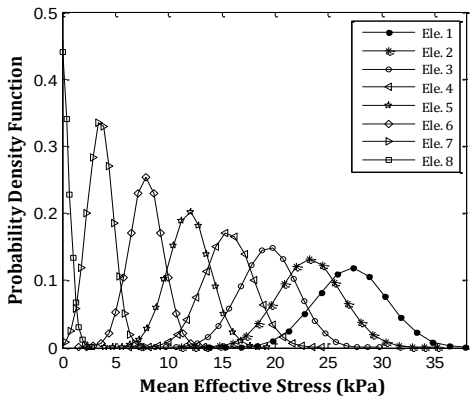

Figure 4: Probability density function of mean .effective stress in depth steps 1.0m

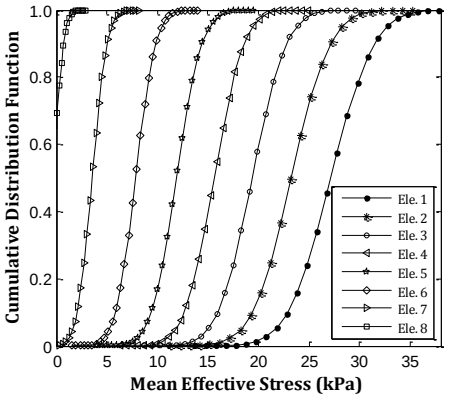

Figure 5: Cumulative density function of mean effective stress in depth steps 1.0m.

Figure 6 shows the probability density function of modified pore pressure ratio in depth steps 1.0m. According to Figure 7, the probability of liquefaction (modified pore pressure ratio equal to 1.0) in the eighth element is approximately equal to 68%. This probability for the ninth and tenth elements is equal to 100% which represents an occurrence of limited liquefaction in eighth element and complete liquefaction in ninth and tenth elements

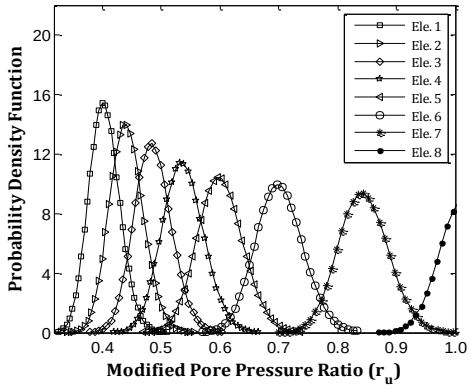

Figure 6: Probability density function of modified pore pressure ratio in depth steps 1.0m.

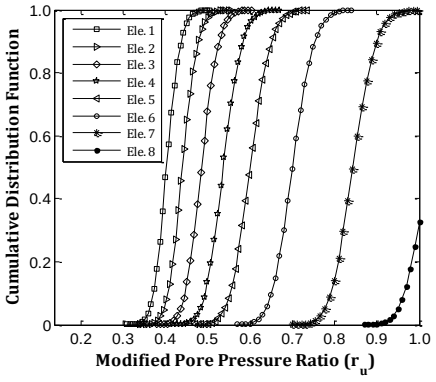

Figure 7: Cumulative density function of modified pore pressure ratio in depth steps 1.0m.

7. Conclusion

The paper is presented the reliability analysis of static soil liquefaction based on probability density function of modified pore pressure ratio at each depth using the random finite element method. The soil behaviour is modelled by an elasto-plastic effective stress constitutive model. Each realization of the Monte Carlo simulation involves a 2D Gaussian random field modelling. Soil parameters such as saturated unit weight, peak friction angle, and initial plastic shear modulus are selected as stochastic parameters which are modelled using a truncated normal probability density function. In addition, the sensitivity analysis of the proposed model indicated that this method can correctly predict the patterns of influence of the stochastic parameters.

References

1. P.M. Byrne, D. Roy,R.G. Campanella and J. Hughes. Predicting liquefaction response of granular soils from pressuremeter tests. In Static and Dynamic Properties of Gravelly Soils 1995. Proceedings of the ASCE National Convention, San Diego, Calif., 23–27 Oct. 1995.

2. P.M. Byrne, S.S. Park, M. Beaty, M. Sharp, L. Gonzalez and T. Abdoun. Numerical modeling of liquefaction and comparison with centrifuge tests. *Canadian Geotechnical Journal*, 41, 193-211, 2004.

3. H. Puebla, P.M. Byrne, R. Phillips. Analysis of CANLEX liquefaction embankments: prototype and centrifuge models. *Canadian Geotechnical Journal*, 34, 641-657, 1997.

4. M. Beaty and P.M. Byrne. An effective stress model for predicting liquefaction behaviour of sand. In Geotechnical earthquake engineering and soil dynamics III, Edited by P. Dakoulas, M. Yegian and R. Holtz *American Society of Civil Engineers, Geotechnical Special Publication*, 75(1), 766–777, 1998.

5. M.B. Jaksa, W.S. Kaggwa and P.I. Brooker. Experimental evaluation of the scale of fluctuation of a stiff clay. In: Melchers RE, Stewart MG, editors. Proceedings 8th international conference on the application of statistics and probability, Sydney, 1999.

Proceedings of the 22nd UK Conference of the
Association for Computational Mechanics in Engineering
2 – 4April 2014, University of Exeter, Exeter

3D-FEM NUMERICAL SIMULATION OF GROUND SURFACE DISPLACEMENT DUE TO SHORT-DISTANCE MULTI-LINE OVERLAPPED SHIELD TUNNELING

***Lei Li and Mengxi Zhang**

Department of Civil Engineering, Shanghai University, 149, Yanchang Road, Shanghai, 200072

*smilelilei@126.com

ABSTRACT

The formation of subway network in metropolis inevitably brings the case of shield tunnels going across the adjacent tunnels at different locations to shield tunnel excavation. Considering the complicated project of four-line overlapped tunnels in Shanghai metro construction, in which the Metro Line 11 below-shield and above-shield cross the short-distance Metro Line 4 tunnels successively, 3D-FEM simulation together with field measurements is employed to study the ground surface displacement. According to the distribution law of earth pressure around the existing tunnels, the face support pressure and grouting pressure change with the advance of shield machine. Based on analysis of numerical results and measured data, the influence of short-distance multi-line overlapped shield tunneling on the ground surface displacement is obtained. The conclusions would be helpful for the construction of similar multi-line overlapped tunnels.

Keywords: *Multi-line Overlapped Tunnels; Shield Tunneling; Ground Surface Displacement; 3D-FEM*

1. Introduction

The ground surface displacement caused by shield tunneling is one of the most important indicators during the tunnel construction. More and more tunnels are being constructed to meet the increasing demands of transportation in metropolises such as Beijing, Shanghai and Guangzhou. As a result, improving an existing subway network inevitably requires new tunnels driving closely across running tunnels. In Japan, Yamaguchi et al. [1] analyzed the behavior of four subway tunnels that run closely each other by collecting numerous monitoring data. Lee et al. [2] performed a series of numerical simulations to investigate the surface settlement troughs, tunnel stability and arching effects that develop during two parallel tunneling. Chehade and Shahrour [3] carried out a numerical analysis of the excavation of twin-tunnels with a particular focus on the influence of both the relative position and the excavation procedure on the soil settlement. Nagel et al. [4] found that the influence of heading face support pressure and grouting pressure on the surface settlements can be realistically described by the use of the holistic proposed simulation model.

Ground surface displacement has been extensively analyzed in the condition of single-line and double-line tunneling. However, the case of Metro Line 11 below-shield and above-shield successively cross the short-distance Metro Line 4 tunnels results in unforeseen impact on ground displacement in Shanghai. For this reason, this paper performs a 3D finite element numerical investigation of ground surface displacement during the construction of short-distance multi-line shield tunnels. Based on the comparison between numerical results and measured data, some conclusions would be helpful for the construction of multi-line overlapped tunnels.

2. Project Background

The new Metro Line 11 tunnels are constructed by two EPB shield machines with diameter of 6.34 m. From Xujiahui station to Shanghai gymnasium station, the Up-line 11 shield and Down-line 11 shield cross from below and above the running Metro Line 4 tunnels with the angle of 75º successively. The minimum vertical clearance between the Line 11 and Line 4 is 1.82 m and 1.69 m respectively. The external diameter D of the Line 11 tunnel is 6.2 m, width of the lining ring is 1.2 m, thickness of the

segment is 0.35 m and the strength grade is C55. Corresponding parameters of the Line 4 tunnel are same to those of the Line 11 tunnel. The mechanical parameters of the soil are summarized in Table 1.

Table 1: Mechanical parameters of the soil

Soil layer	Depth (m)	γ (kN/m^3)	c (kPa)	φ (°)	Es (MPa)	μ
① Fill	0.0~2.0	18.3	15.0	16.0	4.52	0.33
② Silty clay	2.0~3.3	18.5	26.0	17.0	4.48	0.32
③ Muddy silty clay	3.3~6.6	17.4	10.0	16.5	2.54	0.32
④ Muddy clay	6.6~15.0	16.7	11.0	12.5	2.09	0.33
⑤$_1$ Clay	15.0~16.0	17.8	14.0	14.5	3.36	0.26
⑤$_{1a}$ Sandy silt	16.0~20.5	18.2	5.0	33.0	8.21	0.24
⑤$_1$ Clay	20.5~24.8	17.8	14.0	14.5	3.36	0.26
⑤$_3$ Silty clay	24.8~39.8	18.1	16.0	22.5	4.66	0.29

3. 3D-FEM analysis model

In order to study the ground surface displacement induced by short-distance multi-line shield tunneling, a 3D model with dimension of 84 m (direction of the Line 11 excavation) × 84 m (longitudinal direction of the Line4)×60 m (depth) is established, as shown in Fig. 1. An elastic perfectly plastic constitutive relation based on the Drucker-Prager yield criterion is adopted to describe the soil behavior. The soil, tunnel lining and equivalent layer are modeled by 8-nodes solid elements. It should be noted that, after the completion of Up-line 11 tunnel, the Down-line 11 shield starts to move forward. The Young's modulus of the grout changes with excavation step from 0.58 MPa to 1.2 MPa, which is supposed to reflect the process of grout hardening. According to the distribution law of vertical earth pressure around the existing Line 4 tunnels (see Figure 2), the grouting pressure was set to be equal to the vertical earth pressure of working face center(σ_v) and the face support pressure was given by $P=K\sigma_v$ (K is the coefficient of lateral earth pressure).

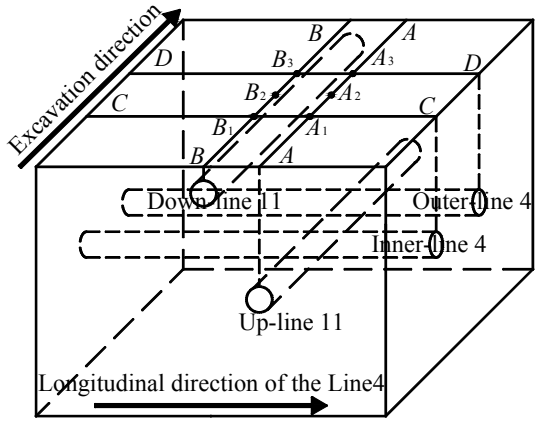

Figure 1: 3D geometric model and observing lines

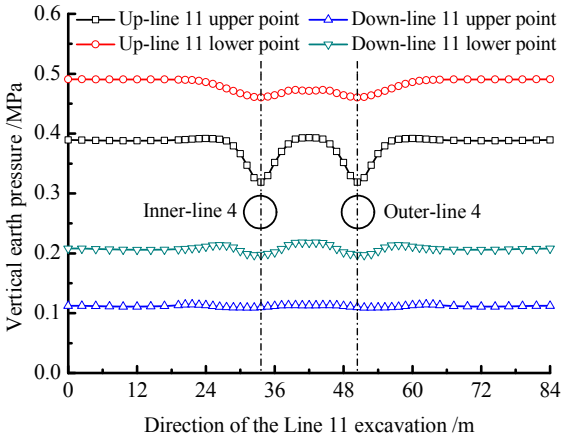

Figure 2: Vertical earth pressure distribution at different positions of new tunnel excavation face

4. Results and comparisons

Construction of the Up-line 11 tunnel. Fig. 3 shows the change of vertical displacements of the points in the longitudinal direction of the Up-line11 tunnel axis with the construction of Up-line11 tunnel. It is noted that the vertical displacements of the points remain stable at around 0.2 mm and decrease gradually before the Up-line11 shield machine reaching the centerlines of existing tunnels. As the shield machine moving forward continually, the settlements of the points would be stable finally. Fig. 4 shows the vertical displacement curve of ground surface at section *CC* and *DD* in different excavation step. The maximum settlement value occurs at the centerline position of the Up-line11 tunnel.

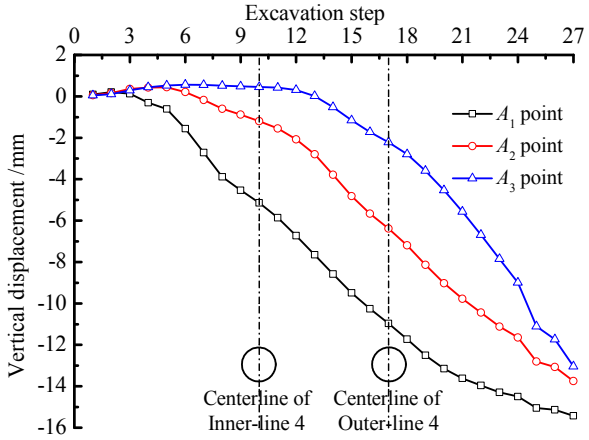

Figure 3: Change of vertical displacements with excavation step

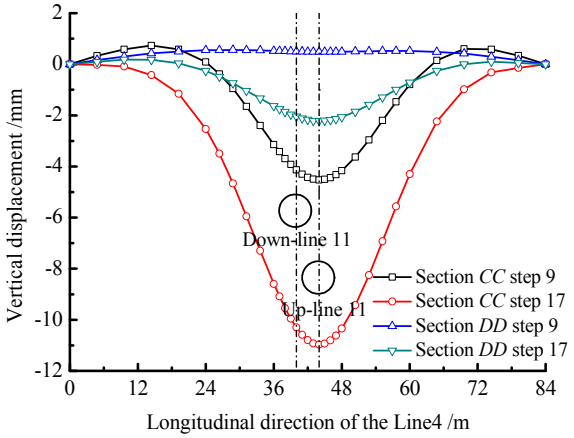

Figure 4: Vertical displacement curve in different excavation step

Construction of the Down-line 11 tunnel. The Down-line 11 shield starts to move forward when the Up-line 11 tunnel has been constructed in the overlapped site. In order to compare with the measured data during the construction of Down-line 11 tunnel, the initial displacement of ground surface is assumed to be 0 mm at the beginning of the construction.

Vertical displacements of the points in the longitudinal direction of the Down-line11 tunnel axis change with the construction of Down-line 11 tunnel are given in Fig. 5. Different from the vertical displacements during the construction of Up-line 11 tunnel, the maximum uplift value of the point increases to 1.5 mm due to the effect of face support pressure. Part uplift of the ground surface appears at section *CC* and *DD*, which is mainly caused by centerlines misalignment of the Line 11 tunnels, as shown in Fig. 6.

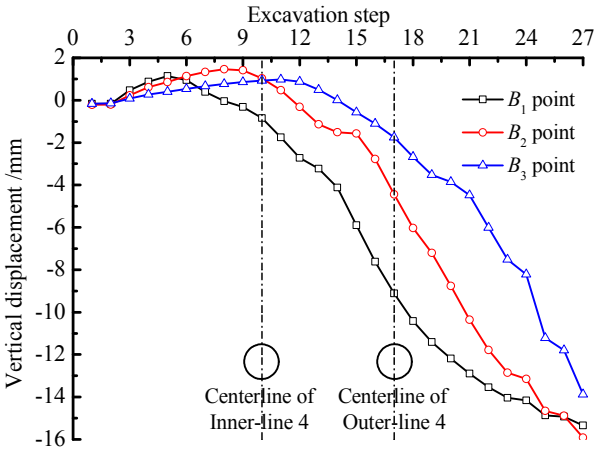

Figure 5: Change of vertical displacements with excavation step

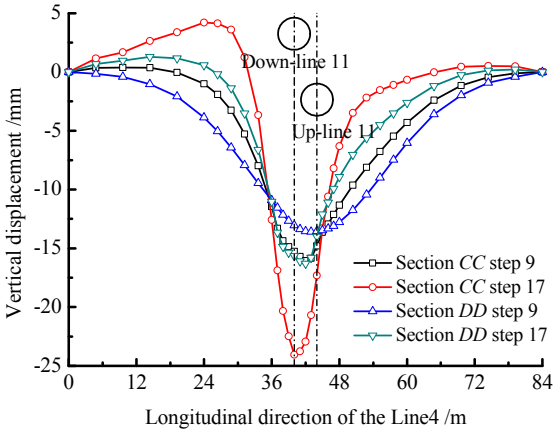

Figure 6: Vertical displacement curve in different excavation step

Analysis of measured data. Because of the complicated project of multi-line overlapped tunnels, strict measurement on the vertical displacements of ground surface in the longitudinal direction of

Line11 tunnel axis is executed. Fig. 7 and Fig. 8 show the measured data of the points during the excavation process of Up-line 11 tunnel and Down-line 11 tunnel respectively.
From the figures, vertical displacement lag of the ground surface is observed during the excavation process. The maximum uplift value of ground surface caused by 1.0*D*-depth Down-line 11 tunneling is greater than the one caused by 3.5*D*-depth Up-line 11 tunneling. In addition, during the construction of shallow tunnel, ground surface uplift is mainly induced by rebound effect of the underlying tunnels which is affected by ground loss and stress release.

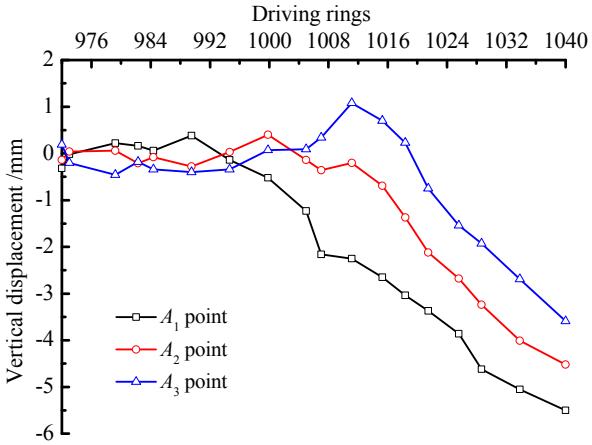

Figure 7: Vertical displacements during the Up-line 11 tunnel construction

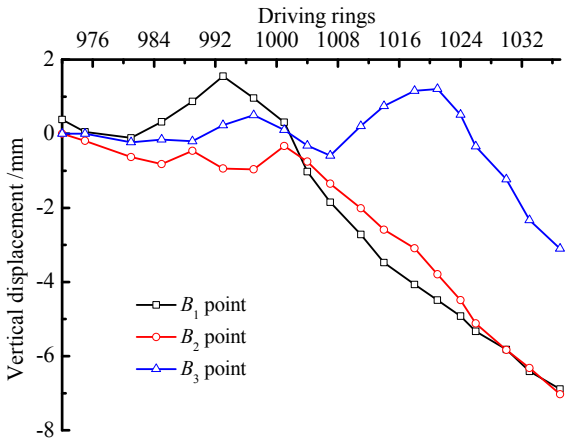

Figure 8: Vertical displacements during the Down-line 11 tunnel construction

5. Conclusions

3D finite element numerical simulation and field measurements have been carried out to investigate the vertical displacements of ground surface due to the construction of short-distance multi-line overlapped shield tunnels in Shanghai. The following conclusions can be obtained from this study.
(1) As a whole, the settlements of ground surface in the longitudinal direction of the Line11 tunnel axis increase gradually with the advance of shield machine.
(2) The maximum settlement values in the longitudinal direction of the Line4 tunnel axis occur at the centerline position of the Up-line11 tunnel which was constructed at first. However, part uplift of the ground surface is observed due to the centerlines misalignment of the Line 11 tunnels.
(3) Results from the measured data show that rebound deformation of the underlying tunnels is the primary cause which results in the uplift of ground surface during the construction of shallow tunnel.

Acknowledgements

The financial assistance from the National Natural Science Foundation of China under Grant No. 41172238 is here in much acknowledged.

References

[1] I. Yamaguchi, I. Yamazaki and Y. Kiritani. Study of ground-tunnel interactions of four shield tunnels driven in close proximity, in relation to design and construction of parallel shield tunnels. *Tunnelling and Underground Space Technology*, 13, 289-304, 1998.

[2] C.J. Lee, B.R. Wu, H.T. Chen and K.K. Chiang. Tunnel stability and arching effects during tunneling in soft clayey soil. *Tunnelling and Underground Space Technology*, 21, 119-132, 2006.

[3] F.H. Chehade and I. Shahrour. Numerical analysis of the interaction between twin-tunnels: influence of the relative position and construction procedure. *Tunnelling and Underground Space Technology*, 23, 210-214, 2008.

[4] F. Nagel, J. Stascheit and G. Meschke. Numerical simulation of interactions between the shield-supported tunnel construction process and the response of soft water-saturated soils. *International Journal of Geomechanics*, 12, 689-696, 2012.

Proceedings of the 22nd UK Conference of the
Association for Computational Mechanics in Engineering
2 - 4 April 2014, University of Exeter, Exeter

A Direct Method to Evaluate Stress Intensity Factors Using Extended BEM

***Ibrahim Alatawi, Jon Trevelyan**

School of Engineering and Computing Sciences, Durham University, South Road, Durham, DH1 3LE

*i.a.alatawi@durham.ac.uk

ABSTRACT

The importance of stress intensity factors (SIFs) in linear elastic fracture mechanics is that they may be readily applied to give fracture safety assessment as well as fatigue life predictions. There are many numerical approaches that aim to capture the stress singularity in some way, and some postprocessing is required to give the SIFs. The proposed method provides a direct evaluation of SIFs with high accuracy and a low number of elements. The solution column reveals the values of K_I and K_{II} without the necessity for postprocessing calculations such as the J-integral. The method takes advantage of a new Extended BEM approach, which limits the additional Degrees of Freedom (DOF) to two per crack-tip; this allows for unlimited elements to be enriched. Auxiliary equations are derived from enforcing continuity of displacement at the crack tip. Numerical examples for mode I and mixed mode problems show a high level of accuracy with a low number of elements.

Key Words: *Enriched BEM, XBEM; Fracture Mechanics, Stress Intensity Factors*

1. Introduction

Cracks existing in engineering structures can grow extremely rapidly when they reach a certain length, leading to serious failure. Determination of crack growth rates and critical length requires an accurate evaluation of the stresses near to the crack-tip. In linear elastic fracture mechanics, William's expansions can provide an accurate evaluation of stresses near the crack-tip [1] once the SIFs are known. However, although analytical SIFs are available for simple geometries, for the majority of cases numerical techniques are required. Contributions of numerical methods in fracture mechanics are well-known. However, some selected previous works that have led to our algorithm for direct calculation of SIFs are briefly discussed.

The Partition of Unity Method (PUM) established the concept of using basis functions with better approximation properties than piecewise polynomials [2]; this has been widely implemented with FEM to model fracture mechanics problems with great success. The use of Extended FEM (XFEM) [3] has led to accurate results being produced from a coarse mesh. Simpson [4] has introduced a technique that might be called the extended BEM (XBEM), to determine SIFs with similar enrichment to XFEM. This shows a high accuracy at low computational rate, but requires a J-integral for accurate SIFs. However, the current method involves revealing accurate values of K_I and K_{II} directly, without the need for such post-processing. This is likely to be of significance particularly in 3D, though this paper considers only 2D. A new auxiliary equation is also introduced to enforce displacement continuity at the crack tip, replacing the need for additional collocation points as used in [4]. The method shows flexibility in the number of enriched elements, which allows more elements to be enriched without increasing the DoFs or degrading the conditioning.

2. Formulation

The formulation of XBEM introduced by Simpson and Trevelyan [5], based on PUM, is used in the same fashion in the current method. The XBEM permits the use of Williams' asymptotic displacement expansions around the crack-tip as an additional basis function. Here the Williams displacement equation can be written as,

$$u_j = K_I \psi_{Ij}(\rho, \theta) + K_{II} \psi_{IIj}(\rho, \theta) \tag{1}$$

where K_I and K_{II} are mode I and mode II SIFs; $\psi_{Ij}(\rho, \theta)$ and $\psi_{IIj}(\rho, \theta)$ are given by the following functions, obtained from Williams expansions,

$$\psi_{Ix} = \frac{1}{2\mu}\sqrt{\frac{\rho}{2\pi}}\cos\frac{\theta}{2}\left[\kappa - 1 + 2\sin^2\frac{\theta}{2}\right] \tag{2a}$$

$$\psi_{IIx} = \frac{1}{2\mu}\sqrt{\frac{\rho}{2\pi}}\sin\frac{\theta}{2}\left[\kappa + 1 + 2\cos^2\frac{\theta}{2}\right] \tag{2b}$$

$$\psi_{Iy} = \frac{1}{2\mu}\sqrt{\frac{\rho}{2\pi}}\sin\frac{\theta}{2}\left[\kappa + 1 - 2\cos^2\frac{\theta}{2}\right] \tag{2c}$$

$$\psi_{IIy} = \frac{1}{2\mu}\sqrt{\frac{\rho}{2\pi}}\cos\frac{\theta}{2}\left[\kappa - 1 - 2\sin^2\frac{\theta}{2}\right] \tag{2d}$$

where ρ and θ are polar coordinates centred at the crack-tip, and κ is a parameter defined as $\kappa = 3 - 4\upsilon$ and $\kappa = \frac{3-\upsilon}{1+\upsilon}$ for plane strain and plane stress, respectively, υ being Poisson's ratio. Eq (1) can be rewritten to approximate the displacement near the crack-tip in the style of Benzley [6]; as follows,

$$u_j = \tilde{K}_I \psi_{Ij} + \tilde{K}_{II} \psi_{IIj} + \sum_{a=1}^{M} N^a u_j^a \tag{3}$$

where terms u_j^a are not nodal displacements but are now more general coefficients used to find the displacement, N^a is the Lagrangian shape function for node a and M is the total number of element nodes. $\tilde{K}_I$ and $\tilde{K}_{II}$ are coefficients playing the role of SIFs K_I and K_{II}, and are yielded as part of the solution vector. The first two terms of Eq. (3) are used to capture the local crack displacement, relative to the crack-tip, while the last term is included to approximate any non-zero displacement of the crack-tip.

The enriched displacement form (3) is used within the Dual Boundary Element Method (DBEM)[7]. DBEM is an ideal technique to model crack problems without giving rank deficiency. The BEM system is formed using the Displacement Boundary Integral Equation (DBIE) when collocating on one crack surface (and all non-crack boundaries) and the Traction Boundary Integral Equation (TBIE) for the opposing crack surface. DBIE can be written in a discretised form as,

$$C_{ij}(\grave{x})u_j(\grave{x}) + C_{ij}(\hat{x})u_j(\hat{x}) + \sum_{n=1}^{Ne} u_j^{na} \int_{-1}^{1} N^a(\xi) T_{ij}(\grave{x}, x(\xi)) J^n(\xi) d\xi + \sum_{a=1}^{Ne} \tilde{K}_l \underbrace{\int_{-1}^{1} T_{ij}(\grave{x}, x(\xi)) \psi_{lj}(\xi) J^n(\xi) d\xi}_{\tilde{P}_{ijl}^n}$$
$$= \sum_{n=1}^{Ne} t_j^{na} \int_{-1}^{1} N^a(\xi) U_{ij}(\grave{x}, x(\xi)) J^n(\xi) d\xi \tag{4}$$

where Ne is the total number of elements, and $J^n(\xi)$ is the Jacobian. T_{ij}, U_{ij} are the usual traction and displacement kernels. If the n^{th} element is unenriched then $\tilde{P}_{ijl}^n = 0, l = I, II$. In addition, as $\theta = \pm\pi$ at the crack surfaces for flat cracks, ψ_{Ij} and ψ_{IIj} are only functions of ξ . Jump terms in the enriched DBIE remain the same as unenriched jump terms; these will be cancelled during implementation. The TBIE can be obtained in numerical form as follows,

$$n_i(\grave{x}) \sum_{n=1}^{Ne} u_k^{na} \int_{-1}^{1} N^a(\xi) S_{kij}(\grave{x}, x(\xi)) J^n(\xi) d\xi + n_i(\grave{x}) \sum_{a=1}^{Ne} \tilde{K}_l \underbrace{\int_{-1}^{1} S_{kij}(\grave{x}, x(\xi)) \psi_{lk}(\xi) J^n(\xi) d\xi}_{\tilde{E}_{kijl}^n}$$
$$= n_i(\grave{x}) \sum_{n=1}^{Ne} t_k^{na} \int_{-1}^{1} N^a(\xi) D_{kij}(\grave{x}, x(\xi)) J^n(\xi) d\xi \tag{5}$$

where S_{kij}, D_{kij} are the usual derivative kernels. If the n^{th} element is unenriched $\tilde{E}_{kijl}^n = 0, l = I, II$. Implementation of the TBIE and DBIE requires considerable care in evaluating the hyper-singular and strongly-singular integrals, and the injection of extra enrichment degrees of freedom requires us to supply auxiliary equations to reach a square linear system.

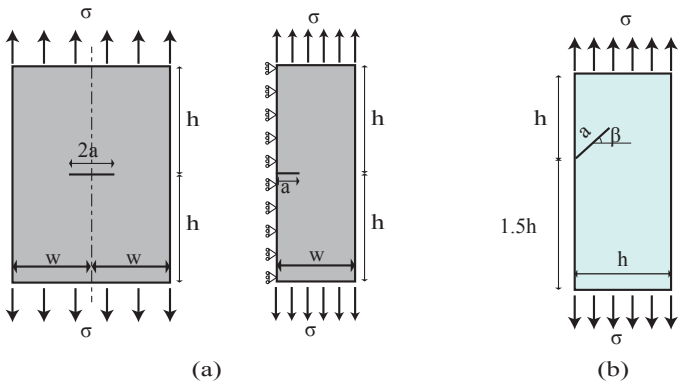

Figure 1: Numerical examples, *a*) Mode I centred crack on a flat plate; *b*) Inclined edge crack on rectangular plate

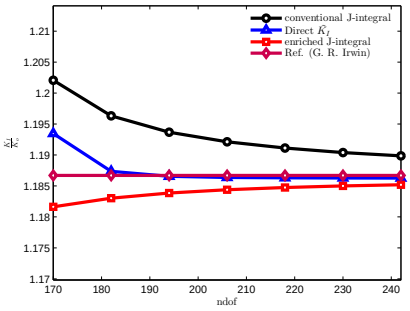

Figure 2: K_I compared to post-process method

3. Crack-tip displacement continuity

The Dual BEM involves a hypersingular integral equation which places requirements on the continuity of displacement derivatives at the collocation point. This cannot normally be achieved because of the C^0 continuity of shape functions at nodes shared between adjacent elements. Therefore, most Dual BEM implementations make use of discontinuous elements. One result of this is that a displacement discontinuity is often observed at the crack tip. While this does not in itself preclude us from obtaining accurate SIFs, it does provide us with an opportunity to design a simple set of auxiliary equations while at the same time enforcing a displacement continuity that is observed in the physical problem being modelled. The crack tip displacement can be approximated by extrapolating over the adjacent elements on the upper and lower crack surfaces. The approximations taken from the two surfaces can be equated to enforce displacement continuity, i.e.

$$\sum_{a=1}^{L} u^a_{j(upper)} N^a = \sum_{a=1}^{L} u^a_{j(lower)} N^a \tag{6}$$

L is the number of nodes used for the crack-tip extrapolation and N^a is the associated Lagrangian shape function. Eq. (6) is considered in both x and y directions independently, and the resulting equations used to form extra rows of the matrix description of the BEM problem. Now, $\tilde{K_I}$ and $\tilde{K_{II}}$ can present the SIFs directly, without requiring the J-integral.

4. Numerical Examples

The first example is a pure Mode I centre crack in a rectangular flat plate under uniaxial traction, with dimensions of $h = 2w = 4a$, as illustrated in Fig.1(a). Because of symmetry, only half of the plate is considered. The problem does not have an exact solution; instead a reference solution is used[8]. Normalised results K/K_0, where $K_0 = \sigma\sqrt{\pi a}$, are shown in Fig. 2 in which the reference solution is plotted as a horizontal line.

In the second example, a mixed mode inclined edge crack in a rectangular flat plate is shown in Fig. 1(b). A solution by Wilson [9] is used as a reference solution. Results have been plotted in Figs. 3 (a) and (b) for K_I and K_{II}, respectively.

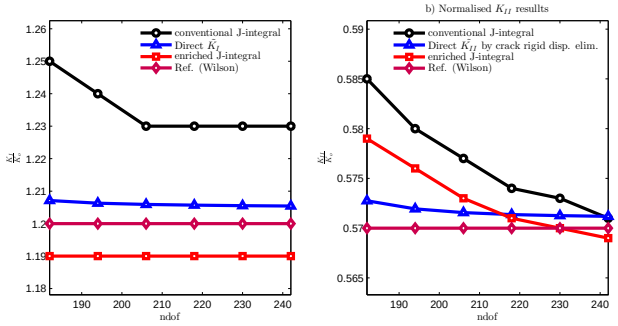

Figure 3: K_I compared to post-process method

In all figures we compare the Direct $\tilde{K}_I$ and $\tilde{K}_{II}$ results against (i) a conventional (unenriched) Dual BEM using the J-integral, and (ii) an enriched Dual XBEM using the J-integral. In all cases the directly obtained SIFs show excellent convergence properties.

5. Conclusions

A direct method has been presented that is able to evaluate SIFs without need for postprocessing (J-integral) calculations. This has been achieved using a Dual XBEM approach in which auxiliary equations are formed by enforcing displacement continuity at the crack tip. Additional DoFs are limited to two per crack-tip, which allows for the enrichment of all crack surface elements for greater accuracy with controlled conditioning. Special treatment must be applied to singular integrals as illustrated in [4]. The results show accurate values for SIFs compared to conventional J-integral based BEM approaches. The method can be extended to 3D, where the removal of the requirement for a J-integral will be helpful.

Acknowledgements

The first author acknowledges the financial support under Ref. No. *S* 11973 by Ministry of Higher Education of Saudi Arabia. We would like to thank Prof. Sergey Mikhailov from Brunel University for his helpful contribution.

References

[1] M. L. Williams. On the Stress Distribution at The Base of a Stationary Crack. *J Applied Mechanic*, 1957, 24, 109-11.

[2] J. M. Melenk and I. Babuška. The Partition of Unity Finite Element Method: basic theory and applications. *Comp Meth Appl Mech Eng*, 1996, 139, 289-314.

[3] T. Belytschko and T. Black. Elastic Crack Growth in Finite Elements with Minimal Remeshing. *International Journal of Fracture Mechanics*, 1999, 45, 601-620.

[4] R. Simpson and J. Trevelyan. A Partition of Unity Enriched Dual Boundary Element Method for Accurate Computations in Fracture Mechanics. *Computer Methods in Applied Mechanics and Engineering*, 2011, 200, 1 - 10.

[5] R. Simpson and J. Trevelyan. Evaluation of J1 and J2 Integrals for Curved Cracks Using an Enriched Boundary Element Method. *Engineering Fracture Mechanics*, 2011, 78, 623-637.

[6] S. E. Benzley. Representation of Singularities with Isoparametric Finite Elements *International Journal for Numerical Methods in Engineering*, John Wiley & Sons, Ltd, 1974, 8, 537-545.

[7] A. Portela, M. H. Aliabadi and D. P. Rooke. The Dual Boundary Element Method: Effective implementation for crack problems *International Journal for Numerical Methods in Engineering*, 1992, 33, 1269-1287.

[8] G. Irwin. Analysis of Stresses and Strains Near the End of a Crack Traversing a Plate. *ASME*, 1957, 24, 361-364.

[9] W. Wilson. Research Report 69-IE7-FMECH-RI. *Westinghouse Research Laboratory*, 1969

Proceedings of the 22nd UK Conference of the
Association for Computational Mechanics in Engineering
2 – 4April 2014, University of Exeter, Exeter

A MULTISCALE STOCHASTIC FRACTURE MODELLING CALIBRATION USING MONTE CARLO SIMULATIONS

R. M. Sencu[1*], Z. Yang[1], Y. C. Wang[1]

[1] School of Mechanical, Aerospace and Civil Engineering, University of Manchester, M13 9PL, UK

*razvan.sencu@manchester.ac.uk

ABSTRACT

The validation of macroscopic fracture modelling of heterogenous materials is strongly related to the effectiveness of the homogenization principle at fine scales. Often because the complete material morphology is missing, artificial repetitive boundary conditions are deployed despite many criticisms on their inadequate local subscale assumptions. This paper applies a recently developed multiscale stochastic fracture modelling approach (MsSFrM) to simulate crack growth in FRP materials. First, image-based models are solved at micro level and mapped onto the macro scale using a two-scales adaptive window principle; and second, the macro scale is solved by using a calibrated heterogeneous cohesive interface crack model based on [6, 7]. Two further enhancements are proposed here, both being able of representing the macro continuum in a stochastic fashion. First, the micro scale is related to various degrees of aggregations (DAG) via Voronoi tessellation statistics; and second, Karhunen-Loeve (KL) material property expansions are used for areas where images cannot be provided.

Keywords*: multiscale stochastic fracture mechanics; cohesive zone modelling (CZM); fibre reinforced plastics (FRPs); Monte Carlo simulation*

1. Introduction

In order to extend the micro mechanical interactions of heterogeneous materials to macro continuum, two options are available. First the random mapping of heterogeneous properties which extends the formulation to semi-infinite continuum, but with a good control of the material property variances; second, cascade scale segmentations such as hierarchical image based reconstructions can be defined in order to ensure that the crack paths and energy conservation principles yields best matching results. While the undamaged plasticity behaviour does not pose any modelling difficulty and most traditional multiscale modelling strategies can be employed, modelling the softening part poses great challenges which are commonly associated with the stochastic character of the crack paths. Crack bias effects arise mainly from random distribution of the inclusions, but also from size effects, local material defects and incompatible boundary conditions.

This paper uses the multiscale stochastic fracture modelling method (MsSFrM) developed by Sencu, et. al. (2014) which is based on image based FRP models. The modelling is done in two different stages. In the first stage, the orthotropic properties of transverse plies at micro-scale were obtained; afterwards, a memory-wise mapping links material properties from micro to macro scale. The local mismatch of properties between meso scale units is evaluated by stress displacement curves from prescribed boundary conditions. Multiple meso scale elements (MeEs) were used to capture most critical failure events. However, when extending the computational domain to full scale, some important morphological information required is unavailable due to limited fields of view. In such cases, bootstrapping algorithms [1] can be further employed to assign continuum properties. Therefore, this paper extends the MsSFrM to a hybrid formulation MsSFrM-H which promises flexibility and accuracy for modelling heterogeneous structural components. The MsSFrM-H framework is aimed at using the available material information in most critical areas (such as the beam notch, corners and areas where stress concentrations are expected) and uses bootstrapped data for the rest of macro continuum. This method should not be confused with concurrent discretisation methods such as [2, 3] or the hierarchical uncoupled approaches in [4, 5]. The benefit of using this

new development is that the computational cost is kept to minimum, while the non-local elasto-plastic disruption of the overall model is also minimized.

2. Stochastic coupling enhancements of MsSFrM

The conceptual formulation of the MsSFrM-H method is shortly presented in Figure 1. The key steps of this method are as follows: image acquisition, image based models reconstruction and simulation by using overlapped windows, adaptive mesh discretisation at macro scale and properties mapping, KL expansions and reconstruction of the overall structural model. The detailed modelling methodology is not presented here.

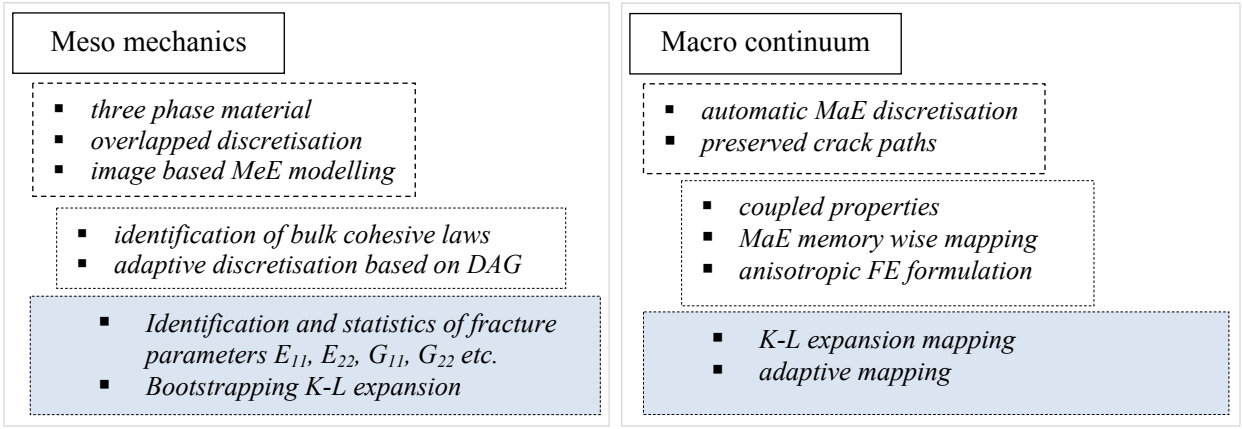

Figure 1: The big picture of MsSFrM-H framework.

A finite number of MeEs are explicitly simulated in fracture modes I and II on the two principal orthonormal directions. The macro scale properties are then approximated based on two overlapping average equations which collect the effects of elements sharing the same edge:

$$G_{f,short} = \int_{\bar{\varepsilon}_{0,pl}}^{\bar{\varepsilon}_{f,pl}} L_1 \bar{\sigma}_{L1} d\bar{\varepsilon}_{pl} + \frac{1}{2}\left(\int_{\bar{\varepsilon}_{0,pl}}^{\bar{\varepsilon}_{f,pl}} L_2 \bar{\sigma}_{L2} d\bar{\varepsilon}_{pl} + \int_{\bar{\varepsilon}_{0,pl}}^{\bar{\varepsilon}_{f,pl}} L_3 \bar{\sigma}_{L3} d\bar{\varepsilon}_{pl} \right) + \int_{\bar{\varepsilon}_{0,pl}}^{\bar{\varepsilon}_{f,pl}} L_4 \bar{\sigma}_{L4} d\bar{\varepsilon}_{pl} \qquad (1)$$

$$G_{f,long} = \frac{1}{4}\left(\int_{\bar{\varepsilon}_{0,pl}}^{\bar{\varepsilon}_{f,pl}} L_1 \bar{\sigma}_{L1} d\bar{\varepsilon}_{pl} + \int_{\bar{\varepsilon}_{0,pl}}^{\bar{\varepsilon}_{f,pl}} L_2 \bar{\sigma}_{L2} d\bar{\varepsilon}_{pl} + \int_{\bar{\varepsilon}_{0,pl}}^{\bar{\varepsilon}_{f,pl}} L_3 \bar{\sigma}_{L3} d\bar{\varepsilon}_{pl} + \int_{\bar{\varepsilon}_{0,pl}}^{\bar{\varepsilon}_{f,pl}} L_4 \bar{\sigma}_{L4} d\bar{\varepsilon}_{pl} \right) \qquad (2)$$

The new MsSFrM-H approach is based on correlation concepts of statistical fibre distribution within individual MeE windows which are transferred to macro scale via Voronoi tessellation cells. Similar interfacial stochastic homogenized cohesive elements are used at macro scale to represent the fluctuations of microscopic deformation fields.

3. Modelling results

The enhancements in this paper can be separated in two main categories according to the scale definition. At meso scale, the MeE size can systematically change according to the target domain which allows the discretisation of difficult computational areas (such as for curved components like pipes, nozzles, ribs etc.). Second, we introduce a new meso scale degree of aggregation (DAG) evaluated based on Voronoi tessellation. This will be further related to the crack initiation and propagation processes. At macro scale, material properties bootstrap is introduced based on Karhunen-Loeve (KL) expansion. The KL process produces best possible basis for expansion.

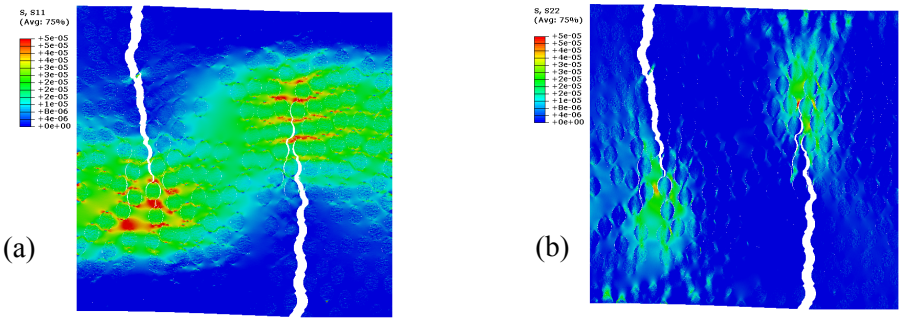

Figure 2: Stress contours on a type 2 failure mode with MeE size 100 μm^2.

Figure 3 explains some methodologies which were used. Both non-overlapped as well as overlapped MeE discretisations were tested. As previously mentioned, different crack paths can arise. It has been observed that in general, the overlapping concept is a better method to solve the deformation compatibility problem and therefore gives more accurate multiscale links.

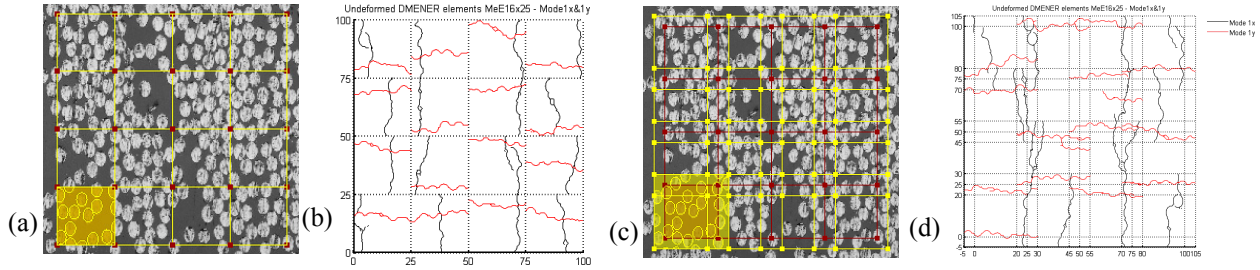

Figure 3: (a) non-overlapping discretisation; (b) crack paths from MeEs in (a); (c) overlapped discretisation; (d) crack paths from MeEs in (c).

In Figure 4 we illustrate the stress-displacement curves and crack path benchmarks as they were obtained from the overlapped series MeE 16x50 against fully detailed meso-scale simulations (typical MeE 100 stress contour plots are shown in Figure 2). The grid size was 25 microns and the simulations were computed on multiple CPUs. The individual crack paths were used to build an adaptive macro mesh which matched the detailed crack paths from different boundary conditions such as mode 1 and mixed modes on x and y directions. The CPU time on a desktop PC i7 – 2600 @3.40 GHz with 8 cores was about 5 to 6 hours per simulation, while when using 48 cores per simulation on the CSF facility at University of Manchester, the average time was 45 min.

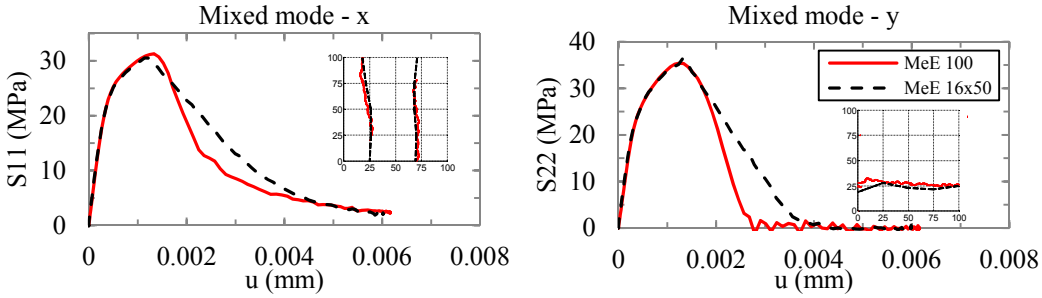

Figure 4: Nonlinear benchmark by using the overlapping concept vs fully detailed simulations.

4. Conclusions

Simulations of a wide range of properties by using traditional non-overlapping discretisation are not always possible due to the bias of the crack paths. The novel overlapping discretisation concept was successfully employed to transfer crack growth from micro to macro on FRP materials. Once the most critical crack locations are known, many discretisation options could be created in order to solve the macro scale. For example, reduced integration order meshes either containing full information about inclusions or by using homogenized continuum solids are all possible. Finally, it is proved that the cohesive crack interface model can be employed to simulate both intra and inter meso to macro scale complicated fracture interactions by using the newly developed MsSFrM-H framework. The hybrid formulation allows the extension of the image based results to further simulate full scale structural components. It is believed that unstructured discretisations can be related to statistical measurements at micro scale, such as the proposed Voronoi DAG. This is an essential step in decomposing the crack probability spectrum in order to shape feasible realizations for modelling the complete macro continuum.

Acknowledgements

This paper would not have been possible without the use of the services and facilities of The University of Manchester and the financial support of this PhD study by US Air Force through grant FA8655-12-1-2100 commissioned via The European Office of Aerospace Research & Development (EOARD). The financial support from EPSRC grant (QUBE) EP/J019763/1 is also greatly appreciated.

References

[1] Allaix, D.L. and V.I. Carbone. Numerical discretization of stationary random processes. *Probabilistic Engineering Mechanics*, 25(3), 2010.

[2] Ghosh, S. and D. Paquet. Adaptive concurrent multi-level model for multi-scale analysis of ductile fracture in heterogeneous aluminum alloys. *Mechanics of Materials*, 65(0), 2013.

[3] Llorca, J., et al. Multiscale Modeling of Composites: Toward Virtual Testing … and Beyond. *JOM*, 65(2), 2013.

[4] Unger, J.F. An FE2-X1 approach for multiscale localization phenomena. *Journal of the Mechanics and Physics of Solids*, 61(4), 2013.

[5] Verhoosel, C.V., et al. Computational homogenization for adhesive and cohesive failure in quasi-brittle solids. *International Journal for Numerical Methods in Engineering*, 83(8-9), 2010.

[6] Yang, Z. and F.X. Xu. A heterogeneous cohesive model for quasi-brittle materials considering spatially varying random fracture properties. *Computer Methods in Applied Mechanics and Engineering*, 197(45–48), 2008.

[7] Yang, Z.J., et al. Monte Carlo simulation of complex cohesive fracture in random heterogeneous quasi-brittle materials. *International Journal of Solids and Structures*, 46(17), 2009.

Proceedings of the 22nd UK Conference of the
Association for Computational Mechanics in Engineering
2 - 4 April 2014, University of Exeter, Exeter

Computational Modelling of Hydraulic Fracture

***Guoqiang Xue[1], Lukasz Kaczmarczyk[1] and Chris J. Pearce[1]**

[1]School of Engineering, University of Glasgow, Rankine Building, Glasgow, G12 8LT

*g.xue.1@research.gla.ac.uk

ABSTRACT

This paper presents initial work on the computational modelling of 3D fluid-driven fractures in rock. In this work, the rock deformation is assumed to be elastic and the fluid flow is considered to be constant along the fracture. Leak-off is not considered at this stage. Propagating fractures are modelled using cohesive interface elements. The model is developed in the context of the finite element method (FEM) and utilises a hierarchic approximation basis [1], allowing for local p-refinement. In this paper, the performance of the interface elements, with higher-order approximation polynomials, will be studied in detail. The dissipative load path is controlled by a local arc-length control methodology [2]. All problems are undertaken in 3D. The model is being incorporated into our open source software package MoFEM [3] and is optimised for high performance computing on distributed memory computers.

Key Words: *fluid-driven fractures; hierarchic element; cohesive interface element; local arc-length control; MoFEM*

1. Introduction

Hydraulic fracture (fracking) is an important technique, widely used in petroleum engineering, underground mining, ground thermal energy exploitation, etc. Fracking has received significant attention by engineers in recent years due to the discovery and exploration of shale gas. Basically, fracking is the process of drilling and injecting fluid (typically water mixed with sand and chemicals) into the ground at high pressure in order to fracture rock and release gas or hydrocarbons.

Fracking is a fluid-driven fracture processing, which requires many aspects to be considered, such as [4]: the flow of fluid on the fracture aperture; the mechanics deformation of the surrounding medium induced by the fluid pressure; the leak-off fluid from the fracture to the rock; the fracture propagation in rock. In this work, fracking is considered to be a quasi-static process, the deformation of rock is assumed to be elastic and the fluid flow is considered to be constant along the fracture. Leak-off is not considered at this stage.

The 3D model is being built using the finite element method (FEM) and utilises a hierarchic approximation basis [1], allowing for local p-refinement. Propagating fractures are modelled using zero-thickness cohesive interface elements. In addition, the local arc-length control methodology is used to capture the dissipative load path [2].

This work is incorporated in MoFEM (Mesh-oriented Finite Element Method), our group's open source software package for multi-physics problems and optimised for high-performance computing [3].

2. Hierarchical finite element method

The 3D domains under consideration are discretised with tetrahedral finite elements and utilise hierarchical basis functions of arbitrary polynomial order, following the work of Ainsworth and Coyle [1]. In this paper, the response of a benchmark problem for different orders of approximation are investigated.

3. Zero-thickness cohesive element

In this paper, cohesive elements are adopted for modelling the hydraulic fracture. A bilinear cohesive damage law between the traction **f** and the displacement jump **g** is adopted across the cohesive surface and is shown in Fig.1 and Fig.2. Linear elastic behaviour is assumed for tractions less than the tensile strength f_t (or the displacement jump is less than g_0), with a high penalty stiffness. For displacements beyond g_0, the traction reduces linearly to zero. When $g = g_0$, the internal parameter κ is equal to 0; this parameter is used in the definition of the water pressure. When κ reaches κ_1, the crack is traction-free [5].

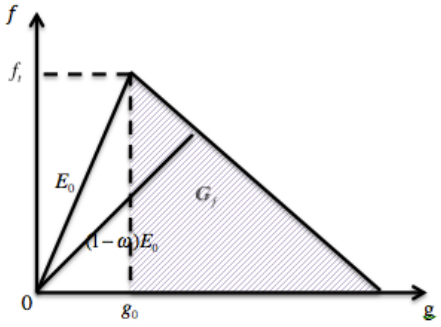

Figure 1: the irreversible bilinear cohesive law

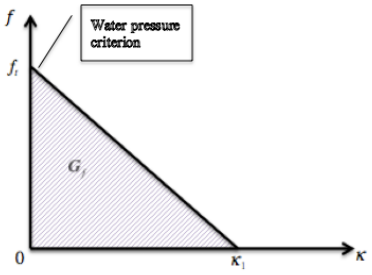

Figure 2: the water pressure criterion in cohesive element

In Figure 1 and 2, ω is damage parameter; E_0 is penalty stiffness $E_0 = \frac{E}{h}$, E is Young Modulus and h is stiffness coefficient; G_f is fracture energy $G_f = \frac{\kappa_1 f_t}{2}$.

4. Local arc-length control

The global load-displacement response of the system can be highly nonlinear, involving snap-back or snap-through phenomena, depending on the material properties, loading, geometry and constraints. As a result, traditional path-following techniques can struggle to trace the post-bifurcation response. In this work, a local arc-length control with line search has been successfully implemented and found to be robust [2, 3].

5. Water pressure effect

At this stage of research, fracking is considered to be quasi-static. That is to say, the rate of crack opening is slow enough so that temporal effects do not need to be taken into account, and the static water pressure acts on both the traction-free crack and the cohesive zone. Following experimental results, the water pressure in the cohesive zone can be assumed to be an exponential function of the crack opening displacement (herein is κ) [6].

$$P = (P_l - P_0)(1 - e^{-r\cdot\kappa}) + P_0 \tag{1}$$

Here P is the water pressure on the interface, P_l is external water pressure, P_0 is the prescribed pressure distribution at the interface before cracking (usually taken as 0), r is a material parameter based on laboratory tests. When $r \to 0$, no water-pressure acts, when $r \to 3/\kappa$, then $P \approx P_l$, i.e. the external pressure fully acts on the interface.

An alternative water pressure function in the cohesive zone could be piece-wise linear, expressed as following:

$$\begin{cases} P = P_l \cdot (\kappa/\kappa_1) & (\kappa \le \kappa_1) \\ P = P_l & (\kappa > \kappa_1) \end{cases} \tag{2}$$

where the water pressure P increases linearly from zero to the external static water pressure P_l.

6. Simple Numerical Example

The model (seen in Fig. 3) is 3D and the thickness is 2m. The initial crack is 2m long and the initial crack opening is 1m. The parameters for the model and the cohesive elements can be seen in Table 1.

Table 1: The parameters of the model

Finite Element		Cohesive Element	
Young-modulous	2e10 Pa	f_t	125e4 N
Possion-ration	0.2	G_f	120 J
h	0.64	β	0

In Table 1, parameter β is a weighting coefficient for the gap of cohesive element, expressed in following equation:

$$g = \sqrt{g_n^2 + \beta \cdot g_t^2} \tag{3}$$

where g_n and g_t are normal and shear displacements of cohesive elements, respectively.

6.1 Case 1

For the problem shown in Fig.3, different orders of approximation are investigated for the same external water pressure and constraints. The results can be seen in Fig.4, where the order of approximation has increased from 1st-order to 5th-order. The external water pressure in the initial crack is 1e6 Pa, the water pressure in the cohesive zone follows the exponential function described above. The results are shown for the first step of the analysis.

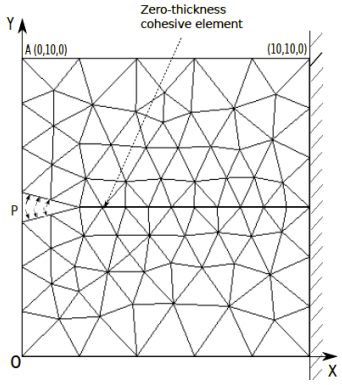

Figure 3: Simplified fracking model

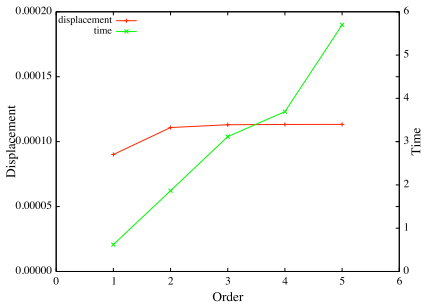

Figure 4: Displacement at point A and computational time.

6.2 Case 2

Here the external water pressure in the initial crack is 1e6 Pa. The water pressure in the cohesive zone follows the exponential function described above for different values of r. 20 load steps are applied and the order of approximation is 2nd-order. The load-displacement response for point A is shown in Fig.5. It is noted that when $r = 1e7$, nearly the full water pressure acts on the interface during the propagation process; and when $r = 1e0$, almost no water pressure acts in the cohesive zone.

6.3 Case 3

Here, all parameters are the same as for Case 2, except that the water pressure in the cohesive zone follows the linear function described above. The load-displacement response for point A is shown in Fig.6, where the response for the linear pressure is compared to no water pressure in the cohesive zone. Fig .8 shows the final deformation of the model.

6.4 Case 4

Here the external water pressure is lowered to 1e5 Pa but extremes of r are considered. The load-displacement response for point A is shown in Fig.7. It should be noted that when $r = 1e7$, snap-back behaviour is observed and the local arc-length control can trace the nonlinear dissipative load path successfully.

Future work will consider fluid flow in the fracture and fluid leak-off.

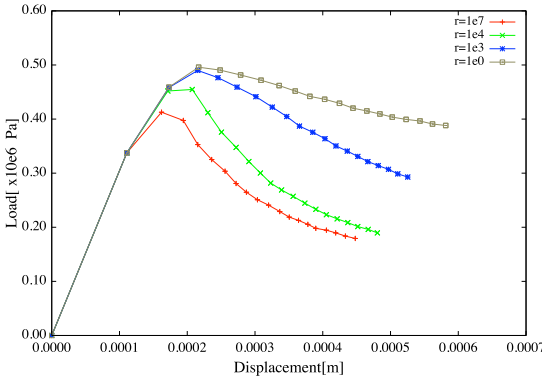

Figure 5: case 2. Load-displacement response

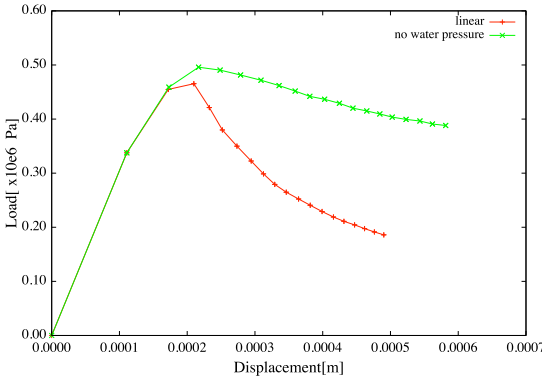

Figure 6: case 3. Load-displacement response

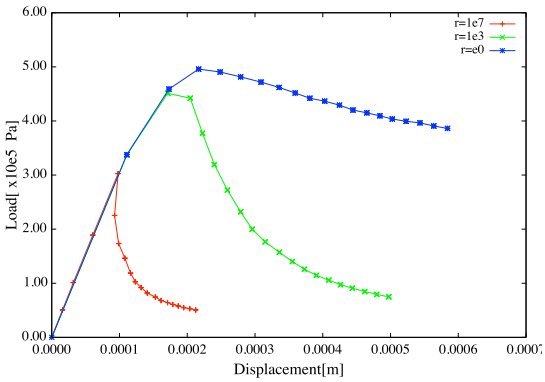

Figure 7: case 4. Load-displacement repsonse

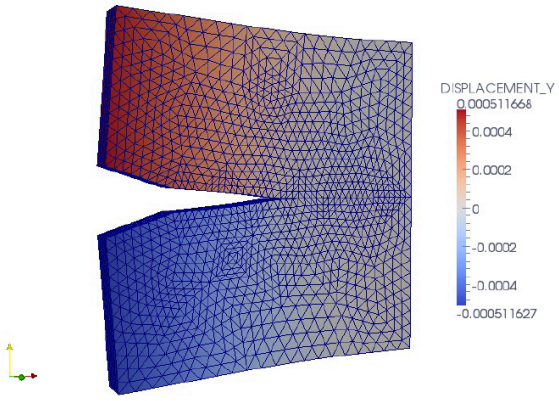

Figure 8: Final deformation of the model

References

[1] M. Ainsworth, J. Coyle, Hierarchic finite element bases on unstructured tetrahedral meshes, International Journal for Numerical Methods in Engineering 58 (14) (2003) 2103–2130.

[2] G. Alfano, M. A. Crisfield, Solution strategies for the delamination analysis based on a combination of local-control arc-length and line searches, International Journal for Numerical Methods in Engineering 58 (7) (2003) 999–1048.

[3] L. Kaczmarczyk (Manager), Mesh Orientated Finite Element Method - (MoFEM v0.0.1), Department of Civil Engineering, School of Engineering, The University of Glasgow, Glasgow, G12 8LT, available at: https://bitbucket.org/likask/mofem-joseph (Accessed date: 26 Jan 2014) (2014).

[4] B. Carrier, S. Granet, Numerical modeling of hydraulic fracture problem in permeable medium using cohesive zone model, Engineering Fracture Mechanics 79 (0) (2012) 312 – 328.

[5] A. Turon, P. Camanho, J. Costa, C. Dávila, A damage model for the simulation of delamination in advanced composites under variable-mode loading, Mechanics of Materials 38 (11) (2006) 1072 – 1089.

[6] G. Alfano, S. Marfia, E. Sacco, A cohesive damage–friction interface model accounting for water pressure on crack propagation, Computer Methods in Applied Mechanics and Engineering 196 (1-3) (2006) 192–209.

Proceedings of the 22nd UK Conference of the
Association for Computational Mechanics in Engineering
2 - 4 April 2014, University of Exeter, Exeter

Extracting stress intensity factors of 3-D cracks using displacement correlation method applied on an unstructured mesh

Morteza Nejati, *Adriana Paluszny and Robert W. Zimmerman

Department of Earth Science and Engineering, Imperial College,
London, United Kingdom

*apaluszn@imperial.ac.uk

ABSTRACT

The displacement correlation technique is applied to extract stress intensity factors of 3D cracks discretised using unstructured hybrid triangle-tetrahedral meshes. The crack surface is discretised by triangles; crack walls are split at all nodes except for those on the tips; and elements on the crack tip are quarter point triangles that have either a *side* or a *corner* on a tip segment. The paper proposes that the low-cost displacement correlation technique can be applied to compute stress intensity factors of such grids, provided that it is performed on *corner* quarter point triangular element. Displacements are interpolated onto a plane normal to the crack front using the element local reference space. The numerical values of the SIFs for a tilted penny-shaped crack embedded in a cube are compared with analytical results. There is a good agreement between the numerical and analytical SIFs along the crack front.

Key Words: *stress intensity factor; displacement correlation; quarter-point element; unstructured mesh*

1. Introduction

Analysing cracked bodies often requires the accurate computation of fracture mechanics parameters such as stress intensity factors (SIFs). In the context of linear elastic fracture mechanics, SIFs fully characterise the stress state around the crack, and can be used to predict propagation. SIFs can be calculated analytically or experimentally for restricted geometric configurations and boundary conditions. Numerical techniques, such as the finite element method, often applied to analyse complex crack problems, require spatial discretisation of the geometric domain. Barsoum [1] and Henshell and Shaw [2] proposed the idea of using quarter-point elements (QPEs) in order to capture the high stress gradient near the crack to accurately compute the singular crack stress field. They independently showed that the singularity at the crack tip can be properly modelled by placing the mid-side node near the crack tip at the quarter-point position. This shift simply results in a nonlinear mapping between the natural and local coordinate systems in a way that singular strains at the crack tip occur, and an inverse square root singularity is modelled throughout the element. Volumetric QPEs, such as the collapsed quarter-point twenty-noded brick element and quarter-point fifteen-noded pentahedral element, are placed around the tip to form a brick-structured mesh [1]. However, in practise, complex geometric multiple crack layouts are best discretised using unstructured meshes which can be generated in a quick non-interactive manner, by a number of mature open-source and commercial meshers, optimised to accurately capture geometry [3]. This paper focusses on the use of a fully unstructured mesh to model 3D crack configurations, and employs the nodal displacement near the crack to extract SIFs using the low-cost displacement correlation technique. Quarter-point triangle and tetrahedral elements are used in an unstructured mesh layout to model singularity along the crack front. The displacement correlation method is then developed to extract the SIFs from FE results directly.

2. Displacement correlation method

Once the finite element simulation has been performed for a particular crack problem, crack tip stress intensity factors can be computed by employing a correlation between the finite element nodal displacements values and the well-known crack tip displacement fields. This method was first developed by for a

general FE solution of a crack problem without using CPEs or QPEs around the crack tip. As the FE results for stresses at crack tip are bounded in these solutions, the FE results are not very accurate very close to the crack tip. Hence, an extrapolation approach was firstly used to compute SIFs from nodal displacements. Shih et al. [4] employed a correlation between the displacement distribution over the quarter-point element and the well known displacement field expressions, to extract the SIFs in 2D crack problems. Ingraffea and Manu [5] then generalised this approach for computing the SIFs in 3D crack problems using collapsed quarter-point twenty-noded brick elements. The displacement correlation approach is conceptually simple and straight forward. Unlike energy approaches which require further numerical integration of the FE results, this method directly uses the finite element nodal values to obtain the SIFs.

Two types of quarter-point tetrahedral elements are generated along the crack front: i) the ones which share an edge with the crack front, side quarter-point tetrahedra (SQPTs); and the ones which share one node with the crack front, corner quarter-point tetrahedra (CQPTs). As the square-root singularity occurs in the whole domain of CQPTs, we shall use the displacement representation of these elements for computing SIFs. In fact, we choose those CQPT elements through which the normal to the crack front passes. Let us assume that $\zeta = 0$ corresponds to the tetrahedal element face which is one of the corner-based quarter-point triangles lies on the crack face (see Fig. 1). The ray normal to the crack front, OP in Fig. 1, is defined by the natural coordinate $0 \leq \psi \leq 0$ in a way that $\psi = 0$ and $\psi = 1$ represents points O and P, respectively. Along this ray, the natural coordinates ξ and η will be: $\xi = \xi_P\psi$ and $\eta = \eta_P\psi$, in which $(\xi_P, \eta_P, 0)$ is the coordinate of point P in natural coordinate system (ξ, η, ζ). Using the shape functions of the tetrahedral element, the relative displacement along the ray OP with respect to crack tip displacement is expressed as:

$$u = \Big(\xi_P(4u_5 - u_2) + \eta_P(4u_7 - u_3)\Big)\psi + 2\Big(\xi_P(u_2 - 2u_5) + \eta_P(u_3 - 2u_7) + 2\xi_P\eta_P(u_6 - u_5 - u_7)\Big)\psi^2 \quad (1)$$

The distance of any point along OP from the crack tip is defined as $r = L_P\psi^2$, in which $L_P = \sqrt{(\xi_P x_2 + \eta_P x_3)^2 + (\xi_P y_2 + \eta_P y_3)^2 + (\xi_P z_2 + \eta_P z_3)^2}$ is the length of line OP. The displacement along the ray OP will therefore be given by:

$$u = \Big(\xi_P(4u_5 - u_2) + \eta_P(4u_7 - u_3)\Big)\sqrt{\frac{r}{L_P}} + 2\Big(\xi_P(u_2 - 2u_5) + \eta_P(u_3 - 2u_7) + 2\xi_P\eta_P(u_6 - u_5 - u_7)\Big)\frac{r}{L_P} \quad (2)$$

The first term in Eq. (2) reproduces the displacement field due to the singular stress field, and the second

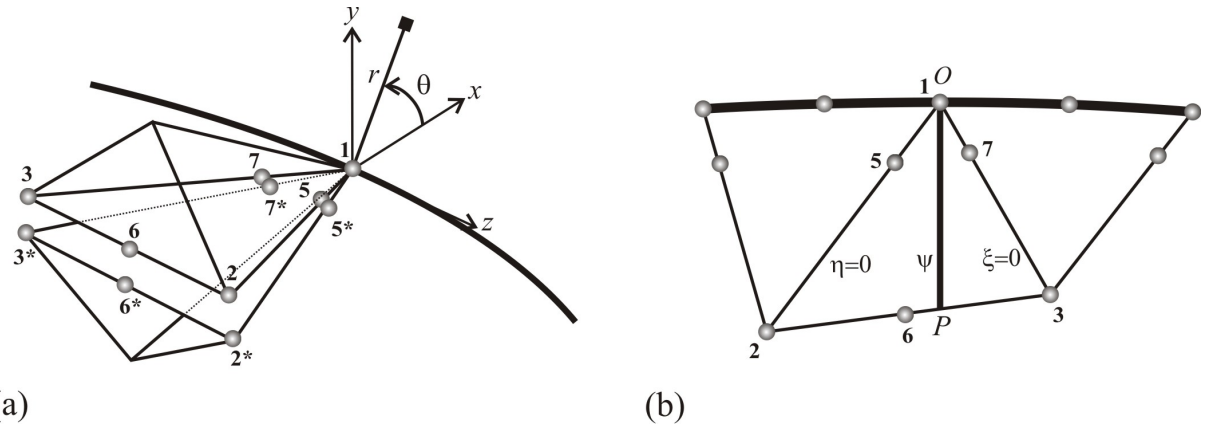

Figure 1: Matching triangular elements used for extracting SIFs.

term represents the displacement due to the constant stress. As we aim to compute the coefficients of singular stress terms, only the first term shall be considered. Similar expressions can be obtained for the displacements in y and z directions (v and w). The relative displacement of the top surface element with respect to the displacement of the bottom surface element is therefore given by:

$$\begin{aligned}
\Delta u &= \left[\xi_P\Big(4(u_5 - u_{5^*}) - (u_2 - u_{2^*})\Big) + \eta_P\Big(4(u_7 - u_{7^*}) - (u_3 - u_{3^*})\Big)\right]\sqrt{\frac{r}{L_P}} \\
\Delta v &= \left[\xi_P\Big(4(v_5 - v_{5^*}) - (v_2 - v_{2^*})\Big) + \eta_P\Big(4(v_7 - v_{7^*}) - (v_3 - v_{3^*})\Big)\right]\sqrt{\frac{r}{L_P}} \\
\Delta w &= \left[\xi_P\Big(4(w_5 - w_{5^*}) - (w_2 - w_{2^*})\Big) + \eta_P\Big(4(w_7 - w_{7^*}) - (w_3 - w_{3^*})\Big)\right]\sqrt{\frac{r}{L_P}}
\end{aligned} \quad (3)$$

On the other hand, the expressions for the relative displacement of the top and bottom crack faces are given from the leading terms in Williams series expansion as:

$$\begin{aligned}
\Delta u &= K_{\mathrm{II}}\Big(\frac{\kappa+1}{\mu}\Big)\sqrt{\frac{r}{2\pi}} + O(r) \\
\Delta v &= K_{\mathrm{I}}\Big(\frac{\kappa+1}{\mu}\Big)\sqrt{\frac{r}{2\pi}} + O(r) \\
\Delta w &= K_{\mathrm{III}}\Big(\frac{4}{\mu}\Big)\sqrt{\frac{r}{2\pi}} + O(r)
\end{aligned} \tag{4}$$

where K_{I}, K_{II}, and K_{III} are the stress intensity factors in modes I, II and III, respectively. $\mu = E/2(1+\nu)$ is the shear modulus, E and ν are the Young's modulus and Poisson's ratio, and the Kolosov constant κ is equal to $3-4\nu$ for plain strain and $(3-\nu)/(1+\nu)$ for plane stress. The assumptions of plane stress on the free surfaces and plane strain elsewhere are also used for 3D crack problems. By equating Eqs. (3) and (4) the following expessions for the SIFs are obtained:

$$\begin{aligned}
K_{\mathrm{I}} &= \sqrt{\frac{2\pi}{L_P}}\Big(\frac{\mu}{\kappa+1}\Big)\Big[\xi_P\Big(4(v_5 - v_{5^*}) - (v_2 - v_{2^*})\Big) + \eta_P\Big(4(v_7 - v_{7^*}) - (v_3 - v_{3^*})\Big)\Big] \\
K_{\mathrm{II}} &= \sqrt{\frac{2\pi}{L_P}}\Big(\frac{\mu}{\kappa+1}\Big)\Big[\xi_P\Big(4(u_5 - u_{5^*}) - (u_2 - u_{2^*})\Big) + \eta_P\Big(4(u_7 - u_{7^*}) - (u_3 - u_{3^*})\Big)\Big] \\
K_{\mathrm{III}} &= \sqrt{\frac{2\pi}{L_P}}\Big(\frac{\mu}{4}\Big)\Big[\xi_P\Big(4(w_5 - w_{5^*}) - (w_2 - w_{2^*})\Big) + \eta_P\Big(4(w_7 - w_{7^*}) - (w_3 - w_{3^*})\Big)\Big]
\end{aligned} \tag{5}$$

3. Results and discussion

Fig. 2*a* schematically shows the configuration of a penny-shaped crack embedded in a cube and the boundary conditions applied on the specimen. The model is discretised using a fully unstructured mesh with triangles on the crack surface and tetrahedral elements elsewhere. The mid-side nodes near the crack front are moved onto the quarter-point position. Fig. 3*b* shows the mesh structure on the crack face. The full specimen was modelled to ensure that an unstructured mesh is generated all over the crack front. The mixed mode stress intensity factors were computed using Eq. (5), and are plotted along the crack front in a normalised form in Fig. 3. Numerical values are in a good agreement with analytical results. The advantages of the displacement correlation approach are simplicity and low computational cost. This method can be used for analysing very complicated crack configurations for which a structured mesh cannot be generated.

References

[1] R.S. Barsoum. On the use of isoparametric finite elements in linear fracture mechanics. *International Journal for Numerical Methods in Engineering*, 10, 25–37, 1976.

[2] R.D. Henshell and K.G. Shaw. Crack tip finite elements are unnecessary. *International Journal for Numerical Methods in Engineering*, 9, 495–507, 1975.

[3] A. Paluszny, R.W. Zimmerman. Numerical fracture growth modeling using smooth surface geometric deformation. *Engineering Fracture Mechanics*, 108, 13–36.

[4] C.F. Shih, H.G. DeLorenzi, M.D. German. Crack extension modeling with singular quadratic isoparametric elements. *International Journal of Fracture*, 12, 647–651, 1976.

[5] A.R. Ingraffea and C. Manu. Stress intensity factor computation in three dimensions with quarter-point elements. *International Journal for Numerical Methods in Engineering*, 15, 1427–1445, 1980.

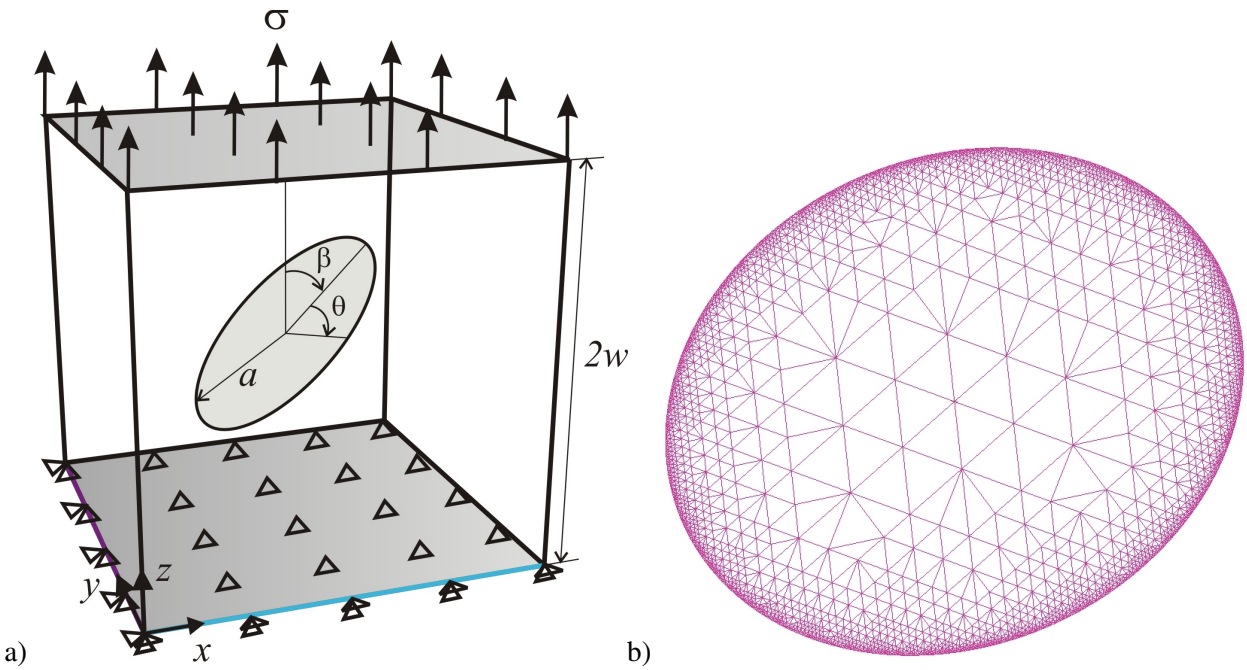

Figure 2: Geometry and boundary conditions. (a) An inclined penny-shaped crack in a cubic body under uniaxial tension. b) Mesh structure around the crack front.

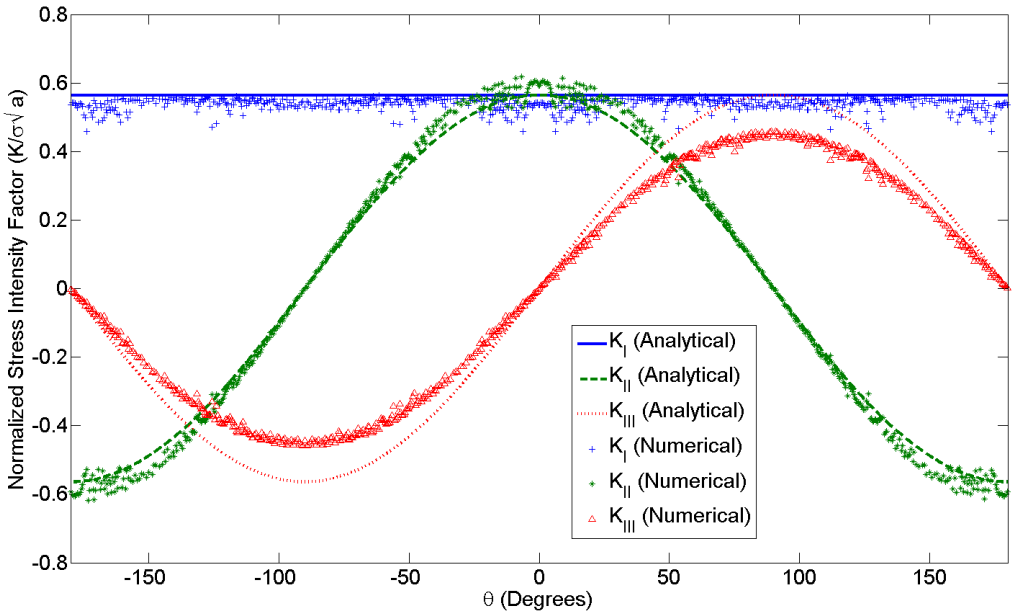

Figure 3: Normalised mixed mode stress intensity factors for an inclined penny-shaped crack in a cubic body ($a/w = 0.1, \beta = 45°$)

.

Proceedings of the 22nd UK Conference of the
Association for Computational Mechanics in Engineering
2 – 4 April 2014, University of Exeter, Exeter

Failure Analysis of 3-D Graphite Bricks in an AGR Core

***Costy Kodsi, Lukasz Kacszmarczyk and Chris J. Pearce**

School of Engineering, Rankine Building, The University of Glasgow, Glasgow, UK, G12 8LT

*c.kodsi.1@research.gla.ac.uk

ABSTRACT

A methodology has been developed to study unstable fracture in multi-body impacts. This has required the combination of two modelling frameworks, namely multi-body contact mechanics and quasi-static crack propagation. This was achieved by developing a number of algorithms for rigid body motion mitigation, crack initiation and Boolean unification between volume elements and the crack surface for coarse mesh generation.

Keywords: *Fracture, rigid body motion, crack initiation, Boolean unification of volume and surface*

1. Introduction

The objective of this research is to develop a methodology for modelling crack propagation in three-dimensional multi-body impact scenarios. The developed methodology makes use of a dynamic multi-body contact finite element analysis code, SOLFEC [1], and a quasi-static crack propagation code, MoFEM [2]. The motivation of this work is the study of crack propagation in graphite bricks in an Advanced Gas-Cooled Reactor (AGR) subjected to abnormal loading conditions.

2. Background

The graphite core in an AGR is a large assembly of graphite bricks stored in an array format organised on top and next to each other with a vertical channel in the middle of each brick that contains the fuel, namely uranium dioxide. These graphite bricks will be idealised as isotropic linear elastic and assumed to behave in a brittle manner.

SOLFEC is based on an implicit formulation of contact conditions, in contrast to commercial codes that typically employ repulsive springs in their contact methodology. This provides a physically accurate representation of reality and permits larger stable time-steps in simulations. SOLFEC has been developed with high performance computing in mind from the onset making it an ideal code for modelling a large number of impacting bodies. However, this capability does not extend to the finite element analysis part of the code. Subsequently, the mesh representing graphite bricks in an impact simulation uses a relatively simple mesh comprising through-depth elements as pictorially depicted in **Figure 1(a)**.

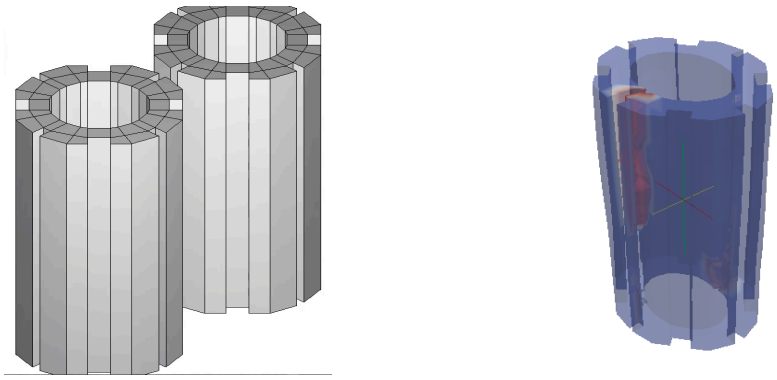

Figure 1. (a) SOLFEC graphite brick mesh, & (b) example of MoFEM crack propagation.

The crack propagation available in MoFEM employs configurational forces and maximum energy dissipation at the crack front. The configurational forces provide the crack propagation direction and the crack propagation criterion is based on Griffith theory. The local topology is modified to accommodate the crack extension and a local hp-adaptive mesh refinement scheme is concentrated on the crack front. The local mesh is adapted through the movement of the nodes on the crack front; mesh refinement and edge decimation maintains the validity of the local mesh. An example of crack propagation can be seen in **Figure 1(b)**. The crack propagation analysis relies on a much more refined mesh than is necessary or practical in SOLFEC and this discrepancy has to be addressed.

3. Method Development

It is assumed fracture events in bodies do not influence the contact force evolution with time. This simply means that the crack propagation will occur faster than the change in boundary conditions in SOLFEC. Furthermore, and most importantly, it is assumed that fracture in one body will not have a bearing on the fracture in other bodies.

An approach for modelling unstable crack propagation can then be formulated, which is represented by the following sequential steps:

(i) SOLFEC implicit contact analysis is executed and run to completion;
(ii) Bodies that will fracture are identified during the simulation and the contact forces as well as corresponding Lagrangian displacement (relative to the reference configuration) on the surface boundary are recorded at the specific time-step;
(iii) Rigid body motion is removed from the displacements of the identified bodies and a denser mesh is generated in preparation for crack propagation analysis;
(iv) Location of crack initiation is determined in the identified bodies and crack propagation to failure is carried out in MoFEM, given the displacement boundary conditions as constraints;
(v) The predicted crack surface is unified with the original SOLFEC mesh and the intersected elements have a denser mesh generated for them to account for the modified geometry;
(vi) SOLFEC is re-run with the fractured bodies to study the impact that cracks have on the overall simulation and on individual graphite bricks.

The bodies that will undergo fracture are identified in SOLFEC using an energetic criterion that monitors the strain energy of each element and has an empirically set threshold.

Algorithms to remove rigid body motion from the displacement, to perform the Boolean operation of unification and to generate the subsequent mesh have been developed. In addition, a crack initiation criterion has been proposed to determine the location(s) of crack initiation in MoFEM, which currently requires manual identification of the affected edges. The algorithms and proposed criterion are briefly documented in the next sections. To facilitate data transfer between SOLFEC, MoFEM and the developed algorithms, the legacy VTK file format has been selected.

4. Rigid Body Motion Removal

The contact forces output by SOLFEC are provided on the surface, while the displacements are given on the nodes. Therefore, a surface-to-node algorithm was written to identify the nodes where the contact forces are applied. The displacements on those nodes are then used as constraint in the crack propagation analysis.

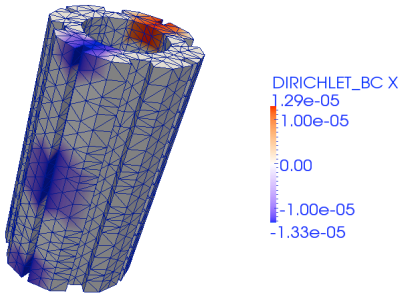

Figure 2. Example of rigid body translation mitigation.

A routine was written to remove the rigid body translation; this involves subtracting the average of the displacements at the identified nodes from the displacement magnitude at each identified node. An

illustration demonstrating the removal of rigid body displacement in a graphite brick is shown in **Figure 2**.

The removal of rigid body rotations is a more involved process. The displacements have to be decomposed into a deformational $\mathbf{u}^d$ and rotational part $\mathbf{u}^r$,

$$\mathbf{u}^d = \mathbf{u} - \mathbf{u}^r, \text{ and} \tag{1}$$

$$\mathbf{u}^r = \left(\mathbf{R} - \mathbf{I}\right)\mathbf{X}, \tag{2}$$

where $\mathbf{R}$ is the rotation operator, $\mathbf{I}$ the identity matrix and $\mathbf{X}$ the reference configuration position vector. The object of this exercise is to determine the rotation operator. One can take advantage of the fact that the anti-symmetric part of the displacement gradient vanishes when there is no rotation. Assuming that the rotation is constant over a body volume V, the anti-symmetric part of the displacement gradient averaged over all the elements can be expressed,

$$\int \left(\left[\frac{\partial \mathbf{u}^d}{\partial \mathbf{X}} \right] - \left[\frac{\partial \mathbf{u}^d}{\partial \mathbf{X}} \right]^T \right) dV = 0. \tag{3}$$

Alternatively, a pseudo-vector applied on the surface boundary can be defined as [3],

$$\mathbf{h} = \int \left(\mathbf{n} \times \mathbf{u}^d \right) dS, \tag{4}$$

where n is the surface spatial normal. An objective function can then be defined and optimized to yield the rotation operator,

$$J\left(\mathbf{R}\right) = \mathbf{h}^T \mathbf{h}. \tag{5}$$

A number of algorithms were implemented and investigated for the optimization procedure: (i) the finite difference method using the complex derivative; (ii) the Cayley transform based method; (iii) a Gauss-Newtonian approach; and a (iv) Newtonian approach based on local parameterization of the manifold $SO(3)$ [4]. The final method was selected as it proved to be the least computationally expensive and to be the most stable for large rotations.

5. Crack Initiation Criterion

A crack initiation criterion has been proposed based on the notion that fracture is a sudden discrete rupture event that suddenly appears at the macroscopic level. A topological asymptotic expansion evaluates the sensitivity of the total potential energy change involved in introducing a hole into an unperturbed (geometrically) elastic system at a point through the expression,

$$D_T\left(x_0\right) = -\frac{1}{2E}\left[\left(\sigma_1 + \sigma_2\right)^2 + 2\left(\sigma_1 - \sigma_2\right)^2\right], \tag{6}$$

where σ_1 and σ_2 are the principal stresses, while E is the Young's modulus. The change in energy is then equated to a critical factor derived from an energy equivalent of Novozhilov's non-local force-based criterion. A more thorough treatment of this criterion is available in [5].

6. Boolean Unification

At the heart of this part of the work is the CGAL library [6] and the contained half-edge data structure, which provides connectivity information of the vertices, edges and faces that compose a shape. TetGen [7] is used as the mesh generator due to the fact that interior surfaces inside the shape volume can be treated as an extension of the boundary. A novel, simple and robust procedure has been developed for unifying the crack surface and the original volume SOLFEC mesh as follows:

(i) Mesh simplification is performed on the crack surface to reduce the triangle count;
(ii) The elements in the original SOLFEC mesh that are intersected by the crack surface are identified and the shared faces in the elements are not included in the following steps;
(iii) The simplified crack surface boundary nodes are aligned with the intersected SOLFEC mesh elements and assigned to the intersected element faces;
(iv) Delaunay triangulation in 2-D is performed on the identified faces to reconstruct them so as to include the crack surface nodes;
(v) The intersected element faces are merged together to form a new shape;
(vi) The simplified crack front mesh and the new shape are unified in the TetGen data structure for purposes of mesh generation;
(vii) The generated mesh is split at the crack surface front and replaces the intersected elements in the original SOLFEC mesh.

Existing CGAL functionality is employed to perform the mesh simplification, intersection tests and Delaunay triangulation. The half-edge data structure is utilised to store face information regarding the intersected vertices and triangulations to produce an efficient algorithm for Boolean unification of a volume with a surface.

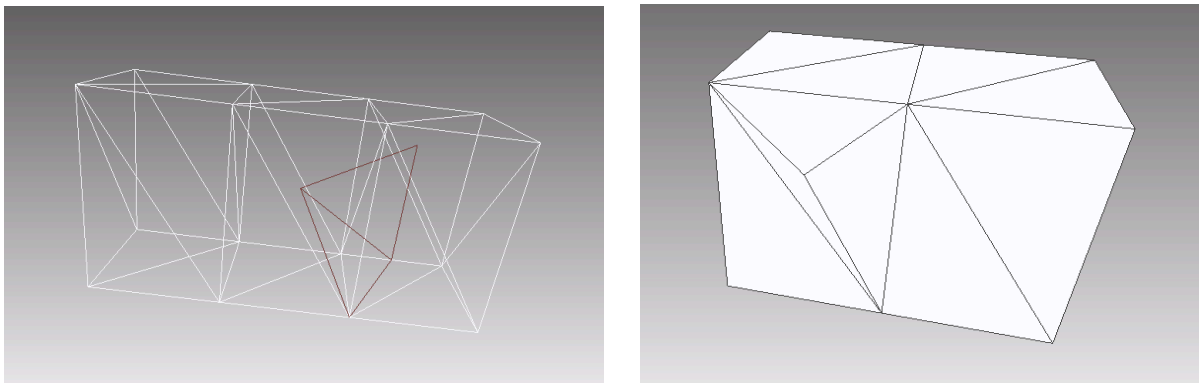

Figure 3. (a) Simple example of surface (red) intersecting volume elements, & (b) volume elements containing intersection identified and reconstructed.

References

[1] T. Koziara and N. Bićanić. A distributed memory parallel multibody contact dynamics code. *International Journal for Numerical Methods in Engineering*, 87(1-5), 437-456, 2011.

[2] Ł. Kaczmarczyk, M. M. Nezhad and C. J. Pearce. Three-dimensional brittle fracture: configurational-force-driven crack propagation. *International Journal for Numerical Methods in Engineering*, 97(7), 531-550, 2014.

[3] Ł. Kaczmarczyk, T. Koziara and C. J. Pearce. Co-rotational formulation for 3d solids: An analysis of geometrically nonlinear foam deformation. *arXiv:1110.5321v2*, April 2013.

[4] C. J. Taylor and D. J. Kriegman. Minimizations on the Lie group SO(3) and related manifolds. Yale Center for Systems Science, New Haven, CT, Tech. Rep. 9405, April 1994.

[5] C. Kodsi, Ł. Kaczmarczyk and C. J. Pearce. Crack Initiation: a discrete non-local energy approach. *In International Conference on Computational Mechanics CM13*, Durham, 2013.

[6] CGAL, Computational Geometry Algorithms Library, *http://www.cgal.org*.

[7] H. Si. On Refinement of Constrained Delaunay Tetrahedralizations. *In Proceedings of the 15th International Meshing Roundtable*, September 2006.

Proceedings of the 22nd UK Conference of the
Association for Computational Mechanics in Engineering
2 - 4 April 2014, University of Exeter, Exeter

Global energy minimization for multi-crack growth in linear elastic fracture using the extended finite element method

***Danas Sutula[1], Pierre Kerfriden[2], Stephane P. A. Bordas[3] and Alexandre Barthelemy[4]**

[1,2]Cardiff University, School of Engineering, The Parade, Cardiff, CF24 3AA, Wales, UK
[3]University of Luxembourg, Engineering, 6 rue Richard Coudenhove-Kalergi, L-1359 Luxembourg
[4]SOITEC, Parc Technologique des Fontaines Chemin des Franques, 38190 Bernin, France

*sutulad@cardiff.ac.uk

ABSTRACT

We investigate multiple fracture evolution under quasi-static conditions in an isotropic linear elastic solid based on the principle of minimum potential elastic energy in the framework of the extended finite element method. The technique enables a minimization of the potential energy with respect to all crack increment directions. Results show that the maximum hoop stress criterion and the energy minimization approach converge to the same fracture path. It is found that the converged solution lies in between the fracture paths obtained by each criterion for coarser meshes. This presents an opportunity to estimate an upper and lower bound of the true fracture path as well as an error on the crack path.

Key Words: *crack propagation; extended finite element method; energy minimisation.*

1. Introduction

In computational fracture mechanics as applied, for example, to damage tolerance assessment, it has been common practice to determine the onset of fracture growth and the growth direction by post-processing the solution of the linear elastostatics problem, at a particular instance in time. For mixed mode loading the available analytically derived criteria that can be used for determining the onset of crack growth typically rely on the assumptions of an idealized geometry e.g. a single crack subjected to remote loading [9, 5] and that the kink angle of the infinitesimal crack increment is small [7]. Moreover, the growth direction given by a criterion that is based on an instantaneous local crack tip field can only be valid for infinitesimally small crack growth increments. Consequently, the maximum hoop stress criterion [4] and other similar criteria [2] disregard the changes in the solution that take place as fractures advance over a finite size propagation. Hence, due to the error committed in time-integration, fractures may no longer follow the most energetically favorable paths that theoretically could be achieved for a specific discrete problem.

2. Methodology

In our approach, we investigate multiple fracture evolution under quasi-static conditions in an isotropic linear elastic solid based on the principle of minimum potential elastic energy, which can help circumvent the aforementioned difficulties. The technique enables a minimization of the potential energy with respect to all crack increment directions taking into consideration their relative interactions. The directions are optimized (in the energy sense) by considering virtual crack rotations to find the energy release rates and its first derivatives in order to determine, via an iterative process, the directions that yield zero energy release rates with respect to all virtual rotations [6]. We use the extended finite element method (XFEM) [1, 8] for discretization of a 2D continuum in order to model an elaborate crack evolution over time, similar in principle to [3], although here we would like to consider hundreds of propagating cracks.

3. Governing equations

The energy release rate with respect to a fracture growth direction θ_i can be obtained by differentiation of the potential energy Π of the system:

$$Gs_i = -\frac{\partial \Pi}{\partial \theta_i} \tag{1}$$

Considering a general case of multiple fractures, the rate of the energy release rate can be obtained as:

$$Hs_{i,j} = \frac{\partial Gs_i}{\partial \theta_j} = -\frac{\partial^2 \Pi}{\partial \theta_i \partial \theta_j} \tag{2}$$

In a discrete setting, the potential energy of a static system can be written as:

$$\Pi = \frac{1}{2} u' K u - u' f \tag{3}$$

where u, K, and f are the displacement vector, the stiffness matrix, and the applied force vector. The energy release rate with respect to an arbitrary crack incitement angle θ_i is defined as the negative variation of the potential energy:

$$Gs_i = -\frac{1}{2} u' \delta_i K u + u' \delta_i f - \delta_i u' (K u - f) \tag{4}$$

in which case the last term in (4) disappears due to assumed equilibrium of the discrete system i.e. $Ku = f$. Hence, the expression for the energy release rate becomes:

$$Gs_i = -\frac{1}{2} u' \delta_i K u + u' \delta_i f \tag{5}$$

where $\delta_i f$ only needs to be accounted for if the applied loads influence the virtual crack rotation, e.g. due to crack face tractions and body-type loads. The rates of the energy release rate, Hs_{ij} are obtained by differentiating Gs_i in (5) with respect to θ_j:

$$Hs_{ij} = -\left(\frac{1}{2} u' \delta_{ij}^2 K u - u' \delta_{ij}^2 f \right) - \delta_j u' \left(\delta_i K u - \delta_i f \right) \tag{6}$$

The variations of displacements $\delta_j u$ in (6) are global, and can be determined from the equilibrium condition and that the variation must vanish, i.e. $\delta_j (Ku - f) = 0$ and thus:

$$\delta u = -K^{-1} (\delta K u - \delta f) \tag{7}$$

Substituting (7) in (6) gives:

$$Hs_{ij} = -\left(\frac{1}{2} u' \delta_{ij}^2 K u - u' \delta_{ij}^2 f \right) + (\delta_j K u - \delta_j f)' K^{-1} (\delta_i K u - \delta_i f) \tag{8}$$

In (8) the second order mixed derivatives $\delta_{ij}^2 K$ and $\delta_{ij}^2 f$ capture the local interaction between the rotations of different crack increments. However, if the crack tips are sufficiently far apart such that no geometrical interactions exist between different rotations, then for $i \neq j$ the interacting terms vanish, i.e. $\delta_{ij}^2 K = 0$ and $\delta_{ij}^2 f = 0$. As such, it only becomes necessary to retain the non-zero self-interactions i.e. $\delta_{ii}^2 K$ and $\delta_{ii}^2 f$. Consequently, by leaving out the cross-interactions, equation (8) reads as:

$$Hs_{ij} = -\left(\frac{1}{2} u' \delta_{ii}^2 K u - u' \delta_{ii}^2 F \right) + (\delta_j K u - \delta_j f)' K^{-1} (\delta_i K u - \delta_i f) \tag{9}$$

Equations (5) and (9) can be used to determine the energy release rates and the rates of the energy release rates associated with the rotation of different crack increments. The problem of finding the most energetically favorable growth directions for the candidate finite length crack increments, denoted by a set I_{inc}, is one requiring that the corresponding energy release rates must vanish i.e. $Gs_i = 0, \ \forall i \in I_{\text{inc}}$. The solution procedure at every time step, t^{n+1} can be cast as Newton-Raphson iterations:

$$\boldsymbol{\theta}_{k+1} = \boldsymbol{\theta}_k - \boldsymbol{H}_k{}^{-1} \boldsymbol{G}\boldsymbol{s}_k \tag{10}$$

where k is the iteration count. The converged solution is attained when $|\boldsymbol{\theta}_{k+1} - \boldsymbol{\theta}_k| \leq \epsilon$, ϵ being the tolerance in the change in the angle of the finite crack increment, e.g. $\epsilon = 0.1^\circ$.

4. Implementation

Although XFEM facilitates mesh independent fracture propagation the enrichment must be updated at each time step. In the current implementation this is achieved by means of a systematic book-keeping of the element enrichment data, addition and removal of enrichment only where necessary, and a consistent updating of the global system of equations. Consequently, moderate computational times are obtained, even in our *Matlab* implementation. In the problems we solve, the greatest cost, by far, is in the solution of the linear system of equations rather than in the assembly/updating.

5. Results and discussion

We compare the fracture paths obtained by different criteria for problems consisting of multiple cracks and verify that, with mesh refinement, both criteria converge to the same fracture path provided the criterion for growth is the same. However, the convergence rate of the energy minimization technique to the converged crack path is found to be only marginally superior to that of the maximum hoop stress criterion. It is found that the converged fracture path lies in between the fracture paths obtained by each criterion for coarser meshes. This presents an opportunity to estimate an upper and lower bound of the true fracture path as well as an error on the crack path. It is found that a more accurate approximation of the fracture path for coarser meshes can be obtained by averaging the directions determined by each criteria individually at every time step. Some results are demonstrated in Appendix A. Although there is no limitation on the number of cracks in the implementation, the example cases presented consider only few cracks as it is sufficient to demonstrate the key idea clearly.

6. Conclusions

Convergence of the maximum hoop stress criterion and the energy minimization towards the true fracture path is found to be similar. However, from numerical experiments it is found that the converged fracture path lies in between the fracture paths obtained by each criterion for coarser meshes. Besides the opportunity to estimate the error on the fracture path for a given mesh, a more accurate approximation of the true fracture path can be obtained by taking the average of the propagation directions given by each criterion separately at every time step. Future work involves optimization of fracture increment lengths as well as the growth directions simultaneously.

References

[1] T. Belytschko and T. Black. Elastic crack growth in finite elements with minimal remeshing. *International Journal for Numerical*, 620(July 1998):601–620, 1999.

[2] P. O. Bouchard, F. Bay, and Y. Chastel. Numerical modelling of crack propagation: automatic remeshing and comparison of different criteria. *Computer Methods in Applied Mechanics and Engineering*, 192(35-36):3887–3908, August 2003.

[3] E. Budyn, G. Zi, N. Moës, and T. Belytschko. A method for multiple crack growth in brittle materials without remeshing. *International Journal for Numerical Methods in Engineering*, 61(10):1741–1770, November 2004.

[4] F. Erdogan and G. C. Sih. On the crack extension in plates under plane loading and transverse shear. *Journal of basic engineering*, 85:519, 1963.

[5] K. Hayashi and S. Nemat-Nasser. Energy-release rate and crack kinking under combined loading. *Journal of Applied Mechanics*, (September 1981):520–524, 1981.

[6] M. A. Hussain, S. L. Pu, and J. Underwood. Strain Energy Release Rate for a Crack Under Combined Mode I and Mode. *Fracture analysis*, 560:1, 1974.

[7] B. L. Karihaloo, L. M. Keer, and S. Nemat-Nasser. Crack kinking under nonsymmetric loading. *Engineering Fracture Mechanics*, 13(4):879–888, 1980.

[8] N. Moës, J. Dolbow, and T. Belytschko. A finite element method for crack growth without remeshing. 150(February):131–150, 1999.

[9] R. J. Nuismer. An energy release rate criterion for mixed mode fracture. *International journal of fracture*, 11(2):245–250, 1975.

Appendix A. Figures

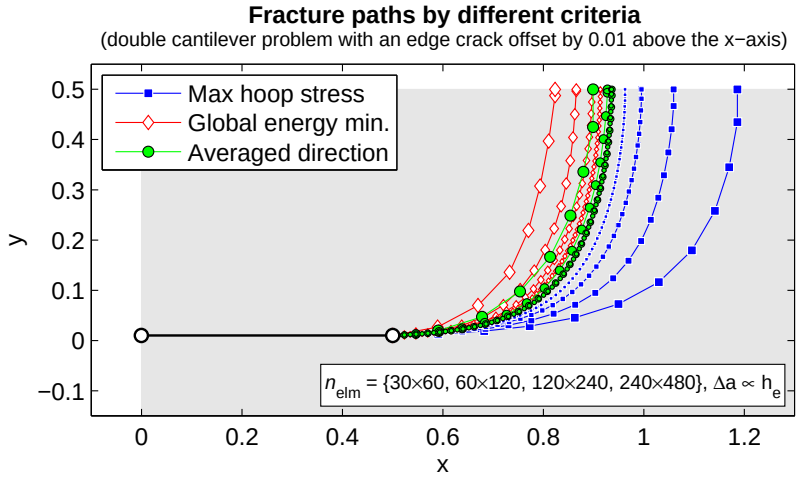

Figure A.1: Fracture paths considering different growth criteria for the double cantilever problem with the initial crack positioned 0.01 above the x-axis. The prying action is exerted by prescribed displacements on the left edge.

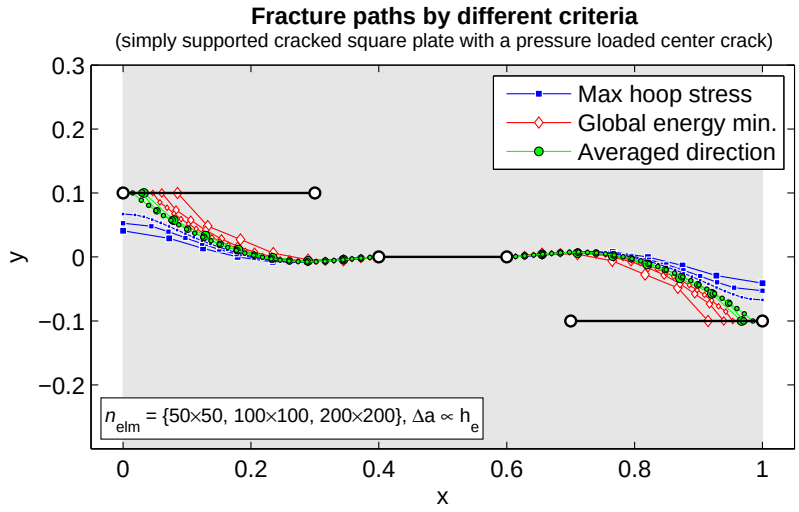

Figure A.2: Fracture paths considering different growth criteria for a simply supported square plate with three pre-existing cracks, where the center crack is subjected to a pressure load acting normal to the crack surface.

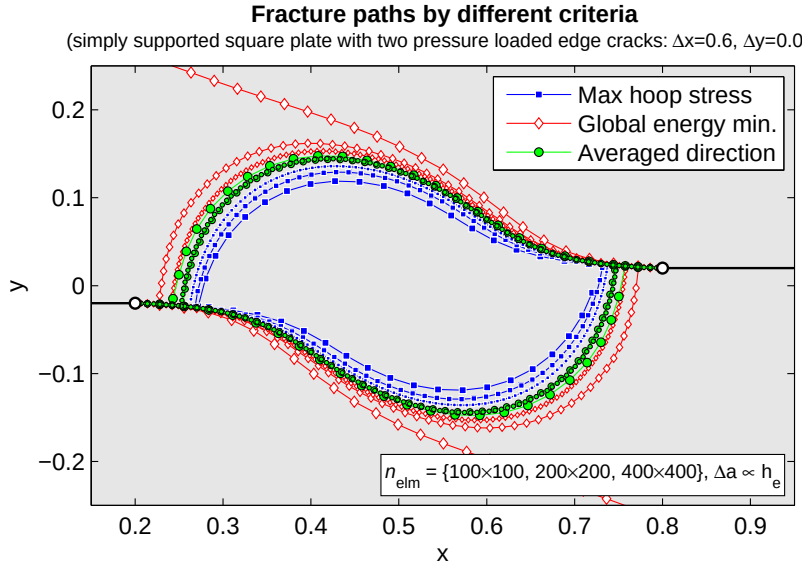

Figure A.3: Fracture paths considering different growth criteria for a simply supported square plate with two initial edge cracks that are loaded by pressure acting normal to the crack surface.

Proceedings of the 22nd UK Conference of the
Association for Computational Mechanics in Engineering
2 – 4April 2014, University of Exeter, Exeter

MESO-SCALE FRACTURE MODELLING OF CONCRETE WITH RANDOM AGGREGATES AND PORES

***X.F. Wang[1], Z.J. Yang[1,2] and J.R. Yates[3]**
[1]School of MACE, the University of Manchester, Manchester, M13 9PL, UK
[2]College of Civil Engineering and Architecture, Zhejiang University, Hangzhou, 310058, China
[3]Simuline Ltd, Derbyshire, S18 1QD, UK

*xiaofeng.wang@manchester.ac.uk

ABSTRACT

Generation and packing algorithms are developed to create models of two-dimensional heterogeneous concrete specimens with randomly distributed circular, elliptical and polygonal pores and aggregates. A recently developed numerical method based on the cohesive crack model is used to simulate meso-scale crack initiation and propagation. Monte Carlo simulations are carried out to evaluate the effects of pore and aggregate shape, porosity and aggregate volume fraction. The nucleation and coalescence of microcracks and propagation of macrocracks are modelled in detail with some important conclusions drawn.

Keywords: *concrete, random packing, Monte Carlo simulation, cohesive elements, meso-scale modelling*

1. Introduction

Concrete is a composite material with a variety of inhomogeneities and its response to mechanical loading is complex. Due to its multi-phase composition and quasi-brittle mechanical behaviour, modelling of concrete for structural engineering analysis is an important and challenging problem [1, 2]. At the mesoscopic scale, it is evident that several parameters, such as the shape, pore and aggregate distribution, aggregate gradation, porosity, aggregate volume fraction and aggregate-mortar interfaces, significantly influence the numerical simulation of the mechanical behaviour of concrete. The majority of researchers treat concrete as a two-phase (mortar and inclusions) or three-phase (mortar, inclusions and interfaces) material at the mesoscale. However, the XCT images [3, 4] clearly show that pores exist in the concrete at this scale. In our paper, we describe the generation of random mesostructure models with circular, elliptical, polygonal aggregates and pores based on prescribed parameters. The models are then meshed automatically, solved by FEM, and statistically analysed to elucidate the effects of mesostructural parameters on the mechanical behaviour.

2. Mesostructure Generation

Wang *et al*. [5] presented a comprehensive procedure using a commonly adopted "taking" and "placing" method to generate a random geometric arrangement of aggregates. A similar procedure is adopted in the present study, which is programmed using MATLAB. The basic idea is to create the aggregates in the concrete in a repeated manner, until the target area is filled. The "input" step reads the controlling parameters for different shapes of aggregates and pores, the "taking" step generates an individual aggregate/pore in accordance with the random size and shape descriptions, and the "placing" step subsequently positions the aggregates and pores into the predefined area in a random manner, subjected to the prescribed physical constraints. The shape of aggregate particles depends on the aggregate type. Generally, gravel aggregates have a circular or elliptical shape, while crushed stone aggregates have an angular shape and are therefore modelled as polygons.

3. Cohesive Crack Model

A recently developed numerical method based on the cohesive crack model is used to simulate meso-scale crack initiation and propagation [2]. Here 4-node zero in-plane thickness cohesive elements are pre-inserted into the existing element edges by an in-house computer program. Fig. 1(a) and Fig. 1(b) shows the initial FE mesh (16 elements and 13 nodes) and FE mesh with inserted cohesive elements

(36 elements, 48 nodes). The element and node numbers are denoted as *E* and *N* respectively. The detailed numbering of elements and nodes in the initial mesh and the mesh with inserted cohesive elements (see Fig. 1) shows the insertion procedure with the new nodes generated at the same positions and interface cohesive elements between the continuum elements. The inserted cohesive elements can be divided into three groups (see Fig. 1(b)); those along mortar-aggregate interfaces (yellow in Fig. 1(b)), inside mortar (green in Fig. 1(b)) and inside aggregates (blue in Fig. 1(b)). In general, aggregates are less likely than mortar to crack. But, in our work additional interface elements are inserted within the aggregates to represent potential cracks, such as in the case of lightweight or high-strength concrete. So in the mesostructure of concrete, a potential crack path may transverse through aggregates, or mortar, or along their interfaces.

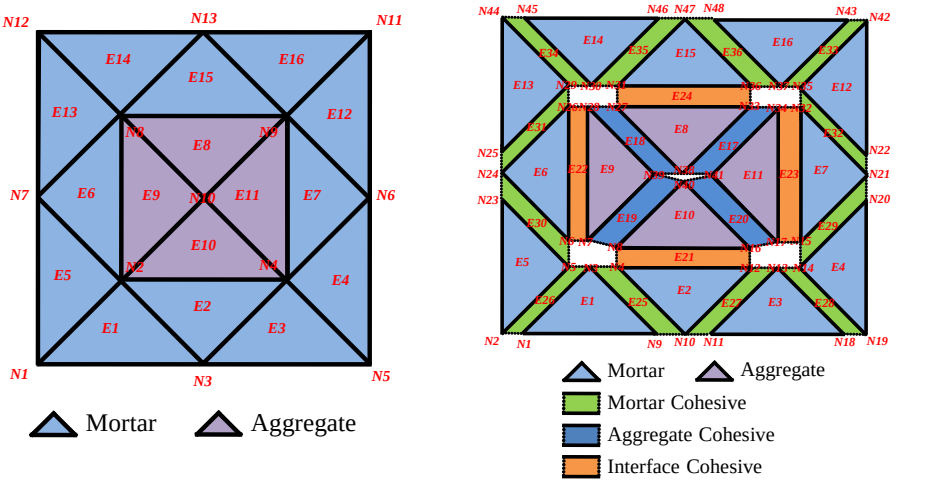

(a) Initial mesh (b) Mesh with zero thickness cohesive elements

Fig. 1. Inserting different cohesive elements into the initial mesh

4. Monte Carlo Simulation

4.1. Effect of aggregate and pore shape

A series of 2D concrete specimens (50mm×50mm, aggregate volume fraction=40%, porosity=2%) with different shapes of aggregates and pores are modelled under a uniaxial tension test. Horizontal displacements are prescribed to all nodes of the left and right surfaces of the specimen, with value equal to zero on the left surface, and a uniformly distributed displacement (0.1mm) on the right surface. Vertical displacements for the same nodes are left free, except for the node at the left lower corner of the specimen, which is fixed to prevent rigid body translation. The material parameters used for the continuum elements are: Young's Modulus E=7×10^4 MPa (aggregates), E=2.5×10^4 MPa (mortar) and Poisson's ratio υ=0.2 (both); for the aggregate-aggregate and mortar-mortar interface elements: elastic stiffness k_n=k_s=10^6 MPa/mm, tensile strength t_n=6 MPa and fracture energy G_f =0.06 N/mm; for the aggregate-mortar interface elements: k_n=k_s=10^6 MPa/mm, t_n=3 MPa and G_f =0.03 N/mm.

The effect of aggregate and pore shape is investigated by performing 100 Monte Carlo simulations while all the other parameters are fixed. Fig. 2 plots the typical crack paths for samples with different shapes of aggregates and pores. Two typical crack types as found in asphalt mixture [6] are observed in the Monte Carlo simulations under a uniaxial tension test: namely, type I cracking with only one dominant crack, and type II cracking with two dominant cracks. The both types of cracking are easily observed in concrete samples with different shapes of aggregates and pores (see Fig. 2(a)-(f)). This is because microcracks first initiate and coalesce in some weaker regions, type I crack develops when the degraded regions are almost in a line, and type II crack develops when the microcrack connection is obstructed by a strong portion. Fig. 3(a)-(f) shows the resulting stress-displacement curves for the 6 groups. The mean stress-displacement curves are plotted, and the mean value and the standard deviation of the peak stress are also calculated. It seems to reveal that the load capacity in the tensile test of the circular and elliptical aggregate samples is greater than that of polygonal ones. The load capacity difference between samples with circular aggregates and elliptical aggregates is about 2% while the difference between samples with circular aggregates and polygonal aggregates is about 6%.

It is postulated that this is because the local stresses are enhanced by the higher stress concentration at the corners of the polygonal aggregates, while the smooth edges of the circular and elliptical aggregates have a more benign stress distribution which delays the fracture event and increases the tensile strength.

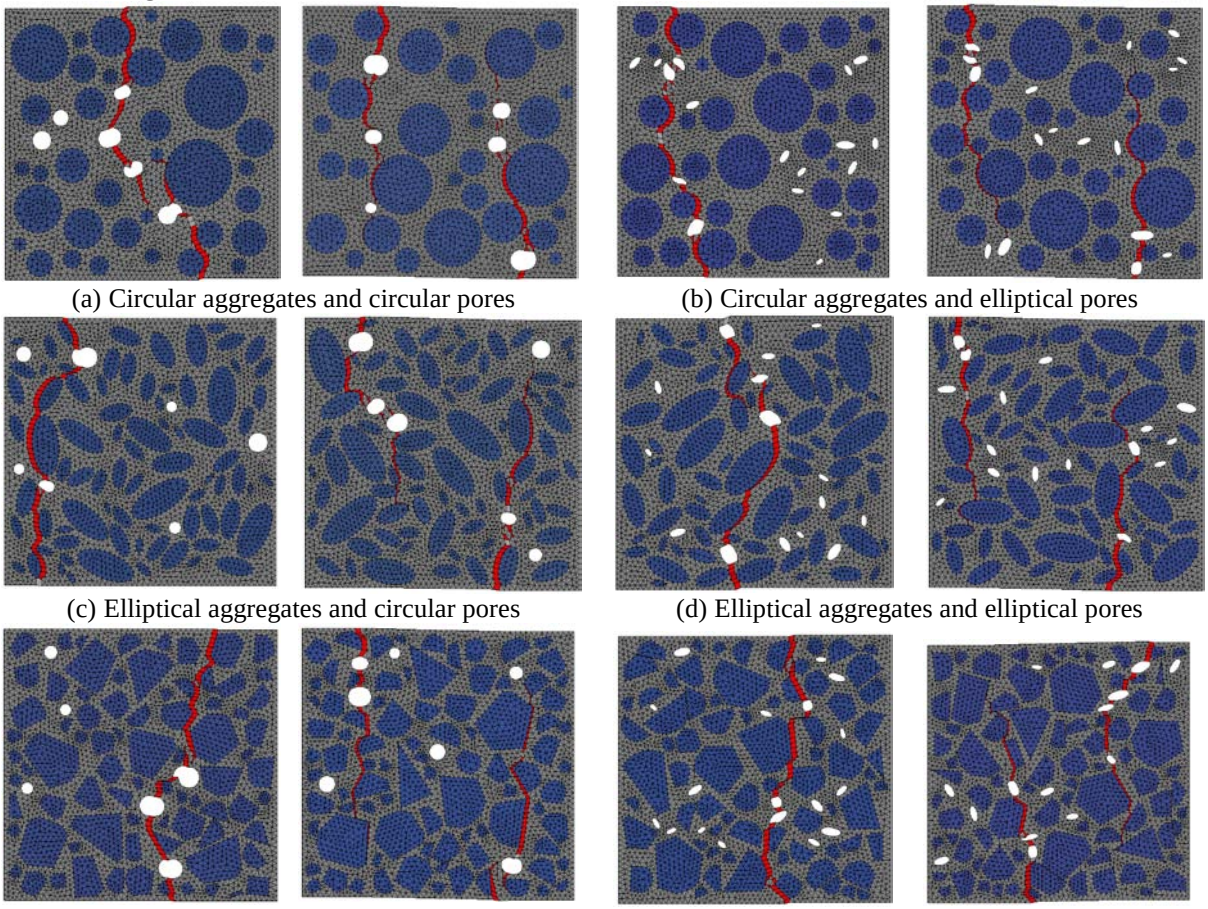

(a) Circular aggregates and circular pores (b) Circular aggregates and elliptical pores

(c) Elliptical aggregates and circular pores (d) Elliptical aggregates and elliptical pores

(e) Elliptical aggregates and elliptical pores (f) Elliptical aggregates and elliptical pores

Fig. 2. Typical type I and type II crack paths for samples with different shapes of aggregates and pores (magnification factor=10)

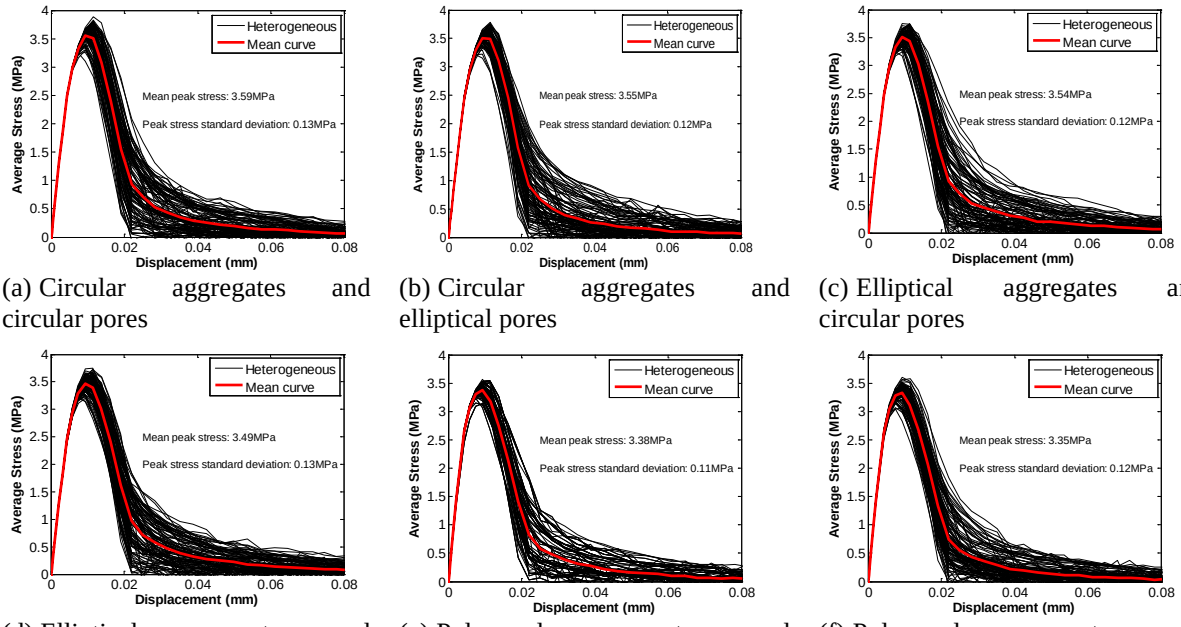

(a) Circular aggregates and circular pores (b) Circular aggregates and elliptical pores (c) Elliptical aggregates and circular pores

(d) Elliptical aggregates and elliptical pores (e) Polygonal aggregates and circular pores (f) Polygonal aggregates and elliptical pores

Fig. 3. Stress-displacement curves for different shapes of aggregates and pores

4.2. Effect of aggregate volume fraction and porosity

In order to investigate the effect of aggregate volume fraction and porosity, concrete samples with circular aggregates and circular pores are chosen. Monte Carlo simulations were carried out under a uniaxial tension test and all the parameters except for aggregate volume fraction and porosity were fixed to the values used in section 4.1. Fig. 5 shows the mean stress-displacement curves of the samples with different aggregate volume fraction and porosity. It can be observed that the mean stress-displacement curve is relatively insensitive to the aggregate volume fraction (see Fig. 5(a)). This may be because the increase of weak interfaces offsets the effect of increase in strong aggregates for this particular material set. As shown in Fig. 5(b), the effect of porosity on the load capacity is more pronounced. This is because the pores enable the cracks to propagate easily through them so that the samples fail quickly. It clearly shows that the pores which exist in the concrete should not be neglected when analyzing the mechanical properties and fracture of concrete.

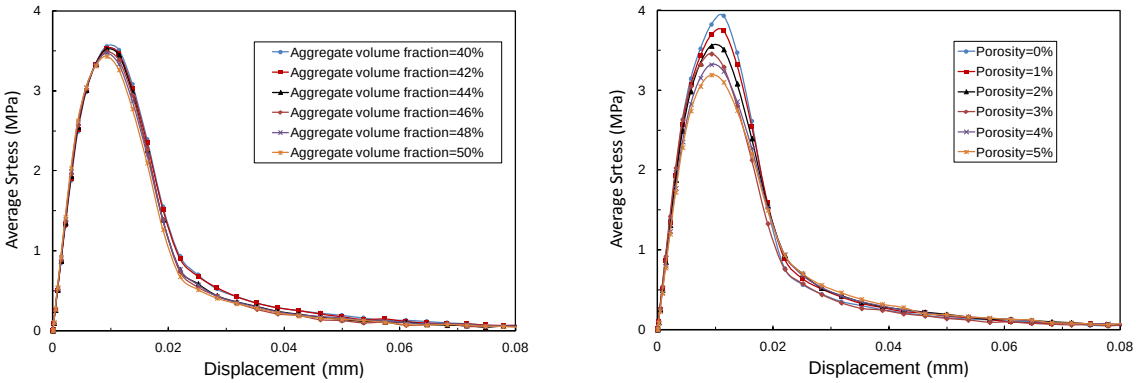

(a) Aggregate volume fraction (b) Porosity

Fig. 4. Effect of aggregate volume fraction and porosity

5. Conclusions

Models of concrete with a random mesostructure comprising circular, elliptical, or polygonal aggregates and pores have been developed in this study. The results obtained from the Monte Carlo simulations of a uniaxial tension test show that the load capacity of the circular and elliptical aggregate samples is greater than that of polygonal aggregates for this particular material set; It is also found that the porosity has a great effect on the load capacity so that the pores should be considered in meso-scale fracture modelling of concrete.

Acknowledgements

XF Wang is funded by an EPS Faculty PhD Studentship from the University of Manchester, UK. ZJ Yang would like to thank the support from EPSRC via grant EP/J019763/1, “QUBE: Quasi-Brittle fracture: a 3D experimentally-validated approach”.

References

[1] Z. Tu and Y. Lu. Mesoscale modelling of concrete for static and dynamic response analysis Part 1: model development and implementation. *Structural Engineering and Mechanics*, 37, 197-213, 2011.

[2] Z. Yang, X. Su, J. Chen and G. Liu. Monte Carlo simulation of complex cohesive fracture in random heterogeneous quasi-brittle materials. *International Journal of Solids and Structures*, 46, 3222-3234, 2009.

[3] W. Ren, Z. Yang, M. Mostafavi, A.S. Mcdonald, and T.J. Marrow. Characterisation of 3d fracture evolution in concrete using in-situ x-ray computed tomography testing and digital volume correlation. *8th International Conference on Fracture Mechanics of Concrete and Concrete Structures*, 1-7, 2013.

[4] W. Ren, Z. Yang and P. Withers. Meso-scale Fracture Modelling of Concrete Based on X-ray Computed Tomography Images. *5th Asia Pacific Congress On Computational Mechanics & 4th International Symposium On Computational Mechanics*, 2013.

[5] Z. Wang, A. Kwan and H. Chan. Mesoscopic study of concrete I: generation of random aggregate structure and finite element mesh. *Computers & structures*. 70, 533-44,1999.

[6] A. Yin, X. Yang, H. Gao and H. Zhu. Tensile fracture simulation of random heterogeneous asphalt mixture with cohesive crack model. *Engineering Fracture Mechanics*, 92, 40-55. 2012.

Proceedings of the 22nd UK Conference of the
Association for Computational Mechanics in Engineering
2 - 4 April 2014, University of Exeter, Exeter

Mixed-dimensional multi-point flux approximation for discrete fracture-matrix simulation

***R. Ahmed[1], M.G. Edwards[1] and M. Pal[2]**

[1]C[2]EC, College of Engineering, Swansea University, Swansea SA2 8PP, Wales UK
[2]Maersk Oil and Gas A/S, 1263 Copenhagen, Denmark.

*R.AHMED.642142@swansea.ac.uk

ABSTRACT

A cell-centered control-volume distributed multi-point flux (CVD-MPFA) finite volume formulation is presented for fractured porous media. Highly conductive fractures are modelled as lower-dimensional (1D) interfaces in between the (2D) matrix cells. Matrix-fracture flux transfer is incorporated into the MPFA formulation efficiently by the transfer function used in the fracture flow equation. The lower-dimensional fracture model is compared to the explicit equi-dimensional model and hybrid-grid method. Highly conductive fractures are efficiently modelled by a lower-dimensional fracture approximation while yielding results that are comparable with equi-dimensional methods.

Key Words: *MPFA; fractured porous; lower-dimensional; interfaces; transfer function*

1. Introduction

The understanding of fluid flow through fractured porous medium has immense importance in environmental and energy production problems. Generally, fractures have higher permeability and lower porosity in contrast to the matrix (main part of porous medium) and act as preferential fluid flow paths. Because of the importance of fractures in reservoirs, increasing effort is devoted to the development of efficient and accurate numerical methods to simulate the fluid flow through fractured porous media. To avoid the deficiencies of the conventional dual-porosity model, discrete-fracture model (DFM) was developed; see e.g. [1, 5, 6]. In this model actual geometry and location of the fracture are honoured in the domain. Generally, fractures are modelled by (n-1) dimensional elements in a n-dimensional problem, for example in 2d, fractures are represented by the lines at the edges of the polygonal matrix elements.
Here, we will focus on the control volume distributed finite-volume method for discrete-fracture method with multi-point flux approximation (MPFA). Recently, T.H. Sandve et al [7] has proposed hybrid-grid approach with MPFA for discrete-fracture modelling. In the hybrid-grid approach, introduced in [4], fractures are (n-1)D in the physical mesh and are expanded to nD in the computational domain. The fracture-fracture intermediate cell is assumed to be of small size so that pressure variation and mass accumulation is zero in that cell. We present and investigate a simplified formulation which couples the CVD-MPFA method (refer to e.g. H.A. Friis et al [2]) with the lower dimensional fracture model in the computational domain without using the hybrid grid approach. The simplified formulation is naturally incorporated into the existing CVD-MPFA framework.

2. CVD-MPFA lower-dimensional fracture formulation

For high permeability and low aperture, the jump in pressure across the fracture is very low. Pressure can be assumed constant along the width of fracture but the velocity jump is non-zero as discussed in [6]. We use the transfer function as presented by H. Hoteit et al. [3], coupled within the cell-centered CVD-MPFA framework. For a matrix domain the nD equation is solved while the (n-1)D equation is solved (simultaneously) for fracture cells:

$$-\nabla \cdot \boldsymbol{K}_m \nabla \phi_m = f_m \quad \text{in} \quad \Omega_m \tag{1}$$

$$-\nabla \cdot \boldsymbol{K}_f \nabla \phi_f = Q_f + f_f \quad \text{in} \quad \Omega_f \tag{2}$$

where $\boldsymbol{K}_f$ is the longitudinal permeability of fracture and Q_f is the transfer function to account for the flux transfer between matrix and fracture cells. The cluster of cells is shown in figure (1(a)) which is typically used in the CVD-MPFA formulation.

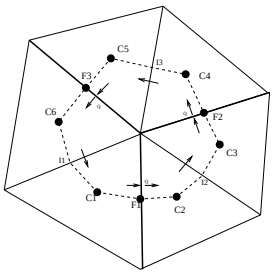

(a) Cluster of matrix cells involving fracture cells as interfaces in between, depicted by bold lines

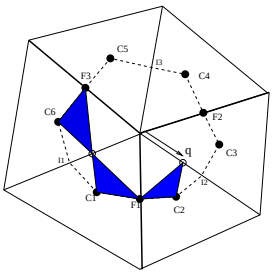

(b) Dual cell with sub-cells of matrix cells. Triangular pressure supports are also shown

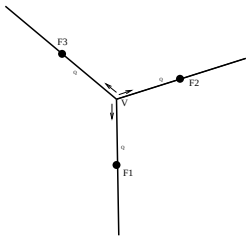

(c) Cluster of 1D fracture cells

Figure 1: Cluster and dual-cell involving fracture cells as interfaces

2.1. Matrix-matrix and matrix-fracture fluxes

For the dual-cell shown in figure(1(b)), we require 3 fluxes on the edges which are not fractures and 6 fluxes on both the sides (right and left) of the edges which are fractures and can be written in matrix form as:

$$\boldsymbol{F} = A^{9\times6}\boldsymbol{\phi}_M + B^{9\times3}\boldsymbol{\phi}_F + C^{9\times3}\boldsymbol{\phi}_I \tag{3}$$

where $\boldsymbol{\phi}_M$ are pressures associated with the matrix cells, $\boldsymbol{\phi}_I$ are pressures on the edges, between matrix cells, which are not fracture cells and $\boldsymbol{\phi}_F$ are pressures related to fracture cells. As in the usual CVD-MPFA formulation, $\boldsymbol{\phi}_I$ are eliminated by imposing continuity of fluxes on both sides of edges. Thus we obtain fluxes in terms of $\boldsymbol{\phi}_M$ and $\boldsymbol{\phi}_F$ only as follows:

$$\boldsymbol{F} = \bar{A}^{9\times6}\boldsymbol{\phi}_M + \bar{B}^{9\times3}\boldsymbol{\phi}_F \tag{4}$$

Fluxes on the edges of fractures are discontinuous across the fracture. The difference in these fluxes on both sides of fracture edges are the half integral of transfer functions for the corresponding 1D fracture cells.

$$\boldsymbol{Q}_{f,1/2} = \boldsymbol{F}_L - \boldsymbol{F}_R \tag{5}$$

$$\implies \quad \boldsymbol{Q}_{f,1/2} = \bar{E}^{3\times6}\boldsymbol{\phi}_M + \bar{F}^{3\times3}\boldsymbol{\phi}_F \tag{6}$$

2.2. Fracture-fracture fluxes

A cluster of 1d fracture cells is represented in figure (1(c)). Pressures are associated with fracture midpoints, and with intermediate vertices between fractures. The outgoing fluxes are computed for every fracture at the vertex, formulated as follows:

$$\boldsymbol{F} = A^{3\times3}\boldsymbol{\phi}_F + B^{3\times1}\phi_V \tag{7}$$

The pressure at the intermediate vertex is eliminated by imposing the condition of mass conservation at the vertex, Kirchhoff's law analogy. We obtain fluxes in terms of fracture cell pressures.

$$\sum_k^3 F_k = 0 \qquad \implies \phi_V = (B_V{}^{1\times1})^{-1} A_V{}^{1\times3}\boldsymbol{\phi}_F$$

$$\implies \quad \boldsymbol{F} = \bar{A}^{3\times3}\boldsymbol{\phi}_F \tag{8}$$

2.3. Global linear system

We use the fluxes, determined in (4) and (8), and transfer function, determined in (6), to complete the discrete conservation scheme of equations (1) and (2) for every matrix cell and fracture cell respectively. A coupled linear system is obtained for matrix cells away from the fracture $\boldsymbol{\phi}_{M_1}$, matrix cells associated with fracture $\boldsymbol{\phi}_{M_2}$ and the fracture cells $\boldsymbol{\phi}_F$:

$$\begin{pmatrix} G_{M_1M_1} & G_{M_1M_2} & O \\ G_{M_2M_1} & G_{M_2M_2} & G_{M_2F} \\ O & G_{FM_2} & G_F \end{pmatrix} \begin{pmatrix} \boldsymbol{\phi}_{M_1} \\ \boldsymbol{\phi}_{M_2} \\ \boldsymbol{\phi}_F \end{pmatrix} = \begin{pmatrix} \boldsymbol{f}_{M_1} \\ \boldsymbol{f}_{M_2} \\ \boldsymbol{f}_F \end{pmatrix} \tag{9}$$

Above coupled system, (9) can be solved monolithically or by iterative solution methods for matrix and fracture pressures. The overall condition number of the global system depends on the fracture permeability and aperture magnitudes.

3. Transport model

We assume high flow in the fractures and the intermediate cell is so small that there is no accumulation inside. If there are n intersecting fractures at the intermediate cell and there are l fluxes going into the intermediate cell then we can compute concentration at intermediate cell, c_{fo}, by the following condition;

$$\sum_{k_1=1}^{l} F_{k_1} c_k = c_{fo} \sum_{k_2=1}^{n-l} F_{k_2} \tag{10}$$

In this way we do not need to include the intermediate cell in overall computations and avoid the restriction of low CFL condition because of the inclusion of the intermediate cell.

4. Numerical Tests

Convergence tests for different aperture and fracture to matrix permeability ratios are presented for a domain with single fracture. The convergence for the 1D fracture model is the same as that obtained for the hybrid-grid method. Also we have compared the 1D fracture results to the results obtained by explicit 2D fracture model and hybrid-grid method. Meshes are shown in figure (2). Pressure and concentration contours are shown in figure (3). Concentration of producer w.r.t time is also shown in figure (4).

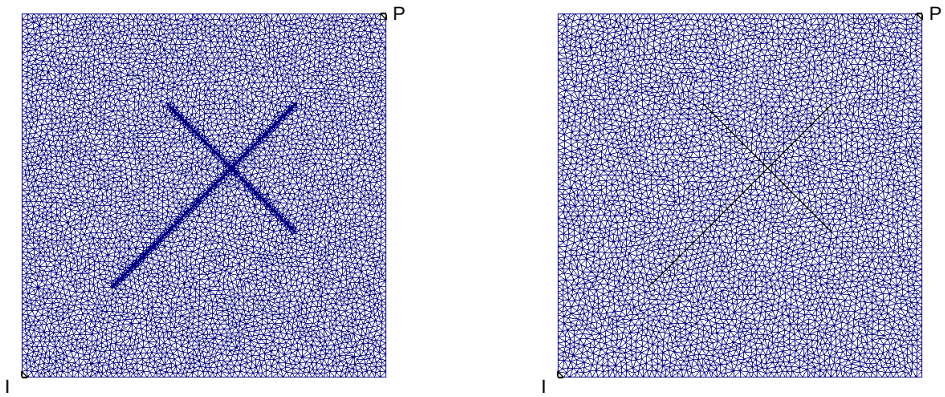

(a) 11984 cells (b) 8648 cells + 80 1D fracture cells

Figure 2: Explicit grid representation of intersecting fractures and mixed-dimensional grid with 1D fractures representation, aperture = 10^{-3}

5. Conclusions

We have presented a CVD-MPFA formulation for discrete fracture modelling and efficient lower-dimensional fracture modelling in computational domain. For thin highly conductive fractures, the lower-dimensional fracture model yields results that rival the hybrid grid method and explicit equi-dimensional modelling of fractures, without extra degrees of freedom in the cluster. In addition the lower dimensional fracture model is naturally coupled with the CVD-MPFA method.

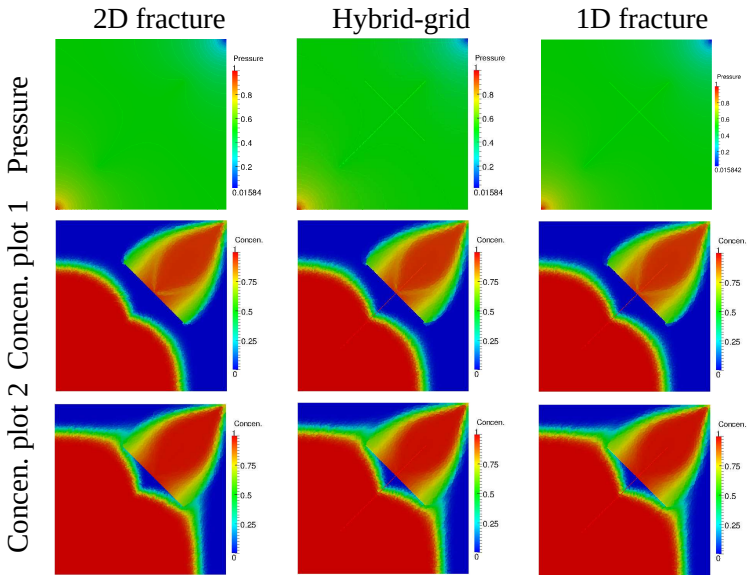

Figure 3: Pressure plot and concentration plots at 5 time units and 8 time units for 2D fracture, Hybrid-grid and 1D fracture model; $k_f = 10^6$.

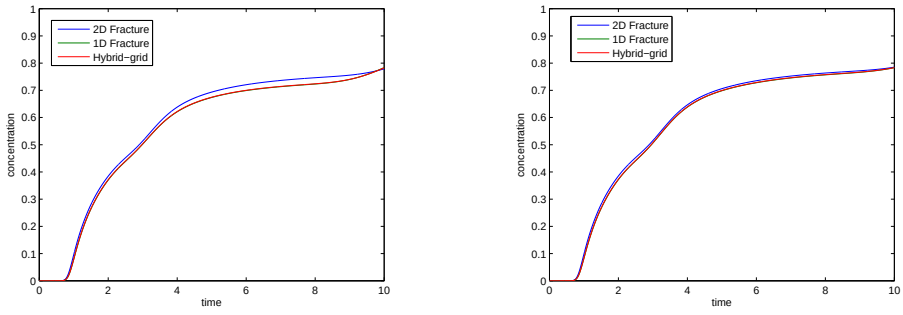

(a) $k_{f_1} = 10^4$ (b) $k_{f_2} = 10^6$

Figure 4: Comparison of concentration plots for two different permeability contrast values.

Acknowledgements

We thank Shell Rijswijk, the Netherlands, for supporting this work and Dr's S. Lamine and B. Huisman for helpful discussion of this work.

References

[1] R. Baca, R. Arnett, and D. Langford. Modeling fluid flow in fractured porous rock masses by finite element techniques. *Int. J. Num. Meth. Fluids*, 4:337–348, 1984.

[2] H.A. Friis, M.G. Edwards, and J. Mykkeltveit. Symmetric positive definite flux-continuous full-tensor finite-volume schemes on unstructured cell-centered triangular grids. *SIAM J. Sci. Comput.*, 31(2):1192–1220, 2008.

[3] H. Hoteit and A. Firoozabadi. An efficient numerical model for incompressible two-phase flow in fractured media. *Advances in Water Resources*, 31:891–905, 2008.

[4] M. Karimi-Fard, L.J. Durlofsky, and K. Aziz. An efficient discrete-fracture model applicable for general-purpose reservoir simulators. *SPE Journal*, 9:227–236, 2004.

[5] M. Karimi-Fard and A. Firoozabadi. Numerical simulation of water injection in 2d fractured media using discrete-fracture model. *SPE REE J*, 4:117–126, 2003.

[6] V. Martin, J. Jaffré, and J.E. Roberts. Modelling fractures and barriers as interfaces for flow in porous media. *SIAM J. Sci. Comput.*, 26:1667–1691, 2005.

[7] T.H. Sandve, I. Berre, and J.M. Nordbotten. An efficient multi-point flux approximation method for discrete fracturematrix simulations. *J Comp Physics*, 231:3784–3800, 2012.

Proceedings of the 22nd UK Conference of the
Association for Computational Mechanics in Engineering
2 – 4April 2014, University of Exeter, Exeter

NUMERICAL MODELLING OF BRITTLE FRACTURE IN GEOLOGICAL MATERIALS

*** John S. Coggan[1], Doug Stead[2] and Fuqiang Gao[2]**

[1]Camborne School of Mines, University of Exeter, Cornwall Campus, Cornwall, UK, TR10 9FE
[2]Earth Sciences, Simon Fraser University, Burnaby, BC, Canada, V5A 1S6

*J.Coggan@exeter.ac.uk

ABSTRACT

Numerical modelling of brittle fracture and failure in geological materials is now possible through a variety of available software. Given the wide scope of numerical applications it is essential for the engineer and geoscientist to fully understand and appreciate the varying strengths and limitations inherent in each of the different methodologies. In this paper we demonstrate the application of brittle fracture modelling from the laboratory to rock mass scale. Examples of brittle fracture simulation in both two and three dimensions to underground and surface mine geometries are presented. The loading conditions, and therefore engineering response of the structure, can be complex as a result of the redistribution of the three-dimensional stress field; this can result in stress-induced fracture and associated failure of the rock at varying scales. The modelling of geological materials is made more complex in view of the potential controlling behaviour of the discrete fracture network. Failure can result from formation of new fractures or extension of pre-existing discontinuities. With increasing scale of the modelled structure the pre-existing discrete fracture network can have a dramatic influence on the modelled behaviour. Hybrid codes that incorporate fracture simulation capabilities have been used to model a wide spectrum of rock-related failure modes, and are particularly well suited to modelling complex instabilities where failure requires yielding, brittle fracture and shearing. The influence of the correct geological model and choice of modelling approach on the simulated failure mechanism is demonstrated.

Keywords: *brittle fracture; numerical modelling; geological model; discontinuity characteristics*

1. Introduction

The role of brittle fracture in rock excavation instability, both in engineered and natural structures, is the subject of considerable on-going research. For example, man-made excavations can vary in size from centimetres (borehole and associated breakout), metres (tunnel and pillar stability) to hundreds of metres (large open pit slopes). The loading conditions, and therefore engineering response of the structure, can be complex as a result of the redistribution of the three-dimensional stress field. This can result in stress-induced fracture and associated failure of the rock at varying scales. The modelling of geological materials is made more complex in view of the potential controlling behaviour of the discrete fracture network. Failure can result from formation of new fractures or extension of pre-existing discontinuities. With increasing scale of the modelled structure the pre-existing discrete fracture network can have a dramatic influence on the modelled behaviour. Stead et al [1] emphasised the diversity of roles and scale of brittle fracture in rock slopes.

2. Brittle fracture

Stead et al [1] suggested that brittle facture may be conveniently considered in terms of primary, secondary and tertiary processes. Primary brittle fracture is considered to include processes that occur prior to the onset of failure. They include: (i) propagation of failure surfaces through fracture tip growth, (ii) coalescence of fractures and failure of intact rock bridges and (iii) shearing along discontinuities involving removal of asperities. These processes may lead to failure through a variety of mechanisms such as sliding along discrete daylighting planes of weakness, step-path failure surface generation and in extreme cases major changes in kinematics through the fracture of keyblocks within an excavation surface. Stead and Coggan [2] described rock slope failure using a total slope failure

analysis terminology. In this framework, primary brittle fracture processes are predominantly associated with the failure initiation or trigger zone.

Following the onset of primary slope movements within a slope, secondary brittle fracture processes may be involved in: (i) development of rear and lateral release surfaces leading toward global slope failure and (ii) internal deformation, fracturing and dilation of the rock slope mass associated with translational failure, toppling or multiple complex interacting mechanisms. Secondary brittle fracture processes, in rock slopes, are associated with a transition from the initiation to transportation stages in a slope failure. They accompany a gradual reduction in rock mass strength and removal of kinematic restraint prior to global rock slope failure and debris transportation.

The final stages in the rock slope brittle fracture involve the comminution of the rock mass associated with transport leading up to final debris deposition. These tertiary brittle fracture processes are recognised to be particularly important when characterising the distance that rock failure debris will travel or 'run-out' of natural slopes. Researchers have characterised the comminution of the rock slope mass using approaches that consider the initial block size distribution in the initiation zone and the final block size in the debris pile. As large open pits become more frequent the need to assess tertiary brittle fracture processes, velocity of transport and run-out extent will increase.

3. Numerical modelling of brittle fracture

The possible approaches to numerical modelling of rock-related failure have been previously described in [1-7], with [3] providing a review of advantages and limitations of each approach. Stead et al [1] emphasised the importance of simulation of brittle fracture at varying scales and the need to incorporate representative discrete fracture networks within model geometry.

Figure 1 shows results of brittle fracture modelling undertaken by [8; 9] with the ELFEN code [10]. These comparative laboratory numerical modelling studies were extremely useful in calibrating the use of the ELFEN code approach against continuum finite element and Voronoi distinct element models. The importance of considering ongoing continuous kinematic changes even at the laboratory scale is indicated from the results of these ELFEN simulations. Karami and Stead [9] further demonstrate the key role of scale when considering simple direct shear in a shear box test.

Figure 2 shows example modelling results from three-dimensional simulation of roof failure in an underground coal mine roadway using 3DEC [11; 12]. A newly developed Trigon logic was employed within the 3DEC modelling to simulate cutter roof failure caused by oblique horizontal stress with respect to roadway advance direction. The roadway roof was represented as an assembly of tetrahedral blocks bonded together through the contact surfaces between them. As the roadway face advanced, stress concentration was observed at the intersecting corner of the major horizontal stress and the roadway roof, with no stress concentration observed at the other corner of the roof. This leads to cutter roof failure immediately behind the advancing face.

Figure 3 shows selected stages of the modelled failure of the 1967 failure of the West face at Delabole Slate Quarry using ELFEN [6; 10] to highlight the initial fracture geometry and subsequent fracture development through extension of pre-existing fractures and development of new fractures in an application to surface excavation. The results highlight the step-path nature of the modelled failure, together with internal fracturing and subsequent rotation and translation of the failed mass.

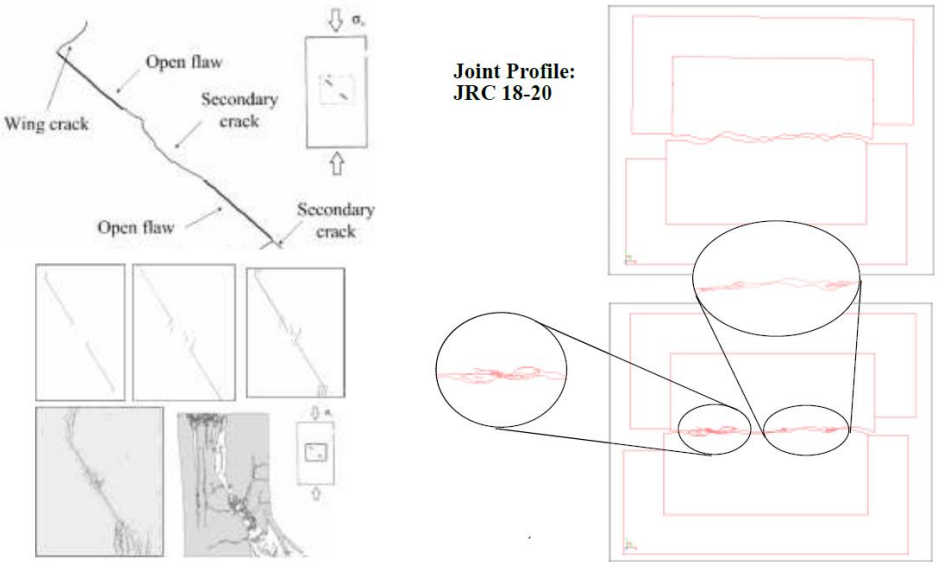

Figure 1: Brittle fracture simulation at the laboratory scale: (a) stages in step-path fracturing under uniaxial compression and (b) direct shear simulation, top low normal stress, bottom high normal stress (after [8])

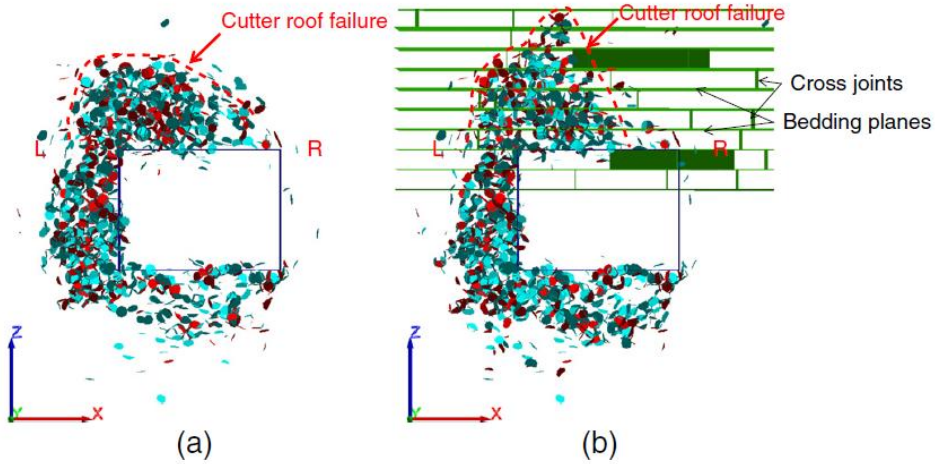

Figure 2: Cutter roof failure captured at 1 m behind the advance face in: (a) Model without pre-existing fractures, (b) model with pre-existing fractures (after [9])

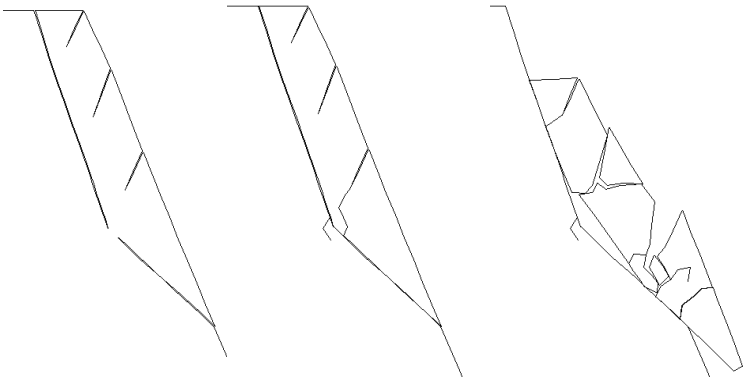

Figure 3: Modelled stages of the 1967 failure at Delabole Slate Quarry showing initial assumed fracture geometry and subsequent fracture development for non-continuous discontinuities

4. Conclusions

Numerical codes that incorporate fracture simulation capabilities can now be used to model a wide spectrum of rock-related failure modes, and are particularly well suited to modelling complex translational/rotational instabilities where failure requires yielding, brittle fracturing and shearing. The results confirm the importance of the correct geological model and correct choice of modelling approach based on likely failure mechanism (whether material, discontinuity or a combination of both material and discontinuity controlled failure). There is, however, a need to appreciate both model and parameter uncertainty within the chosen approach, together with both spatial and temporal changes in material behaviour. With ever increasing computing power there has been a drive towards more realistic modelling with increasingly complex representation of the rock mass. With more sophisticated three-dimensional models it remains important however to be aware of both model and parameter uncertainty.

References

[1] D. Stead, J.S. Coggan, D. Elmo and M. Yan, M. Modelling brittle fracture in rock slopes: Experiences gained and lessons learned. *In: Proceedings of the International Symposium on Rock slope Stability in Open Pit Mining and Civil Engineering*, Perth, Australia, 239-252, 2007.

[2] D. Stead and J.S Coggan. Numerical modelling of rock slopes using a total slope failure approach. *In: Landslide from Massive Rock Slope Failure*, Eds., S. Evans, R. Hermans and Strom, A. Springer, Netherlands,131-142, 2006.

[3] D. Stead, E. Eberhardt and J.S. Coggan. Developments in the characterization of complex rock slope deformation and failure using numerical modelling techniques. *Engineering Geology*, 83, 217-235, 2006.

[4] E. Eberhardt, D. Stead and J.S. Coggan. Numerical analysis of initiation and progressive failure in natural rock slopes – the 1991 Randa rockslide. *International Journal of Rock Mechanics & Mining Sciences*, 41, 69-87, 2004.

[5] R.J. Pine, J.S. Coggan, Z. Flynn Z and D. Elmo. The development of a comprehensive numerical modelling approach for pre-fractured rock masses. *Rock Mechanics and Rock Engineering*, 39, 5, 395-419, 2006.

[6] J.S. Coggan, R.J. Pine, T.D. Styles and D. Stead. Application of hybrid finite/discrete element modelling for back-analysis of rock slope failure mechanisms. In*: Proceedings of Slope Stability 2007, International Symposium on Rock Slope Stability in Open Pit Mining and Civil Engineering*, 12-14 September, 267-277, 2007.

[7] J.S. Coggan, F. Gao, D. Stead and D. Elmo. Numerical modelling of the effects of weak immediate roof lithology on coal mine roadway stability. *International Journal of Coal Geology*, 90–91 (1), 100–109, 2012.

[8] M. Yan, D. Elmo and D. Stead. Characterization of step-path failure mechanisms: A combined field based numerical modelling study. *In: Proceedings of 1st Canada-U.S. Rock Mechanics Symposium*. Vancouver, 493-501, 2007.

[9] A. Karami and D. Stead. Asperity degradation and damage in the direct shear test: A hybrid DEM/FEM approach. *Rock Mechanics and Rock Engineering*, 41, 229-266, 2008.

[10] Rockfield Software Ltd. ELFEN User Manual, Swansea, UK. www.rockfield.co.uk, 2007.

[11] Itasca. 3DEC Version 4. 0. Itasca Consulting Group Inc., Minneapolis, Minnesota, 2011.

[12] F. Gao and D. Stead. Discrete element modelling of cutter roof failure in coal mine roadways. *International Journal of Coal Geology*, 116-117, 158-171, 2013.

Proceedings of the 22nd UK Conference of the
Association for Computational Mechanics in Engineering
2 - 4 April 2014, University of Exeter, Exeter

THREE DIMENSIONAL BRITTLE FRACTURE: CONFIGURATIONAL -FORCE -DRIVEN CRACK PROPAGATION

***Ł. Kaczmarczyk[1], Chris Pearce[1]**

[1]School of Engineering, University of Glasgow, G12 8LT, UK

*Lukasz.Kaczmarczyk@glasgow.ac.uk

ABSTRACT

This paper presents a solution strategy for quasi-static brittle fracture in three dimensional solids. The paper briefly set outs the theoretical basis for determining the initiation and direction of propagating cracks based on concept of configurational mechanics. Attention is focused on load control enforcing dissipative loading path, consistent fracture with Griffith's theory and resolution of by the finite element mesh. Cracks are restricted on to the element faces and the mesh is adapted in order to align with the predicted crack direction. A local mesh improvement procedure is developed to maximise mesh quality in order to improve accuracy and solution robustness and to reduce the influence of the initial mesh on the direction of propagating cracks. The performance of this modelling approach is demonstrated on three numerical examples that qualitatively illustrate its ability to predict complex crack paths. All problems are three-dimensional, including a torsion problem that results in the accurate prediction of a doubly-curved crack. Finally hierarchical hp-adaptivity is studied in order to improve approximation of displacements and crack geometry. Since the presented methodology is based on face splitting, and since no changes in approximation function space are introduced, it could be easily implemented in commercial finite element systems.

Key Words: *fracture; configurational forces; crack path; mesh adaptivity; mesh quality; arc-length control*

1. Introduction

Fracture is a pervasive problem in materials and structural engineering and the predictive modelling of crack propagation remains one of the most significant challenges in solid mechanics. A computational framework for modelling crack propagation must be able not only to predict the initiation and direction of cracks but also provide a numerical setting to accurately resolve the crack path.

Finite element method (FEM) is, on the face of it, not well adopted to the resolution of cracks, i.e. changes of topology. Nevertheless, strategies for discretization of the discontinuities in the context of FEM can be categorized into two main types: smeared and discrete. The former is attractive form the point of view that the problem can be solved within continuum setting, without need of approximation of discontinuities or changing mesh connectivity. However, as strain localization occurs, or crack is approximated in averaged sense like in phase-field methods, causes numerical difficulties and requires regularization. Discrete approaches on the other hand are able to directly approximate macroscopic crack geometry. Discrete approaches describe fractures in a more natural and straightforward manner in terms of displacement jumps and tractions. Developments in discrete approaches include introducing embedded displacement jumps within finite elements via additional enhanced strain modes (for example [1]) or can be based on partition of unity, e.g. [2].

A potentially straightforward approach is to restrict the path to element faces. Such approach means that that the predicted path can be strongly influenced by the mesh and strongly influence crack surface area strongly affecting total crack release energy. The crack geometry dependence on mesh can be somehow reduced by using very fine, unstructured meshes, but this could be computationally expensive analysis which unrealistic crack release surface energy. It is worth to notice that the authors [3, 4] have shown that,

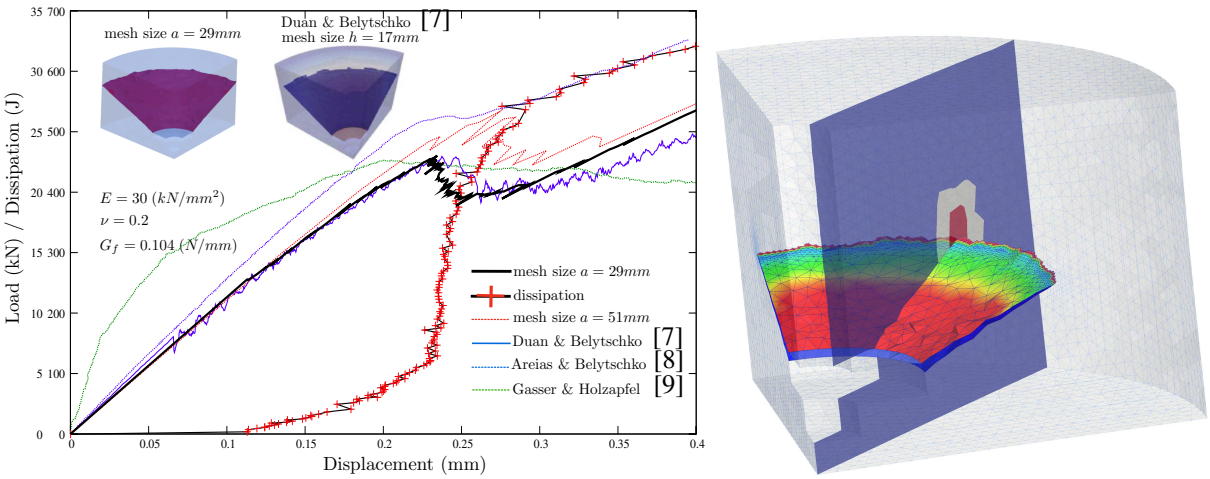

Figure 1: Pull-out test load displacement path and energy dissipation . On the right hand figure: The contour plot on the crack surface presenting density of strain energy. The contour plot on the slice presenting approximation order, blue color: linear approximation, white: quadratic approximation, red: cubic approximation. Figure on the right hand side shows final crack surface.

when modelling energy is released by crack opening, for cohesive element methodology, and heterogeneous microstructures, the crack propagation is largely controlled by the need for the mesh to resolve the heterogeneities. However, in the modelling of ideally brittle homogeneous materials, studied here, this is clearly not the case.

In addition to the need yo resolve crack within the context of the Finite Element Method, it is necessary to employ a rational means of determining the direction of crack propagation and crack propagation criterion. This is particular difficult for three-dimensional case where crack front is approximated on the finite element edges. The approach taken in this paper is principally based on the principle of maximal energy dispassion, with configurational forces, which at crack front at material and spatial equilibrium, determine direction of crack front propagation. Similar technique was successfully adopted by a number of authors, but here we mainly follow the work of [5, 6]. Such an approach for predicting the crack path can be coupled with local r-adaptivity to mitigate the influence of the mesh.

We are primarily concerned in this chapter with solving crack propagation in large three-dimensional problems. The efficiency of such problems, with large numbers of degrees of freedom (DOFS), usually requires the use of an iterative solvers for solving system of algebraic equations. In such case the we must control element quality in order to optimise matrix conditioning, thereby increasing the computational efficiency of the solver. This in could difficulty in methods such as XFEM where enrichment functions not only increase band of the stiffness matrix but also deteriorate matrix conditioning. This paper also shows how controlling mesh quality improves crack path predictions and robustness of the solution algorithm.

Two numerical examples are presented for crack propagation that demonstrate the ability of formulation to accurately predict crack paths, as well as demonstrate mesh independence and influence of both mesh adaptivity and controlling mesh quality on the solution obtained.

2. Example

Solution strategy presented in this paper is implemented for parallel shared memory computers. The two core libraries are used for this implementation, MOAB: A mesh-oriented database [10] to store data on mesh, input and output operations and access all information about mesh topology. The parallel matrices and vectors are implemented using PETSc: Portable, Extensible Toolkit for Scientific Computation [11]. For the solution of linear system of equations and other algebraic operations are implemented with PETSc. For parallel mesh partitioning is used ParMetis [12] using PETSc native interface. Calculations are executed on ARCHIE-West academic super computer for the west of Scotland.

Three numerical examples are presented for crack propagation in three-dimensions that demonstrate the ability of the formulation to accurately predict crack paths, as well as demonstrate mesh independence and the influence of both mesh adaptivity and controlling mesh quality on the solution obtained.

2.1. Pull out test

This example consists of a pull-out test of a steel anchor embedded in a concrete cylindrical block. This numerical examples is compared with results of Duan & Areias, Belytschko [7, 8] and Gasser & Holzapfel [9]. All geometrical data could be obtained form [7, 8, 9]. Analysis is made for Young-modulus $E = 30000\text{N/mm}^2$, Poison ratio $\nu = 0.2$ and Griffith energy $G_f = 0.106\text{N/mm}$. Following [7] to represent the steel anchor effect, we impose vertical displacement. The anchor stem is not explicitly modelled. Other examples and detailed description of presented methodology can be found in paper [13].

Acknowledgements

This work was supported by EDF Energy Nuclear Generation Ltd. The views expressed in this paper are those of the authors and not necessarily those of EDF Energy Nuclear Generation Ltd. Analyses were undertaken using the EPSRC funded ARCHIE-WeSt High Performance Computer (www.archie-west.ac.uk). EPSRC grant no. EP/K000586/1.

References

[1] J. Oliver, *Modelling strong discontinuities in solid mechanics via strain softening constitutive equations. part 1: fundamentals*, International Journal for Numerical Methods in Engineering, 39(21), 35753600, 1996.

[2] G. Wells, *Discontinuous modelling of strain localisation and failure*, PhD thesis, Technische Universiteit Delft, 2001.

[3] Ł. Kaczmarczyk, C.J. Pearce, *A corotational hybrid-Trefftz stress formulation for modelling cohesive cracks*, Computer Methods in Applied Mechanics and Engineering, 198, 1298-1310, 2009.

[4] Ł. Kaczmarczyk, C.J. Pearce, N. Bićanić, E. de Souza Neto, *Numerical multiscale solution strategy for fracturing heterogeneous materials*, Computer Methods in Applied Mechanics and Engineering, 199, 1100-1113, 2010.

[5] C.Miehe, E.Gürses,M.Birkle,*A computationalframeworkofconfigurational-force-driven brittle fracture propagation based on incremental energy minimization*, International Journal of Fracture, 145, 245-259, 2007.

[6] E. Gürses, C. Miehe, *A computational framework of three-dimensional configurational-force-driven brittle crack propagation*, Computer Methods in Applied Mechanics and Engineering, 198, 1413-1428, 2009.

[7] Q. Duan, J.H. Song, T. Menouillard and T. Belytschko, *Element-local level set method for three-dimensional dynamic crack growth*, International Journal for Numerical Methods in Engineering, 80, 1520-1543, 2009.

[8] Areias PMA, Belytschko T. *Analysis of three-dimensional crack initiation and propagation using the extended finite element method*. International Journal for Numerical Methods in Engineering 2005; 63:760-788.

[9] Gasser TC, Holzapfel GA. *Modeling 3D crack propagation in unreinforced concrete using PUFEM. Computer Methods in Applied Mechanics and Engineering* 2005; 194(2526):2859-2896.

[10] Satish Balay and Jed Brown and Kris Buschelman and William D. Gropp and Dinesh Kaushik and Matthew G. Knepley and Lois Curfman McInnes and Barry F. Smith and Hong Zhang, *PETSc Web page*, http://www.mcs.anl.gov/petsc, 2012.

[11] Timothy J. Tautges Ray Meyers, Karl Merkley, Clint Stimpson, Corey Ernst, *MOAB: A MESH-ORIENTED DATABASE*, Sandia Report, Sandia National Laboratories, 2004.

[12] R. Bender, P. Klinkenberg, Z. Jiang, B. Bauer, G. Karypis, N. Nguyen, M. Perera, B. Nikolau, and C. Carter. Flora: Morphology, Distribution, *Function Genomics of Nectar Production in Brassicaceae*, Functional Ecology of Plants Volume 207, Issue 7, pp. 491-496, 2012.

[13] Kaczmarczyk, L., Mousavi Nezhad, M., and Pearce, C. (2014) Three-dimensional brittle fracture: configurational-force-driven crack propagation. International Journal for Numerical Methods in Engineering, 97 (7). pp. 531-550.

Proceedings of the 22nd UK Conference of the
Association for Computational Mechanics in Engineering
2 – 4April 2014, University of Exeter, Exeter

3D MESO-SCALE IMAGE-BASED FRACTURE MODELLING OF CONCRETE USING COHESIVE ELEMENTS

***Wenyuan Ren[1], Zhenjun Yang[1,2] and Rajneesh Sharma[1]**

[1] School of Mechanical, Aerospace and Civil Engineering, the University of Manchester, M13 9PL
[2] College of Civil Engineering and Architecture, Zhejiang University, China, 310000

*Wenyuan.ren@manchester.ac.uk

ABSTRACT

This paper extended the 2D meso-scale image-based models to 3D by using a small volume proportion of images obtained from an X-ray computed tomography test. The real microstructure of concrete specimen was characterized as three phases: aggregate, cement and voids (which is empty areas). Zero-thickness cohesive interface elements were embedded in cement phase to represent the potential cracks (no cracks allowed to propagate through aggregate particles). The average stress-strain curve of the 3D mesh under uniaxial tension was compared with a 2D simulation result. The crack propagation process in 3D was illustrated together with the final crack surfaces.

Keywords: *Concrete; X-ray computed tomography; Image based modelling; Cohesive interface element; Meso-scale model*

1. Introduction

As a quasi-brittle composite material, concrete has been widely used in many civil and industrial structures. Due to the existence of intrinsic heterogeneity at nano, micro, meso and macro scales, it is very complicated to model fracture behaviour of both microcracks and macrocracks, such as initiation and coalescence. Traditionally, numerical models are obtained by computer programmes and the material heterogeneity is realized either by random distributed material properties controlled by correlated functions [1-3] or by randomised positions and shapes of inclusions [4-7]. Monte Carlo simulation method can be used to get the statistical analysis because of the ease of using computer programmes. However, most of these studies assume the morphologies, which are mathematical representations.

The innovation of this paper is to build the 3D meso-scale model with realistic internal microstructure by transforming images obtained from X-ray computed tomography (XCT) into a 3D finite element (FE) mesh, which is acknowledged as image-based modelling method [8]. In the companion paper [9], the two-dimensional (2D) meso-scale FE meshes based on XCT images were used along with pre-embedding cohesive interface elements to simulate crack propagation processes in concrete under uniaxial tension loading. In this paper, a three-dimensional (3D) model is built by cropping a $10\times10\times10$ mm^3 volume from the whole image model (size of $37.2\times37.2\times37.2$ mm^3). The zero-thickness cohesive interface elements (CIEs) are embedded in cement using an in house computer programme to simulate potential cracks.

2. Image-based modelling

The proposed method involves the following steps:

1) Creating the 3D image model from XCT test. The detailed reconstruction and segmentation process of the concrete specimen from XCT test can be found in [10]. Here, a randomly selected small volume cube (10 mm^3) was cropped from a large specimen. Figure 1 shows the 3D image, in which blue and grey colours represent aggregates and cement paste respectively;
2) Generating mesh. The software package of Simpleware [11] is used to directly transform the 3D image into a fine 3D Mesh;

3) Inserting the cohesive interfaces elements (CIEs). The CIEs (known as COH3D6 and COH3D8 in Abaqus [12]) are inserted in cement and on aggregate-cement interfaces (different material properties are assigned) using the same approach as used for 2D in [9].The cracks are not allowed to be propagated in aggregates due to their high strength. The final image-based 3D mesh is shown in figure 2;
4) Assigning material properties and conducting analysis. The material properties used for 2D simulations [9] are considered and shown in Table 1. Due to the lack of experimental data, the shear components of initial stiffness and cohesive strength are assumed to be the same as the normal ones. The periodic boundary conditions are applied. A displacement controlled loading of un-notched specimen under uniaxial tension is simulated. Abaqus/Explicit solver is selected because of its high efficiency and convergence advantage for simulations of material degradation.

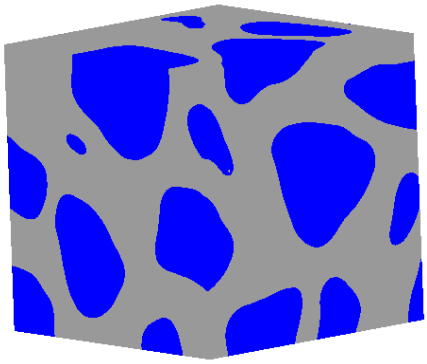

Figure 1: 3D image of concrete specimen

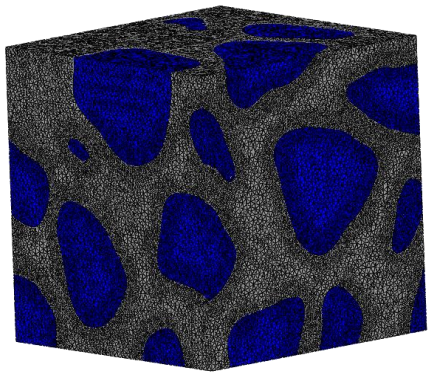

Figure 2: Image based 3D mesh

Table 1: Material properties

	Elastic modulus (MPa)	Poisson's ratio	Density (kg/m^3)	Initial stiffness (MPa/m)	Tensile strength (MPa)	Fracture energy (N/m)
Aggregate	70000	0.2	2500	/	/	/
Cement	25000	0.2	2200	/	/	/
CIE_CEM	/	/	2200	10^9	6	60
CIE_INT	/	/	2200	10^9	3	30

3. Numerical simulation results

Figure 3 shows the energy curves of model, including Kinetic energy, Strain energy, Internal energy and External work. Figure 3 concludes that the energy balance is obtained: the kinetic energy remains less than 5% of the internal energy; meanwhile, the internal energy is almost identical to the external work) as expected for a quasi-static analysis.

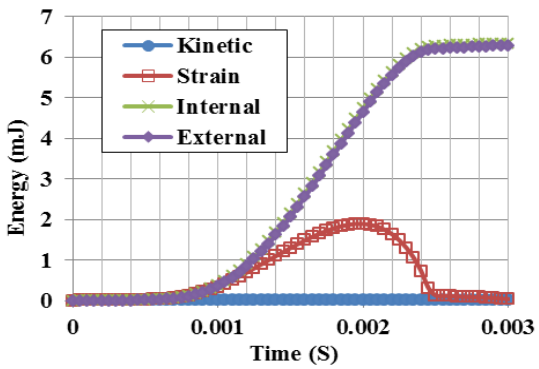

Figure 3: Energy curves of the whole model

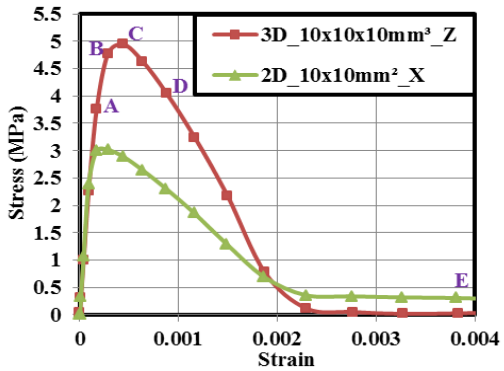

Figure 4: Stress-strain curves of 2D and 3D models

Figure 4 shows the average stress-strain curves of the 3D simulation and a 2D model having the same material properties and boundary conditions. The pre-peak stiffness is identical for both, however with different peak values (4.94 MPa for 3D and only 3.01 MPa for 2D). One reason is that microcracks in 3D are more difficult to get interconnected to form macrocracks due to the arbitrary shapes of the 3D aggregate particles. The 3D model seems to be more brittle (stiffer softening slope) than 2D.

Figure 5 shows the process of initiation and coalescence of microcracks and macrocracks (corresponding to the points marked A, B, C, D and E in figure 4). The blue areas in figure 5 represent aggregates. The orange and red (darker) colours represent the microcracks exist on aggregate-cement interfaces and within cement. A lot of microcracks first only initiated on aggregate-cement interfaces (Point A). At point B, more microcracks appeared on aggregate-cement interfaces. Some of interfacial ones begin to coalesce and get connected by newly formed cracks in cement. Most of interfacial cracks formed before peak value (point C), meanwhile more and more cracks in cement increased gradually (point D) and finally the specimen failed into two pieces (point E). The cracked specimen is shown in figure 5(f).

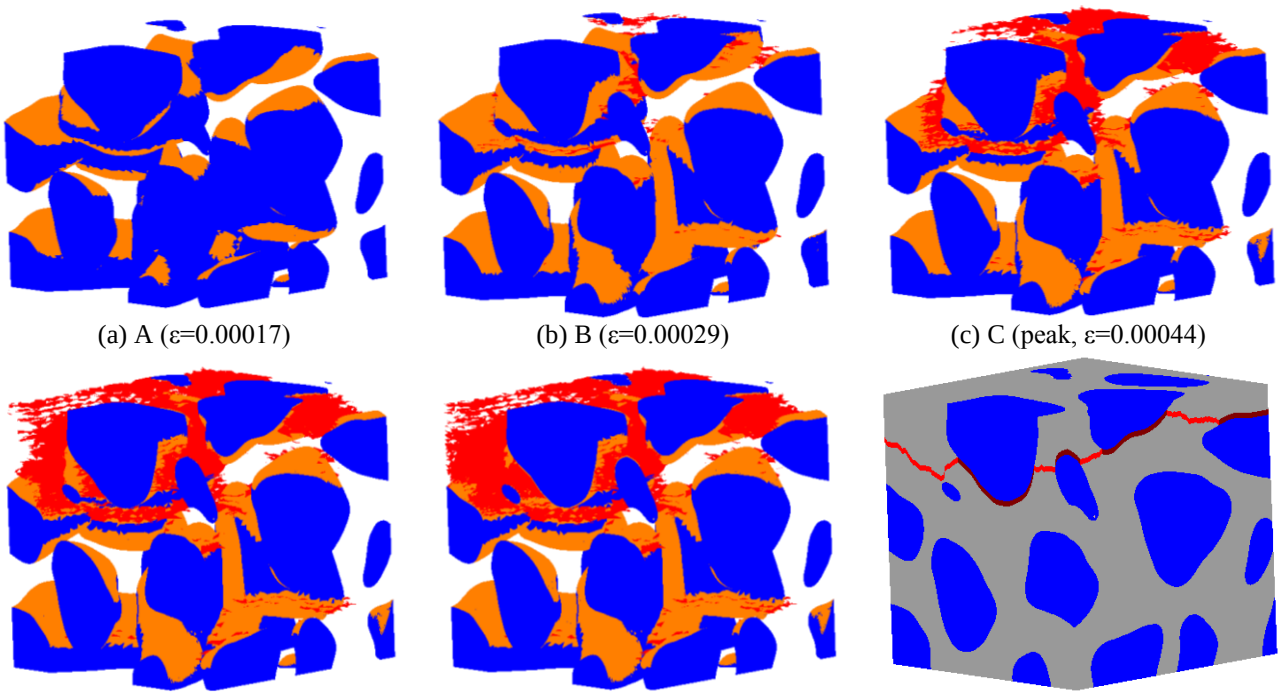

(a) A (ε=0.00017) (b) B (ε=0.00029) (c) C (peak, ε=0.00044)

(d) D (ε=0.00086) (e) E (ε=0.00375) (f) Final macrocrack

Figure 5: The initiation and propagation of micro and macro cracks

The final cracked surfaces are shown in figure 6 and the 3D visualisation of crack path is plotted in figure 7. The numbers (①-⑤) represent five aggregates (in blue colour) around the cracking surface.

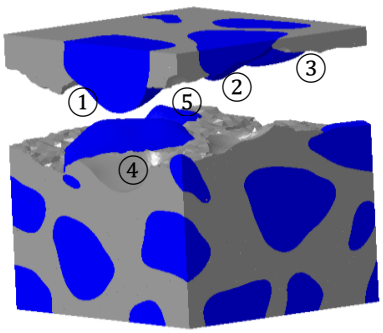

Figure 6: Final cracked pieces

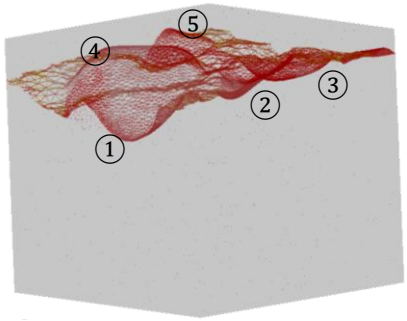

Figure 7: 3D crack surfaces (SDEG>0.9)

As no cracks are allowed through aggregates, the crack surfaces always formed around particles. The numbers (①-⑤) in figure 7 are the corresponding places in Figure 6 which caused the resulting crack path.

4. Conclusions

3D meso-scale FE image-based model is developed to simulate crack propagation process in concrete under uniaxial tension loading. The average stress-strain curve of the 3D mesh is compared with a 2D analysis by using same material inputs and boundary conditions. The curves show that the 3D model predicts a higher peak strength and stiffer softening slope. The features of initiation and coalescence of microcracks into macrocracks were illustrated. The final 3D crack surface shows that cracks are always formed along the surfaces of aggregates. The proposed imaged-based modelling technique shows a powerful way to study fracture mechanics of the composites with realistic internal structures. Moreover, the meso-scale simulation results could be also used to predict more realistic macro behaviour of concrete by multiscale analysis. Though there is a limitation of proposed modelling method: the computational cost. It is high due to the use of a very fine mesh and a large amount of inserted cohesive elements. This is unavoidable as the particles in the real materials always exhibit highly heterogeneous and the resultant mesh is very fine. However, with the help of parallel computing, the computation time could be greatly reduced when explicit solver is selected.

Acknowledgements

The research is funded by a Royal Society Research Grant and an EPSRC grant (No. EP/J019763/1).

References

[1] Z.J. Yang and X. Frank Xu. A heterogeneous cohesive model for quasi-brittle materials considering spatially varying random fracture properties. *Computer Methods in Applied Mechanics and Engineering*, 197(45–48): 4027-4039. 2008.

[2] Z.J. Yang, X.T. Su, J.F. Chen and G.H. Liu. Monte Carlo simulation of complex cohesive fracture in random heterogeneous quasi-brittle materials. *International Journal of Solids and Structures*, 46(17): 3222-3234. 2009.

[3] X.T. Su, Z.J. Yang and G.H. Liu. Monte Carlo simulation of complex cohesive fracture in random heterogeneous quasi-brittle materials: A 3D study. *International Journal of Solids and Structures*, 47(17): 2336-2345. 2010.

[4] G. Lilliu and J.G.M. van Mier. 3D lattice type fracture model for concrete. *Engineering Fracture Mechanics*, 70(7–8): 927-941. 2003.

[5] C. López, I. Carol and A. Aguado. Meso-structural study of concrete fracture using interface elements. I: numerical model and tensile behavior. *Materials and Structures*, 41(3): 583-599. 2008.

[6] A.Y. Yin, X.H. Yang and Z.J. Yang. 2D and 3D Fracture Modeling of Asphalt Mixture with Randomly Distributed Aggregates and Embedded Cohesive Cracks. *Procedia IUTAM*, 6(0): 114-122. 2013.

[7] Ł. Skarżyński and J. Tejchman. Calculations of fracture process zones on meso-scale in notched concrete beams subjected to three-point bending. *European Journal of Mechanics - A/Solids*, 29(4): 746-760. 2010.

[8] R. Sharma, P. Mahajan, and R.K. Mittal. Fiber bundle push-out test and image-based finite element simulation for 3D carbon/carbon composites. *Carbon*, 50(8): 2717-2725. 2012.

[9] W.Y. Ren, Z.J. Yang and P. Withers. Meso-scale Fracture Modelling of Concrete Based on X-ray Computed Tomography Images, *APCOM & ISCM*, Singapore. 2013.

[10] Z.J.Yang, W.Y. Ren, M. Mostafavi, S.A. McDonald and T.J. Marrow. Characterisation of 3d fracture evolution in concrete using in-situ X-ray computed tomography testing and digital volume correlation. *VIII International Conference on Fracture Mechanics of Concrete and Concrete Structures*, Toledo. 2013.

[11] Simpleware, ScanIP, +FE and +CAD Version 4.3 Reference Guide, Simpleware Ltd. Exeter, UK. 2011.

[12] Abaqus, Abaqus 6.10 Online Documentation, Internet Manual, 2010.

Proceedings of the 22nd UK Conference of the
Association for Computational Mechanics in Engineering
2 – 4April 2014, University of Exeter, Exeter

USING SEMI-FUZZY RMR TO DETERMINE THE REQUIRED SUPPORT SYSTEM FOR GHESHLAGH COAL MINE

***Mahdi Mahdizadeh[1], Navid Navid Hosseini[1], Payman Afzal[1,2], Daryoush Kaveh Ahangaran[1,2], Amir Bijan Yasrebi[2]**

[1]Department of Mining Engineering, South Tehran branch, Islamic Azad University, Tehran, Iran
[2]Camborne School of Mines, University of Exeter, Cornwall Campus, Penryn, TR10 9EZ, UK

* mahdizadeh67@gmail.com

ABSTRACT

It is very important to have a comprehensive recognition of rocks on the way in designing underground spaces because this highly affects the determination of support system. Rock rating system is known as one of the ways of rocks analysis such as Q and RMR. However, RMR rating system is more common in mining studies. In this system, different parameters are applied and then each part of a rock mass is scored and finally the intended support system needed for the tunnel is suggested. The parameters entering to RMR are classified into two groups of quantitative and qualitative ones and are placed in one specific classification accordingly. Since quantitative parameters are not fixed yet, it is hard to determine an exact threshold between the classifications and devote a specific amount to one certain group. To solve this problem, membership functions can be defined for each one of the quantative parameters and the output point of every parameter can be figured out by fuzzy sets. Fuzzy inference system calculated the points related to the quantitative parameters and other parameters are classified based on quality and they are scored in the normal way. Ultimately, the amount of RMR is obtained from adding the points of every one of the parameters. The current essay evaluates the final results of the semi-fuzzy method due to the support system in every part of the mine which is sampled. These studies demonstrate that the semi-fuzzy method is well able to determine the support system required for mining tunnels.

Key Words: *Rock classification, RMR semi-fuzzy, Fuzzy inference system, Gheshlagh coal mine*

1. Introduction

One of the most common methods determining the support system required for underground mines is to use Rock Mass Rating system (RMR) [1]. This rating system first analyzes 10 different quantative and descriptive parameters and then it classifies every part of the tunnel which has almost similar conditions with one another in one group and it also suggests their required support system. Table 1 indicates the parameters required for rating based on being either quantative or qualitative. In RMR system, according to the fact that the amount of each parameter is placed in which interval of the tables, the point related to that parameter is calculated. One of the outstanding disadvantages of these types of classifications is being fixed near the thresholds. To solve this problem; the changes of results near these thresholds can become milder according to their degree of membership in every one of the classes using fuzzy inference system. It is simply to prevent sudden changes in the output amount near the thresholds. It is not also necessary to define fixedness for qualitative parameters because the input amounts of these parameters are descriptive and they don't have an exact threshold to make the output amounts are unclear that is why semi-fuzzy method is suggested for their research.

Table 1: Comparing quantitative and qualitative (Descriptive) parameters

Quantitative Parameters	Value Range	Rating Range	Descriptive Parameters	Value Range	Rating Range
Uniaxial Compressive Strength of rock material	1 - >250 MPa	0 - 15	Groundwater conditions	Flowing -Completely dry	0 - 15
Rock quality designation (RQD)	0 - 100	3 - 20	Infilling	Soft filling -Hard filling	0 - 6
Spacing of discontinuities	< 60 mm - > 2 m	5 - 20	Weathering	Decomposed -Unweathered	0 - 6
Orientation of discontinuities	0-90 (Degree)	(12) - 0	Roughness	Slickensided -Very rough	0 - 6
Discontinuity length	> 20 m - < 1 m	0 - 6			
Separation (aperture)	> 5 mm - None	0 - 6			

2. The Specifications of the under Study Mine

Gheshlagh coal mines also called Rudbare Gheshlagh mine is known as the oldest mine in Golestan Province and placed in the 35 km away from Azadshahr to Shahrud road and 6 km further in the auxiliary road and it ends to two Rudbar and Shahrud villages. Each village is 3 km away from the mine. Figure 1 shows the situation of Gheshlagh coal mine in roads map.

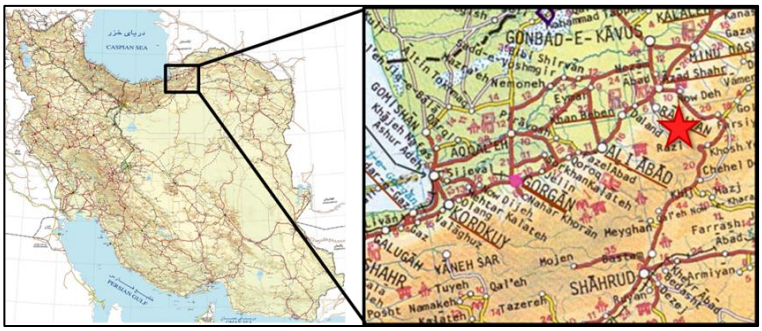

Figure1: the situation of Gheshlagh mine

3. Rock Mass Rating(RMR)

Bieniawski represented the system of Rock Mass Rating (RMR) as a rock geomechanical rating [2]. As mentioned RMR uses 10 input parameters and rates each parameter according to Table 2.

Table 2: Classification parameters and their ratings

Parameter		Range of values						
Quantitative Parameters								
Strength of intact rock material	Point Load Strength Index (MPa)	>10	4-10	2-4	1-2	For this low range Uniaxial Compressive test is preferred		
	Uniaxial Compressive Strength (MPa)	> 250	100 - 250	50 - 100	25 - 50	5 - 25	1 - 5	< 1
Rating		15	12	7	4	2	1	0
Drill core quality RQD (%)		90-100	75-90	50-75	25-50	< 25		
Rating		20	17	13	8	3		
Spacing of discontinuities		> 2 m	0.6 - 2 m	200mm - 600mm	100mm - 200mm	< 60 mm		
Rating		20	15	10	8	5		
Discontinuity length (m)		<1	1 - 3	3 - 10	10 - 20	> 20		
Rating		6	4	2	1	0		
Separation (aperture)		None	< 0.1 mm	0.1mm - 1.0mm	1mm - 5mm	> 5 mm		
Rating		6	5	4	1	0		
Orientation of discontinuities		Strike perpendicular to tunnel axis				Strike parallel to punnel axis		Dip < 20
		Drive with dip		Drive against dip		Dip 20 - 45	Dip 45 -90	Irrespective of strike
		Dip 45 - 90	Dip 20 - 45	Dip 45 - 90	Dip 20 - 45			
Descriptive Parameters								
Groundwater conditions		Completely dry	Damp	Wet	Dripping	Flowing		
Rating		15	10	7	4	0		
Infilling		None	Hard >5mm	Hard <5mm	Soft >5mm	Soft <5mm		
Rating		6	4	2	2	0		
Weathering		Unweathered	Slightly weathered	Moderately weathered	Highly weathered	Decomposed		
Rating		6	5	3	1	0		
Roughness		Very rough	Rough	Slightly rough	Smooth	Slickensided		
Rating		6	5	3	1	0		

By reviewing existing support system in tunnels which installed in this mine for many years and the proposed support system in RMR, table 3 shows suggestion to determine the required support instrument for each class of systems.

Table 3: Required support systems for each classes of RMR

Class	Support	Rating	Required support system	
			Applied support in the under study mine	General support system (According to RMR)
I	No support	81-100	Generally, no support required except for occasional spot bolting	
II	Light support	61-80	Occasional wood frame and lagging in wall where required	Locally, bolts in crown 3 m long, spaced 2.5 m, with occasional wire mesh, 50 mm shotcrete in crown where required,
III	Moderate support	41-60	Systematic wood frames with 1.5-2 m spacing and lagging in crown (and sides if required).	Systematic bolts 4 m long, spaced 1.5-2 m in crown and walls with wire mesh in crown, 50-100 mm shotcrete in crown and 30 mm in sides.
IV	Heavy support	21-40	Systematic steel sets 1-1.5 m spacing, required lagging in tectonized zones in crown and wall.	Systematic bolts 4-5 m long, spaced 1-1.5 m in crown and wall with wire mesh, 100-150 mm shotcrete in crown and 100 mm in sides, Light to medium ribs spaced 1.5 m where required.
V	Very Heavy support	0-20	Systematic steel sets 0.75- 1 m spacing, lagging in crown and wall and crete lining if required.	Systematic bolts 5-6 m long, spaced 1 - 1.5 m in crown and walls with wire mesh and bolt invert, 150-200 mm shotcrete in crown, 150 mm in sides, and 50 mm on face, medium to heavy ribs spaced 0.75 m with steel lagging and forepoling if required, close invert.

4. Fuzzy Inference System

Fuzzy inference system turns the data of input space into the output one by fuzzy logic. This is done by membership functions and fuzzy rules [3]. In fact, membership function defines the input membership degree in every one of the classes [4]. The output amount matched with the input is obtained by multiplying the point of every set in the correlation co-efficiency of the input amount to that set and then adding up all points. For example, the uniaxial compressive rock strength is MPa 48. Scoring is placed in the second group and it must get point 4 while the uniaxial compressive strength is MPa 52 for another rock and it is placed in the third group and it need point 7. This sudden change of point can be milder through membership functions. According to the uniaxial compressive strength (Fig 2), the output point related to the strength is MPa 48 is 5.3 and for the strength MPa52, it is 5.7.

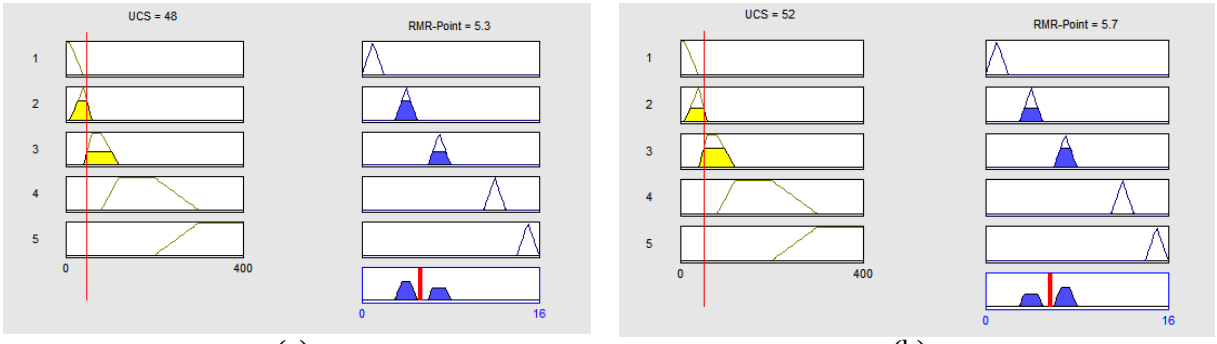

(a) (b)

Figure 2: UCS rating in semi-fuzzy RMR, (a) UCS=48MPa, (b) UCS=52MPa

Figure 3 represents the input and output membership functions related to quantative parameters.

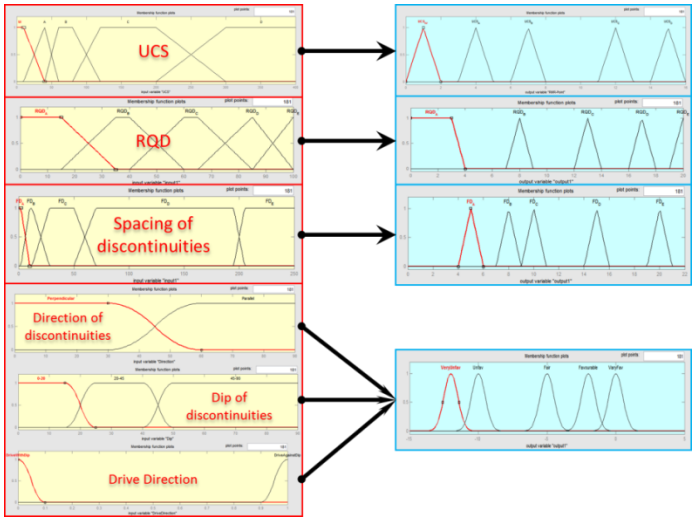

Figure 3: Input and outputs membership functions of quantitative parameters

5. Results Analysis

In this research, 45samples were taken from different parts of the tunnel and the information related the parameters required were recorded in RMR. Then, the supporting class of every one of these parts calculated by RMR semi-fuzzy method and compared with real facts. Table 4 compares these results with one another and it proves that 63% of this method is matched with the current supporting.

Table 4 : RMR results for 30 samples with their real classes

Sample No.	RMR	Support Class	Existing Support System	Sample No.	RMR	Support Class	Existing Support System	Sample No.	RMR	Support Class	Existing Support System
1	52.7	Moderate	Heavy	14	52.0	Moderate	Light	32	49.9	Moderate	Very Heavy
3	58.9	Moderate	Heavy	16	48.3	Moderate	Light	33	50.1	Moderate	Heavy
5	57.9	Moderate	Moderate	18	69.9	Light	Light	35	54.9	Moderate	Moderate
5-1	49.4	Moderate	Heavy	19	80.1	No Support	No Support	37	50.1	Moderate	Moderate
6	69.3	Light	Light	21	49.6	Moderate	Light	38	51.3	Moderate	Moderate
8	60.9	Light	Light	23	60.4	Light	Light	39	55.2	Moderate	Moderate
10	48.6	Moderate	Light	24	40.9	Moderate	Heavy	40	54.5	Moderate	Light
11	69.5	Light	Light	26	49.9	Moderate	Moderate	41	60.4	Light	Light
12	49.4	Moderate	Moderate	27	59.1	Moderate	Moderate	42	69.4	Light	Light
13	48.9	Moderate	Moderate	29	44.6	Moderate	Moderate	45	38.2	Heavy	Heavy

6. Conclusions

By comparing the results of the semi- fuzzy RMR with the results in mine, this system specifies that fuzzy making is a part of quantative parameters and not fuzzy making the quantative parameters highly affects the power of RMR separation method. Holistically, there are limitations in supporting equipments in the understudy mine; it is both economically and technically beneficial to apply a new scientific method in this mine or other similar mines.

References

[1] H. Jalalifar, S. Mojeddifar, A. A. Sahebi, Prediction of Rock Mass Rating using Fuzzy Logic with Special Attention to Discontinuities and Ground Water Conditions, *11th Underground Coal Operators' Conference*, University of Wollongong & the Australasian Institute of Mining and Metallurgy, 115-120, (2011).

[2] Z.T. Bieniawski, *Engineering rock mass classifications*, (1989).

[3] S. Guillaume, Designing Fuzzy Inference Systems from Data: An Interpretability-Oriented Review, *IEEE transactions on fuzzy systems*, Vol. 9, No. 3, (2001).

[4] L. A. Zadeh, *Fuzzy Sets*, Information and Control, 8(3), pp. 338-353, (1965).

Proceedings of the 22nd UK Conference of the
Association for Computational Mechanics in Engineering
2 – 4April 2014, University of Exeter, Exeter

AN EQUILIBRIUM FINITE ELEMENT MODEL FOR SHELLS WITH LARGE DISPLACEMENTS

***Edward A. W. Maunder[1], Bassam A. Izzuddin[2]**

[1]College of Engineering, Mathematics & Physical Sciences, University of Exeter, North Park Road, Exeter, EX4 4QF
[2]Department of Civil & Environmental Engineering, Imperial College, London, SW7 2AZ

*e.a.w.maunder@exeter.ac.uk

ABSTRACT

A facetted quadrilateral shell element based on Reissner-Mindlin theory and a hybrid equilibrium formulation is presented. Each side of an element has six rigid body freedoms as well as six additional modes of deformation. The element is incorporated within a co-rotational framework, upgrading its applicability to large displacement geometric non-linear analysis. Numerical examples are included concerning the pinched hemisphere benchmark problem for both linear and geometrically non-linear behaviour. Results are included regarding the convergence of the radial displacements of the loaded points, and distributions of stress-resultants. All results from the hybrid models are compared with those from similar meshes of 9-noded conforming elements.

Keywords: *finite elements; equilibrium; shells; large rotations.*

1. Introduction

The formulation of equilibrium shell elements is not so well suited to curved elements, either with curved boundaries or with curved surfaces, as are conforming elements. However, the general use of faceted models for curved shells is widely accepted as a valid simplification, and it thus seems justified to investigate the use of flat straight-sided equilibrium shell elements in this context. In general, the motivation for the use of equilibrium models is the expectation that, compared with conforming models, much stronger forms of equilibrium are determined without loss of accuracy concerning displacements, albeit that displacements are only determined at the sides of elements.
Recent work [4] has indicated good results can be obtained with such elements to model linear elastic behaviour of a folded plate and a curved shell having zero Gaussian curvature. In this paper we extend the formulation to model cases where small strains can be assumed and local behaviour continues to be linear elastic, but displacements become large enough to produce non-linear behaviour in a global sense.

2. Hybrid equilibrium quadrilateral flat shell element

We consider a co-rotational formulation of a quadrilateral hybrid equilibrium flat shell macro-element which combines four triangular primitive elements [4]. We assume moment fields and side rotations of degree 2, together with membrane and transverse shear force fields and side translations of degree 1. The plate bending behaviour is governed by Reissner-Mindlin theory, and the sides are assumed to be initially straight. The 12 kinematic parameters associated with a side include its 6 rigid body freedoms plus 6 additional modes of deformation. The conjugate static parameters consist of 6 resultant forces/moments plus 6 self-balanced distributions of stress-resultants. Thus each side has a separate rigid body drilling degree of freedom, but the transverse fibres are not free to rotate independently, as would be the case with micropolar theory, or at the nodes of an element which exploits Allman's incompatible shape functions to interpolate drilling rotations [5].
Special consideration needs to be given at the interfaces between elements which are not coplanar. Without additional distributions of drilling rotation, the twisting rotations of fibres cannot necessarily be transferred to an adjacent element. Two alternative assumptions are made: (a) the additional modes of twisting are assumed to be free to occur and the conjugate torsional moments are released at an

interface; or (b) the additional modes of twisting are assumed to be transferred between elements even though their axes of rotation are in different directions. In case (a) we have a strictly equilibrated model in terms of stress-resultants, but in case (b) where torsional moments are not released, the self-balanced modes of torsion are not codiffusive, and we have a so-called quasi-equilibrium model. Of course in the case of modelling curved shells, their shapes are only approximated by a facetted model, and equilibrium must be understood to be with reference to that model.

When the response of a model involves large displacements, including large rotations, the co-rotational formulation follows a similar procedure as in [1,2]. Global and local element Cartesian axes are used as indicated in Figure 1, where the effective nodes of the element are located at the midpoints of the sides. The local coplanar $(\bar{x}, \bar{y})$ axes bisect the lines joining nodes (42,13) and (13,24) respectively, and the $\bar{z}$ axis is normal to the plane of the element.

3. Analysis of the pinched hemisphere benchmark problem

The performance of the element is assessed when either small or large rotations occur for the benchmark problem [6] of the pinched hemisphere, radius 10m, thickness 40mm, with an 18° opening. The hemisphere is modelled by the quadrant in Figure 2 by using appropriate symmetry conditions on the boundary. Solutions are compared with those produced from models based on 9-noded curved conforming elements [1], which models are susceptible to locking.

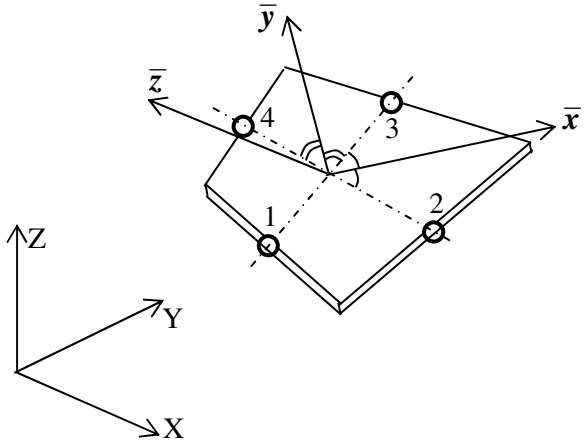

Figure 1: global and local Cartesian reference axes for the flat quadrilateral element.

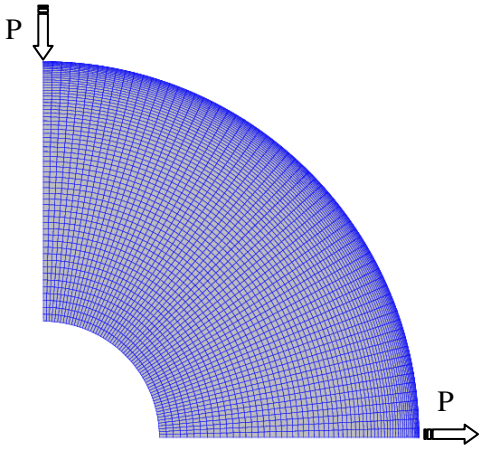

Figure 2: Plan view of quadrant of hemisphere with radial pinch loads.

The convergence of the radial displacements of the pinch points are compared in Figure 3(a) for a small load P = ±1kN with regular meshes containing 4, 8, 16, and 32 elements uniformly distributed along each boundary curve. It should be noted that the theoretical value of 94mm is based on linear elastic theory [6], and this amounts to nearly 2.5 times the shell thickness.

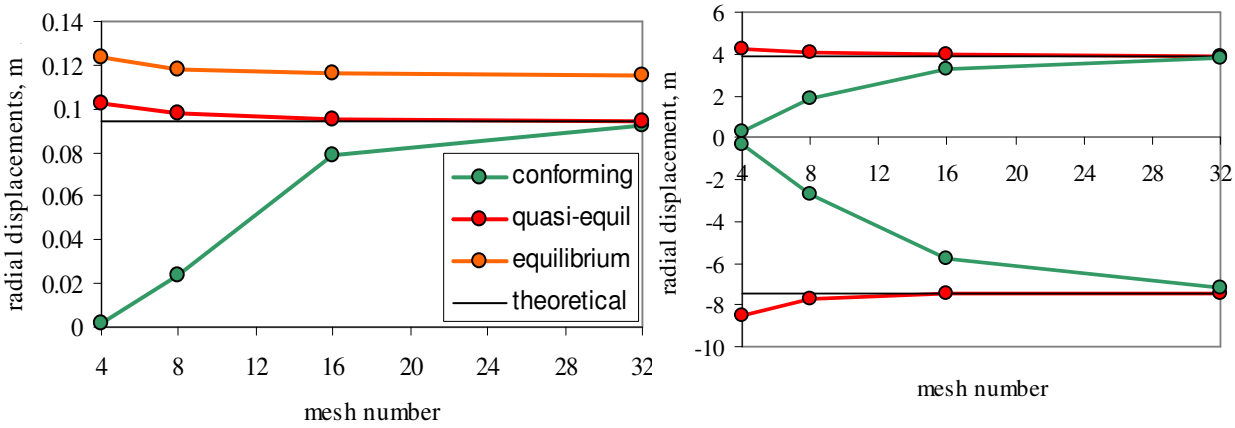

(a) approximately linear behaviour with loads ±1kN (b) non-linear behaviour with loads ±160kN

Figure 3: convergence of the radial displacements at the pinch points.

Figure 3(b) includes results for both the equilibrium and the quasi-equilibrium models, and it can be seen that they are both giving upper bounds to the radial displacements. However, it must be noted that these results refer to facetted model geometries that change as the mesh is refined. The vertices of the quadrilateral elements always lie in the midsurface of the shell, but the structural nodes are offset from the midsurface as a result of the facetted approximation. Clearly, the quasi-equilibrium models tend towards the true solution as the mesh is refined and adjacent elements approach being coplanar. However, the equilibrium models remain too flexible due to the release of the torsional moments at element interfaces. The conforming models represent the shape of the shell more precisely, but, as expected, are too stiff with a tendency towards membrane locking in the coarser meshes.

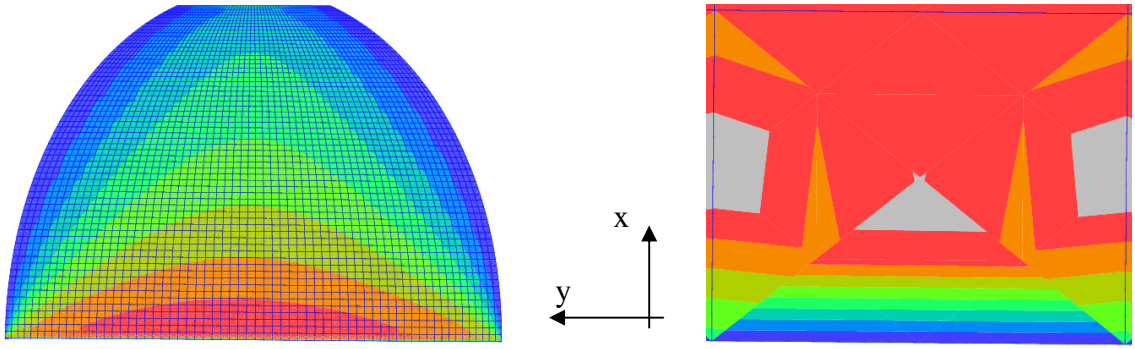

(a) Mxy (blue: 0 to red: 0.60kNm/m) quasi-equilibrium model (b) Mxy central element at bottom edge

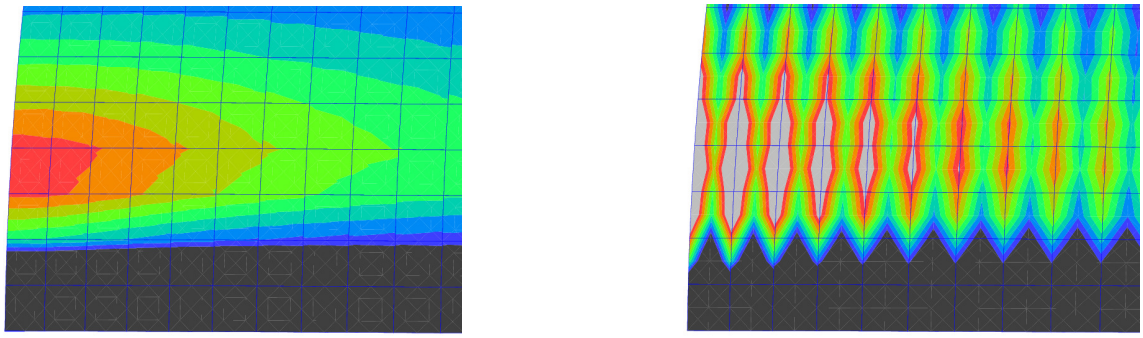

(c) quasi-equilibrium model (d) conforming model

Ny tension (blue: 0 to red: 20kN/m), patch of 7x10 elements adjacent to the outward pinch force

(e) quasi-equilibrium model (f) conforming model

Ny compression (blue: -100 to red: 0kN/m), patch of 2x10 elements adjacent to the outward pinch force

Figure 4: contours of moment and membrane force stress-resultants from 64x64 meshes; axes *x,y* refer to longitudinal and latitudinal directions respectively.

The contours of moment stress-resultants are generally in agreement in both types of model, e.g. Mxy in Figure 4(a), with an important exception. The conforming model shows Mxy to be at its maximum value on the bottom edge of the hemisphere, whereas the quasi-equilibrium model indicates high local gradients in Mxy, which moments correctly become zero, as prescribed, on the bottom edge as indicated in Figure 4(b). The gradient in Mxy also correctly reflects the presence of a boundary layer which contains concentrations of transverse shear forces Qzy.

The distributions of membrane forces, e.g. circumferential forces Ny, are better recovered from the quasi-equilibrium model, as indicated in Figures 4(c to f), where the results from the conforming model tend to oscillate in a typical, but unrealistic, way.

The results from the models when P = ±1kN contain small differences between the inward and outward displacements of the loads, as well as small differences from expected symmetric or

antisymmetric contours of stress-resultants. These differences indicate that geometric non-linear behaviour is already present at this load.
When the load P = ±160kN, geometric non-linear behaviour is very evident, as indicated in Figure 5, and in the convergence towards different magnitudes of radial displacement at the pinch points, as shown in Figure 3(b). The converged values agree with those in [3] to within 0.5% for the quasi-equilibrium model, and within 3.6% for the conforming model with 32x32 meshes.

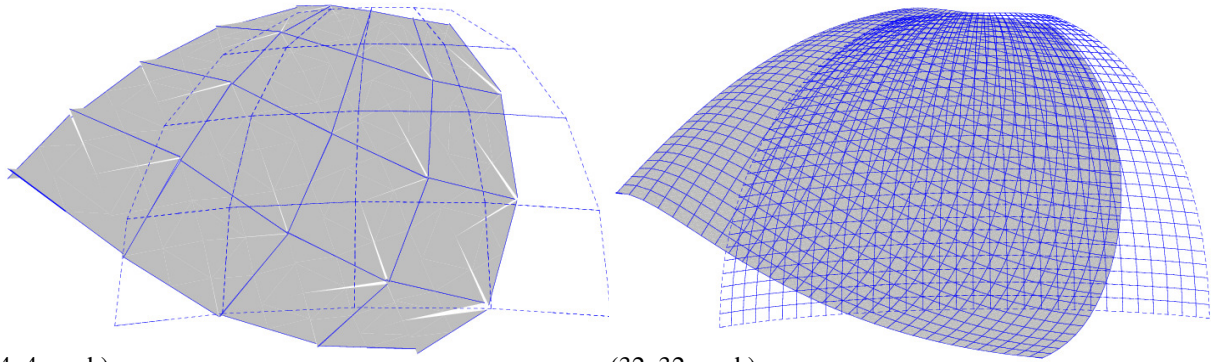

(4x4 mesh) (32x32 mesh)
Figure 5: deflected shapes of the quasi-equilibrium model at ±160kN.

As with the linear case, the quasi-equilibrium model gives apparent upper bounds to the magnitudes of both radial displacements, with even the coarsest 4x4 mesh providing excellent results in this respect. This is in stark contrast with the conforming model which is far too stiff for coarse meshes. However it is observed that for the 4x4 mesh, some of the facetted elements become quite distorted and warped out of their planes. A consequence of this is that local equilibrium of nodal forces and moments can be violated without a non-linear formulation of the local element response.

4. Conclusions

The radial displacements of the pinch points from the quasi-equilibrium hybrid models converge monotonically as upper bounds to the reference solutions of the benchmark problem for both linear and geometrically non-linear forms of behaviour. The equilibrium model which releases the self-balanced modes of torsion gives greater upper bounds, and appears to converge to a more flexible solution. As expected, unlike the conforming model, there is no evidence of locking in either form of hybrid model. The distributions of stress-resultants from the quasi-equilibrium models tend to converge more rapidly towards useful forms for the design engineer compared with the conforming models. Future research is required to investigate the formulation of a non-planar macro-element.

References

[1] B.A. Izzuddin and Z.X. Li, A co-rotational formulation for large displacement analysis of curved shells, in: Deeks, Hao (Eds.), *Developments in Mechanics of Structures and Materials*, Taylor & Francis Group, London, 1247-1253, 2004.

[2] B.A. Izzuddin, An enhanced co-rotational approach for large displacement analysis of plates, *Int. J. Numer. Meth. Engng.* **64**, 1350-1374, 2005.

[3] C.C. Celigoj, A strain- and displacement-based variational method applied to geometrically non-linear shells, *Int. J. Numer. Meth. Engng.* **39**, 2231-2248, 1996.

[4] E.A.W. Maunder and B.A. Izzuddin, A hybrid equilibrium element for folded plate and shell structures, *Int. J. Numer. Meth. Engng.* **95**, 451-477, 2013.

[5] H. Nguyen-Van, N. Mai-Duy, T. Tran-Cong, An improved quadrilateral flat shell element with drilling degrees of freedom for shell structural analysis, *Computer Modeling in Engineering & Sciences*, **49**, 81-112, 2009.

[6] R.H. Mac Neal and R.L. Harder, A proposed standard set of problems to test finite element accuracy, *Finite Elements in Analysis and Design*, **1**, 3-20, 1985.

Proceedings of the 22nd UK Conference of the
Association for Computational Mechanics in Engineering
2 – 4April 2014, University of Exeter, Exeter

ASSESSING THE REMAINING SAFE LIFE OF CONCRETE SEWER PIPES USING STOCHASTIC FINITE ELEMENT METHOD

***Asaad Faramarzi[1], Amir M. Alani[1]**

[1]Faculty of Engineering & Science, University of Greenwich, Central Avenue, Chatham Maritime, ME4 4TB

*A.Faramarzi@gre.ac.uk

ABSTRACT

In this paper a stochastic finite element model is developed to investigate the probability of failure of cementitious buried sewer pipes under combined effects of corrosion and stresses. Using the developed model, the effects of different random variables including traffic loads, pipe material and corrosion on the remaining safe life of the cementitious sewer pipes are explored. A numerical example is presented to demonstrate the application of the proposed model in evaluating the effect of the contributing parameters to the probability of failure of concrete sewer pipes. The stochastic finite element model provides a practical tool for both designers and asset managers to predict the reliable service life of the system.

Keywords: *Stochastic finite element method; cementitious sewer pipes; probability of failure; concrete corrosion; random variables*

1. Introduction

Underground sewer pipes are important and vital infrastructures that play a crucial role in the economy, prosperity, quality of life and especially the health of a country. These essential structures are designed to resist and operate safely under various external loads and environmental conditions. However the degradation of sewer pipes over their service life in combination with the effect of overlaying soil and surface traffic loads can sometimes cause failures in sewer pipes. It is known that for cementitious sewer pipes, corrosion is the main cause of degradation [1]. The corrosion can cause reduction in structural strength of the pipeline, leading to pipe collapse. Therefore considering the effect of corrosion in the analysis and design of cementitious sewer pipes is essential for developing advanced model(s) to predict the likelihood of collapses of sewer systems. In order to provide an accurate prediction of remaining safe life of the sewer pipes, all the parameters that affect and control the process of deterioration and failure of pipes, the interaction of different mechanisms of failure, and their effect on remaining safe life of sewer pipes should be considered. Due to the large degree of uncertainty relating to the factors that are involved in the operation of underground sewer systems - in particular corrosion - it is more rational to model the failure of sewer pipes as a stochastic process. To fulfil this, a comprehensive model has been developed and is reported in this paper that takes into consideration all parameters contributing towards the failure of cementitious sewer pipes using stochastic finite element method (SFEM). SFEM can determine the prospect of failure of sewer pipes throughout their intended service life. Particular attention is paid to simulate the corrosion using the stochastic finite element model and to investigate its interaction with other mechanisms of failure and their effect on the remaining safe life of sewer pipes. The results provided by the proposed stochastic finite element model can help asset managers and owners to make risk-informed and cost-minimised decisions with respect to when, where, what and how interventions are required to ensure the safety and integrity of existing pipelines during their whole life of service.

2. Stochastic Finite Element Method

The stochastic finite element method (SFEM) is a powerful numerical tool in computational stochastic mechanics. SFEM can be classified as an extension of the classic deterministic finite element approach to the stochastic framework i.e. to the solution of static and dynamic problems with stochastic mechanical, geometric and/or loading properties [2]. The general formulation of a SFEM can be written in the following form [3]:

$$\mathbf{K}(\theta)\mathbf{U}(\theta) = \mathbf{F}(\theta) \quad (1)$$

where K is the global stiffness matrix, U and F represent the nodal displacement and force vectors and θ represents the randomness of the parameters. The above equation is the stochastic representation of the static finite element problems and the uncertain response of structure (i.e. $U(\theta)$) and other quantities of interest such as stresses $\sigma(\theta)$, and strains $\varepsilon(\theta)$ can be obtained by solving Equation 1. In this paper a stochastic finite element model based on the Monte Carlo simulation (MCS) technique is developed to analyse the probability of failure of underground cementitious sewer pipes. In the MCS-based SFEM, a deterministic finite element problem (Equation 1) is solved a large number of times and the response variability is calculated using statistical relationships. The MCS method does not involve any simplification or assumption which makes it a robust and universal technique to treat complex stochastic problems. The developed code is employed incrementally over the time in order to account for the degradation of the sewer pipe and predict the probability of failure of the sewer pipes throughout their service life. In the MCS code, for every simulation, the limit state function(s) is checked using the finite element method (i.e. if the resultant stress has exceeded the yield stress) and the probability of failure is obtained using the following equation [4]:

$$P_f^i = \frac{N_f}{N} \quad (2)$$

where $P_f{}^i$ is defined as the probability of failure of each limit state function, N_f is the number of simulations when the limit state function is violated, and N is the total number of simulations. In a series system, where more than one limit state function exist, the failure of any of the limit state functions implies the failure of the system. If the individual failures are mutually independent, then the probability of the system can be obtained from Equation 3 [4]. In this equation P_f is the probability of failure of the system, and m is the number of limit state functions defined for the system.

$$P_f = 1 - \prod_{i=1}^{m}(1 - P_f^i) \quad (3)$$

Effect of Corrosion

Concrete corrosion due to sulphuric acid attack is known to be one of the main contributory factors in the degradation of concrete sewer pipes. In this study it is assumed that the corrosion of concrete sewer pipes is dependent on the age of the pipe and can be presented using a power law model. The power law model to predict the biogenic sulphuric acid corrosion of concrete pipes can be presented in the form of the following equation:

$$\mathrm{C} = \alpha\, T^{\lambda} \quad (4)$$

where C is the corrosion of the pipe, α is a multiplying coefficient, λ is an exponential coefficient, and T is the age of the pipe. The data provided in Meyer [5] are utilised to estimate the coefficients in Equation 4 using an exponential regression. Due to a large degree of uncertainty of corrosion process, the corrosion and consequently the coefficients in Equation 4 are considered as stochastic parameters. At every finite element simulation the amount of corrosion is obtained using Equation 4 and the finite element input file is updated via re-meshing the pipe domain using the new coordinates after considering the corrosion. The strength of the concrete pipe is expected to be reduced as a result of the reduction of pipe wall thickness.

3. Numerical Example

In this section a numerical example is considered to evaluate the performance of the developed SFEM in predicting the probability of failure of concrete sewer pipes subject to stresses and corrosion. The finite element (FE) model of the problem consists of a concrete pipe with a circular section buried underground and surrounded by a homogenous soil. The model is subjected to self-weight and an external traffic load applied on the surface of the model. The FE model is assumed to be two

dimensional with plane strain geometrical condition. In order to draw conclusions that are not affected by a particular example, the problem is scaled with respect to the external diameter of the pipe and the variations of different normalised parameters are investigated. Figure 1 shows the geometry and normalised parameters of the problem.

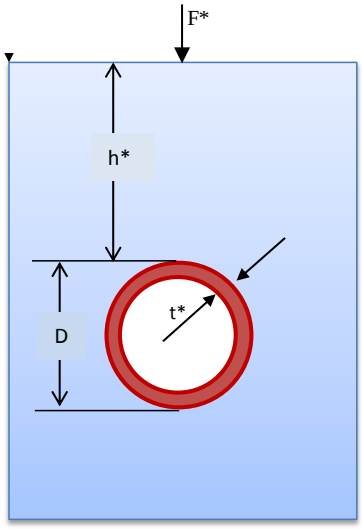

Figure 1: Geometry and parameters used in the FE model

Table 1: Random variables used for the SFEM

Symbol	Description	Mean	Coefficient of variation
f_c	Concrete maximum compressive strength	35 MPa	0.1
F^*	Traffic load	20	0.25
I_f	Load impact factor	1.5	0.15
α	Corrosion multiplying coefficient	3.5×10^{-5}	0.1
λ	Corrosion exponential coefficient	1.5	0.15

In addition to the deterministic parameters such as diameter and thickness of the pipe, there are some parameters that are considered as stochastic or random parameters. Using the existing studies on the reliability analyses of underground pipelines and performing a number of pilot simulations, five parameters were chosen as random variables. The normal distribution has been adopted for these random variables since only means and variances were available. These parameters, their mean and their coefficient of variation (cv) are presented in Table 1.

Results and discussion

After choosing the type of each parameter (deterministic or stochastic) and creating the FE models, the time-dependant SFEM were performed for different values of scaled parameters in order to study their effect on the probability of failure of concrete sewer pipes. Figure 2 shows the results of the SFEM on probability of failure of the example sewer pipe under various normalised traffic loads over its service life. It can be seen that as the traffic load increases the probability of failure of sewer pipes grows rapidly. In addition it can be noted that initially the probability of failure is zero or very small for all cases; however as the effect of corrosion emerges (usually after the first 20 years) the probability of failure increases rapidly. To further investigate the effect of traffic load on the service life of concrete sewer pipes subject to stresses and corrosion, the following analysis was also carried out. Let us assume that the acceptable probability of failure (P_f) is 10%, or 20% or 30% (equivalent of a remaining safe life of 90%, 80% and 70% respectively). The service life of each FE model (each model has a different normalised traffic load) can be evaluated using the results provided by the SFEM (Figure 3). It can be seen in Figure 3 that the service life of the sewer pipe is reduced significantly with a non-linear trend as the traffic load increases. For example if the traffic load is doubled (i.e. F^* increases from 10 to 20) then the service life of the sewer pipe is reduced from 60 years to zero years for the acceptable probability of failure of 10%. A similar trend can also be seen for other presumed acceptable values of probability of failure (i.e. $P_f = 20\%$ and $P_f = 30\%$).

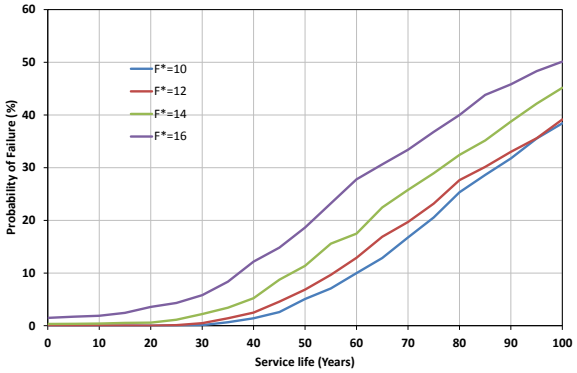

Figure 2: Probability of failure of concrete sewer pipe for different values of scaled traffic load versus service-life

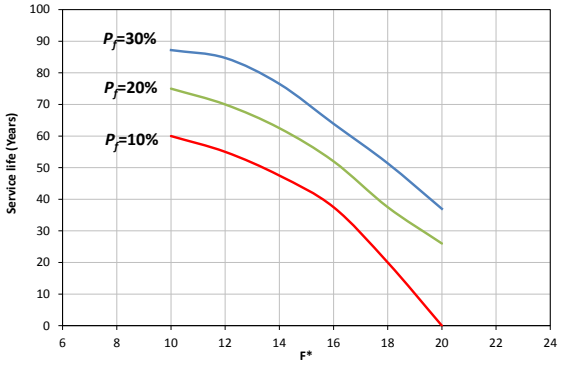

Figure 3: The variation of traffic load (normalised) with the service life of sewer pipes

4. Summary and Conclusions

In the present study a stochastic finite element model was utilised to predict the probability of failure of concrete sewer pipes under combined effects of internal corrosion and stresses. Uncertainties involved in pipe material, traffic load and corrosion are considered to develop the stochastic finite element model. A nonlinear time-dependent model was chosen to predict the corrosion in concrete sewer pipes. A normalised numerical example was employed to investigate the effect of both deterministic and probabilistic parameters on the probability of failure of sewer pipes. Two mechanisms of failure (i.e. corrosion and shear failure) were adopted to define the limit state functions. The results of the numerical simulations revealed a nonlinear relationship between most of the parameters and the probability of failure of sewer pipes. The results of the developed stochastic finite element model can be used to improve the performance and planning of existing sewer systems, by providing better predictions for the probability of failure of sewer pipes compared to the existing approaches. The model can bring together the effect of contributing parameters in the probability of failure of the system being studied in a numerical framework with high precision. Using the stochastic finite element model it is possible to study the effect of each parameter on the failure of the system and their interaction with each other. The SFEM also provides a time-dependant reliability analysis for predicting the remaining safe life of sewers, which provides a means to better manage the existing sewers and plan resources during their whole life of service. Further improvement in the predictions provided by model can be achieved by collecting additional data on the corrosion rate of concrete sewer pipes.

Acknowledgements

This research was funded by a grant from the UK Engineering and Physical Sciences Research Council (EPSRC) grant number EP/1032150/1 (Assessing Current State of Buried Sewer Systems and Their Remaining Safe Life).

References

[1] A.M. Alani, A. Faramarzi, M. Mahmoodian, K.F. Tee. Prediction of sulphide build-up in filled sewer pipes. *Environmental Technology*. In press available online http://dx.doi.org/10.1080/09593330.2014.881403, 2013.

[2] G. Stefanou. The stochastic finite element method: Past, present and future. *Computer Methods in Applied Mechanics and Engineering*, 198, 1031-1051, 2009.

[3] M.F. Pellissetti and G.I. Schuëller. Scalable uncertainty and reliability analysis by integration of advanced Monte Carlo simulation and generic finite element solvers. *Computers & Structures*, 87, 930–947, 2009.

[4] R.E. Melchers, *Structural Reliability Analysis and Prediction*, 2nd edition, John Wiley & Sons, 1999.

[5] W.J. Meyer. Case study of prediction of sulphide generation and corrosion in sewers. *Water Pollution Control Federation*, 52, 2666-2674, 1980.

Proceedings of the 22nd UK Conference of the
Association for Computational Mechanics in Engineering
2 – 4April 2014, University of Exeter, Exeter

CO-ROTATIONAL FORMULATION FOR SANDWICH PLATES AND SHELLS

Yating Liang[1], *Bassam A. Izzuddin[1]

[1]Dept. of Civil and Environmental Engineering, Imperial College, London, SW7 2AZ

*b.izzuddin@imperial.ac.uk

ABSTRACT

A 9-noded co-rotational shell element based on a layer-wise theory is proposed for the nonlinear analysis of three-layered sandwich plates/shells with soft core. The cross-sectional zigzag effect of planar displacements is considered by assuming a layer-wise linear zigzag function specific to stiff/soft/stiff sandwich construction. A novel zigzag function is introduced into the Reissner-Mindlin element formulation leading to seven displacement freedoms per node. Meanwhile, a piecewise linear-constant-linear distribution of the transverse shear stress through thickness is also assumed, which leads to three stress parameters per node. By employing the Hellinger-Reissner variational principle at each layer, stress parameters can be expressed in terms of displacement parameters and thus eliminated, and the governing equations can be obtained. The proposed shell element is formulated in a co-rotational framework allowing for large displacement analysis. For computational efficiency, additional displacement fields related to the zigzag effect are defined in a shell coordinate system so that co-rotational transformations of nodal forces and stiffness associated with these freedoms are excluded. To address the locking issue of the proposed shell element, an optimisation approach is adapted to the sandwich shell element. Two nonlinear examples are used to illustrate the effectiveness of the proposed element.

Keywords: *sandwich plates/shells; zigzag function; locking; assumed strain; shell coordinate system*

1. Introduction

Sandwich structures, which comprise a relatively flexible core sandwiched by stiff face sheets, have been widely used in engineering practice. These are characterised by zigzag displacements and interlaminar continuity of transverse stresses due to the large face-to-core modular ratio. In this work, a 9-noded sandwich shell element is proposed for nonlinear analysis of sandwich plates and shells.

2. Zigzag Planar Displacement Fields

A 9-noded sandwich shell element based on a layer-wise theory has been developed and implemented in ADAPTIC [1], which assumes that planar displacement fields are layer-wise linear through thickness. The element is an extension of a previous 9-noded shell element [2,3] to a 3-layered application, which is formulated in a co-rotational framework to allow for nonlinear analysis. The optimisation approach proposed by Izzuddin [3] has been adapted to this element to address locking.
The transverse displacement field is assumed to be constant through the thickness, while planar displacement fields are derived by adding a zigzag-shaped component to the original Reissner-Mindlin displacement terms, which are expressed as:

$$\begin{Bmatrix} u(\xi,\eta,\zeta) \\ v(\xi,\eta,\zeta) \end{Bmatrix} = \begin{Bmatrix} u_0(\xi,\eta) \\ v_0(\xi,\eta) \end{Bmatrix} + \frac{h}{2}\zeta \begin{Bmatrix} \theta_x(\xi,\eta) \\ \theta_y(\xi,\eta) \end{Bmatrix} + \Lambda(\zeta) \begin{Bmatrix} \vartheta_x(\xi,\eta) \\ \vartheta_y(\xi,\eta) \end{Bmatrix} \tag{1}$$

where (ξ,η,ζ) is the element natural coordinate system, in which $\zeta = \pm 1$ at the top/bottom surface; u_0 and v_0 are planar displacement fields of the middle surface; θ_α $(\alpha = x, y)$ is the rotation in α -direction of the cross-section with reference to initial geometry; ϑ_α $(\alpha = x, y)$ is the additional displacement field; $\Lambda(\zeta)$ is the zigzag-shaped function. For three-layered sandwich plates/shells whose faces are stiffer than the core, the zigzag effect is dominated by the mode that has identical rotations in the faces. Therefore, the mode in Figure 1 is used as the zigzag function $\Lambda(\zeta)$.

3. Shell Coordinate System

The proposed sandwich shell element has seven freedoms per node (five Reissner-Mindlin freedoms plus two additional freedoms associated with sectional warping). The five Reissner-Mindlin

displacement variables are local co-rotational freedoms transformed from their global counterparts. Since external loading is usually associated with traditional freedoms only, it is unnecessary to define the additional freedoms in the global coordinate system as those Reissner-Mindlin freedoms. Instead, a specific local shell coordinate system independent of the co-rotational framework is proposed within which additional freedoms are defined. The orientations of the shell coordinates are obtained by rotating the element coordinates by an angle β extracted at that point. This angle β is a function varying throughout the shell surface, which is defined such that at a node shared by two or more elements, the orientations of the shell coordinate systems at that node are exactly or close to identical. Despite possible second-order violation of continuity, this shell coordinate system is computationally efficient with mesh refinement, hence excluding co-rotational transformations related to the additional freedoms. By denoting $\{\bar{\vartheta}_x, \bar{\vartheta}_y\}$ the additional displacement fields defined in the shell coordinate system, the following relationship is obtained:

$$\begin{Bmatrix} \vartheta_x \\ \vartheta_y \end{Bmatrix} = \begin{bmatrix} \cos\beta & -\sin\beta \\ \sin\beta & \cos\beta \end{bmatrix} \begin{Bmatrix} \bar{\vartheta}_x \\ \bar{\vartheta}_y \end{Bmatrix}. \tag{2}$$

Substituting Equation (2) into Equation (1) gives:

$$\begin{Bmatrix} u(\xi,\eta,\zeta) \\ v(\xi,\eta,\zeta) \end{Bmatrix} = \begin{Bmatrix} u_0(\xi,\eta) \\ v_0(\xi,\eta) \end{Bmatrix} + \frac{h}{2}\zeta \begin{Bmatrix} \theta_x(\xi,\eta) \\ \theta_y(\xi,\eta) \end{Bmatrix} + \Lambda(\zeta) \begin{bmatrix} \cos\beta & -\sin\beta \\ \sin\beta & \cos\beta \end{bmatrix} \begin{Bmatrix} \bar{\vartheta}_x \\ \bar{\vartheta}_y \end{Bmatrix} \tag{3}$$

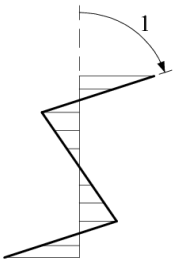

Figure 1: Schematic plot of the zigzag function.

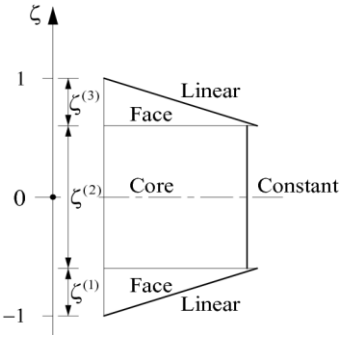

Figure 2: Assumed distribution of transverse shear stress through thickness.

4. Assumed Transverse Shear Stress Fields

If the face-to-core modular ratio is relatively large, distribution of the transverse shear stress through the thickness exhibits a piecewise linear-constant-linear pattern. Therefore, a shear stress distribution as shown in Figure 2 is assumed. For computational efficiency, transverse shear stresses at the three layers are assumed to be mutually independent, though resulting in possible violation of C^0 continuity at laminar interfaces. The assumed transverse shear stresses are expressed as:

$$\boldsymbol{\tau}_{AS} = \begin{Bmatrix} \tau_{13,AS} \\ \tau_{23,AS} \end{Bmatrix}; \tau_{\alpha 3,AS} = \begin{cases} \omega_{\alpha 3}^{(1)} \left(1 + \dfrac{2\left(\zeta - \zeta_0^{(1)}\right)}{\zeta^{(1)}} \right) & \zeta_-^{(1)} \le \zeta < \zeta_+^{(1)} \\ \omega_{\alpha 3}^{(2)} & \zeta_-^{(2)} \le \zeta < \zeta_+^{(2)} \\ \omega_{\alpha 3}^{(3)} \left(1 - \dfrac{2\left(\zeta - \zeta_0^{(3)}\right)}{\zeta^{(3)}} \right) & \zeta_-^{(3)} \le \zeta < \zeta_+^{(3)} \end{cases} \tag{4}$$

where $\boldsymbol{\omega}^{(k)} = \left\{\omega_{13}^{(k)}, \omega_{23}^{(k)}\right\}^T$ is the vector of stress variables for Layer (k); $\zeta^{(k)} = \zeta_+^{(k)} - \zeta_-^{(k)}$; $\zeta_+^{(k)}$ and $\zeta_-^{(k)}$ are values of ζ at the top and bottom of Layer (k); $\zeta_0^{(k)}$ is the value of ζ in the middle of Layer (k).

5. The Hellinger-Reissner Variational Principle

Consistently with layer-wise theories, each individual layer is regarded as a pseudo Reissner-Mindlin shell. The vector of 45 pseudo freedoms at Layer (k), $\mathbf{U}_{ps}^{(k)}$, can be expressed in terms of the vector of the 45 local freedoms $\mathbf{U}_C$ and the vector of 18 additional freedoms $\mathbf{U}_A$:

$$\mathbf{U}_{ps}^{(k)} = \mathbf{T}_{ps,C}^{(k)}\mathbf{U}_C + \mathbf{T}_{ps,A}^{(k)}\mathbf{U}_A \tag{5}$$

in which $\mathbf{T}_{ps,C}^{(k)}$ and $\mathbf{T}_{ps,A}^{(k)}$ are transformation matrices. With the use of pseudo freedoms $\mathbf{U}_{ps}^{(k)}$, strains at Layer (k) are obtained via von Karman's equations.

The Hellinger-Reissner principle is employed at each individual layer, which gives both the relationship between the stress and displacement parameters and the weak form of equilibrium. At Layer (k), the Hellinger-Reissner variation of the model is expressed as

$$\begin{aligned}\delta\Pi_R = &\int_A \left(\delta\boldsymbol{\varepsilon}_m^{(k)T}\boldsymbol{\sigma}_m^{(k)} + \delta\boldsymbol{\varepsilon}_b^{(k)T}\boldsymbol{\sigma}_b^{(k)} + \delta\boldsymbol{\varepsilon}_s^{(k)T}\int_{h_-^{(k)}}^{h_+^{(k)}} \boldsymbol{\tau}_{AS}^{(k)} dz \right) dA + \int_A \left(\int_{h_-^{(k)}}^{h_+^{(k)}} \delta\boldsymbol{\tau}_{AS}^{(k)T}\left(\boldsymbol{\varepsilon}_s^{(k)} - \boldsymbol{\varepsilon}_{s,AS}^{(k)}\right) dz \right) dA \\ &-\delta W_{ext}^{(k)} = 0 \qquad \forall \delta\mathbf{U}_C, \delta\mathbf{U}_A, \delta\boldsymbol{\omega}^{(k)}\end{aligned} \tag{6}$$

where terms with subscripts 'm', 'b', and 's' represent respectively the membrane, bending and transverse shear stresses/strains; $\boldsymbol{\varepsilon}_{s,AS}^{(k)}$ are transverse shear strains obtained from assumed stress fields. The stress parameters $\omega_{\alpha 3}^{(k)}$ can be expressed in terms of displacement parameters by the use of the second integral in Equation (6). Further manipulation of Equation (6) gives the weak form of equilibrium at Layer (k):

$$\begin{aligned}&\left(\delta\mathbf{U}_C^T\left(\mathbf{T}_{ps,C}^{(k)}\right)^T + \delta\mathbf{U}_A^T\left(\mathbf{T}_{ps,A}^{(k)}\right)^T\right)\int_A \left(\left(\mathbf{B}_m^{(k)}\right)^T\mathbf{D}_m^{(k)}\boldsymbol{\varepsilon}_m^{(k)} + \left(\mathbf{B}_b^{(k)}\right)^T\mathbf{D}_b^{(k)}\boldsymbol{\varepsilon}_b^{(k)} + \left(\mathbf{B}_s^{(k)}\right)^T\mathbf{D}_s^{(k)}\boldsymbol{\varepsilon}_s^{(k)}\right)dA \\ &-\delta W_{ext}^{(k)} = 0 \quad \forall \delta\mathbf{U}_C, \delta\mathbf{U}_A\end{aligned} \tag{7}$$

where $\mathbf{B}_m^{(k)}$, $\mathbf{B}_b^{(k)}$, and $\mathbf{B}_s^{(k)}$ represent respectively the first derivative of $\boldsymbol{\varepsilon}_m^{(k)}$, $\boldsymbol{\varepsilon}_b^{(k)}$, and $\boldsymbol{\varepsilon}_s^{(k)}$ with respect to $\mathbf{U}_{ps}^{(k)}$; $\mathbf{D}_m^{(k)}$, $\mathbf{D}_b^{(k)}$, and $\mathbf{D}_s^{(k)}$ are generalised constitutive matrices, in which $\mathbf{D}_s^{(k)}$ incorporates the effect of the assumed transverse shear stress distribution.

6. Nodal Forces and Tangent Stiffness Matrices

Using Equation (7), the nodal forces $\mathbf{f}_C$ and $\mathbf{f}_A$ can be obtained:

$$\mathbf{f}_C = \sum_{k=1}^{3}\mathbf{T}_{ps,C}^{(k)T}\int_A \left(\mathbf{B}_m^{(k)T}\mathbf{D}_m^{(k)}\boldsymbol{\varepsilon}_m^{(k)} + \mathbf{B}_b^{(k)T}\mathbf{D}_b^{(k)}\boldsymbol{\varepsilon}_b^{(k)} + \mathbf{B}_s^{(k)T}\mathbf{D}_s^{(k)}\boldsymbol{\varepsilon}_s^{(k)}\right)dA \tag{8}$$

$$\mathbf{f}_A = \sum_{k=1}^{3}\mathbf{T}_{ps,A}^{(k)T}\int_A \left(\mathbf{B}_m^{(k)T}\mathbf{D}_m^{(k)}\boldsymbol{\varepsilon}_m^{(k)} + \mathbf{B}_b^{(k)T}\mathbf{D}_b^{(k)}\boldsymbol{\varepsilon}_b^{(k)} + \mathbf{B}_s^{(k)T}\mathbf{D}_s^{(k)}\boldsymbol{\varepsilon}_s^{(k)}\right)dA \tag{9}$$

The element tangent stiffness matrices related to $\mathbf{U}_C$ and $\mathbf{U}_A$ are also readily available:

$$\mathbf{k}_C = \frac{\partial\mathbf{f}_C}{\partial\mathbf{U}_C^T};\ \mathbf{k}_A = \frac{\partial\mathbf{f}_A}{\partial\mathbf{U}_A^T};\ \mathbf{k}_{CA} = \mathbf{k}_{AC}^T = \frac{\partial\mathbf{f}_C}{\partial\mathbf{U}_A^T}. \tag{10}$$

The co-rotational transformation of local nodal forces $\mathbf{f}_C$ and tangent stiffness matrices are:

$$\mathbf{f}_G = \mathbf{T}^T\mathbf{f}_C \tag{11}$$

$$\mathbf{k}_G = \frac{\partial\mathbf{f}_G}{\partial\mathbf{U}_G^T} = \frac{\partial^2\mathbf{U}_C^T}{\partial\mathbf{U}_G\partial\mathbf{U}_G^T}\mathbf{f}_C + \mathbf{T}^T\mathbf{k}_C\mathbf{T};\ \mathbf{k}_{GA} = \mathbf{k}_{AG}^T = \frac{\partial\mathbf{f}_G}{\partial\mathbf{U}_A^T} = \mathbf{T}^T\mathbf{k}_{CA}. \tag{12}$$

It is obvious that co-rotational transformations regarding $\mathbf{f}_A$ and $\mathbf{k}_A$ are excluded, which enhances the computational efficiency of the element.

7. Examples

Two nonlinear examples are provided to examine the effectiveness of the proposed shell element (SS-AO3). Equilibrium paths are plotted in Figure 4 and 6. Results with the first order shear deformation theory (FSDT-AO3) are also plotted for comparison. Solution of 3D models (i.e. BK20 in Example 1, and SOLSH190 in Example 2) are used as reference solution. In each example, the

result with FSDT-AO3 elements deviates from the reference solution, which gives a stiffer response, thus showing the importance of incorporating the zigzag effect in these examples. On the other hand, the equilibrium path of a relatively coarse mesh with SS-AO3 elements coincide with the reference solution, which verifies the adopted zigzag function, the assumed transverse shear stress distribution, and the defined shell coordinate system. It is also clear that the proposed element is free of shear and membrane locking with the application of the optimisation approach to each individual layer. Therefore, the results of the coarse meshes with SS-AO3 elements prove the computational efficiency and accuracy of the proposed 9-noded sandwich shell element.

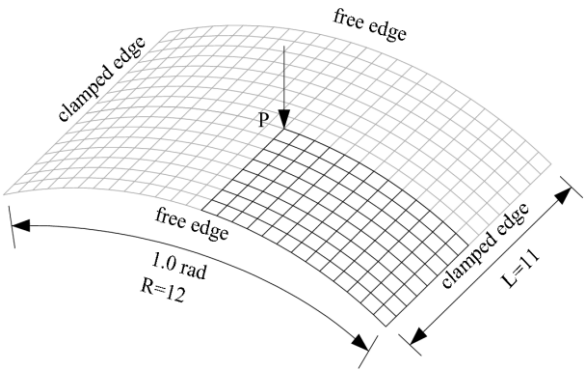

Figure 3: Cylindrical sandwich shell under point load (Example 1).

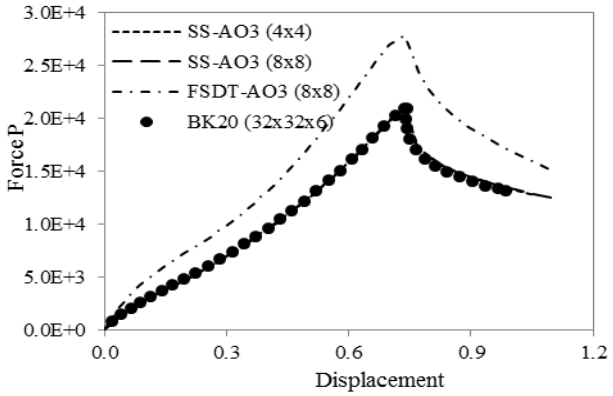

Figure 4: Comparison of equilibrium paths of Example 1 with different elements.

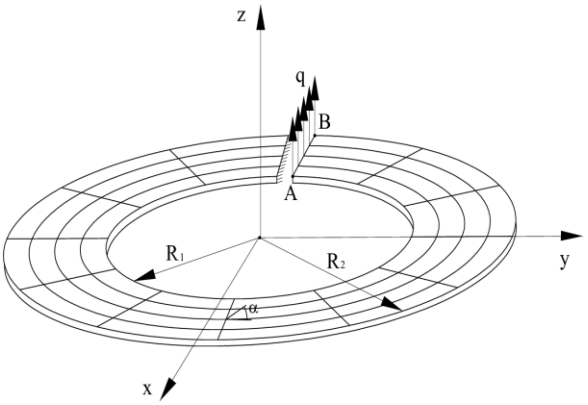

Figure 5: Annular sandwich plate under end shear with (0/0/0) layup (Example 2).

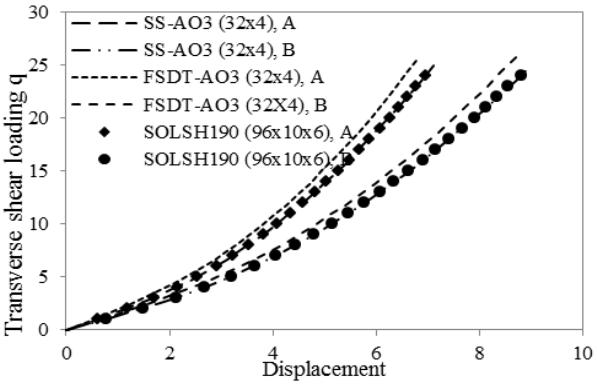

Figure 6: Comparison of equilibrium paths of Example 2 with different elements.

8. Conclusions

This paper presents a 9-noded shell element for nonlinear analysis of sandwich plates/shells. A novel zigzag displacement function specific to sandwich structures is introduced, and a simple distribution of transverse shear stresses through thickness is also assumed in the formulation. Additional freedoms associated with the zigzag effect are defined in a specific shell coordinate system for computational efficiency. Numerical examples have verified the accuracy and effectiveness of the proposed element.

References

[1] B. Izzuddin, Nonlinear Dynamic Analysis of Framed Structures. PhD Thesis, Imperial College, University of London, 1991.

[2] B. Izzuddin, Z. Li, A Co-rotational Formulation for Large Displacement Analysis of Curved Shells, in: Deeks & Hao (eds), Developments in Mechanics of Structures and Materials, pp. 1247-1253, 2004.

[3] B. Izzuddin, An optimisation approach towards lock-free finite elements, in: B. H. V. Topping (editor), Proceedings of the Eleventh International Conference on Civil, Structural, and Environmental Engineering Computing, 2007.

Proceedings of the 22nd UK Conference of the
Association for Computational Mechanics in Engineering
2 – 4April 2014, University of Exeter, Exeter

DELAY OPTIMIZATION IN REAL TIME DYNAMIC SUBSTRUCTURING TESTS ON A CABLE-DECK SYSTEM

***Maria R. Marsico[1] and David J. Wagg[2]**

[1]College of Engineering, Mathematics and Physical Sciences, University of Exeter, EX4 4QF, Exeter, UK
[2]Department of Mechanical Engineering, Sir Frederick Mappin Building, Mappin Street, Sheffield, S1 3JD, UK

*m.r.marsico@exeter.ac.uk

ABSTRACT

The dynamics of cable-stayed bridges are complex, in particular because of the complex interaction between the deck and all the cables. The whole bridge is difficult to model and to reproduce in the laboratory, moreover, the presence of many cables complicates the modeling process. As a result, the substructuring technique often represents an efficient solution for capturing its behaviour. The cable available at the Earthquake Engineering Laboratory of the University of Bristol (UK) is representative of a full scale cable on the Second Severn Crossing, a cable-stayed bridge in United Kingdom. Using this example several parameters can be considered in order to extend the developed theory to a general cable for cable-stayed bridges. The 5.4m long steel cable has been experimentally observed interacting with the deck that has been modelled numerically as a single degree-of-freedom system. The cable is excited at the bottom through a vertical actuator that transfers the input force, generated by the numerical model, to the physical structure. A time lag exists due to the latency in the acturator and the input is effectively applied later than expected. Delay compensation has been optimized in the range of the exciting frequencies and several values have been found and correlated to the magnitudes of the applied forces. Various tests have been conducted in order to compare the response of the system in the absence of delay compensation, and optimizing delay compensation. It has been shown that both the accuracy of the results and the detection of the stability boundaries of the cable are sensitive to the delay compensation process.

Keywords: *cable-stayed bridge, cable-deck interaction, delay compensation, hybrid tests, substructuring technique, time lag.*

1. Introduction

Real-time dynamic substructuring (RTDS) is a kind of hybrid testing technique. Essentially, the whole system is divided into two parts. One part of the system is physically built in the laboratory. The remaining part is modelled in the computer and it interfaces with the physical model - see [1,2,5]. RTDS technique has been adopted for the present research, to conduct tests on a cable representative of a full scale cable for a cable-stayed bridge, that interacts with the deck [3-4].
The numerical model (deck) generates the input signal. The latter is acquired by the transfer system, which is an actuator that in turn excites the physical model (cable). The signal is then acquired and closes the control loop by feeding back to the numerical model, and a new input signal is generated. The response of the physical model depends on the effective input signal, which is affected by delay.
Several approaches have been proposed to compensate for the transfer system error in RTDS tests - see [7-8] and reference therein. The authors, beside those approaches already in use, consider the online adaptive forward prediction (AFP) technique. The AFP algorithm is adopted to create a new reference signal in the time domain. The reference signal is used as the transfer system demand, then eliminating the response delay and obtaining nominally zero synchronization error between each transfer system and its numerical model [7].
This paper is concerned with the significant effects of delay compensation on the reliability of the results in RTDS tests. Section 2 is devoted to the experimental setup of the cable-deck system. In Section 3, the online adaptive forward prediction algorithm is presented. Section 4 is concerned with the effect of delay on the reliability of the results in RTDS tests conducted on the cable-deck system.

2. Cable-deck experimental setup

The theory on the cable-deck interaction considers a single degree-of-freedom system [3-4]. The mass-spring-damper model simulates the behaviour of a bridge deck, which is connected at the lower end of an inclined cable. The angle of inclination of the cable, θ, is measured from the horizontal line in the gravity plane. The cable is vertically excited at its lower (deck) support at a frequency close to its second natural frequency, which leads the cable to experience in-plane and out-of-plane vibrations. The purpose of exciting the inclined cable is

to identify its nonlinear dynamics and to mark the stability boundary of the semi-trivial solution. The latter physically corresponds to the point at which the cable starts to have an out-of-plane response when both input and previous response were in-plane.
The cable, available at the Earthquake Engineering Research Laboratory of the University of Bristol, UK, (Fig. 1) is a single wire steel cable with diameter $0.78 \cdot 10^{-3}$m and length L=5.4m, inclined at an angle $\theta = 22.6°$. The cable interacts with the numerical model of the deck through a vertical actuator. It has been designed to reproduce the behaviour of a real cable on the Second Severn Crossing, a motorway bridge in the South West of the UK [3]. In accordance with this purpose, 21 lead masses have been attached, spaced at 0.25m, except the one on the top and the one on the bottom that distance 0.20m by the ends of the cable [5]. The parameters that significantly influence the similitude of the scaled cable with the real cable have been non dimensionalised. This approach enables to extend the theory to a general inclined cable interacting with the deck, with the same nondimensional parameters.
The tension in the cable is measured by a single axial esse shape load cell, which is connected to the cable at the upper end. At the bottom of the cable, a multiaxial six-degree-of-freedom load cell measures the applied force, and a linear variable displacement transducer (LVDT) with limit displacement of ±10mm, measures the vertical displacement corresponding to the applied force. The hydraulic actuator, in displacement control, is able to apply a maximum force of 10kN and a maximum displacement of ±150mm. The acquisition system consists of two cameras, one along the cable that records in-plane modes, and one in front of it that records out-of-plane modes. The vibrations of 21 discretised points of the cable, which correspond to the added lead masses, are tracked by the Imetrum Video Gauge System (VGS). Each test has been performed, ensuring consistency of the initial setting parameters since they are considerably sensitive to the external conditions.
Moreover, free vibration tests on the cable have been conducted to measure the viscous-damping ratio ξ_n and, a reasonable damping ratio of ξ_n=0.02% has been assumed for the first four considered modes.

3. Delay in RTDS tests conducted on a cable-deck system

Experimental tests on the cable-deck system have been performed to mark the stability boundaries, such as when the cable is excited in the second in plane mode and it responds with either of the other modes. The investigation has been restricted to four modes, such as the first and the second both in plane and out of plane modes.
The tests conducted to identify the cable-deck interaction are carried out in real-time, so that the complex dynamic behaviour is captured as accurately as possible. Whereas, when RTDS tests are performed, the transfer system introduces into the desirable displacement signal a delay, τ, which will significantly affect the feedback force.
Delay in hybrid tests can be represented by two components. One, e_1, is a function that describes the accuracy of the numerical models compared to the appropriate variable in the complete emulated system. The other, e_2, represents the degree of synchronization between each transfer system and its numerical model. Both terms, e_1 and e_2, are coupled and, when substructuring complex systems, the only measure of accuracy is the degree of synchronization, e_2, which in practice is never equal to zero in RTDS tests - see [7] for the full derivation.
The effectiveness of the control algorithm is measured by using the subspace plots approach. The design interface displacement of the numerical model is plotted versus the actual position of the transfer system. Thus, the amount of delay is online predicted and a new reference signal is generated to ideally eliminate the response error. The ideal delay compensation corresponds to narrow the ellipse that plots the desirable input displacement versus the acquired input displacement, to the maximum axis inclined at 45° and the minimum axis close to zero. Any introduced delay in substructuring tests transforms the ideal straight line into an ellipse.

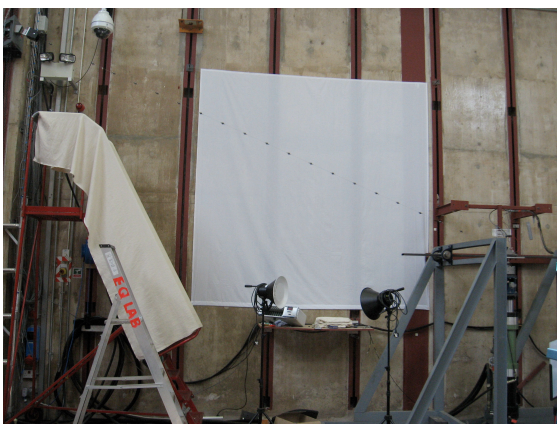

Figure 1: Cable-deck experimental setup at EERL, University of Bristol, UK.

Online procedures of delay estimation and adaptive mechanisms have been used to correct the delay parameter and to account for the system dynamics, which in fact may be varying during the test. Those procedures include the online adaptive forward prediction technique that is used by the authors to conduct RTDS tests on the cable-deck system. The AFP algorithm removes the need for tuning both the magnitude of the forward prediction and the amplitude gain for each different excitation condition. This tuning is a need for the basic Forward Prediction (FP) algorithm. Moreover, the AFP algorithm achieves high levels of synchronization for frequency dependent and transient plant conditions by closing the control loop and using the feedback dynamics of the transfer system [7]. This technique can appropriately be used when there is no knowledge of the plant dynamics and when there is transient or frequency dependent plant behaviour.
The approach used here follows the AFP technique, which is based on a polynomial estimation algorithm to compensate for the delay present in the transfer system [7]. The prediction algorithm is:

$$\delta(t)' = (P_{N,n,\underline{\Delta}}[\delta])(t+\rho) \quad (1)$$

where δ is the target displacement coming form the substructuring, $P_{N,n,\underline{\Delta}}[\delta]$ is the least squares fitting Nth-order polynomial through the n time-point pairs $(t, \delta(t))$, $(t-\underline{\Delta}, [\delta(t-\underline{\Delta})),\ldots., (t-(n-1)\underline{\Delta}, \delta(t-(n-1)\underline{\Delta}))$; ρ is the amount of the FP. The sampling time step, $\underline{\Delta}$, used in the RTDS tests is 1ms for experimentation.

4. Estimation of delay and effect on RTDS tests

A number of RTDS tests has been conducted on the cable-deck system to observe the cable's behaviour [6]. The ratio $q=\omega_g/\omega_2$, between the deck's natural frequency and the cable's second natural frequency, has been fixed as $q = 0.98$. Further tests have been conducted for $q = 1$ and $q = 1.04$, aiming to develop a general theory. The cable has been observed in the range of the excitation frequencies of $-0.03 \leq \mu \leq +0.03$, where $\mu=\Omega/\omega_2-1$ is a parameter accounting for the oscillator's frequency, and the second in-plane frequency of the cable.
Figure 2a shows the synchronization subspace plot for tests conducted when the cable is excited and it responds in the second in-plane mode, Z_2: then it is stable. Delay has been evaluated by essentially measuring the shift time between two sine wave excitations in the time domain and the value of $\tau=12$ms has been assessed (Fig. 2b). Panels c and d in Fig. 2, state the response of the cable shacked by sine waves, which are exciting its second in-plane mode for $\mu=+0.01$. The top panel shows the results from a typical test performed in the absence of delay compensation: the response of the system is substantially away from the ideal response, which is recognisable when the ellipse condenses in a line (Fig. 2d).
Steady state RTDS tests have been performed on the cable-deck system to mark the stability boundaries. Figure 3 shows the Z_2 stability boundary of the cable interacting with a deck for $\mu=+0.03$. The cable has been excited in the second in-plane mode and the maximum displacement of the quarter point has been recorded by the VGS, before that the cable vibrates in either of the out-of-plane modes.
The analytical curve shown in Fig. 3, plots the normalised amplitude of the quarter point, Z_2, against the normalised applied displacement, Δ. The curve has been defined by following the theory on the nonlinear dynamics of the cable as discussed in [4]. The parameter $\mu=+0.03$ has been chosen because the S-shape is more distinguishable then the comparison with the experimental results is appreciable. The experimental results from tests conducted with delay compensation of 12ms - stars in Fig. 3 -, follow the lower boundary branch of the S-shape curve and capture the second branch of the Z_2 response. The experimental points upon the third higher branch of the S-shape curve state the presence of higher Z_2 stability branches, which have been defined in [5].
Whereas, the experimental results from tests conducted in the presence of delay, partially catch the first lower branch and do not predict possible higher branches of the Z_2 response of the cable interacting with the deck - see the circles in Fig. 3.

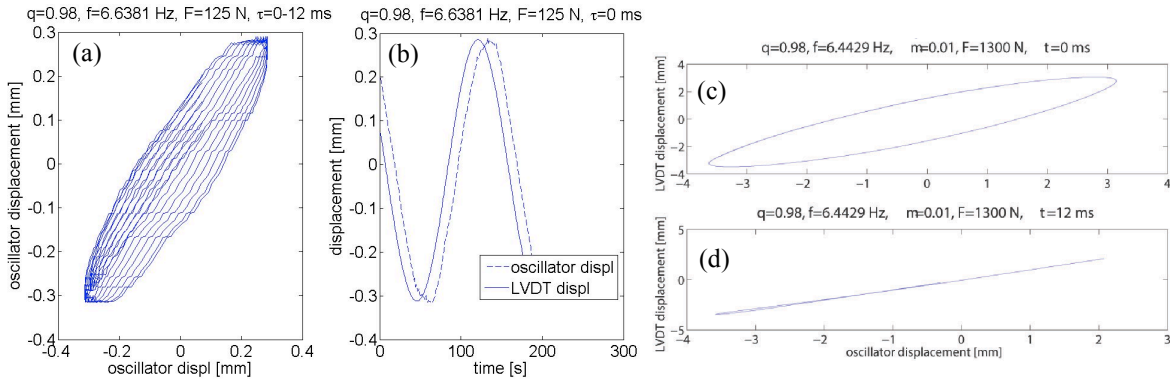

Figure 2: Estimation of delay compensation.

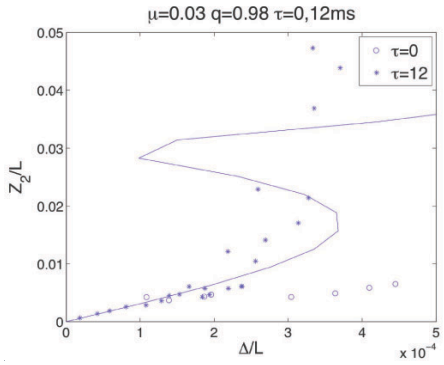

Figure 3: Second in-plane stability boundary affected by delay compensation.

Moreover, neither the second nor the third branch of the Z_2 response in the range of $2 \cdot 10^{-4} \leq \Delta/L \leq 3 \cdot 10^{-4}$ is captured by the circle points. It is evident that the presence of delay, in the form as afore discussed, has a significant effect on the prediction of the cable behaviour.

5. Conclusions

This work is concerned with the significant effect of delay on the reliability of real-time dynamic substructuring tests performed on a cable-deck system. The cable is physically present at the Earthquake Engineering Research Laboratory of the University of Bristol, UK, and the deck is modelled numerically, as a single-degree-of-freedom system. The singularity of the real-time susbstructuring technique is that the characteristics of the numerical model, which simulates the deck, can be changed in real-time, without any physical change. The cable is observed interacting with different decks and a general stability theory is experimentally validated.
The adaptive forward prediction technique has been used to compensate for the delay error, which is present in the transfer system when real-time dynamic substructuring tests are performed. It is based on a polynomial estimation algorithm that removes the need for tuning both magnitude of the forward prediction and amplitude gain for each different excitation conditions. The experimental tests conducted with compensated delay of τ =12ms capture significant aspects of the behaviour of the cable-deck system. A discrepancy between the analytical model and the experimental data is still evident for high combination of excitation force and frequency. On of the reasons of such discrepancy is that the analytical model in fact does not include the dynamic effect of the cable on the deck, which is included in the performed RTDS tests.

Acknowledgements

The author would like to acknowledge the support from the Engineering and Physical Sciences Research Council (EPSRC), under the grant EP/F030711/1.

References

[1] A. Blakeborough, J. Sieber, S. Neild, D. Wagg, B. Krauskopf. The development of real-time substructure testing. *Philosofical Transaction of the Royal Society of London* A, 34(15), pp.1869–1891,2011.

[2] O. Bursi and D. Wagg. *Modern testing techniques for Substructural System*. Springer-Verlag, 2008.

[3] V. Gattulli, L. Martinelli, et al. Non-linear oscillations of cables under harmonic loading using analytical and finite element models. *Comput. Meth. Appl. Mech. Eng*., (193) pp.69–85, 2004.

[4] J. Macdonald, M. Dietz, S. Neild, A. Gonzalez-Buelga, A. Crewe, D. Wagg. Generalized modal stability of inclined cables subjected to support excitations. *J. Sound & Vibr*, (329), pp.4515–4533, 2010.

[5] M.R. Marsico, V. Tzanov, D. Wagg, et al. Bifurcation analysis of parametrically excited inclined cable close to two-to one internal resonance. *J. Sound & Vibr*, 24(330), pp.6023-6035, 2011.

[6] M.R. Marsico, D. Wagg, et al. Real time dynamic substructuring tests on a cable-deck system in absence of delay, *Network Earthq Eng Simulation*, Dataset, 2013, DOI:10.4231/D3VX0635F.

[7] M. Wallace, D. Wagg, S. Neild. An adaptive polynomial based forward prediction algorithm for multi-actuator real-time dynamic substructuring. *Proceedings of the Royal Society*, 461, pp.3807–3826, 2005.

[8] B. Wu, Q. Wang, et al. Equivalent force control method for generalized real-time substructure testing with implicit integration. *Earth Eng & Str Dynamics*, 36, pp.1127–1149, 2007.

Proceedings of the 22nd UK Conference of the
Association for Computational Mechanics in Engineering
2 – 4April 2014, University of Exeter, Exeter

Dynamic Modeling and Analysis for Flexible Space Web

***Zhang Qingbin[1], Feng zhiwei[1] and Yang tao[1]**

[1] College of Aerospace Science and Engineering, University of National University of Defence Technology, 410073, Deya Rd. 109, Changsha, Hunan, P. R. China

*qingbinzhang@sina.com

ABSTRACT

As a new type of structure for advanced concepts in space exploration, flexible web system shows the important and potential applications in various space explorations. The dynamic behaviour of flexible web is investigated by using finite segment method. The flexible web is modelled as a set of semi-damp springs with masses lumped at appropriated nodes. The internal forces produced by the semi-damp springs are modelled based on the experimental result of cables. The motion equations of each node are derived by Newton's law with considering internal elastic force and external forces including the aerodynamic force and gravity. Then a flexible multibody systems model is build to predict the dynamics behaviour of the space web. The effective area, flight rang, and web shape in the orbital environment is compared with the one in ground for various size of web and deployment velocity. The results can be used to the design and analysis of the future space web application system.

Keywords: *dynamic modelling; Newton's law; flexible web*

1. Introduction

Flexible net system which can be used to capture failed satellites is of increasing interest in many aerospace applications. Several on-going studies indicate the potential. ROGER sponsored by ESA employed flexible tether-net to capture the target, which could be a satellite or an upper stage or another debris part. With funding from the DARPA, Star Inc. revealed plans for a spacecraft equipped with nets called Electrodynamics Debris Eliminator (EDDE). University of Tokyo has been proposing a large space membrane structure named "Furoshiki Satellite" as a promising candidate for the future structure for those missions requiring large area in space, such as a solar cell or a large communication antenna [1].

Flexible net systems can be regarded as complex tethers system, and there are two basic approaches which are often used to model general tethers system. Recently, some numerical and experimental investigations were performed for this new type of spacecraft. Mattias employed the commercial software LS-DYNA to demonstrate a robust method for space webs spinning deployment [2]. Onoda investigated a constant angular velocity-deployment and stabilization of a spinning solar sail [3]. Zhai developed a capture error compensate strategy using feedforward control method [4].

This paper aims to build a high-fidelity simulation model for flexible net system, which can predict the behaviours for space debris removal. In the presented mathematical model, the flexible net is modelled as a series of point mass connected by semi-spring-dampers. Meanwhile, the tether properties such as stiffness and damp ratio are obtained from experiment data, the aerodynamic force of each segment is considered for ground test. The dynamic model is firstly verified by ground test. The simulation results are in well agreements with experiment data. Then, characteristics of space flexible net, such as shape and strain distribution, are investigated for the given mission of orbital capture.

2. Space net system

As shown in Fig.1, the space net capture mechanism is generally consisting of some flying weights, a container and a flexible net. The flexible net can be stowed in a canister, which is in the mid of the four flying weights. Once it has the task to capture the target, each flying weight would be firstly accelerated by a spring or explosive device, and immediately pull out the net. After some time, the flexible net along with the flying weights would unwrap and fly to the target until that it hit the target at some speed and tangle around it totally. There are three aspects to model this process, namely, deployment, free flying and terminal covering. This paper focuses on the dynamic modelling of deployment and free flying.

As shown in Fig.2, there are two manners for ejecting nets. One method is that the net is deployed by the flying weights located the corner of nets, another method is that the net is firstly deployed from the center point, and then opened by the flying weights.

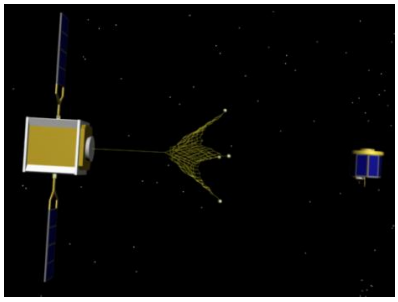

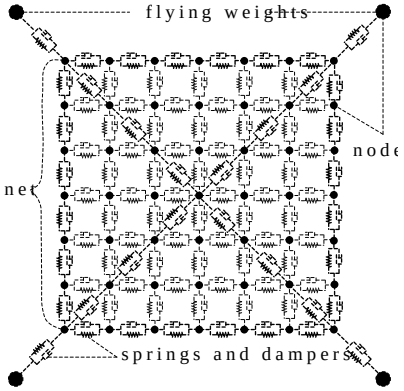

Fig.1: Scene of orbital capturing Fig. 2: Finite segment model of flexible net

3. System model

As shown in figure 3, the segment l_{ij} conect the i^{th} and j^{th} mass point. Each tether segment is assumed to be a semi-spring and damper, which can only afford tension.

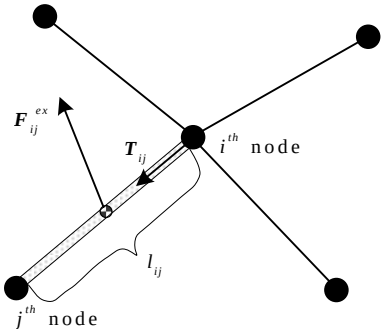

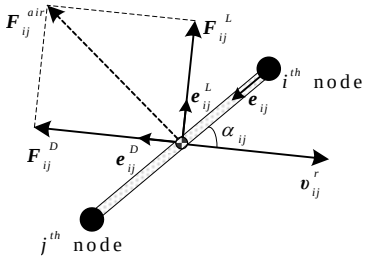

Fig. 3: Semi-spring model for tether segment Fig. 4: Aero force acted on tether segment

For the sake of simplicity, the aerodynamics and gravitational force are lumped to each point mass by taking half from adjacent segment. Then the equations of motions of i^{th} tether node can be given by

$$m_i \ddot{\boldsymbol{r}}_i = \sum_{j\in R(i)} \boldsymbol{T}_{ij} + \sum_{j\in R(i)} \frac{1}{2}\boldsymbol{G}_{ij} + \sum_{j\in R(i)} \frac{1}{2}\boldsymbol{F}_{ij}^{D} + \sum_{j\in R(i)} \frac{1}{2}\boldsymbol{F}_{ij}^{L} \tag{1}$$

Where $R(i)$ is the index set related with i^{th} node. It should be noted that all the above-mentioned equations of motion for flying weights and tether nodes are nonlinear, and the nonlinearity is obviously caused by the rigid body motions and the aerodynamic forces.

In this work, the forces on each tether segment include the gravity, lift and drag. Gravities which act on both flying weights and tether nodes are assumed to be invariant with altitude, can be obtained by

$$\boldsymbol{G}_i = m_i \boldsymbol{g} \tag{2}$$

For the aerodynamic forces acting on the tether segment can be determined from cross flow principle. As shown in figure 4, each tether segment is treated as an ideal cylinder with no porosity. The aerodynamic lift and drag coefficients are defined as functions of the segment angle of attack α_{ij}. The lift and drag coefficients C_{ij}^{D}, C_{ij}^{L} for an inclined cylinder are given

$$C_{ij}^{D} = C_{ij}^{f} + C_{ij}^{b}\sin^{3}\alpha_{ij} \approx 0.022 + 1.1\sin^{3}\alpha_{ij}$$
$$C_{ij}^{L} = C_{ij}^{b}\sin^{2}\alpha_{ij}\cos\alpha_{ij} \approx 1.1\sin^{2}\alpha_{ij}\cos\alpha_{ij} \quad (3)$$

Where C_{ij}^{f} and C_{ij}^{b} are skin-friction and cross flow drag coefficient. Hence, the drag and lift vectors can be written as

$$\boldsymbol{F}_{ij}^{D} = \frac{1}{2}\rho^{air}C_{ij}^{D}d_{ij}l_{ij}^{0}\left\|\boldsymbol{v}_{ij}^{r}\right\|^{2}\boldsymbol{e}_{ij}^{D}$$
$$\boldsymbol{F}_{ij}^{L} = \frac{1}{2}\rho^{air}C_{ij}^{L}d_{ij}l_{ij}^{0}\left\|\boldsymbol{v}_{ij}^{r}\right\|^{2}\boldsymbol{e}_{ij}^{L} \quad (4)$$

where $\boldsymbol{v}_{ij}^{r}$ is the wind velocity of the center of segment l_{ij}, $\boldsymbol{e}_{ij}^{D}$ and $\boldsymbol{e}_{ij}^{L}$ are drag and lift vectors respectively.

The elastic forces of tether segments are due to the spring and damper characteristics of the tether, these forces are parallel to the direction of the tether segment. There are certain circumstances where the tether loses tension. However, a tether cannot sustain compression forces. The elastic force in segment l_{ij} is thus given by

$$T_{ij} = \begin{cases} 0 & l_{ij} \le l_{ij}^{0} \\ p(\varepsilon_{ij}) + c_{ij}\dot{\varepsilon}_{ij} & l_{ij} > l_{ij}^{0} \end{cases} \quad (5)$$

Where ε_{ij} the strain in segment is (i, j), $\dot{\varepsilon}_{ij}$ is the strain rate, k_{ij} is the elastic constant, and c_{ij} is the damping constant.

4. Simulation Results

It is very important to do a lot of ground tests for verifying and improving the dynamic model, since it is very expensive and difficult to do experiments in space environment. The space net mechanism for ground tests is illustrated in figure 5. The mechanism is constructed by ejecting device and net storing chest. The net for tests is rectangular with for

Two characteristic parameters are very important for the orbital capture operation, one is the effective area which is determined by four flying-weights, and the other is the range of flying-weights. Therefore, numerical simulations were compared with the experiments results in figure 5 and figure 6. It is clear that the solutions obtained by mathematic model consist with those by ground test. The difference between numerical simulation and ground test is caused by wind gust, which is stasis in magnitude and orientation. The above-mentioned simulation results show the variety of the presented dynamics model.

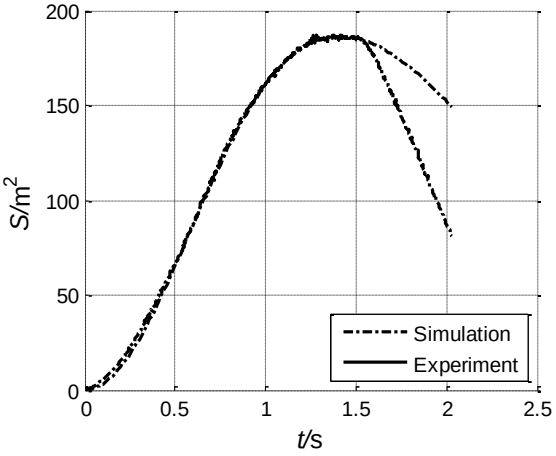

Fig. 5: Area of net during deployment

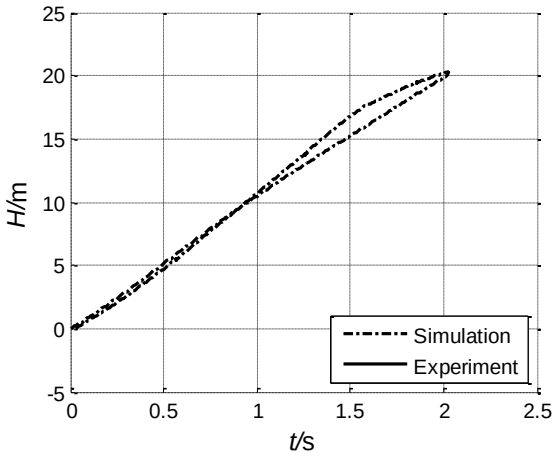

Fig. 6 Flight range of net during deployment

Error! Reference source not found. Figure 7 shows the shapes of space net at various instants, along with the tension in each tether segments. Note that it is very difficult to obtain the positional information of nets due to its painful thickness, and the position information of flying weights can be accurately obtained using optical instruments. It should be emphasized that there is a remarkably difference between the orbit and ground environment, meaning that an important issue is to correct the modeling for orbital capture mission. The aerodynamic forces can be neglected for the case of orbital capture, while the gravity of GEO is very smaller than ground.

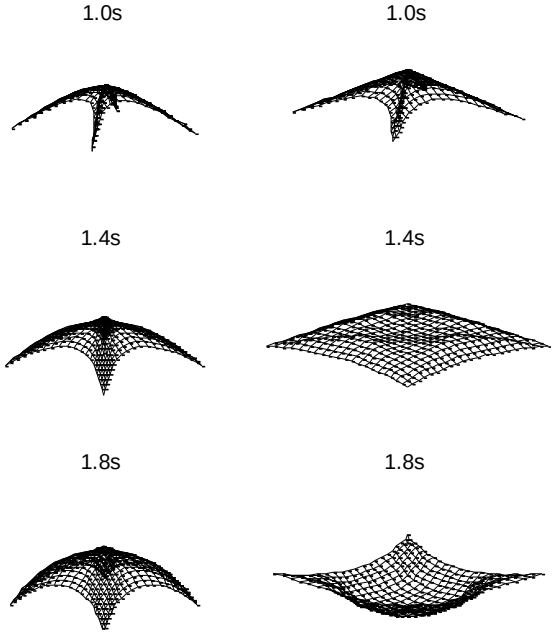

(a) Ground simulation (b) Orbital simulation

Fig. 7: The shape of space nets during deployment

In practice, the effective area of flexible net which is mainly determined by initial ejection velocity is very important for the design of orbital capture. A set of numerical results are obtained to assess the effect of ejection velocity for flying weights. The ejection speed used is 10m/s, then behaviour of net are investigated for the ejection angle of 15° and 30° respectively. As illustrated in figure 8, a bigger speed of ejection of flying weights result in a larger projection area of flexible net, along with a shorter range. For another case, the two different ejection angles with same speed are investigated. The comparison of projection area of the net is plotted in figure 9. All these simulations highlight that it is very important to select an appropriate ejection velocity for the given capture mission.

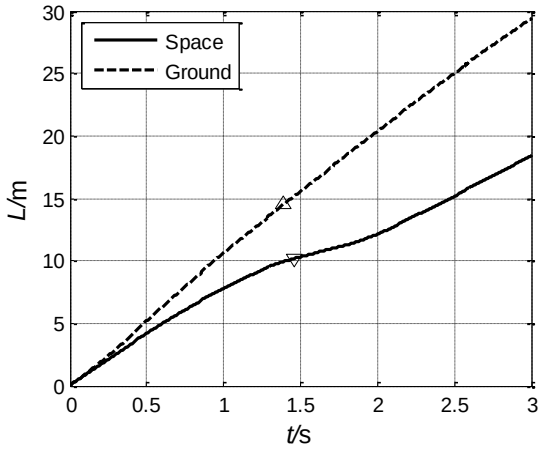

Fig. 8: Flight range of the center of space nets

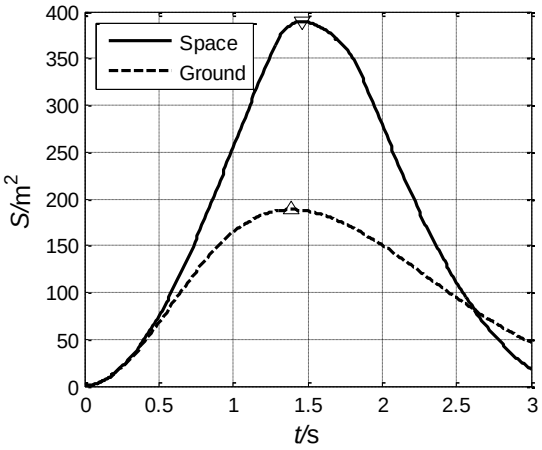

Fig. 9: The curve of effective area

5. Conclusions

Lightweight flexible net systems have potential applications for space debris removal, and require appropriate modeling techniques. Deployment of space nets is a contemporary issue for advanced concepts in space exploration. A nonlinear model was developed using a lumped-mass approach, along with a variable-mass tether segment to describe deployment. The simulation results match well with experiment data, which demonstrated the variety of the presented model. Because of its generality, this model would be useful for other investigators working with nets or webs in space.

Acknowledgements

This study was co-supported by the National Natural Science Foundation of China (Grant No 11272345). The authors would also like to thank the anonymous reviewers for their critical and constructive review of the manuscript.

References

[1] Shinichi Nakasukaa,et al，Large membrane“Furoshiki Satellite”applied to phased array antenna and its sounding rocket experiment, *Acta Astronautica*, 58 (2006) 395-400

[2] Mattias Gärdsback, Gunnar Tibert. Deployment Control of Spinning Space Webs, *Journal of guidance, control, and dynamics*, vol. V32, No. 1, 2009

[3] Onoda, J., Takeuchi, S., and Aoki, Y. A preliminary investigation of a spin-stabilised

[4] Guang Zhai, Yue Qiu,Bin Liang,Cheng Li, On-orbit capture with flexible tether–net system *Acta Astronautica* 65 (2009) 613-623

Proceedings of the 22nd UK Conference of the
Association for Computational Mechanics in Engineering
2 – 4April 2014, University of Exeter, Exeter

KRIGING MODELS FOR COMPENSATING THERMAL RESPONSE IN MEASUREMENTS FROM BRIDGE MONITORING

***R. Kromanis and P. Kripakaran**

College of Engineering, Mathematics and Physical Sciences, University of Exeter, North Park Road, Exeter EX4 4QF

*rk296@exeter.ac.uk

ABSTRACT

Recent studies in structural health monitoring have shown that bridge response to temperature effects masks effects of live loads and critical defects on structural behaviour in measurements collected from long-term monitoring. This paper aims to resolve this challenge by applying kriging surrogate models for compensating thermal response in measurements. Initially kriging models are trained for thermal response prediction from distributed temperature and response measurements collected over a period when the structure is known to behave normally. Later these models are used to predict thermal response from real-time measurements of distributed temperatures. The proposed approach is studied on a continuously-monitored laboratory truss structure exposed to accelerated temperature variations in healthy and damaged conditions. Results show that kriging surrogate models accurately predict thermal response and thereby offer support for detection of anomalous structural behaviour.

Keywords: *structural health monitoring, kriging surrogate model, thermal response, data interpretation*

1. Introduction

Accurate understanding of structural behaviour of bridges can assist bridge managers and owners in optimal maintenance of these valuable assets. Structural health monitoring (SHM), which is seen as a means to identify real structural behaviour, is often limited by the difficulty in inferring structural performance from measurements. Commonly employed model-based methods are resource-intensive requiring experts to create complex finite element (FE) models. In contrast, data-driven methods, which are solely based on the interpretation of collected measurements, show promise for revealing previously unseen structural behaviour without requiring expensive modeling [5]. However, the sensitivity of both model-based and data-driven methods is severely limited by the effects of continuously changing environmental conditions, which can neither be fully captured nor accurately modeled using current approaches.

Of the various environmental parameters, temperature variations are increasingly recognized as the key factor governing quasi-static structural response of bridges [3,10,12]. Consequently, accounting for thermal response is critical in understanding long-term measurements from bridge monitoring. For most bridges, measured structural response can be approximated as its thermal response [1,8]. This premise is validated in previous research [9] in which regression algorithms such as support vector regression and artificial neural networks are employed for generating statistical models capable of predicting response from distributed temperatures.

This study investigates if kriging surrogate models can provide more accurate and reliable estimates of thermal response compared to other previously studied statistical regression models. Kriging models are widely used as surrogates for complex finite element models in computationally expensive tasks such as design optimization and have the potential to accurately capture the relationship between distributed temperature measurements and structural response. This paper presents preliminary results from a study undertaken to evaluate this hypothesis on measurements collected from a continuously monitored laboratory truss.

2. Surrogate Models

Figure 1 illustrates our approach of using surrogate models to understand measurements from structural health monitoring (SHM). The concept is similar to many existing data-driven strategies for measurement interpretation. However, the novelty is in its capability to systematically compensate for thermal effects. This paper is mainly concerned with two stages - surrogate model generation and real-time model application. Measurements from a monitored bridge are collected and communicated for storage and processing. They are initially treated for noise and outliers in data-sets. Subsequently, principal component analysis (PCA) is employed to reduce the dimensionality of data-sets. Specifically, this research uses PCA to transform correlated temperature inputs into a set of uncorrelated variables, often referred to as principal components (PCs) [6].

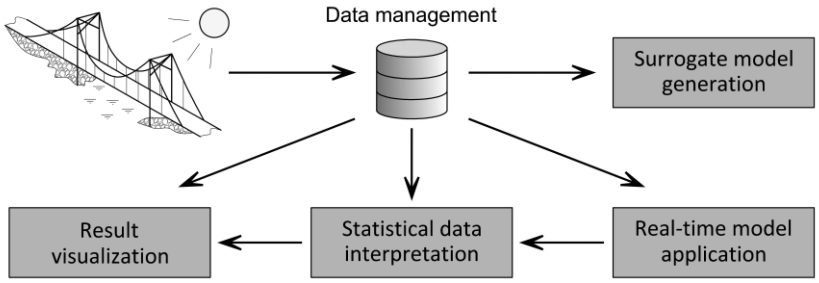

Figure 1: Structural health monitoring paradigm with surrogate model

The optimal size and period of training sets for surrogate models is dependent on the nature of measurements. For generating reliable models, training sets must cover the full range of variability expected in measurements [15]. However, decreasing the number of individual measurement time-points in the training set only marginally reduces prediction accuracy of surrogate models [9]. Therefore, even though large data-sets may be available, a small subset may be sufficient for model training. While many regression algorithms evaluate the accuracy of prediction models on a subset of the training set, in this study we use measurements collected after the training period to evaluate the prediction accuracy. Root mean square deviation (RMSD) is employed to measure the difference between time-series of predicted and measured response. The overall accuracy of the model, i.e., the performance with respect to all sensor locations, is evaluated in terms of its RMSD and accuracies at individual sensor locations are taken into account by considering its range of measurements.

3. Kriging Modeling and Prediction

Kriging is a powerful interpolation and spatial averaging tool originally developed for spatial analysis in geostatistics and hydrosciences [4,13]. Conceptually, kriging is a regression-based approach, where a model is created from optimal interpolation between given data points, which are weighted in accordance to their spatial covariance [2]. A description of the mathematics behind kriging analysis can be found in [14]. In this study DACE: A Matlab kriging toolbox [11] is chosen to create surrogates. The construction of surrogates is a one-step process requiring input and output data, selection of regression and correlation functions [11] and a kriging hyper-parameter (θ) [7].

4. Case Study: Laboratory Truss

A truss, composed of aluminium sections and monitored in the structure lab at the University of Exeter, serves as a test-bed for the study. The layout of the truss is shown in Figure 2 (left). It is 0.5m heigh and spans 3.2m. Double channel sections are form top and bottom chords and outer diagonals, and flat bars are used for other elements. All joints are connected with six bolts. Three infrared heaters, located 0.5m above and 0.2m behind the truss, are employed to alter temperature across the entire truss. Heaters are automatically switched on for 45 minutes every 1½ hours thus emulating diurnal temperature cycles. Measurements are collected every 10 seconds with 540 measurements in a full simulated diurnal cycle. Structural response closely follows temperature variations as shown by

plots of temperature and strain variations over a diurnal cycle in Figure 2 (right).

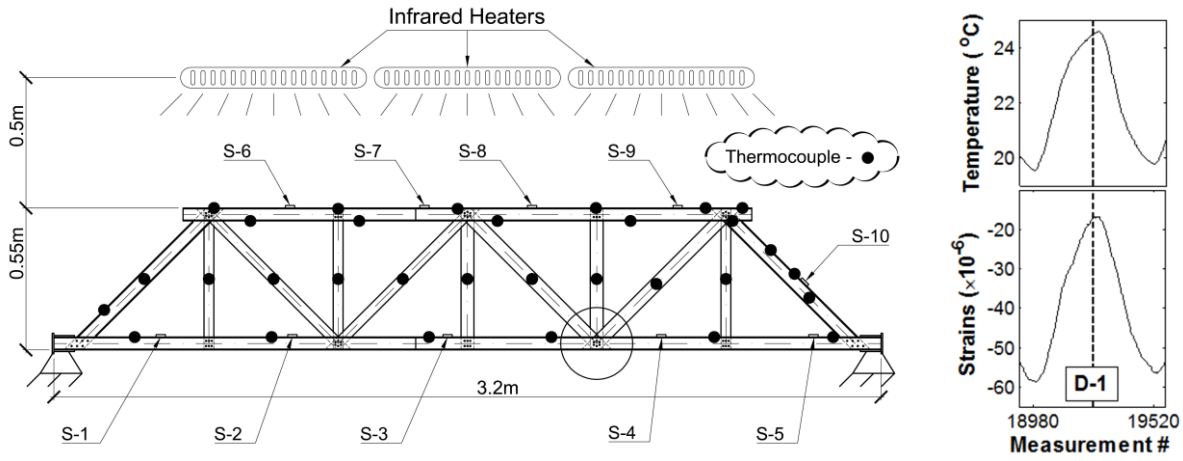

Figure 2: Sketch of the truss (left) showing the location of strain gauges (S-i, i = 1, 2, …, 10), thermocouple (black dots) and damage location (circled joint); Plots of temperature (top right) and strain (bottom right) measurements collected at the bottom chord of the truss over a simulated diurnal cycle.

The truss is monitored under normal and damaged conditions. Damage is introduced abruptly by removing bolts from joints. The performance of surrogate models is evaluated on measurements collected over a period of 64 simulated days. In this period two-stage damage is introduced. D-1 corresponds to the first stage when three bolts are removed from the joint located left to the strain gauge S-4 (Figure 2 (left) - circled joint) and D-2 to the second stage when two additional bolts are removed from the same joint. D-1 and D-2 are introduced on the 36th and 52nd simulated days. Measurements from the first twelve simulated days form the training set and those from the next four simulated days form the test set.

5. Results

Kriging models are trained and tested for a number of model parameter settings. Prediction accuracy depends on choice of pre-processing methods, training and test periods, and number of input time-points. The best prediction accuracy is achieved when $\theta = 10$, and first-order polynomial regression and exponential correlation models are chosen.

RMSD of less than 2% of measured range of each sensor for the test period is achieved using a small number of PCs. The range of response depends on the location where measurements are taken. Figure 3 (left) shows that there is good agreement between measured and predicted strain time-histories. The overall performance of kriging surrogate models is demonstrated in Figure 3 (right), where RMSDs for each sensor are evaluated versus the number of PCs. This study aims to find surrogate models capable of predicting response with high accuracy while, at the same time, being computationally inexpensive by limiting the number of PCs. As can be observed from Figure 3 (right), minimum RMSD is obtained when using 14 PCs. However, the accuracy only improves marginally when the number of PCs is increased beyond 7.

6. Conclusions

The following conclusions can be drawn from this study:

- Kriging surrogate models accurately predict thermal response from distributed temperatures.
- Prediction accuracy is high even if only the first few PCs of temperature measurements are used as input to surrogate models.

Future work will (i) investigate the interpretation of PE signals for anomaly detection using signal processing techniques and (ii) compare obtained results with previously employed approaches.

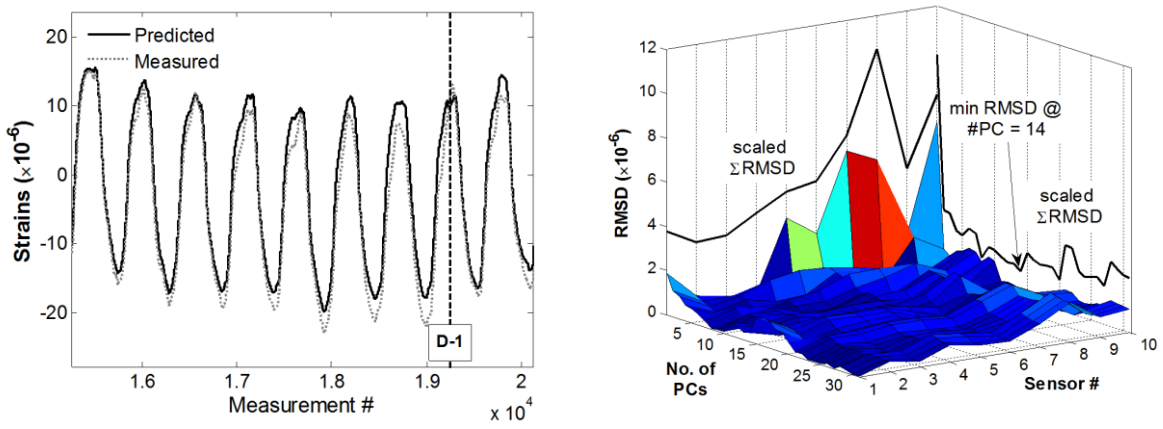

Figure 3: A portion of predicted and measured strain time-series of S-4 (left) and a surface plot of prediction accuracy of measurements for each sensor and number of PCs.

References

[1] F.N. Catbas, M. Susoy, D.M. Frangopol, Structural health monitoring and reliability estimation: Long span truss bridge application with environmental monitoring data. *Engineering Structures*, 30, 2347–2359, 2008.

[2] N. Cressie, The origins of kriging. *Mathematical Geology*, 22, 239–252, 1990.

[3] E.J. Cross, K.Y. Koo, J.M.W. Brownjohn, K. Worden, Long-term monitoring and data analysis of the Tamar Bridge. *Mechanical Systems and Signal Processing*, 35, 16–34, 2013.

[4] J.P. Delhomme, Kriging in the hydrosciences. *Advances in Water Resources*, 1 (5), 251–266, 1978.

[5] J.A. Goulet, A. Der Kiureghian, Forecasting anomalies using monitoring data and dynamic Bayesian networks. 6th International Conference on Structural Health Monitoring of Intelligent Infrastructure, 2013.

[6] I.T. Jolliffe, *Principal Component Analysis*, 2nd Editon, Springer-Verlag Inc. New York, 2002.

[7] I. Kaymaz, Application of kriging method to structural reliability problems. Structural Safety, 27, 133–151, 2005.

[8] R. Kromanis, P. Kripakaran, Support vector regression for anomaly detection from measurement histories. *Advanced Engineering Informatics*, 27, 486–495, 2013.

[9] R. Kromanis, P. Kripakaran, Predicting thermal response of bridges using regression models derived from measurement histories. *Computers & Structures*, In Press, 2014.

[10] V. Livina, E. Barton, A. Forbes, Tipping point analysis of the NPL footbridge. *Journal of Civil Structural Health Monitoring*, DOI: 10.1007/s13349-013-0066-z, 2013.

[11] S.N. Lophaven, H.B. Nielsen, J. Søndergaard. *DACE-A Matlab Kriging toolbox*, version 2.0, 2002.

[12] J. Mata, Interpretation of concrete dam behaviour with artificial neural network and multiple linear regression models. *Engineering Structures*, 33, 903–910, 2011.

[13] M.A. Oliver, R. Webster, Kriging: a method of interpolation for geographical information systems. *International Journal of Geographical Information System*, 4 (3), 313–332, 1990.

[14] M.L. Stein, *Interpolation of spatial data: some theory for kriging*, Springer, 1999.

[15] K. Worden, H. Sohn, C.R. Farrar, Novelty Detection in a Changing Environment: Regression and Interpolation Approaches. *Journal of Sound and Vibration*, 258, 741–761, 2002.

Proceedings of the 22nd UK Conference of the
Association for Computational Mechanics in Engineering
2 - 4 April 2014, University of Exeter, Exeter

PERFORMANCES OF RUBBER BEARINGS BY VARYING THE RUBBERS PROPERTIES

***Maria R. Marsico[1] and Harry J. Norman[1]**

[1]College of Engineering, Mathematics and Physical Sciences, University of Exeter, Exeter, EX4 4QF

*m.r.marsico@exeter.ac.uk

ABSTRACT

Base isolation is a well-consolidated technology, normally used in buildings to reduce the damages from seismic events. The elastomeric bearings are the most common base isolation devices, essentially consisting of vulcanised layers alternately of rubber and thin steel, and they typically have steel plates at the top and at the bottom. They are stiff in the vertical direction, to carry the vertical load that a structure imparts, whereas they are flexible in the horizontal direction to allow for movement during ground oscillations. Multilayer rubber bearings can experience a form of instability called buckling, which is significantly affected by the properties of the rubber. For instance, the bulk compressibility of the rubber, despite being a hard parameter to measure, reduces the effective compression modulus of the rubber-steel composite. As a consequence, it reduces the buckling load of the bearing. This effect is much considerable when the dimensionless measure of the aspect ratio of the single layer of the elastomer - the first shape factor - increases up to 30-40, which is an ordinary range for commercial bearings. Extensive research has been conducted into the design of base isolation bearings to optimise their performances, resulting then in saved lives and in reducing the damages inflicted on buildings during a seismic event. In order to characterise the stability behaviour in multilayer bearings when the rubber properties vary, an analytical investigation was conducted. Three shear moduli have been considered and the effect on the buckling load in both circular and square bearings has been observed. The bulk compressibility has been also included for the bearings with shape factor greater than 10. Further, a finite element model was used to validate the analytical model and to investigate the effects that the rubber properties have on the bearings coping with a seismic event.

Key Words: *Elastomeric Bearing; Buckling Load; Shear Modulus; Bulk Compressibility; Finite Element Model*

1. Introduction

The elastomeric bearings are the most common base isolation devices, which have been used for buildings especially in earthquake prone areas, since the early 1980s [5]. They essentially consist of vulcanised layers alternately of rubber and thin steel, and they typically have steel plates at the top and at the bottom. They are stiff in the vertical direction, to carry the vertical load that the superstructure imparts, whereas they are flexible in the horizontal direction to allow for movement during ground oscillations.

A significant aspect of a rubber bearing design is the prediction of its instability. The buckling load of a base isolation bearing, together with the concept of the effective reduced area due to the horizontal displacement, have been comprehensively studied by Kelly and Konstantinidis in [5]. They suggest that the effect of bulk compressibility should be included into the design of the traditional rubber bearings, which have the shape factor $S > 10$, where S is a dimensionless measure of the aspect ratio of the single layer of the elastomer. A relevant study on the tension buckling in the rubber bearings was conducted by Kelly and Marsico [6] that investigates the effects of the cavitations in the rubber.

The rubber used for seismic isolators is typically categorised into either high or low damping rubber. Especially when concerning high damping rubber, it is difficult to accurately estimate the bulk modulus of the rubber. Moreover, high damping rubber can express nonlinear behaviour and the assumption that the rubber is incompressible overestimates the buckling load [5].

2. Analytical model of rubber bearing

The analytical model adopted to predict the buckling instability load in multilayered elastomeric bearings is based on the theory proposed by Haringx, and later applied by Gent [5, 4] on the problem of the stability of multilayered rubber compression springs. The buckling load, P_{crit}, is defined as:

$$P_{crit} = (P_S \cdot P_E)^{1/2} \ . \tag{1}$$

P_S is given by $P_S = G \cdot A \cdot \frac{h}{t_r}$, where G is the shear modulus, A is the area of the bearing, t_r is the total thickness of the rubber in the bearing and h is the total height of the bearing (rubber plus steel). P_E is the Euler buckling load for the standard column and it is given by $P_E = \frac{\pi^2}{h^2} \cdot \frac{1}{3} \cdot E_c \cdot I \cdot \frac{h}{t_r}$, where I is the moment of inertia of the cross section of the bearing, about the axis of bending. E_c is the instantaneous compression modulus of the rubber-steel composite - see [5] for an extensive discussion.

2.1. Effect of horizontal displacement and bulk modulus

The critical load, as defined in Eq. 1, provides acceptable values when either the bearing states in the undeformed position or it is slightly horizontally displaced. It is essentially controlled by the horizontal stiffness of the bearing, K_H, which is defined as $K_H = \frac{GA}{t_r}$. However, structural bearings are always required to support vertical loads, P, which reduces the horizontal stiffness to:

$$K_H = \frac{GA_S}{h} \cdot \left[1 - \left(\frac{P}{P_{crit}}\right)^2\right] \ , \tag{2}$$

where the effective shear area, $A_S = A \cdot h/t_r$. In addition, the horizontal displacement experienced by a bearing during a seismic event, reduces the bearing cross sectional area that effectively supports the load, to A_r. As a consequence, the horizontal stiffness even reduces.

Although Kelly et al. [5] suggest that complex non linear analysis is required for the bearings that, during a seismic event, experience peak vertical load combined with peak horizontal displacement, the following approximation for the critical load is reasonably acceptable:

$$P_{crit(A_r)} = P_{crit} \frac{A_r}{A} \ . \tag{3}$$

In the simplified analytical model, the deformation of the rubber is typically assumed as a constant volume one and the rubber is considered incompressible. Those assumptions are valid in most of the applications and give reasonable results in the prediction of the buckling load. However, studies on the bearings agree that the effect of the rubber bulk modulus, K, should be taken into account in the definition of the critical load in the bearings with shape factor $S > 10$ [5]. Then, the formula for the critical load for circular and square bearings becomes respectively:

$$P_{crit(K)} = \frac{GS\pi A_r}{t_r} \cdot \left[2 \cdot \left(1 - \frac{3GS^2}{K}\right)\right]^{\frac{1}{2}} \quad P_{crit(K)} = \frac{GS\pi A_r}{t_r} \cdot \left[\left(\frac{6.73}{3} - \frac{6.73GS^2}{K}\right)\right]^{\frac{1}{2}} \ . \tag{4}$$

2.2. Low and High Damping rubber

The parameters of the rubber that significantly influences the buckling behaviour are the shear modulus, G, and to a certain extent the bulk modulus, K. The hardness of the rubber is measured on the Shore durometer scale by using the International Rubber Hardness Degree (IRHD), which varies between 0 for liquid and 100 for hard plane surface. Lindley [7] gives a range of K values, based on IRHD values varying from 30 to 75 IRHD, from 1000 to 1300 N/mm^2, whereas Fuller et al. [3] give values ranging from 2000 to 3500 N/mm^2.

The amount of damping in base isolation bearings has a significant effect on the amplitude of the structure's oscillations. Low damping rubber is either natural rubber or a synthetic rubber such as neoprene. Low damping rubber shows linear behaviour up to shear strains of 100% and normally has damping in the range of 2-3% of the critical one, along with not being subject to creep. Conversely, high damping rubber consists of natural rubber with the addition of particulates filler increasing the damping up to almost 20%. Nevertheless, it exhibits nonlinear behaviour at shear strains less than 20% [5].

3. Buckling load varying the rubber's properties

The buckling behaviour of a rubber bearing was firstly investigated analytically through a linear analysis. Two models have been considered. The geometry of the circular model has been defined by considering existing manufactured bearings with $S<10$ [2] and the square bearing has been modelled by equating the bearing cross sectional areas, stating the other dimensions the same in both bearings. Three different shear moduli G, respectively equal to $0.294N/mm^2$, $0.55N/mm^2$, and $1.1N/mm^2$, as representative of low, medium and high damping rubbers have been chosen. The influence of the applied load on the horizontal stiffness, K_H, for the three rubbers is shown in Fig. 1, where it is evident that bearings with high initial K_H have a more rapid reduction in the horizontal stiffness as the load reaches the critical load.

The effect of the horizontal displacement on the buckling load was investigated by introducing the concept of the reduced area, as afore stated in Eq. 3. The reduced area has been evaluated for the horizontal deflections, expressed as a function of the side length (a) or diameter (ϕ) of the bearing. Figure 2 shows the effect of the horizontal displacement on the buckling load. For the square bearing - thin lines - a linear reduction in buckling load is shown, whereas for the circular bearing - thick lines - the reduction is apparently nonlinear. It is also shown that the buckling load is zero when the horizontal deformation of the bearing is equal to the width of the bearing. On the contrary, studies demonstrated that the bearing has still the capacity to resist a load under large horizontal deformation and that the concept of reduced area underestimates the critical load at high strains [8]. The plausible reason of this incongruity is that the analytical model does not take into account the nonlinear behaviour of rubber, that can occur at high strains and can be more prevalent in high damping due to the addition of fillers.

The bulk effect on the buckling load has been investigated on two new rubber bearing models, circular and square, with $S=30$. The dimensions have been chosen to be comparable with the commercial bearings' ones [5]. Both bearings shown in Fig. 3 have been modelled by using a commercial software package Abaqus [1]. The steel layer was modelled as an elastic material and the rubber layer was modelled by using a hyperelastic model, which is normally valid for materials that show instantaneous elastic response up to large strains. The buckling load is investigated by varying the rubber properties of the bearings.

The buckling load was investigated by using the eigenvalue buckling prediction procedure, along with the Modified Riks Algorithm, MRA. The eigenvalue buckling prediction works by estimating the elastic buckling by an eigenvalue extraction. It gives appreciable values when concerning the behaviour of stiff structures, where the response before buckling is linear. Negative eigenvalues indicate that the analysed model would buckle if the load was applied in the opposite direction.

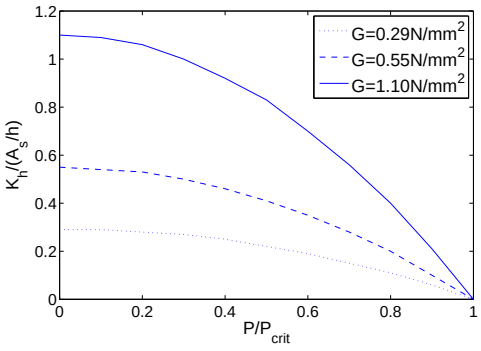

Figure 1: The influence of a vertical load on the horizontal stiffness for three different rubbers.

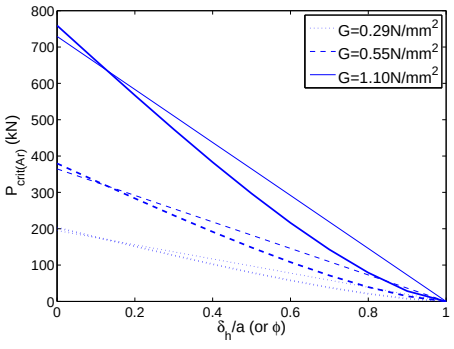

Figure 2: Effect of horizontal displacement on critical load: square and circular bearings (thin and thick lines).

4. Results and Conclusions

The finite elements models predict the buckling load in compression to be larger than the one predicted analytically, P_{crit}, for both square and circular bearings - see Tables 1 and 2. However, the finite elements analysis validates the analytical model by showing that any increase in G will result in an increase in P_{crit}.

In addition, the buckling analysis conducted with the software Abaqus produces some negative eigenvalues, which indicates that the bearing would buckle if the load was reversed, i.e. a tensile load not a compressive load. For both square and circular bearing the buckling load in tension, $P_{crit(\lambda:T)}$, is less than

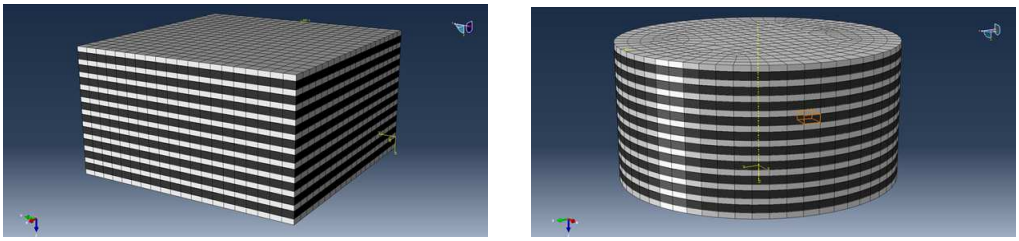

(a) Square bearing (b) Circular bearing

Figure 3: Finite Element model of the bearings. The grey layers represent the steel shims and the black layers represent the rubber layers.

the buckling load in compression, $P_{crit(\lambda:C)}$. This agrees with the theory developed by [6], who found that the tensile buckling load is always less than the compressive load.

Table 1: Critical buckling load for square bearing

G (N/mm^2)	$P_{crit}(kN)$	$P_{crit(\lambda:T)}(kN)$	$P_{crit(\lambda:C)}(kN)$
0.29	198.86	389.32	440.41
0.55	364.53	475.44	554.64
1.10	729.06	698.76	891.14

Table 2: Critical buckling load for circular bearing

G (N/mm^2)	$P_{crit}(kN)$	$P_{crit(\lambda:T)}(kN)$	$P_{crit(\lambda:C)}(kN)$
0.29	202.89	409.07	457.62
0.55	379.53	500.20	575.58
1.10	759.05	741.96	921.63

Acknowledgements

The authors would like to acknowledge the Tun Abdul Razak Research Centre, TARRC, for giving access to experimental data on high damping rubber.

References

[1] Abaqus, . (2011). *Users Manual Volume 111: Materials*. Dassault Systemes Simulia Corp, Providence, RI, USA.

[2] Bridgestone (2011). *Design Characteristics of High Damping Rubber Bearing*.

[3] Fuller, K., M. J. Gregory, J. A. Harris, A. H. Muhr, A. D. Roberts, and A. Sevenson (1988). *Engineering use of natural rubber, Chapter 19 in Natural rubber science and technology*. New York.

[4] Gent, A. (1964). Elastic stability of rubber compression springs. *J. Mech. Eng. Sci. 6*(4), 318–326.

[5] Kelly, J. and D. Konstantinidis (2011). *Mechanics of Rubber Bearings for Seismic and Vibration Isolation*. John Wiley & Sons Inc.

[6] Kelly, J. and M. Marsico (2013). Tension buckling in rubber bearings affected by cavitation. *Engineering Structures 56*, 656–663.

[7] Lindley, P. B. (1992). *Engineering design with natural rubber*. Munich: 5th ed. Malaysian Rubber Producers' Research Association, MRPRA.

[8] Nagarajaiah, S. and K. Ferrell (1999). Stability of elastomeric seismic isolation bearings. *J. Struct. Eng. 125*(9), 946–954.

Proceedings of the 22nd UK Conference of the
Association for Computational Mechanics in Engineering
2 - 4 April 2014, University of Exeter, Exeter

A COMPUTATIONAL FRAMEWORK FOR LARGE STRAIN ELECTROMECHANICS

R. Ortigosa[a], A. J. Gil[a] and J. Bonet[a]

[a]Civil & Computational Engineering Centre, College of Engineering, Swansea University, Swansea SA2 8PP, UK

{577350; a.j.gil; j.bonet}@swansea.ac.uk

ABSTRACT

In this paper, a new computational framework is presented for the analysis of large strain electromechanics. The framework is not restricted to either energy harvesters or smart actuators, but it is applicable to the wide spectrum of piezoelectric polymers. In nonlinear elasticity, the condition of polyconvexity characterises admissible strain energy functionals in the large strain regime. The objective of this work is the extension of this condition to the field of electromechanics, where a new energy functional is introduced as a polyconvex combination of both strain and electric field variables. A series of valid variational mixed formulations will be presented and discretised in space with the Finite Element Method, where the resulting system of nonlinear algebraic equations is solved via the Newton-Raphson method after consistent linearisation. Finally, a series of numerical examples are presented in order to assess the capabilities of the new formulation.

Key Words: Energy harvesting; Piezoelectricity; Polyconvexity; Large deformations; Electro-mechanics; Finite Element Method

1. Introduction

The earliest piezoelectric materials to be discovered, i.e. crystals, have shown limited applicability due to their high stiffness and brittleness. The recent advent of piezoelectric polymers has meant a turning point in the development of piezoelectricity. The circumvention of the drawbacks associated with their crystal predecessors has broadened considerably their applications as actuators, power generators and energy harvesters.

Piezoelectric polymers have traditionally been used as smart actuators in microelectromechanical systems. However, their ability to emulate the functioning of biological muscles as well as their large strain capabilities, have recently triggered the emergence of new exciting applications, such as artificial muscles. The large strain capabilities and large piezoelectric coefficients associated to piezoelectric polymers, confer them also with attractive properties within the field of power generation and energy harvesting. There is currently a growing need for these kinds of applications. For instance, piezoelectric eels are used as part of submarine devices in long endurance military missions. The energy-harvesting eel is designed to extract energy from the wake of a bluff body in an ocean current. The basic configuration is a leading bluff body trailed by a thin flexible piezoelectric eel. The bluff body generates vortices which excite a flapping motion of the eel. The eel deformation results in strain of the piezoelectric membrane, which in turn generates a voltage across the material.

The existing framework for the numerical simulation of piezoelectric materials requires an enhancement as a result of the development of these new polymers, capable of undergoing large deformations. Unlike crystals, the classical linearised theory can no longer be applied for a reliable computer simulation. In this paper, a nonlinear variational formulation for piezo-hyperelastic materials is introduced with the help of an extended internal density functional U constructed on the basis of strain and electric field variables. A variety of energy functionals can then be introduced by exploiting the properties of the piezoelectric polymer under investigation.

2. Mathematical requirements: Polyconvexity.

Polyconvexity is nowadays well accepted as a fundamental mathematical requirement that must be satisfied by admissible strain energy functionals used to describe elastic materials in the large strain regime. Essentially, the strain energy Ψ per unit of undeformed volume must be a function of the deformation gradient $\boldsymbol{F}$ via a convex multi-valued function U of $\boldsymbol{F}$, its cofactor $\boldsymbol{H}$ and its determinant J as

$$\Psi\left(\boldsymbol{\nabla}_0 \boldsymbol{x}\right) = U\left(\boldsymbol{F}, \boldsymbol{H}, J\right), \tag{1}$$

where $\boldsymbol{\nabla}_0 \boldsymbol{x}$ is the gradient operator of the spatial configuration with respect to the initial undeformed configuration. The three strain measures $\boldsymbol{F}$, $\boldsymbol{H}$ and J have work conjugate stresses $\boldsymbol{\Sigma}_{\boldsymbol{F}}$, $\boldsymbol{\Sigma}_{\boldsymbol{H}}$ and Σ_J, respectively, defined by

$$\boldsymbol{\Sigma}_{\boldsymbol{F}} = \frac{\partial U}{\partial \boldsymbol{F}}, \qquad \boldsymbol{\Sigma}_{\boldsymbol{H}} = \frac{\partial U}{\partial \boldsymbol{H}}, \qquad \Sigma_J = \frac{\partial U}{\partial J}. \tag{2}$$

In electro-mechanics, above expression (1) must be extended in order to account for electric field variables. An enhanced energy density functional Ψ is defined as a function of the deformation gradient $\boldsymbol{F}$ and the material gradient of the electrical potential φ via a convex multi-valued function U of $\boldsymbol{F}$, $\boldsymbol{H}$, J and the electric displacement vector $\boldsymbol{D}_0$ as

$$\Psi\left(\boldsymbol{\nabla}_0 \boldsymbol{x}, \boldsymbol{\nabla}_0 \varphi\right) = U\left(\boldsymbol{F}, \boldsymbol{H}, J, \boldsymbol{D}_0\right). \tag{3}$$

Analogously to formulae (2), a new conjugate vector of $\boldsymbol{D}_0$, the material electric field $\boldsymbol{E}_0$, is defined as

$$\boldsymbol{E}_0 = \frac{\partial U}{\partial \boldsymbol{D}_0}. \tag{4}$$

The set of conjugate variables enables the directional derivative of the combined electro-mechanical internal energy density to be expressed as

$$DU\left[\delta \boldsymbol{F}, \delta \boldsymbol{H}, \delta J, \delta \boldsymbol{D}_{\boldsymbol{0}}\right] = \boldsymbol{\Sigma}_{\boldsymbol{F}} : \delta \boldsymbol{F} + \boldsymbol{\Sigma}_{\boldsymbol{H}} : \delta \boldsymbol{H} + \Sigma_J \delta J + \boldsymbol{E}_{\boldsymbol{0}} \cdot \delta \boldsymbol{D}_{\boldsymbol{0}}. \tag{5}$$

3. Variational principles in nonlinear electromechanics.

Numerous authors have previously incorporated the concept of polyconvexity for solid mechanics into computational models for both isotropic and non-isotropic materials for a variety of applications [3]. The standard approach consists of ensuring that the strain energy density satisfies first the polyconvexity condition and then proceed towards a computational solution by re-expressing the energy density in terms of the deformation gradient alone.

A mixed formulation can be derived in which the deformation gradient, its cofactor and its determinant are retained as fundamental problem variables by means of a Hu-Washizu mixed variational principle [4]. Moreover, we can generalise this concept to the electromechanical problem by including the electric displacement as a new variable in the variational principle. The resulting formulation opens up new interesting possibilities in terms of using various interpolation spaces for different variables, leading to enhanced formulations.

A possible variational principle can be introduced in terms of the total potential energy Π_U as follows,

$$\Pi_U(\boldsymbol{x}, \varphi, \boldsymbol{F}, \boldsymbol{H}, J, \boldsymbol{\Sigma}_{\boldsymbol{F}}, \boldsymbol{\Sigma}_{\boldsymbol{H}}, \Sigma_J, \boldsymbol{D}_0) = \min_{\boldsymbol{x}, \boldsymbol{F}, \boldsymbol{H}, J, \boldsymbol{D}_0} \left\{ \max_{\varphi, \boldsymbol{\Sigma}_{\boldsymbol{F}}, \boldsymbol{\Sigma}_{\boldsymbol{H}}, \Sigma_J} \left\{ \int_V U(\boldsymbol{F}, \boldsymbol{H}, J, \boldsymbol{D}_0)\, dV + \right.\right.$$

$$\left.\left. \int_V \boldsymbol{\Sigma}_{\boldsymbol{F}} : (\boldsymbol{F}_{\boldsymbol{x}} - \boldsymbol{F})\, dV + \int_V \boldsymbol{\Sigma}_{\boldsymbol{H}} : (\boldsymbol{H}_{\boldsymbol{x}} - \boldsymbol{H})\, dV + \int_V \Sigma_J (J_{\boldsymbol{x}} - J)\, dV - \int_V \boldsymbol{D}_0 \cdot \boldsymbol{\nabla}_0 \varphi\, dV - \Pi^{ext}(\boldsymbol{x}, \varphi) \right\} \right\} \tag{6}$$

where $\boldsymbol{F}_x$, $\boldsymbol{H}_x$ and J_x represent the deformation gradient, the cofactor and the determinant of the spatial configuration $\boldsymbol{x}$. In addition, $\Pi^{ext}(\boldsymbol{x}, \varphi)$ represents the external work generated from mechanical and electrical body and surface effects. Alternatively, a different ordering in equation (6) leads to the following

variational principle,

$$\Pi_\Upsilon(\boldsymbol{x},\varphi,\boldsymbol{\Sigma_F},\boldsymbol{\Sigma_H},\Sigma_J,\boldsymbol{D}_0,\boldsymbol{E}_0)=\min_{\boldsymbol{x},\boldsymbol{D}_0}\left\{\max_{\varphi,\boldsymbol{\Sigma_F},\boldsymbol{\Sigma_H},\Sigma_J,\boldsymbol{E}_0}\left\{\int_V \Upsilon(\boldsymbol{\Sigma_F},\boldsymbol{\Sigma_H},\Sigma_J,\boldsymbol{E}_0)\,dV\right.\right.$$
$$\left.\left.+\int_V \boldsymbol{\Sigma_F}:\boldsymbol{F_x}\,dV+\int_V \boldsymbol{\Sigma_H}:\boldsymbol{H_x}\,dV+\int_V \Sigma_J J_{\boldsymbol{x}}\,dV-\int_V \boldsymbol{D}_0\cdot(\boldsymbol{\nabla}_0\varphi-\boldsymbol{E}_0)\,dV-\Pi^{ext}(\boldsymbol{x},\varphi)\right\}\right\} \tag{7}$$

where the energy density functional Υ is defined by means of the Legendre transform as

$$\Upsilon(\boldsymbol{\Sigma_F},\boldsymbol{\Sigma_H},\Sigma_J,\boldsymbol{E}_0)=\boldsymbol{\Sigma_F}:\boldsymbol{F}+\boldsymbol{\Sigma_H}:\boldsymbol{H}+\Sigma_J J+\boldsymbol{D}_0\cdot\boldsymbol{E}_0-U(\boldsymbol{F},\boldsymbol{H},J,\boldsymbol{D}_0) \tag{8}$$

Two alternative variational principles could also be defined leading to saddle-point type problems, obtained from the internal energy U by means of the Legendre transform as follows,

$$\Gamma(\boldsymbol{F},\boldsymbol{H},J,\boldsymbol{E}_0)=U(\boldsymbol{F},\boldsymbol{H},J,\boldsymbol{D}_0)-\boldsymbol{D_0}\cdot\boldsymbol{E_0}$$
$$\Sigma(\boldsymbol{\Sigma_F},\boldsymbol{\Sigma_H},\Sigma_J,\boldsymbol{D}_0)=U(\boldsymbol{F},\boldsymbol{H},J,\boldsymbol{D}_0)+\boldsymbol{\Sigma_F}:\boldsymbol{F}+\boldsymbol{\Sigma_H}:\boldsymbol{H}+\Sigma_J J \tag{9}$$

4. Constitutive models for piezo-hyperelastic materials.

The convex nature of the internal energy density $U(\boldsymbol{F},\boldsymbol{H},J,\boldsymbol{D_0})$ makes this energy the most suitable for the definition of constitutive laws. The definition of constitutive laws based on saddle-point functionals (i.e $\Gamma(\boldsymbol{F},\boldsymbol{H},J,\boldsymbol{E}_0)$ and $\Sigma(\boldsymbol{\Sigma_F},\boldsymbol{\Sigma_H},\Sigma_J,\boldsymbol{D}_0)$) is a cumbersome task, specially in two an three dimensional problems.

Although the energy density $\Upsilon(\boldsymbol{\Sigma_F},\boldsymbol{\Sigma_H},\Sigma_J,\boldsymbol{E}_0)$ is convex, it is not as trivial as in the case of the energy density $U(\boldsymbol{F},\boldsymbol{H},J,\boldsymbol{D_0})$ to impose physical restrictions, as for instance material frame indifference by creating invariants of the conjugate stresses $\boldsymbol{\Sigma_F},\boldsymbol{\Sigma_H}$ and Σ_J. Therefore, we propose formulating constitutive laws using the internal energy density U satisfying the polyconvexity restriction. However, this energy only appears in the variational principle associated to the total potential energy functional Π_U defined in equation (6). The use of the alternative variational principles requires to express the derivatives of the associated internal energies in terms of the internal energy U by exploiting their relations through the appropriate Legendre transforms.

As an example, we present a simple isotropic constitutive law for the internal energy U which satisfies the polyconvexity restriction (3), namely

$$U(\boldsymbol{F},\boldsymbol{H},J,\boldsymbol{D}_0)=\frac{\mu}{24}\left((\boldsymbol{F}:\boldsymbol{F})^2+(\boldsymbol{H}:\boldsymbol{H})^2+72\frac{(\boldsymbol{D}_0\cdot\boldsymbol{D}_0)^2}{\mu^2\varepsilon^2}+6\frac{\boldsymbol{F}\boldsymbol{D}_0\cdot\boldsymbol{F}\boldsymbol{D}_0}{\mu\varepsilon}+6\frac{\boldsymbol{H}\boldsymbol{D}_0\cdot\boldsymbol{H}\boldsymbol{D}_0}{\mu\varepsilon}\right)+f(J)\,. \tag{10}$$

The function f is added to guarantee the stress and electric displacement free conditions in the origin, namely

$$\left.\frac{\partial U}{\partial \boldsymbol{F}}\right|_{\boldsymbol{F}=\boldsymbol{I},\boldsymbol{D}_0=\boldsymbol{0}}=\boldsymbol{0};\quad \left.\frac{\partial U}{\partial \boldsymbol{H}}\right|_{\boldsymbol{F}=\boldsymbol{I},\boldsymbol{D}_0=\boldsymbol{0}}=\boldsymbol{0};\quad \left.\frac{\partial U}{\partial J}\right|_{\boldsymbol{F}=\boldsymbol{I},\boldsymbol{D}_0=\boldsymbol{0}}=\boldsymbol{0};\quad \left.\frac{\partial U}{\partial \boldsymbol{D_0}}\right|_{\boldsymbol{F}=\boldsymbol{I},\boldsymbol{D}_0=\boldsymbol{0}}=\boldsymbol{0}. \tag{11}$$

A typical expressions for the function f can be

$$f(J)=-\frac{3\mu}{2}\ln J+\frac{\lambda}{2\varepsilon^2}\left(J^k+J^{-k}\right). \tag{12}$$

The coefficients μ, ε, λ and k are material parameters necessary for the characterisation of the material. This is achieved by performing a match in the origin, i.e. $\boldsymbol{F}=\boldsymbol{I},\boldsymbol{D}_0=\boldsymbol{0}$, between the constitutive tensors derived from the proposed energy functional and the experimentally obtained tensors available in the linearised regime (i.e. small strains and small electric field)

$$\boldsymbol{C}|_{\boldsymbol{F}=\boldsymbol{I},\boldsymbol{D}_0=\boldsymbol{0}}=\boldsymbol{c};\quad \boldsymbol{\mathcal{P}}|_{\boldsymbol{F}=\boldsymbol{I},\boldsymbol{D}_0=\boldsymbol{0}}=\boldsymbol{p};\quad \boldsymbol{\mathcal{H}}|_{\boldsymbol{F}=\boldsymbol{I},\boldsymbol{D}_0=\boldsymbol{0}}=\boldsymbol{H};\quad \boldsymbol{\mathcal{A}}|_{\boldsymbol{F}=\boldsymbol{I},\boldsymbol{D}_0=\boldsymbol{0}}=\boldsymbol{\epsilon}, \tag{13}$$

where $\boldsymbol{C}$, $\boldsymbol{\mathcal{P}}$, $\boldsymbol{\mathcal{H}}$ and $\boldsymbol{\mathcal{A}}$ are the elastic, piezoelectric, electrostrictive and dielectric material tensors, respectively. From the previous match, the necessary material parameters can be obtained either by identification or optimisation.

5. Numerical results.

The resulting variational formulations are discretised in space with the help of the Finite Element Method, where the resulting system of nonlinear algebraic equations are solved via the Newton-Raphson method after consistent linearisation. A series of numerical examples will be presented in order to demonstrate the robustness and applicability of the formulation. Figure 1 shows an example in which an electric field applied across the thickness of a composite shell leads to an electrically induced buckling configuration. Figure 2 shows an example in which a composite transversely anisotropic slab is subjected to an electric field in the plane of the undeformed configuration leading to an out-of-plane deformation.

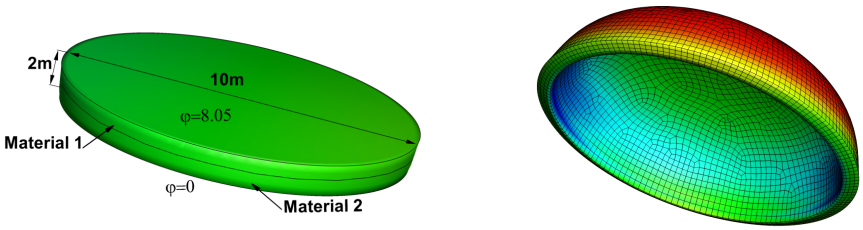

(a) Initial configuration (b) Stress σ_{zz} in deformed configuration

Figure 1: Composite shell subjected to transverse electric field: electrically induced buckling.

(a) Initial configuration (b) Electric displacement D_z in deformed configuration

Figure 2: Anisotropic composite slab subjected to potential gradient in the plane of the undeformed configuration.

6. Conclusions and further research.

A nonlinear variational framework for the numerical simulation of piezo-hyperelastic polymers has been presented. An extended energy density functional has been introduced satisfying the physical and mathematical requirements established by polyconvexity. A mixed variational formulation has been implemented in which the deformation gradient, its cofactor, its determinant and the electric displacement field are retained as fundamental problem variables by means of a Hu-Washizu type variational principle. Application of the Legendre transform on the internal energy or, equivalently, rearrangement of the terms in the variational principle allows to derive alternative mixed variational formulations. The resulting different formulations are resolved numerically with the aid of the Finite Element Method, using suitable interpolations for the newly introduced variables.

References

[1] J.M. Ball, Convexity conditions and existence theorems in non-linear elasticity. *Archive for Rational Mechanics and Analysis*, 63, 337–403, 1977.

[2] R. Ortigosa, A.J. Gil and J. Bonet, On the developement of constitutive laws for large strain hyperelastic piezoelectric materials, *Euromech Solid Mechanics Conference*, 2012.

[3] J. Schröder, Anisotropic Polyconvex Energies on the Basis of Crystallographic Motivated Structural Tensors. *Journal of the Mechanics and Physics of Solids*, 56, 3486–3506, 2008.

[4] J. Bonet, A.J. Gil and R. Ortigosa, A computational framework for polyconvex large strain elasticity. *Computer Methods in Applied Mechanics and Engineering*, under review.

Proceedings of the 22nd UK Conference of the
Association for Computational Mechanics in Engineering
2 – 4April 2014, University of Exeter, Exeter

ANALYSIS OF THERMAL STRESS DISTRIBUTION IN BRAKE DISC DURING SINGLE BRAKING UNDER NON-AXISYMMETRIC LOAD

Adam Adamowicz

Faculty of Mechanical Engineering, Bialystok University of Technology, 45C Wiejska Street, Bialystok 15-351, Poland

*a.adamowicz@pb.edu.pl

ABSTRACT

The aim of this paper was to analyse the state of the thermal stresses in brake disc caused by the transient temperature field during the braking process. The study is a continuation of the previous investigations of the author concerning finite element analysis of the temperature distributions in a pad-disc brake system. Knowing the transient temperature field, the FE model to determine the corresponding quasi-static stresses in a such tribosystem was proposed. A numerical simulation of a single braking process for the axisymmetric (2D) and 3D arrangements of the disc brake was carried out. It was assumed that the contact pressure on the friction surfaces is constant and uniformly distributed, and the angular speed decreases linearly. The calculations do not take into account any mechanical loads. The evolutions and the spatial distributions of the components of the stress tensor and the equivalent Huber-Mises stress in the brake disc are analysed. Based on the results of calculations some conclusions have been drawn. Both computational models show similar trends of the changes in equivalent Huber-Mises stress. The axisymmetric model does not reveal the changes in stress caused by the periodic heating by friction zone and it can be used to determine the average values of stress during a single rotation of a disc at high rotational speeds. The highest Huber-Mises stress occurred near the mean radius of the pad (3D FE model) shortly after the start of braking and on the inner edge of the disc at the end of the braking process (both of the computational models).

Keywords: *frictional heating; temperature; thermal stresses; pad-disc brake system; finite element method*

1. Introduction

During braking the stationary pads are pressed to the rubbing path of the rotating disc and the mechanical energy is converted into heat. Friction elements of a brake are exposed to mechanical and thermal load. The temperature on the contact surfaces rises rapidly, which results in temperature gradients and the stress due to thermal expansion. Interactions between the temperature and the stress are coupled. In calculations this relationship is often omitted analysing the heat conduction and the thermoelasticity problems separately [1-3].
Under certain conditions, the modelling of the brake disc heating during braking process can be implemented as an axisymmetric problem. The heat flux which is variable in time and depends on the radius, acts in this case on the entire surface of the rubbing path of the disc. Then the size of the heat flux is reduced as many times as the surface area of the pad is smaller than area of the friction path. This calculation scheme works well when determining the average temperatures reached on the friction surfaces. An assumption of the axisymmetric state of the thermal loads in the brake disc is obviously simplification, since in the real process the brake disc is heated by moving zone under the brake pad. The remaining area is cooled through heat conduction into the disc and convection to the environment. However during a single braking the effect of heat exchange with the environment can be omitted [4]. The axisymmetric model can be considered at high rotational speed, at low speed the three-dimensional model should be used. This study is a comparison of two computational models, the axisymmetric and the three-dimensional for calculation of thermal stresses occurring in the brake disc during braking.

2. Statement of the problems

Consider a single braking process from the initial angular speed ω_0 to standstill during $t_s = 3.96$ s, for the pad-disc brake system shown in Tab. 1. The displacement of the pads induces on the disc working surfaces the constant and uniformly distributed pressure $p_0 = 1.47$ MPa. The angular speed due to friction decreases linearly. It is assumed that the material of the disc is uniform, isotropic, and its physical properties as well as operating parameters (e.g. coefficient of friction f) are temperature independent. The heating process is described by the linear theory of heat conduction (parabolic type). The heat transfer through convection and thermal radiation is neglected. The corresponding thermal stresses are determined from the solution of the linear system of equations of uncoupled thermoelasticity [5] and due to the symmetry of the disc about the mid-plane, the computational region is restricted to the half of its thickness. It was assumed that at the initial time moment, the temperature of the disc is constant and equal to the ambient temperature $T_0 = T_a = 20$ºC. The dimensions and the properties of materials of the pad and the disc are given in Tab. 1.

Table 1: Dimensions of the disc brake and operations parameters from

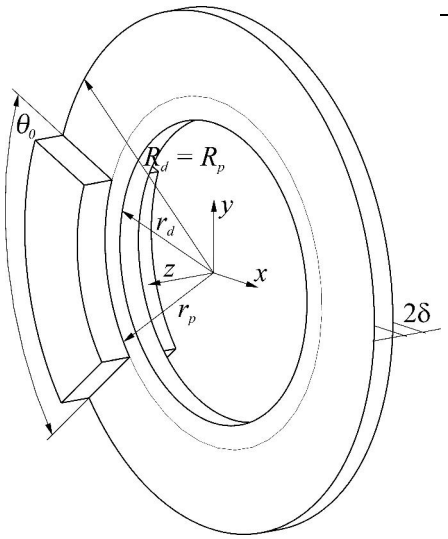

Parameter	disc (ChNMKh)	pad (FMC-11)
inner radius, r_d, r_p [mm]	66	76.5
outer radius, R_d, R_p [mm]	113.5	
pad arc length, θ_0 [deg]		64.5
thickness, δ [mm]	5.5	10
thermal conductivity, K [W/(mK)]	51	34.3
density, ρ [kg/m^3]	7100	4700
thermal diffusivity, $K \times 10^5$ [m^2/s]	1.44	1.46
Young's modulus, E [GPa]	99.97	
Poisson's ratio	0.29	
thermal expansion coefficient, α_T [K^{-1}]	1.08 10^{-5}	
initial angular speed, ω_0 [s^{-1}]	88.464	
braking time, t_s [s]	3.96	
contact pressure, p_0 [MPa]	1.47	
coefficient of friction, f	0.5	

Two computational models using the finite elements were developed: the axisymmetric and the three-dimensional. In solving the problem of heat conduction the boundary conditions shown in Fig. 1a and 1b were applied. The heat flux density of the heating brake disc has been determined on the basis of the relationship:

$$q_d(r,t) = \gamma f \omega(t) r p_0, \; r_p \le r \le R_p, \; 0 \le t \le t_s, \tag{1}$$

where γ is the heat partition ratio:

$$\gamma = \frac{\sqrt{K_d \rho_d c_d}}{\sqrt{K_d \rho_d c_d} + \sqrt{K_p \rho_p c_p}}. \tag{2}$$

In the case of axisymmetric problems (Fig. 1a), the intensity of the heat flux was additionally reduced by a factor incorporating a real contact area between the pad and the disc. Implementation of the calculation of these problems is described in detail in [1] and [2].

To solve the problems of thermoelasticity, the boundary conditions shown in Fig. 1c were used. The nodes placed in the plane of symmetry of the disc ($z = -\delta$) is fixed in a z direction. The 3D model requires additional constraints in order to avoid the mechanism. Boundary conditions imitate the supports of the floating brake disc, which can expand under the influence of temperature without hindrance.

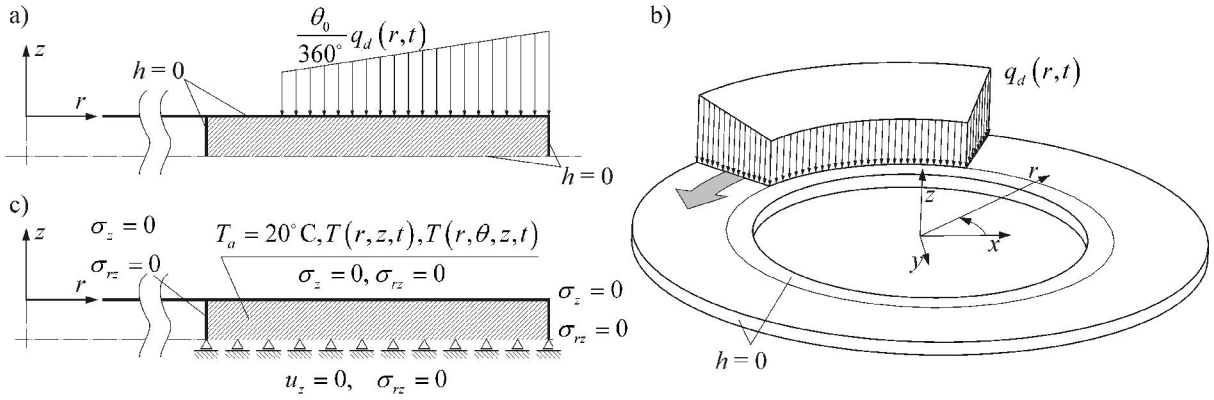

Figure 1: Boundary conditions for heat conduction problem: a) axisymmetric model; b) 3D model; c) thermoelasticity problem

3. Numerical analysis

The numerical calculations were carried out by using the finite element method based on the software package MSC.Patran/Nastran [6]. The developed computational models were tested using the finite element mesh with different densities. Finally, the disc region of the axisymmetric model was divided into 209000 triangular three-node axisymmetric linear finite elements 'CTRIAX6' and 105561 nodes. The 3D model consisted of 86040 'CHEXA8' type elements and 102960 nodes. At the first stage of the analysis, the solution of the transient heat conduction problem, allowed to obtain the distribution of the temperature fields for the specific time steps. The results of these calculations were then used as the boundary conditions for the solution of the thermoelasticity problem. This process has been automated by the developed of the original software, written in Python. Sample results are shown in Fig. 1 and Fig. 2.

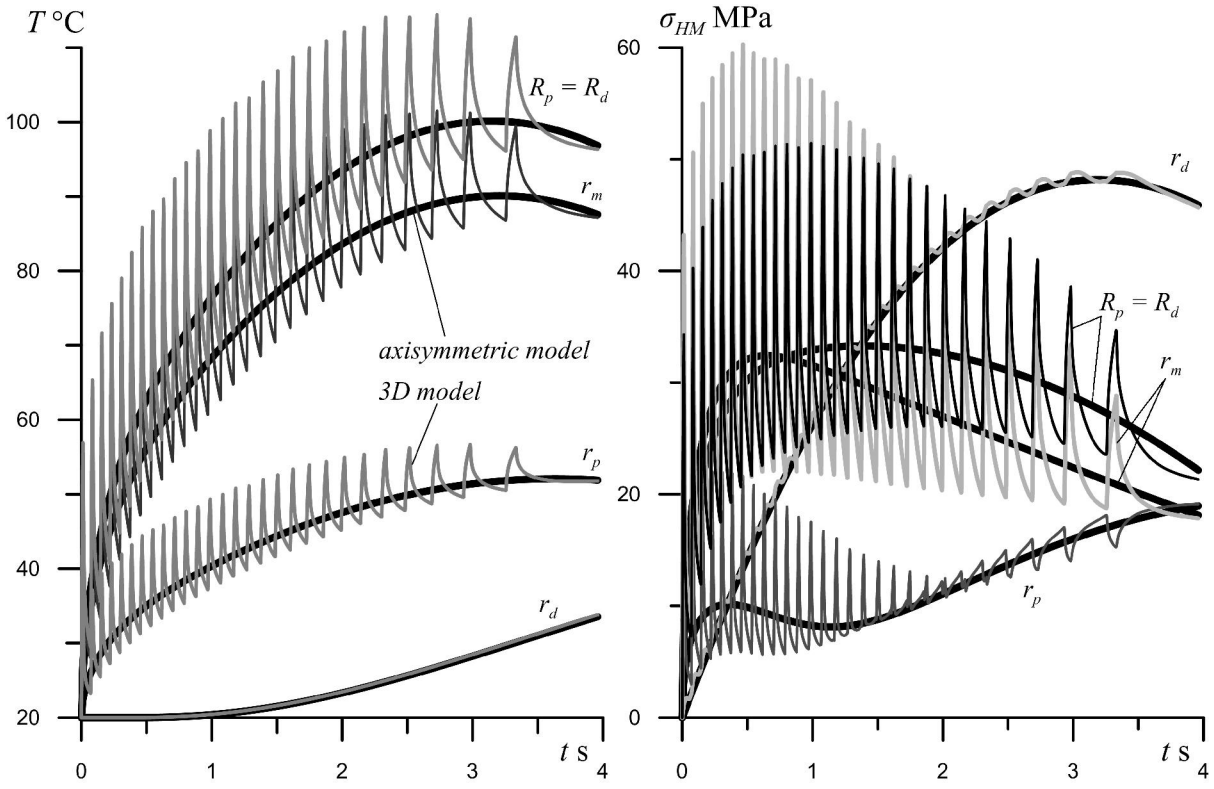

Figure 2: Temperatures and corresponding Huber-Mises thermal stress σ_{HM} on the disc surface during braking at various radii.

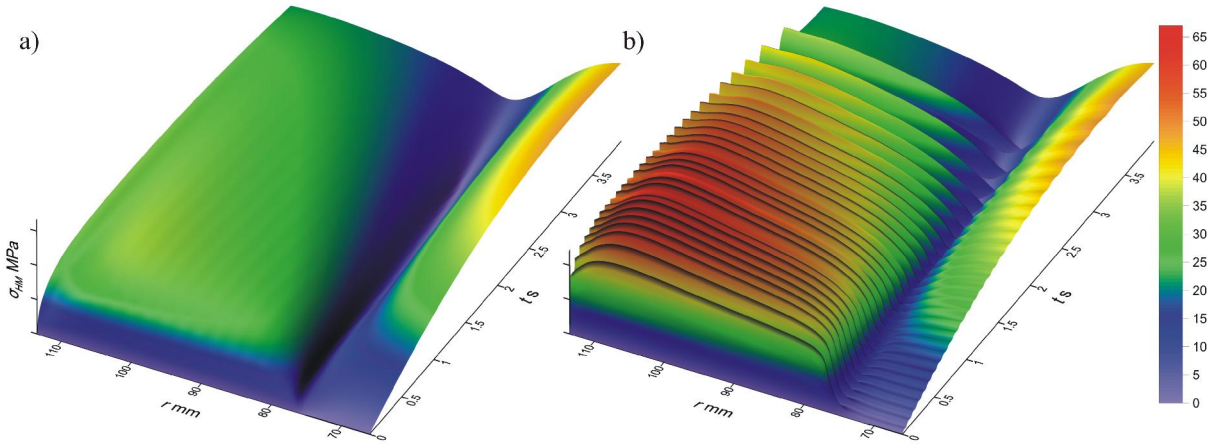

Figure 3: Equivalent Huber-Mises stress σ_{HM} changes on the disc surface during braking: a) axisymmetric model, b) 3D model

4. Conclusions

Based on the obtained results general conclusions about the usefulness of both computational models can be formulated. The axisymmetric model reveals the trends of the average level of thermal stresses induced in the disc. It is easier to use and quicker to set up calculations. The model correctly identified the most strenuous disc areas (between the medium and the outer radius of the rubbing path at the beginning of braking and the inner radius of the disc at the end of braking). However, the maximum stress values obtained are lower than in the 3D model. The axisymmetric model is not suitable for predicting of the fatigue cracking processes occurring on the surface of the brake disc. The periodic heating and cooling of the surface layer of the brake disc results in the cyclic changes in the thermal stress with the amplitude of about 40 MPa, which gives the basis for using the fatigue cracking criteria. The full thermal and mechanical stress state can only be given using a three-dimensional model.

Acknowledgements

The present article is financially supported by the National Science Centre in Poland (research project No 2011/01/B/ST8/07446).

References

[1] A.A. Yevtushenko, P. Grzes, Axisymmetric finite element model for the calculation of temperature at braking for thermosensitive materials of a pad and a disc, Numer Heat Transfer, Part A Applications, Vol. 62, pp. 211–230, 2012.

[2] A. Adamowicz, P. Grzes, Analysis of disc brake temperature distribution during single braking under non-axisymmetric load, Appl. Therm. Eng., Vol. 31, pp. 1003–1012, 2011.

[3] A. Adamowicz, P. Grzes, Three-dimensional FE model for calculation of temperature of a thermosensitive disc, Appl. Therm. Eng., Vol. 50, 572–581, 2013.

[4] A. Adamowicz, P. Grzes, Influence of convective cooling on a disc brake temperature distribution during repetitive braking, Appl. Therm. Eng., Vol. 31, 2177-2185, 2011.

[5] O.C. Zienkiewicz, R.L. Taylor, J.Z. Zhu, The finite element method: its basis and fundamentals, sixth ed., Elsevier Butterworth-Heinemann, Amsterdam, 2005.

[6] MSC.Nastran Thermal Analysis User's Guide, 2002.

Proceedings of the 22nd UK Conference of the
Association for Computational Mechanics in Engineering
2 – 4April 2014, University of Exeter, Exeter

BREAKING PERIODICITY IN MATERIAL SIMULATIONS

***Jan Novák[1,2], Martin Doškář[1], Martin Horák[1]**

[1]Department of Mechanics, Faculty of Civil Engineering, Czech Technical University in Prague, Thákurova 7/2077, Prague 6, 166 29
[2]Institute of Structural Mechanics, Faculty of Civil Engineering, Brno University of Technology, Veveří 331/95, Brno, 602 00

*novakj@cml.fsv.cvut.cz

ABSTRACT

In this paper an approach to modelling of heterogeneous materials is presented. It is based on incorporating the concept of Wang tilings in microstructure compression and reconstruction techniques. Unlike the Periodic Unit cell approach, where a complete microstructural information is stored within a single cell, the set of simpler domains, so called Wang tiles, is used, thereby allowing for breaking the periodic nature of reconstructed microstructure representations. A potential of the concept in synthesis of microstructure-informed enrichment functions for Generalized Finite Element environments is also discussed and accompanied with preliminary results.

Keywords: *microstructure synthesis; Wang tiling; enrichment strategy*

1. Introduction

The sustainable environmental tendencies lead to a highly optimized design of majority of consumer products. In Materials Engineering, this is mirrored by a race towards miniaturization, top product performance, and optimal energy consumption. A potential solution to these contradicting requirements is brought by custom designed composite materials, which finds the use of virtual laboratories to link the knowledge of characteristic physical processes taking place at the level of constituents with macro-scale behaviour.
To contribute this goal, the generalization of a popular periodic unit cell approach to modelling of heterogeneous materials is presented. It rests on the idea of stochastic Wang tilings to represent random material microstructures or fine scale local field patterns that can be used as the microstructure-informed enrichment functions in Generalized Finite Element environments. Preliminary result are outlined and discussed.

2. Wang tilings

The concept of Wang tiles was introduced by Hao Wang in 1961 as a method to decide whether an arbitrary representative of a certain class of logic statements can be proven by means of axioms of mathematical logic [1, 2]. Since, Wang tiles, sets, and tilings have been the subject of vigorous studies in Discrete Mathematics [3], Theory of quasicrystals and Biology [4, and references therein]. From the perspective of Computer Graphics and Game industry, the ability of Wang tiles to produce non-periodic planar representations of arbitrary sizes was first noticed by Stam [5]. This work then inspired our current research which brought the concept to Materials Engineering community [4].
Wang tiles can be described as square, dominoe-like pieces, alternatively called tetraminoes, with codes assigned to edges [1]. The edges are denoted by codes with respect to cardinal directions as W-west, N-north, E-east and S-south, $\delta, \alpha, \gamma, \alpha$ – tile 1 in Figure 1a. The tiles and edges are designed such that a tiling morphology can be recovered for arbitrarily large plane, including infinitely large ones, by placing the tiles in a regular square lattice while controlling the conformity of adjacent edge codes.
For the purpose of Materials Engineering the stochastic sets [7] seem to be the optimal choice [4]. These tile sets are not strictly aperiodic from the definition (can produce periodic tilings), however,

provide more freedom in the sense of their design while better preserving random nature of synthesized microstructures.
With the term valid tiling we understand such a tiling in which no empty spots in the tilling lattice are allowed and all edge codes are conforming, sometimes called “ground state” [6]. In order to assemble tiles into a valid tiling the stochastic algorithm proposed by Cohen at al. [7] was used. It works as follows. The tiles from the set are placed in column by column, row by row order in the lattice. In each step the subset of tiles that satisfy the edge constrains given by the previously placed tiles is filtered out of the entire set and a tile from the subset is randomly chosen and placed, an illustration of this procedure is shown in Figure 1b. The stochastic nature of the procedure is determined by the random choice of the tile to be placed yielding the condition that at least two different tiles for each admissible north-western combination of edges must be contained in the set.

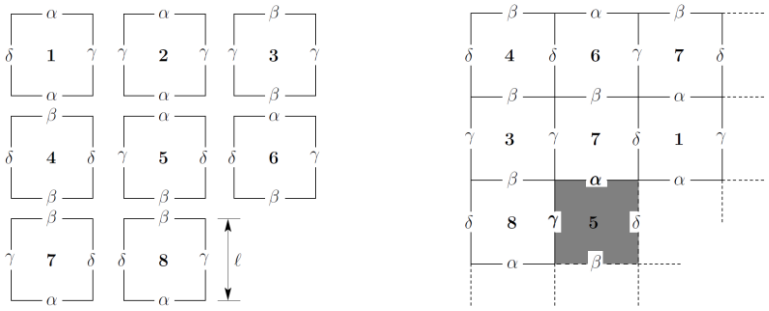

Figure 1: a) Example of Wang tile set consisting of 8 tiles, b) single step of stochastic tiling algorithm

3. Tile morphology design

Contrary to our previous work [4], the tile morphologies used in this contribution were designed by means of the automatic procedure proposed by Cohen at al [7]. This approach makes use of samples subtracted directly from the reference microstructures, squares 1-4 in Figure 2a. In particular, each tile is created as a square cut rotated by $\pi/4$ from the four partially overlapping samples that are positioned with respect to the edge codes of the manufactured tile, see Figure 2b. The straight diagonal cuts within the four-sample conglomerate ensure compatibility of the microstructure morphology across the edges. So far, the procedure seems fairly straightforward, however, its uneasy part is to fuse the samples within the overlapping region without any visible defects in the morphology along the quilting paths, red curves in Figure 2b. Here we have employed the modified version of the Freeman’s [10] Image Quilting algorithm that prefers the quilting path running through a fully percolated phase, i.e. the phase for which the two-point probability and the two-point cluster functions are identical. [8].

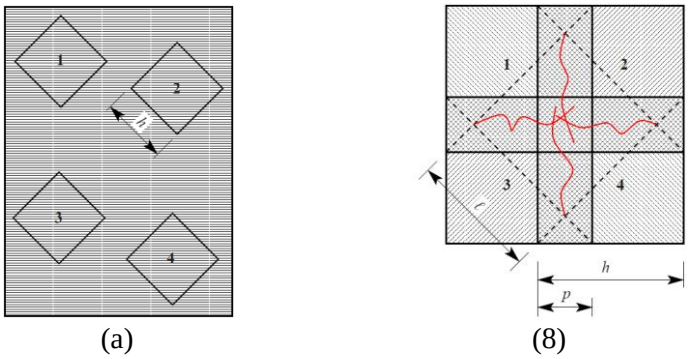

Figure 2: Schematic of automatic tile design

Moreover, in order to substantially reduce parasitic long-range orientation order artefacts while keeping a low number of tiles in the set we employed the idea of patches added to the centre of each

tile [9]. To determine the optimal design parameters the sensitivity of the choice of the sample edge length *h* and the overlap width *p* was tested. The objective of the analysis was to determine the smallest dimensions of tiles that are representative to the choice of a set diversity and type of the reference microstructure. The ability of sets, in other words "compressed systems", to approximate reference microstructures was quantified by means of statistical descriptors, in particular, the two-point probability and two-point cluster functions.

4. Results

In Figure 3a, we show the reference microstructure of a random hard-disk monodispersion. The appropriate synthesis of the microstructure made up of the 12-tile set is depicted in Figure 3b. It consists of only 9 tiles (separated by green dashed lines) due to the visualization purposes, however, can be extended to arbitrary sizes with apparent repetitive effects. These are mirrored by means of secondary extremes in the two point probability function which are displayed in Figure 3c (including data for sets of higher diversities).

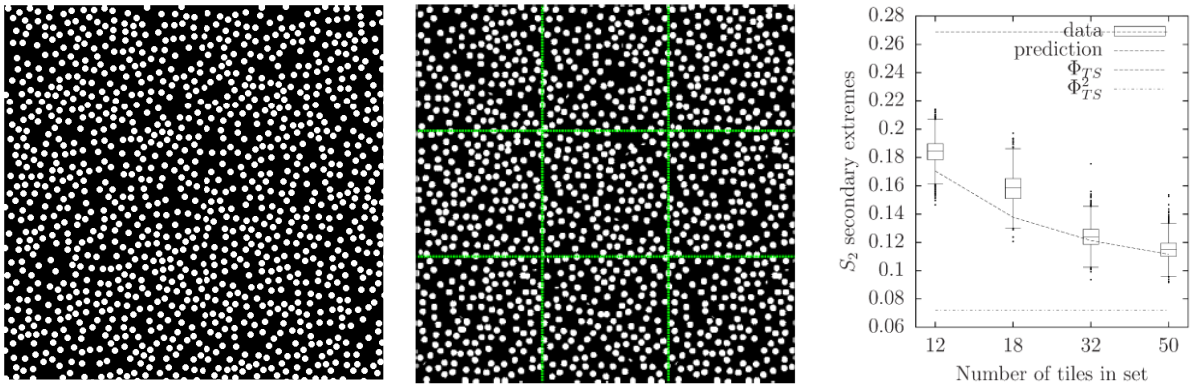

(a) (b) (c)

Figure 3: Hard-disk monodispersion, a) reference specimen, b) synthesis - a tiling consisting of 9 tiles, c) spatial statistics of the reconstructed (synthesized) microstructure

Another two target material systems along with their synthesized representations are shown in Figure 4.

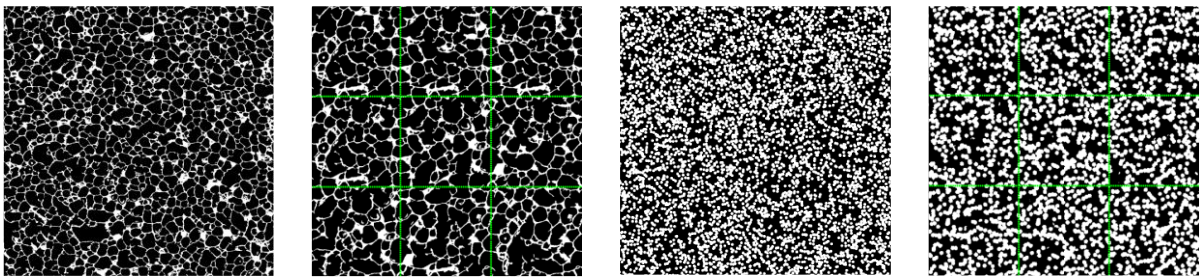

(a) (b) (c) (d)

Figure 4: Alporas® and permeable-disk monodispersion, a, c) reference specimen, b, d) synthesized representations consisting of 9 tiles

The last example of synthesized morphology patterns contains a single component of the local displacements in hard-disk monodisperse medium from Figure 3. The reference patterns of displacement perturbation field are obtained as the Eshelby solution to multiple inhomogeneity problem with a unitary strain excitation in *x* direction while the remaining two vanish, Figure 5a. We can observe a clear discontinuities along the tile boundaries in the synthesized patterns displayed in Figure 5b. The local relative error is displayed in Figure 5c. It shows the error magnitude locally less than 20%, and less than 5% overall.

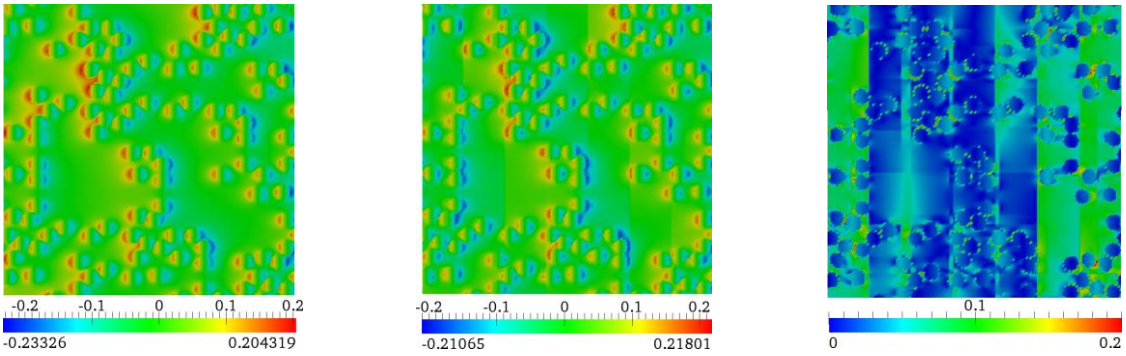

u_x, reference (a) u_x, synthesis (b) u_x, rel-error (c)

Figure 5: Local displacements, a) reference solution, b) synthesized solution, c) local relative error

5. Conclusions

In this contribution we have outlined a method for synthesis of microstructural patterns that goes beyond periodic representations based on a single Periodic Unit Cell. It rests on the concept of Wang tiles. It can be useful in compression and reconstruction techniques for heterogeneous random materials. Moreover, the above results show that the approach can be used in order to reconstruct microstructure-informed local fields that can be exploited in enrichment numerical strategies.

Acknowledgements

The European Social Fund, grant No. CZ.1.07/2.3.00/30.0005 "creation of excellent interdisciplinary research teams at the Brno University of Technology", and the Czech Science Foundation, grant No. 1324027S (MD), are gratefully acknowledged.

References

[1] H. Wang, Proving theorems by pattern recognition-II, *Bell Systems Technical Journal*, 40 (1), 1–42, 1961.

[2] H. Wang, Games, logic and computers, *Scientific American*, 213 (5), 98–106, 1965.

[3] K. Culik II, An aperiodic set of 13 Wang tiles, *Discrete Mathematics*, 160 (1), 245–251, 1996.

[4] J. Novák, A. Kučerová, J. Zeman, Compressing random microstructures via stochastic Wang tilings, *Physical Review E*, 86 (4), 040104, 2012.

[5] J. Stam, Aperiodic texture mapping, *European Research Consortium for Informatics and Mathematics*, 1997.

[6] D. Aristoff, C. Radin, First order phase transition in a model of quasicrystals, *Journal of Physics A: Mathematical and Theoretical*, 44 (25), 255001, 2011.

[7] M. Cohen, J. Shade, S. Hiller, O. Deussen, Wang tiles for image and texture generation, *ACM Transactions on Graphics*, 22 (3), 287–294, 2003.

[8] M. Doškář, Wang tilings for Real word Material Systems, MSc thesis, CTU in Prague, 2014.

[9] P. Somol, M. Haindl, Novel path search algorithm for image stitching and advanced texture tiling, *WSCG'2005 Full Papers Conference Proceedings*, Science Press, UNION Agency, Plzen, 155–162, 2005.

[10] A. Efros, W. Freeman, Image quilting for texture synthesis and transfer, *Proceedings of the 28th annual conference on Computer graphics and interactive techniques*, 341–346, 2001.

Proceedings of the 22nd UK Conference of the
Association for Computational Mechanics in Engineering
2 - 4 April 2014, University of Exeter, Exeter

Computational Modelling of Braided Fibre for Concrete Reinforcement

***M. Cortis, L. Kaczmarczyk and C.J. Pearce**

The University of Glasgow, Rankine Building, School of Engineering, Oakfield Avenue, Glasgow, G12 8LT, United Kingdom

*m.cortis.1@research.gla.ac.uk

ABSTRACT

This paper presents numerical modelling of braided fibre, to be used as concrete reinforcement. Ultimately, a corrosive and fire resistant concrete will be produced.

A Cubit script (geometry and mesh software) was created to mesh braided yarns under different geometric parameters. Fibres were represented using elastic transversely isotropic materials, for which the fibre directions for every yarn were precisely determined from the gradients of the resultant stream functions of potential flow problems. Applying an elastic interfaces between yarns to preventing penetration and having free sliding, convergence studies were conducted on a coarse and fine mesh, using hierarchical higher order approximation [1] for uniform p- and hp-refinement.

Key Words: *Fibre Reinforced Concrete; Composite; Bond Strength; Interface Cohesion Elements; Hierarchical Refinement*

1. Introduction

This paper presents a numerical investigation into the modeling of braided carbon fibre ropes. These ropes can provide an alternative to steel reinforcement in concrete, whereby the braiding can provide good bond adhesion between the fibre and concrete [2] and mitigate the need for weak resin binders [3]. In order to realize this ambition and to develop an appropriate modeling framework, a number of modeling challenges need to be overcome. First, an accurate geometrical representation of the complex geometry of the braided rope needs to be achieved. Second, the fibre direction during deformation needs to be accurately determined. Third, the interface between fibre yarns needs to be modeled. Novel hierarchic approximation functions [1] are also adopted and the paper demonstrates the convergence performance of h, p and hp-refinement. The fibres are modeled as transversely isotropic, although restricted to linear elasticity in this paper.

2. Numerical Modelling Approach

2.1. Mesh Modelling

Due to the lack of tools for modelling braided geometries, a flexible Python/APERPRO script was written in Cubit to generate 12-strand plaited sinnet geometry as shown in Figure 1. The algorithm of this script is as follows: a) sets of vertices representing the centre of axis for every yarn were created following the pattern of braiding, b) axis splines were formed along every set of vertices, c) circular surfaces were extrude along the same splines to form the braiding geometry. The input parameters were: i) the diameter of the yarn, ii) permissible tolerance between the yarns, iii) pitch and iv) the number of turns required. The interfaces between the yarns were created by subtracting one yarn from the overlapping adjacent one. Two square clamps were modelled at both ends of the braided model. Tetrahedral mesh was generated using Cubit mesh generator. The respective boundary conditions and material parameters were assigned in Cubit and directly read by MoFEM (Mesh Oriented Finite Element Method, our group's open-source FEM software).

Figure 1: Type of Braided Fibre Modelled

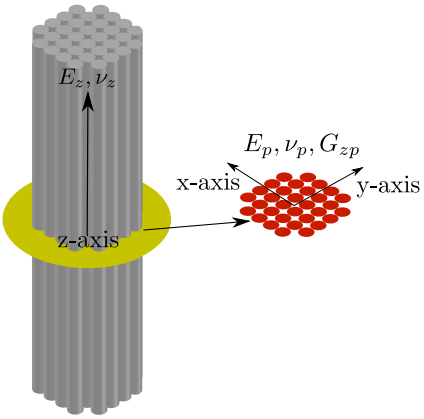

Figure 2: 5 Material Parameters for Transversely Isotropic Material (with reference to fibres)

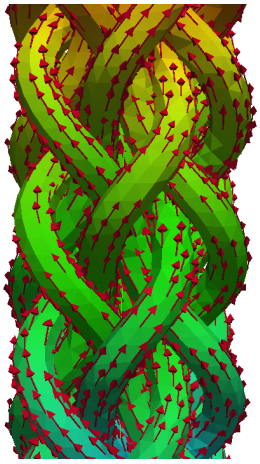

Figure 3: Flow Direction Vectors in Rope Model

2.2. *Transversely Isotropic Material*

A suitable material to represent fibre yarns was chosen to be transversely isotropic material. This material is described by 5 independent material parameters, which are the principal stiffness E_z, and poisson's ratio ν_z along the transverse direction (z-axis) of the fibre and the stiffness E_p, poisson's ratio ν_p and shear modulus G_{zp} in the plan of orthotropy (xy plane) as shown in Figure 2.

The fibre directions can be determined from the spline axes of the yarns. However, this is inaccurate when non-uniform cross-section are considered and/or rapid change of direction exists. An alternative way of obtaining the fibre directions is to solve a steady laminar incompressible potential flow problem, where the gradients of the stream function ψ are the resultant flow velocities defining the fibre directions $\mathbf{F}$ at every Gauss point as shown in Figure 3. By using a higher order approximation for the potential flow solution very accurate stream functions are computed for coarse meshes.

To transform the material response between the local fibre direction and global axes, the axis of rotation is expressed as $\mathbf{A} = \mathbf{F} \times \mathbf{Z}$, where $\mathbf{Z}$ is the unit vector $(0, 0, 1)$ representing the global z-axis and the angle of rotation is expressed by $\theta = \cos^{-1} \frac{\mathbf{F}.\mathbf{Z}}{\|\mathbf{F}\| \|\mathbf{Z}\|}$. This rotation matrix can be computed from $\mathbf{R} = \mathbf{I} + \sin\theta\mathbf{N} + (1 - \cos\theta)\mathbf{N}^2$, where $\mathbf{I}$ is the identity matrix, $\mathbf{N} = \frac{\Omega}{\omega}$, $\omega = +\sqrt{A_1^2 + A_2^2 + A_3^2}$ and $\Omega = \begin{bmatrix} 0 & -A_3 & A_2 \\ A_3 & 0 & -A_1 \\ -A_2 & 0 & 0 \end{bmatrix}$.

2.3. *Interface Elements*

Interface elements represented by prism elements in the FE mesh, were inserted between yarns, and an elastic cohesive model was used for its formulation [2]. Orthogonal penetration/separation of the interface was controlled using a stiffness about thousand times the principal material stiffness, while no stiffness was used to control shear movement, i.e. fibre were free to slide.

2.4. *Convergence Study*

A convergence study was conducted using p, h and hp-refinement on the problem described in Section 2.1. Hierarchical higher order (HO) approximation was used to perform uniform p-refinement up to 4^{th} order polynomial, where a minimum of 45 Gauss points were necessary for the numerical integration. Hierarchical HO shape functions for edges, faces and volumes were constructed using standard linear nodal shape functions (used in linear FEs) and legendre polynomials, as described by Ainsworth [1]. This allows local p-refinement, which is computationally cheaper that global p-refinement. However, the work presented here is restricted to global p-refinement.

Two meshes were considered: coarse mesh (49,624 elements) and a fine mesh (396,992 elements). The coarse mesh was analysed using 1^{st}, 2^{nd}, 3^{rd} and 4^{th} order approximations. The fine mesh was analysed using 1^{st}, 2^{nd} and 3^{rd} (5,823,150 DOF) order approximation.

The error was computed as $|u_z - u_z^h|$, where u_z is the displacement of a random node, and u_z^h is the displacement at the same location on the coarse mesh with 5^{th} order approximation. The 5^{th} order p-refined mesh is assumed to provide the reference solution.

3. Results

Creating the geometry and mesh using a Python/APRPRO script has proven to be an effective dynamic solution to generate braided type geometries. The flexibility of this script is not only the capability of varying the parameters of such braiding, but could be easily adopted for other types of braiding. Loose braiding was formed and hence pre-stressing using nonlinear geometry (large rotations and small strains) is required at a later stage.

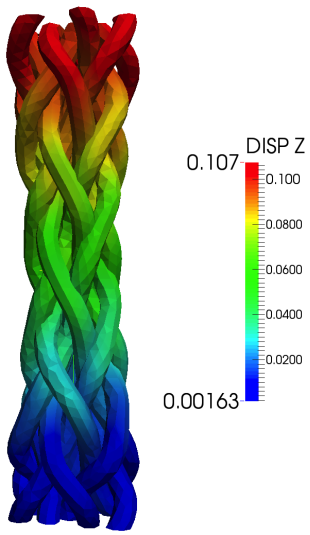

Figure 4: Linear Elastic Material with interface between yarns

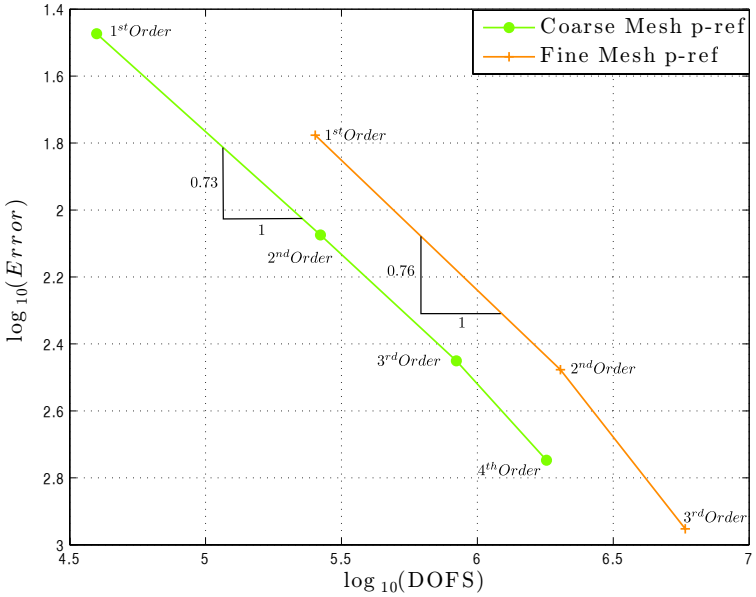

Figure 5: Convergence Results for Coarse and Fine Mesh with different order of approximation

Isotropic steel material was used for the clamps (not shown in fig. 4), and carbon fibre transverse isotropic material properties was used for the yarns. Figure 4 shows the deformed shape of the braided rope. Negligible penetration between yarns was observed.

P-refinement on the coarse and fine mesh resulted in similar rates of convergence (Figure 5). This reflects the theoretical rates of convergence for both the energy and displacement norms [4].

P-refinement on the coarse mesh is found to be the optimal refinement, achieving accurate results with the least number of DOFs. Hence uniform hp-refinement is not recommended in this case, although one might investigate the use of adaptive p and/or hp-refinement, where the theory suggest an exponential rate of convergence would be achieved.

4. Conclusions

An effective method was achieved to model and mesh complex geometries such as braided ropes. Mechanical modelling of such geometries, required the implementation of an appropriate material, i.e. transverse isotropy, that well represent the behaviour of the individual fibre yarns. Although such a material could be orientated using the centre axis of the yarns as a mean of representing the fibre directions, this would lead to problems when the model is subject to large deformations and yarn cross-sections do not remain uniform. An effective solution for this problem, was to solve a potential flow problem, where by the velocity vectors at every gauss point (later used as the fibre directions) were computed using the gradients of the resultant stream function (ψ). Furthermore, convergence studies, shows that although a local error was computed (a nodal displacement was used to compute the error), linear convergence holds with the theory, achieving about 93% of accuracy for 2^{nd} order of approximation with the coarse mesh.

After this initial study, the process to investigate the bond behaviour between the fibre rope and concrete will be as follows:

- Include a non-linear interface between the yarns.
- Pre-stress the rope model using large rotations/small strains.
- A better representation of the geometry using higher order elements.
- Implement the potential flow solution for every iteration of the nonlinear mechanical analysis, hence fibre direction will be updated every time the geometry changes.
- Encase the pre-stress ropes in concrete and use a suitable cohesive damage law for the interface
- Investigate the pull-out bond strength for plain and ribbed braided ropes
- Implement concrete fracture to investigate cracking induced by reinforcement

Acknowledgements

The research work undertaken in this publication is funded by the Strategic Educational Pathways Scholarship (Malta). The scholarship is part-financed by the European Union European Social Fund (ESF) under Operational Programme II Cohesion Policy 2007-2013, "Empowering People for More Jobs and a Better Quality of Life".

References

[1] M. Ainsworth, J. Coyle, Hierarchic finite element bases on unstructured tetrahedral meshes, International Journal for Numerical Methods in Engineering 58 (14) (2003) 2103–2130.

[2] M. Cortis, L. Kaczmarczyk, C. J. Pearce, Computational modelling and experimental investigation of the bond behaviour between concrete and braided fibre ropes, in: International Conference on Computational Mechanics (CM13), no. March, 2013.

[3] A. Katz, N. Berman, Modeling the efect of high temperature on the bond of FRP reinforcing bars to concrete 22 (2000) 433–443.

[4] L. Demkowicz, Computing with hp-adaptive finite elements: Volume 1 One and Two Dimensional Elliptic and Maxwell Problems, Chapman & Hall/CRC Applied Mathematics and Nonlinear Science Series, Taylor & Francis, 2006.

Proceedings of the 22nd UK Conference of the
Association for Computational Mechanics in Engineering
2 – 4April 2014, University of Exeter, Exeter

CONSTITUTIVE MODELLING FOR CYTOSKELETAL CONTRACTILITY OF SMOOTH MUSCLE CELLS

***Tao Liu**

Department of Civil Engineering, University of Nottingham, Nottingham, NG7 2RD

*Tao.Liu@nottingham.ac.uk

ABSTRACT

A group of constitutive equations have been presented for cytoskeletal contractility of idealized one-dimensional smooth muscle cells, which capture the main features of biochemical responses and mechanical responses induced by a rise in the intracellular calcium ion level. The constitutive equations are employed to simulate shortening induced deactivation for smooth muscle cells. The results obtained by simulation agree well with experimental measurements reported in references [1]. A model is developed to extend the 1D constitutive equations for two-dimensional and three-dimensional cytoskeletal networks of SMCs. The 2D version of the model has been incorporated, as the user defined subroutine (UMAT), into commercially finite element package ABAQUS® Standard. The UMAT is used to investigate swine carotid media strips under electrical stimulation and contraction of a hollow airway and a hollow arteriole buried in a soft matrix subjected to multiple Ca2+ stimulations.

Keywords: *Smooth muscle cell; finite element simulation; bio-chemo-mechanical modelling; cytoskeletal contractility*

1. Introduction

As the contractile component of hollow organs such as the intestines, the airways and blood vessels, smooth muscle cells react to stimulations, such as electrical field and calcium ion (Ca2+) transients, by contracting the hollow organs. Abnormal contractility of smooth muscle cells is an important cause of many diseases, such as asthma, incontinence and hypertension. For example, airway hyperresponsiveness is a characteristic of asthma and generally ascribed to the excessive contraction of airway smooth muscle cells. In past decades, significant progress has been made in developing experimental techniques to measure mechanical responses, mainly contraction, of smooth muscle cells or smooth muscle cell based tissues under various conditions. As the recent development, Tan et al. [2]has measured the distribution of force exerted by a smooth muscle cell by seeding the smooth muscle cell on a bed of poly (dimethylsiloxane) (PDMS) micro-posts and determining the deflections of the posts. Alford et al.[3] has employed vascular muscular thin film (vMTF) method to measure the dynamic stress generation during contraction of microfabricated tissues of vascular smooth muscle with differing tissue and cell-level architecture. Due to complexity of the problem, most experimental investigations focus on details of individual elements regulating contractility of smooth muscle cells, but an integrative understanding of how the different regulatory elements function together remains elusive. Hence, interpretation on experimental measurements at cell or tissue level remains a challenge. The aim of the article is to develop a constitutive model that is capable of describing the bio-chemo-mechanical features in contractility of smooth muscle cells.

2. Constitutive model for one-dimensional smooth muscle cells

(i) Bio-chemical model

Let $\dot{\varepsilon}_{\max}$ and $\dot{\varepsilon}$ represent the maximum shortening strain rate and strain rate of a smooth muscle cell, respectively. The biochemical model can be written as

$$\frac{d[M]}{dt} = -k_1[M] + k_2[MP] + \left(k_7 - k_9 \frac{k_{10}}{\xi}\frac{\dot{\varepsilon}}{\dot{\varepsilon}_o}\right)[AM] \quad (1)$$

$$\frac{d[MP]}{dt} = \left(-k_8 \frac{k_{10}}{\xi}\frac{\dot{\varepsilon}}{\dot{\varepsilon}_o} + k_4\right)[AMP] + k_1[M] - (k_2 + k_3)[MP] \quad (2)$$

$$\frac{d[AMP]}{dt} = k_3[MP] + k_6[AM] - \left(k_4 + k_5 - k_8 \frac{k_{10}}{\xi}\frac{\dot{\varepsilon}}{\dot{\varepsilon}_o}\right)[AMP] \quad (3)$$

$$\frac{d[AM]}{dt} = k_5[AMP] - \left(k_6 + k_7 - k_9 \frac{k_{10}}{\xi}\frac{\dot{\varepsilon}}{\dot{\varepsilon}_o}\right)[AM] \quad (4)$$

where , $[\mathrm{M}]$, $[\mathrm{MP}]$,$[\mathrm{AMP}]$ and $[\mathrm{AM}]$ are non-negative and non-dimensional quantities with $[\mathrm{M}]+[\mathrm{MP}]+[\mathrm{AMP}]+[\mathrm{AM}]=1$, representing fractions of free unphosphorylated , phosphorylated , attached dephosphorylated and attached phosphorylated myosin, respectively, ξ phosphorylation level of myosin, $\xi = [\mathrm{MP}]+[\mathrm{AMP}]$ and k_1, ... , k_{10} are the rate constants which can be obtained by fitting the model behavior against experimental data .

(ii) Relation of active contraction stress versus strain rate

Following the Hill's equation and considering the effect of phosphorylation of myosin, the relation between active contraction stress s and strain rate $\dot{\varepsilon}$ of the smooth muscle cell under isotonic contraction can be given as

$$\frac{\sigma}{\sigma_o} = \frac{1 + \frac{k_{10}}{\xi}\frac{\dot{\varepsilon}}{\dot{\varepsilon}_o}}{1 - \frac{1}{\xi}\frac{\dot{\varepsilon}}{\dot{\varepsilon}_o}} \qquad \text{if} \quad -\frac{\xi}{k_{10}} \le \frac{\dot{\varepsilon}}{\dot{\varepsilon}_o} \le 0 \quad (5)$$

$$\sigma/\sigma_o = 0 \qquad \text{if} \quad \frac{\dot{\varepsilon}}{\dot{\varepsilon}_o} \le -\frac{\xi}{k_{10}} \quad (6)$$

$$\sigma/\sigma_o = 1 + \frac{(1+k_{10})}{\xi}\frac{\dot{\varepsilon}}{\dot{\varepsilon}_o} \qquad \text{if} \quad \frac{\dot{\varepsilon}}{\dot{\varepsilon}_o} > 0 \quad (7)$$

where $\dot{\varepsilon}_o$ is a reference strain rate, $\dot{\varepsilon}_o > 0$. The value of attached cross bridges, $h = [\mathrm{AM}]+[\mathrm{AMP}]$, can be related to isometric contraction stress, s_o, of a smooth muscle via

$$s_o = \frac{s_{\max}}{[h]_{\max}} h \quad (8)$$

where $s_{\max}$ is the maximal tension corresponding to the maximal number of attached cross bridges $[h]_{\max} = \max([\mathrm{AMP}]+[\mathrm{AM}])$ that is permitted by biochemistry .

3. Constitutive model for 2D/3D cytoskeleton of smooth muscle cells

Let $\bar{\boldsymbol{\sigma}}$ and $\bar{\mathbf{D}}$ denote macroscopic Cauchy stress and rate-of –deformation, respectively. Employing compatibility, the true strain rate $\dot{\varepsilon}^{(k)}$ along axis of the *k*th stress fiber can be related to $\bar{\mathbf{D}}$

$$\dot{\varepsilon}^{(k)} = \bar{D}_{ij} n_i^{(k)} n_j^{(k)} \qquad \text{(summation over } i \text{ and } j\text{)} \quad (9)$$

For well-developed stress fibers, i.e., $m \to \infty$, we have

$$\bar{\sigma}_{ij} = \frac{1}{\pi}\int_{-\pi/2}^{\pi/2} \sigma n_i n_j d\theta + \sigma_{pij} \qquad \text{(for 2D)} \qquad (10)$$

$$\bar{\sigma}_{ij} = \frac{1}{2\pi}\int_{-\pi/2}^{\pi/2} d\omega \int_{0}^{\pi} \sigma n_i n_j \sin\varphi d\varphi + \sigma_{pij} \text{ (for 3D)} \qquad (11)$$

where angles θ, ω and φ are defined in Fig.1 and $\boldsymbol{\sigma}_p$ is the Cauchy stress for passive behaviour of the cell. The passive elasticity, provided mainly by intermediate filaments, nuclei and cell membrane, need to be included in the contractile response of a cell. As shown in Eqs. (10) and (11), additive decomposition of the active stress and passive stress is assumed as the stress fibers act in parallel with intermediate filaments and the cell membrane. Here, for simplicity, the passive component of a cell is assumed to behave like a neo-Hookean solid. The 2D version of the constitutive model described above has been implemented into commercially available finite element software ABAQUS® Standard via user-defined subroutine UMAT to solve plane strain/plane stress problems.

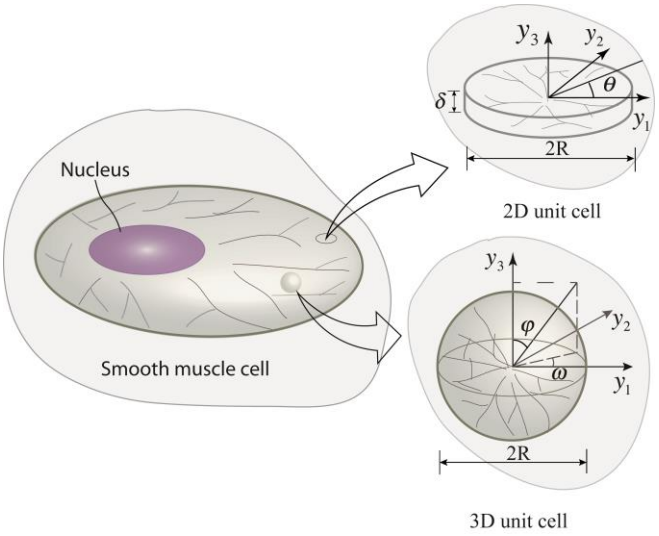

Figure 1 Two-dimensional (2D) representative volume element (RVE) and three-dimensional (3D) representative volume element (RVE) employed to analyse a two-dimensional cytoskeleton network and a three-dimensional cytoskeleton network, respectively, in a smooth muscle cell.

4. Simulation for 2D smooth muscle cells

In this section, six-node quadratic plane stress triangle element (CPS6 in ABAQUS notation) and plane strain triangle element (CPE6) are employed to analyze plane stress and plane strain problems, respectively, under finite deformation setting, i.e. the effects of geometry changes on momentum balance and rigid body rotations are taken into account.

Several authors have experimentally examined the contraction of hollow organs subjected to Ca^{2+} stimulation , which has motivated the finite element simulation on the contraction of a hollow airway, with internal radius 100 mm and external radius 140 mm, and a hollow arteriole, with internal radius 40 mm and external radius 66.6 mm, buried in a 400 mm × 640 mm passive matrix material, clamped at two opposite edges with remaining edges free, subjected to multiple Ca^{2+} stimulations.It is assumed that the out-of-plane dimension is much longer than the in-plane ones. Therefore, the problem can be simplified as a plane strain boundary value problem. No attempt was made to calibrate material properties or intracellular Ca^{2+} concentration against existing experimental studies in this paper. The passive matrix material was treated as a neo-Hookean solid with $\kappa = 7800$ N/m^2 and $\bar{E} = 9360$ N/m^2 representing soft tissues such as lung. The material properties of bovine tracheal smooth muscle [4] are employed in the simulation for both the airway and arteriole. The rate constants of k_1, k_6 are chosen to represent three consecutive stimulations, namely, as shown in Fig.2. The

passive property of bovine tracheal smooth muscle was assumed to be same to that of swine carotid media, i.e., $\kappa = 7840$ N/m^2 and $\bar{E} = 4704$ N/m^2 . The sensitivity of k_8 and k_9 is studied with $k_8 = k_9$.

The time evolutions of relative areas, defined as the area of hollow organ at current configuration normalized by that at initial configuration, of the airway and the arteriole are shown in Fig.2*d* and *e* for selected values of k_8, k_9. The contours of maximum principle true strain at *t*=300 s for selected values of k_8, k_9 is shown in Fig. 2 *a, b* and *c*. These figures show (i) lower values of k_8, k_9 correspond to more reduction of areas in hollow organs, (ii) if the same values of k_8, k_9 were applied to the airway and the arteriole, the relative areal changes of the airway and the arteriole are almost identical, (iii) the deformed shapes of hollow organs may be sensitive to the strain field in the matrix material and (iv) even though the values of k_1, k_6 decline to zero after each stimulation, these hollow organs still keep in contracted state.

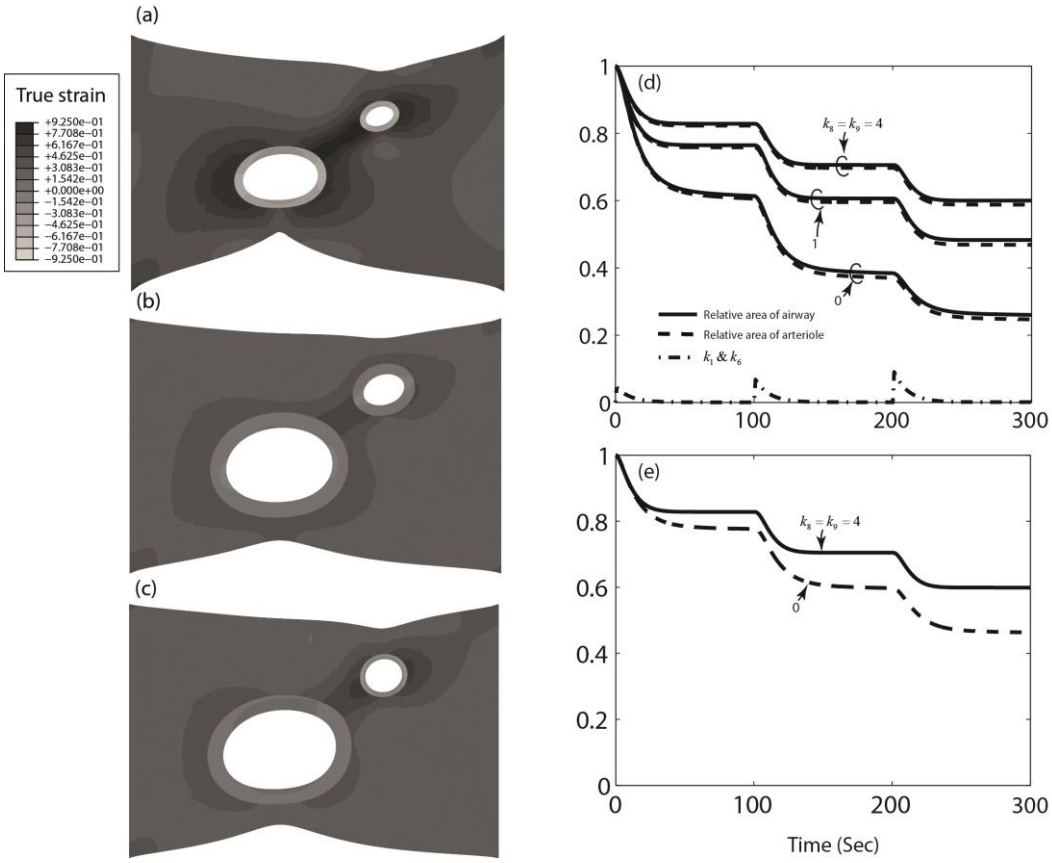

Fig.2 Contours of maximum principle true strain at t= 300 s with $k_8, k_9 = 0$ s^{-1} (*a*) and $k_8, k_9 = 4$ s^{-1} (*b*) for both airway and arteriole and $k_8, k_9 = 4$ s^{-1} for airway and $k_8, k_9 = 0$ s^{-1} for arteriole (*c*).Time histories of relative areas of both the airway and the arteriole for selected values of k_8 and k_9 (*d*) and (*e*). The time history of k_1, k_6 is shown in (*d*).

References

[1] T. Liu, A constitutive model for cytoskeletal contractility of smooth muscle cells. *Proceeding of the Royal Society of London A,* 470, 2164, 2014.

[2] J.L. Tan, J. Tien, D.M. Pirone, D.S. Gray , K., Bhadriraju and C.S.,Chen, Cells lying on a bed of microneedles: an approach to isolate mechanical force. *Proc. Natl Acad. Sci. USA* 100, 1484-1489**,**2003.

[3] P.W. Alford, A.P. Nesmith, J.N. Seywerd, A.Grosberg and K.K. Parker, Vascular smooth muscle contractility depends on cell shape. *Integr.Biol.* 3, 1063-1070, 2011.

Proceedings of the 22nd UK Conference of the
Association for Computational Mechanics in Engineering
2 - 4 April 2014, University of Exeter, Exeter

Finite strain modelling for the curing process in magneto-viscoelasticity

***M. Hossain[1], P. Saxena[1] and P. Steinmann[1]**

[1] Chair of Applied Mechanics, University of Erlangen-Nuremberg, Germany

*mokarram.hossain@ltm.uni-erlangen.de

ABSTRACT

In this contribution, we present a phenomenologically motivated magneto-viscoelastic coupled finite strain framework for simulating the curing process of polymers in the presence of a magneto-mechanically coupled load. In the fabrication of magneto-sensitive polymers, micron-size ferromagnetic particles are used in the uncured stage. Chemical reactions during curing impart a continuous change of stiffness properties that can be modelled by an appropriate constitutive relation where the temporal evolution of material parameters is considered. Here few numerical examples are demonstrated in the case of a magneto-viscoelastically coupled load which predict some common features in polymers undergoing curing processes in finite strain regime.

Key Words: *magneto-sensitive polymers; curing; coupled problem; magneto-viscoelasticity*

1. Introduction

In recent years the so-called smart materials have been invented where the magnetorheological elastomers (MREs) or magneto-active elastomers are a relatively new group of smart materials. The mechanical properties such as the shear modulus of MREs can be enhanced by the application of an externally applied magnetic field. Applications of MREs include different components in automotive industry, civil engineering devices, e.g. suspension bushing, brakes, smart springs in dynamic vibration absorber, building vibration isolation, noise barrier system and sensors. During curing process, the application of a magnetic field results in anisotropic elastomers where the magnetic particles are aligned strictly in a particular orientation. In the curing process of polymers, a series of chemical reactions occur which transform a viscoelastic fluid into a viscoelastic solid. Due to successive reactions, polymer chains cross-link to each other. Hence, the formation of new chemical bonds allows the chains to come closer. Such packing of chains will yield a decrease in specific volume which is noted as the volume or curing shrinkage.

Several publications reported experimental works both on isotropic and anisotropic magneto-sensitive polymeric composites that were obtained either by the application of an externally applied magnetic field or without a magnetic field. A considerable amount of literature is devoted to address the modelling and simulation issues of isotropic and anisotropic magneto-active elastomers in large deformation frameworks. However, there is no constitutive model, to the best of the authors' knowledge, that can predict material parameter evolution as well as stiffness gain during curing process in the presence of a magnetic field or a magnetic induction. Therefore, a finite strain framework, since elastomeric matrix can undergo large deformations when excited by an external magnetic induction, is essential to predict the curing process behaviour under the application of a magneto-mechanically coupled load. The proposed modelling framework is within the hypoelastic concept of our previously published purely mechanical curing model [3]. In order to capture the magneto-mechanically coupled load, a phenomenologically motivated convolution integral type energy potential is proposed that consists of three parts, i.e. a pure mechanical part, a pure magnetic part and a magneto-mechanically coupled part.

2. Curing-dependent viscoelastic model

Continuous chain cross-linking occurs due to chemical reactions in the curing process of polymers. Such chemical cross-linking yields increasing stiffness of a material under curing which can be conceptualised

as the addition of more and more spring-like elements to the already formed network. This stiffness changing process can be realized with the following potential function

$$\begin{aligned}\Phi(t) &= \frac{1}{2}\int_0^t [\mathcal{A}'(s):[\boldsymbol{E}(t)-\boldsymbol{E}(s)]]:[\boldsymbol{E}(t)-\boldsymbol{E}(s)]ds + \frac{1}{2}\int_0^t [\mathcal{K}'(s)\cdot[\mathbb{B}(t)-\mathbb{B}(s)]]\cdot[\mathbb{B}(t)-\mathbb{B}(s)]\,ds \\ &+ \int_0^t [\mathcal{C}'(s)\cdot[\mathbb{B}(t)-\mathbb{B}(s)]]:[\boldsymbol{E}(t)-\boldsymbol{E}(s)]ds. \end{aligned} \tag{1}$$

In Eqn (1) $\mathcal{A}'(s) = d\mathcal{A}(s)/ds, \mathcal{K}'(s) = d\mathcal{K}(s)/ds$ and $\mathcal{C}'(s) = d\mathcal{C}(s)/ds$, where $\boldsymbol{E}$ is the Green-Lagrange strain tensor and $\mathbb{B}$ is the magnetic induction vector in the material configuration. The three tensors $\mathcal{A}, \mathcal{C}, \mathcal{K}$ are time-dependent fourth order, third order and second order magnetoelastic moduli tensors, respectively, i.e. $\mathcal{A}(t) = \frac{\partial^2\Omega(t)}{\partial\boldsymbol{E}\partial\boldsymbol{E}}$, $\mathcal{C}(t) = \frac{\partial^2\Omega(t)}{\partial\boldsymbol{E}\partial\mathbb{B}}$, $\mathcal{K}(t) = \frac{\partial^2\Omega(t)}{\partial\mathbb{B}\partial\mathbb{B}}$, where $\Omega(t)$ is a coupled energy function for magneto-elastic polymers with time dependent material parameters. Obeying the second law of thermodynamics and after rigorous calculations following relations are obtained

$$\dot{\boldsymbol{S}}(t) = \frac{1}{2}\mathcal{A}(t):\dot{\boldsymbol{C}}(t) + \mathcal{C}(t)\cdot\dot{\mathbb{B}}(t), \quad \dot{\mathbb{H}}(t) = \frac{1}{2}\mathcal{C}^t(t):\dot{\boldsymbol{C}}(t) + \mathcal{K}(t)\cdot\dot{\mathbb{B}}(t). \tag{2}$$

The classical approach in viscoelastic rubber-like material modelling is the multiplicative decomposition of the deformation gradient into elastic ($\boldsymbol{F}_e$) and viscous ($\boldsymbol{F}_v$) parts which motivates a similar approach of deformation decomposition in the case of a magnetic induction into elastic and viscous internal variables $\mathbb{B}_e$ and $\mathbb{B}_v$, respectively, such that

$$\boldsymbol{F} = \boldsymbol{F}_e\boldsymbol{F}_v, \qquad \mathbb{B} = \mathbb{B}_e + \mathbb{B}_v. \tag{3}$$

Following the analogy of a multiplicative decomposition of the deformation gradient and an additive decomposition of the magnetic induction vector, the total magneto-mechanical energy stored in a body can be decomposed into an equilibrium part and a non-equilibrium part

$$\Omega(\boldsymbol{C}, \boldsymbol{C}_v, \mathbb{B}, \mathbb{B}_v) = \Omega_{eq}(\boldsymbol{C}, \mathbb{B}) + \Omega_{neq}(\boldsymbol{C}, \boldsymbol{C}_v, \mathbb{B}, \mathbb{B}_v) \tag{4}$$

where the equilibrium part is

$$\Omega_{eq} = \frac{\mu}{4}\left[1 + \alpha_e \tanh\left(\frac{I_4}{m_e}\right)\right]\left[\,[1+n]\,[I_1-3] + [1-n]\,[I_2-3]\,\right] + qI_4 + rI_6 + \frac{1}{8}\kappa\,[\ln I_3]^2 - \frac{1}{2}\mu\ln I_3, \tag{5}$$

and the non-equilibrium part is

$$\begin{aligned}\Omega_{neq}(\boldsymbol{C}, \boldsymbol{C}_v, \mathbb{B}, \mathbb{B}_v) &= \frac{\mu_v}{2}\left[\boldsymbol{C}_v^{-1}:\boldsymbol{C} - 3\right] + q_v[\,[\mathbb{B}-\mathbb{B}_v]\otimes[\mathbb{B}-\mathbb{B}_v]\,]:\boldsymbol{I} \\ &+ r_v\left[[\boldsymbol{C}\,[\mathbb{B}-\mathbb{B}_v]\,]\otimes[\boldsymbol{C}\,[\mathbb{B}-\mathbb{B}_v]\,]\right]:\boldsymbol{I} + \frac{1}{2}\kappa_v\,[\ln J_e]^2 - \mu_v\ln J_e. \end{aligned} \tag{6}$$

In the above equations I_1, I_2, I_3, I_4, I_6 are the standard scalar strain invariants in magnetoelasticity, $\mu, \alpha_e, m_e, n, q, r, \kappa, \mu_v, \kappa_v, q_v, r_v$ are material parameters and $J_e = \det\boldsymbol{F}_e$. Two thermodynamically consistent evolution equations for the viscous internal variables are

$$\frac{d\mathbb{B}_v}{dt} = \frac{2\mu_0}{T_m}\left[q_v\boldsymbol{I} + r_v\boldsymbol{C}^2\right][\mathbb{B}-\mathbb{B}_v], \qquad \frac{d\boldsymbol{C}_v}{dt} = \frac{1}{T_v}[\boldsymbol{C}-\boldsymbol{C}_v], \tag{7}$$

see Saxena et al. [2] for details. Now the stress and the magnetic field are decomposed as

$$\boldsymbol{S} = \boldsymbol{S}_{eq} + \boldsymbol{S}_{neq}, \qquad \mathbb{H} = \mathbb{H}_{eq} + \mathbb{H}_{neq}. \tag{8}$$

To extend the cure-dependent magneto-elastic constitutive framework developed in Eqn (2), we blend the idea of a fully-cured magneto-viscoelastic modelling as in Saxena et al. [2] and the idea of a purely mechanical viscoelastic cure-dependent model as in Hossain et al. [3]. Henceforth, the blended idea will be to add the non-equilibrium responses (stress and magnetic field) in Eqn (8) with the magneto-elastic curing formulations developed in Eqn (2), i.e.

$$\boldsymbol{S}^{n+1} = \boldsymbol{S}^n_{eq} + \frac{1}{2}\mathcal{A}^{n+1}:[\boldsymbol{C}^{n+1}-\boldsymbol{C}^n] + \mathcal{C}^{n+1}\cdot[\mathbb{B}^{n+1}-\mathbb{B}^n] + \boldsymbol{S}^{n+1}_{neq} \tag{9}$$

$$\mathbb{H}^{n+1} = \mathbb{H}^n_{eq} + \frac{1}{2}\mathcal{C}^{t,n+1}:[\boldsymbol{C}^{n+1}-\boldsymbol{C}^n] + \mathcal{K}^{n+1}\cdot[\mathbb{B}^{n+1}-\mathbb{B}^n] + \mathbb{H}^{n+1}_{neq}. \tag{10}$$

Now the non-equilibrium part of the energy function is required for the derivation of the non-equilibrium stress and magnetic field, i.e.

$$\begin{aligned} \boldsymbol{S}_{neq} &= \mu_v[\boldsymbol{C}_v^{-1} - \boldsymbol{C}^{-1}] + \kappa_v \ln J_e \boldsymbol{C}^{-1} + 2r_v \mathbb{B}_e \otimes [\boldsymbol{C}\mathbb{B}_e] + 2r_v\,[\boldsymbol{C}\mathbb{B}_e] \otimes \mathbb{B}_e, \qquad (11) \\ \mathbb{H}_{neq} &= 2q_v \mathbb{B}_e + 2r_v \boldsymbol{C}\mathbb{B}_e, \qquad (12) \end{aligned}$$

where $\boldsymbol{C}_v$ and $\mathbb{B}_v$ are mechanical and magnetic internal variables, respectively. To get the current state of the mechanical and magnetic internal variables, Eqns $(7)_1$ and $(7)_2$ need to be integrated.

3. Numerical Examples

In this section, we present some numerical examples to show the capability of the proposed cure-dependent magneto-viscoelastic model. To obtain current states for the total stress as well as for the magnetic field the relations need to be integrated. For simplicity, we use an Euler-backward type implicit integrator resulting following updates for the algorithmic stress as

$$\boldsymbol{S}^{n+1} = \boldsymbol{S}^n_{eq} + \frac{1}{2}\mathcal{A}^{n+1} : [\boldsymbol{C}^{n+1} - \boldsymbol{C}^n] + \mathcal{C}^{n+1} \cdot [\mathbb{B}^{n+1} - \mathbb{B}^n] + \boldsymbol{S}^{n+1}_{neq}, \qquad (13)$$

and the algorithmic magnetic field vector is as follows

$$\mathbb{H}^{n+1} = \mathbb{H}^n_{eq} + \frac{1}{2}\mathcal{C}^{t,n+1} : [\boldsymbol{C}^{n+1} - \boldsymbol{C}^n] + \mathcal{K}^{n+1} \cdot [\mathbb{B}^{n+1} - \mathbb{B}^n] + \mathbb{H}^{n+1}_{neq}. \qquad (14)$$

In Eqns (13) and (14), $[\bullet]^n = [\bullet](t_n)$, $t_{n+1} = t_n + \Delta t$ and Δt is a time step. The deformation gradient $\boldsymbol{F}$ and the magnetic induction vector $\mathbb{B}$ are input variables for the mechanical and magnetic load cases, respectively. As per definition of a uniaxial tension test, the specimen is elongated only in one direction, i. e. $\lambda_1 = \lambda$, while the other two lateral directions are free to move. In a three-dimensional setting, the complete deformation gradient ($\boldsymbol{F}$) reads

$$\boldsymbol{F} = \begin{bmatrix} \lambda_1 & 0 & 0 \\ 0 & \lambda_2 & 0 \\ 0 & 0 & \lambda_3 \end{bmatrix} \qquad (15)$$

and the magnetic induction vector ($\mathbb{B}$) is as follows

$$\mathbb{B} = \begin{bmatrix} B_1 \\ 0 \\ 0 \end{bmatrix}. \qquad (16)$$

For the particular numerical experiments presented below, the following numerical values of the material parameters are used unless otherwise stated to have a different value for individual computation

$$\begin{aligned} \alpha_e &= 0.3, m_e = 1\ \mathrm{T}^2, n = 1, \nu = 0.4, \mu_0 = 4\pi \times 10^{-7}\ \mathrm{N/A}^2, q = 1/\mu_0, \\ \mu_v &= 5 \times 10^5\ \mathrm{MPa}, q_v = 5/\mu_0, r_v = 1/\mu_0. \qquad (17) \end{aligned}$$

Firstly it is required to verify whether the developed cure-dependent magneto-viscoelastic model can capture few important phenomena that happen during the curing process, i.e. the stiffness gain due to the continuous chain crosslinking with an advancement of time and the stress relaxation during a holding period under a purely mechanical or a purely magnetic load. Moreover, it is also essential to check if the model can provide a correct behaviour in the case when the mechanical strain rate becomes zero and/or the magnetic induction rate is zero. A four-step mechanical and magnetic load is applied to assess the capability of the model. Several homogeneous numerical tests show that the framework can capture relevant phenomena observed in a magneto-mechanical coupled curing process, e.g. two of them are presented in Figs (1) and (2). Figure (1,a) which shows the mechanical stress over curing time indicating

the stress increment in the second deformation phase (during 45-50 sec) is higher than the first deformation phase (0-5 sec). It is more vivid if we plot the mechanical stress over stretch which basically illustrates the stiffness gain during the holding time, cf. Fig (1, b). Figure (2) shows that the increment of the magnetic field is larger in the second load step than the first step. Moreover, the model can capture the physical phenomenon upon which it is based, i.e. if the mechanical strain rate becomes zero and/or the magnetic induction rate is zero, there are no increments in total stress and in magnetic field.

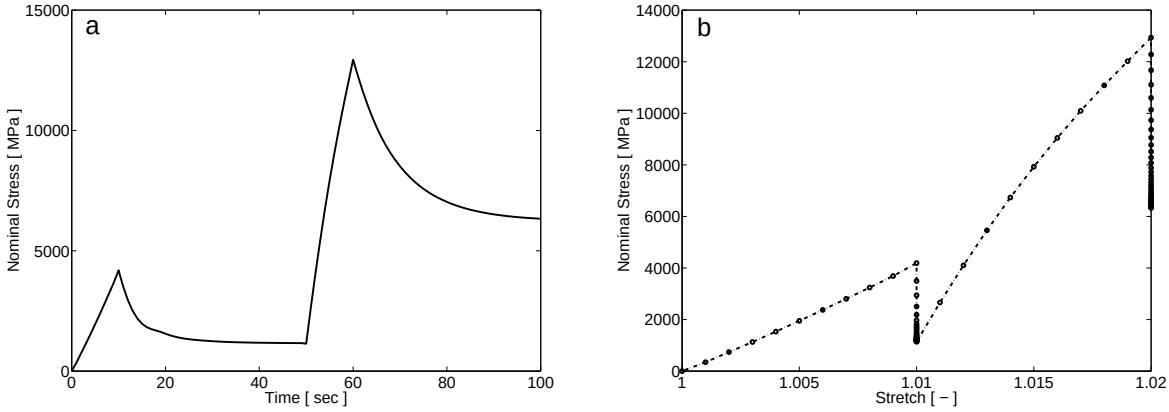

Figure 1: Magneto-viscoelastic curing model : (a) Purely mechanical stress over curing time as produced from a four-phase purely mechanical loading (b) Purely mechanical stress vs stretch that highlights stiffness gain in successive loading phases. The stress relaxation is decelerated in the second holding phase due to a time-evolving characteristics of the mechanical relaxation parameter, T_v

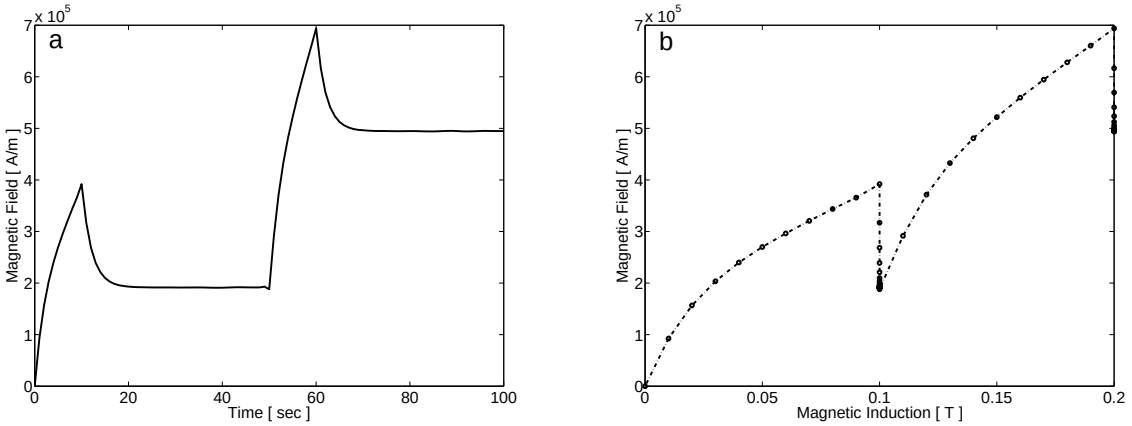

Figure 2: Magneto-viscoelastic curing model: (a) Magnetic field over curing time with respect to a four-phase purely magnetic load (b) Magnetic field vs magnetic induction that highlights stiffness gain due to continuous chain crosslinking. However, the stress relaxation in the two holding phases are the same due to a constant value of the magnetic relaxation parameter, T_m

References

[1] Hossain M, Saxena P, Steinmann P (2013) Modelling the curing process in magneto-sensitive elastomeric materials, submitted

[2] Saxena P, Hossain M, Steinmann P (2013) A theory of finite deformation magneto-viscoelasticity, IJSS, 50(24): 3886-3897

[3] Hossain M, Possart G, Steinmann P (2010) A finite strain framework for the simulation of polymer curing. Part II: Viscoelasticity and shrinkage, Comput. Mech. 46(3):363-375

Proceedings of the 22nd UK Conference of the
Association for Computational Mechanics in Engineering
2 – 4April 2014, University of Exeter, Exeter

HIGH TEMPERATURE PROTECTIVE COATINGS FOR AVIATION GAS TURBINES

A.J. Pashayev[1], A.S. Samedov[2], *T.B. Usubaliyev[3] and R.S. Agaverdiyev[4]

[1]Department of Aircosmic Instruments, National Academy of Aviation, Bina, 25th km, Baku, AZ1045
[2]Department of Aircraft and Aviation Engines, National Academy of Aviation, Bina, 25th km, Baku, AZ1045
[3]Engineering Department, Silk Way Technics, Heydar Aliyev International Airport, Baku, AZ1044
[4]Engineering Department, Silk Way Technics, Heydar Aliyev International Airport, Baku, AZ1044

*TUsubaliyev@swt.az

ABSTRACT

Results of experimental-calculated investigations on development of mathematical models of forecasting of composition and obtaining new protective coating (CrAlPtV) for gas turbine blades on the basis of correlation-regression analysis, analysis of quantitative ratio and physical-chemical characteristics in view of nuclear radius and type of crystal lattice of elements are presented. The number of experiments, time and temperature was determined by the method of experiment planning. On the basis of the differential thermal and X-ray analysis results was confirmed absence of phase transitions and phase stability of alloys in temperature 20÷1500°C.

Keywords: *aviation gas turbine engines; blades; protective coating; CrAlPtV; phase and thermal analysis*

Introduction

The durability of high-temperature aviation gas turbine engines (GTE) blades in many respects depends on a right choice of protective coating. Coatings allow improving flight-technical characteristics of engines, to reduce a consumption of air on cooling, to save fuel, to increase temperature of a gas stream on 100-150K. The coating should be at the same time heat-resistant and thermal barrier, i.e. capable is considerable to reduce temperature on the surface of details and to resist high-temperature oxidative corrosion [1].
Level of reliability of the turbine blade is connected with creation of efficient composition "superalloy – corrosion-resistant coating". Applied the modern nickel superalloys for GTE blades possess necessary level of long strength, however have low corrosion resistance to products of combustion and don't provide requirements imposed to lifetime of blades [2]. Therefore, for ensuring necessary durability of protective coating, along with a right choice of composition, is necessary to consider also the processes, occurring on border of blade and coating, directly influencing their operational reliability. The purpose of work is development of scientific-methodical bases of a choice of composition and obtaining new protective coatings for gas turbine blades, providing durability and extension of aviation GTE lifetime.

Thermal protection problems of gas-turbine engines

Researches demonstrate that base shortcomings of protective coatings are possible because of the incomplete take into consideration structural characteristics of blades and coatings alloys. Therefore, at choice of coatings composition is necessary based from the principle "structure-property" [2]. For this purpose is necessary taking into consideration nuclear radiuses and crystal structure of coating elements and protected surface.
To increases operational reliability of coatings it is necessary to achieve bilateral diffusion with the main metal of blade. Bilateral diffusion can be achieved at observance of size factor, when nuclear radiuses of coating elements differ no more than 15% from nuclear radiuses of basic element of protected alloy and if elements of coating and alloy have identical type of a crystal lattice. Determination of the maximum and minimum value nuclear radiuses of elements entering into composition of coating is calculated by:

$$R_{max/min} = R_{main.met} \pm 0{,}15R_{main.met} \quad (1)$$

When nuclear radiuses of elements are close to each other, at synthesis atoms in knots of crystal lattice are replaced with other atoms and internal energy of crystal lattice practically doesn't change, i.e. connection behaves as a unit.

Along with a right choice of composition, for providing necessary durability of coating also take into consideration the processes, occurring on border of blade and coating, directly influencing their operational reliability. It promotes getting the solid solutions unlike usual chemical compounds of metals with variable structure which can change over a wide range.

For the purpose of concrete realization of the presented method - account of size factor, crystal structure of alloys elements with use of Darken-Gurry method were carried out analysis of physical-chemical characteristics of the metals consisting basis of gas turbines elements and protective coatings, used for vanes and blades [3]. On the basis of this analysis is shown, that existence of numerous phases negatively influences to operational characteristics of alloys.

For carrying out the analysis nuclear radiuses, electronegativity and crystal structures data of considered alloys of gas turbine blades were collected.

For reliability of the above we will consider solubility nature of the elements, which are part of alloys with Darken-Gurry method. For the creation of the diagram, we used nuclear radius of elements, corresponding to coordination number 12 (CN12) and value of electronegativity. It should be noted that electronegativity has the strongest impact on composition and a structure of alloys and dominates over geometrical factors and an arrangement of energy levels. The high difference of electronegativity has impact on composition of a being formed phase and depends on effective number of valence electrons. The diagrams for an alloy IN738 of blade and for protective coating CoCrAlY respectively are given in Fig.1.

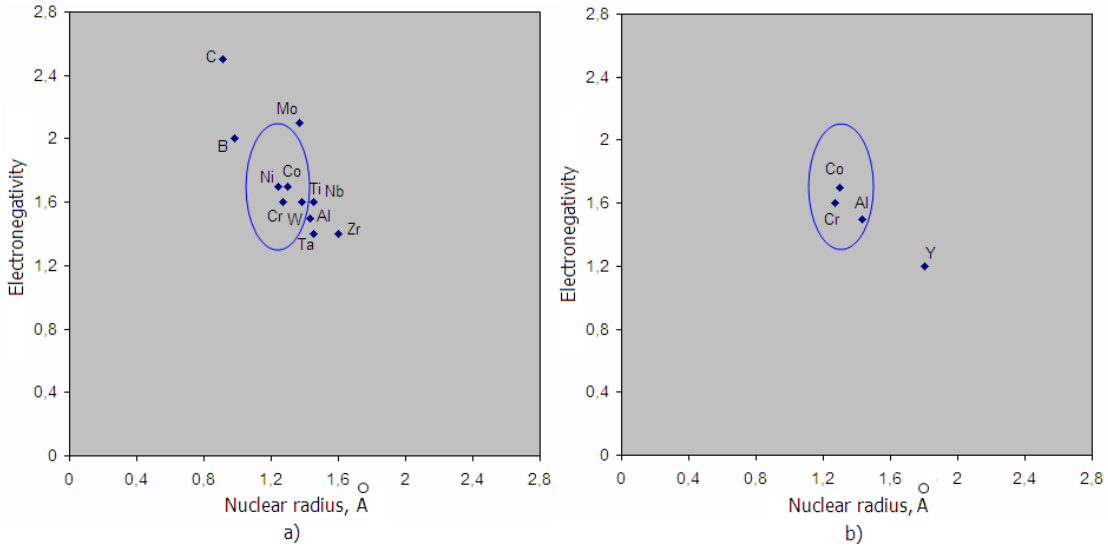

Figure 1: Darken-Gurry diagrams for alloys IN738 and CoCrAlY

For definition of ellipse area are calculated upper and lower bounds of electronegativity (±0.4) and nuclear radius (±15%) of solvent element. From the analysis of Fig.1a follows that elements Co, Cr and W located in an ellipse, will form wide areas of solid solutions with Ni, but elements Ti, Nb, Al, Zr, Ta, Mo, C and B, which didn't get in an ellipse form only very limited solid solutions. In a coating, at which solvent is Co, not all elements get to an ellipse. In an ellipse there are only elements, Co, Cr and Al, but Y is out of an ellipse (Fig. 1b). Thus, metals - Co, Cr and Al will form unlimited, but Y limited solid solutions. As Y is located rather far from ellipse border, even can not form solid solution with these elements. However, according to the fundamental requirements imposed to alloys of blades and coatings of the gas turbines, it is necessary to consider the above factors, especially size factor and uniformity of structure, which has an important role in formation of structure of alloys, diffusion between an alloy of blade and coating alloy [4].

Modeling and Analysis

Searches of new high-temperature coatings are connected, first of all, with optimization of chemical composition of new compounds with use essentially new physical effects, also with development of new technological processes and again created coatings. Problems of properties forecasting and synthesis of alloys are especially difficult and at the present time are formulated only on which obtaining necessary information is expected.

At mathematical modeling of composition of the heat-resisting coating with use of physical-chemical characteristics of the alloy elements, at the first stage was decided the problem of a choice of the factors defining solubility in each other of elements and the most perspective components of an alloy. For this purpose is created new approach to a problem of forecasting of composition of the protective coating for gas turbine blades. This problem decides methods of statistics of straight lines by means of the correlation and regression analysis.

For the solution of this problem is created the database on chemical composition of the protective coatings containing data more than 504 alloys, published in various sources of search more than 50 years. For carrying out researches of structure and physical-chemical properties of alloys, and also the analysis of possibility of obtaining some solid solutions was collected information on various microscopic characteristics of the coating elements, such as radius of atoms, types of a crystal lattice, density, electron configuration and arrangement of energy levels of atom, ionic radius and electronegativity by Pauling, ionization energy of atom, etc.

By means of STATISTICA 6.0 program are analyzed primary and intermediate phases of solid solution, carried out the forecast of substitutional and interstitial solid solutions and executed the assessment of quality of empirical parameters.

Basis of the database STATISTICA 6.0 is the databank, containing data on atoms of 23 elements – Co, Cr, Ni, Al, Y, Ta, W, Si, Hf, Mn, Mo, Ti, Zr, Pt, C, La, Re, Nb, Fe, V, Sn, Ru, Ir, which were used as parameters of the model developed at the following stage.

On the basis of the correlation analysis were obtained coefficients at pair interactions of elements. The results on importance of linear dependences between elements of coating were calculated by estimates of values of correlation coefficients.

The most significant communications exist between independent variables x_2 and x_1, which makes 0.31, between x_2 and x_4 is 0.52, between x_2 and x_5, which makes 0.06, between x_2 and x_9 is 0.05, between x_2 and x_{14} is 0.24, between x_2 and x_{20}, which makes 0.67 and between x_2 and x_{22} is 0.36. Thus, the analysis of the results obtained has demonstrated that the correlation coefficients considerably differ from zero and have rigid positive dependence.

On the basis of the regression analysis is obtained the multidimensional linear model for forecasting of composition of protective coatings:

$$y = 23.18366 + 0.0247x_1 - 0.2945x_4 + 0.6003x_5 + 0.1482x_9 - 0.2121x_{14} - 4.3905x_{20} - 0.2786x_{22} \quad (2)$$

After obtaining the regression formula, adequacy of model is checked on coefficient of determination and multiple correlations, and also by Fischer's criterion [5]. The determination coefficient for considered model is R^2=0.8549, coefficient of multiple correlation is R=0.924648, significant by Fischer's criterion F=50.702.

Such approach allowed to effectively use the correlation-regression analysis on formation of composition and quantitative ratios of elements of the protective coating as a first approximation, that was very important for experiment planning. On the basis of the elements choice, having the greatest correlation communications with definition of intervals of their percentage, the analysis of physical-chemical characteristics taking into account the nuclear radius, type of crystal lattice and on Darken-Gurry method is offered method and is created composition for new four-component high-temperature protective coating on the basis of chrome (CrAlPtV) for gas turbine blades [6].

Experimental investigations

For carrying out researches was used the method of experiment planning, on the basis were specified ranges of temperatures, time and number of experiments. The results of calculation are given in Table 1.

Table 1: Main results of experiment planning

Composition	Temperature of experiments, ^{0}C	Time of experiments, hours	Annealing temperature, ^{0}C	Annealing time, hours	Number of experiments
Cr-Al-Pt-V	1000÷1500	6	1100	60	16

Application of a method of experiment planning at investigation and synthesis of protective coating alloys allowed reducing time and material inputs. At synthesis of components in a solid condition was a need of control not only chemical composition of alloy, but also the organization of its microstructure. It is caused by strong dependence as chemical and many physical properties from characteristics of the structural organization of a solid body at various hierarchical levels.

Experimental studies were applied ceramic synthesis method. Synthesis was carried out under vacuum in corundum crucibles in order to avoid the reaction of metals with quartz at high temperatures.

Results of X-ray of the obtained samples showed that all maximums appear under the same corner (Fig. 2). To obtain more accurate maximums or more perfect structure of alloys, samples are sustained till 60 o'clock at 1100^{0}C temperature (annealing). From X-ray diffractions of the samples after annealing was shown, that structure of alloys has not changed, and even few stabilized. Thus, the results of XRD analysis showed that all samples of the alloys (solid solutions) regardless of the content of metals are single-phase system and have the same structure.

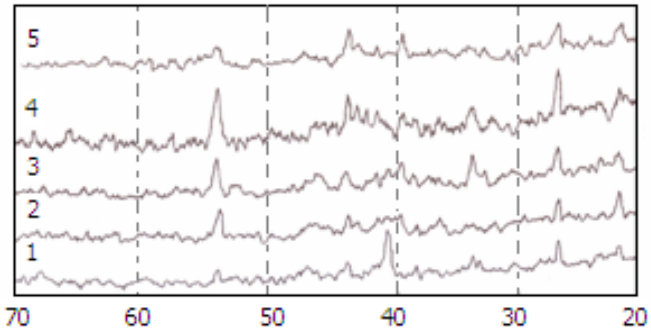

Figure 2: XRD spectrum of obtained alloys (1 - 54Cr28.2Al11.3V6.5Pt, 2 - 59Cr26.7Al9.3V5Pt, 3-64Cr25.2Al7.3V3.5Pt, 4 - 69Cr23.7Al15.3V2Pt, 5 - 74Cr22.1Al3.4V0.5Pt)

For studying thermal stability of the alloys was carried out the differential thermal analysis (DTA). The DTA results of samples of all 16 alloys show that in thermograms aren't observed the endothermic and exothermic effects, characterizing a difference of temperatures [7]. It means that when heating in studied samples of alloys aren't occurred physical or chemical processes and all alloys are stable in the temperature range 20-1500^{0}C.

Investigation of mechanical and physical properties of the alloys, interrelation of these properties with percentage of constituent elements, and also interrelation between these properties showed that between them there is an accurate regularity. Table 2 gives the mechanical and physical properties of obtained alloy. It means that the alloys have stable structure and obtaining stable structure is connected with a right choice of chemical composition of an alloy. The analysis of exploited coating alloys for blades of GTE showed that at a choice of their composition takes into account only physical properties of constituent elements, therefore are as a result obtained multiphase structures or in the majority cases mechanical mixes with those metals which didn't react. It is absolutely clear that various phases or mechanical mixes with various physical and mechanical properties in a working environment will behave differently. It finally can lead to formation of defects, cracks inside and on a surface of alloys and erosion and will influence to stability, durability of protective coatings for GTE.

Table 2: Mechanical and physical properties of obtained CrAlPtV alloy

Material	Hardness	Density, kg/m^3	TLEC, K^{-1}	Thermal conductivity, W/m^2K	Heat capacity $J/(g \cdot K)$
Cr-Al-Pt-V	3348	20.13	10.75	9.37	13.87

The results of calculations and experimental investigations suggest that offered protective coating for blades of GTE will have enough high durability, stability of composition at influence of high temperatures and hostile environment and the improved adhesion with the main materials of blades.
It should be noted that the durability of coatings, except the listed factors still depends from a method of their applying, from a material of bond on which are applied this coating and from observed all main requirements.

Conclusions

For the purpose of increasing the thermal and structural resistant of GTE blade coatings is offered new approach to forecasting of protective coating composition on the basis of the analysis of physical-chemical characteristics of alloys taking into account the size factor, type of crystal lattices and Darken-Gurry method.
It is revealed that bilateral diffusion can be achieved at observance of a size factor when nuclear radiuses of coating elements differ no more than 15% from nuclear radiuses of basic element of a protected alloy and if coating elements and a protected alloy have identical type of crystal lattice.
The mathematical model is developed for forecasting of coating composition on the basis of investigation of physical-chemical characteristics and the correlation-regression analysis of constituent elements.
As a result of calculations and experimental investigations is offered the new four-component high-temperature protective coating on the basis of chrome for the gas turbine blades.
The Complex physical-chemical experimental investigations confirmed structural stability of an alloy. On the basis of DTA and XRD analyses corroborated lack of phase transitions and stability of the obtained alloys in the temperature range $20\text{-}1500^0$C.

Acknowledgements

This work has been performed at National Academy of Aviation. The authors wish to thank their colleagues who have directly or indirectly contribute to this paper.

References

[1] K.D. Sheffer and D.K. Gupta. Current status and future trends in turbine application of thermal barrier coatings. *Journal of Engineering Gas Turbines Power*, Vol. 110, p.605, 1988.

[2] Yu.S. Eliseev, N.V. Abraimov and V.V. Krimov. *Processing and coatings in aircraft engines industry*. Moscow, Vysshaya Shkola, 1999.

[3] L. Darken and R.W. Gurry. *Physical chemistry of metals*. New York, McGraw Hill, 1953.

[4] A.J. Pashayev, A.S. Samedov, T.B. Usubaliyev. Method of producing protective coatings on gas turbine blades, EO patent 012224, August 28, 2009.

[5] A.S. Samedov and T.B. Usubaliyev. Complex method source structure of protective coating for gas turbine blades. *Aerospace Engineering and Technology*, 2(49), 73-77, 2008.

[6] A.J. Pashayev, A.S. Samedov, T.B. Usubaliyev, Method of selecting protective coatings for gas turbine blades, AZ patent I20090182, October 19, 2009.

[7] T.B. Usubaliyev. Research of structural and physical-chemical characteristics of Cr-Al-Pt-Me system alloys for protective coatings. *Herald of aeroenginebuilding*, 2, 273-278, 2012.

Proceedings of the 22nd UK Conference of the
Association for Computational Mechanics in Engineering
2 – 4April 2014, University of Exeter, Exeter

Homogeneous Response of Random Structured Material Concrete with Realistic Microstructure

R. Sharma[1], W. Ren and Third Zhenjun Yang*[1,2]

[1] School of Mechanical, Aerospace and Civil Engineering, University of Manchester, UK, M13 9PL
[2] College of Civil Engineering and Architecture, Zhejiang University, China

* zhenjun.yang@manchester.ac.uk

ABSTRACT

The realistic microstructure of the concrete has been reconstructed using X-ray tomography images and numerically simulated to obtain the effective elastic properties. The concrete under consideration was made of 5 mm coarse aggregate and cement (includes three phases cement, aggregates and macro-pores). 3D reconstructed image of the concrete cube specimen of size 40 mm^3 were converted to the finite element mesh. Also, five smaller cubical regions of size two times of coarse aggregate had been cropped to establish a statistical representative volume element (RVE) for concrete. Asymptotic homogenization technique along with periodic boundary conditions was used to obtain the elastic stiffness coefficients. Elastic stiffness matrices were obtained along with associated uncertainties for each case of RVE's. The obtained stiffness matrices for all cases were fully populated. However the shear-extension and shear-shear coupling were very small as compared to extension – extension, hence can be neglected. The cubical symmetry was observed for all cases as expected for concrete and mean values of engineering constants were closer to the isotropic case, as anisotropy ratios are nearly 1. Hence the concrete can be considered as isotropic with effective values of E= 34 GPa and μ=0.2 (Young's modulus and Poison' ratio respectively). The investigation also revealed that a smaller RVE can be considered for the concrete provided the scatter in the properties should be minimum. Later the effect of cement damage was also studied by modelling the damage initiation and propagation using damage-plasticity model for cement stiffness degradation. The strength of the concrete in tension and shear is obtained as 3.72 and 1.65 MPa respectively.

Keywords: *Homogenisation of concrete; Statistical RVE; Image based modelling; Elastic properties of concrete; Fracture of concrete*

1. Introduction

Recent developments in the field of non-destructive reconstruction techniques e.g. X-ray tomography, neutron radiography etc. have given a new insight to the material researchers for the exploration of the inherent material structure and flaws. Many applications of the X-ray tomography can be found in the area of biomedical, particulate composite, reinforced composites, ceramics and geological materials etc. [1]. Initial studies based on tomographic images are limited to the quantification of the inherent flaws such as micro cracks, voids and distribution of the phases [2]. Recently, the 3D images of the material obtained through tomography were used to study the mechanical behaviour by descritizing them into finite element meshes [1, 3]. In this way the effects of random size, shape and distribution of the different phases in the microstructure were modelled directly in finite element analysis. However, sometimes these studies were limited to a very small domain and the representation of the overall behaviour of the response differs with the domain selection. Therefore, an accurate measure to define the representative volume element (RVE) is very important, when the random quantities are associated to the domain. The window approach was generally adopted in the literature, where the size of the window was determined by optimizing the response for the domain and it was assumed that the same response is applicable for whole material [4]. Another approach of defining the effective response for material was taking the volume average of the responses obtained from different windows of different locations and also reporting the associated standard deviations [3]. A more efficient way to represent the randomness in the response is to report the mean and associated scatter for the different realisations. It is also shown by the Kanit et al. [5] that the scatter minimises for a

sufficient number of the realisations for a particular size of RVE. Therefore, a RVE can be considers with having sufficient numbers of the realisation associated to minimum scatter in the response.
In present study the homogenous elastic properties were obtained for concrete by considering the statistical RVE. Asymptotic homogenisation technique with periodic boundary condition was used with finite element analysis.

2. Material

Material under the consideration in this study was concrete, made of 5mm coarse aggregate and ordinary Portland cement. A cubical specimen from a concrete plate of age 28 days was taken out for the investigations. X-ray computed tomography (XCT) facility available in the school of materials at the University of Manchester is used to scan the specimens. Details of the parameters used during the scan are given in Table 1.

Table 1. XCT parameters used during the scan

X-ray tube: energy/intensity		Radiograph acquisition		Volume reconstruction	
Voltage (kV)	Current (mA)	Angular displacement (°)	Exposure time (ms)	Pixel size (μm)	Reconstructed volume (voxels)
160	0.06	0.18	2000	37.2	1000 × 1000 ×1000

3. Homogenisation

Asymptotic homogenisation along with periodic boundary conditions was used to obtain the elastic homogenised stiffness matrix for the concrete. In this technique six loading cases were analysed using six boundary conditions in the finite element method to get the special average of the responses, which are referred as homogenous response [3]. The general constitutive relation in terms of asymptotic homogenization can be expressed as

$$\left\langle \sigma_{ij} \right\rangle = C^{H}_{ijkl} \left\langle \varepsilon_{kl} \right\rangle \tag{1}$$

Here C^{H}_{ijkl} is the homogenised stiffness matrix. $\left\langle \sigma_{ij} \right\rangle$ and $\left\langle \varepsilon_{ij} \right\rangle$ are the respective macro stress and strain tensors and can be expressed as

$$\left\langle \sigma_{ij} \right\rangle = \frac{1}{v} \int_{v} \sigma_{ij} \, dv \tag{2}$$

and

$$\left\langle \sigma_{ij} \right\rangle = \frac{1}{v} \int_{v} \varepsilon_{ij} \, dv \, . \tag{3}$$

The components of the C^{H}_{ijkl} matrix are obtained by applying one by one six individual load cases of the strains by keeping one strain to unity and other equal to zero. In this way one can get one by one all six column of the stiffness matrix. The associated periodic conditions are given as

$$u_{x=0} = v_{y=0} = v_{y=ly} = w_{z=0} = w_{z=lz} = 0 \text{ , and } u_{x=lx} = \varepsilon_{11} lx \tag{4}$$

$$u_{x=0} = u_{x=lx} = v_{y=0} = w_{z=0} = w_{z=lz} = 0 \text{ , and } v_{y=ly} = \varepsilon_{22} ly \tag{5}$$

$$u_{x=0} = u_{x=lx} = v_{y=0} = v_{y=ly} = w_{z=0} = 0 \text{ , and } w_{z=lz} = \varepsilon_{33} lz \tag{6}$$

$$u_{x,y,z=0} = u_{x=lx,y=ly,z=lz} = v_{z=0} = w_{y=ly} = w_{y=0} = 0 \text{ , and } v_{z=lz} = \varepsilon_{23} lz \tag{7}$$

$$u_{z=0} = v_{x,y,z=0} = v_{x=lx,y=ly,z=lz} = w_{x=lx} = w_{x=0} = 0 \text{ , and } u_{z=lz} = \varepsilon_{13} lz \tag{8}$$

$$u_{y=0} = v_{x=lx} = v_{x=0} = w_{x,y,z=0} = w_{x=lx,y=ly,z=lz} = 0 \text{ , and } u_{y=ly} = \varepsilon_{12} ly \tag{9}$$

The material properties for the aggregates and cement were taken from the literature. The aggregates were assumed elastic with Yong's modulus as E=70GPa and Poisson's ratio as μ=0.2 [1]. The elastic constants for cement were considered as E=25GPa and μ=0.2 [1]. The fracture parameters; fracture energy release rate and strength were as 100mJ and 3MPa respectively [6,1]. The results for the elastic stiffness matrix and effect of the cement damage are discussed in details in next section.

4. Discussion on results

The investigation was divided in two parts, first to get the homogenised effective elastic properties for the concrete along with associated uncertainties and second to establish the strengths of concrete for tension and shear loading by considering the cement damage on the established RVE. The RVE size, two times of the coarse aggregate has been investigated for 5 different microstructures from the domain of 40 mm^3. Also the full domain was analysed to get the elastic constants. The obtained stiffness matrices were fully populated with the coupling terms as shown by one of them in Table 2.

$$C_{ijkl}^{H} = \begin{bmatrix} 37.58839 & 9.442843 & 9.436502 & 0.140611 & 0.541544 & -0.01888 \\ 9.442842 & 38.27575 & 9.402096 & 0.317694 & 0.183541 & 0.19474 \\ 9.436502 & 9.402097 & 37.87667 & 0.029753 & 0.23479 & -0.05446 \\ 0.171311 & 0.271645 & 0.021141 & 14.22495 & 0.013007 & 0.392824 \\ 0.513155 & 0.211675 & 0.32043 & 0.001754 & 14.17137 & 0.108761 \\ -0.08736 & 0.056749 & -0.07653 & 0.317769 & 0.062619 & 14.23183 \end{bmatrix}$$

However, shear-extension and shear-shear coupling terms are of one order less than the extension-extension terms and hence can be ignored. The mean values of the coefficients of C_{ijkl}^{H} along with standard deviations associated are given as below.

$$C_{ijkl}^{H} = \begin{bmatrix} 37.79 \pm 0.61 & 9.36 \pm 0.12 & 9.4 \pm 0.12 & & & \\ 9.36 \pm 0.12 & 37.98 \pm 0.54 & 9.39 \pm 0.1 & & & \\ 9.4 \pm 0.12 & 9.39 \pm 0.1 & 38.22 \pm 67 & & & \\ & & & 14.11 \pm 0.16 & & \\ & & & & 14.2 \pm 0.20 & \\ & & & & & 14.22 \pm 0.17 \end{bmatrix}$$

One can obtain the engineering constants for the concrete by considering the cubical symmetry of the stiffness coefficients as given in Table 2.

Table 1. Homogenised effective engineering constants.

E11	34.08 ± 0.58 GPa	μ12	0.20 ±0.002	G12	14.11 ±0.17 GPa
E22	34.26 ±0.51 GPa	μ 13	0.20 ±0.003	G13	14.20 ±0.20 GPa
E33	34.48 ±0.64 GPa	μ 23	0.20 ±0.002	G23	14.22 ±0.17 GPa

Also, the measure of the anisotropy in the planes can be determined as

$$A = \frac{2G(1+\mu)}{E} \tag{10}$$

A is anisotropy ratio and is equal to1for the isotropic material. The concrete can be considered as isotropic as A=0.99 for all the plans for the mean values. Hence the concrete is isotropic having engineering constants as E= 34 GPa and μ=0.2. The six load cases were also investigated for the effect of the cement damage during the loading history to determine the strengths of the concrete. The

stress-displacements curves of all five RVE's for normal loadings are given in Fig.1a and for the shear loading are shown in Fig.1b.

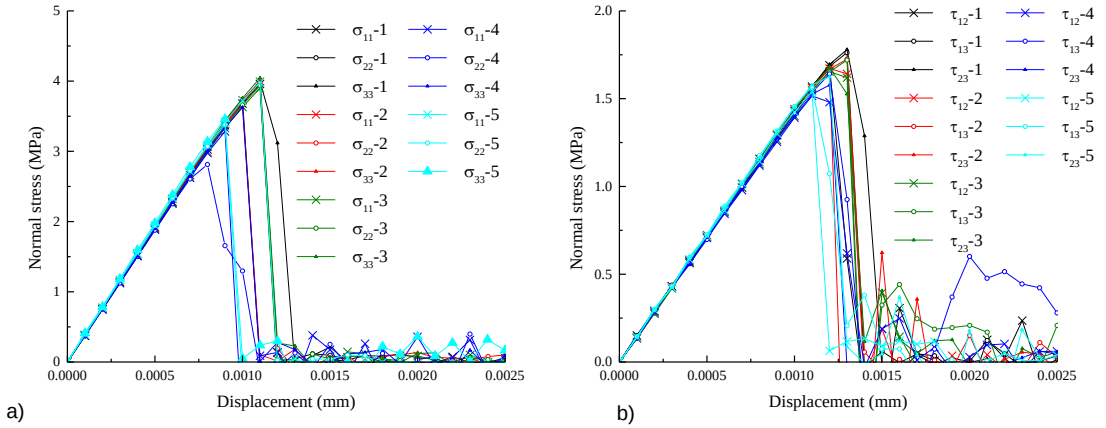

Figure 1: Stress-displacement curves for all six loading cases of RVE's (here, (In σ_{ij}-k) σ_{ij} represents the stress tensor and –k, represents RVE number).

The mean strength for all directions in tension loading condition is obtained as 3.72±0.37 MPa. Only in one case was observed below 3MPa and having a different trend in the post peak stress-displacement curve. In this particular case, the specimen had failed form the vicinity of the y-boundary due to the segregation of the coarse aggregates in the region of the domain. The shear behaviour was almost similar for all the cases and the average shear strength is obtained as 1.65±0.08 MPa.

5. Conclusions

The realistic microstructure of the concrete has been investigated to obtain the homogenised stiffness and strength properties of the concrete. An RVE of the size of 10mm, which is 2 times of the size of coarse aggregate has been analysed with 5 different microstructure using periodic boundary conditions. The concrete is observed nearly isotropic as the ratio of the isotropy is near to one. The Young's modulus is obtained as 34 GPa and Poison's ratio is 0.2. The strengths of the concrete in shear and normal direction are 3.72 and 1.65 MPa respectively.

Acknowledgements

Authors are thankful to Royal Society Research Grant and EPSRC grant (No. EP/J019763/1) for providing funds to this research.

References

[1] Wenyuan Ren, Zhenjun Yang, and Phil Withers. Meso-scale Fracture Modelling of Concrete Based on X-ray Computed Tomography Images, APCOM & ISCM Singapore, 11-14 December, 2013.

[2] R. Sharma, V.V. Deshpande, A.R. Bhagat, P. Mahajan, R.K. Mittal. X-ray tomographical observations of cracks and voids in 3D carbon/carbon composites, *Carbon*, 60, 335-345, 2013.

[3] R. Sharma, A.R. Bhagat, P. Mahajan. Finite element analysis for mechanical characterization of 4D inplane carbon/carbon composite with imperfect microstructure. *LAJSS*. 11, 170-184, 2014.

[4] T. Kanita, F. N'Guyena, S. Foresta, D. Jeulina, M. Reedc, S. Singletond. Apparent and effective physical properties of heterogeneous materials: Representativity of samples of two materials from food industry. *Comput. Methods Appl. Mech.Engg*. 195, 3960-3982, 2006.

[5] T. Kanit, S. Forest, I. Galliet, V. Mounoury, D. Jeulin, Determination of the size of the representative volume element for random composites: statistical and numerical approach, *IJSS*, 40, 3647–3679, 2003.

[6] K. Benzarti, C. Perruchot, M.M. Chehimi. Surface energetics of cementitious materials and their wettability by an epoxy adhesive, *Colloids and Surfaces A*. 286, 78–91, 2006.

Proceedings of the 22nd UK Conference of the
Association for Computational Mechanics in Engineering
2 - 4 April 2014, University of Exeter, Exeter

MIXED FINITE ELEMENT FORMULATIONS FOR STRAIN GRADIENT ELASTICITY IN FEniCS

***Veena Phunpeng[1] and Pedro M. Baiz[2]**

[1,2]Department of Aeronautics, Imperial College London, South Kensington Campus, London, SW7 2AZ

*v.phunpeng10@imperial.ac.uk and p.m.baiz@imperial.ac.uk

ABSTRACT

Classical (local) elastic theories do not include micro-structural length scales of the material. To study size effects in micro/nano materials, nonlocal/strain gradient elastic theories are proposed. These could provide an efficient way to account for the important scale size effects. Within this paper a mixed-type finite element formulation is presented using triangular elements of C^0 continuity. Material behaviour of a perfectly bonded bimaterial subjected to a shear stress σ_{21}^{∞} is investigated. The finite element analysis was implemented using a framework that provides an automated, efficient solution of differential equations (FEniCS Project). Numerical results are presented and compared with analytical solutions.

Key Words: *boundary layer problem; strain-gradient elasticity; mixed formulations; FEniCS*

1. Introduction

Classical (local) elastic theories consider that stresses at a point are a functions of the strains at the same point. This assumption is valid for most continuum/macro scale simulations but in general it does not hold for micro/nano scales. To study the issue of size effects, theories which consider the material behaviour at a point as a function of the deformation of the surrounding have been proposed, these are usually refered as nonlocal or strain gradient theories. Nonlocal theories state that the stress at a point depends on the strain at all points in the continuum body [6]. In certain cases, there is a direct equivalence between nonlocal stress theories and strain gradient theories. Of the two approches, strain gradient theories are well known to be simpler to solve/implement. They have previously been considered in serveral published works, using either the mixed-type finite element formulation [1, 8] or meshless methods [9]. The difficulty of using numerical approximation of strain gradient elasticity with the finite element method (FEM) is the continuity of strains that requires C^1 continuity. In this paper, C^1 continuous finite element can be avoided by a mixed-type formulation. Establishing mixed formulations was also not an easy task in the past. Fortunately, thanks to the FEniCS project [3], development of complex mixed finite element formulations has become extremely easy. The present paper shows the advantages of using the FEniCS environment to implement a mixed formulations of strain gradient elasticity with a wide range of element types. Accuracy is assessed with a well known benchmark example.

2. Strain Gradient Elasticity

Mindlin [4] and Toupin [7] developed a theory of linear elasticity in which the strain energy density W depends not only on the first derivative of displacement (strain, ε_{ij}) but also the second derivative of displacement (strain gradient, η_{ijk}),

$$W = W(\varepsilon_{ij}, \eta_{ijk}) \tag{1}$$

The second order deformation gradient (η_{ijk}) are defined in three differenct ways [1, 2, 4, 7]. In this paper, Strain-Gradient Elasticity based on Type-I formulation is considered - which the strain gradient is the second derivative of the displacement,

$$\eta_{ijk} = \partial_i \partial_j u_k \tag{2}$$

In 1965, Mindlin [5] derived that the stress σ_{ij} and double stress τ_{ijk} are conjugated with the strain and the second order deformation gradient,

$$\sigma_{ij} = \frac{\partial W}{\partial \varepsilon_{ij}}, \qquad \tau_{ijk} = \frac{\partial W}{\partial \eta_{ijk}} \tag{3}$$

Applying the principle of virtual work, the equalibrium equation for a quasi static solid is [8, 2],

$$\partial_i(\sigma_{ik} - \partial_j \tau_{jik}) - b_k = 0 \tag{4}$$

where b_k is a body force vector. For a solid (the domain, Ω, shown in Fig.1), the solution of the displacement field u_i is investigated through the known boundary conditions on Ω, such as displacement $\hat{u}_i$ on the surface $d\Gamma_D$, and traction t_i on the surface $d\Gamma_N$.

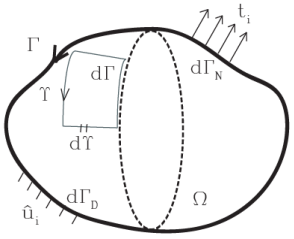

Figure 1: Linear Elastic Domain Problem

The variational form of the total strain energy in a domain Ω can be written as

$$\delta \int_\Omega W d\Omega = \int_\Omega (\sigma_{ij}\delta\varepsilon_{ij} + \tau_{ijk}\delta\eta_{ijk}) d\Omega \tag{5}$$

Using the divergence theorem, the previous equation can be reformulated as a first variation of the strain energy density, giving

$$\begin{aligned} \delta \int_\Omega W d\Omega = &- \int_\Omega (\partial_i \sigma_{ik} - \partial_i \partial_j \tau_{ijk}) \delta u_k d\Omega \\ &+ \int_\Gamma [n_j(\sigma_{jk} - \partial_i \tau_{ijk})\delta u_k + n_i \tau_{ijk} \partial_j \delta u_k] d\Gamma \end{aligned} \tag{6}$$

For the last term of the surface integral, a decomposition of $\partial_j \delta u_k$ on the boundary surface is defined as

$$\partial_j \delta u_k = D_j \delta u_k + n_j D \delta u_k \tag{7}$$

where

$n_i = i^{th}$ component of the unit surface normal vector
$D(.) = n_k \partial(.)/\partial x_k$ = surface normal gradient operator
$D_j(.) = (\delta_{jk} - n_j n_k)\partial(.)/\partial x_k$ = surface gradient operator

Using this definition and Stoke's surface divergence theorem on a surface, Γ, it is possible to obtain

$$\int_\Gamma D_j(n_i \tau_{ijk} \delta u_k) d\Gamma = \oint_\Upsilon n_i k_j \tau_{ijk} \delta u_k d\Upsilon + \int_\Gamma (D_p n_p) n_i n_j \tau_{ijk} \delta u_k d\Gamma \tag{8}$$

Then the last term in the surface integral (Eq.6) then becomes,

$$\begin{aligned} \int_\Gamma n_i \tau_{ijk} \partial_j \delta u_k d\Gamma = &\int_\Gamma [n_j(\sigma_{jk} - \partial_i \tau_{ijk,i}) + n_i n_j \tau_{ijk}(D_l n_l) - D_j(n_i \tau_{ijk})] \delta u_k d\Gamma \\ &+ \int_\Gamma n_i n_j \tau_{ijk} D \delta u_k d\Gamma + \Sigma_m \oint_\Upsilon \triangle(n_i k_i \tau_{ijk}) \delta u_k d\Upsilon \\ &= \int_\Gamma t_k \delta u_k d\Gamma + \int_\Gamma r_k D \delta u_k d\Gamma + \Sigma_m \oint_\Upsilon p_k \delta u_k d\Upsilon \end{aligned} \tag{9}$$

The final form of the principle of virual work can then be written as

$$\int_\Omega [\sigma_{ij}\delta\varepsilon_{ij} + \tau_{ijk}\delta\eta_{ijk}] d\Omega = \int_\Omega b_k \delta u_k d\Omega + \int_\Gamma [t_k \delta u_k + r_k D \delta u_k] d\Gamma + \Sigma_m \oint_\Upsilon p_k \delta u_k d\Upsilon \tag{10}$$

3. Mixed-type Finite Element Formulation

From the principle of virtual work (Eq.10), the procedure of finite element requires C^1 continuous elements. Due to the complexities involved with the implementation of C^1 FEM formulations, it is common to reformulate Eq.10 as a mixed formulation in which higher order terms (e.g. strains) are modelled as independent variables. To derive the weak form of the principle of virtual work, kinematic constraints are introduced by defining,

$$\psi_{ij} = u_{j,i} \tag{11}$$

By making use of divergence theorem, the strain energy density (Eq.10) on the domain Ω can be rewritten as [8]

$$\int_\Omega [\sigma_{ij}\delta\varepsilon_{ij} + \tau_{ijk}\delta\eta_{ijk} + \tau_{ijk,i}(\delta u_{k,j} - \delta\psi_{jk})]d\Omega = \int_\Omega b_k\delta u_k d\Omega + \int_\Gamma [t_k\delta\psi_k + n_j r_k \delta u_{k,j}]d\Gamma \tag{12}$$

When applying a mixed finite element formulation, we have to enforce the first variational form of the constraints by introducing Lagrange multipliers, defined as

$$\rho_{jk} = -\tau_{ijk,i} \tag{13}$$

The constraints are enforced by writing Eq.11 as a variational form, using an arbitrary variation of the Lagrange multipliers, $\delta\tau_{ijk,i}$, giving a set of extra conditions,

$$\int_\Omega (\psi_{jk} - u_{k,j})\delta\rho_{jk} d\Omega = 0 \quad \text{(no sum on j and k)} \tag{14}$$

After rewriting Eq.12 and Eq.14, the final modified virtual work formulation becomes

$$\begin{aligned}
\int_\Omega (\sigma_{ij}\delta\varepsilon_{ij} - \rho_{jk}\delta u_{k,j})\, d\Omega &= \int_\Omega b_k\delta u_k\, d\Omega + \int_\Gamma t_k\delta\psi_k\, d\Gamma \\
\int_\Omega (\tau_{ijk}\delta\eta_{ijk} + \rho_{jk}\delta\psi_{jk})\, d\Omega &= \int_\Gamma n_j r_k \delta u_{k,j}\, d\Gamma \\
\int_\Omega (\psi_{jk} - u_{k,j})\delta\rho_{jk}\, d\Omega &= 0 \quad \text{(no sum on j and k)}
\end{aligned} \tag{15}$$

4. Numerical Examples

The mixed formulation introduced above was tested with a well known benchmark example (bimaterial system subjected to uniform shear stress). In the numerical model a domain with the dimension of $100l \times 100l$ represents the bimaterial system. The boundary conditions are shown in Fig.2 and consist of a shear stress on the upper and lower surfaces. To avoid the rigid body motion, the left-bottom corner is set $u = v = 0$ and the right-bottom corner is set $v = 0$. The shear modulus and nonlocal paremeter of two materials are assumed [8, 9]

$$\mu_1 = 2\mu_2 \qquad \text{and} \qquad l_1 = l_2 = l \tag{16}$$

The results for triangular elements using different discretization are presented in Fig.3 and are compared with the analytical soultion [8].

5. Conclusions

In this paper, a 2D mixed finite element formulation was presented based on strain gradient elasticity. The numerical results using triangular elements in FEnicS show that the higher-order discretization is in excellent agreement with the analytical solutions [8]. This suggests that more complicated problems without analytical solutions can be solved accurately using this technique.Thanks to the features provided by the FEniCS project, it has become extremly easy and fast to implement complex FEM formulations.

References

[1] E. Amanatidou and A. Aravas. Mixed finite element formulations if strain-gradient elasticity problems. *Comput. Methods Appl. Mech. Engrg.*, 191, pp.1723-1751, 2002.

[2] D.C. Lam and F. Yang, A.C. Chong and J. Wang and P. Tong. Experiments and theory in strain gradient elasticity. *J. Mech. Phys. Solids.*, 51, pp.1477-1508, 2003.

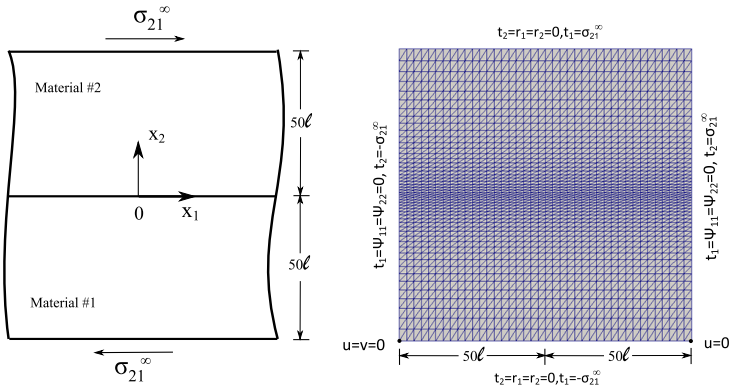

Figure 2: : A bimaterial under uniform shear and sketch of mesh

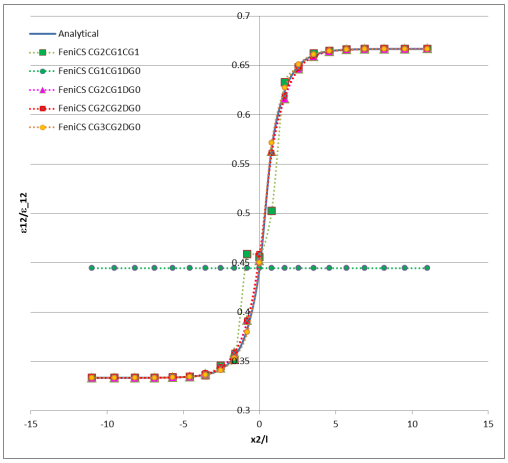

Figure 3: : The comparison of the normolized strain on various discreatizations

[3] A. Logg and K.-A. Mardal and G. N. Wells. *Automated Solution of Differential Equations by the Finite Element Method*, Springer, 2012, [doi:10.1007/978-3-642-23099-8]

[4] R.D. Mindlin. Micro-structure in Linear Elasticity. *Arch. Rational Mech. Anal*, 10, pp.51-78, 1964.

[5] R.D. Mindlin. Second gradient of strain and surface tension in linear elasticity. *Int. J. Solids Struct.*, 1, pp.417-438, 1965.

[6] R.D. Mindlin and N.N. Eshel. On first strain-gradient theories in linear elasticity. *Int. J. Solids Struct.*, 4, pp.109-124, 1968.

[7] R.A. Toupin. Elastic Matreials with couple stresses. *Arch. Rational Mech. Anal.*, 11, pp.385-414, 1962.

[8] J. Y. Shu and W. E. King and N. A. Fleck. Finite elements for materials with strain gradient effects. *Int. J. Numer. Meth. Engng.*, 44, pp.373-391, 1999.

[9] Z.Tang, S. Shen and S.N. Atluri. Analysis of Materials with Strain-Gradient Effects: A Meshless Local Petrov-Galerkin(MLPG) Approach, with Nodal Displacements only. *CMES-Comp. Model. Eng.*, 4, pp.177-196, 2003.

[10] O.C. Zienkiewicz and R.C. Taylor. *The finite element method: Volume 1 the basis*, 5^{th} Edition, Butterworth-Heinemann, 2000.

Proceedings of the 22nd UK Conference of the
Association for Computational Mechanics in Engineering
2 - 4 April 2014, University of Exeter, Exeter

MULTISCALE MODELLING OF THE TEXTILE COMPOSITE MATERIALS

***Zahur Ullah, Łukasz Kaczmarczyk, Michael Cortis and Chris J. Pearce**

School of Engineering, Rankine Building, The University of Glasgow, Glasgow, UK, G12 8LT

*Zahur.Ullah@glasgow.ac.uk

ABSTRACT

This paper presents an initial computational multiscale modelling of the fibre-reinforced composite materials. This study will constitute an initial building block of the computational framework, developed for the DURCOMP (providing confidence in durable composites) EPSRC project, the ultimate goal of which is the use of advance composites in the construction industry, while concentrating on its major limiting factor "durability". The use of multiscale modelling gives directly the macroscopic constitutive behaviour of the structures based on its microscopically heterogeneous representative volume element (RVE). The RVE is analysed using the University of Glasgow in-house parallel computational tool, MoFEM (Mesh Oriented Finite Element Method), which is a C++ based finite-element code. A single layered plain weave is used to model the textile geometry. The geometry of the RVE mainly consists of two parts, the fibre bundles and matrix, and is modelled with CUBIT, which is a software package for the creation of parameterised geometries and meshes. Elliptical cross sections and cubic splines are used respectively to model the cross sections and paths of the fibre bundles, which are the main components of the yarn geometry. In this analysis, transversely isotropic material is introduced for the fibre bundles, and elastic material is used for the matrix part. The directions of the fibre bundles are calculated using a potential flow analysis across the fibre bundles, which are then used to define the principal direction for the transversely isotropic material. The macroscopic strain field is applied using linear displacement boundary conditions. Furthermore, appropriate interface conditions are used between the fibre bundles and the matrix.

Key Words: *multiscale modelling; composite material; Transverse isotropy; MoFEM; CUBIT*

1. Introduction

Conventional materials, e.g. steel, aluminium and metallic alloys can no longer satisfy the demands for materials with exceptional mechanical properties and ultimately requires the design of new material [1]. These new materials are designed by changing their microconstituents at a scale, which is very small as compared to the physical structures. Due to the complicated micro-structure of these materials, direct macro-level modelling is not possible and requires a detailed modelling at the micro-level. Textile or fabric composites is a class of these new materials which provides full flexibility of design and functionality due to the mature textile manufacturing industry and is commonly used in many engineering applications, including ships, aircrafts, automobiles, civil structures and prosthetics [2]. Numerous analytical and computational methods have been proposed to analyse textile composite materials, which includes the calculation of the overall macro homogenised response and properties from the micro-heterogeneous representative value element (RVE) [3] and is often referred as micro-to-macro transition or homogenisation [4].

This paper presents the computational multiscale modelling of the textile composites, using the University of Glasgow in-house computational tool MoFEM. The RVE in this case consists of fibre bundles and matrix, which is modelled and meshed in CUBIT using a Python parametrized script. CUBIT also facilitates the insertion of interfaces between the fibres and matrix. Transversely isotropic material are used for the fibres and isotropic martial are used for the matrix. Five material parameters are required

for the transversely isotropic material, i.e. E_p, ν_p, E_z, ν_{pz} and G_{zp} where E_p and ν_p are Young's modulus and Poisson's ratio in the transverse direction respectively, while E_z, ν_{pz} and G_{zp} are the Young's modulus, Poisson's ratio and shear modulus in the fibre directions respectively. For the matrix part, only two material parameters are required, i.e. Young's modulus E and Poisson's ratio ν. Although, periodic boundary conditions [5, 6] gives better estimates of the homogenised response and properties as compared to traction and linear displacement boundary conditions, linear displacement boundary conditions are used in this paper due to its simple implementation. This will subsequently be extended to periodic boundary conditions in future work. Fibre directions are calculated at each integration point by solving a potential flow problem.

2. Theoretical background

Computational multiscale modelling is used in this paper to analyse the textile composite materials, in which a heterogeneous RVE is associated with each integration point of the macro-homogenous structure as shown in Figure 1, in which $\overline{B} \subset \mathbb{R}^3$ and $B \subset \mathbb{R}^3$ are macro and micro domains respectively. The calculation of the RVE boundary conditions from the macro-strain

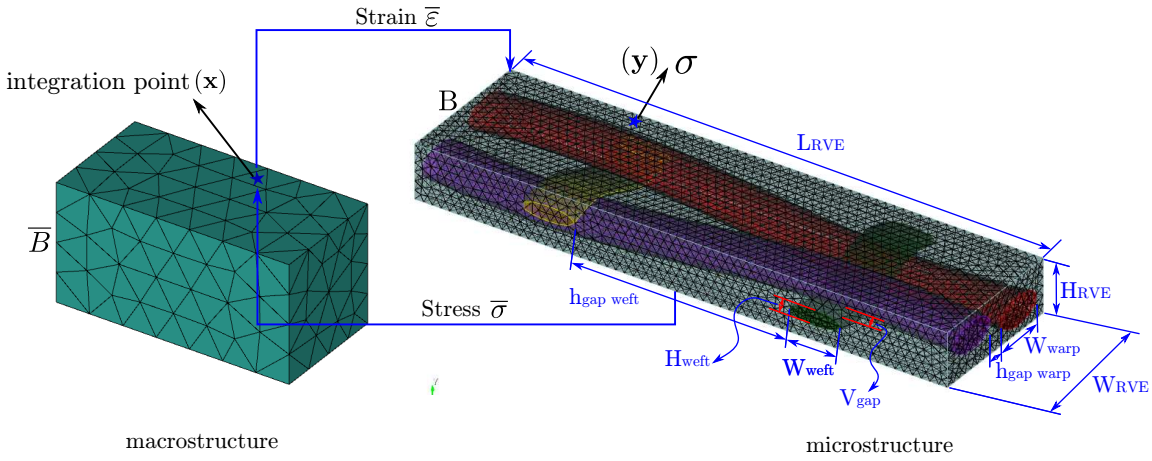

Figure 1: Transition from macro-to-micro and micro-to-macro

$\overline{\boldsymbol{\varepsilon}} = \begin{bmatrix} \overline{\varepsilon}_{11} & \overline{\varepsilon}_{22} & \overline{\varepsilon}_{33} & 2\overline{\varepsilon}_{12} & 2\overline{\varepsilon}_{23} & 2\overline{\varepsilon}_{31} \end{bmatrix}^T$ at macroscopic integration point $\mathbf{x} = \begin{bmatrix} x_1 & x_2 & x_3 \end{bmatrix}^T$ is known as macro-to-micro transition, while subsequent calculation of the homogenised stress $\overline{\boldsymbol{\sigma}} = \begin{bmatrix} \overline{\sigma}_{11} & \overline{\sigma}_{22} & \overline{\sigma}_{33} & \overline{\sigma}_{12} & \overline{\sigma}_{23} & \overline{\sigma}_{31} \end{bmatrix}^T$ and tangent moduli is known as micro-to-macro transition. The macro-strain is applied as linear displacement boundary conditions, which leads to satisfaction of Hill-Mandel principle [7], i.e.

$$\overline{\boldsymbol{\varepsilon}} : \overline{\boldsymbol{\sigma}} = \frac{1}{V} \int_V \boldsymbol{\varepsilon} : \boldsymbol{\sigma} dV, \tag{1}$$

where V is the volume of the RVE, while $\boldsymbol{\sigma}$ and $\boldsymbol{\varepsilon}$ are stresses and strains associated with a point $\mathbf{y} = \begin{bmatrix} y_1 & y_2 & y_3 \end{bmatrix}^T$ of the RVE. The micro displacement field $\mathbf{u} = \begin{bmatrix} u_1 & u_2 & u_3 \end{bmatrix}^T$, is written as

$$\mathbf{u} = \mathbf{u}^* + \widetilde{\mathbf{u}}, \tag{2}$$

where $\mathbf{u}^*$ is known as Taylor displacements and $\widetilde{\mathbf{u}}$ is the unknown displacement fluctuations. The Taylor component is written as

$$\mathbf{u}_i^* = \mathbb{D}_i^T \overline{\boldsymbol{\varepsilon}}, \qquad i = 1, 2, \cdots n, \tag{3}$$

where n is the number of nodes and $\mathbb{D}_i$ is the coordinate matrix and is given as [4]

$$\mathbb{D}_i = \frac{1}{2} \begin{bmatrix} 2y_1 & 0 & 0 \\ 0 & 2y_2 & 0 \\ 0 & 0 & 2y_3 \\ y_2 & y_1 & 0 \\ 0 & y_3 & y_2 \\ y_3 & 0 & y_1 \end{bmatrix}_i . \tag{4}$$

Finally, the homogenised stress is calculated as

$$\overline{\boldsymbol{\sigma}} = \frac{1}{V}\sum_{i=1}^{n_b} \mathbb{D}_i \mathbf{f}_i^{ext}, \tag{5}$$

where n_b is the number of nodes on the boundary ∂B of the RVE, and $\mathbf{f}_i^{ext}$ is the external nodal force vector.

3. Numerical example

A sample RVE, which was used in [2], is used here with the same geometrical and material parameters, as shown in Figure 1, where the subscripts warp and weft represent the corresponding directions of fibre bundles. The geometrical and material parameters are defined in Table 1. This RVE is referred

Parameters	Values	Parameters	Values
W_{warp}	0.3	W_{weft}	0.3
H_{warp}	0.1514	H_{weft}	0.0757
$h_{gap\,warp}$	0.09	$h_{gap\,weft}$	1.2
L_{RVE}	3.0	v_{gap}	0.012
W_{RVE}	0.8		
H_{RVE}	0.3		

Fibres properties					Matrix Properties	
E_p	E_z	ν_p	ν_z	G_{pz}	E	ν
40	270	0.26	0.26	24	35	0.35

Table 1: REV geometrical and material properties (all dimensions in mm while E and G are in GPa)

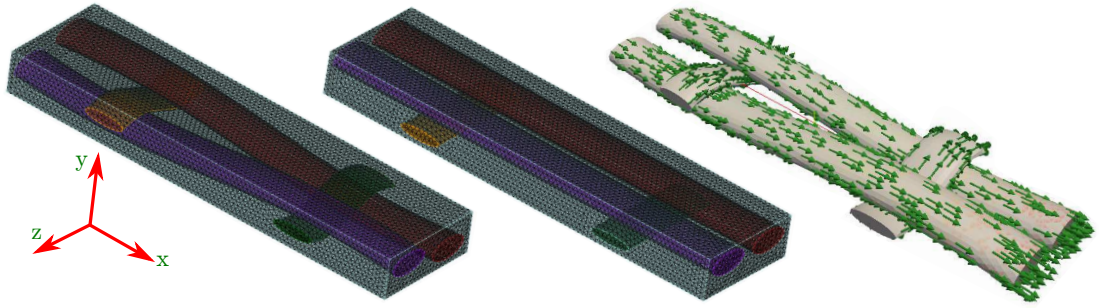

(a) Textile RVE (b) $0^o/90^o$ non-crimp RVE (c) Fibres directions

Figure 2: Crimp and non-crimp RVEs and sample fibre directions

as unbalanced, where the dimensions of fibre bundles are different in warp and weft directions. The manufacturing processes and crossing of the warp and weft yarn will lead to non-circular cross sections of the fibre bundles; therefore, elliptical cross sections are used in this paper, which are then sweeped over the cubic spline fibres' path to generate the fibres. Four-node tetrahedral elements are used for both the fibre bundles and the matrix, while six-nodes prism elements are used as an interface between fibres and matrix.

The textile RVE is analysed using two different meshes with 41,193 and 106,011 DOFs and is subjected to 1 % strain in x direction, i.e. $\overline{\varepsilon}_{xx}$. The finest mesh and coordinates system are shown in Figure 2(a), where x and z are warp and weft directions respectively, while sample fibre directions vector are shown in Figure 2(c). The resulting homogenised stress $\overline{\sigma}_{xx}$ versus applied strain $\overline{\varepsilon}_{xx}$ for the two meshes and a reference value from [2] are shown in Table 2, in which Mesh-2 with 106,011 DOFs provides satisfactory results. The small difference between current and reference results may be due to the use of lenticular cross-sections for the fibres, use of 8-node 3D linear brick element and 4- node linear tetrahedron element for fibres and matrix respectively and the use of perfect bonding between fibres and matrix in [2]. Furthermore, The effect of fibres dimensions and crimp pattern are analysed, for which a new $0^o/90^o$ non-crimp RVE with 103,095 DOFs (shown in Figure 2(b)) is generated and is subjected to the same strain state. Comparison of the homogenised stress $\overline{\sigma}_{xx}$ for both crimp and non-crimp RVEs are given in Table 3, where relatively lower value of homogenised stresses $\overline{\sigma}_{xx}$ in the crimp RVE is due to the waviness of the fibre bundles. Furthermore, both crimp and non-crimp RVEs are subjected to 1 % strain in z direction, i.e. $\overline{\varepsilon}_{zz}$ and comparison of their homogenised stress in the z direction, i.e. $\overline{\sigma}_{zz}$ are shown in

Table 3, where again $\overline{\sigma}_{zz}$ is lower for the crimp RVE. Due to the small size and higher waviness of the weft fibre bundles, the values of $\overline{\sigma}_{zz}$ are relatively smaller than the corresponding values of $\overline{\sigma}_{xx}$.

	$\overline{\sigma}_{xx}$ (MPa)		
$\overline{\varepsilon}_{xx}$ (%)	Mesh-1	Mesh-2	Reference
1	749.82	508.771	541.278

Table 2: $\overline{\sigma}_{xx}$ versus $\overline{\varepsilon}_{xx}$ for different mesh levels

	$\overline{\sigma}_{xx}$ (MPa)	
$\overline{\varepsilon}_{xx}$ (%)	Crimp	Non-Crimp
1	508.771	751.507

	$\overline{\sigma}_{zz}$ (MPa)	
$\overline{\varepsilon}_{zz}$ (%)	Crimp	Non-Crimp
1	83.9317	125.065

Table 3: Comparison of $\overline{\sigma}_{xx}$ versus $\overline{\varepsilon}_{xx}$ and $\overline{\sigma}_{zz}$ versus $\overline{\varepsilon}_{zz}$ for crimp and non-crimp RVE

4. Conclusions

This paper described an initial computational modelling framework for the DURACOMP project. Textile composite RVE geometry, which consists of two parts, i.e. fibre bundles and matrix is modelled and meshed using CUBIT, where fibres are modelled using cubic spline with elliptical cross sections. The University of Glasgow in-house computational tool MoFEM is used to analyse the RVE using transversely isotropic material for the fibre bundles and isotropic material for the matrix. Linear displacement boundary conditions and elastic interfaces between fibre bundles and matrix are used in this paper. Direction of the fibre bundles are calculated using a potential flow analysis. Two different level of meshes are used to solve the RVE, and it is found that the homogenised stress calculated in the case of Mesh-2 are in a good agreement with the reference solution. It is also found that homogenised stress in the case of the crimp RVE is lower than the corresponding non-crimp RVE. Furthermore, it is also observed that due to the relatively smaller dimensions and more waviness pattern for the weft fibre bundles, the homogenised stress $\overline{\sigma}_{zz}$ is lower than the corresponding stress $\overline{\sigma}_{xx}$ in the warp direction.

Acknowledgements

The authors gratefully acknowledge the support of the UK Engineering and Physical Sciences Research Council through the Providing Confidence in Durable Composites (DURACOMP) project (Grant Ref.: EP/K026925/1).

References

[1] D. Perić, E.A. de Souza Neto, A.J. Carneiro Molina, and M. Partovi. *Computational Methods in Applied Sciences*, volume 7, pages 165–185. Springer Netherlands, 2007.

[2] T. W. Chua. Multi–scale modeling of textile composites. Master's thesis, Department of Mechanical Engineering, Technische Universiteit Eindhoven, January 2011.

[3] V.G. Kouznetsova. *Computational homogenization for the multi-scale analysis of multi-phase materials*. PhD thesis, Technische Universiteit Eindhoven, The Netherlands, 2002.

[4] C. Miehe and A. Koch. Computational micro-to-macro transitions of discretized microstructures undergoing small strains. *Archive of Applied Mechanics*, 72(4-5):300–317, 2002.

[5] Ł. Kaczmarczyk, C. J. Pearce, and N. Bićanić. Scale transition and enforcement of RVE boundary conditions in second-order computational homogenization. *International Journal for Numerical Methods in Engineering*, 74(3):506–522, 2008.

[6] G. Soni, R. Singh, M. Mitra, and B. G. Falzon. Modelling matrix damage and fibre-matrix interfacial decohesion in composite laminates via a multi-fibre multi-layer representative volume element (M^2RVE). *International Journal of Solids and Structures*, 51(2):449 – 461, 2014.

[7] R. Hill. On constitutive macro-variables for heterogeneous solids at finite strain. In *Proceedings of the Royal Society of London. Series A, Mathematical and Physical Sciences*, volume 326, pages 131–147. The Royal Society, 1972.

Proceedings of the 22nd UK Conference of the
Association for Computational Mechanics in Engineering
2 - 4 April 2014, University of Exeter, Exeter

Viscoelastic Modelling of Wood-Water Interactions Using Finite Difference Modelling

***Euan Richardson[1], Dr Karin de Borst[1]**

[1]School of Engineering, University of Glasgow, Rankine Building, Glasgow, G12 8QQ

*e.richardson.1@research.gla.ac.uk

ABSTRACT

Timber is a naturally occurring material, with properties adapted to its local environment. Moisture has a pronounced effect on the strength, stiffness and dimensional stability of timber. One particular concern in moisture induced warping, both during the drying process and during construction and the lifespan of any building. The current focus of the project is to model the viscoelastic response of the timber in reaction to a change of humidity conditions. The model makes use of a Zener spring-dashpot method to model both the instantaneous elastic response as well as the time dependent, poroelastic material behaviour. Flory-Huggins Isotherm is used to model the interaction between molecular chains of amorphous cellulose and the moisture influx while Ficks law of diffusion is used to assess the rate of diffusion through the wood fibre. A finite difference scheme is to be used to model the constitutive equations over the length of a single wood fibre. The results from the model will be compared to experimental results of sorption kinetics of softwoods. Recent research into sorption kinetics has determined that the rate limiting step in moisture sorption in timber could be due to substrate swelling rather than the process being diffusion limited. The model will assess whether this is the case of if the moisture sorption is a more complex interplay of the various processes. The current model will serve as the starting point in an attempt to create a multi-scale model to create an accurate set of hygro-mechanical properties for softwood.

Key Words: *Wood; Sorption; Viscoelastic; Finite Difference*

1. Introduction

Wood is a highly complex heterogeneous material with a multi-scale hierarchical structure, incorporating properties over many length scales. It is naturally occurring and thus the structure is adapted to its local environment. This makes timber an inherently unpredictable material to work with. A major issue that arises from the unpredictable properties is moisture induced distortion. During the drying process (or after), changes in moisture content can lead to changes within the microstructure of the timber. This in turn leads to dimensional changes that can be observed on the macroscopic scale. The key to mitigating the issue of moisture induced distortion is to understand and be able to predict how moisture interacts on the smallest length scales within the timber. The aim is to model the moisture sorption behaviour of the cell wall and determine the rate determining step in sorption kinetics within wood i.e. whether solvent migration is diffusion or mechanically limited. This information will be related to the macroscale deformation effects by multiscale modelling in the future. The model will include the viscoelastic effects of stress relaxation and creep which occur over time and their relationship with varying moisture content.

2. Cell Wall Structure

At the microstructural level softwood consists of three main polymers, cellulose, hemicellulose and lignin. The wood cell wall itself is a multilayer composite structure (shown in figure 1) and consists of a primary cell wall, a secondary cell wall (containing 3 layers denoted S1, S2 and S3 layers) and the lumen contained within [3]. Both the primary and secondary cell walls contain cellulose, hemicellulose and lignin.

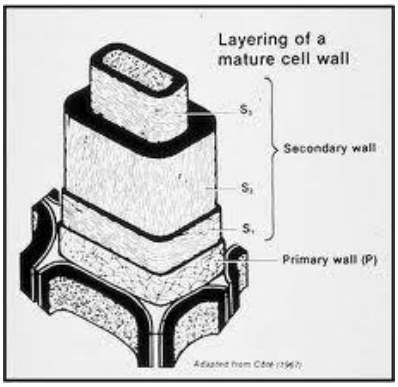

Figure 1: : Cell Wall Structure

In the secondary cell wall the cellulose chains form fibres which are embedded in a non-cellulosic polymer matrix. The cellulose is split into both crystalline and semi-crystalline (amorphous) components, and it is the amorphous component which interacts most strongly with water. This hygroscopic water is bound to the cell wall by forming hydrogen bonds with the hydroxl groups within amorphous cellulose, hemicelluloses and a small amount of hydroxyl groups within the lignin matrix. The amount of hygroscopic water within the cell wall is limited both by the number of sorption sites and the number of water molecules that can be held per sorption site. When water enters the cell wall it causes a swelling of the cell wall material. The water then accupies the space between the microfibrils, forcing them apart and thereby opening up new sorption sites [2]. It is unclear yet whether it is this deformation of the cell wall polymers or the rate of diffusion that is the rate determining step in sorption kinetics of wood.

3. Sorption Model

3.1. Model Outline

The aim is to create a sorption model of the wood cell wall due to interaction with water that incorporates the viscoelastic behaviour of the cell wall. To do this a 1D model resolved in the direction of the water flow across the wood cell wall is modelled. Experimental evidence has suggested that cellulose fibres have amorphous zones connecting crystalline chains in series. The high stiffness of crystalline cellulose constrains deformations of the crystalline sections in the direction of the fibre. The amorphous sections contain the lignin and hemicellulosic matrix material. The organization of crystalling and amorphous sections will be investigated by modelling both sections seperately. The corresponding sorption models

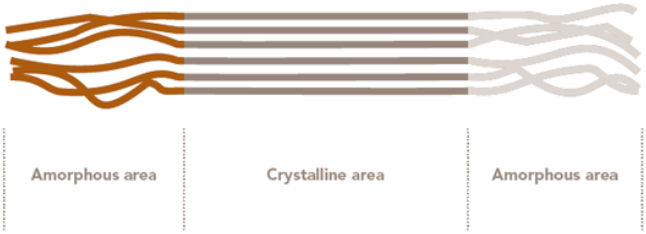

Figure 2: : Example of Amorphous and Crystalline polymers linked in series

will be combined in series, shown in figure 2, according to their relative volume fractions. This will produce a predicted overall swelling response of the cell wall. A parallel arrangement of crystalline and amorphous sections will also be investigated to determine which arrangement best relates to experimental results for sorption isotherms. The model will intially focus on the S2 layer as this makes up around 80 percent of the mass of a wood fibre.

3.2. Constitutive Equations

Taking a similar approach to Hu and Suo's study into elastomeric gels [5], the viscoelastic material behaviour of the cell wall is described by a Zener model. Unlike the Kelvin-Voigt and Maxwell model, the Zener model can accurately describe both stress relaxation and creep. We formulate the sorption model in terms of the conservation of mass, kinetics of deformation and solvent migration and the balance

of forces. The following relationship, representing a zener spring model, describes a dual process with the elastic response represented by a single spring working in parallel with the viscoelastic response, represented by a spring (elastic) in series with a dashpot (viscous):

$$\sigma_{ij} + \frac{\mu - \mu_0}{\Omega}\delta_{ij} = 2G^{\alpha}\left[\epsilon_{ij} + \frac{\nu^{\alpha}}{1-2\nu^{\alpha}}\epsilon_{kk}\delta_{ij}\right] + 2G^{\beta}\left[(\epsilon_{ij} - \hat{\epsilon}_{ij}) + \frac{\nu^{\beta}}{1-2\nu^{\beta}}(\epsilon_{kk} - \hat{\epsilon}_{kk})\delta_{ij}\right] \tag{1}$$

The strains within spring α are denoted by ϵ_{ij} and the strains within spring β are represented by $\epsilon_{ij} - \hat{\epsilon_{ij}}$. G^{α} and G^{β} represent the shear moduli of the two springs while ν^{α} and ν^{β} are Poisson's ratio. The strain rate of the dashpot is related to the viscosity by

$$\frac{\partial\hat{\epsilon_{ij}}}{\partial t} = \frac{G^{\beta}}{\hat{G^{\beta}}}\left[(\epsilon_{ij} - \hat{\epsilon_{ij}}) + \frac{\nu^{\beta} - \hat{\nu^{\beta}}}{(1-2\nu^{\beta})(1+\hat{\nu^{\beta}})}(\epsilon_{kk} - \hat{\epsilon_{kk}})\right] \tag{2}$$

where $\hat{G^{\beta}}$ and $\hat{\nu^{\beta}}$ represent the constants that specify the viscous behaviour of the dashpot.

The Flory-Huggins theory for interaction within polymer solutions is used to model the energy of mixing of wood with water, within the wood fibres, taking into account both entropy and enthalpy changes. It is a statistical mechanical treatment of a polymer solution and in this case will be used as a starting point for predicting a sorption isotherm from the various activation energies of the solutions and polymers. In the theory of Flory-Huggins the change of Gibb's free energy upon mixing is formulated as

$$\Delta G_m = RT[n_1 ln\phi_1 + n_2 ln\phi_2 + n_1\phi_2\chi_{12}] \tag{3}$$

where the terms n_1 and ϕ_1 represent the number of moles and volume fraction of the solvent (in this case water) respectively while n_2 and ϕ_2 represent the same for the polymer. The term χ_{12} is the polymer-solvent interaction parameter and is a material specific parameter. R is the gas constant and T is the absolute temperature.

Fick's 2nd law of diffusion is used to predict how the diffusion changes the concentration within the polymer i.e. how the flux direction goes from an area of high concentration to an area of lower concentration. We formulate Fick's law in terms of chemical potential μ as the driving force

$$\frac{\partial\mu}{\partial t} = D\frac{\partial^2\mu}{\partial x^2} \tag{4}$$

where D represents the diffusion coefficient.

Molecular incompressibility is assumed and thus it is assumed that any uptake of solvent is accommodated due to elastic deformation of the cell wall. This yields a relation between the volumetric strain and the moisture concentration, depending on the molecular size of water.

4. Finite Difference Scheme

A finite difference scheme is used to obtain numerical solutions of the sorption model. An implicit Euler (backwards time centred) scheme is used which gives better performance than an explicit scheme in this case due to the slow rate of diffusion and the relatively long relaxation times making the time steps relatively large. The high effort of solving an implicit system of time equations at each step pays off as numerical stability is ensured. The following equation shows the backwards time centred space relationship

$$\frac{\mu_{i,j+1} - \mu_{i,j}}{\Delta t} = D\frac{\mu_{i+1,j+1} - 2\mu_{i,j+1} + \mu_{i-1,j+1}}{\Delta x^2} \tag{5}$$

where Δt represents the time step and Δx represents the distance between different spatial points. The position in time is represented by j and the spatial position by i. $\mu_{i,j}$ is the known value for chemical potential and the implicit scheme will solve for $\mu_{i+1,j+1}, \mu_{i,j+1}$ and $\mu_{i-1,j+1}$ in the forward time step.

From the model, sorption isotherms will be predicted and will be compared with experimentally measured sorption idotherms. It is expected that in both adsorption and desorption, a sigmoidal shaped isotherm will be obtained. Firstly the model will be validated against obtained sorption isotherms for

cotton fibres [4]. Cotton fibres are almost purely made of cellulose. Thus, the amorphous matrix in the model only consists of amorphous cellulose, which makes the identification of the required input parameters of the model easier.

The next step will be to compare model results for sitka spruce with similarly obtained results [1] for sorption isotherms and to compare the rate determining steps observed within the cell wall sorption.

References

[1] Callum AS Hill, Andrew Norton, and Gary Newman. Analysis of the water vapour sorption behaviour of sitka spruce [picea sitchensis (bongard) carr.] based on the parallel exponential kinetics model. Holzforschung, 64(4):469473, 2010.

[2] Emil Tang Engelund, Lisbeth Garbrecht Thygesen, Staffan Svensson, and Callum AS Hill. A critical discussion of the physics of wood water interactions. Wood science and technology, 47(1):141161, 2013.

[3] R Cristian Neagu, E Kristofer Gamstedt, Stig L Bardage, and Mikael Lindstrom. Ultrastructural features affecting mechanical properties of wood fibres. Wood Material Science and Engineering, 1(3-4):146170, 2006.

[4] Yanjun Xie, Callum AS Hill, Zaihan Jalaludin, and Dongyang Sun. The water vapour sorption behaviour of three celluloses: analysis using parallel exponential kinetics and interpretation using the kelvin-voigt viscoelastic model. Cellulose, 18(3):517530, 2011.

[5] Yuhang Hu and Zhigang Suo. Viscoelasticity and poroelasticity in elastomeric gels. Acta Mechanica Solida Sinica, 25(5):441458, 2012.

Proceedings of the 22nd UK Conference of the
Association for Computational Mechanics in Engineering
2 - 4 April 2014, University of Exeter, Exeter

AN HP-FEM FRAMEWORK FOR THE SIMULATION OF COUPLED MAGNETO-FLUID EFFECTS

***D. Jin[1], P.D. Ledger[1] and A.J. Gil[1]**

[1]Civil and Computational Engineering Centre,
College of Engineering, Swansea University, Swansea SA2 8PP, United Kingdom

*536040@swansea.ac.uk

ABSTRACT

The physical understanding of coupled electro-magneto-mechanics has long since been an important topic for scientists. However, computational methods have only recently been applied to this field. In this paper, we will focus on solving the fully coupled nonlinear magneto-fluid problem using the *hp*-finite element method and a consistent Newton-Raphson linearisation strategy, for both conducting and non-conducting magnetic fluids with magnetostrictive effects, extending our previous work in [1]. Numerical results, including verification of the quadratic convergence of our Newton-Raphson implementation, are presented.

Key Words: *Coupled Magneto-fluid; Magnetostriction; hp-Finite Elements; Consistent Linearisation; Magnetohydrodynamics*

1. Introduction

Coupled magneto-fluid effects are important for a number of applications, including the industrial production of aluminium and the restriction of blood flow during surgery. Understanding the mechanisms that cause the magnetic field to influence the fluid flow and the flow patterns required to change the magnetic properties of the medium are crucial for these applications. To do this cost-effectively, computational mechanics must be applied.

Our present research is focused on the solution of coupled magneto-fluid problems where the fluid is Newtonian and incompressible. The presence of an electromagnetic field exerts stresses on the fluid field. Meanwhile, the strain rate of the fluid flow alters the magnetic properties of the fluid by magnetostriction, resulting into a nonlinear fully coupled system. Further non-linearity can be introduced by the constitutive behaviour of a ferro-magnetic fluid. The finite element method is employed to discretise the problem and the resulting non-linear algebraic equations are consistently linearised via a Newton-Raphson strategy. The complexity of the equations requires spatial discretisation of the velocity, pressure and magnetic fields by different element types in order to satisfy the LBB constraint. High accuracy is achieved by using high order (or *hp*-) versions of these finite elements.

In order to study the effectiveness and accuracy of our simulations, a series of benchmark problems, including the flow around a rigid cylinder and the lid-driven cavity flow, are extended to consider their behaviour for conducting and non-conducting fluids at low and high Reynolds numbers under the influence of a magnetic field of varying intensity.

2. Basic Formulations

The fluid motion can be described by the Navier-Stokes equations with the constitutive law for incompressible viscous fluid and the electromagnetic field is governed by the Maxwell equations with appropriate electromagnetic constitutive laws. The stationary formulations are shown in Table 1. Here, ρ is the fluid density, $\boldsymbol{u}$ is the fluid velocity, $[\sigma_F]$ is the fluid stress tensor, $\boldsymbol{f}$ is the total body force, p is the pressure, $\hat{\mu}$ is the viscosity, $[I]$ is the identity tensor and $[d(\boldsymbol{u})]$ is the strain rate tensor. $\boldsymbol{E}$ and $\boldsymbol{H}$ are

Table 1: Navier-Stokes equations and Maxwell's equations and the corresponding constitutive laws

Navier-Stokes equations	Maxwell's equations
$\rho(\nabla \boldsymbol{u})\,\boldsymbol{u} - \nabla \cdot [\sigma_F] = \rho \boldsymbol{f}$ $\nabla \cdot \boldsymbol{u} = 0$	$\nabla \times \boldsymbol{E} = 0$ $\nabla \times \boldsymbol{H} = \boldsymbol{J}$ $\nabla \cdot \boldsymbol{D} = \rho_e$ $\nabla \cdot \boldsymbol{B} = 0$
$[\sigma_F] = -p\,[I] + 2\hat{\mu}\,[d(\boldsymbol{u})]$	$\boldsymbol{B} = [\mu_r]\,\boldsymbol{H}$ $\boldsymbol{D} = [\epsilon_r]\,\boldsymbol{E}$

the electric and magnetic field intensity vectors, respectively. The vectors $\boldsymbol{D}$ and $\boldsymbol{B}$ are the electric and magnetic flux intensities, respectively. The electric current density is denoted by $\boldsymbol{J}$ and ρ_e denotes the volume charge density. The relative permittivity and permeability tensors are denoted by $[\epsilon_r]$ and $[\mu_r]$, respectively.

The existence of a magnetic field exerts a stress field $[\sigma_H]$ on the fluid, which appears in $\boldsymbol{f} = \nabla \cdot [\sigma_H] + \tilde{\boldsymbol{f}}$, and the magnetic field properties, especially the permeability $[\mu_r]$, are influenced by the fluid strain rate. With this two way coupling, the Navier-Stokes and Maxwell equations result in a fully coupled non-linear set of governing equations. The fully coupled equations, the coupling mechanisms and the suitable weak variable spaces considered in this work are summarised in Table 2. We remark that the detailed formulations for constitutive laws for magnetostrictive effects can be found in [2] and those for the conducting fluid with conductivity s are available in [3] and [4].

Table 2: Coupling mechanisms, including the strong form for the fully coupled governing equations and the suitable weak variable spaces for conducting and non-conducting fluids

$\boldsymbol{J} = \boldsymbol{0}$ non-conducting fluid	$\boldsymbol{J} = \boldsymbol{J}(\boldsymbol{E}, \boldsymbol{B})$ conducting fluid
$\rho(\nabla \boldsymbol{u})\,\boldsymbol{u} - \nabla \cdot ([\sigma_H] + [\sigma_F]) = \rho \tilde{\boldsymbol{f}}$ $\nabla \cdot \boldsymbol{u} = 0$ $\nabla \cdot ([\mu_r]\,\boldsymbol{H}) = 0$ $\boldsymbol{H} = -\nabla \phi, (\nabla \times \boldsymbol{H} = \boldsymbol{0})$	$\rho(\nabla \boldsymbol{u})\,\boldsymbol{u} - \nabla \cdot ([\sigma_H] + [\sigma_F]) = \rho \tilde{\boldsymbol{f}}$ $\nabla \cdot \boldsymbol{u} = 0$ $\nabla \cdot ([\mu_r]\boldsymbol{H}) = 0$ $\nabla \times s^{-1} \nabla \times \boldsymbol{H} + \nabla r - \nabla \times (\boldsymbol{u} \times [\mu_r]\,\boldsymbol{H}) = \boldsymbol{g}$
$[\sigma_H] = \sigma(\boldsymbol{H} \otimes \boldsymbol{H}, \boldsymbol{H} \cdot \boldsymbol{H})$ $[\mu_r] = \mu_r([d(\mathbf{u})])$ or $[\mu_r] = \mu_r(\mathbf{H})$	$[\sigma_H] = \sigma(\boldsymbol{H} \otimes \boldsymbol{H}, \boldsymbol{H} \cdot \boldsymbol{H})$ $[\mu_r] = \mu_r([d(\mathbf{u})])$
$\boldsymbol{u} \in \boldsymbol{H}^1(\Omega), p \in L^2(\Omega), \phi \in H^1(\Omega)$	$\boldsymbol{u} \in \boldsymbol{H}^1(\Omega), p \in L^2(\Omega)$, $\boldsymbol{H} \in \boldsymbol{H}(curl, \Omega), r \in H^1(\Omega)$

The weak formulation can be derived from the strong form stated in this table and the resulting non-linear system of equations are consistently linearised via a Newton-Raphson strategy. For full details we refer to [2].

3. Numerical Discretisation

To ensure accuracy, the $hp-$finite element discretisation of Schöberl and Zaglmayr [5] is used for the simplicial triangulation of Ω in two–dimensions, with the suitable hierarchic conforming finite element spaces for each of the variables shown in Table 2. For a non-conducting fluid, the magnetic field intensity $\boldsymbol{H}$ can be described as gradient of a potential field. In this case, a discretisation of $\boldsymbol{H}^1(\Omega), H^1(\Omega)$ and $L^2(\Omega)$ are required. For a conducting fluid, the curl-curl equation can not be simplified and $\boldsymbol{H}$ must be discretised by $\boldsymbol{H}(curl, \Omega)$ conforming edge elements. Note that in order to satisfy the LBB condition, the polynomial degree must be chosen as P_p, P_{p-2} for fluid velocity and pressure, respectively.

The scheme for a non-conducting fluid is able to simulate magnetostrictive effects. It can also simulate the more complicated non-linear constitutive behaviour of a ferro-fluid. The implementation has been benchmarked using classic benchmark problems (lid-driven cavity and flow past a cylinder) without the magnetic intensity and has been extended to include the behaviour under the presence of a magnetic field. The benchmarking procedure and results for the coupled mechanic-fluid problems for single phase non-

conducting fluid can be found in [2]. The scheme for a conducting fluid can be employed to simulate magnetohydrodynamics (MHD) problems. The implementation has been benchmarked with the well-known Hartmann flow problem, an L-shape domain problem with a smooth solution as well as an L-shaped domain with a singular solution. These interesting results will be presented in the presentation.

4. Numerical Results

We focus on presenting the results that show how the flow patterns are influenced by the presence of a magnetic field for conducting and non-conducting fluids with multiple phases.

The geometry of the background fluid is square in to which are placed fluid droplets with differing electromagnetic properties. In our case, nine small cylinders are placed inside the square domain. The background fluid and inner fluid are both either conducting or non–conducting, but with different parameters, depending on the problem being solved, as listed in Table 3. For both cases, the background fluid is moving in a horizontal direction and a uniform magnetic field is then applied in either a horizontal or vertical direction depending on whether a non-conducting or conducting fluid are considered.

Table 3: The parameters for inside and outside fluids (μ_0 is permeability for free space)

Non conducting fluid (ferro -fluid)			Conducting fluid (MHD)		
Parameters	Inside fluid	Outside fluid	Parameters	Inside fluid	Outside fluid
ρ	1320	1000	ρ	2700	1000
$\hat{\mu}$	80	1	$\hat{\mu}$	810	100
μ_r	1.002	0.99	μ_r	1.002	0.99
			s	$2/\mu_0$	$1/\mu_0$

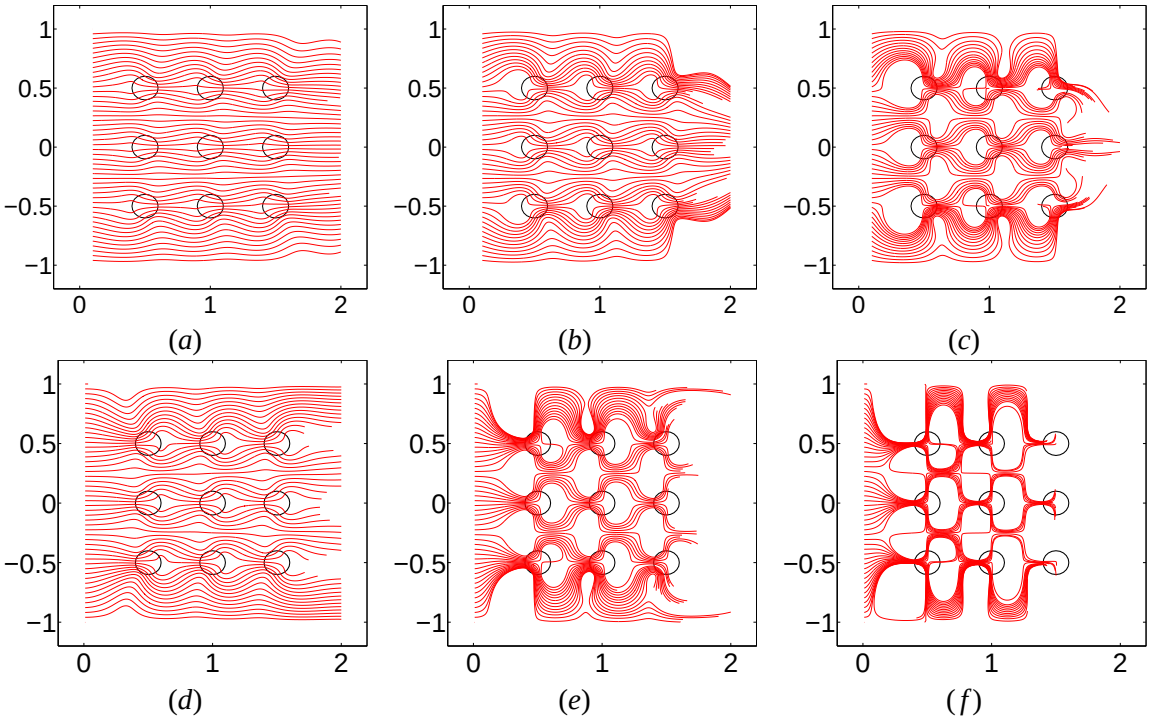

Figure 1: Multiple phase problem for non-conducting fluid (a), (b), (c) and for conducting fluid (d), (e), (f) with increasing magnetic field.

In many applications, multiple phases with different magnetic properties must be taken into account when considering conducting and non-conducting fluids. The behaviour of several ferro-fluid droplets inside a non-ferro background fluid under the increasing magnetic field are simulated in Figure 1 (a), (b), (c) by using our high order approach. This simulation is motivated by a biomedical application of the treatment of retinal detachment and extends the examples of [6]. The corresponding behaviour of

different conducting fluid under the increasing magnetic field is shown in Figure 1 (*d*), (*e*), (*f*). This simulation is motivated by a MHD problem of the industrial production of aluminium [7].

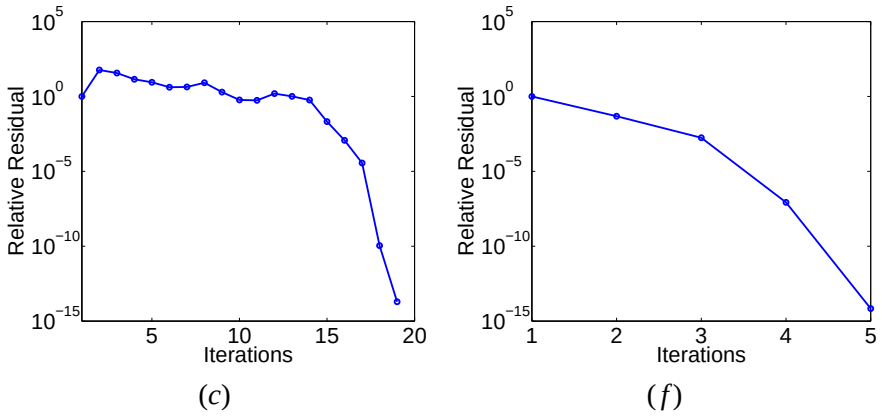

Figure 2: Quadratic convergence plots for a non–conducting and conducting fluid, cases (*c*) and (*f*) from Figure 1.

Figure 2 shows the quadratic convergence plot for the relative residual for conducting and non-conducting simulations for cases (*c*) and (*f*) of Figure 1. The Newton-Raphson strategy clearly shows quadratic convergence for both the non-conducting and conducting cases. The first case needs more steps to converge due to the additional non-linearity arising from the ferro-fluid. The convergence is only limited by the finite precision of our approach. Note that the convergence behaviour will be influenced by the parameters in Table 3 and the magnitude of $\boldsymbol{H}$. In particular, for the same parameters, the larger the magnitude of $\boldsymbol{H}$, the more iterations that are required to reach convergence.

5. Conclusions

The coupled formulations for conducting and non-conducting fluids are implemented in a monolithic manner and solved by means of a Newton–Raphson strategy in conjunction with consistent linearisation for single and multiple phase problems. A finite element discretisation employing *hp*-finite elements has been used to ensure high levels of accuracy. A series of well known benchmark problems are simulated under the influence of an magnetic intensity field for the two–dimensional case. On going current work includes the extension to three–dimensional problems and we intend to report on progress in this direction during our presentation.

References

[1] A.J. Gil and P.D. Ledger. A coupled *hp*–finite element scheme for the solution of twodimensional electrostrictive materials. *International Journal for Numerical Methods in Engineering*, 91(11), 1158-1183, 2012.

[2] D. Jin, P.D. Ledger and A.J. Gil. An *hp*-fem framework for the simulation of electrostrictive and magnetostrictive materials. *Computers and Structures*, 133, 131-148, 2014.

[3] P. Houston, D. Schötzau and X. Wei. A mixed DG method for linearised incompressible magnetohydrodynamics. *Journal of Scientific Computing*, 40, 281-314, 2009.

[4] F. Armero and J.C. Simo. Long-term dissipativity of time-stepping algorithms for an abstract evolution equation with applications to the incompressible MHD and Navier-Stokes equations. *Computer Methods in Applied Mechanics and Engineering*, 131, 41-90, 1996.

[5] J. Schöberl and S. Zaglmayr. High order Nédélec elements with local complete sequence properties. *International Journal for Computation and Mathematics in Electrical and Electronic Engineering*, 24, 374-384, 2005.

[6] S. Afkhami, Y. Renardy, M. Renardy, J.S. Riffle and T. St Pierre. Field-induced motion of ferro-fluid droplets through immiscible viscous media. *Journal of Fluid Mechanics*, 610, 363-380, 2008.

[7] J.-F. Gerbeau, T. Lebievre and C. Le Bris. Simulation of MHD flow with moving interfaces. *Journal of Computational Physics*, 184, 163-191, 2003.

Proceedings of the 22nd UK Conference of the
Association for Computational Mechanics in Engineering
2 - 4 April 2014, University of Exeter, Exeter

AN IMMERSED STRUCTURAL POTENTIAL METHOD FRAMEWORK FOR INCOMPRESSIBLE FLEXIBLE/RIGID/MULTI-PHASE FLOW INTERACTION

L. Yang[1], A. Arranz Carreño[2], A.J. Gil[1] and J. Bonet[1]

[1]Civil & Computational Engineering Centre, College of Engineering, Swansea University, Swansea SA2 8PP
[2]Department of Mathematics, College of Science, Swansea University, Swansea SA2 8PP

{530567; a.arranz-carreno; a.j.gil; j.bonet}@swansea.ac.uk

ABSTRACT

In this paper, a general framework for the computational simulation of Fluid-Structure Interaction (FSI) problems involving rigid/flexible solids and multiphase flows is presented. The proposed methodology builds upon the Immersed Structural Potential Method (ISPM) developed by the authors [1, 2] for the simulation of single-phase FSI problems. Several numerical examples are presented to showcase and benchmark the proposed methodology in the solution of complex multi-body multi-phase problems.

Key Words: *Immersed Structural Potential Method (ISPM); rigid body constrains; level set method; augmented Lagrangian method*

1. Introduction

The numerical solution of incompressible flexible/rigid/multi-phase flow interaction problems is extremely important and commonplace in many engineering applications: from costal engineering, civil engineering to ship hydrodynamics. In general terms, two main families of methodologies have been used in practice: body-fitted approaches [3] and immersed type methods [1, 2, 4]. Methods of each family have some strengths and weaknesses, but within the body-fitted methodologies, the main disadvantage is the cost of mesh update and re-meshing algorithms, a factor particularly important in the case of three-dimensional simulations. As an alternative to such methodologies, Peskin [4] originally introduced the Immersed Boundary Method (IBM) for the solution of heart valve problems, where the computation is performed on a background Cartesian grid and a body force is added to the fluid to account for the presence of a solid.

There have been several extensions of immersed methodologies since their inception. One such extension to the original IBM is the Immersed Structural Potential Method (ISPM), introduced by the authors [1, 2] for the solution of single-phase FSI problems with highly deformable structures, such as those present in typical haemodynamic problems. In such scenarios, the methodology is robust and efficient, but the consideration of rigid, or very stiff structures, can be a limiting factor. For such problems, the authors have opted for extending the methodology by adding a Lagrange multiplier field to enforce the rigid body constraints, and solve the arising mixed formulation using a Least Squares projection approach [5]. Moreover, for the case of immersed structures with a density substantially different to that of the surrounding fluid, an extension of the original methodology is required to avoid numerical instabilities. In this work, both issues will be addressed and the original framework extended to allow for multi-phase flows by means of the Level Set Method [6]. The efficient iterative solution of the corresponding non-constant diffusion (anisotropic) pressure-Poisson equation that arises in the modified fractional step method is then solved efficiently using a geometric multigrid solver in combination with segregation of the rigid constraints.

2. Methodology

In immersed techniques an underlying Eulerian mesh is employed to discretise the fluid. For the case of an incompressible Newtonian fluid, the time-dependent Navier-Stokes equations tend to be solved (due to computational efficiency) by means of a fractional step method that uncouples velocity and pressure unknowns. In order to extend the methodology first for multiphase flows, we consider the continuum domain $\Omega \subset \mathbb{R}^n$, $n = 2, 3$ and a partition into disjoint sets Ω_i that will represent each of the possible fluid phases, i.e. $\Omega = \cup_i \Omega_i$, $\Omega_i \cap \Omega_j = \emptyset, i \neq j$. The Level Set Method [7] is employed to "capture" the interfaces of the different phases as they evolve in time. A regularised Heaviside function H_i, i.e. a smooth approximation of the characteristic or indicator function χ_{Ω_i}, is evaluated for each phase Ω_i by means of the corresponding vector level set function $\boldsymbol{\phi}$, i.e. $H_i = H_i(\boldsymbol{\phi})$. Such regularisations are constructed so that the partition of unity property that the true characteristic functions satisfy also holds, i.e. $\sum_i H_i \equiv 1$. This identity allows us to consider the linear momentum conservation equation for a control volume $V \subset \Omega$ as

$$\int_V \frac{\partial}{\partial t} (\rho(\boldsymbol{H})\boldsymbol{u})\, dv + \int_{\partial V} (\rho(\boldsymbol{H})\boldsymbol{u} \otimes \boldsymbol{u} + p\boldsymbol{I} - \sigma'(\boldsymbol{H})) \cdot \boldsymbol{n} da = \int_V \boldsymbol{g} dv$$

where $H_i = [\boldsymbol{H}]_i$ is the vector of regularised Heaviside functions, $\rho(\boldsymbol{H})$ is the (non-constant, space-varying) density of the fluid as a function of the regularised Heaviside vector $\boldsymbol{H}$ and $\sigma'(\boldsymbol{H})$ is the deviatoric component of the stress tensor of the corresponding continuum phase. In addition, for an incompressible fluid, the following constraint has to be satisfied

$$\nabla \cdot \boldsymbol{u} = 0.$$

Upon solution by means of a fractional step method, the following non-constant diffusion (anisotropic) Poisson equation has to be solved to determine the pressure field

$$\nabla \cdot \left(\frac{1}{\rho(\boldsymbol{H})} \nabla \psi \right) = div(\boldsymbol{u}^*),$$

where ψ is an increment to the pressure field and $\boldsymbol{u}^*$ is an intermediate stage, non-divergence free, approximation to the velocity field. This is accomplished efficiently by use of a geometric multigrid Poisson solver. The above methodology allows for the simulation of multi-phase flows with high ratios of physical phase properties (e.g. density or viscosity).

For the inclusion of a deformable structure with initial domain Ω_0^s immersed in the fluid domain Ω, the body force $\boldsymbol{g}$ above is computed using the ISPM [1, 2], based on a Marker and Cell (MAC) spatial discretisation. A deviatoric energy functional Π^s corresponding to the deformable structure is integrated using a quadrature rule with integration points a_p and weights W^{a_p}, thus "tracking" in a Lagrangian fashion the mechanical response of the flexible structure

$$\Pi^s(\varphi) = \int_{\Omega_0^s} \hat{\Psi}^s(\varphi) dV \approx \sum_{a_p} \hat{\Psi}^s(\varphi^{a_p}) W^{a_p},$$

where φ is the solid mapping and $\hat{\Psi}^s$ is the deviatoric strain energy density. The FSI forces term $\boldsymbol{g}$ can be computed then as

$$f_i^{A_i} = \int_{\Omega_0^s} \tau_i'^s \cdot \nabla \zeta^{A_i}(\boldsymbol{x^s}) dV \approx \sum_{a_p} W^{a_p} \tau_i'^{s,a_p} \cdot \nabla \zeta^{A_i}(\boldsymbol{x}^{a_p}),\ g_i^{A_i} = f_i^{A_i} / (\prod_{j=1}^{j=n} \Delta x_j) \quad i = x_1, \ldots, x_n$$

where ζ^{A_i} is a suitable interpolating kernel function [2] centred at edge A_i. In the original methodology [1], the FSI interaction force $\boldsymbol{g}$ included both the deviatoric contribution to the interaction forces and the inertial term, due to the different densities of solid and fluid phases. Unfortunately, in the case of explicit time integration algorithms, the inertial contribution can lead to unstable computations for large density ratios. In the proposed extension, the ISPM is used to compute only the deviatoric component, leaving the inertial contribution to be dealt with in an Eulerian manner by the above multi-phase fluid solver.

Another limitation of the original ISPM is the modelling of very stiff or rigid structures, as the corresponding interaction term dominates the stability of the fluid solver and forces extremely small time-steps. For a rigid body occupying $\Omega^{RB} \subset \Omega$, the following additional constraint on the velocity field has to be fulfilled

$$\boldsymbol{u} = \boldsymbol{\omega} \times (\boldsymbol{x} - \boldsymbol{x_0})$$

where $\boldsymbol{x_0}$ is the instant centre of rotation and $\boldsymbol{\omega}$ is the angular velocity. The rigid body is "tracked" in a Lagrangian way using a collection of integration points, in a similar fashion to the ISPM. A Lagrange multiplier field $\boldsymbol{\lambda}$ is added to the formulation to enforce the above constraint. In order to simplify the enforcement of such constraint, a weighted Least-Squares projection of the velocity field is performed. The spatial semi-discretisation is carried out using a staggered Finite Volume scheme on a Cartesian standard Marker-and-Cell (MAC) grid, where the level set and the pressure field are defined at the cell centres and the normal component of velocities, Lagrange multipliers and forces are defined at the cell faces, arriving at

$$\begin{aligned}
\frac{\mathcal{M}}{\Delta t}\boldsymbol{U}_{n+1} + \mathcal{G}\boldsymbol{P}_{n+1} + \mathcal{H}\lambda_{n+1} &= \frac{\mathcal{M}}{\Delta t}\boldsymbol{U}_n - C(\boldsymbol{U})_{n+1/2}(\rho(\boldsymbol{\phi})\boldsymbol{U}) - \mathcal{V}(\boldsymbol{U}_{n+1}) + G(\boldsymbol{U}_{n+1}),\\
\mathcal{D}\boldsymbol{U}_{n+1} &= 0,\\
\mathcal{A}\boldsymbol{U}_{n+1} &= \boldsymbol{U}_R,\\
\frac{\boldsymbol{\phi}_{n+1} - \boldsymbol{\phi}_n}{\Delta t} + C(\boldsymbol{U})_{n+1/2}(\boldsymbol{\phi}) &= 0,
\end{aligned}$$

where $\mathcal{M}, \mathcal{G}, C, \mathcal{V}, \mathcal{D}$ and $\mathcal{A}$ denote the discrete mass, gradient, convective, viscous term, divergence and Least-Squares projection operator respectively, and $\boldsymbol{U}_n$, $\boldsymbol{P}_n$ and λ_n denote the discrete velocity, pressure and Lagrange multiplier at time t_n. Note that $\mathcal{D}$ and $\mathcal{H}$ are the adjoint operators of $\mathcal{G}$ and $\mathcal{A}$ respectively. The above discrete system is solved by means of the fractional step method in conjunction with an Uzawa-type algorithm.

3. Numerical examples

In this section we present the numerical simulation of the sinking and fluttering of a rigid body in a viscous fluid with the framework presented above. The physical domain is the rectangle 15×40, discretised with a series of Cartesian meshes, the finest of which is composed of 240×640 cells, filled with a Newtonian viscous fluid of viscosity $\mu = 10^{-5}$ and density $\rho = 10^3$. A rigid rectangle of size 5×0.5 m is rotated clockwise an angle of $\pi/3$ and translated such that its geometrical centre is at position $(3.4665, 35.96)$ with respect to the bottom left corner of the fluid domain (see Figure 1a). The rigid solid has a density 1.5 times that of the fluid and is discretised using 5760 integration points. The total run-time for the case with the finest mesh is 1 hour using a 2.4 GHz Intel Core 2 Duo CPU. In Figure 1b and 1c we can observe convergence of the evolution over time of the position and velocity of the bottom left corner of the rectangle for a series of discretisations. In Figure 2, in a series of snapshots of the solution, it can be observed how the rigid solid sinks and flutters as it creates vortices in its wake.

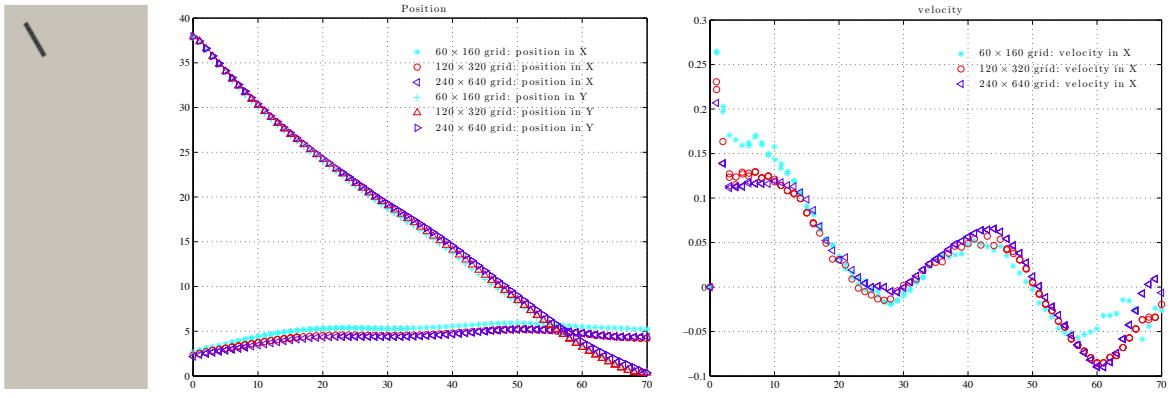

(a) (b) (c)

Figure 1: (a) Geometry of the problem; (b) Evolution with respect to time of the x and y position of the bottom left corner of the rigid rectangle for a series of mesh discretisations; (c) Corresponding velocity of the same point with respect to time for a series of meshes.

4. Conclusions

In this work, we presented a general unified framework for the simulation of incompressible rigid/flexible/multi-phase flow problems that offers a series of advantages. First, the use of a novel

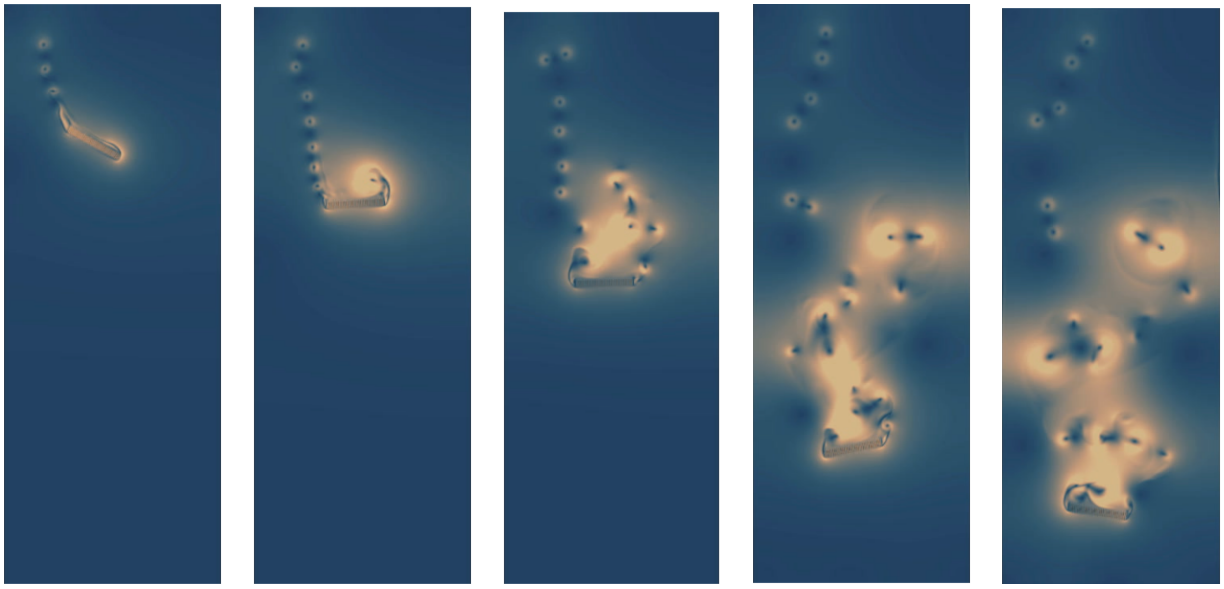

Figure 2: Snapshots of the solution for the problem of a rigid solid sinking and tumbling in a viscous fluid.

weighted least square projection scheme allows for the easy incorporation of complex rigid body motions. Second, all constraints are segregated in the system, combining fractional steps and the augmented Lagrange Method, reducing the overall computational cost. By means of an efficient geometric multigrid Poisson solver, it is shown that the framework can also be used to simulate scenarios with large density ratios between phases and/or solids.

Acknowledgements

This work is financially supported by the Zienkiewicz Scholarship, College of Engineering, Swansea University.

References

[1] A. Gil, A. Arranz Carreño, J. Bonet, O. Hassan, The immersed structural potential method for haemodynamic applications, Journal of Computational Physics 229 (2010) 8613–8641. doi:10.1016/j.jcp.2010.08.005.

[2] A. J. Gil, A. Arranz Carreño, J. Bonet, O. Hassan, An enhanced Immersed Structural Potential Method for fluid–structure interaction, Journal of Computational Physics 250 (0) (2013) 178 – 205. doi:10.1016/j.jcp.2013.05.011.

[3] C. Wood, A. J. Gil, O. Hassan, J. Bonet, A partitioned coupling approach for dynamic fluid-structure interaction with applications to biological membranes, International Journal for Numerical Methods in Fluids 57 (5) (2008) 555–581. doi:10.1002/fld.1815.

[4] C. S. Peskin, Flow patterns around heart values: a numerical method, Journal of Computational Physics 10 (1972) 252–271.

[5] K. Taira, T. Colonius, The immersed boundary method: A projection approach, Journal of Computational Physics 225 (2) (2007) 2118 – 2137. doi:10.1016/j.jcp.2007.03.005.

[6] M. Sussman, P. Smereka, S. Osher, A Level Set Approach for Computing Solutions to Incompressible Two-Phase Flow, Journal of Computational Physics 114 (1) (1994) 146 – 159. doi:10.1006/jcph.1994.1155.

[7] J. A. Sethian, Level Set Methods and Fast Marching Methods: Evolving Interfaces in Computational Geometry, Fluid Mechanics, Computer Vision, and Materials Science, 2nd Edition, Cambridge University Press, 1999.

Proceedings of the 22nd UK Conference of the
Association for Computational Mechanics in Engineering
2 – 4April 2014, University of Exeter, Exeter

COMPUTATIONAL MODELLING OF AN ESTUARY IN THE FRAME OF THE OPTIMISATION OF TIDAL FARMS

***M. Garcia-Oliva[1], G. Tabor[1] and S. Djordjevic[1]**

[1]College of Engineering, Mathematics and Physical Sciences, University of Exeter, North Park Road, Exeter EX4 4QF, United Kingdom

*mg391@exeter.ac.uk

ABSTRACT

Computational simulations are used in an increasing range of applications for coastal environments. Despite their advantages in comparison to other methods, there are still some uncertainties over the features involved, sometimes connected to the complexity of the large scale physical processes.
A 2D numerical simulation based on a Finite Volume Method (Mike21 by DHI) has been developed to study the hydrodynamic behaviour of the flow in the Solway Firth as a basis for the optimisation of tidal farms. The aim is to find a configuration with the maximum energy extraction and the minimum impact on flood risk. The boundary conditions applied in the model consisted of the highest tides and a storm surge. The results for the maximum water levels and velocities identified the areas with high risk of flooding and the potential locations for the tidal farms, respectively.
Due to the lack of observed data for turbulence in the estuary, a sensitivity analysis has been carried out to determine how the hydrodynamic results would be affected by this parameter. Regarding the integration of turbines in the estuarine model, results from a detailed 3D Computational Fluid Dynamics (OpenFoam) model of individual turbines and groups of them are used to account for the interactions within the farm and with the surrounding environment. Different configurations of tidal farms will be included in the simulations and optimised by means of nature-inspired genetic algorithms and advanced methodologies, such as artificial neural networks.

Keywords: *CFD; FVM; Hydrodynamics; Optimisation;Turbines*

1. Introduction

Computational simulations are used increasingly in different applications for coastal environments, ranging from representations of the near-field effects of structures deployed in a certain location up to the far-field effects of marine energy extraction at ocean scales. The current study is focused on computational simulations related to the environmental interactions of tidal farms in estuaries. Although there are some advantages in the simulations in terms of the balance between accuracy of results and computational costs in comparison to other methods, like simplified analytic approaches or physical models, the connection between different scales (in this case, tidal farm and estuary) within the model results in a high complexity. This project integrates both scales with the aim of providing a better understanding of the effect of tidal farms in estuaries.

The current study is focused on the Solway Firth area, which is a highly energetic estuary located in the West coast of Great Britain, between England and Scotland. The purpose is to optimise the layout of tidal farms in terms of maximum energy extraction and minimum environmental impact. The latter is represented by the influence that turbines could have on the existing water levels in the area. Flood risk is preferred here to other environmental parameters, such as suspended sediment concentration or changes in the morphology of the seabed, because it can be directly assessed with the same model used to calculate the extracted power. On the other hand, the cost of damages caused by flooding is very important from a social perspective.

2. Methodology

In order to achieve the integration between the different scales involved in the study, two kinds of

models have been used: a Computational Fluid Dynamics (CFD) model and a Finite Volume Method solver. The detailed three-dimensional (3D) CFD modelling will provide results about the interactions of turbines within the farm. On the other hand, the computational demand of the CFD is very high to be used directly in the optimisation process. Therefore, a 3D FVM model (Mike3 by DHI) with a lower computational time is being compared with the CFD in the same cases. These models will be a basis for the optimisation of the energy output in the scale of the farm. In relation to the estuary, a 2D FVM system (Mike21 by DHI) has been used to assess the flood risk in the situation without turbines and these results will be compared with the cases including the optimised configurations of tidal farms. Finally, the comparisons will be used to find the solution which minimises the flood risk in the estuary.

3. Turbines and tidal farms modelling

CFD models have been developed to provide detailed information about wake formation and interactions between turbines. In this project the design of the turbines is based on the horizontal transverse flow type called Momentum Reversal Lift turbine, as can be seen from figure 1. Several situations have been performed in OpenFOAM, including individual turbines and groups of them [5, 6, 7, 8]. Currently, a model is being created to represent a group of thirty turbines in two different configurations, related to the experimental testing that will be carried out in the Allwaters tank in order to validate the results of the CFD models. The Allwaters facility is a curved tank located in the University of Edinburgh with the ability of recreating currents in any direction and situations with waves and currents at the same time. [11]

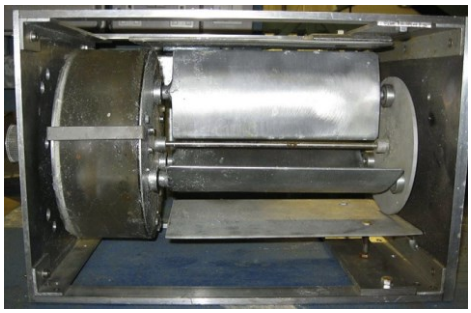

Figure 1: MRL turbine

In order to compare the aforementioned models with an application which can gives similar results with a reduced computational demand, Mike3 models have been developed consisting of three vertical layers. The central layer is referred to the turbine position and the upper and lower layers are related to the by-pass flows, according to the Linear Momentum Actuator Disk Theory, which allows studying the losses from turbulent wake mixing [4].

4. Estuary modelling

A numerical model of the Solway Firth Estuary has been defined by means of Mike21. The domain of the model is delimited by the inland boundary to the North-East, close to convergence of the rivers Esk and Eden, and by the open sea boundary at the South-West, between Head Abbey (Kirckcudbright Bay) and St Bee's Head (Workington). The domain is covered by an unstructured flexible mesh created through the interpolation of bathymetry and terrain data. The former were obtained from the Celtic Seas dataset, provided by the British Oceanographic Data Centre [2], with a resolution of 30 arc seconds and 1 arc minute for the latitude and longitude, respectively. The terrain in the coastline was included between the shoreline and the 10 m elevation isoline and it was represented by points from the Profile Contour dataset, provided by the Ordnance Survey, with a vertical resolution between 5 and 10 m. The domain was divided in several subdomains with different refinements according to the areas where a higher accuracy was necessary

The duration of the preliminary simulation consisted of four tidal cycles and it was referred to an extreme scenario based on the 1 in 200 years return period event for the highest tide plus the atmospheric surge. The water elevations for this event were calculated following the guidance of the Environment Agency for the design of flood defences presented by McMillan et al. [1] and the data from the Admiralty Tide Tables 2013 and included as a boundary condition in the open sea boundary. Wind data have been obtained from Carlisle airport.

The value of the bed resistance was set to a constant value of the Manning's roughness coefficient according to the existing sediments in the seabed and varying according to Land Cover values in the Coastline, taken in ArcGis format from the UK Land Cover Map (LCM2007)**.** The land cover indexes were converted into Manning's roughness coefficients for natural floodplains. Due to the lack of data about turbulence in this area, a sensitivity analysis was carried out and the results showed that there was little influence of this parameter on the results. Therefore, a value of 0.28 for the Smagorinsky coefficient was adopted.

Figure 2 shows the results for the initial hydrodynamic model for the mean water levels and current velocities in the estuary. The maximum values give an idea about the areas at risk of flooding and the potential locations of tidal farms, respectively. These results are in good agreement with the information showed by the flood risk maps provided by the Environment Agency [3] and the Scottish Environment Protection Agency [10], as well as with the annual velocities from the UK atlas of marine renewable energy resources [12].

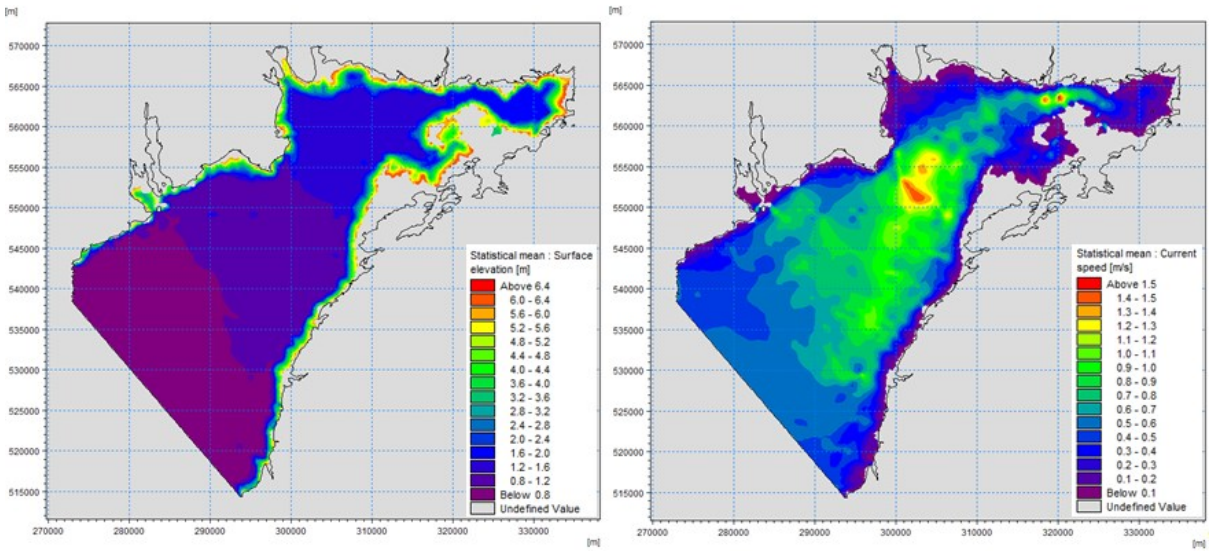

Figure 2: Mean water elevations and velocities from Mike21 model in the Solway Firth estuary, averaged over four tidal cycles.

The model has been calibrated according to the observed sea levels from the gauge station, with coordinates 54˚44.0'N and 3˚53.0' W, on 30th April 1977, being this dataset provided by the British Oceanographic Data Centre [2]. Data for the river flows on the previous date have been provided by the National River Flow Archive [9].

The model will include the main rivers along the boundary represented as sources. The peak flows for the 1:200 years return period are being obtained through the Environment Agency and the Scottish Environment Protection Agency. Further work will also include the evaluation, in terms of damages and monetary costs, and the comparison of flood risk levels from the model without and with the tidal farms in order to be introduced in next stages of the optimisation process. For that purpose the data about urban areas in the estuary are being collected.

5. Optimisation

Optimisation techniques based on genetic algorithms, will be applied to get the best configuration of tidal turbines within the farm in terms of the maximum power output. These configurations will then be included in the estuary model to assess the flood risk. Advanced techniques such as artificial neural networks will be used at this stage to improve the layout of the farm in order to have the minimum impact on flood risk.

6. Conclusions

Further work will focus on Mike3 models of individual turbines and groups of them and the comparison with OpenFOAM results, which are being validated through experimental testing. These models will be integrated in the optimisation process in order to determine the configuration that could extract maximum energy from the flow.

Results from the 2D estuarine model without tidal farms show good agreement with the official data sources and give an idea about the locations with high levels of flood risk and the potential locations for the tidal farms. Turbines will be included in a direct way as drag forces against the flow and the model will be used as a basis to provide the layout of the tidal farm with the minimum induced flood risk.

Acknowledgements

This research was conducted as part of the '*Optimal Design of Very Large Tidal Stream Farms: for Shallow Estuarine Applications*' project commissioned and funded by the UK Engineering and Physical Sciences Research Council (EPSRC). The authors would also like to acknowledge the support and software licence provided by DHI.

References

[1] A. McMillan, C. Batstone, D. Worth, J. Tawn, K. Horsburgh, and M. Lawless, *Coastal flood boundary conditions for uk mainland and islands. project sc060064/tr2: Design sea levels*, 2011.

[2] *British oceanographic data centre*. http://www.bodc.ac.uk/. Accessed: 2014-01-28.

[3] *Environment agency*. http://www.renewables-atlas.info/. Accessed: 2014-01-28.

[4] G. Houlsby, S. Draper, M. Oldfield, et al., Application of linear momentum actuator disc theory to open channel flow, *Report no. OUEL*, vol. 2296, no. 08, 2008.

[5] M. Berry, CFD Analysis of a Single MRL Tidal Turbine, *Proceedings of the 2nd Oxford Tidal Energy Workshop*, pp.37-38, 2013.

[6] M.G. Gebreslassie, G.R. Tabor and M.R. Belmont , Cfd simulations for investigating the wake states of a new class of tidal turbine, *Journal of Renewable Energy and Power Quality*, 10(241), 2012

[7] M.G. Gebreslassie, G.R. Tabor and M.R. Belmont, Numerical simulation of a new type of cross flow tidal turbine using OpenFOAM Part I: Calibration of energy extraction, *Renewable Energy*, 50:994-1004, 2013

[8] M.G. Gebreslassie, G.R. Tabor and M.R. Belmont, Numerical simulation of a new type of cross flow tidal turbine using OpenFOAM Part II: Investigation of turbine-to-turbine interaction. *Renewable Energy*, 50:1005-1013, 2013

[9] *National river flow archive*, http://www.ceh.ac.uk/data/nrfa/data/search.html. Accessed: 2014-01-28.

[10] *Scottish environment protection agency*, http://www.sepa.org.uk/flooding.aspx. Accessed: 2014-01-28.

[11] T. Davey, I. Bryden, D. Ingram, A. Robinson, J. Sinfield, and A. Wallace, The all-waters test facility- a new resource for the marine energy sector, *Proceedings of the 4th International Conference on Ocean Energy,* Dublin, Ireland, 2012.

[12] *Uk atlas of marine renewable energy resources*, http://www.renewables-atlas.info/. Accessed: 2014-01-28.

Proceedings of the 22nd UK Conference of the
Association for Computational Mechanics in Engineering
2 – 4April 2014, University of Exeter, Exeter

FLUID-STRUCTURE INTERACTION SIMULATION OF PARACHUTE FINITE MASS INFLATION

***Gao Xinglong[1], Zhang Qingbin[1] and Tang Qiangang[1]**

[1]College of Aerospace Science and Engineering, University of National University of Defence Technology, 410073, Deya Rd. 109, Changsha, Hunan, P. R. China

*qingbinzhang@sina.com

ABSTRACT

Parachute inflation has a sophisticated fluid-structure interaction (FSI) dynamic behaviour. This paper describes the simulation technique for life saving parachute inflation in a finite mass scenario. Combing with the CFD/CSD and FEM techniques, the computational FSI models were developed by Arbitrary Lagrangian Euler coupling method embedding in the LS-DYNA transient dynamic code. Prior to 2012, the infinite mass inflating simulation of parachute was analyzed by us, where the parachute does not influence the freestream air velocity; such models can be compared with the tests conducted in a wind tunnel. In finite mass scenario, a more complex inflation phase and FSI dynamics of parachute was investigated. The 3D visualization of canopy deformation, as well as the variability of dropping velocity and overload was obtained. Specifically, the evolvement of vortex in fluid field was analyzed to understand the FSI mechanism of parachute inflation. This technique could be further used in the parachute's airdrop test as a true prediction.

Keywords: *fluid-structure interaction; parachute inflation;Arbitrary Lagrangian Euler*

1. Introduction

As a kind of decelerator, parachute has been widely used in recovery and life-saving system. During parachute's working process, inflation is a critical step for the decelerating, and has always been a challenge work for a long period since 1960s'[1]. Fluid mechanics is unsteady, viscous often compressible flow about a porous body with large shape changes, the parachute is a tension structure that undergoes large transient deformations constructed by nonlinear materials with complex strain, and all of the above disciplines are strongly coupled. So it's difficult to converge the computation of FSI coupling equations for parachute inflation, thus people have built some simplified dynamic inflation models for parachute to predict filling time and drag forces[2, 3], some are also integrated with ballistic fight-path equations to compute the trajectory and stability for parachute-load system[4], for the trajectory computation of parachute-load system, the initial conditions is determined by the performance of parachute opening process.
The aim of this paper is to discuss the use of the LS-DYNA Explicit Finite Element Analysis (FEA) tool for simulation of parachute inflation dynamics.

2. Fluid-structure interaction approach

The applications described in this paper involve the modeling of a channel air flow interacting with a porous and inflatable structure. The fluid here is solved by utilizing a Eulerian formulation on Cartesian grid that overlaps the structure, while the latter is discretized by Lagrangian shells and cables. The parachute we investigated in this paper is a life saving slot-parachute with 24 suspension lines, and 8 radial gaps are placed symmetrically on connecting area of 8 gores (as shown in figure 1).

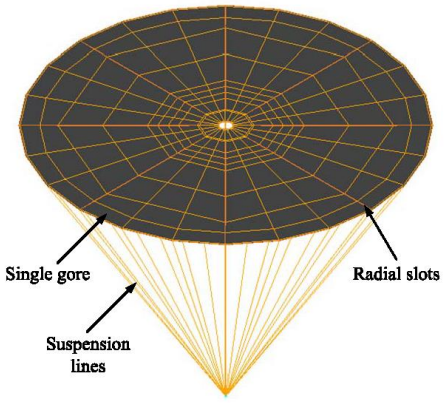

Figure 1: Slotted canopy layout.

The parachute opening velocity of airdrop process is commonly relative low, although the fluid field during parachute inflation is typical time-variant spatial domain, it can be considered as incompressible viscid flow. Let f and (0, T) be the spatial and temporal domains, $\partial\Omega^f$ denote the boundary of domain. Introducing the ALE formulation, the finite mesh can be freely moved and the fluid particles coordinates are $X_i(t)$, (i=x, y, z)， where $t\in(t, T)$, thus the N-S governing equations of incompressible flow in reference coordinates are

$$\frac{\partial \boldsymbol{v}}{\partial t}+(\boldsymbol{v}-\boldsymbol{w})\cdot\nabla\boldsymbol{v}-\frac{1}{\rho_f}\boldsymbol{\sigma}=\boldsymbol{g} \tag{1}$$

Where $\boldsymbol{v}$ and ρ_f is the fluid velocity and density, $\boldsymbol{w}$ is the mesh velocity in reference coordinates. If $\boldsymbol{w}$ = 0, Equation (1) is the Euler formulation, and if $\boldsymbol{v}$ = $\boldsymbol{w}$, it's the Lagrangian formulation.

In FSI problems, the computation of coupling interface is a key technique for the conversation of energy must be ensured. Generally, it's impossible to implement the total matching between structural and fluid mesh. Here we implemented the Multi-Material ALE method (MMALE) in LS-DYNA code for solving this problem. LS-DYNA code allows running models with non-coincident structure and fluid meshes. The MMALE method combines Lagrangian and Eulerian methods. Which means for Lagrangian step, the mesh moves with the material in the first part of the step, while for Eulerian step, the mesh is smoothed out to minimize the element distortion and material flow between elements, the fluid characteristics are re-computed at the initial node locations by a procedure called "advection".

For Newton fluid, the stress tensor can be defined as

$$\boldsymbol{\sigma}=-p\boldsymbol{I}+\mu\left(\nabla\boldsymbol{v}+(\nabla\boldsymbol{v})^T\right) \tag{2}$$

Here, $\boldsymbol{p}$ is pressure, $\boldsymbol{I}$ is 2 rank unit tensor, and μ is dynamic viscosity coefficient, both the Dirichlet and Neuman-type boundary conditions are accounted for, represented as

$$\boldsymbol{v}=\boldsymbol{g}(t) \text{ on } \partial\Omega_1^f \tag{3}$$

$$\boldsymbol{n}\cdot\boldsymbol{\sigma}=\boldsymbol{h}(t) \text{ on } \partial\Omega_2^f \quad ` \tag{4}$$

Where $\partial\Omega_1^f$ denotes the velocity boundary of fluid field, and $\partial\Omega_2^f$ denotes attached boundary, which is just the boundary of the interaction between flow and canopy structure. The initial fluid velocity condition at intake boundary is

$$\boldsymbol{v}(x,0)=\boldsymbol{v}_0 \text{ on } \Omega_0 \tag{5}$$

Here we move the bottom layer elements as the pressure inlet elements, as depicted in figure 2, and the velocity boundary is easily to be imposed and p=0, on the outflow boundary.

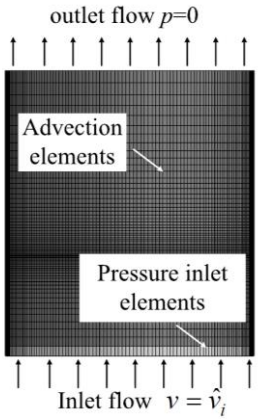

Figure 2: Fluid boundary profile

Solid elements with momentum advection advantage are suitable for solving the N-S equations of fluid, and second order van Leer MUSCL scheme is used to calculate the values of the solution variables in the transport fluxes to achieve second order accurate monotonic results, this algorithm is accurate, stable, conservative, and monotonic. To improve the computation efficiency, we choose the single point integral of ALE multi-material method rather than the total volume integral.

3. Numerical models

Both the structure and fluid domain can be meshed independently. Initially, the parachute is already developed from the package, and constructed in conical profile with simplified fold of each gore in radial direction. The structure meshes were constructed by the canopy and suspension lines and the parachute model were meshed by 2D tetrahedral shell and 1D discrete beam elements (as shown in figure 3).

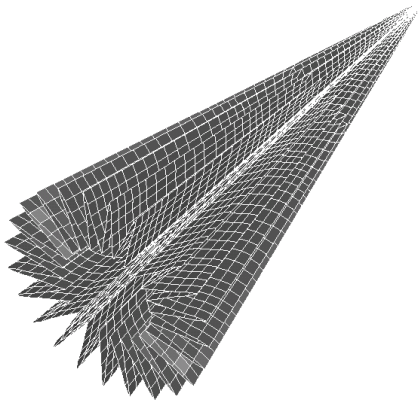

Figure 3: Initially folded canopy mesh

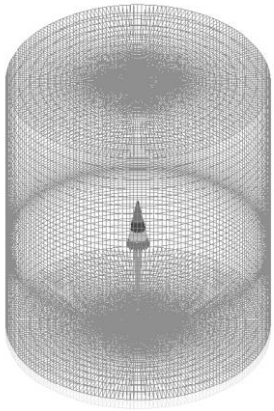

Figure 4: Fluid domain mesh

The fluid was meshed by 3D hexahedron elements (as depicted in figure 4). The statistical information of FE model is illustrated in table 1.

Table 1: Statistic information of parachute system numerical model

	Elements		Materials	Parts
	Types	Numbers		
Canopy	Tetrahedral Shell	14888	*MAT_FABRIC	Part1~6
Fluid	Hexahedral Solid	649440	*MAT_IDEAL_GAS	Part7
Ropes	Discrete Beam	1872	*MAT_CABLE	Part8
Total	666200		3	8

4. Results

The coupled numerical model simulates the FSI performance of finite mass inflation and trajectory motion of a typical slot-parachute that either is used for personnel/cargo or being used in airdrop experiments. Numerical results from a sum of several computation cases with different initial free dropping velocity will be presented and compared to the experimental results.

4.1 Opening process

Parachutes are stochastic systems with large scatter of their performance characteristic, and various parameters can affect the inflating performance of parachute dramatically, and the influence of stochastic wind is not considered in this paper. Figure.5(a)~(f) shows the 3-D deformation of canopy shape from the initial stretched shape at time equal to 0.0 s up to time equal to about 2.0s when canopy fully inflated.

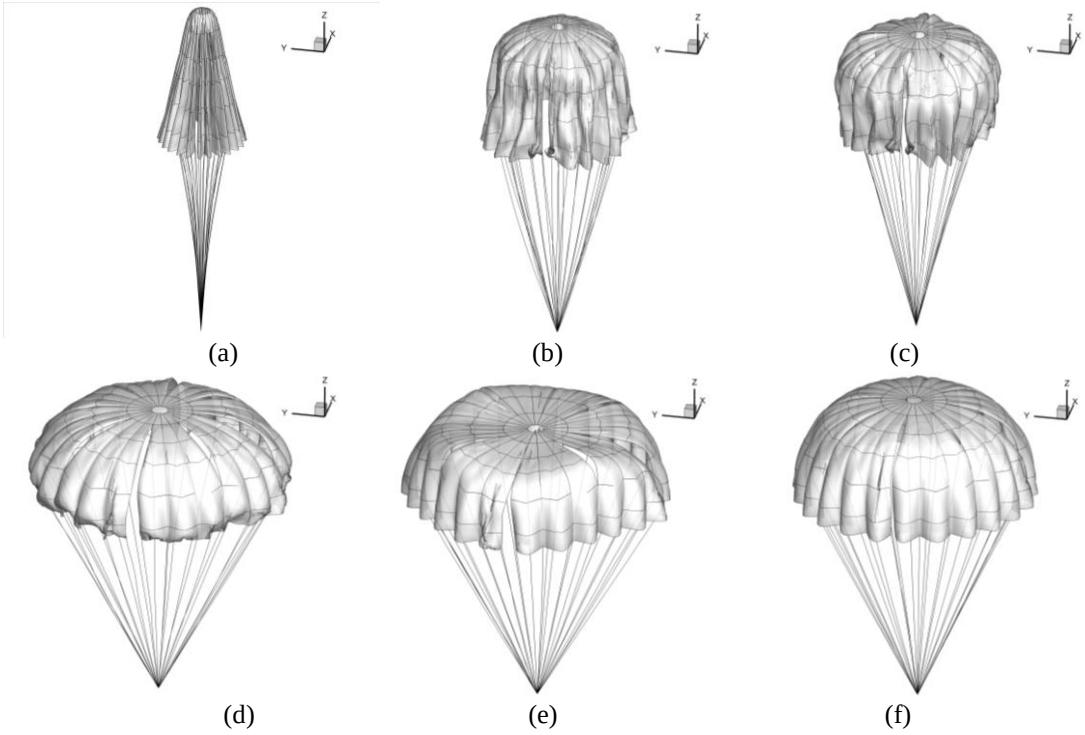

Figure 5: 3-D canopy shape during inflation vs time: (a) 0.18, (b) 0.54, (c) 0.62, (d) 0.95, (e) 1.6, (f) 2.0

4.2 Inflation performance

Figure 6 plots the numerically predicted load acceleration vs time curve and experimental curves from airdrop test. The weight of load is 300 kg, so the peak overload of simulation and experiment is 23.44g and 21.36g, it can be seen from the figures that these two curves are very close considering the approximations used in the model.

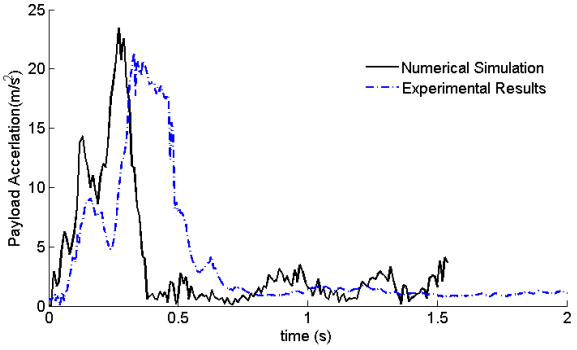

Figure 6: Drag force vs time (numerical and experimental)

The instant velocity when canopy is stretched equal to the initial velocity of opening, figure 7 shows the change of velocity of parachute-load system, the velocities reduced rapidly at the beginning of opening for the high overloads, and then tend to keep steady as the balance between the drag forces and aerodynamic forces on canopy.

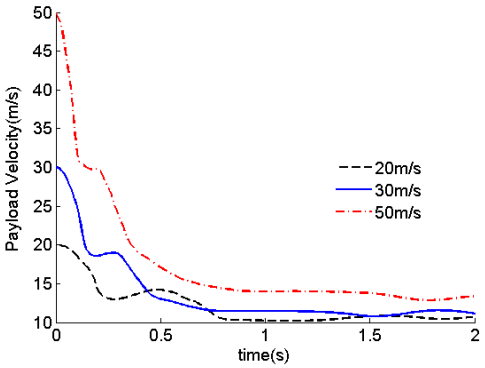

Figure 7: Parachute-load system's velocity comparison vs time

4.3 Fluid-structure interaction

Figure 8 illustrates the details of fluid domain around parachute during inflation process, the FSI model also predicts a phenomenon known as wake recontact. Wake recontact can occur in finite mass openings during or soon after the load has undergone maximum deceleration. The wake trailing the opening canopy is moving close to the speed of the load. As a result, when the load undergoes its maximum deceleration, the wake contacts the apex of the canopy. The recontacting wake results in a negative differential pressure that indents the apex of the canopy. This phenomenon can also be seen in figure 5(e).

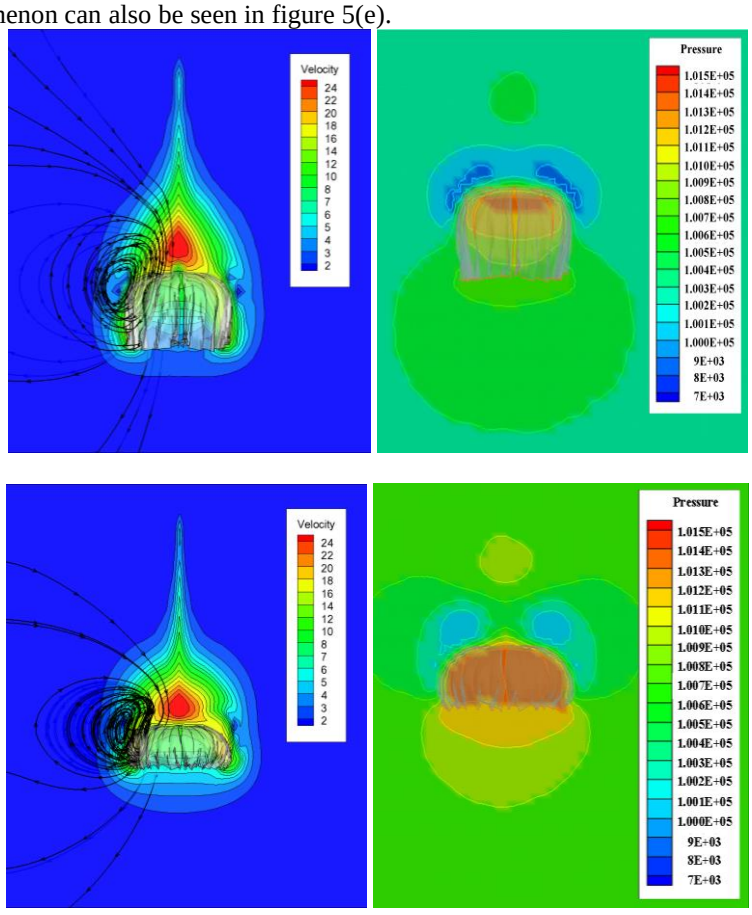

Figure 8: CFD pressure distributions and velocity vectors during opening

The structure response of canopy under the act of aerodynamic pressure can also be seen from fig. 10, from the distribution of von mises stress and equivalent plastic strain on the canopy, we can know that the red area near the top of canopy experience high levels of fabric strength, the central area of each gore also suffer higher tensile than the average level of whole canopy.

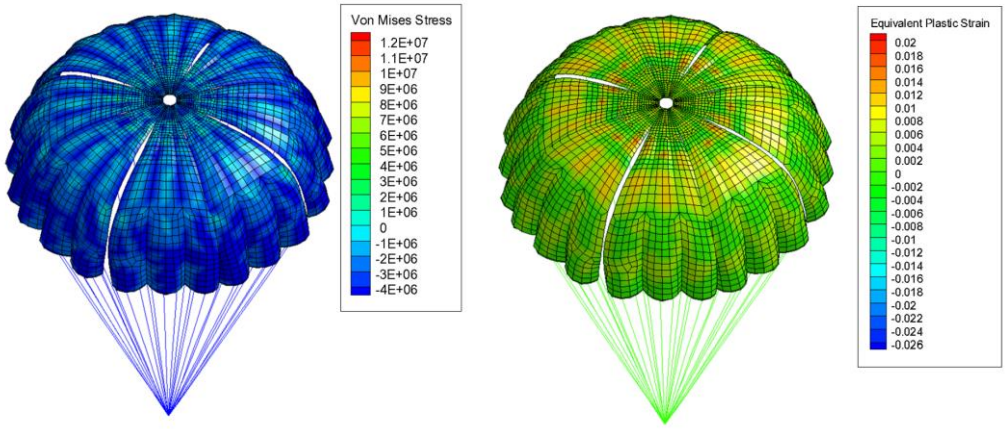

Figure 9: Von mises stress and equivalent plastic strain distributions during opening (left is von mises stress results, right is equivalent plastic strain results)

5. Conclusions

This paper presented a study on FSI phenomenon of parachute during finite mass inflation process in low speed and altitude, the results of the numerical model were compared with experimental results obtained from the airdrop test, and curves from different work conditions of the numerical models were also compared and investigated. The ALE technique is capable of reproducing the FSI phenomenon of parachute during opening process, both the structure dynamics of canopy and fluid field evolvement around parachute were simulated visually and analyzed. The changing rules of canopy's shape and overload were in good agreement with experimental data, which prove the good inflating performance of this kind of slots parachute. As mentioned in Introduction, this numerical approach can be part of integrated simulation system of parachute airdrop, and is now being increasingly applied in parachute research field. Future study should consider much more uncertainties and probability in environmental factors like gust.

Acknowledgements

This study was co-supported by Research Project of Chinese National University of Defense Technology (No. JC13-01-04) and the National Natural Science Foundation of China (Grant No: 51375486). The authors would also like to thank the anonymous reviewers for their critical and constructive review of the manuscript.

References

[1] K.E. French, The initial phase of parachute inflation, in: *2nd AIAA Aerodynamic Deceleration Systems Conference*, 23-25 September 1968, Sunnyvale, Californial, AIAA Paper No. 68-927.

[2] J.M. Macha, A simple, approximate model of parachute inflation, *AIAA Journal*, 18 (1993) 44-53.

[3] D. Wolf, A simplified dynamics model of parachute inflation, in: *4th AIAA Aerodynamics Deceleration Systems Conference*; 21-23 May 1973, Palm Springs, California, AIAA Paper No. 73-451.

[4] H. Johari, K.J. Desabrais, A coupled fluid-structure parachute inflation model, in: *7th AIAA Aerodynamic Decelerator Systems Technology Conference and Seminar*, 19-22 May 2003, Monterey, California, AIAA Paper No. 2003-2146.

Proceedings of the 22nd UK Conference of the
Association for Computational Mechanics in Engineering
2 - 4 April 2014, University of Exeter, Exeter

Higher Resolution Cell-Centred Finite-Volume Schemes on Unstructured Grids for Multi-Phase Flow in a Porous Medium

***Ya-Wei Xie[1], Michael G. Edwards[1], Mayur Pal[2]**

[1]Civil and Computational Engineering Centre, College of Engineering, Swansea University

[2]Maerskoil, Denmark

*717023@swansea.ac.uk

ABSTRACT

A higher resolution unstructured finite-volume method is presented for subsurface reservoir simulation. The flow equations involve an essentially hyperbolic convection equation coupled with an elliptic pressure equation resulting from Darcy's law together with mass conservation. The focus is on the convective flux approximation on unstructured grids, based on Barth-Jespersen and Darwish et al. The governing equations are discretized by a standard cell-centred finite volume scheme in space and by multi-stage Runge-Kutta scheme in time. The numerical flux approximations are of second order Godunov-type, with a flux-limiter for higher resolution with accompanying maximum principle. A comparison of performance between first order and higher resolution methods applied to two phase flow problems in porous medium is presented.

Key Words: *Two-phase flow; unstructured grids; maximum-principle; TVD; positive scheme*

1. Introduction

Key aspects of subsurface reservoir flow simulation include capture of fluid flow fronts and shock fronts which involve steep flow gradients in saturation and concentration. The geometric complexity of many reservoirs requires that the flow equations be approximated on unstructured grids. Standard methods involve use of the single-point upstream weighting (first order upwind) scheme for convection. The first order scheme is highly diffusive and introduces a large amount of numerical diffusion into the solution causing spreading of crucial flow fronts and consequent flow variables. Following the previous work by Michael G. Edwards[4, 5], this work presents the development of higher resolution methods[1, 2, 3, 6, 7, 8] that can reliably compute flow solutions in porous media with steep fronts while ensuring a maximum principle is maintained, so as to prevent spurious oscillations in the solution.

1.1. Governing Equations

The equations governing two phase flow involve:
the pressure equation:

$$-\nabla \cdot (\lambda \mathbf{K} \nabla p) = q \tag{1}$$

where $\lambda, \mathbf{K}, \nabla p$ are the mobility, permeability and pressure gradient respectively and the saturation equation:

$$\phi \frac{\partial s}{\partial t} + \nabla \cdot f_w(s) \vec{u}_T = q_w \tag{2}$$

where s and $f_w(s)$ are the aqueous saturation and fractional flow, and $\vec{u}_T = -\mathbf{K}\lambda\nabla p$ is the total velocity and ϕ is porosity.

2. Description of The Unstructured Solver

2.1. Positive Scheme for Hyperbolic Equation

Lemma 1: A positivity criterion
The semi-discrete approximation of equation (2)*, with U_i representing discrete saturation at node i, is expressed in the form*:

$$\frac{dU_i}{dt} = L(U) = b_i U_i + \sum_{j \neq i} b_j U_j \,, \tag{3}$$

where all the b_j, $j \neq i$, are non-negative and $b_i \in \mathbb{R}$. Then the corresponding explicit first-order scheme preserves positivity under an appropriate CFL-like condition.

The first-order positive scheme for the i^{th} cell is written in the form

$$a_i \frac{dU_i}{dt} = - \sum_{j \in V(i)} (\vec{V}_{ij} \cdot \vec{\eta}_{ij})^+ U_i - \sum_{j \in V(i)} (\vec{V}_{ij} \cdot \vec{\eta}_{ij})^- U_j \tag{4}$$

where a_i is the i^{th} cell area, U_i the conservative variable, $\vec{V}_{ij}$ is the j^{th} cell face flux and the superfixes denote the local upwind sign dependent coefficients.

Lemma 2 The upwind scheme (4) is positive under the CFL condition:

$$\frac{\Delta t}{a_i} \sum_{j \in V(i)} (\vec{V}_{ij} \cdot \vec{\eta}_{ij})^+ \leq 1 \tag{5}$$

The formulation of the limited higher resolution scheme is given by

$$a_i \frac{dU_i}{dt} = - \sum_{j \in V(i)} (\vec{V}_{ij} \cdot \vec{\eta}_{ij})^+ (U_i + \frac{1}{2} L_{ij}(U)) - \sum_{j \in V(i)} (\vec{V}_{ij} \cdot \vec{\eta}_{ij})^- (U_j + \frac{1}{2} L_{ji}(U)) \tag{6}$$

where $L_{ij}(U), L_{ji}(U)$ are the respective slope-limited gradients used for higher order reconstruction at edge j of cell i and edge i of cell j respectively.
Two types of limiter are considered below.

2.2. The Barth-Jespersen Scheme

Here we review the Barth-Jespersen scheme[7]. The gradient ∇U_i is computed via least squares of local subtriangle gradients. The limiter proposed by Barth and Jespersen is designed to make sure the reconstructed values (e.g. $U_{ij} = U_i + \frac{1}{2} L_{ij}(U)$) satisfy:

A: The reconstruction must not decrease below the minimum or exceed the maximum of the neighbouring cell averages;

B: The difference in the interpolated values at the i-th edge and the difference in the corresponding cell-averages should have the same sign.

Barth-Jespersen Limiter:

$$\Phi_j = \begin{cases} min(1.0, \frac{M_i - U_i}{U_{ij} - U_i}), U_{ij} > U_i \\ min(1.0, \frac{m_i - U_i}{U_{ij} - U_i}), U_{ij} < U_i \\ 1.0, \ otherwise \end{cases} \tag{7}$$

where

$$m_i = min_{j \in N_i} U_j, M_i = max_{j \in N_i} U_j,$$

N_i is the set of direct neighbours of cell i, $\Phi_i = min_{j \in N_i}[\Phi_j]$.

And then the modified slope $L_{ij}(U) = \Phi_i \Delta x_{ij} \cdot \nabla U_i$.

To satisfy the property B, an edge-by-edge check is performed on the reconstructed values. If condition B is violated, the reconstructed values will be substituted by the cell-average constants. However the best results are obtained without property B which causes some spreading of the solution.

2.3. The TVD Scheme

Implementation of a TVD based method on an unstructured grid requires the definition of a virtual upwind node. Based on the work of *A. Jameson*[1] and *Darwish et al.*[2], the information in the upwind direction depends either on the extrapolations or interpolations of values on neighbouring cells and the cell geometry. Here we extend the TVD based scheme directly to a cell-centred finite volume method on unstructured grids by interpolation of the known data.

See figure 1 as examples of the grids, the local formulation for the reconstruction $U_f = U_C + \frac{1}{2}L_f(U)$.

$$\begin{aligned} L_f(U) &= \Phi(r_f)\Delta U_f \\ r_f &= \frac{U_C - U_U}{U_D - U_C} = \frac{2\nabla U_C \cdot r_{CD}}{\Delta U_f} - 1 \\ \Delta U_f &= U_D - U_C \end{aligned} \tag{8}$$

where $\Phi(r_f)$ is any known slope or flux limiter, which can be described by Sweby diagram.

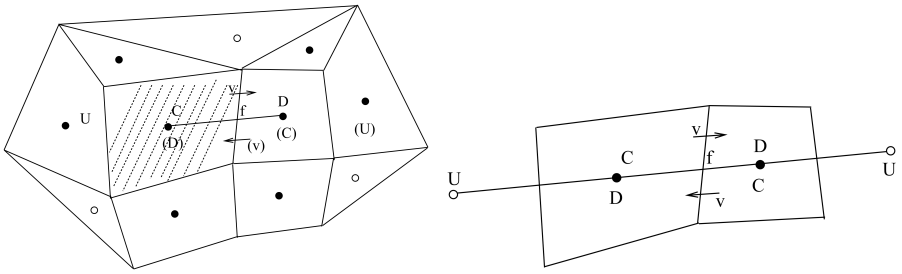

Figure 1: Left: stencils for flux limiting in unstructured mesh; Right: advection node notation in unstructured mesh

3. Results

Due to space limitation only one case is presented, which involves quarter five spot flow. A triangle mesh with union-jack type pattern is used and $CFL = 0.2$.

Test Case : Quarter-five spot
Initial conditions:
saturation:

$$S_0(\vec{x}) = S_{wc} = 0.001, \vec{x} \in [0,2] \times [0,2], \tag{9}$$

permeability has a unit matrix.
Boundary conditions:
An injection well(bottom LHS), where flow rate and saturation are specified, with $q = 100$, $s = 1$, and at the production well (top RHS), pressure is specified as $p = 0$.
For the saturation equation, ghost cells are used with reflected values. Neumann conditions are imposed for pressure with zero normal flow on the solid walls, output time 0.5.
The results for linear and nonlinear fluxes are shown in Figure 2.

4. Conclusions

We have presented an unstructured cell-centred finite-volume framework for higher resolution methods for porous media flow computation. Our current results indicate that the Barth-Jesperson (BJ) method yields higher resolution results with significant improvement in front and shock resolution compared to the standard first order method. Further formulations are being investigated. A Darwish based method is also included however BJ proves to be the most robust to date.

Acknowledgements

We thank Shell for funding this project and Dr's Sadok Lamine and Bastiaan Huisman of Shell for helpful discussions. We thank Raheel Ahmed of C2EC, Swansea University for the Pressure equation solver.

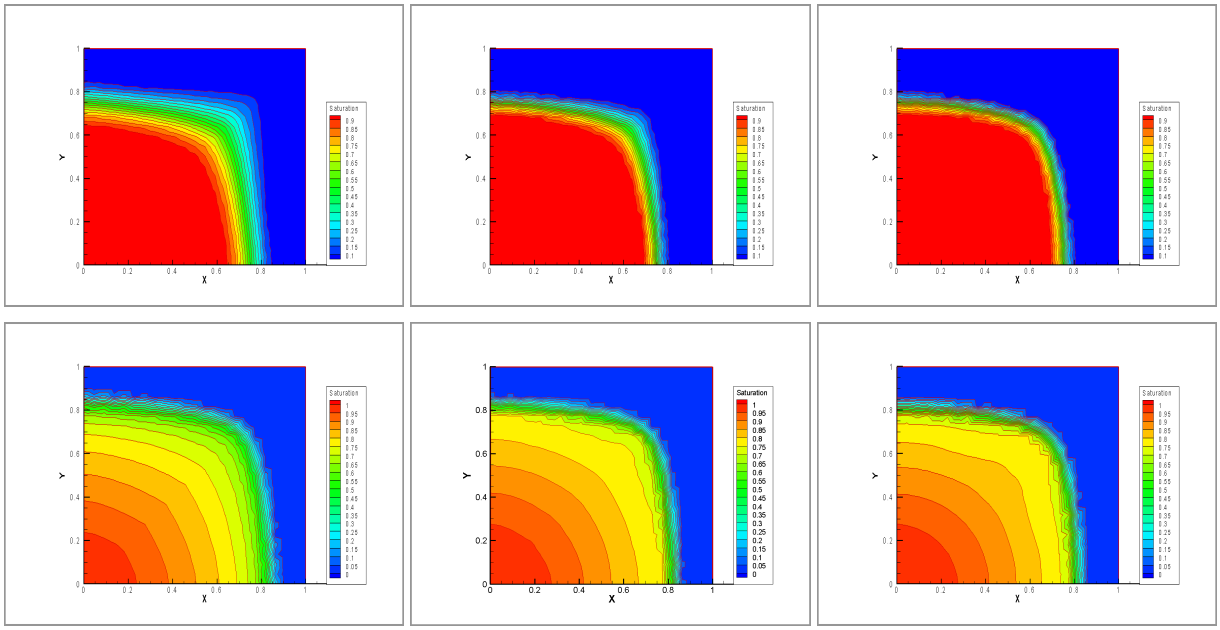

Figure 2: : upper case: linear; bottom case: nonlinear case; left: first order; centre: Darwish scheme(minmod) + RK3; right: BJ scheme + RK3

References

[1] A. Jameson. Artificial diffusion, upwind biasing, limiters and their effect on accuracy and multigrid convergence in transonic and hyperbolic flows, AIAA paper 3359, 1993.

[2] Darwish et al. TVD schemes for unstructured grids, International Journal of Heat and Mass Transfer, 46, 599-611, 2003.

[3] M. E. Hubbard. Multidimensional slope limiters for MUSCL-type finite volume schemes, Numerical Analysis Report 2/98, Department of Mathematics, University of Reading, Reading, UK, 1998.

[4] Michael G. Edwards. A higher-order Godunov scheme coupled with dynamic local grid refinement for flow in a porous medium, Computer methods in applied mechanics and engineering, 131, 287-308, 1996.

[5] Michael G. Edwards. Higher-resolution hyperbolic-coupled-elliptic flux-continuous CVD schemes on structured and unstructured grids in 2-D, International Journal for Numerical Methods in Fluids, 51, 1059-1077, 2006.

[6] Randall. J. Leveque. Finite-Volume Methods for Hyperbolic Problems, cambridge university press, 2004.

[7] T. Barth, D.C. Jespersen. The design and application of upwind schemes on unstructured meshes, AIAA paper 89-0366, 1989.

[8] X. D. Liu. A maximum principle satisfying modification of triangle based adaptive stencils for the solution of scalar hyperbolic conservation laws, SIAM Journal Numerical Analysis, 701-716, 30, 1993.

Proceedings of the 22nd UK Conference of the
Association for Computational Mechanics in Engineering
2 - 4 April 2014, University of Exeter, Exeter

Modelling of Micro-scale Droplets Subject to Surface Acoustic Waves

***Ross J.D. Mackenzie[1], Julien Reboud[1], Łukasz Kaczmarczyk[1] and Chris J. Pearce[1]**

[1]School of Engineering, University of Glasgow, Oakfield Avenue, Glasgow, G12 8LT

*r.mackenzie.2@research.gla.ac.uk

ABSTRACT

Surface acoustic wave devices are being used in more and more areas, especially within the food and medical industries. Prototypes of such devices are expensive and time consuming to produce but are a necessary requirement for physical testing. However, the need for physical prototypes can be reduced through the use of a computational framework developed for the prediction of micro-scale fluid droplets subject to surface acoustic waves. This paper continues the work already undertaken by the authors by predicting the period of oscillation, and experimenting with different forms of excitation to reproduce data from the laboratory.

Key Words: *surface acoustic waves; surface tension; Updated Arbitrary Lagrangian Eulerian formulation*

1. Introduction

This paper presents a computational framework for modelling fluid droplets, including surface tension, using an Updated Arbitrary Lagrangian Eulerian (UALE) formulation. This approach permits accurate tracking of the fluid surface and reduces the need for remeshing, compared to traditional approaches. The paper specifically builds on the work presented by the authors in [1]. The governing equations are based upon an axisymmetric *weak form* of the Navier-Stokes equations for incompressible Newtonian fluids. Additional contributions from the surface tension force and contact line force are assembled into the force vector and stiffness matrix, following the work of Saksono and Perić [2]. These additional contributions arise from the Laplace-Young equation and thus are directly related to the curvature of the fluid-air interface. The use of equal order interpolation functions for pressures and velocities leads to oscillations in the pressure field. These oscillations are overcome by the use of the pressure Laplacian stabilisation (PLS) technique proposed by Oñate et al. [3]. This technique leads to a pressure Laplacian term as seen in many other stabilisation techniques, and, in addition, a boundary term calculated over the boundary of the fluid domain only. The resulting computational framework showed a good correlation to analytical solutions for problems involving the prediction of the equilibrium shape of sessile droplets subject to gravity alone.
Laplacian mesh smoothing and a simple mesh refinement algorithm is replaced by the approach described in [4], and the results of this are discussed.
Further work has been undertaken to predict the period of oscillation of droplets floating in zero-gravity and experimentation with different forms of excitation to reproduce laboratory results of droplet attenuation via surface acoustic waves.

2. Dynamic Analysis of Floating Droplets

Of the examples examined in [1], only the equilibrium shape was determined as dynamic oscillations were removed via artificially increasing the fluid viscosity. However, if the computational framework is to be successful, it must also be able to examine problems involving oscillations. The work of Rayleigh [5], calculated an analytical period of oscillation for water droplets floating in zero-gravity, assuming no viscous effects and small amplitude oscillations. Following [5], the calculated analytical period for the first three modes ($n = 2, 3, 4$) with an unperturbed spherical radius $R = 0.0125cm$ and amplitude

$A = 0.2R$, giving an approximate volume of $8.3nL$, are $T = 3.63 \times 10^{-4} sec$, $T = 1.87 \times 10^{-4} sec$, and $T = 1.21 \times 10^{-4} sec$ respectively. In zero-gravity environments, droplets will conform to near perfect spheres as this is the shape with the smallest surface area. The surface area is minimised to reduce the out-of-balance forces due to surface tension. In 2D, droplets will conform to near perfect circles, therefore, the initial non-equilibrium geometry of each droplet provides the potential energy. A FE mesh is created consisting of 580 nodes and 1067 triangular elements for each mode of oscillation; the geometric centre of each droplet is fixed. The parameters listed in Table 1, water at 20°C, are used in each case.

Table 1: Parameters for analysis of floating droplets

Parameter	Value	Parameter	Value
Fluid viscosity, μ	$1.01 \times 10^{-2} dyne \cdot s/cm^2$	Stabilisation, β	1.0
Fluid density, ρ	$0.998 g/cm^3$	Mesh viscosity, μ_{mesh}	$1 \times 10^{-3} dyne \cdot s/cm^2$
Surface tension, γ	73dyne/cm	Time step, Δt	$1 \times 10^{-7} sec$

A point on the surface of each droplet is traced in time and the computed period, as shown in Figure 1(a) for the first three modes of oscillation are $T = 3.74 \times 10^{-4} sec$, $T = 1.92 \times 10^{-4} sec$, and $T = 1.23 \times 10^{-4} sec$ respectively. The computed period of oscillation is slightly larger than the analytical, with a difference of less than 3% in each case. This difference can be attributed to the fact that Rayleigh neglects viscous effects and assumes small amplitude oscillations, whereas the computational framework includes viscous effects and assumes large deformations. For the droplets under investigation, the computational framework out-performs the computational model based upon a purely Lagrangian mesh developed by Saksono and Perić [6]. Figure 1(b) depicts the geometric evolution for the fourth mode.

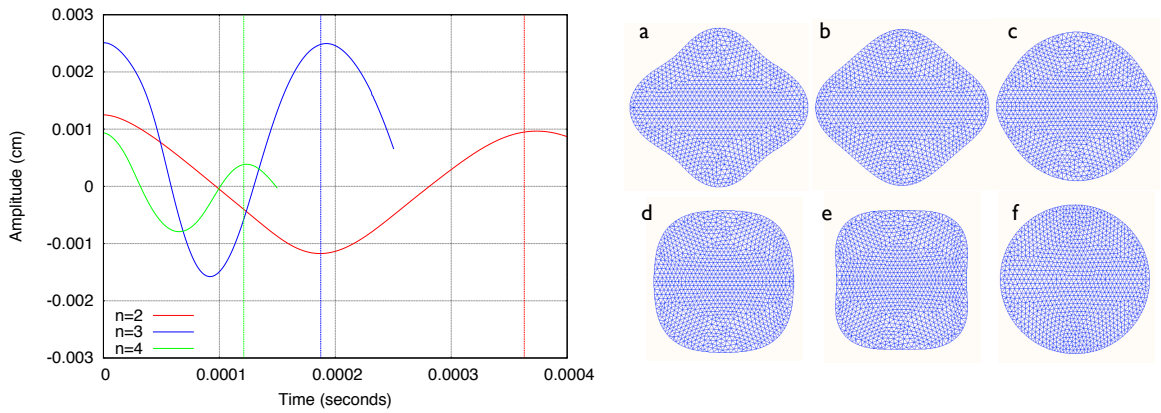

(a) Comparison of computed and analytical period of oscillation for the first three modes

(b) Droplet oscillations for fourth mode at various time instants: (a) $t = 0$, (b) $t = T/8$, (c) $t = T/4$, (d) $t = 3T/8$, (e) $t = T/2$, (f) $t = \infty$

Figure 1: Geometric evolution and calculated period

3. Mesh Optimisation

Laplacian smoothing works from the premise that a high quality mesh is uniform and has nodes separated by equal distances. However, the opposite is not true, a good mesh need not have equidistant nodes. Due to this premise, Laplacian smoothing induces excessive and unnecessary nodal displacements in mesh initially deemed good. Every nodal displacement produces non-linearities which have negative effects on the rate of convergence and the efficiency of the solution. The form of Laplacian smoothing adopted utilises a mesh viscosity parameter; poor choice of this parameter can cause severe mesh distortion, see Figure 2. Additionally, although somewhat effective in 2D, Laplacian smoothing is not effective in 3D and causes mesh shrinkage after repeated iterations. With this in mind, an alternative mesh improvement approach that is driven by a quality measure q is proposed that uses a log-barrier as an objective function and expresses every angle ϕ as a function of the worst angle φ in the solution space.

$$q = \frac{\sin^2(\phi)}{2(1-\varphi)} - \log(\sin(\phi - \varphi)) \tag{1}$$

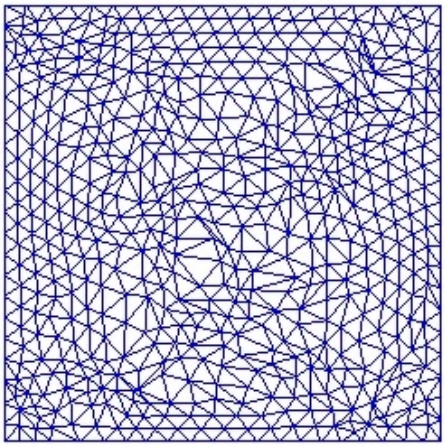

Figure 2: Poor choice of mesh viscosity parameter when using Laplacian smoothing

Several examples have been undertaken to compare the outcomes using Laplacian smoothing and the new mesh improvement approach. Whilst there are fewer mesh-related problems using the new mesh improvement approach, simulations using this alternative method have taken much longer to complete. However, with the current aim to extend the framework from axisymmetric to 3D, and therefore changing from triangular elements to tetrahedral elements, the new mesh improvement approach will provide much better quality results than Laplacian smoothing.

4. External Excitation

Collaborating with the Bioelectronics Group at the University of Glasgow, the computational framework is used to predict the response of a 10μL water droplet with a 65° contact angle sitting on a vibrating speaker oscillating at 100Hz. A velocity is applied to the nodes on the base of the droplet to replicate the vibrating speaker. This velocity is calculated from the measured displacement of a point marked on the speaker in the laboratory. Results from the computational framework show good correlation to the high-speed video data, with the form of oscillation and the amplitude of oscillation approximately equal, see Figure 3(a) where the modelled droplet geometry is overlaid with the geometry as seen in the laboratory. Whilst the motions are not the same initially, due to a difference in momentum, the modelled droplet very quickly oscillates in phase, and with the same amplitude, as seen in the laboratory.
An alternative approach to this problem examined a time-dependent contact angle of the form in Equation 2:

$$\Delta\alpha = \alpha_0 + A\sin(\omega t) \tag{2}$$

Using amplitude $A = 25$, frequency $\omega = 1000Hz$ and initial contact angle $\alpha_0 = 65°$, produces the response as shown in Figure 3(b). Whilst this response is very different from that seen in the laboratory, very interesting behaviour occurs in the form of violent oscillations followed by ejection of material from the main droplet. The two ejected droplets are near-perfect circles in shape and are ejected at speeds in excess of 3.5m/s.

5. Conclusions

The computational framework successfully predicts both the equilibrium geometry and period of oscillations of sessile droplets and floating droplets, giving confidence in the model to move toward more complex behaviour.
An alternative mesh optimisation method has been examined and whilst results are somewhat improved, computational time is vastly increased, However, when the framework is extended to 3D, the Laplacian smoothing will be ineffective and the new quality measure will be utilised.
Replicating a water droplet on a speaker produced good results in terms of the form and amplitude of oscillation.

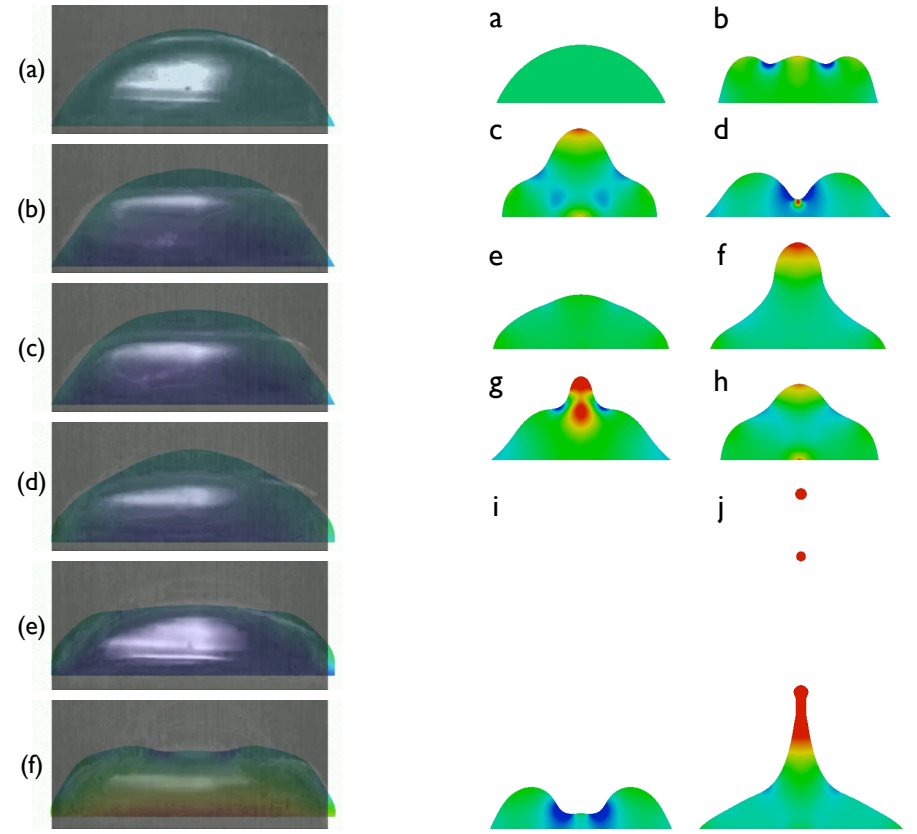

(a) Response of droplet with excitation of base superimposed onto video from laboratory

(b) Response of droplet with time-dependent contact angle

Figure 3: Response of droplets subject to different forms of excitation

Acknowledgements

The support of the Engineering and Physical Sciences Research Council (EPSRC) through grant DTA EP/P50418X/1 is gratefully acknowledged and appreciated.

References

[1] R.J.D. Mackenzie, Ł. Kaczmarczyk and C.J. Pearce. An axisymmetric pressure stabilised predictive model of surface tension in micro-fluids, in: *21st UK Conference on Computational Mechanics (ACME-UK)*, 2013.

[2] P.H. Saksono and D. Perić. On Finite Element Modelling of Surface Tension: Variational Formulation and Applications Part I: Quasistatic Problems. *Computational Mechanics* 38 (3) 265-281, 2005.

[3] E. Oñate, S.R. Idelsohn and C.A. Felippa. Consistent pressure Laplacian stabilization for incompressible continua via higher-order finite calculus. *International Journal for Numerical Methods in Engineering*, 87 (1-5):171-195, 2011.

[4] A.Kelly, Ł. Kaczmarczyk and C.J. Pearce. ALE Mesh Updating using Mesh Optimisation. *Proceedings of the 22nd International Meshing Roundtable* (2013).

[5] L. Rayleigh. On the Capillary Phenomena of Jets. *Proceedings of the Royal Society of London*, 29(196-199):71-91, (1879).

[6] P.H. Saksono and D. Perić. On Finite Element Modelling of Surface Tension: Variational Formulation and Applications Part II: Dynamic Problems. *Computational Mechanics* 38 (3) 251-263, 2005.

Proceedings of the 22nd UK Conference of the
Association for Computational Mechanics in Engineering
2 - 4 April 2014, University of Exeter, Exeter

Multi-dimensional models of the interior of stars

***J. Pratt[1], M. Viallet[2], I. Baraffe[1],C. Geroux[1], T. Goffrey[1], M.V. Popov[3], D. Folini[3], R. Walder[3]**

[1]College of Engineering, Mathematics and Physical Sciences, University of Exeter, Exeter, EX4 4QL, UK
[2]Max-Planck Institut für Astrophysik, Karl-Schwarzschild-Strasse 1, 85748 Garching, Germany
[3]Center of Research in Astrophysique, ENS-Lyon, 69364 Lyon, Cedex 07, France

Correspondence: *j.l.pratt@exeter.ac.uk

ABSTRACT

Current physical understanding of the evolution of stellar interiors is drawn from one-dimensional calculations. In these simulations, nonlinear anisotropic processes like turbulent convection, shear, rotation, and MHD are modeled using simple phenomenological approaches. In order to understand the high quality data produced from recent space-missions like CoRoT, Kepler, and GAIA, it is necessary to develop multi-dimensional hydrodynamical simulations. We describe the three dimensional, time implicit, fully compressible, hydrodynamical code `MUSIC`, developed to address early stages of the evolution of stellar interiors in unprecedented detail. `MUSIC` solves the hydrodynamical equations in a spherical geometry using a finite volume method. We present early results of turbulent convective flows.

Key Words: *implicit time integration: finite volume methods: turbulence simulation: convection: compressible hydrodynamics*

1. Introduction

The evolution of stellar interiors is characterized by three dimensional nonlinear processes that develop over a wide range of temporal and spatial scales. The MUlti-dimensional Stellar Implicit Code (`MUSIC`), currently under development as part of the ERC project TOFU, will provide a detailed picture of long-term stellar development. This project is intended to fill the gap between sophisticated stellar formation simulations that examine short periods of time and simple one-dimensional calculations that follow the complete stellar evolution process.

The European Space Agencies' current missions CoRoT[1] and GAIA[2] monitor stellar motion and will produce massive amounts of stellar seismology data over the next few years. The NASA mission Kepler[3] will produce similar data targeted to stars in our galaxy. Each of these observational programs accumulates data on stellar pulsation by closely observing the changing brightness of many stars. Pulsation frequency depends on the internal sound-speed, density structure, rotational profile, and magnetic field structure of a star. The amplitude and phase of stellar pulsation are directly impacted by turbulent convection in the stellar interior. Turbulent convection underlies the fundamental processes of heat transport, mixing, rotation, shear, and the stellar dynamo.

2. Simulation

Turbulent convection is typically modeled using one of three approaches: the Boussinesq hydrodynamic equations[4], the anelastic hydrodynamic equations[5], or the compressible hydrodynamic equations[6]. The Boussinesq approximation neglects differences in density except in the buoyancy force and equation of state. This is an accurate approximation for convection when the extent of the simulation volume is much less than the density and pressure scale heights. Realistically, Boussinesq simulations can be performed either to examine large physical domains where the pressure and density do not change dramatically: the ocean, planetary cores or mantles [7, 8], atmospheres [9], or in the cores of massive stars.

Boussinesq simulations are often also performed to examine a small part of the convection zone of a star[10, 11].

Because density typically varies by several orders of magnitude in a star, the Boussinesq approximation cannot accurately treat the expansion of fluid convecting through the whole star; either an anelastic or a compressible model is needed. The anelastic approximation assumes that the stellar flows remain subsonic, but a compressible simulation makes no such assumptions[12]. Because our ultimate goal is to study a wide range of Mach number scales $10^{-8} \lesssim M \lesssim 1$, and to simulate a whole star, `MUSIC` has been developed as a compressible hydrodynamic simulation. `MUSIC` can operate as an implicit large eddy simulation to study a large section of a star, or as a direct numerical simulation to study a small portion of a star.

In its current form, the `MUSIC` simulation evolves the inviscid compressible hydrodynamic equations for density ρ, momentum $\rho\boldsymbol{u}$, and internal energy ρe:

$$\frac{\partial}{\partial t}\rho = -\nabla \cdot (\rho \boldsymbol{u}) \tag{1}$$

$$\frac{\partial}{\partial t}\rho\boldsymbol{u} = -\nabla \cdot (\rho \boldsymbol{u}\boldsymbol{u}) - \nabla p + \rho \boldsymbol{g} \tag{2}$$

$$\frac{\partial}{\partial t}\rho e = -\nabla \cdot (\rho e \boldsymbol{u}) + p \cdot \boldsymbol{u} + \nabla \cdot (\chi \nabla T). \tag{3}$$

Here $\boldsymbol{g}$ is the gravitational acceleration vector. The thermal conductivity $\chi = 16\sigma T^3/3\kappa\rho$ is defined using the Stefan-Bolzmann constant σ and the Rossland mean opacity κ. At high temperature, opacity is interpolated from the OPAL tables [13]; at low temperature opacity is calculated from the tables of Ferguson *et al.* [14]. The compressible hydrodynamic equations (1-3) are closed by determining the gas pressure $p(\rho, e)$ and temperature $T(\rho, e)$ from a tabulated equation-of-state appropriate for a mixture of hydrogen, helium and solar metallicity. These tables were calculated by solving the Saha equation and taking into account partial ionization of atomic species. Because an initial state for `MUSIC` is extracted from one-dimensional data, the equation of state used is identical for the one-dimensional stellar evolution code.

The compressible hydrodynamic equations (1-3) are solved in a spherical wedge. In our current simulations, this wedge covers 80% of the stellar radius, excluding only the stellar core. `MUSIC` uses spherical coordinates: radius r, colatitude θ, and longitude ϕ. To enable direct comparison between two and three dimensional flows, `MUSIC` also includes the possibility of performing two dimensional calculations on a wedge where symmetry in ϕ is assumed. Two and three dimensional simulations can be performed on the same initial state of a star.

The equations are discretized on a staggered grid, using a finite volume approach. Physical quantities are interpolated to the grid using an upwind limited interpolation similar to the monotone upwind schemes for conservation laws (MUSCL) method [15].

2.1. Implicit time integration

Our objective is to study processes in stellar evolution that develop on scales much longer than the dynamical time-scale. To allow time steps larger than the Courant-Friedrich-Lewy (CFL) limit permits in time-explicit methods, time integration in `MUSIC` is implicit. Obtaining convergence of an implicit scheme can be delicate and computationally demanding. In `MUSIC`, the system of equations is discretized with the Crank-Nicholson scheme.

To solve the compressible hydrodynamic equations we standardly use an inexact Newton method. We solve the linearized system for the Newton direction, and apply each new direction iteratively until a specified error tolerance is reached. We use an algebraic preconditioner, typically an ILU preconditioner [16], to speed up the convergence of this scheme.

The inexact Newton solver with an algebraic preconditioner calculates and stores an approximate Jacobian. A low-storage alternative is the Jacobian free Newton Krylov (JFNK) solver [17] that has recently been implemented in the `MUSIC` framework. Instead of storing a Jacobian, JFNK methods use matrix vector products that can be estimated efficiently with finite difference methods. Our JFNK solver uses a physics-based preconditioner [18] designed to target precisely the physical processes that cause the

system to become stiff. By using a semi-implicit solution as a preconditioner a JFNK method can be designed to converge for a large range of CFL numbers. A basic preliminary comparison [19] of iterative solvers against direct solvers using MUMPS[20] has been performed. A thorough study of the results of the Jacobian free Newton Krylov solver is underway in MUSIC, and will be discussed in this contribution.

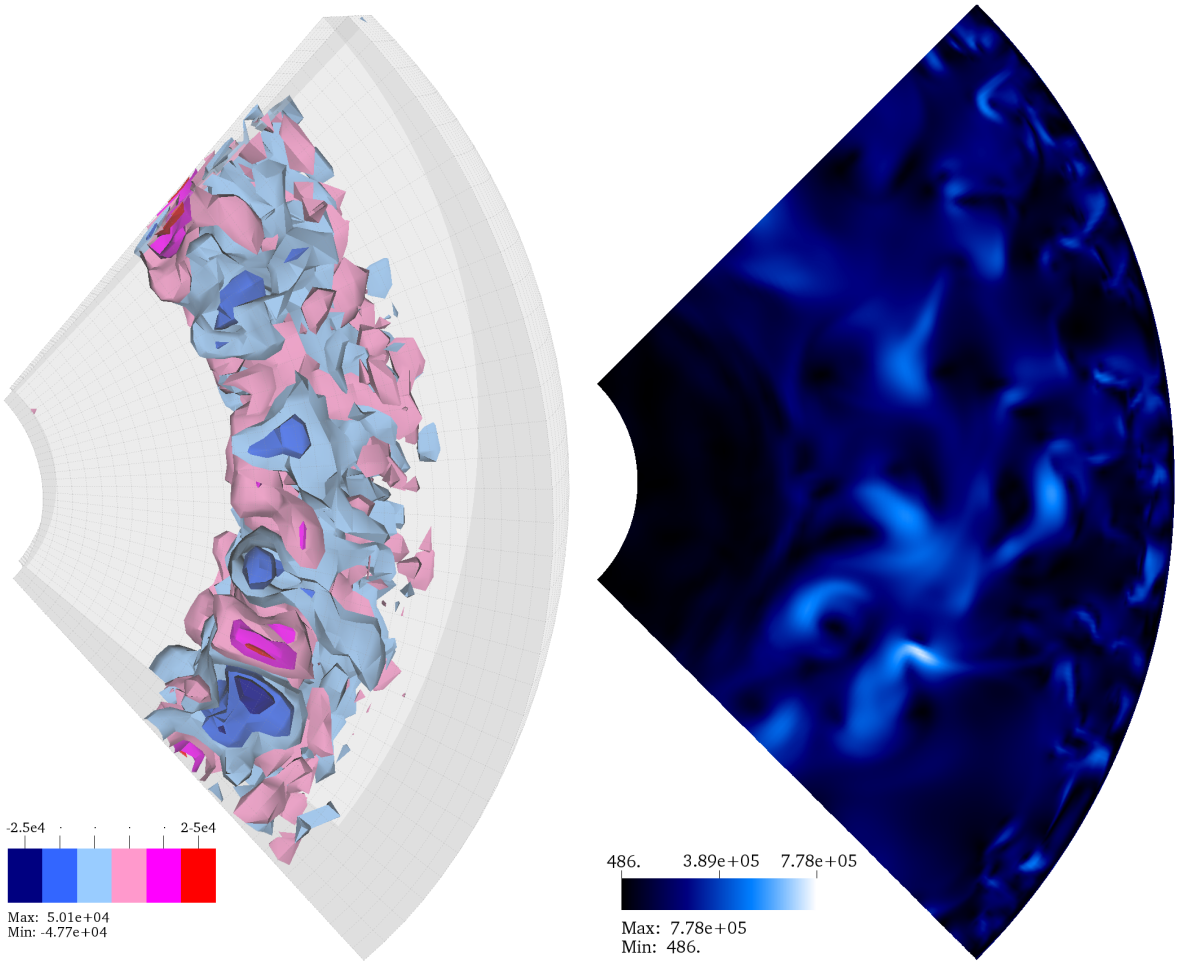

Figure 1: (Left) contours of radial velocity (cm/s) during developing convection in a low resolution 3D young sun calculated using a JFNK solver. (Right) a snapshot of velocity magnitude during steady-state turbulent convection in a 2D young sun calculated using an ILU preconditioner.

2.2. *Boundary conditions*

We impose periodicity on the boundary conditions in θ and ϕ. Radial boundaries require more sophisticated treatment, and several possibilities have been implemented in MUSIC. Because the choice of boundary conditions can dramatically affect the physical outcome of the simulation, we work towards more realistic surface boundary conditions. Currently the radial boundary can be (1) non-penetrative, $u_r = 0$ (2) stress-free, $\frac{\partial}{\partial r}(u_r/r) = 0$ (3) constant energy flux (4) energy flux set to the black-body radiation of the Stefan-Boltzmann law, σT^4, where T is the temperature and σ is the Stefan-Boltzmann constant. Boundary condition (4) makes sense only at the surface of the star.

3. Results

At an early stage in its evolution the interior of the sun was fully convective from the central regions to the surface, making it an ideal setting to study large-scale, strong convection. This large convection zone is shown in Figure 1 for a sun a few million years in age. Understanding convective overshooting [21], turbulent mixing, and dynamo action are the ultimate goals for our study of turbulent convection in the young sun. In this contribution we present the first steps in this work. We evaluate how successfully MUSIC captures large-scale compressible phenomena like the expansion and contraction of convecting fluid.

Acknowledgements

The research leading to these results has received funding from the European Research Council under the European Unions Seventh Framework (FP7/2007-2013)/ERC grant agreement no. 320478. Simulations were performed on the SGI Altix ICE 8200 cluster ZEN at the University of Exeter and the DiRAC Complexity machine, jointly funded by STFC and the Large Facilities Capital Fund of BIS.

References

[1] E. Guggenberger, *et al.*, The CoRoT star 105288363: strong cycle-to-cycle changes of the Blazhko modulation, MNRAS 415 (2) (2011) 1577–1589.

[2] J. de Bruijne, Science performance of GAIA, ESAs space-astrometry mission, Astrophys Space Sci 341 (1) (2012) 31–41.

[3] W. J. Chaplin, *et al.*, Ensemble asteroseismology of solar-type stars with the NASA kepler mission, Science 332 (6026) (2011) 213–216.

[4] F. Busse, Non-linear properties of thermal convection, Rep. Prog. Phys. 41 (12) (1978) 1929.

[5] C. Jones, P. Boronski, A. Brun, G. Glatzmaier, T. Gastine, M. Miesch, J. Wicht, Anelastic convection-driven dynamo benchmarks, Icarus 216 (1) (2011) 120–135.

[6] N. H. Brummell, S. M. Tobias, F. Cattaneo, Dynamo efficiency in compressible convective dynamos with and without penetration, Geophys. Astrophys. Fluid Dyn. 104 (5-6) (2010) 565–576.

[7] A. Anufriev, C. Jones, A. Soward, The Boussinesq and anelastic liquid approximations for convection in the earths core, Phys. Earth Planet. Inter. 152 (3) (2005) 163–190.

[8] U. Hansen, D. Yuen, Extended-Boussinesq thermal–chemical convection with moving heat sources and variable viscosity, Earth Planet. Sc. Lett. 176 (3) (2000) 401–411.

[9] F. Busse, A simple model of convection in the Jovian atmosphere, Icarus 29 (2) (1976) 255–260.

[10] F. Busse, Differential rotation in stellar convection zones, ApJ 159 (1970) 629.

[11] J. Pratt, A. Busse, W.-C. Müller, Fluctuation dynamo amplified by intermittent shear bursts in convectively driven magnetohydrodynamic turbulence, A&A 557 (2013) 76.

[12] G. Glatzmaier, Introduction to Modeling Convection in Planets and Stars: Magnetic Field, Density Stratification, Rotation, Princeton University Press, 2014.

[13] C. A. Iglesias, F. J. Rogers, Updated OPAL opacities, ApJ 464 (1996) 943.

[14] J. W. Ferguson, *et al.*, Low-temperature opacities, ApJ 623 (1) (2005) 585.

[15] B. Thornber, A. Mosedale, D. Drikakis, D. Youngs, R. Williams, An improved reconstruction method for compressible flows with low mach number features, J. Comput. Phys. 227 (10) (2008) 4873–4894.

[16] Y. Saad, ILUM: a multi-elimination ILU preconditioner for general sparse matrices, SIAM J. Sci. Comput. 17 (4) (1996) 830–847.

[17] D. A. Knoll, D. E. Keyes, Jacobian-free Newton–Krylov methods: a survey of approaches and applications, J. Comput. Phys. 193 (2) (2004) 357–397.

[18] H. Park, R. R. Nourgaliev, R. C. Martineau, D. A. Knoll, On physics-based preconditioning of the Navier–Stokes equations, J. Comput. Phys. 228 (24) (2009) 9131–9146.

[19] M. Viallet, I. Baraffe, R. Walder, Comparison of different nonlinear solvers for 2D time-implicit stellar hydrodynamics, A&A 555 (2013) A81.

[20] P. R. Amestoy, *et al.*, A fully asynchronous multifrontal solver using distributed dynamic scheduling, SIAM J. Matrix Anal. Appl. 23 (1) (2001) 15–41.

[21] S. M. Tobias, N. H. Brummell, T. L. Clune, J. Toomre, Transport and storage of magnetic field by overshooting turbulent compressible convection, ApJ 549 (2) (2001) 1183.

Proceedings of the 22nd UK Conference of the
Association for Computational Mechanics in Engineering
2 – 4April 2014, University of Exeter, Exeter

PRESSURE GAUGE PLACEMENT DESIGN FOR WATER NETWORK HYDRAULIC CALIBRATION

***Xiongfei Xie[1], Mahmood Nachabe[2] and Bo Zeng[3]**

[1]Pinellas County Department of Environ. & Infrastr., 14 S. Fort Harrison Ave., Clearwater, FL 33756, USA
[2]Department of Civil and Environmental Engineering, University of South Florida, Tampa, FL 33620, USA
[3]Department of Industrial and Management Systems Eng., University of South Florida, Tampa, FL 33620, USA

*xxie2@mail.usf.edu

ABSTRACT

Hydraulic model is widely used to simulate and predict the behaviour of water distribution system. Model input parameters shall be adjusted to ensure the simulation results to meet field measurements. This procedure is referred to as model calibration. Typical hydraulic model parameters include pipe sizes, lengths, friction coefficients and water demands. Pressure gauges and flow meters can be used to calibrate pipe friction coefficients. However, high manufacturing and installation costs prohibit the application of flow meters. This paper provides a novel approach to minimize the quantity of pressure gauges used for the calibration of pipe friction coefficients. Three questions are investigated. (1) What is the minimum number of pressure gauges needed? (2) Where to put them? (3) How many combinations of pressure gauge placement are available? Preliminary investigation shows that at least three pressure gauges are needed to calibrate one pipe friction coefficient. Based on this principle, the mathematical expressions of the pipe friction coefficients between any two pressure gauge locations are developed and two-dimension relationship matrices are generated. Then, mixed integer programming (MIP) algorithm is developed to solve the three questions. The model frame is demonstrated in a hypothetical pipe network which has four pipe friction coefficients. Calculation shows that at least five pressure gauges are needed to calibrate this network and totally 58 location combinations are obtained.

Keywords: *water distribution system; pipe friction coefficient; sampling design; mixed integer programming*

1. Introduction

Drinking water is produced at water treatment facilities and delivered to end users through water distribution system, which typically consists of pipes, valves, storage tanks, fire hydrants, pump stations and control equipments. Water distribution system hydraulic model is a digitized representation of the water network. Model input parameters shall be adjusted so that the simulated results match field measurements. The parameters normally include pipe length, diameters, pipe friction coefficient, valve status and water demands. The calibration of pipe friction coefficients has been studied extensively. Pressure gauge is inexpensive instrument for the calibration of pipe friction coefficients. The purpose of optimization of pressure gauge placement is to provide the best trade-off between pressure gauge cost and model prediction accuracy.

Walski [1] was among the first to suggest where to observe pressure heads and flows to collect data for model calibration. Bush [2] developed three simple, yet efficient methods for sensor placement design: the max-sum, weighted sum, and max-min methods. These methods were based on a Jacobian matrix and inspired by D-optimality criteria. Most of the current methodologies used for sensor placement design are based on the sensitivity matrix analysis. The paradox of this method is that the true value parameters are not known beforehand. An iterative method is normally used to address this puzzle: first, the parameters are estimated based on a combination of historical information, reconnaissance-level data collection, and the experiences of engineers and operators; second, these pre-assumed parameter values are used to develop the sensitivity matrix and generate a suboptimal sensor placement design; and third, the suboptimal sensor placement design is used to collect data and evaluate the initial parameter estimations. This procedure is repeated until differences between the updated parameter estimations and previous estimated values are minimized. The literature review shows that existing approaches cannot provide a definitive guide to practitioners on how to balance the modeling and calibration with the quality of decisions that could be made based on calibrated models. Therefore, most utilities still rely on a set of simple and pragmatic rules based on previous experiences [3]. This paper presents an innovative approach on sensor placement design, the originality of this methodology lies that a prior knowledge or estimation of pipe friction loss coefficients is not necessary.

2. Methodology

A hypothetical pipe network is presented in Figure 1 to illustrate the methodology. It has 29 demand nodes and 36 pipes. The pipe parameters are listed in Table 1. The pipes fall into four groups, and each group has same friction coefficient. Only pressure gauges are allowed to be installed; and flow meter is not used in the research. This is to simulate the field condition that all the pipes are buried underground and the only way of calibration is attaching pressure gauges to fire hydrants, which are above ground and easily accessible. The placement of pressure gauges is limited to 29 locations, which are named as SP-1 and SP-29.

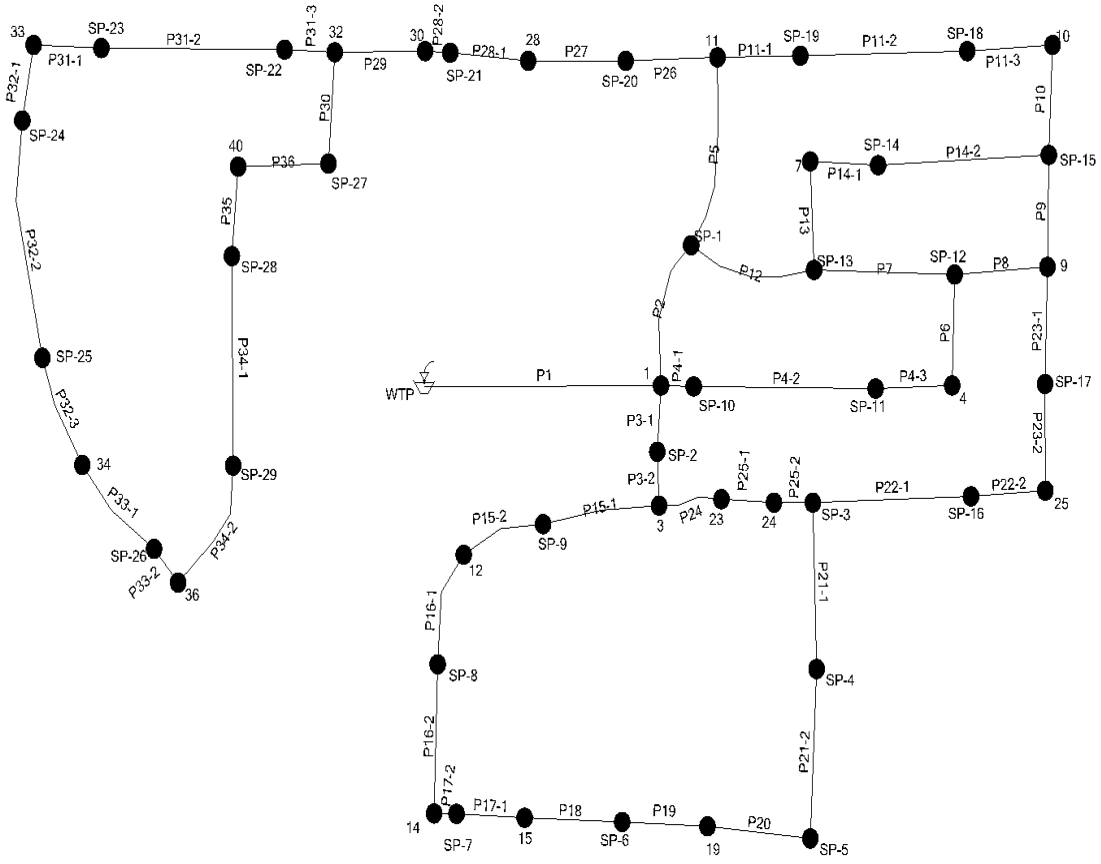

Figure 1 - Schematic pipe network (TIFF)

Pipe 21.2 in Fig. 1 is selected to illustrate the calculating of pipe friction coefficient. To calibrate pipe friction coefficient C_1 of this pipe, following information shall be obtained: pressures at junctions SP-4 and SP-5, and flow of this pipe. The math expression is shown in Eq. 1. However, the flow of pipe 21.2 is not measurable. A third pressure gauge has to be installed in SP-3. A new math formula; Equation 2 is created.

$$P_4 - P_5 = \frac{10.67 \times L_{21.2} \times Q_{21.2}^{1.852}}{C_1^{1.852} \times d_{21.2}^{4.87}} \tag{1}$$

$$P_3 - P_4 = \frac{10.67 \times L_{21.1} \times Q_{21.1}^{1.852}}{C_1^{1.852} \times d_{21.1}^{4.87}} \tag{2}$$

Where P_3 is the pressure at SP-3 (m of water); L is the pipe length (m); Q is the flow inside pipe (m3/s); and, d is the pipe diameter (m). These two equations contains two independent variables, $Q_{21.2}$ and C_1, Therefore, unique solutions are obtained. Since the pipe friction coefficients are not known, flow directions in the pipes are not determined either. However, this does not affect the calculation of pipe friction coefficients. When pipe friction coefficient of Pipe 21.1 is not C_1, three pressure gauges are still sufficient. However, a new flow

condition, such as increasing water consumption at SP-5, shall be performed to create two more equations. Therefore, at least three pressure gauges are needed to calculate one pipe friction coefficient; this is referred to as Three Point Principle in this paper.

Table 1. Water distribution system pipe data

ID	Length (m)	Dia. (cm)	Type	ID	Length (m)	Dia. (cm)	Type	ID	Length (m)	Dia. (cm)	Type
P1	61	40.64	3	P15.1	110	20.32	2	P28.1	90	20.32	4
P2	111	25.4	2	P15.2	67	20.32	2	P28.2	21	20.32	4
P3.1	40	25.4	4	P16.1	61	20.32	2	P29	79	20.32	4
P3.2	43	25.4	4	P16.2	129	20.32	2	P30	81	20.32	3
P4.1	42	25.4	1	P17.1	67	20.32	2	P31.1	61	20.32	1
P4.2	152	25.4	1	P17.2	12	20.32	2	P31.2	152	20.32	1
P4.3	61	25.4	1	P18	85	20.32	3	P31.3	52	20.32	1
P5	140	25.4	2	P19	61	20.32	3	P32.1	92	20.32	1
P6	79	20.32	3	P20	91	20.32	3	P32.2	152	20.32	1
P7	126	20.32	1	P21.1	122	20.32	1	P32.3	69	20.32	1
P8	82	20.32	3	P21.2	122	20.32	1	P33.1	76	20.32	2
P9	81	20.32	2	P22.1	122	20.32	4	P33.2	40	20.32	2
P10	79	20.32	3	P22.2	84	20.32	4	P34.1	152	20.32	4
P11.1	61	20.32	1	P23.1	67	20.32	4	P34.2	113	20.32	4
P11.2	152	20.32	1	P23.2	61	20.32	4	P35	70	20.32	3
P11.3	73	20.32	1	P24	57	20.32	4	P36	81	20.32	3
P12	109	20.32	1	P25.1	55	20.32	4				
P13	78	20.32	2	P25.2	21	20.32	4				
P14.1	73	20.32	1	P26	82	20.32	4				
P14.2	136	20.32	1	P27	85	20.32	4				

Based on this priciple, 29 two-dimension matrices are generated. Each represents one potential location for placing pressure gauge. Each matrix has the dimension of 29 rows and five columns. Columnes one through four correspond four pipe friction coefficients repsectively. Matrix 5 is taken as example to demonstate how these matrices are created. The fourth row in this matrix is [1 0 0 0 1], which shows that relationship when placing pressure gauges in SP-4 and SP-5. It is observed that puting pressure gauges in this two locations can not solve C_1, but it is directly helpful to solve C_1. Therefore, element in the first column is assigned with "1". Meanwhile, the element in fifth column is assigned with "1" too. Therefore there are two variables in one equation. This embodies the inability of solving one pipe friction coefficients when placing only two pressure gauges. The second through the fourth columns are all filled with "0", this suggests that placing pressure gauges in these two points provides no help to the solutions of C_2 through C_4. To solve C_1, one more pressure gauge shall be installed in a third location, such as SP-3. The third row in Matrix 5 is [2 0 0 0 1]. Two equations will be created when pressure gauges are placed in these three points, where C_1 can be solved. Using the same logic, 29 matrices are created.

Mixed integer programming (MIP) optimization algorithm is developed in the research. The objective of the MIP algorithm is to minimize sampling points selected from the 29 allowable locations, as follows:

$$\sum_{i=1}^{29} x_i \tag{3}$$

Where x_i is a binary variable used to represent whether pressure gauge is placed at point i; it takes 1 when pressure gauge is installed at this point, and zero otherwise.

To compute four pipe friction coefficients, four independent equations are needed, which constitute the constraints for the MIP algorithm. A collection with five locations, e.g., SP-4, SP-5, SP-8, SP-9, and SP-16, is used to explain how the constraints are formulated mathematically. Placing pressure sensors in these five points means selecting Matrices 4, 5, 8, 9, and 16 and rows 4, 5, 8, 9, and 16 from each matrix. This constitutes a set of 5*4/2=10 equations. If by linear combination, i.e., multiplying with certain coefficients, these 10 equations generate an equation that contains only C_1, written as a unit row vector [1 0 0 0 0 0]. This sampling combination is said to be able to solve C_1. Similarly, if this selection of sampling points can generate four equations, each is

the function of C_1 through C_4, respectively; this selection of locations is said to be able to solve the four pipe friction coefficients. Mathematically, these constraints of MIP algorithm are expressed as:

$$\sum_{i=1}^{29}\sum_{j=1}^{29} x_i \times x_j \times \lambda_{i,j} \times Matrix_i(j, C_1, C_2, C_3, C_4) = [01000] \quad (4a)$$

$$\sum_{i=1}^{29}\sum_{j=1}^{29} x_i \times x_j \times \lambda_{i,j} \times Matrix_i(j, C_1, C_2, C_3, C_4) = [01000] \quad (4b)$$

$$\sum_{i=1}^{29}\sum_{j=1}^{29} x_i \times x_j \times \lambda_{i,j} \times Matrix_i(j, C_1, C_2, C_3, C_4) = [00100] \quad (4c)$$

$$\sum_{i=1}^{29}\sum_{j=1}^{29} x_i \times x_j \times \lambda_{i,j} \times Matrix_i(j, C_1, C_2, C_3, C_4) = [00010] \quad (4d)$$

The nonlinear formulation is converted into a mixed integer linear programming question (MILP). Linear programming is classified as exact algorithm because it is guaranteed to find an optimal solution and to prove its optimality. The MILP is implemented by GAMS (General Algebraic Modeling System), a high-level mathematical programming and optimization modeling system [4]. The linear programming solver CPLEX 12.1 is employed to solve the model.

3. Results and discussions

The calculation results reveal that the answer to the first question is 5. Additionally, the solver can also find where the five points are located in the WDS in each calculation. By restricting the solution different from existing ones, a new solution, i.e., a new combination of sampling points can be derived. Finally, 58 sets of solutions were obtained, as shown in Table 2.

Table 2. List of pressure gauge placement locations

Solutions	Pressure Gauge Locations				
1	22	25	26	27	29
2	24	25	26	28	29
---	---	---	---	---	---
58	4	5	8	9	17

Using the pressure measurement at any location combinations shown in Table 2, four pipe friction coefficients can be obtained. When the hydraulic model is absolutely accurate and field measurement contains no errors, all these sensor location combinations are equivalent. In practice, however, errors exist in field measurements and model construction. These errors lead to the inaccuracy in calculation of pipe friction coefficients. As a result, these location combinations are not equivalent. Some provides more accurate estimation of pipe friction coefficients. This will be investigated in the next phase of study.

4. Conclusions

This paper presents a novel approach to pressure sensor placement design for calibrating pipe friction coefficients. The advantage of this method, compared to the traditional iterative sensitivity matrix method, is that a prior knowledge or estimation of pipe friction loss coefficients is not necessary.

This technique was applied in a pilot water distribution system; it can be used in large-scale WDS without any changes in the algorithm since a large distribution system can be divided into several small systems, and each small system can be calibrated individually.

References

[1] T. Walski. Technique for calibrating network models. *Journal of Water Resources Planning and Management*, 109 (4), 360–372, 1983.

[2] C. Bush. Sampling design methods for water distribution model calibration. *Journal of Water Resources Planning and Management*, 124 (6), 334–344, 1998.

[3] D. Savic. Quo vadis water distribution model calibration? *Urban Water Journal*, 6 (1), 3–32, 2009.

[4] A. Brooke. *General algebraic modelling system: a user's guide*. Washington, DC. Commun. 2003.

Proceedings of the 22nd UK Conference of the
Association for Computational Mechanics in Engineering
2 – 4April 2014, University of Exeter, Exeter

ANALYSIS OF THE DYNAMIC RESPONSE OF A LARGE DEEP KARST AQUIFER BY DATA-DRIVEN MODELLING

***Angelo Doglioni[1] and Vincenzo Simeone[1]**

[1]Department of Civil Engineering and Architecture, Technical University of Bari, via E. Orabona 4, 70125, Bari, ITALY

*a.doglioni@poliba.it

ABSTRACT

The analysis of the dynamic response of a deep karst aquifer to precipitation is a complex problem, due to the structure of the aquifer, which may origin non-linear variations of the groundwater table. However, karst aquifers may be one of the main water resources for those regions characterized by poor presence of shallow water and medium-high permeable soils. This work presents an analysis of the dynamic response of the large aquifer of central Apulia, south Italy, based on a data-driven approach, namely Evolutionary Polynomial Regression. Four wells were monitored, and for each of them about 15 years of monthly average levels are available. In particular, the dynamic response of the aquifer is modelled in terms of prediction of the groundwater levels as function of total monthly precipitations and past measured groundwater levels. A single model, as closed-form equation, is obtained for each well and then these models are compared, highlighting the differences and the similarities among the responses of each well.

Keywords: *data-driven; groundwater levels; dynamic response; Evolutionary Polynomial Regression; karst aquifer.*

1. Introduction

Karst aquifers are complex systems characterized by heterogeneous infiltration paths, which can be preferential direct flow paths as well as denoted by manifold interlayers with variable hydraulic conductivities. For these reasons, the time evolution of the groundwater table levels of a deep karst aquifer cannot be linear and with a short lag with respect to rainfall as expected. It may show multiple lags, as well as non-linear behaviours.
Data-driven modelling constitutes an appealing alternative to physically based modelling for investigating the aquifer dynamics, whereas timeseries of groundwater data are available. This work presents the outcomes of the use of the multi-objective evolutionary modelling technique, Multi-objective Evolutionary Polynomial Regression (EPRMOGA) [5], for groundwater level fluctuation prediction. EPRMOGA is a multi-objective evolutionary modelling technique successfully applied to multiple problems related to natural systems [2][4][6]. It proved quite effective at modelling the dynamic relationship between groundwater levels and rainfall heights for specific cases, related to porous aquifers [3][6]. The main practical advantage of EPRMOGA is its ability of returning closed-form polynomial equations, allowing for conjecturing on the physical relationship between the main variables of the investigated phenomena. In particular, here the relationship between water table levels and rainfall is investigated, for a deep karst aquifer hosted by the Apulian limestone basement in south-east Italy. In particular, four timeseries ranging on about 15 years of monthly data are available. Starting from these data, four equations are here identified and discussed, in terms of differences and similarities of the structures and of the selected inputs.

2. The deep karst aquifer of central Apulia – southeast Italy

The investigated aquifer is located in the central part of Apulia region, figure 1, namely Murgia, it is a large Mesozoic carbonate platform constituted by a sequence of detrital and bistromal limestones and dolomitic limestone, karstified, sometimes severely. This wide platform is a large asymmetric horst, with a NW-SE direction, its morphostructural features were superimposed by tectonics with direct

fault having their main orientation according NW-SE and NE-SW directions. Wide folds with a large curvature radius gently deform Murgia. The morphology is normally quite flat, and the limestone layers are normally sub-horizontal with small inclination rarely higher than 10°-15°. Toward the Adriatic sea side, Murgia gently slopes, with a sequence of little terraces and scarps parallel to the coast, while the lower zones are overlain by discontinuous and thin upper Pliocene to lower Pleistocene transgressive calcarenites, deposited in shallow and agitated marine waters [8][9]. The limestones and dolomitic limestones are karstified and originating a characteristic hydrogeological domain [1], where the hydraulic base level of groundwater circulation corresponds to sea level. The permeability of this karst aquifer is due to fractures and karst phenomena, which allow rainfall to infiltrate quite easily and reasonably quickly. This implies that quick responses to rainfall are expected, while the recharge period starts from September/October of each year ending at the following February/March. Figure 1 shows the sampling wells from which four timeseries of phreatimetric data are available. These are named in the order: A, B, C and D. Data are available for the years ranging between 1975 and 1990. Finally, for each sampling well a timeseries of monthly total data, covering the same time interval of phreatimetric data is available. It is noteworthy that rainfall data are collected nearby the wells, this assumption is reasonable since due to the medium-high permeability of soils, infiltration conditioning the groundwater levels is supposed to be mostly local.

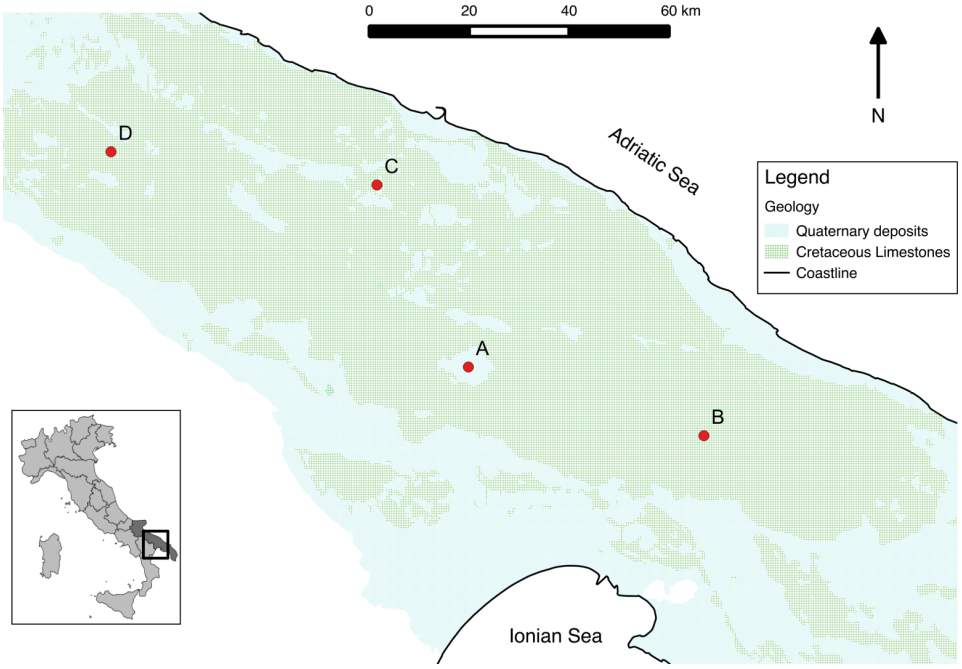

Figure 1: The region hosting the aquifer and location of the sampling points.

3. Multi-Objective Evolutionary Polynomial Regression - EPRMOGA

EPRMOGA is a two-stages methodology: it is firstly made a structural model identification based on a Genetic Algorithm [7], afterwards an estimation of the constant values is made, based on a least-square approach. In this the preliminary contribute of the user is particularly valuable, since she/he can broadly assume the main structure of the model, potentially involved functions, maximum length of the polynomial structures, candidate exponents and objective functions. This does not mean the user has to assume an equation, but just some assumptions about the structures of the equations, in order to set a limit to the evolutionary search, i.e. to the space of solutions. During the search for the equations, EPRMOGA can simultaneously optimize three objective functions at most. These are the minimization of the Sum of Squared Errors, the minimization of the number of monomial terms and the minimization of the percentage of input selected among the candidates given by the user. This constitutes a multiobjective approach, where three conflicting functions are simultaneously optimized. EPRMOGA already proved to fit particularly to those cases where the input to the process and the boundary conditions are not completely clear or known a-priori [2][4][6], as for the problem at stake.

The comparison between the models found the four wells will show how EPRMOGA is able to return reasonably good predictions of water table levels as well as models consistent with the dynamics of the aquifer and with their different response to rainfall due to local different hydrogeological characteristics.

4. Results and discussion

EPRMOGA returned a set of models for each sampling wells. Among these, an equation is chosen for each well. These are in the order for A, B, C and D:

$$H_t = 9.2147 \cdot 10^{-5} \cdot P_{t-3}^2 + 1.7567 \cdot 10^{-5} \cdot P_{t-2}^2 P_{t-5}^{0.5} + 0.00010327 P_{t-1}^2 + 0.95456 H_{t-1} + 3.9395 \quad (1)$$

$$H_t = 0.00031945 P_{t-1}^{0.5} P_{t-3} P_{t-4}^{0.5} + 8.9153 \cdot 10^{-6} P_{t-1}^{0.5} P_{t-2} P_{t-5} P_{t-6}^{0.5} + 0.90301 H_{t-1} + 4.9879 \quad (2)$$

$$H_t = 2.6457 \cdot 10^{-6} \cdot P_t \cdot P_{t-1}^2 + 0.9884 \cdot H_{t-1} \quad (3)$$

$$H_t = 0.00056017 P_t P_{t-1}^{0.5} P_{t-2}^{0.5} + 0.27321 H_{t-2} + 0.48127 H_{t-1} + 0.05312 \quad (4)$$

Where H is average monthly the piezometric height and P is the total monthly rainfall. The subscripts represent the time delay in months. These models show some differences, which denote behaviours not typical of fractured karst aquifers. In fact, the response of the aquifer varies among the wells, even if the aquifer is the same. Moreover, there are lags between rainfall and level variations. Equation (1) shows the term of persistence, as well as terms related to rainfall up to 5 months before the level to be predicted. This hybrid behaviour seems to be between a karst and a porous aquifer and then this may be related to a local poor fracturing of limestones. Equation (2) shows a persistence term, which actually has a lower influence on the output than the previous models, as well as rainfall terms ranging between 1 to 6 months before the output. Similarly to equation (1) this is a hybrid behaviour, typical of complex flow paths and of the presence of poorly permeable layers. Equation (3) is reasonable for a karst aquifer, it shows a strong persistence term, H_{t-1}, while the rainfall terms rely on the precipitations of the same month or the month before the level prediction. Rainfall does not show exponents lower than 1, this implies a direct effect of rainfall on groundwater levels, as expected by fractured media. Equation (4) shows a peculiar behaviour, the most influencing rainfall terms are those of the same month of the prediction and those of the two months before, even if these have 0.5 as exponent. This is typical of a karst aquifer, since the temporally closer precipitations are the most determining on the level variations. A further interesting but difficult to be interpreted characteristic is the persistence: there are two terms H_{t-1} and H_{t-2}, their presence may be relate to the inertia of the aquifer or to unknown extra inputs as well as to a pressurized flow of the aquifer, which is consistent with the high oscillations of the levels. The following figures 2a-2d show the time plot of the measured levels and of the predicted levels at 1, 6 and 12 months ahead, for the test set of data, i.e. data not used by EPRMOGA for model identification.

5. Conclusions

The dynamic response of the deep karst aquifer of Murgia, southeast Italy, was here investigated, by identifying four models, starting from four timeseries of available data. The wells are located relatively far from each other, in order to cover as much as uniformly the hydrogeological catchment of the aquifer. Similar models were expected, however this is not the case, since the returned models, corresponding to the local behaviours of the aquifer are different from each others. This may be related to local flow paths or local permeability variations. In this scenario, the use of a data-driven approach as EPRMOGA was very important, since on the one hand it allowed to model the groundwater levels variations and on the other hand, it returned closed form equations, which permit to advance some physical speculations on the aquifer. Finally, it is important to emphasize that like for all the data-driven approaches, EPRMOGA returned interpolative equations, with good generalization abilities. However, since these are interpolative models, their physical interpretation cannot be considered exhaustive, it should be coupled with direct physical observations and possibly by physically based analysis.

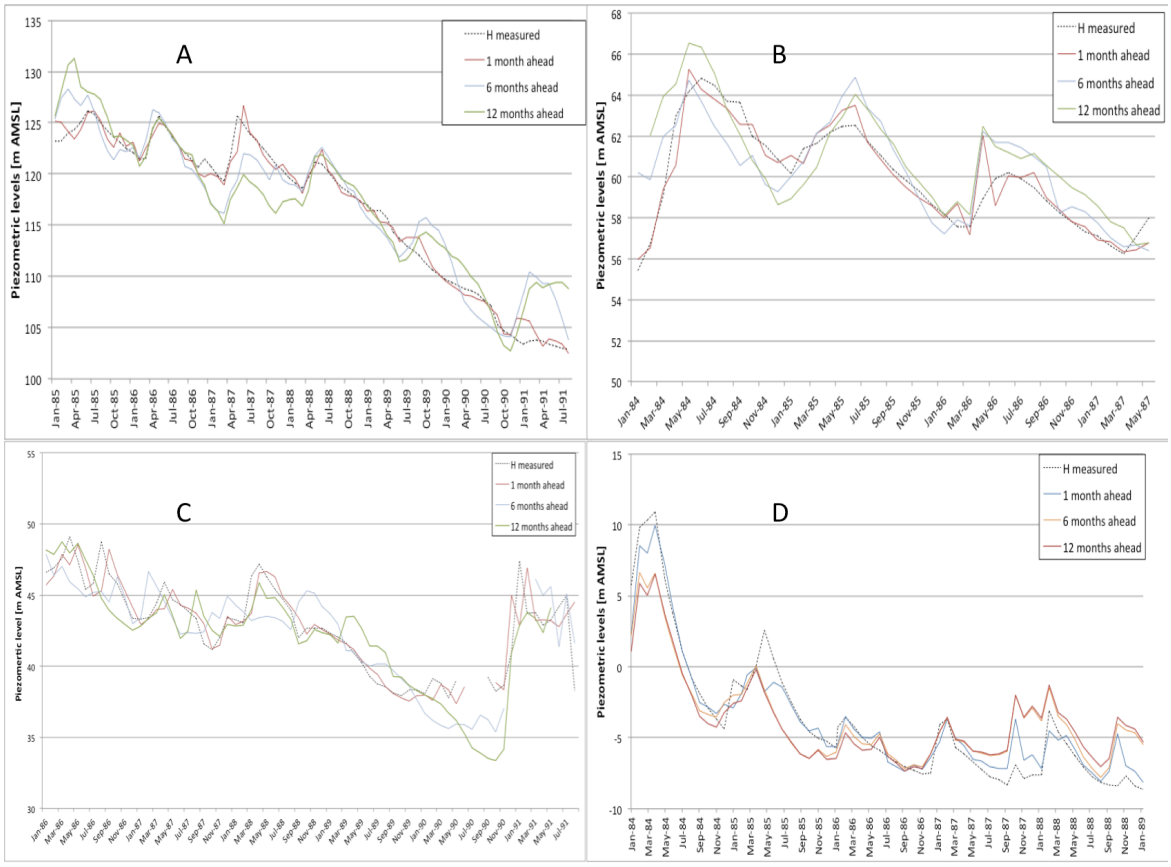

Figure 2: Time plot of the groundwater levels and of their predictions – test set.

References

[1] V. Cotecchia, D. Grassi and M. Polemio. Carbonate aquifers in Apulia and seawater intrusion. *Giornale di Geologia Applicata (Italian Journal of Engineering Geology)*, 1, 219–231, 2005.

[2] A. Doglioni, F. Fiorillo, F.M. Guadagno and V. Simeone. Evolutionary polynomial regression to alert rainfall-triggered landslide reactivation alert. *Landslide*, 9(1), 53-62, 2012.

[3] A. Doglioni, A. Galeandro and V. Simeone. A data-driven model of the shallow porous aquifer of south Basilicata – Italy. *Advances in the Research of Aquatic Environment - Environmental Earth Sciences*, 4, 233-240, 2011.

[4] A. Doglioni, D. Mancarella, V. Simeone, O. Giustolisi. Inferring groundwater system dynamics from time series data. *Hydrolog. Sci. J.*, 55(4), 593-608, 2010.

[5] O. Giustolisi and D.A. Savic. Advances in data-driven analyses and modelling using EPR-MOGA. *J. Hydroinform.*, 11(3–4), 225–236, 2009.

[6] O. Giustolisi, A. Doglioni, D.A. Savic, and F. di Pierro. An Evolutionary Multi-Objective Strategy for the Effective Management of Groundwater Resources. *Water Resour. Res.*, 44, W01403, 2008.

[7] O. Giustolisi, A. Doglioni, D. Laucelli and D.A. Savic. A proposal for an effective multiobjective non-dominated genetic algorithm: the OPTimised Multi-Objective Genetic Algorithm, OPTIMOGA, *Report 2004/07, School of Engineering Computer Science and Mathematics, Centre for Water Systems, University of Exeter*, UK, 2004.

[8] G. Ricchetti, N. Ciaranfi, E. Luperto Sinni, F. Monelli and P. Pieri. Geodinamica ed evoluzione sedimentaria e tettonica dell'Avampaese apulo. *Mem. Soc. Geol. Ital.*, 41, 57–82, 1988.

[9] M. Tropeano and L. Sabato. Response of Plio-Pleistocene mixed bioclastic–lithoclastic temperate-water carbonate system to forced regression; the Calcarenite di Gravina Formation, Puglia, SE Ital. In: Hunt, D., Gawthorpe, R. (Eds.), *Sedimentary Responses to Forced Regressions. Geol. Soc. London. Spec. Publ.*, 172, 217–243, 2000.

Proceedings of the 22nd UK Conference of the
Association for Computational Mechanics in Engineering
2 – 4April 2014, University of Exeter, Exeter

IDENTIFICATION OF MORPHOLOGICAL ANOMALIES BY 2D DISCRETE WAVELET TRANSFORM

***Angelo Doglioni[1] and Vincenzo Simeone[1]**

[1]Department of Civil Engineering and Architecture, Technical University of Bari, via E. Orabona 4, 70125, Bari, ITALY

*a.doglioni@poliba.it

ABSTRACT

Digital elevation models processing is a hot topic for identifying the main topographic features of an area. In particular, medium resolution digital elevation models are of particular interest for analysing regional phenomena, like geomorphological evolution and ongoing or past tectonic processes. The key point of these analyses is the extraction of these features from elevation models. In this context, an effective approach is constituted by 2D discrete wavelet transforms. These allow for a multi-scale decomposition, which permits to extract details of digital elevation models, normally not clearly evident looking just at the topography. These details are often associable to anomalies or singularities of the topography, which may be related by a careful geomorphological interpretation to regional tectonic processes or, more in general, to landscape evolution phenomena, i.e. big landslides, erosion, etc.

Keywords: *Digital elevation model; 2D discrete wavelet transform; landscape evolution; tectonics; geomorphology.*

1. Introduction

Identification and delineation of anomalies of the topographic surface can be of support in delineating morphological shapes due to tectonics or landscape evolution processes. The numerical analyses applied to Digital Elevation Models (DEM) constitute a valid methodology to this kind of studies, allowing for a detailed and relatively accurate identification of topographic anomalies, which may be related to large or local geomorphological phenomena. The reasonable availability of DEMs encourages these analyses, since DEMs are matrixes of elevation values suitable for signal processing [10]. Global or quasi-global medium resolution DEMs, such as ASTER GDEM Ver. 2, SRTM, etc., allow for regional studies, which provide an overview on processes involving large areas.
This work introduces a numerical analysis of DEM based on 2D Discrete Wavelet Transform (DWT) [2]. This aims at decomposing DEMs into high and low frequencies, the earlier representative of details and the latter representing a lower resolution approximation of the DEM itself. In particular, 2D DWT allows for identifying high-frequency components of elevation data, by a progressive data filtering. The localization of high-frequency components is of support to the identification of topographic anomalies, such as scarps, faults, streams, etc. [5]. The methodology here presented is applied to a relatively large area, of south Italy, the central Apulia foreland, where a large calcareous highland called Murgia outcrops. This is characterized by peculiar morphologies, which, even if apparently uniform, may be related to deep geological structures [3][7]. 2D DWT is here used in order to outline the anomalies of the topographic surface of Murgia area in order to highlight them by using a numerical technique and to advance geological interpretations.

2. Background to the methodology

Wavelet transform is decomposition into space–frequency space of a data series. This permits for the analysis of localized variations within data. Different frequency components can be studied and analysed with the proper resolutions matching to their scales [2]. This approach can be easily adapted to distributed data, in particular elevation data coming from a grid-based description of earth surface, i.e. a DEM, thus providing accurate spatial information in terms of slope variations, being sensitive to

minimal variations. Discrete Wavelet Transform (DWT) is an orthogonal function applied to a finite set of data. DWT is orthogonal: a signal passed twice through the transformation is unchanged, and it is assumed the input signal as a set of discrete-time samples. DWT is based on a set of functions defined by a recursive difference equation:

$$\phi(x) = \sum_{k=0}^{M-1} c_k \phi(2x - k) \tag{1}$$

M is the specified number of nonzero coefficients, which is arbitrary, and referred to as the order of the wavelet. The values of the coefficients are not arbitrary; they are determined by constraints of orthogonality and normalization. The area under the wavelet is required to be one. This class of wavelet functions is bounded to be zero outside of a small interval. This allows the wavelet transform to operate on a finite set of data, i.e. compact support. The commonly used functions for transforms are a few sets of well-defined coefficients resulting in a function provided with a discernible shape. Manifold mother wavelet functions exist, the specific choice of a mother wavelet depends on data to be analysed. The choice of a proper mother wavelet for DEM analysis is dependent on the resolution of the DEM, conditioning the description of terrain detail. Regional analyses of medium-low resolution DEMs can be based on the biorthogonal 1.3 wavelet [2]. Biorthogonal wavelets use two scaling functions, these generate different multiresolution analysis and then two wavelets, one for decomposition and the other for reconstruction. Detail coefficients of 2D DWT applied to a DEM are here analysed, since their variations represent discontinuities of DEM. Moreover, 2D DWT can be exerted to further levels, assuming a higher scale number of the transform. This may return further results, in terms of identification of the anomalies of land surface. Differently from an analysis based of slope, curvature and aspect mapping, this approach returns sharp maps of variations of elevations at high scale, even minimal, which can be used as a starting point for successive and more localized analysis, based traditional methodologies [4][5][8].

3. General description of the investigated region

The introduced methodology is tested on Murgia area. This is a highland located in the central part of Apulia region, extreme southeast of Italy. Murgia highland is a large Mesozoic carbonate platform made up by a sequence of limestones and dolomitic limestone often karstified, sometimes to a severe degree. This wide platform is like a large asymmetric horst, with a NW-SE direction. Its morphostructural features depend on regional tectonics, in fact direct faults developing along NW-SE direction exist [7]. Wide folds, characterized by large curvature radii, gently deform Murgia highland. Its morphology is diffusively flat, while limestone layers are normally sub-horizontal with inclination rarely higher than 10°-15°. Towards the Adriatic sea side, north-east of the highland, Murgia is gently sloping, with a sequence of small terraces and scarps parallel to the coast. Lower elevated areas, i.e. relatively close to the coastline, are overlain by discontinuous and thin upper Pliocene to lower Pleistocene transgressive sandstone.

4. Results of the analysis and discussion

The 2D DWT is applied to the medium resolution ASTER GDEM v2 [11], a 30 m grid raster DEM. This DEM is processed by 1.3 biorthogonal 2D DWT, returning some potentially interesting results.
The following figure 1a shows the used DEM and the location of the investigated region, while figure 1b represents the map of detail coefficients of level 3 biorthogonal 1.3 2D DWT evaluated along N-S direction. Higher values of detail coefficients are associated with discontinuities of DEM or sudden variations in terms of elevation or slope. Therefore, if for some reasons the topography locally varies, detail coefficients will increase their moduli. However, the map of these local variations may be helpful in giving objective evidences, by numerical values of the detail coefficients of 2D DWT, of large-scale anomalies or structures. In fact, detail coefficients of 2D DWT are sensitive to variations of elevation, thus allowing for delineating patterns contained in topography that may be potentially related to geological or tectonic structures. These otherwise would be hardly detectable, even looking at slope or aspects maps.

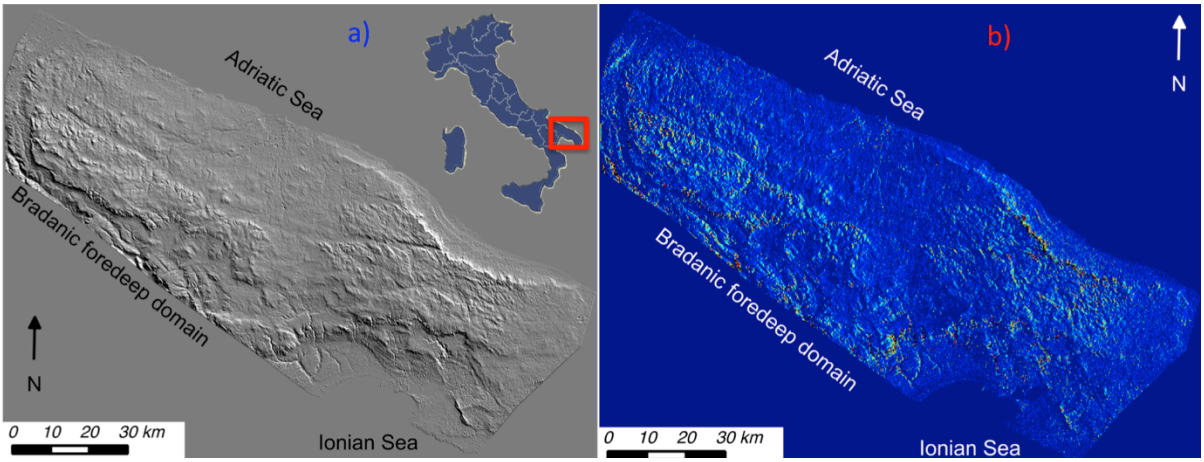

Figure 1: a) hillslope of the used DEM; b) Detail coefficients of level 3 biorthogonal 1.3 DWT, along N-S direction and location of the region.

Looking at figure 1b, higher values of detail coefficients correspond to the west side of Murgia, at the bound between the Apulian foreland and the Bradanic foredeep domain. The southeast side shows a zone, between the Ionian and Adriatic coast, where detail coefficients are quite scattered, with high values diffusively spread. Central and north of Murgia show polarized stripes of high values, along NW to SE direction, in particular where there are the steps of elevation increment. Finally, high values of detail coefficients show on the south and northeast bound of Murgia. Here the high values of detail coefficients are concentrated along well-defined directions, which permit to outline the main ephemeral stream network and particularly the deep valleys, namely Gravine. These particularly are on the south side of Murgia tableland, directed towards the Ionian coast [1][6]. Despite figure 1b provides information about the main structural features of Murgia, it is still quite complex, since detail coefficients widely range thus making their interpretation difficult. The next step of this analysis is then to filter the detail coefficients, assuming a threshold value under which they are no more mapped. This is supposed to highlight those discontinuities of the topography, which are meaningful and of certain interpretation. Figure 2 show the maps of the filtered detail coefficients superimposed to the DEM and to the map of the main tectonic structures.

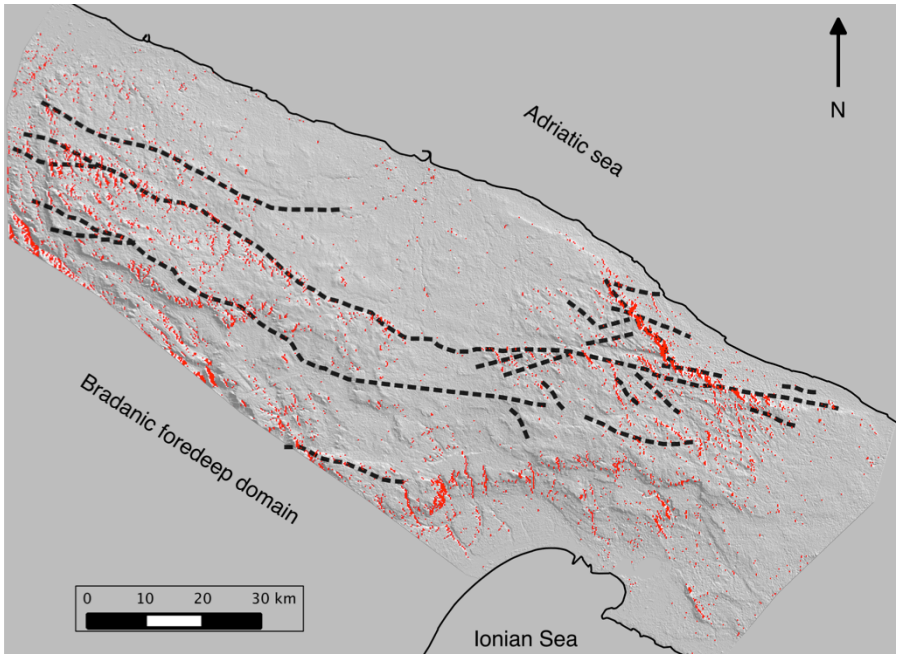

Figure 2: Filtered detail coefficients of level 3 biorthogonal 1.3 DWT, threshold value 30 and main tectonic structures.

Starting from an initial range of variation of detail coefficients comprised between 0 and 358, two new maps are constructed, assuming in 30 as threshold value. This new map is interesting, since clearly delineating the variations of elevation data, which may correspond to more relevant macro phenomena. On the one hand, the central area of Murgia, east and north-east, does not show high detail coefficients, thus highlighting a relative uniformity of the topography. On the other hand, the zones characterized by high values of detail coefficients are quite interesting since these may be interpreted as consequence of stresses, which diffusively disturbed the bedrock causing cracks and changes of elevations and slopes. It is noteworthy that the singularities highlighted by the presented approach barely correspond to the main structural features of Murgia highland reported by [7] in a past study based on traditional geostructural analyses.
For this reason, these areas are worth of further investigations, since apparently biased by geological-structural phenomena.

5. Conclusions

The results of an investigation on the effects of regional tectonics on topography based on the 2D DWT applied to a DEM are here presented. The analysis focuses on Murgia highland in Apulia foreland, south east of Italy. The results of the proposed approach are interesting, since they evidence how it is possible to delineate the main discontinuities and singularities, possibly due to tectonic stresses or ongoing processes, by processing a DEM. Even if this analysis cannot be considered exhaustive for providing a certain interpretation to the discontinuities of a DEM, it is of support for starting further geomorphological investigations as well as to clean a DEM from the excess of information they provide. Moreover, the 2D DWT is a numerical technique, then the returned results allow for a numerical classification of the discontinuities of a DEM and then for extracting common patterns from elevation data. Finally, mapping the spatial variability of detail coefficients is a further important advantage of this approach, since it allows for spatially delineating the details of DEM.

References

[1] M.C. Cristino, A. Doglioni, V. Simeone. Preliminary results about morphological characteristics of ephemeral stream catchments in Apulia region, South Italy. *Rend. Online Soc. Geol. It.*, 24, 70 – 72, 2013.

[2] I. Daubechies, *Ten lectures on wavelets*, SIAM, Philadelphia, 1992.

[3] C. Doglioni, M. Tropeano, F. Mongelli and P. Pieri. Middle late Pleistocene uplift of Puglia: an “anomaly” in the Apenninic foreland. *Mem. Soc. Geol. It.*, 51, 101-117, 1996.

[4] A. Doglioni. The use of discrete wavelet transform for the analysis of topographic surface for geological purposes. *Rend. Online Soc. Geol. It.*, 24, 104 – 106, 2013.

[5] A. Doglioni and V. Simeone. Geomorphometric analysis based on discrete wavelet transform. *Environmental Earth Sciences*. In press, doi: 10.1007/s12665-013-2686-3, 2013.

[6] A. Doglioni, V. Simeone and O. Giustolisi. The activation of ephemeral streams in karst catchments of semi-arid regions. *Catena*, 99, 54-65, 2012.

[7] V. Festa. Cretaceous structural features of the Murge area (Apulian Foreland, Southern Italy). *Eclogae Geologicae Helvetiae*, 96, 11-22, 2003.

[8] A. Galeandro, A. Doglioni, A. Guerricchio and V. Simeone. Hydraulic stream network conditioning by a tectonically induced, giant, deep-seated landslide along the front of the Apennine chain (south Italy). *Natural Hazards and Earth System Sciences*, 13, 1269-1283, 2013.

[9] M. Kalbermatten, D. Van De Ville, P. Turberg, D. Tuia and S. Joost. Multiscale analysis of geomorphological and geological features in high resolution digital elevation models using the wavelet transform. *Geomorphology*, 138(1), 352-363, 2012.

[10] A.V. Oppenheim and R.W.Schafer, *Digital Signal Processing*, Prentice Hall, 1975.

[11] ASTER GDEM ver. 2, http://asterweb.jpl.nasa.gov/gdem.asp, 2011.

Proceedings of the 22nd UK Conference of the
Association for Computational Mechanics in Engineering
2 – 4April 2014, University of Exeter, Exeter

LATERAL LOAD BEARING CAPACITY MODEL FOR PILES IN COHESIVE SOILS

***A. Ahangar-Asr[1], A. A. Javadi[2], A. Johari[3] and Y. Chen[4]**

[1]School of Architecture, Computing and Engineering, University of East London, UK
[2]College of Engineering, Mathematics and Physical Sciences, University of Exeter, UK
[3]Department of Civil and Environmental Engineering, Shiraz University of Technology, Shiraz, Iran
[4]Department of Civil Engineering, University of Shanghai for Science and Technology, Shanghai, China

*a.ahangar-asr@uel.ac.uk

ABSTRACT

In this research work an evolutionary approach is proposed to develop a structured polynomial model for predicting the lateral load bearing capacity of piles in undrained conditions. The proposed polynomial regression technique is an evolutionary data mining methodology that generates a transparent and structured representation of the behaviour of a system directly from raw data. It can operate on large quantities of data in order to capture nonlinear and complex relationships between contributing variables. Field measurement data from literature was used to develop the proposed model. Comparison of the proposed model predictions with the field data shows that the EPR model is capable of capturing, predicting and generalising predictions to unseen data cases the lateral load bearing capacity of piles with very high accuracy. The merits and advantages of the proposed methodology are also discussed.

Keywords: *load bearing capacity, piles, cohesive soils*

1. Introduction

Some research contributions have revealed that solving equations of static equilibrium can be an effective way of designing axially loaded piles, whereas, design of laterally loaded piles will only be possible by solving nonlinear differential equations. Poulos and Davis [1] implemented a methodology based on elasticity, by adopting a previously developed soil model to analyse the behaviour of piles. However, their proposed approach was not suitable for the nonlinear analysis of behaviour of soil and pile systems. The analysis of nonlinear soil behaviour has been conducted by Matlock and Reese [2] and Portugal and Seco e Pinto [3]. Portugal and Seco e Pinto [3] also utilized the finite element method for numerically predicting the behaviour of laterally loaded piles. This methodology is widely used in analysis and design of deep foundations despite the presence of uncertainties in such predictions due to the variability of soil properties. Semi-empirical methods were also suggested for analysis and design of laterally loaded piles and for predicting their load bearing capacity (e.g., Hansen [4], Broms [5] and Meyerhof [6]).
Lee and Lee [7] utilized neural networks to predict the ultimate bearing capacity of piles based on data simulated using previously suggested models and also in situ pile loading test results. Abu-Kiefa [8] used a probabilistic neural network model, generalized regression neural network (GRNN), to predict the pile load bearing capacity considering the contributions of the tip and shaft separately and also the total load bearing capacity of piles driven into cohesionless soils.
Artificial neural networks have mostly been used to predict the vertical load bearing capacity of piles and their performance is usually measured based on the coefficient of correlation (R).
The results of previous works have shown that artificial neural network offers great capabilities and advantages in modelling the behaviour of materials and systems. However, it is generally accepted that ANNs also suffer from a number of shortcomings. One of the main shortcomings of the neural network based approach is that the optimum structure of the neural network (e.g., the number of input layers, hidden layers and transfer functions) needs to be identified a priori through a time consuming trial and error procedure. Another main drawback of the neural network approach is the large complexity of the structure of ANN. This is because the neural network stores and represents the

knowledge in the form of weights and biases which are not easily accessible to the user. Artificial neural networks are considered as black-box systems as they are unable to explain the underlying principles of prediction and the effect of inputs on the output [9].
In this paper an evolutionary-based data mining approach is proposed to model the bearing capacity of laterally loaded piles in undrained conditions. EPR provides a structured and transparent representation of the model in the form of mathematical (polynomial) expressions to describe the complicated behaviour of systems. The proposed methodology overcomes most of the issues and drawbacks associated with the neural network modelling approach by providing clear insight into the behaviour of the system and the levels of contribution of the influencing parameters in the developed models.

2. Evolutionary Polynomial Regression (EPR)

EPR is a data-driven method based on evolutionary computing, aimed to search for polynomial structures representing a system. A general EPR expression can be presented as [10]:

$$y = \sum_{j=1}^{n} F(X, f(X), a_j) + a_0 \qquad (1)$$

where y is the estimated vector of output of the process; a_j is a constant; F is a function constructed by the process; X is the matrix of input variables; f is a function defined by the user; and n is the number of terms of the target expression. The general functional structure represented by F(X, f(X), a_j) is constructed from elementary functions by EPR using a Genetic Algorithm (GA) strategy. The GA is employed to select the useful input vectors from X to be combined. The building blocks (elements) of the structure of F are defined by the user based on understanding of the physical process. While the selection of feasible structures to be combined is done through an evolutionary process, the parameters a_j are estimated by the least square method. This technique uses a combination of the genetic algorithm to find feasible structures and the least square method to find the appropriate constants for those structures. In particular, the GA allows a global exploration of the error surface relevant to specifically defined objective functions. By using such objective (cost) functions some criteria can be selected to avoid the overfitting of models, push the models towards simpler structures and avoid unnecessary terms representative of the noise in the data. An interesting feature of EPR is in the possibility of getting more than one model for a complex phenomenon. The user physical insight can also be used to make hypotheses on the elements of the target function and on its structure. Selecting an appropriate objective function, assuming pre-selected elements based on engineering judgment, and working with dimensional information enable refinement of final models. The level of accuracy at each stage is evaluated based on the coefficient of determination (COD) i.e., the fitness function as:

$$\mathbf{COD} = 1 - \frac{\sum_{N} (\mathbf{Y}_a - \mathbf{Y}_p)^2}{\sum_{N} \left(\mathbf{Y}_a - \frac{1}{N} \sum_{N} \mathbf{Y}_a \right)^2} \qquad (2)$$

where Y_a is the actual output value; Y_p is the EPR predicted value and N is the number of data on which COD is computed. If the model fitness is not acceptable or the other termination criteria (in terms of maximum number of generations and maximum number of terms) are not satisfied, the current model goes through another evolution in order to obtain a new model. Detailed explanation of the method can be found in [10].

3. Database

Field measurements from literature were used to develop and evaluate the proposed EPR model. From among 38 data cases [11] 80% were used to train the EPR model and the remaining cases were kept

unseen to EPR during the model development process and were used in the model evaluation stage to examine generalization capabilities of the created model.

4. EPR Model

Among developed models provided by EPR, the shortest model with the least possible number of terms and with the highest value of coefficient of determination was selected to represent the lateral load bearing capacity of piles (the following equation):

$$Q_u = \frac{7.02 \times 10^{-14}}{(D.S_u)^2 e} + 6.41 \times 10^{-6} D.S_u.L^2 \qquad (3)$$

where Q is the lateral load bearing capacity of piles, D is the diameter of the pile, L is the depth of embedment of the pile in soil, e is eccentricity of load and S_u is the undrained shear strength of the soil.

After training, the performance of the trained EPR model was examined using the validation dataset which had not been introduced to EPR during training. Figures 1 and 2 compare the predicted values of the lateral load bearing capacity by the proposed model with the actual field measurement data used for training and validation stages respectively. The figures show a very good correlation between the predictions of the EPR model and the actual data both for modelling and validation datasets. Table one also shows the coefficient of determination values for training and testing data cases used to develop the proposed model.

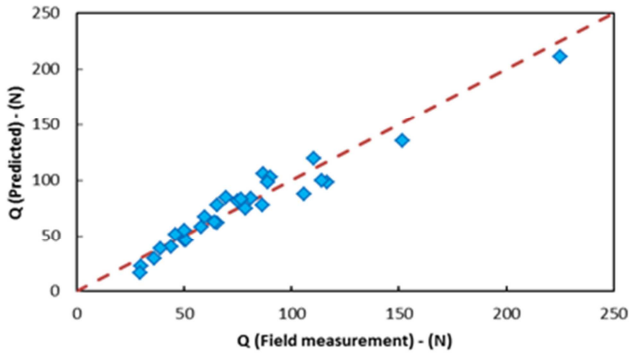

Figure 1: EPR predictions against field measurement values for lateral load bearing capacity values (Training data)

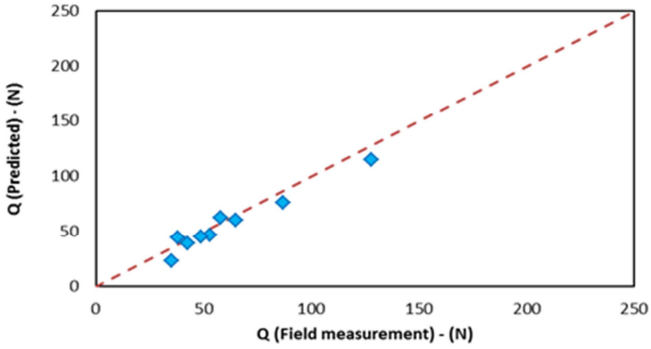

Figure 2: EPR predictions against field measurement values for lateral load bearing capacity values (Testing data)

Table 1: training and testing COD values for the EPR model

Model	COD (%) Training data	COD (%) Validation data
Evolutionary polynomial regression (EPR)	85	86

5. Discussion and conclusions

In this paper, a new approach was presented to develop an evolutionary-based model for predicting lateral load bearing capacity of piles. An EPR model was developed and validated using a field measurement database from literature, created based on tests on model piles. The model prediction results were compared with the actual measured data. Comparison of the results showed that the developed EPR model provides accurate predictions for lateral load bearing capacity of piles with the interesting capability of generalising the predictions to unseen data cases. The developed model presents a structured and transparent representation allowing a physical interpretation of the problem that gives the user an insight into the relationship between the lateral load bearing capacity and its various contributing parameters. Another interesting feature of EPR is that as more data become available the model could be retrained to produce more accurate and comprehensive predictions.

References

[1] H. G. Poulos and . E. . H. Davis, Pile foundation analysis and design, New York: Wiley, 1980.

[2] H. Matlock and L. C. Reese, "Generalized solutions for laterally loaded piles," *Trans ASCE,* vol. 127, p. 1220–48., 1962.

[3] J. C. Portugal and . P. S. Seco e Pinto, "Analysis and design of pile under lateral loads," in *Proceedings of the 11th international geotechnical seminar on deep foundation on bored and auger piles,* Belgium, 1993.

[4] B. Hansen, "The ultimate resistance of rigid piles against transversal force," in *Bulletin No.12,* Copenhagen, 1961.

[5] B. B. Broms, "Lateral resistance of piles in cohesive soils," *J Soil Mech Found Eng, ASCE,* vol. 90(SM2), p. 27–63, 1964.

[6] G. G. Meyerhof, "Bearing capacity and settlement of pile foundations," *J Geotech Engrg, ASCE,* vol. 102, no. 3, p. 196–228, 1976.

[7] I. M. Lee and J. H. Lee, "Prediction of pile bearing capacity using artificial neural networks," *Comput Geotech,* vol. 18, no. 3, p. 189–200, 1996.

[8] M. A. Abu-Kiefa, "General regression neural networks for driven piles in cohesionless soils," *J Geotech Geoenv Engrg, ASCE,* vol. 124, no. 12, p. 1177–85, 1998.

[9] A. T. Goh, F. H. Kulhawy and C. G. Chua, "Bayesian neural network analysis of undrained side resistance of drilled shafts," *J Geotech Geoenv Eng, ASCE,* vol. 131, no. 1, p. 84–93, 2005.

[10] O. Giustolisi and D. A. Savic, "A Symbolic Data-driven Technique Based on Evolutionary Polynomial Regression," *Journal of Hydroinformatics,* vol. 8, no. 3, p. 207–222, 2006.

[11] K. M. Rao and K. . V. Suresh, "Measured and predicted response of laterally loaded piles," in *Proceedings of the sixth international conference and exhibition on piling and deep foundations,* India, 1996.

Proceedings of the 22h UK Conference of the
Association for Computational Mechanics in Engineering
2 – 4 April 2014, University of Exeter, Exeter

MODELLING SWELLING INDUCED LATERAL PRESSURE TRANSMISSION CONTROL ON RETAINING STRUCTURES IN EXPANSIVE SOILS

A.Ahangar-Asr[1*], L. Fonseca[1], R Carvalheira[1], I. Silva[1], S. Penha[1], L. Braga[1]
A. A. Javadi[2], A. Johari[3]

[1]School of Architecture, Computing and Engineering, University of East London, UK E16 2RD
[2]College of Engineering, Mathematics and Physical Sciences, University of Exeter, UK EX4 4QF
[3]Department of Civil and Environmental Engineering, Shiraz University of Technology, Shiraz, Iran

*a.ahangar-asr@uel.ac.uk

ABSTRACT

An In this research work the complicated phenomena of swelling behaviour of expansive soils is modelled using an evolutionary approach proposed to develop a structured polynomial model for predicting the lateral swelling pressure of soils on retaining structures considering the effect of EPS geofoam implemented to control the transmitted lateral swelling pressures to the structures. The proposed evolutionary polynomial regression technique possesses the capability of generating a transparent and structured representation of the behaviour of a system from raw data. Field measurement data from literature was used to develop the proposed model. Comparison of the developed model predictions with the field measurement data revealed that the proposed model is robustly capable of capturing, predicting and generalising predictions to unseen data cases. The merits and advantages of the proposed methodology are also discussed.

Keywords: *lateral swelling pressure, expansive soils, retaining structures*

1. Introduction

Damages to constructions and structures of different types induced by expansive soils are extensive and are described in detail in civil and geotechnical engineering literature [1]. Due to the non-homogenous nature of soils and also contribution of a variety of parameters to their swelling behaviour no mathematically and theoretically comprehensive models has been presentenced so far to be able to completely predict the swelling aspect of the behaviour soils. Different materials with high compressibility characteristics of different types have so far been used in geotechnical engineering structures to deal with the swelling pressure problems related to expansive soils including bales of hay, glass-fiber and cardboard [2]. Due to the nature of these materials, in general, their stress–strain and volume change behaviour is not completely predictable for engineers. In fact, using some of these materials might result in potential explosion hazard because of the generation of methane gas due to anaerobic decomposition of organic materials in confined conditions [3]. Geofoam is one of the materials with desirable compressibility characteristics for engineers to be used as an expansion induced stress absorbent material. The great advantage of this material is that it does not have the hazardous nature as some other materials with similar compressibility properties. There are different types of geofoam with the potential of application to construction industry; however, selecting a suitable type of geofoam must be done considering engineering characteristics and also cost and environmental implications. Experience indicates that most useful geofoam material is EPS geofoam from compressibility point of view [4].
According to literature, geofoams and particularly EPS are widely implemented in geotechnical engineering applications including roads and pavements [4], embankments [5] and retaining structure [6]. In this paper a new approach is presented to develop a model to predict the lateral swelling pressure of expansive soils on adjacent structures considering the effect of EPS geofoam. The proposed evolutionary polynomial regression technique introduces a new unified, clear and physically plausible framework in which different aspects of soil behaviour can be directly captured from experimental data and be

represented in the form of mathematical expressions. The developed models are capable of satisfactorily explaining the physics of the problem. The capabilities of the suggested methodology are demonstrated in this study by applying it to experimental data from literature [7] and developing a model to predict the controlling effect of EPS in swelling pressure transmission to structures.

2. Modelling technique

Evolutionary polynomial regression is a data-driven method based on evolutionary computing, aimed to search for polynomial structures representing a system. A general EPR expression can be presented as [8]:

$$y = \sum_{j=1}^{n} F(X, f(X), a_j) + a_0 \quad (1)$$

where $\boldsymbol{y}$ is the estimated vector of output of the process; $\boldsymbol{a_j}$ is a constant; $\boldsymbol{F}$ is a function constructed by the process; $\boldsymbol{X}$ is the matrix of input variables; $\boldsymbol{f}$ is a function defined by the user; and $\boldsymbol{n}$ is the number of terms of the target expression. The general functional structure represented by $F(X, f(X), a_j)$ is constructed from elementary functions by EPR using a Genetic Algorithm (GA) strategy. The GA is employed to select the useful input vectors from X to be combined. The building blocks (elements) of the structure of F are defined by the user based on understanding of the physical process. While the selection of feasible structures to be combined is done through an evolutionary process, the parameters a_j are estimated by the least square method. This technique uses a combination of the genetic algorithm to find feasible structures and the least square method to find the appropriate constants for those structures. In particular, the GA allows a global exploration of the error surface relevant to specifically defined objective functions. By using such objective (cost) functions some criteria can be selected to avoid the overfitting of models, push the models towards simpler structures and avoid unnecessary terms representative of the noise in the data. An interesting feature of EPR is in the possibility of getting more than one model for a complex phenomenon. A further feature of EPR is the high level of interactivity between the user and the methodology. The user physical insight can be used to make hypotheses on the elements of the target function and on its structure. Selecting an appropriate objective function, assuming pre-selected elements based on engineering judgment, and working with dimensional information enable refinement of final models. The level of accuracy at each stage is evaluated based on the coefficient of determination (COD) i.e., the fitness function as:

$$\mathbf{COD} = 1 - \frac{\sum_{N} (\mathbf{Y}_a - \mathbf{Y}_p)^2}{\sum_{N} \left(\mathbf{Y}_a - \frac{1}{N} \sum_{N} \mathbf{Y}_a \right)^2} \quad (2)$$

where $\boldsymbol{Y_a}$ is the actual output value; $\boldsymbol{Y_p}$ is the EPR predicted value and $\boldsymbol{N}$ is the number of data on which COD is computed. If the model fitness is not acceptable or the other termination criteria (in terms of maximum number of generations and maximum number of terms) are not satisfied, the current model goes through another evolution in order to obtain a new model. Detailed explanation of the method can be found in [8], [9].

3. The proposed model

Thirty six cases of data from experimental measurements [4] were used to develop the proposed model in this study. Data was divided into training and validation cases. Two input parameters were used to develop the suggested EPR model for predicting the swelling behaviour of expansive soils with application of EPS geofoam as a stress absorbent material. The two input parameters were considered to be the time (T) in minutes and the thickness (t) of the EPS geofoam implemented to control swelling effects on the structure adjacent to the heaving soil in millimetres. The output parameter was the lateral swelling pressure (LSP) in kPa transmitted to the structure.

$$LSP = 4.6 \times 10^{-3} T - 3.6 \times 10^{-4} T.t + 1.5 \times 10^{-5} T.t^2 - 1.8 \times 10^{-7} T.t^3 - 2.3 \times 10^{-13} T^3 \quad (3)$$

Table 1 represents the values of the coefficient of determination (COD) for training and testing sets of data. Figures 1 shows comparison between the suggested evolutionary polynomial regression-based model predictions with experimental measurements for training data. After completing the training stage, the developed model was validated using a second set of data that was kept unseen to EPR in the training time. This was done to examine the generalisation capabilities of the developed model to cases that have not been seen by EPR in the model training and development process. Figure 2 shows the result of comparisons made between the EPR model predictions for testing (unseen) cases of data and the experimental measurements. It can be seen that the suggested model is capable of predicting swelling pressure for testing cases of data to a high level of accuracy. The results shows that the EPR methodology has robustly and accurately been capable of capturing, reproducing and generalising the relationship between the contributing parameters to the swelling pressure development and transmission in expansive soils considering the controlling effect of EPS geofoam.

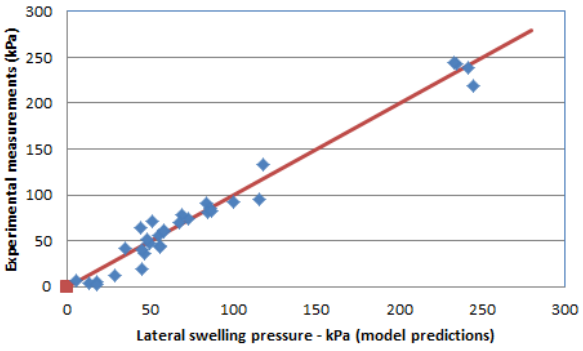

Figure 1. Comparison between the predicted swelling pressure values and the actual data (training)

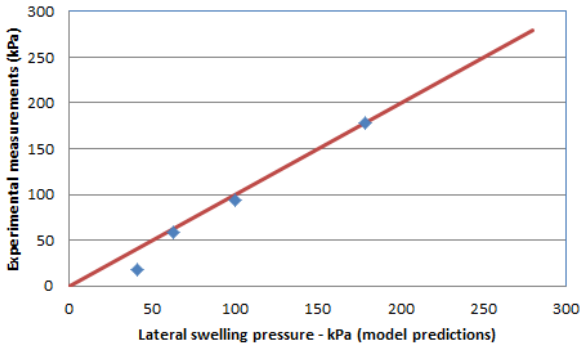

Figure 2. Comparison between the predicted swelling pressure values and the actual data (testing)

Table 1: COD values for the developed prediction model

EPR model	COD values (%)
Train	96
Test	98

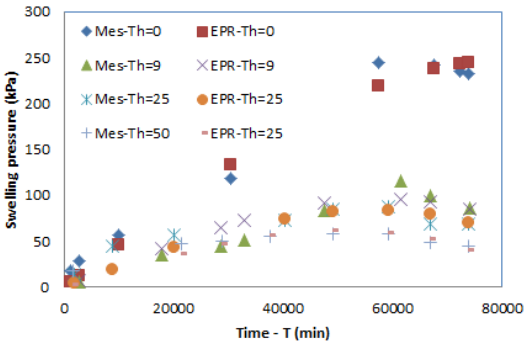

Figure 3. EPR predictions and experimenttal measurements for different EPS thicknesses (Mes=Measurement; Th= EPS thickness mm)

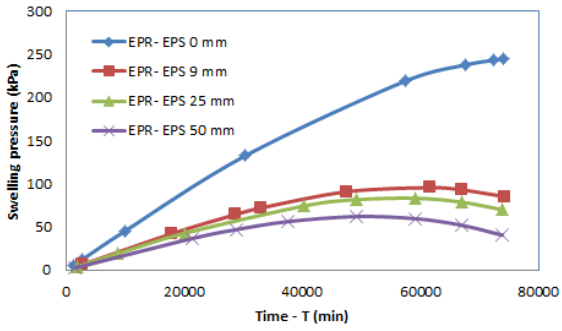

Figure 4. Model predictions of the swelling pressure (effects of time and EPS thickness)

Figure 3 shows the swelling pressure against the time graph for different thicknesses of the EPS geofoam and also for the case that no geofoam is used between the soil and structure, for both experimental data and EPR model predictions. A close consistency can be easily noticed between the developed model predictions and experimental measurements. Figure 4 shows EPR predictions for all 4 tested cases (no geofoam, 9mm, 25mm and 50mm EPS geofoam). According to the test results, by using EPS geofoam the swelling pressure is largely taken by the EPS and the amount of pressure being transmitted to the structure is substantially reduced [7]. From figure 4 it is evident that the expected effect of EPS geofoam

(as seen in tests [7]) is correctly captured by EPR and accurate predictions are also produced by the developed model. According to figure 4, also the positive effect of increasing thickness of the EPS geofoam layer in controlling the transmitted lateral pressures to the structure is correctly foreseen.

4. Summary and conclusion

An EPR model was developed and validated using a database of experiments involving 36 cases of test data. The model predictions were compared to the experimental data. Comparison of the results shows that the developed EPR model provides accurate predictions of the swelling pressure transmitted to the structures from the cohesive soils surrounding them due to heaving. The data used to develop the model included the thicknesses of EPS geofoam material, a highly compressible material, placed between the structure and the soil to absorb the heaving pressure from the soil side with the aim of reducing the transmitted swelling pressures to the structures. The developed model was also shown to be able to correctly and accurately predict the effect of presence of EPS geofoam in controlling the swelling pressures being passed to the structures. According to the model, as expected, placing even a thin (9 mm) layer of EPS hugely affects the swelling pressure applied by the soil to the structure. Increasing the thickness of the EPS geofoam layer increases the pressure control effect of the material and helps reduce the lateral compressing effect of the cohesive soil on the structure. The developed model presents a structured and transparent representation of the swelling control effect of EPS geofoam on structures allowing a physical interpretation of the problem that gives the user an insight into the relationship between the swelling behaviour of soil and contributing/controlling parameters. From practical point of view, the EPR models presented in this paper is very accurate and easy to use. In the EPR approach, no pre-processing of the data is required and there is no need for normalization or scaling of the data. Performance of the model is being validated using an unseen set of data. This allows examining the generalization capabilities of the developed model. Thus, an unbiased performance indicator is obtained on the real capabilities of the model. Also, as more data becomes available the quality of the prediction can be easily improved. This can be done by retraining EPR using the more comprehensive set of data to achieve more general, effective and accurate models.

References

[1] G. Xeidakis, P. Koudoumakis and A. Tsirambides, “Road construction on swelling soils: the case of Strymi Soils, Rhodope, Thrace, Northern Greece,” *Bull Eng Geol Environ,* vol. 63, pp. 93-101, 2004.

[2] J. S. Horvath, “The compressible inclusion function of EPS geofoam,” *Geotext Geomembrane,* vol. 15, pp. 77-120, 1997.

[3] U. Ground engineering, “Data collection will clarify clayboard doubts,” Thomas Telford, April 1991.

[4] G. Beinbrech and R. Hillmann, “EPS in road construction—current situation in Germany,” *Geotext Geomembranes,* vol. 15, no. 1-3, p. 39–57, 1997.

[5] H. L. Riad, A. L. Ricci, P. W. Osborn and J. S. Horvath, “Expanded polystyrene (EPS) geofoam for road embankments and other lightweight fills in urban environments,” in *Soil and rock America - 2003; 12th Panamerican Conference on soil mechanics and geotechnical engineering/39th US rock mechanics symposium Cambridge*, Massachusetts, USA, 2003.

[6] S. Zarnani and R. J. Bathurst, “Experimental investigation of EPS geofoam seismic buffers using shaking table tests,” *Geosynth Int,* vol. 14, no. 3, p. 165–177, 2007.

[7] S. B. Ikizler, . M. Aytekin and E. Nas, “Laboratory study of expanded polystyrene (EPS) geofoam used with expansive soils,” *Geotext Geomembranes,* vol. 26, no. 2, p. 189–195, 2008.

[8] O. Giustolisi and D. A. Savic, “A Symbolic Data-driven Technique Based on Evolutionary Polynomial Regression,” *Journal of Hydroinformatics,* vol. 8, no. 3, pp. 207-222, 2006.

[9] A. A. Javadi and M. Rezania, “Applications of artificial intelligence and data mining techniques in soil modelling,” *Geomechanics and Engineering, An International Journal,* vol. 1, no. 1, pp. 53-74, 2009.

Proceedings of the 22nd UK Conference of the
Association for Computational Mechanics in Engineering
2 – 4April 2014, University of Exeter, Exeter

LEVEL SET OPTIMISATION METHOD FOR CONTINUOUS FIBRES PATHS

***Christopher J. Brampton[1] and H. Alicia Kim[2]**

[1]Department of Mechanical Engineering, University of Bath, Bath, United Kingdom, BA2 7AY

*c.j.brampton@bath.ac.uk

ABSTRACT

Advanced fibre placement (AFP) composite manufacturing technology offers a means to tailor the fibres for complex loading environments and significantly improve the overall structural efficiency. This paper introduces a new method to optimise the continuously varying fibre paths using a level set method. The paths of the fibre tows are defined by constant level set function values, describing a series of continuous equally spaced fibre paths. Sensitivity is derived and used to update the level set function. This optimises the fibre paths to minimize structural compliance, while maintaining the continuous fibre paths, producing a solution that can be manufactured using AFP. The optimisation method is demonstrated on a test problem of an out of plane loaded plate. It is then applied to design an inter-tank plate of a space shuttle propellant tank structure.

Keywords: *composite fibre path optimisation; advanced fibre placement; level set method;*

1. Introduction

The orientation of the fibres of composite laminates can be optimized to significantly improve structural performance over the traditional quasi-isotropic fibre construction without increasing the weight [1]. Advanced fibre placement (AFP) manufacturing technology offers a greater flexibility in tailoring the structure of composite panels by laying down fibre tows in curved and continuously varying paths. However, how to design the optimal fibre paths for a composite structure remains an unresolved research problem.

One approach is to optimise the fibre angles of piece-wise constant finite elements however, the continuity of fibre angles between elements is not easily enforced, often leading to solutions with large changes in fibre orientation between elements [2, 3], that cannot be manufactured using AFP techniques. The problem is also non-convexed so this approach is dependent on the initial solution [3]. Lamination parameters can be used to optimise stiffness properties of an anisotropic element [4]. However the suitability of the solution for AFP manufacture depends on the construction of continuous fibre paths from the lamination parameters, [5]. Another approach is to represent the fibre paths as a curvilinear function, optimising their coefficients [1, 6]. This ensures the continuity of fibre angles in the final solution, but reduces the design space and may lead to a sub-optimal solution [3].

The level set method has fast become a popular approach to moving boundary and front tracking problems in a wide range of fields such as image processing, interface motion tracking, and topology optimisation, due to the flexibility in describing complex change of boundaries [7, 8]. This paper introduces a new optimization method for composite fibre paths using the level set method. This method directly optimizes the fibre paths ensuring continuity of the fibre angles between elements like the curvilinear parameterization, but with a greater flexibility in fibre path definition.

2. Method

The level set function (lsf) is an implicit signed distance function, with values stored at the finite element nodes. The path of the primary fibre path is defined by the path of the locations where the lsf function is equal to zero (φ=0). The other fibre paths are defined by constant level set function values, describing a series of continuous equally spaced fibre paths through the laminate, shown in figure 1.

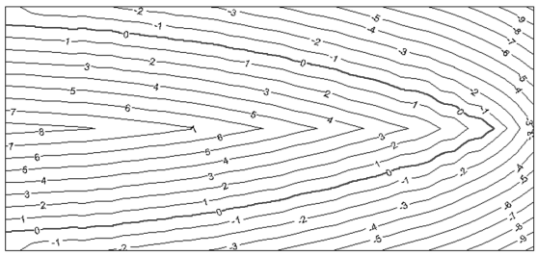

Figure 1: Fibre paths defined by lines with constant integer level set function values.

Since the fibres follow the constant lsf path, the elmental fibre orientation can be defined to be perpendicular to the maximum gradient of the level set function over the element, as shown in figure 2. The elemental fibre orientation can be calculated in each element using Eq. (1), where x and y are the global coordinates, i is the local node number and N_i is the element shape functions for each node.

$$\theta_e = \frac{\pi}{2} + \arctan\left(\frac{d\varphi/dy}{d\varphi/dx}\right) \qquad \text{where: } \frac{\partial\varphi}{\partial x} = \sum_i^4 \frac{\partial N_i}{\partial x}\varphi_i \quad \text{and} \quad \frac{\partial\varphi}{\partial y} = \sum_i^4 \frac{\partial N_i}{\partial y}\varphi_i \qquad (1)$$

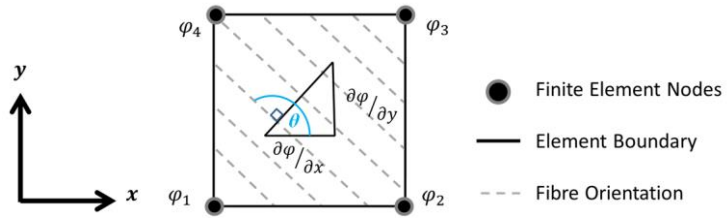

Figure 2: Definition of the fibre orientation within a finite element from the level set function.

The level set fibre path optimisation method to minimise structural compliance, E, is as follows.

1. Initialise the level set function values to describe the initial fibre paths of a laminate.
2. Calculate the element fibre orientation, θ_e, from the nodal level set function values.
3. From the element fibre orientations calculate the stiffness and solve the linear elastic problem.
4. Calculate the sensitivity of the global compliance to changes in the element fibre orientation using the energy based sensitivity analysis from Luo & Gea (1998) [3].
5. Calculate the sensitivity of the element, e, fibre orientation to change in lsf value of node i, using Eq.(2).

$$\frac{\partial\theta_e}{\partial\varphi_i} = \left(\frac{\partial N_i}{\partial y}\left(\frac{\partial N_i}{\partial x}\varphi_i + \sum_{\substack{p=1\\p\neq i}}^4 \frac{\partial N_p}{\partial x}\varphi_p\right) - \frac{\partial N_i}{\partial x}\left(\frac{\partial N_i}{\partial y}\varphi_i + \sum_{\substack{p=1\\p\neq i}}^4 \frac{\partial N_p}{\partial y}\varphi_p\right)\right) \Bigg/ \left(\frac{\partial N_i}{\partial x}\varphi_i + \sum_{\substack{p=1\\p\neq i}}^4 \frac{\partial N_p}{\partial x}\varphi_p\right)^2 \left[\left(\frac{\frac{\partial N_i}{\partial y}\varphi_i + \sum_{\substack{p=1\\p\neq i}}^4 \frac{\partial N_p}{\partial y}\varphi_p}{\frac{\partial N_i}{\partial x}\varphi_i + \sum_{\substack{p=1\\p\neq i}}^4 \frac{\partial N_p}{\partial x}\varphi_p}\right)^2 + 1\right] \qquad (2)$$

6. Use the Hamilton Jacobi formulation and the sensitivities to update the local lsf values around the primary fibre path using Eq.(3), where $\Delta\theta_{max}$ is the move limit set for stability, and ne is the number of elements that neighbour node i and are intercepted by the primary tow path.

$$\varphi_i^{iter+1} = \varphi_i^{iter} + \Delta\theta_{\max} \sum_{e=1}^{ne} \frac{\partial E}{\partial\theta_e}\frac{\partial\theta_e}{\partial\varphi_i} \qquad (3)$$

7. Update the level set function values for the rest of the nodes using the fast marching method [8]. The level set function now describes a set of improved evenly spaced fibre paths.
8. Check for convergence, if change in structural compliance is less than a user set critical value.
9. If procedure hasn't converged return to step 2 to begin the next iteration.

3. Test Model: Plate Under Out of Plane Load

As an example the fibre paths of a square plate, with four simply supported corners and an out-of-plane load applied at the centre, will be optimised, figure 3A. The plate is modelled by 30 × 30 four-

node bilinear Kirchoff shell elements. The material properties are E_L=137.9GPa, E_T=10.34GPa, ν_{LT} = 0.29, ν_{TL} = 0.021, G_{LT} = G_{LW} = 6.89GPa and G_{TW} = 3.7GPa. The initial fibre paths, figure 3B, are obtained from the lsf function of an isotropic topology optimisation solution [7]. The level set optimisation procedure is applied to these initial fibre paths with the move limit, $\Delta\theta_{max}$, set at 5°.

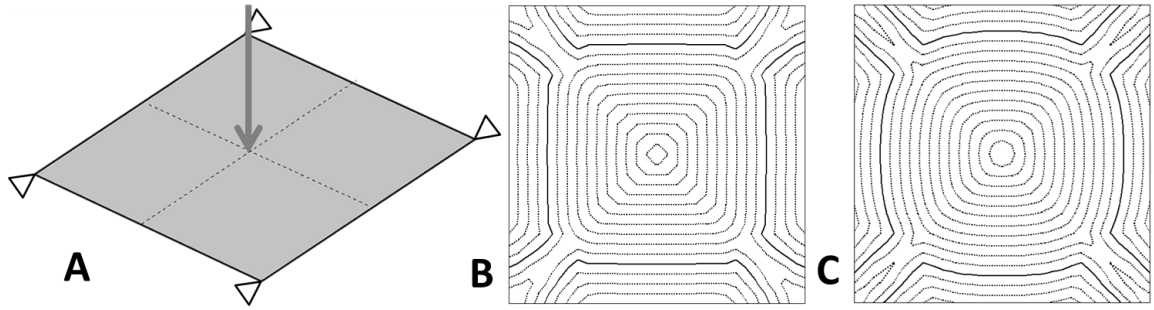

Figure 3: A, Definition of the out of plane loaded plate optimisation problem. B, Initial solution of the out of plane loaded plate for level set tow paths optimisation. C, Optimised tow paths solution. The solid line in figures B and C indicates the primary fibre path where the level set function, φ=0.

The optimisation procedure converges after 1500 iterations, producing the result shown in figure 3C. The anisotropic level set fibre paths optimisation refines the orientation of the fibre paths to reduce the overall compliance by 20%.

4. Application: Shuttle Inter Tank Plate Optimisation

A realistic design problem is now optimised, the inter-tank plate from the external fuel tank of the shuttle orbiter launch system. The inter tank plate transfers the load from the solid rocket boosters to the fuel tank. A simplified model of the inter-tank plate is to be optimised, assuming that it is a curved plate of uniform thickness with no holes. Symmetry is assumed so only half the plate is modelled. The model was meshed using a 66×28 four-node bilinear Kirchoff shell elements. The loading conditions and mesh are shown in figure 4. The composite material properties are the same as the Plate model in section 3.

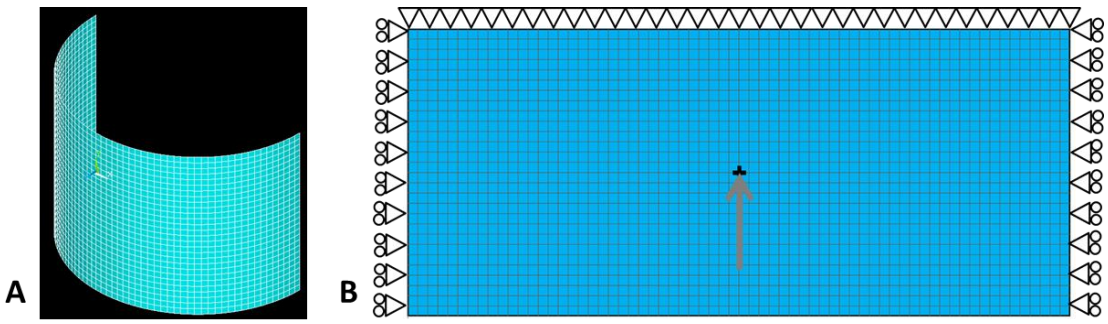

Figure 4: Shuttle inter-tank plate model mesh in 3D. B, Shuttle inter-tank plate model mesh and loading conditions represented in 2D.

The level set function is initialised manually by observation of an unconstrained element based optimisation solution for the same problem, to describe the fibre paths shown in figure 5A. Multiple primary level set paths are used in this model to satisfy the regional demands on the orientation of the fibre paths. When multiple primary fibre paths are used the element fibre orientation is controlled by the primary fibre path it is closest too. Using fibre cutting and tow drop techniques, regions of different fibre paths can be constructed in the same laminate using AFP manufacturing [1]. The initial fibre path orientation is optimized using the level set optimisation procedure with the move limit, $\Delta\theta_{max}$, set at 5°.

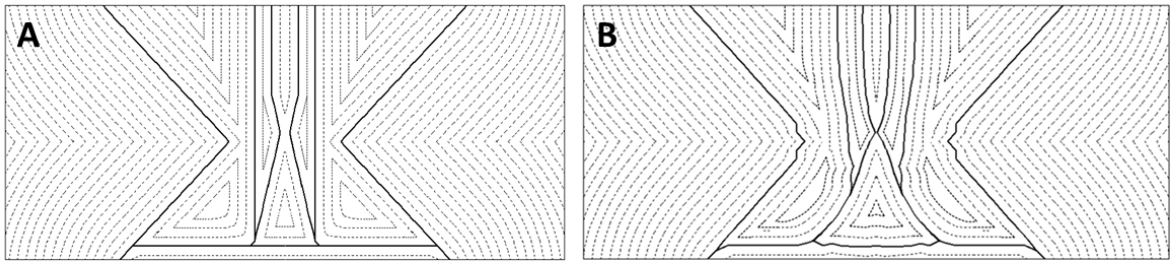

Figure 5: A, Initial tow paths of the shuttle inter-tank plate model for level set tow paths optimisation with multiple level sets. B, Optimum fibre paths solution for shuttle inter-tank plate. The solid line in figures B and C indicates the primary fibre path where the level set function, $\varphi=0$.

The optimisation procedure converges after 440 iterations, producing the result shown in figure 5B. An 8.28% reduction in the structural compliance from the initial design is achieved by the level set optimization method's refinement of the fibre paths. The compliance of the optimal level set solution is 5.4% higher than the unconstrained elemental solution of the same problem, as would be expected given the greater constraint on the level set optimal solutions. However the element solution could not be manufactured due to discontinuities in the element fibre orientations. The extra constraints upon the level set solution produce continuous fibre paths that could be manufactured using AFP.

5. Conclusion

In the test cases the level set method was able to optimize the orientation of the fibre paths to significantly reduce the overall compliance of the structure and produce a solution that could be manufactured by the AFP technique. However it is evident that the solution is dependent on the initial solution. Also the level set fibre path optimisation is slow; a small move limit is required to achieve a stable convergence. Further research is needed to reduce the dependency of the level set optimisation method on the initial solution and to obtain faster convergence. However this work demonstrates the feasibility of using a level set method to optimise composite fibre paths.

Acknowledgements

We would like to thank Dr. Chauncey Wu from NASA Langley Research Center for valuable input during this project.

References

[1] K.C. Wu Design and Analysis of Tow-Steered Composite Shells Using Fiber Placement. *American Society for Composites, 23rd Annual Technical Conference Memphis,* TN, Sept 9-11 2008.

[2] J.H. Luo, H.C. Gea. Optimal orientation of orthotropic materials using an energy based method. *Structural Optimization*, 15, 230-236, 1998a

[3] H. Ghiasi, K. Fayazbakhsh, D. Pasini, L. Lessard. Optimum stacking sequence design of composite materials Part II: Variable stiffness design. *Composite Structures*, 93, 1-13, 2010.

[4] S. Setoodeh, M.M. Abdalla, Z. Gürdal. Design of variable–stiffness laminates using lamination parameters. *Composites Part B: Engineering*, 37(4-5) 301-309, 2006.

[5] J.M.J.F. van Campen, C. Kassapoglou, Z. Gürdal, Generating realistic laminate fiber angle distributions for optimal variable stiffness laminates, *Composites: Part B*, 43 354-360, 2012.

[6] Z. Wu, P.M. Weaver, R. Gangadharan, B.C. Kim. Buckling analysis and optimisation of variable angle tow composite plates. *Thin-Walled Structures* 60: 163-172, 2012

[7] P.D. Dunning, H.A. Kim. Investigation and improvement of sensitivity computation using the area-fraction weighted fixed grid FEM and structural optimization. *Finite Elements in Analysis and Design*, 47, 933-941, 2011.

[8] J.A. Setian Level set methods and fast marching methods. *Cambridge University, Press, New York, 2nd edition.*

Proceedings of the 22nd UK Conference of the
Association for Computational Mechanics in Engineering
2 – 4April 2014, University of Exeter, Exeter

OPTIMISATION OF A VENTURI MIXER DESIGN TO PROMOTE EFFICIENT COMBUSTION IN A PRE-MIX BURNER

***Jennifer S. Thompson[1], Oubay Hassan[2], David Carswell[3], Sam Rolland[4] Nicholas P. Lavery[5] and Johann Sienz[6]**

[1 to 6] College of Engineering, University of Swansea, Swansea, SA2 8PP

*jennifer.thompson@swansea.ac.uk

ABSTRACT

A goal driven optimisation process has been undertaken for a Venturi-type premixer. Premixers are used to supply the correct mixture of fuel and oxidiser to a premix burner; providing the correct quantity of excess air results in a reduction of nitrogen oxides (NOx). A computational fluid dynamic (CFD) simulation has been undertaken using FLUENT 14.0, verified by experimental data. This CFD model has been used in Ansys workbench's "Design Exploration" software to establish an optimised design of the premixer, considering four geometrical parameters and their effect on two Objective Functions; the completeness of mix of the fuel and oxidiser, and the correct quantity of excess air.

Keywords: *Premix; Venturi; CFD; Optimisation*

1. Introduction

Natural gas processing facilities require gas pressure reducing stations; where, the high pressure at which gas has been transported through pipelines is reduced to a lower pressure for processing. As the pressure is reduced, due to the Joule Thompson effect, the temperature also reduces i.e. isenthalpic. Therefore, in order to keep the gas temperature elevated above 0°C, a shell-pipe heat exchanger is utilised; the radiant section of which can employ a premix burner, supplied by Venturi-type entrainment premixers (Figure 1).

Figure 1: Venturi-type entrainment mixers (left image) supply a premix burner (right image)

In premix burners the fuel and oxidiser are completely mixed prior to the initiation of combustion. Increasing the excess air results in a leaner mix, lower flame temperature and reduced levels of nitrogen oxides (NOx) emissions. Minimising pollutant emissions such as NOx is a desired outcome due to the health risks that these pollutants pose. Considering the pressure let down system, optimal combustion conditions require that the burner should be supplied with a mixture containing 30% excess air. If a premixed flame is termed stoichiometric when the fuel and oxidiser consume each other completely, producing only carbon dioxide and water; then, a lean premixed flame involves an excess of oxidiser in the reaction, with an additional oxygen component found in the combustion products [1]. The stoichiometric air-to-fuel ratio (AFR) can be calculated from the reaction equation and can be quoted in terms of mass or volume.

Considering this design of entrainment premixer, which operates utilising the law of conservation of momentum; the fuel stream is used to inspirate the oxidiser. The fuel is supplied at a high velocity

after passing through a very small orifice. At this orifice, the oxidiser is made available as an (initially) stationary source. As the fuel's velocity is dissipated through expansion, to maintain the momentum of the motive fluid, additional air must be entrained into the flow [1, 2]. The passage of a fluid through a constriction, causing a pressure drop and subsequent increase in velocity is termed the Venturi effect; and is why this type of premixer can be referred to as Venturi-type.

The primary objective of the current work is to utilise computational fluid dynamics (CFD) to undertake a 2D axisymmetric analysis of the premixer. The model is to be compared to experimental results, prior to utilising a Goal Driven Optimisation (GDO) process in the Ansys Workbench 14.0, "Design Exploration" software [3]; establishing if the premixer's geometry is optimised. Two Objective Functions have been identified, which consider both the premixer's ability to draw in the correct quantity of excess air; and, the completeness of mix between the fuel and air.

2. Experimental procedure

In order to establish confidence in the CFD results and subsequent optimisation of the premixer, experimental work was undertaken to establish the effect of adjuster plate position (see Figure 2) and pressure on the velocity of the flow through the mixer. Intrusive methods of velocity measurement were utilised, including both a vane anemometer, 65mm in diameter, providing a measurement range of 0.4 to 30 m/s ($\pm$ 2%), Figure 2; and a thermoanemometer straight probe (i.e. a hot wire anemometer), with a velocity range of 0 to 50 m/s ($\pm$ 3%). Different devices were used to ensure accurate, repeatable readings were established at critical locations within the flow. Several readings were taken with the thermoanemometer at the mixer outlet, to establish a velocity profile. At the measurement locations, flow disruptions were not expected e.g. shock waves; therefore, intrusive methods were deemed acceptable and the timeliest approach to implement [4].

Figure 2: Adjuster plate position was altered (left image) and the average velocity was recorded (right image)

3. Computational model

Several previous CFD based investigations of other designs of premixers have been undertaken [2, 5-8. A review of these works enabled the most appropriate simulation methodology to be identified. The CFD for this study was undertaken using the commercially available FLUENT v14.0 software [3]. FLUENT utilises a cell-centred finite volume method and the governing equations were discretised with a second order upwind scheme, using the SIMPLE algorithm to couple the momentum and pressure equations [3]. After assessment of several turbulence models, including the Standard κ-ε [5], Realisable κ-ε [6], Enhanced κ-ε [7] and the κ-Ω [8] models; the first one was identified as the most appropriate. A full convergence and mesh sensitivity study was undertaken, with the steady state solution considered converged when data extracted from the mixer's outlet was found to differ by no more than 1%. Several meshes were constructed, each with elements focussed in the region of the issuing jet and at the walls. Mesh independence was achieved with a mesh consisting of 46,000 elements, i.e. element dimension of δ; with meshes having been considered in the range of 4δ to δ/4.

The boundary conditions are labelled in Figure 3, the gas was supplied at a pressure of 1.4bar (gauge); the pressure at the air inlet and at the mixer's outlet was set as atmospheric. When simulating the mix between natural gas and air, the percentage mass of each constituent was required as a boundary condition. The species transport model in FLUENT predicts the local mass fraction of each

species Y_i, by solution of a convection-diffusion equation (1) for the i^{th} species [3]:

$$\frac{\partial}{\partial t}(\rho Y_i) + \nabla . (\rho \vec{v} Y_i) = -\nabla . \vec{J_i} + R_i + S_i \quad (1)$$

Where, R_i is the net rate of production of the species i by chemical reaction (discounted if no reaction) and S_i is the rate of creation plus any user-defined sources.

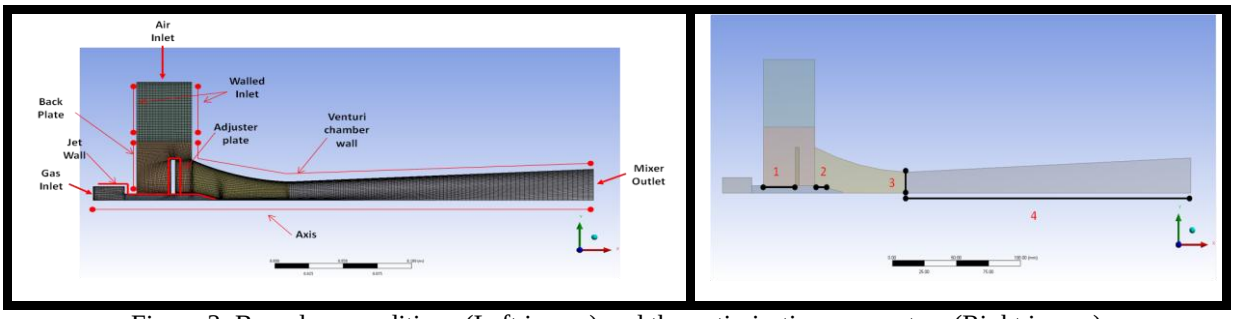

Figure 3: Boundary conditions (Left image) and the optimisation parameters (Right image)

There are four parameters under consideration for the optimisation of the premixer, clearly identified in Figure 3: (1) position of the adjuster plate, which controls the inspirated air; (2) length of the gas jet; (3) radius of the venturi chamber's throat; and (4) length of the chamber. In a general optimisation problem, the aim is to minimise a function, the "Objective Function". For this problem two Objective Functions have been identified: the mass AFR value being representative of a mixture of 30% excess air; and, completeness of mix, by attaining a standard deviation value of zero for the mixture constituents at the outlet. The goal driven optimisation process in Ansys workbench provides several options for Design of Experiments and Response Surface generation [3]. On consideration of the options available, the Optimal Space Filling with central composite design (CCD) sampling and the Kringing Meta model have been used to generate the design space. The multi-objective genetic algorithm (MOGA) [3] was used for the optimisation of the defined Objective Functions.

4. Results

4.1 Experimental results and comparison with the model

Area average velocity readings were measured at the mixer's outlet at an operating pressure of 1.4bar (gauge). These were compared with the simulation results. As clearly shown in Figure 4 below, a similar trend was captured, where pulling back the adjuster plate beyond a certain distance from the venturi chamber inlet, no longer had any effect on the quantity of air inspirated. The average velocity values maximised to approximately 18 m/s (experimentally), and 16.5 m/s (simulated); a less than 10% difference. Additionally, the straight probe velocity values measured at various locations and at different operating pressure values also compared favourably, with the model generally found to over predict by no more than 10%. In particular, the velocity values at the air inlet were found to be simulated very accurately (< 5% error). Subsequently, it can be concluded that the simulation has accurately captured the fluid dynamics of the premixer.

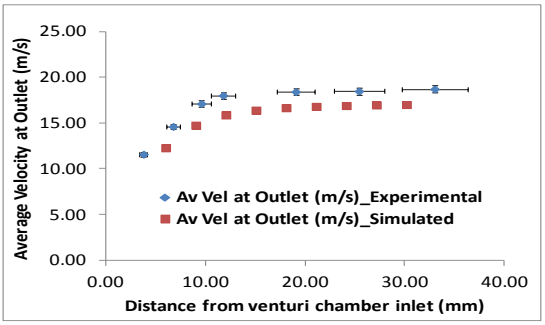

Figure 4: Experimental and CFD results showing the effect of adjuster plate position on velocity at the mixer's outlet (vertical error bars of ± 2% quoted for device and horizontal error bars of ± 10% for parallax error).

4.1 Optimisation

The optimisation process was undertaken by considering parameters (1) to (4) over restricted ranges based on the limitations of size of the premixer, due to restricted space for installation in the gas pressure reducing station. Figure 5, shows the quantified effect of the four parameters on the Objective Functions: the mass AFR value associated with 30% excess air; and, the extent of mixedness, measured by the standard deviation values provided for methane (the main constituent of natural gas) and air. It is evident that the radius of the throat is the most influential design parameter on both mixedness and air-fuel ratio and that the length of the jet (2) has no effect on the quantity of air drawn in by the mixer, but does affect the quality of mixing.

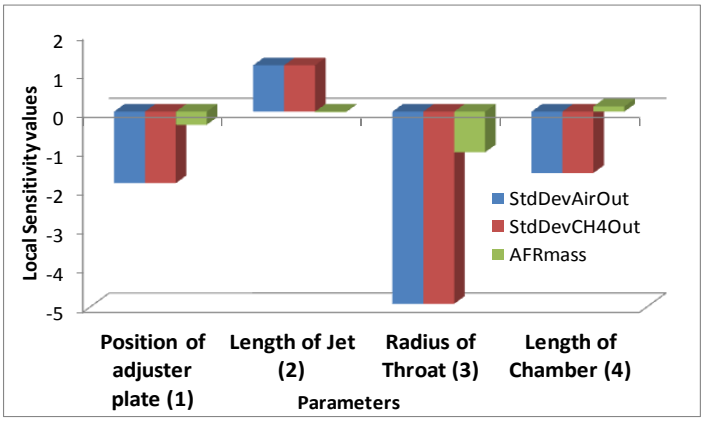

Figure 5: Local sensitivities of the four parameters considered for optimisation of the premixer

The optimisation process provided three "Candidate Points", which were all verified against simulated values. Generally, the optimisation suggested a 4.55% increase in the length of the chamber (4); a 3.3% increase in the radius of the throat; a 150% increase in the length of the jet (2); with the adjuster plate located at approximately a mid-location.

5. Conclusions and Future work

A numerical model of a venturi type premixer has been shown to be comparable to experimental data, to within 10% of velocity values measured, illustrating similar trends of flow behaviour. Based on this, a goal driven optimisation has been undertaken which has suggested minor modifications to the premixer's geometry that will improve the completeness of mixing between air and natural gas whilst achieving the correct ratio of fuel to oxidiser for cleaner combustion. Potentially, future work could consider a more radical alteration to the premixer's design, to assess if further improvements could be attained.

References

[1] C.E. Baukal. The John Zink Combustion Handbook, CRC Press, 2001.

[2] J. Zhang. Micro Injection Fuel/Air Premixer/Combustion, Phd Thesis, Louisiana State University, 2007.

[3] Ansys Inc. Software, www.ansys.com, (accessed 2013).

[4] T. B. Gatski and J. Bonnet, *Compressibility, Turbulence and High Speed Flow*, 2nd Edition, Elsevier, 2013.

[5] D. Danardono et al. Optimization the design of venture gas mixer for syngas engine using 3D CFD modelling. *Journal of Mechanical Science and Technology*, 25, 2285-2296, 2011.

[6] R. Kamali and A. Binesh, The importance of sensitive parameters on the combustion in a high velocity oxygen-fuel spray system, *International Communications in Heat and Mass Transfer*, 36, 978-983, 2009.

[7] E. Smith et al, The round jet inflow-condition anomaly for the κ-ε turbulence model, University of Adelaide, 2001.

[8] R. Morgans et al, Application of the revised Wilcox (1998) κ-Ω Turbulence model to a jet in co-flow. *2nd Internal Conference on CFD in the Minerals and Process Industries (CISRO, Melbourne)*, 1999.

Proceedings of the 22nd UK Conference of the
Association for Computational Mechanics in Engineering
2 – 4April 2014, University of Exeter, Exeter

RESEARCH ON POTABLE WATER NETWORK AUTOMATIC FLUSH DEVICE OPERATION OPTIMIZATION

***Xiongfei Xie[1], Mahmoud Nachabe[2] and Bo Zeng[3]**

[1]Pinellas County Department of Environ. and Infra., 14 S. Fort Harrison Ave., Clearwater, FL 33756, USA
[2]Department of Civil and Environmental Engineering, University of South Florida, Tampa, FL 33620, USA
[3]Department of Industrial and Management Systems Eng., University of South Florida, Tampa, FL 33620, USA

*xxie2@mail.usf.edu

ABSTRACT

Maintaining adequate chlorine residual in the water distribution system is crucial to the health of end users and the integrity of system. Depleting un-chlorinated water from pipe line via automatic flush device (AFD) is a feasible measure to maintain water quality. This paper presents an innovative optimization method to minimize the discharge volume for 24-hr horizon through AFD. Three constraints are imposed: maintaining minimum chlorine residual, minimum system pressure, and maximum amount of AFD starts per day. Two parameters are used to describe AFD working conditions: opening extent and open/close status. Accordingly, the single objective optimization problem is solved in two stages: 1) determining the base discharge rate of each AFD; and, 2) developing operation pattern of each AFD. In the first stage, each AFD opens all the time, discharge flow rates of AFD are the decision variables. A reduced gradient algorithm is used to reduce the discharge rates. In the second stage, decision variables are the discharge patterns of these AFD. One day is divided into certain time intervals. AFD is either open or closed in one time interval. Simulated annealing is used to search global optimum. EPANET 2.0 is used as hydraulics and water quality simulator. Matlab code is developed to guide the searching of optimal solution. The method is applied to the water network located at the south Pinellas County.

Keywords: *water distribution system; water quality; automatic flushing device; optimization*

1. Introduction

Drinking water distribution system typically consists of pipes, valves, storage tanks, fire hydrants and control equipments. Sufficient chlorine residual helps to maintain water quality and the integrity of the water system [1]. One of the most widely used methods is to flush distribution pipes to deplete un-chlorinated water by opening automatic flush device (AFD) or manually opening fire hydrant, blowoff valves. Operating AFD needs less labour than manually opening fire hydrants. Therefore, AFD is gaining popularity in water utilities.

AFD can be initiated either by timer or chlorine sensor, installed in the distribution system. Due to financial and technical reasons, chlorine sensor is not widely used to control AFD. The prerequisite of AFD operation optimization is to determine the chlorine residual in the pipe network; a well calibrated water quality model is needed. Therefore, using timer controlled AFD working in concert with well calibrated water model is a feasible method to minimize AFD discharge. Currently, most AFD in water utilities controlled by timers are programmed empirically.

Literature review shows that no studies have been directly aimed at minimizing AFD discharge. Similar researches, such as operation optimization of pump schedules to minimize energy costs, were reviewed. A variety of optimization algorithms have been developed. Examples include Boolean integer nonlinear programming [2], evolutionary algorithm [3], ant colony algorithm [4] and linear programming greedy (LPG) algorithm [5], to name a few. This paper presents an EPANET-simulation based method to minimize the flushing volume in water distribution system. This is formulated as a single objective operation optimization problem where AFD flushing volume is minimized through optimized AFD opening extent and open/close control strategy.

2. Methodology

Consider a water distribution system with M junction nodes, N automatic flush devices, which are operated for T time intervals. The objective function is the minimization of the total AFD discharge volume

$$E = \sum_{t=1}^{T} \sum_{n=1}^{N} Q_{n,t} \times L \tag{1}$$

where $Q_{n,t}$ = the discharge rate of AFD n at time t (L/min); L = the length of time interval (min). This optimization problem is subject to three constraints: water quality, hydraulics and operation respectively. They are given as

$$C_{m,t} \geq C_{\min} \quad 1 \leq m \leq M \tag{2}$$

$$P_{m,t} \geq P_{\min} \quad 1 \leq m \leq M \tag{3}$$

$$S_n \leq S_o \quad 1 \leq n \leq N \tag{4}$$

where $C_{m,t}$ = the chlorine residual of node m at time t (mg/l); C_{min} = the specified minimum chlorine concentration (mg/l); $P_{m,t}$ = the pressure at Node m at time t (m of water); P_{min} = the minimum allowable pressure in the water distribution system (m of water); S_n = the number of starts for AFD n; and, S_o = the maximally allowable AFD starts per day, it is determined by the AFD characteristics.

Accordingly, discharge rate Q for each AFD is decomposed as a base discharge rate multiplying the open/close status of the AFD. It is given as

$$Q_{n,t} = Q_{n,B} \times D_{n,t} \tag{5}$$

where $Q_{n,B}$ = the base discharge rate for AFD n, which describes AFD open extent; and, $D_{n,t}$ = the open/close status of AFD n at time t. Accordingly, this research is formulated as a two stage optimization problem. The first stage is to determine the base discharge rate Q_B for each AFD. It is a continuous control optimization problem since its solution space is continuous. The second stage is to determine the AFD flow patterns. It is formulated as a discrete-time control optimization problem.

To calculate base discharge rate, each AFD is initially turned on to its full extent and all the time in the EPANET simulation. Discharge rate Q for each AFD is controlled to decrease at a pace proportional to the concentration difference between AFD and the chlorine concentration lower limit until the chlorine residual limit is violated. The calculated discharge rates are the minimum open extents of these AFD. They are used to calculate the initial open time in next stage of study.

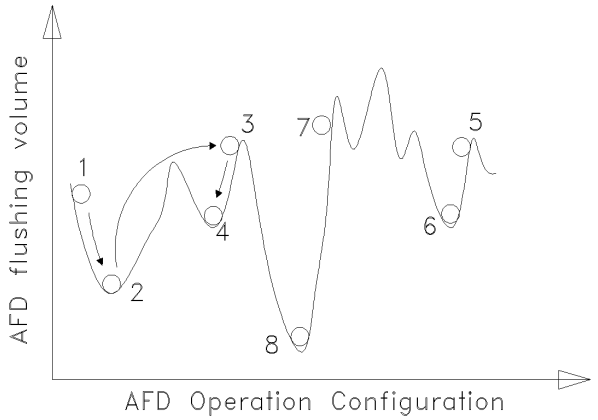

Figure 1. Searching global optimum (TIFF)

Initial open duration for each AFD is calculated using a simple reverse proportion method. The results are shown in the third column in Table 1. The procedure of searching global minimum is described as a ball rolling downhill and jumping valley to valley as shown in Figure 1. The ball trajectory shows the evolution of objective function. AFD open time length is reduced slowly to reach local minimum. Sensitivity analysis is used to detemine which AFD shall be selected, at which moment, and how long the AFD open time length shall be reduced during the rolling downhill operation. Simulated annealing method is used to determine the availablity of jumping valley to valley. Simulated annealing is an optimization approach for searching the global minimum of a highly nonlinear problem that may possess several local minima [6]. Simulated annealing has been reported to be used in optimizing pump scheduling in water distribution systems [7], and water network design [8]. In addition, it has been applied in water resource engineering [9] and irrigation water system design [10], to name a few. The procedure will find mumerious local minima, the lowest of them is global minimum.

3. Model Application

Gulf Beach pump station service area in south Pinellas County, Florida, is selected for case study. It serves a small city with 6,500 residents and a park with 8,800 visitors per day. 14 AFD are installed in the pipe network. Approximately 48% of the outflow from the pump station, 2,550 m^3/d, is discharged through AFD. EPANET is used to simulate chlorine residuals. The optimization methodology is programmed into Matlab code. EPANET simulation time length is 10 days. The hydraulic and water quality time steps are both set at five minutes. The simulation results of last 24 hours are saved for analysis. The minimum chlorine residual is 2.0 mg/l. Water pressure shall be no less than 14 meter of water everywhere in the pipe network. Each AFD starts at most four times every day.

4. Results and discussions

The AFD discharge volume calculation is presented Fig. 2. There are two curves in this figure. The upper curve shows the evolution of AFD discharge volume, and the lower curve records the minimum values from the first to the most recent iteration. It is observed that AFD discharge volume, i.e. the objective function, stabilizes after fifteenth iteration of calculation. From utility engineer and operators' viewpoints, this is a near optimum with sufficient accuracy. The results reveal that the minimum discharge volume is 120 m^3/d, which is significantly less than the current discharge rate of 2,550 m^3/d. The AFD open schedules are presented in Table 1. It shows that all the AFD open less four times per day. The minimum pressure of the pipe network is 36 meter of water.

Table 1. Automatic flush devices optimal open schedules when they are opened at full extents

			Open (min)		
AFD #	Flow (L/min)		Initial Length	Optimal Length	Optimal Open Schedule
AFD-37	458		115	0	
AFD-38	443		130	0	
AFD-39	447		80	25	(00:00-00:25)
AFD-40	435		115	30	(00:00-00:15) (10:00-10:15)
AFD-41	428		100	20	(00:00-00:20)
AFD-42	432		110	30	(23:45-00:15)
AFD-43	420		95	15	(01:45-02:00)
AFD-44	379		175	35	(0:00-0:20) (02:00-02:15)
AFD-45	397		105	20	(00:00-00:20)
AFD-46	375		130	35	(08:00-08:15) (23:40-24:00)
AFD-47	356		200	60	(23:00-24:00)
AFD-48	310		150	0	
AFD-49	310		145	0	
AFD-50	238		210	55	(23:05-24:00)

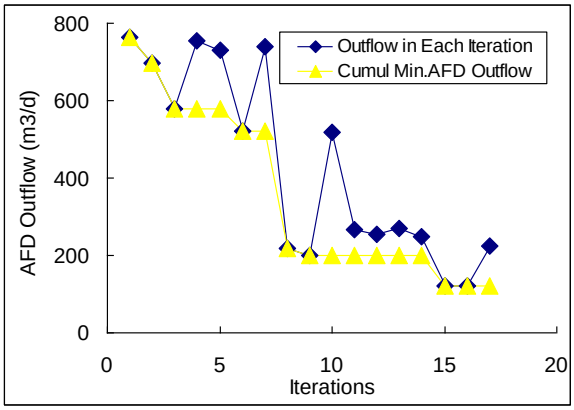

Figure 2. Optimal AFD discharge volume (TIFF)

5. Conclusions

This paper provides an insightful approach on AFD operation optimization in the water distribution system. This methodology has two stages. In the first stage, the solution space is continuous, reduced gradient method is used to determine base AFD discharge rates. In the second stage, the feasible region to the optimization problem is discrete, simulated annealing is used to search AFD operation patterns. Originality of this research lies in the approach of using gradient-based method to quickly explore and narrow down the solution space; and employing heuristic method to intensively exploit the optimal solution. We applied this method to a chloramined water system. The results suggest that water flushing volume calculated by optimal AFD operation configuration is much less than current field practice. Since this methodology is developed based on EPANET simulation, it can be readily applied to chlorinated or any other water distribution system that EPANET can simulate.

Acknowledgements

This paper is funded in part by University of South Florida.

References

[1] U.S. EPA. *The effects of disinfectant residuals in the distribution system. EPA-68-C-00-113*. Office of Ground Water and Drinking Water, U.S. EPA, Washington, D.C., 2006.

[2] A. El Mouatasim. Boolean integer nonlinear programming for water multireservoir operation. *Journal of Water Resource Planning and Management*, 138 (2), 176–181, 2012.

[3] M. Lopez-Ibanez. *Operation optimization of water distribution networks*. PhD dissertation, Edinburgh Napier University, pp. 40-77, 2009.

[4] M. Lopez-Ibanez. Ant colony optimization for optimal control of pumps in water distribution networks. *Journal of Water Resource Planning and Management*, 134 (4), 337-346, 2007.

[5] C. Giacomello. Fast hybrid optimization method for effective pump scheduling. *Journal of Water Resource Planning and Management*, 139 (2), 175–183, 2013.

[6] S. Kirkpatrick. Optimization by simulation annealing. *Science*, 220 (4598), 671-680, 1983.

[7] G. McCormick. Derivation of near-optimal pump schedules for water distribution by simulated annealing. *Journal of the Operational Research Society*, (55) 7, 728-736, 2004.

[8] J. Tospornsampan. Split-pipe design of water distribution network using simulated annealing. *International Journal of Computer and Information Engineering*, (1) 3, 154-164, 2007.

[9] X. Wang. An eco-environmental water demand based model for optimising water resource using hybrid genetic simulated annealing algorithms. Part I. Model development. *Journal of Environmental Management*, (90) 8, 2628-2635, 2009.

[10] R. Martinez. Application of several meta-heuristic techniques to the optimization of real looped water distribution networks. *Water Resource Management*, 22 (10), 1367-1379, 2008.

Proceedings of the 22nd UK Conference of the
Association for Computational Mechanics in Engineering
2 – 4April 2014, University of Exeter, Exeter

Weight Optimization of Laminated Composite Structures using Genetic Algorithm

Mokhtar Jalilian * [1], Nasser Taghizadieh [2]
[1]Master Student of Structural Engineering, Department of Civil Engineering, University of Tabriz, Tabriz, Iran
[2]Associate Professor of Faculty of Civil Engineering, University of Tabriz, Tabriz, Iran

Jaliliyan-mokhtar90@ms.Tabriz.ac.ir
ntaghiza@tabrizu.ac.ir

ABSTRACT

Structural weight optimization is a very important issue that has to be considered in construction. Structural optimization of the design is such that compliance with both the technical aspects of the implementation cost is minimal weight. Due to the weight of the structures, especially buildings and structures used in aerospace industry can Volume fraction in the layer can be made of composite materials and structures so that the minimum weight is required to satisfy certain conditions. Such composites can be characterized as having low density, good thermal stability, high fatigue resistance, high mechanical strength noted. These plates consist of alternating thin paste is obtained. Therefore, due to the increasing use of mechanical behavior of materials is essential. In this study, the minimum weight beam made of ceramic composite materials - metal is specified as the natural frequency of the structure is satisfied. Natural frequency of the structure is obtained using the Generalized Differential Quadrature (GDQ). After using evolutionary genetic algorithm, the weight of the structure is optimized to achieve maximum natural frequency of the structure.
Keywords: *Optimization; Genetic Algorithms; Laminate Composites ; Weight; Frequency*

1. Introduction

The beam structures occupy a leadership position in civil, architectural, aeronautical, and marine engineering, since they give rise to optimum conditions for dynamic behaviour, strength and stability. in other words, these structures support applied external forces efficiently by virtue of their geometrical shape. The study of the vibration of beam of revolution is an important aspect in the successful applications of these structures. Due to high strength and resistance to temperature change, the composite beam can be applied to military aircraft propulsion system, structures of civil. Tornabene (1) has used four-parameter power law distribution to study the behavior of moderately think functionally graded conical and cylindrical shells and annular plates. Optimization is implemented for various objective functions in mechanical problems, such as buckling Loads (2), weight (3,4) fundamental frequencies (2), deflection (3), etc. The aim of this study is to optimize generalized power-law distribution for maximizing the first natural frequency with constraint on the density of composite beam using genetic algorithm. The Frequency of beam is obtained by numerical technique termed the generalized differential quadrature (GDQ) method based on the DQ Technique (5). This research to minimize the weight of the composite beam made of ceramic - metal. It is stated that the natural frequency of the structure so that it can satisfy. Genetic Algorithms is applied to optimize the weight of the composite beam.

2. Laminate Composites

In this study, a Multi -Layer Composite beam are studied ceramic - metal mechanical properties.
Gradual Changes is in the properties of the laminated beam volume fraction of material changes to the beam axis.

Figure - 1 show on elastic foundation

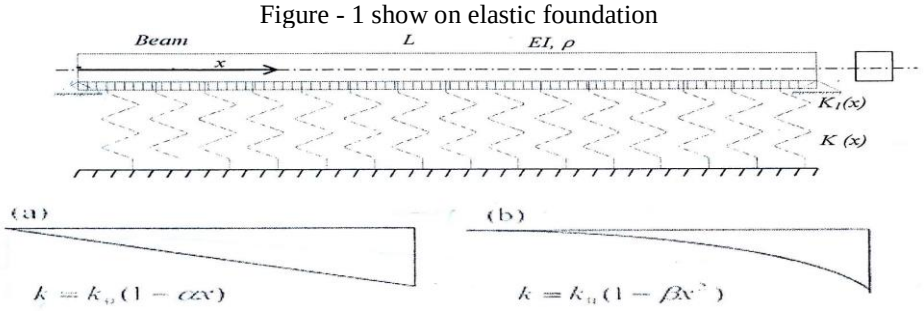

$$\rho(Z) = (\rho_c - \rho_m)V_C + \rho_m$$
$$E(Z) = (E_c - E_m)V_C + E_m$$
$$\nu(Z) = (\nu_c - \nu_m)V_C + \nu_m$$

Where ρ_m , Em , ν_m ,V_m and ρ_c , Ec , ν_c ,V_c represent mass density, Youn's modulus , Poisson's ratio and volume fraction of the metal and ceramic constituent materials respectively .
In the present work, V_c is considered as follow:

$$V_C = \begin{cases} V_{C1} & -\frac{h}{2} \le z < -\frac{h}{2} + h_1 \\ V_{C2} & -\frac{h}{2} + h_1 \le z \le -\frac{h}{2} + h_1 + h_2 \\ V_{C3} & -\frac{h}{3} - h_4 < z < \frac{h}{2} - \frac{h}{4} \\ V_{C4} & \frac{h}{2} - \frac{h}{3} < z < \frac{h}{2} \end{cases}$$

$\Omega = \omega L^2 \sqrt{\frac{\rho_m A}{E_m I}}$ E_C=380 GPa , ρ_c=3800 kg/m^3 , E_m=70 GPa , ρ_m=2707 kg/m^3

Rest vibrating beam on elastic equation is as follows. [6]

$$-D\frac{\partial^4 w}{\partial x^4} - \frac{\partial}{\partial x}(K_1 \frac{\partial_w}{\partial x}) - K_0(1-0.2x)w - \rho A \frac{\partial^2 w}{\partial t^2} = 0 \qquad 0 \le x \le L$$

K1 and K0 are the elastic modulus of the base.

$$D = \int_{\frac{-h}{2}}^{\frac{h}{2}} Q_{11}\ z^2\ dz$$

To obtain the natural frequency of vibration of the beam as a function of the eigenvalues is written in the mode shape of the transverse momentum.

$$w(x,t) = W(x)e^{-i\omega t}$$

3. GDQ solution of governing equations

The GDQ approach was developed by Shu and Coworkers (7,8) that approximates the spatial derivative of a function of given grid point as a weighted linear sum of all the functional value at all grid point in the whole domain. In GDQ method, the *n*th order partial derivative of a continuous function f(x,z) with respect to x at a given point x_i can be approximated as a linear sum of weighting values at all of the discrete point in the domain of x ,i.e.

$$\frac{\partial f^{n(x_i z)}}{\partial x^n} = \sum_{k=1}^{N} c_{ik}^{(n)} f(x_{ik}, z), \qquad i = 1,2..., N \qquad n = 1,2..., N-1$$

Where *N* is the number of sampling points, and c_{ik}^n is the x_i dependent weight Cofficients.

4. Genetic Algorithm

GA are probably the best-known EA, receiving substantial attention in recent in years. The first attempt to use EA took place in the sixties by a team of biologists (3) and was focused in building a computer program that would Simulate the process of evolution in nature. However, the GA model used in this study and in many other structural design applications refers to model introduced and studied by Holland and co-workers (3). In general the term genetic algorithm refers to any population-based model that uses various operators (selection-crossover-mutation) to evolve. In the basic genetic algorithm each member of this population will be a binary or a real valued string, which is sometimes referred to as a genotype or , Alternatively, as a chromosome.

5. Structural optimization

The term optimal structure is very vague. This is because a structure can be optimal in different aspects. These different aspects are called objectives, and may for instance be the weight, cost or stiffness of the structure. A numerical evaluation of a certain objective is through an objective

function, f, which determines the goodness of the structure in terms of weight, cost or stiffness [11]. Of course, the optimization has to be done within some constraints; otherwise it's a problem without a well defined solution [9]. Firstly, there are design constraints, like a limited geometrical extension or limited availability of different structural parts. Secondly, there are behavioral constraints [9] on the structure that denotes the structural response under a certain load condition. Here may, for instance, limits on displacements, stresses, forces and dynamic response be sorted. Finally, there is one obvious demand that is valid for all structures, and it is kinematical stability, otherwise they are mechanisms [10]. This can be seen as a behavioral constraint. Structures that lie within the constraints are called feasible solutions to the optimization problem.

6. Optimization Procedure

The objective of optimization in this paper is to find best values of the parameters, (V_{c1}, V_{c2}, V_{c3}, V_{c4}, h1/h, h2/h,h3/h). In generalized power low distribution so that to maximize fundamental frequency parameter of composite beam. There is an important point that considered parameters must be obtained so that the ceramic volume fraction is between zero and one ($0 \leq v_c \leq 1$). Also, Therefore, the constrained optimization problem is defined as:

$$\textit{Minimize} \qquad f(h1/h, h2/h, h3/h, V_1, V_2, V_3, V_4) = \rho$$

$$\textit{Subject to} \quad \begin{cases} -\Omega \geq 32.5760 \\ 0 \leq V_C \leq 1 \\ 0 \leq h1/h, h2/h, h3/h \leq 1 \end{cases}$$

If GDQ method is applied for frequency parameters, the optimization process becomes so complicated and time consuming.

Figure 2**:** convergence of the GA to the optimal solution

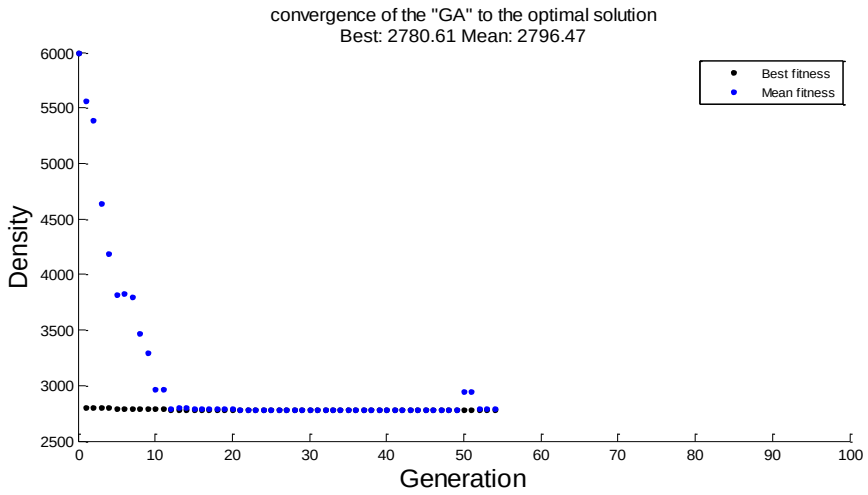

Table 1: comparison of the Genetic Algorithm

Optimum parameters								
h1	h2	h3	Vc1	Vc2	Vc3	Vc4	ρ (kg/m^3)	-Ω
0.79	0.01	0.451	0.815	0.318	0	0	2780.6058	-32.5760

7. Conclusion

With proper alignment layer and changes in the volume fraction of material using a genetic algorithm can be more frequency the lower the density of a ceramic beam reached 100%. Because the result of many factors involved including elastic substrate, the volume fraction ,thickness.

References

[1] Tornabene,F.,Free vibration analysis of functionally graded conical cylindrical shell and annular plate structures with a for- parameter power- low distribution. Comput Meth Appl Mech Engrg. 198(2009)2911-2935.

[2] Abouhamze M,Shakeri M.Multi-objective stacking sequence optimization of laminated cylindrical

[3] Walker M,Smith R.A technique for the multi objective optimization of laminated composite structures using genetic algorithms and finite element analysis. Compos Struct 2003;62(1):123-8.

[4] Soremekun G, Gurdal Z, Haftka RT, Waston LT. Composite laminate design optimization by genetic algorithm with generalized elitist selection. Compos Struct 2001;79:131-43.

[5] Bellman R.,Kashef B.G.,Casti J., Differential Quadrature:a technique for a rapid solution of nonlinear partial differential equations, Journal of Computational Physics 10,1972,40-52.

[6] K.Y. Lam , L. Hua , Influence of initial pressure on frequency characteristics of a rotating truncated circular conical shell , Int.J.Mech.

[7] Shu,C.:DifferentialQuadratureanditsApplicationinEngineering.Springer,Berlin(2000).

[8] Shu,C.,Richards BE,Application of generalized differential quadrature to solve two-dimensional incompressible NavierStockes equations ,Int.J.Numer Meth.Fluid, 1992,15,791-798.

[9] Christensen, Peter W. Klarbring, Anders. An Introduction to Structural Optimization. (2008). Springer Netherlands.

[10] Tsai, Lung-Wen. Mechanism design: enumeration of kinematic structures according to function. (2001). New York: CRC Press.

Proceedings of the 22nd UK Conference of the
Association for Computational Mechanics in Engineering
2 - 4 April 2014, University of Exeter, Exeter

A hybrid IGAFEM/IGABEM formulation for two-dimensional stationary magnetic and magneto-mechanical field problems

***S. May[1], M. Kästner[2], S. Müller[2] and V. Ulbricht[2]**

[1]School of Engineering, University of Glasgow, Glasgow G12 8LT, UK
[2]Institute of Solid Mechanics, TU Dresden, D-01062 Dresden, Germany

*s.may.2@research.gla.ac.uk

ABSTRACT

In this work a hybrid IGAFEM/IGABEM coupling is presented to solve a stationary magnetic field problem. IGABEM is used to model the free space while IGAFEM is applied to a magnetisable solid with a heterogeneous structure. The solution of the stationary magnetic field problem is then utilised to solve a magneto-mechanical field problem with IGAFEM. With this approach, meshing of the infinte free space is not necessary for solving both field problems.

Key Words: *NURBS; BEM; FEM; hybrid methods; magneto-mechanics*

1. Introduction

The concept of isogeometric analysis [1] has already been implemented to solve field problems using Finite Element (FEM) and Boundary Element Methods (BEM) but coupling of both methods has not been applied. In the current work, an isogeometric FEM/BEM coupling is proposed and applied to two-dimensional stationary magnetic field problems. While FEM is used to model bodies with magnetisable particles, the BEM domain accounts for the free space surrounding these bodies, see Fig. 1. Both methods are coupled on the surface of the bodies. Due to this hybrid IGAFEM/-BEM approach, the free space does not have to be meshed and truncation errors are avoided for problems to be solved on open, infinite or semi-infinite domains. Once the solution for the stationary magnetic field problem is obtained using the isogeometric FEM/BEM method, IGAFEM is used to solve a one-sided coupled magneto-mechanical field problem in the domain of the bodies with magnetisable particles. This one-sided coupling is realised by a magnetic stress tensor computed from the solution of the field variable for the stationary magnetic field problem. To summarise, the following staggered solution procedure is used:

(i) *Hybrid IGAFEM/IGABEM* is applied to compute the magnetic field in Ω_∞, i. e. within and outside of the magnetisable solid.

(ii) *IGAFEM* is used in a mechanical analysis step in Ω_{FEM} considering magnetic loads resulting from the magnetic field obtained in step (i) to simulate magneto-mechanical interactions in the magnetisable body which covers only Ω_{FEM}.

For more details see also [2].

2. Continuum formulation of the boundary value problems

2.1. Stationary magnetic boundary value problem

The stationary magnetic problem is given by the Poisson equation

$$A_{,ii} = -\mu J \ \text{ in } \ \Omega_\infty \ . \tag{1}$$

With the definition of the normal derivative of the magnetic potential $Q = A_{,i} n_i$, jump conditions across an interface Γ can be written as

$$[\![A]\!] = 0 \qquad \text{and} \qquad \left[\!\!\left[\frac{Q}{\mu} \right]\!\!\right] = -K \ \text{ on } \ \Gamma \ . \tag{2}$$

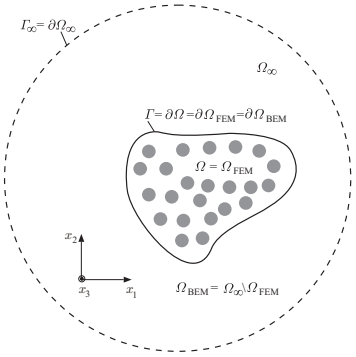

Figure 1: Modelling problems on infinite or semi-infinite domains Ω_∞ using a hybrid approach by coupling FEM and BEM on the common boundary Γ. While FEM can be used to model heterogeneous materials with complex history dependent constitutive relations in Ω_{FEM}, BEM is applied to account for fields in the free space Ω_{BEM}.

2.2. Magneto-mechanical boundary value problem

The coupled magneto-mechanical problem can be carried out in Ω_{FEM} only. The mechanical balance of equilibrium is formulated in terms of the symmetric total stress tensor $t^{\text{tot}}_{kl} = t^{\text{tot}}_{lk}$

$$t^{\text{tot}}_{ij,i} + \rho f_j = 0 \;\text{ in }\; \Omega_{\text{FEM}} \;, \qquad [\![t^{\text{tot}}_{ij}]\!] n_i = -p_j \;\text{ on }\; \Gamma. \tag{3}$$

As discussed in more detail in [3], the symmetric total stress tensor

$$t^{\text{tot}}_{ij} = {}_{\text{E}}t_{ij} + \hat{t}_{ij} \tag{4}$$

can be decomposed into the *symmetric* pseudo-mechanical stress ${}_{\text{E}}\mathbf{t}$ and the pseudo-magnetic stress tensor $\hat{\mathbf{t}}$, which is entirely defined by magnetic quantities

$$\hat{t}_{ij} = H_i B_j - B_i M_j - \frac{1}{2}\left(\frac{1}{\mu_0} B_q B_q - 2 M_q B_q\right)\delta_{ij}. \tag{5}$$

Boundary conditions have to be set-up for Γ as follows

$$u_i = \bar{u}_i \quad \text{on } \Gamma_u \qquad \text{and} \qquad t^{\text{tot}}_{ij} n_i = \bar{p}_j \quad \text{on } \Gamma_p. \tag{6}$$

In this work, no mechanical surface tractions are considered. Hence, the effective surface traction

$$\bar{p}_j = \hat{t}^{\text{BEM}}_{ij} n^{\text{FEM}}_i \tag{7}$$

reduces to purely magnetic contributions of the surrounding free space. To compute the pseudo-magnetic stress tensor $\hat{\mathbf{t}}^{\text{BEM}}$ from equation (5) on the boundary Γ_p, the magnetic induction $\mathbf{B}$ or equivalently the necessary gradient of the magnetic potential can be calculated by solving

$$\begin{bmatrix} n^{\text{BEM}}_1 & n^{\text{BEM}}_2 \\ x_{1,\psi} & x_{2,\psi} \end{bmatrix} \begin{bmatrix} A_{,1} \\ A_{,2} \end{bmatrix} = \begin{bmatrix} Q_{\text{BEM}} \\ A_{,\psi} \end{bmatrix}. \tag{8}$$

3. Numerical formulation for the two field problems

3.1. Hybrid IGABEM/FEM formulation for the stationary magnetic field problem

Coupling of the IGABEM/-FEM formulations for the stationary magnetic field problem using the jump conditions

$$\underline{\mathbf{A}}_{\text{FEM}}\big|_\Gamma = \underline{\mathbf{A}}_{\text{BEM}} \quad \text{and} \quad \frac{1}{\mu_{\text{FEM}}|_\Gamma}\underline{\mathbf{Q}}_{\text{FEM}} = -\frac{1}{\mu_{\text{BEM}}}\underline{\mathbf{Q}}_{\text{BEM}} \tag{9}$$

yields the following system of equations

$$\begin{bmatrix} \underline{\underline{\mathbf{K}}}_A & \frac{\mu_{\text{FEM}}|_\Gamma}{\mu_{\text{BEM}}}\underline{\underline{\mathbf{T}}} \\ \underline{\underline{\tilde{\mathbf{H}}}} & \underline{\underline{\mathbf{G}}} \end{bmatrix} \begin{bmatrix} \underline{\mathbf{A}}_{\text{FEM}} \\ \underline{\mathbf{Q}}_{\text{BEM}} \end{bmatrix} = \begin{bmatrix} \underline{\mathbf{P}}_A \\ \underline{\mathbf{A}}_S \end{bmatrix} \tag{10}$$

which can be solved for the unknowns $\underline{\mathbf{A}}_{\text{FEM}}$ and $\underline{\mathbf{Q}}_{\text{BEM}}$.

3.2. IGAFEM formulation for the magneto-mechanical field problem

Since we consider a non-linear stress-strain relation for the magneto-mechanical field problem, the non-linear system of equations

$$\underline{\mathbf{f}}_{u}^{\text{int}} = \underline{\mathbf{f}}_{u}^{\text{ext}} \tag{11}$$

with

$$\underline{\mathbf{f}}_{u}^{\text{int}} = \bigcup_{e=1}^{E} \int_{\Omega_{\text{FEM}}^{e}} \underline{\underline{\mathbf{B}}}_{u}^{e^{T}} \, \mathrm{E} \underline{\mathbf{t}}^{e} \, \mathrm{d}\Omega^{e} \quad \text{and} \quad \underline{\mathbf{f}}_{u}^{\text{ext}} = \bigcup_{\tilde{e}=1}^{\tilde{E}} \int_{\Gamma_{p}^{\tilde{e}}} \underline{\underline{\mathbf{N}}}_{u}^{e^{T}} \, \bar{\underline{\mathbf{p}}}^{\tilde{e}} \, \mathrm{d}\Gamma^{\tilde{e}} - \bigcup_{e=1}^{E} \int_{\Omega_{\text{FEM}}^{e}} \underline{\underline{\mathbf{B}}}_{u}^{e^{T}} \, \hat{\underline{\mathbf{t}}}^{e} \, \mathrm{d}\Omega^{e} \tag{12}$$

defining the discretised magneto-mechanical field problem is solved iteratively for $\underline{\mathbf{u}}_{\text{FEM}}$ using a Newton-Raphson scheme.

4. Demonstration

4.1. Magnetisable cylinder in an inhomogeneous magnetic field

The first demonstration problem is illustrated in Fig. 2(a) and has been investigated in more detail in [3]. Contour plots for the solution of the magnetic potential are shown in Fig. 2(c). For the stationary

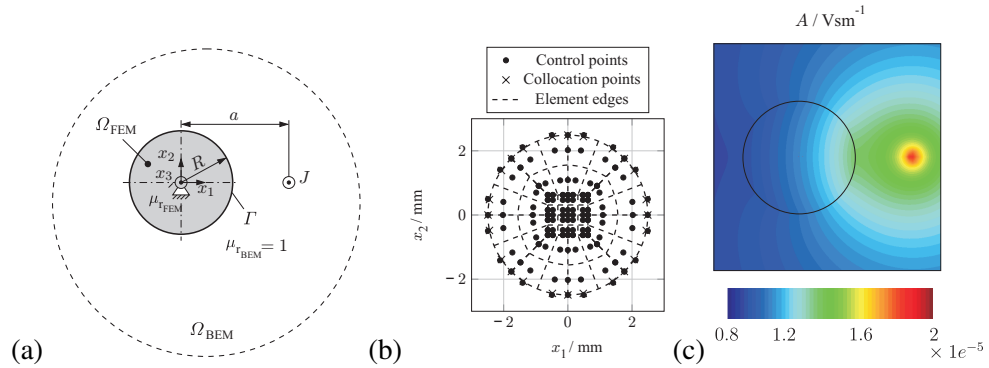

Figure 2: (a) Setup of the demonstration problem, (b) NURBS mesh for the magnetisable cylinder and (c) contour plot of the magnetic potential obtained from the numerical solution of the stationary magnetic BVP

magnetic field problem, the normalised error norm $\|A\|_{L_2}$ in the domain Ω_{FEM} is calculated. In order to assess the quality of the solution of the coupled magneto-mechanical field problem, the relative error for the force $|\Delta F_1|$ is evaluated.

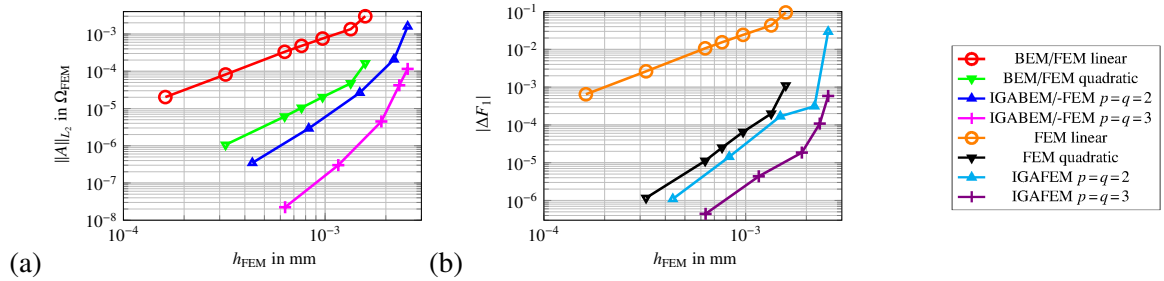

Figure 3: Results of the convergence analysis: (a) normalised error norm of the magnetic potential $\|A\|_{L_2}$ in the domain Ω_{FEM} (b) relative error $|\Delta F_1|$

4.2. Heterogeneous magnetoactive material in an external field

The following example illustrates the modelling of magnetostriction by the hybrid IGAFEM/-BEM approach. It considers an elliptic sample which consists of magnetisable particles embedded in a soft polymeric matrix according to Fig. 4.
Two principal loadings are considered. The horizontal orientation of the coil generates a magnetic field $\bar{\mathbf{B}} = \left[\bar{B}_1,\ 0\right]^T$ (red in Fig. 4 (a)), while the vertical arrangement leads to $\bar{\mathbf{B}} = \left[0,\ \bar{B}_2\right]^T$ (blue in Fig. 4 (a)).

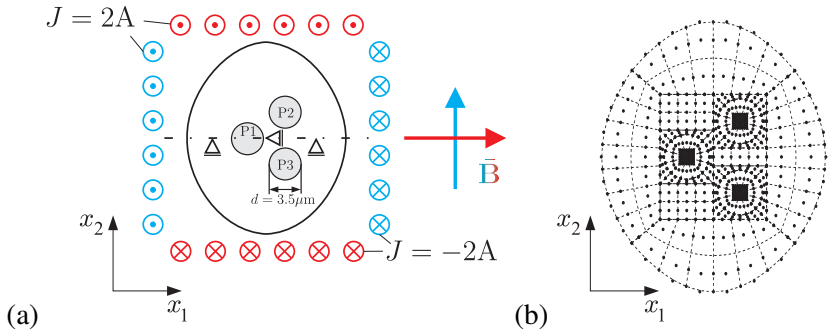

Figure 4: Heterogeneous magnetoactive sample consisting of magnetisable particles and a polymeric matrix: (a) model arrangement with two possible external magnetic fields and (b) NURBS mesh.

While the particles are modelled isotropic linear elastic, a viscoelastic material model is used to represent the polymeric matrix. The magnetic potential as well as the deformation of the sample at the end of the simulation are illustrated in Fig. 5 for both orientations of the magnetic field $\bar{\mathbf{B}}$. It can be seen that the magnetically induced attractive or repulsive interactions of the particles cause either an elongation or contraction of the sample, i.e. a magnetostrictive effect can be observed.

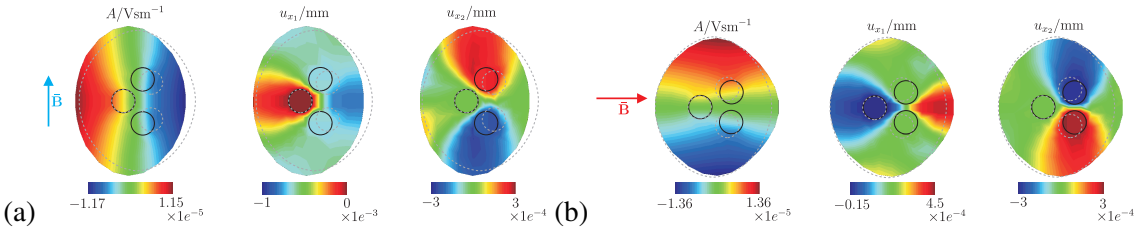

Figure 5: Local magnetic stray field resulting from the particle magnetisation and magnetically induced deformation of an elliptic sample for (a) a vertically, and (b) a horizontally aligned magnetic field $\bar{\mathbf{B}}$.

5. Conclusion

Isogeometric analysis has been used to solve two-dimensional stationary magnetic and coupled magneto-mechanical field problems. The magnetic problem was handled by a hybrid IGAFEM/-BEM approach. While the IGAFEM was utilised to model the magnetisable body, the IGABEM was used to account for the infinite domain representing the free space surrounding the magnetisable body. As a consequence, no meshing of the free space was required. The subsequent solution of the magneto-mechanical field problem was obtained from applying IGAFEM to discretise the domain of the magnetisable body, hence, allowing for inelastic material behaviour. Magnetic contributions to the total stress as well as to the surface traction acting on this body were obtained from the solution of the stationary magnetic field problem provided by the hybrid IGAFEM/-BEM method.

References

[1] T. Hughes, J. Cottrell, Y. Bazilevs, Isogeometric analysis: CAD, finite elements, NURBS, exact geometry and mesh refinement, Computer Methods in Applied Mechanics and Engineering 194 (3941) (2005) 4135–4195.

[2] S. May, M. Kästner, S. Müller, V. Ulbricht, A hybrid IGAFEM/IGABEM formulation for two-dimensional stationary magnetic and magneto-mechanical field problems, Computer Methods in Applied Mechanics and Engineering (2014) accepted.

[3] M. Kästner, S. Müller, J. Goldmann, C. Spieler, J. Brummund, V. Ulbricht, Higher-order extended FEM for weak discontinuities level set representation, quadrature and application to magneto-mechanical problems, Int. J. Numer. Meth. Engng 93 (13) (2013) 1403–1424.

Proceedings of the 22nd UK Conference of the
Association for Computational Mechanics in Engineering
2 - 4 April 2014, University of Exeter, Exeter

AN ISOGEOMETRIC MODEL FOR EARTHQUAKE FAULT RUPTURE WITH WEAKENING FRICTION

***Julien Vignollet[1], Stefan May[1] and René de Borst[1]**

[1]School of Engineering, University of Glasgow, G12 8LT, Glasgow, United Kingdom

*julien.vignollet@glasgow.ac.uk

ABSTRACT

The objective of this contribution is to investigate the performance of isogeometric analysis when applied to cohesive zone problems with existing interfaces under dynamic loading. An application of interest is earthquake engineering, and in particular the dynamic rupture of geological faults. We use non-uniform rational B-splines, together with Bézier operators, which allow to model complex fault geometries. The fault discontinuity is inserted by locally increasing a knot multiplicity. The traction at this interface is modelled with a slip-weakening friction law. Some features of this preliminary work are presented on an idealised example, where spurious traction oscillations are reported at the interface.

Key Words: *Isogeometric analysis; slip-weakening friction; plasticity; dynamics*

1. Introduction

Seismic events are particularly complex phenomenon, overlapping a number of branches in mechanics such as dynamics, fracture, poro-elasticity and plasticity. Although the holy grail of earthquake prediction, with regard to both time and location, seems out of reach today [4], computational models can provide valuable insight to describe earthquake processes such as initiation and propagation.
This work represents the first step toward the modelling of earthquake rupture dynamics. The double objective is to participate to the current and active exploration of the performances of isogeometric analysis, but also to provide an alternative framework to existing models, which tend to use finite differences or boundary integral element methods.

2. Model

In this paper, we focus on an idealised 2D representation of the fault Γ_d and surrounding bulk Ω as shown in Fig. 1. The pre-defined interface Γ_d is assumed to run across the whole body, and is created by the insertion of a knot value with multiplicity $p+1$ at the desired location, where p is the polynomial order (see example on Fig. 2a). For more details, refer to [6] and [2].

The linear momentum balance is:

$$\operatorname{div}\boldsymbol{\sigma} = \rho\ddot{\mathbf{u}} \qquad \mathbf{x} \in \Omega, \tag{1}$$

where $\boldsymbol{\sigma}$ denotes the Cauchy stress in the bulk, ρ the bulk density and $\ddot{\mathbf{u}}$ the acceleration of a material point.

The strong form is completed with the boundary conditions at the external boundaries and the discontinuities (where the jump $[\![\mathbf{u}]\!]_d$ defines the relative displacement between both sides of the discontinuity):

$$\mathbf{u} = \bar{\mathbf{u}} \qquad \mathbf{x} \in \Gamma_u, \tag{2a}$$

$$\boldsymbol{\sigma}\mathbf{n} = \bar{\mathbf{t}} \qquad \mathbf{x} \in \Gamma_t, \tag{2b}$$

$$\boldsymbol{\sigma}\mathbf{n} = \mathbf{t}([\![\mathbf{u}]\!]_d) \qquad \mathbf{x} \in \Gamma_d. \tag{2c}$$

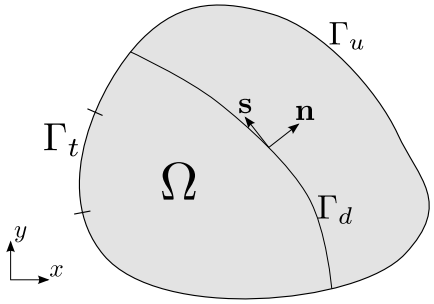

Figure 1: Schematic representation of the fault Γ_d and surrounding body Ω

The discretised weak form of Eqs. (1)-(2) can then be derived to obtain the internal force vector in matrix-vector notations:

$$\mathbf{f}_{\text{int}} = \int_{\Omega} \mathbf{B}^{\mathrm{T}} \boldsymbol{\sigma} \, d\Omega + \int_{\Gamma_d} \mathbf{M}^{\mathrm{T}} \mathbf{t}(\llbracket \mathbf{u} \rrbracket_d) \, d\Gamma_d. \tag{3}$$

In the above, the standard operator $\mathbf{B}$ is defined as to obtain the infinitesimal strain vector by the product $\boldsymbol{\varepsilon} = \mathbf{B}\mathbf{u}_b^e$, with $\mathbf{u}_b^e$ the element vector of nodal displacements in the bulk. The operator $\mathbf{M}$ is defined so that the jump vector at the discontinuity results from the product $\llbracket \mathbf{u} \rrbracket_d = \mathbf{M}\mathbf{u}_d^e$, with $\mathbf{u}_d^e$ the element vector of nodal displacements at the interface Γ_d (see [6] for more details). The operator $\mathbf{B}$ contains the derivatives of the bivariate NURBS basis, while $\mathbf{M}$ aggregates the univariate NURBS parametrisation of the interface.

At the interface, the elastic stress-slip relationships are defined in the local coordinate system of the discontinuity Γ_d

$$\mathbf{t}_d(\llbracket \mathbf{u} \rrbracket_d) = t_n \mathbf{n} + t_s \mathbf{s} \tag{4}$$

$$= k_n \llbracket u \rrbracket_n \mathbf{n} + k_s \Big(\llbracket u \rrbracket_s - \llbracket u \rrbracket_s^p \Big) \mathbf{s}. \tag{5}$$

The parameters k_n and k_s are dummy stiffnesses modelling a rigid interface. $\llbracket u \rrbracket_n$ and $\llbracket u \rrbracket_s$ respectively represent the normal and tangential jumps (i.e. $\llbracket \mathbf{u} \rrbracket_d = \llbracket u \rrbracket_n \mathbf{n} + \llbracket u \rrbracket_s \mathbf{s}$), while $\llbracket u \rrbracket_s^p$ is the plastic slip along the shearing direction $\mathbf{s}$.

A plastic slip weakening model is used, with the yield function defined as:

$$f(t_s, \kappa) = \|t_s\| - \tau^{\mathrm{y}}(\kappa), \tag{6}$$

where the slip-weakening function τ^{y} decreases as the accumulated plastic slip κ (where, for each increment, $\dot{\kappa} = |\dot{\llbracket u \rrbracket}_s^p|$) increases, as proposed in [1]:

$$\tau^{\mathrm{y}}(\kappa) = \begin{cases} \tau_p - \dfrac{\tau_p - \tau_r}{D_c} \kappa & \kappa \leq D_c \\ \tau_r & \kappa > D_c. \end{cases} \tag{7}$$

In Eq. 7, τ_p is the peak shear strength and τ_r the residual shear strength, i.e. the shear strength once the accumulated plastic slip has reached the critical slip-weakening distance D_c.

We use an associated flow rule to relate the increment of plastic slip $\dot{\llbracket u \rrbracket}_s^p$ to the incremental plastic multiplier $\dot{\lambda}$:

$$\dot{\llbracket u \rrbracket}_s^p = \dot{\lambda} \frac{\partial f}{\partial t_s} = \dot{\lambda} \, \mathrm{sign}(t_s). \tag{8}$$

Finally, the plastic problem is fully defined by the addition of the usual Kuhn-Tucker complementary conditions:

$$\dot{\lambda} \geq 0 \qquad f(t_s, \kappa) \leq 0 \qquad \dot{\lambda} f(t_s, \kappa) = 0. \tag{9}$$

3. Results

3.1. Earthquake initiation

Initial tests are performed on the idealised 1x2mm^2 plate (see Fig. 2a), where the fault is aligned with the y-axis. The following parameters, which have no physical relevance, have been arbitrarily chosen. The elastic constants are $E = 20$GPa and $\nu = 0.25$, while the density is $\rho = 4000$kg/m^3. Along the fault, the peak and residual shear strengths are $\tau_p = 20$MPa and $\tau_r = 1$MPa and the critical slip-weakening distance is $D_c = 0.01$mm. The sample is sheared vertically using the ramp event shown in Fig. 2b. In order to initiate early slipping within the geometry, two interface elements at the centre of the fault have their peak shear strength reduced to $\tau_p = 5$MPa.

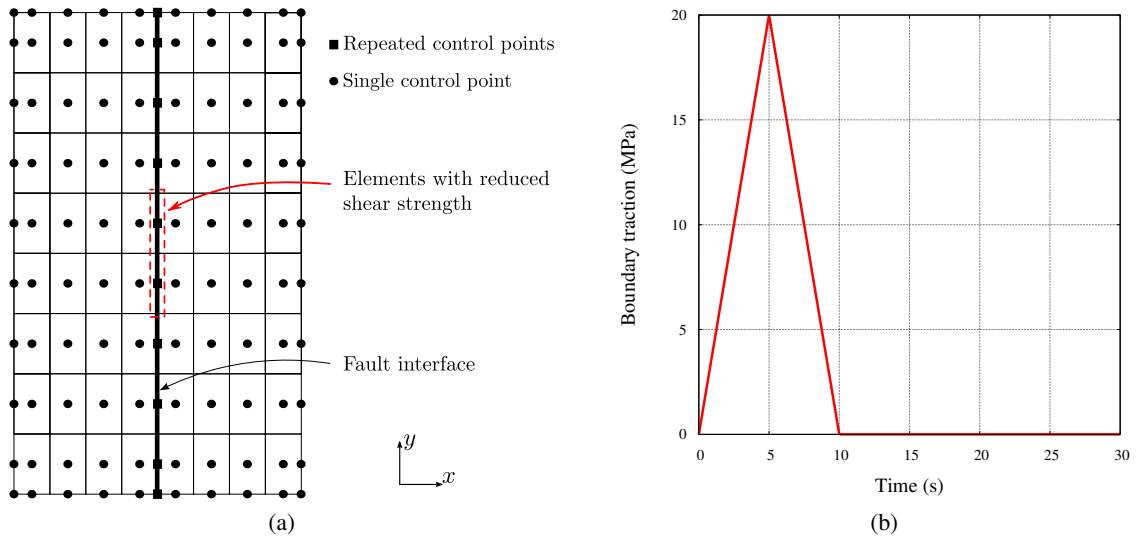

Figure 2: (a) Quadratic (p=2) mesh in the physical space. Solid lines represent the edges of the Bézier elements. Control points are interpolatory at the boundary and at the interface where repeated control points lie. The knot vectors are ξ = [0, 0 , 0, 1/8, 1/4, 3/8, 1/2, 1/2, 1/2, 5/8, 3/4, 7/8, 1, 1, 1] and η = [0, 0, 0, 1/8, 1/4, 3/8, 1/2, 5/8, 3/4, 7/8, 1, 1, 1] (b) Ramp shear traction applied to the right edge

Due to inertia, the shear wave $\sigma_{xy} = 5$MPa only reaches the fault at time $t = 5s$, which initiates plastic slip across the weakened elements (Fig. 3a). At $t = 9s$, the shear along the remaining of the interface attains its yield value of $\tau_r = 20$MPa, and plastic slip occurs along the whole interface (Fig. 3b). As the plastic slip increases, the shear strength at the interface weakens, e.g. to 15MPa on Fig. 3c.

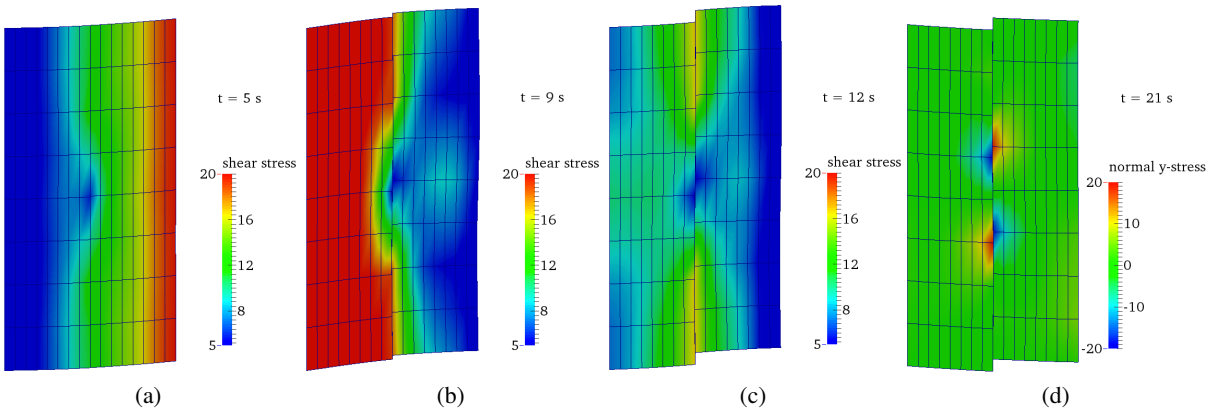

Figure 3: Deformed mesh magnified 40 times with shear stress contour plot (a)-(b)-(c) and normal stress σ_{yy} (d)

As a result of local internal slip, normal stresses build up at the crack tips (see Fig. 3d), as reported in [5]. These tend to give rise to off-fault rupture, which will be accounted for in subsequent models.

3.2. Spurious traction oscillations at the interface

In Eq. 5, penalty stiffnesses k_n and k_s were introduced to model the initially rigid interface. It is well known that for standard FEM, this may give rise to spurious traction oscillations (see e.g. [3]). As reported in [2], the Bézier interface elements suffer from similar deficiencies. This can be seen on Fig. 4, where the traction along the interface is depicted at the end of the plastic step for various values of the dummy stiffness k_s. In this case, oscillations occur when k_s = 1e8 MPa/mm and k_s = 1e9 MPa/mm. The solutions for k_s = 1e7 MPa/mm and k_s = 1e10 MPa/mm are identical, while the traction is slightly different when k_s = 1e6 MPa/mm due to the larger elastic jump resulting from the low dummy stiffness.

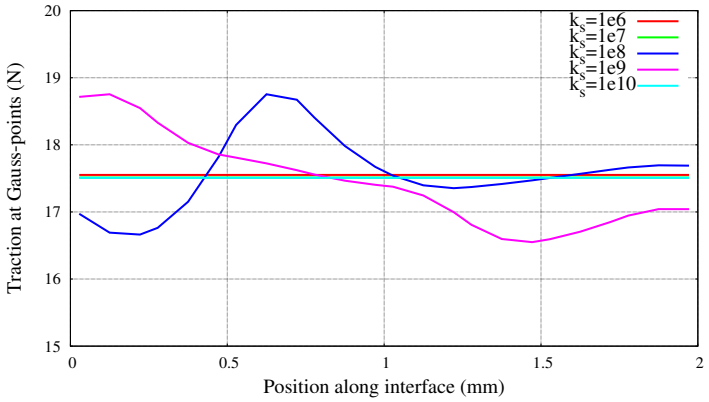

Figure 4: Traction distribution along the interface Γ_d for various values of the dummy stiffness k_s.

4. Conclusions and future work

In the first step of this ongoing work, a dynamic frictional slip weakening model was implemented in an isogeometric framework. It was shown that numerical integration at the fault interface requires more attention, as the Gauss quadrature gives rise to spurious oscillations for the traction. This model is still at an inceptive stage and a number of features still need to be implemented in order to model realistic seismic events. First, non-reflecting infinite elements will be used to absorb bouncing elastic waves at the boundaries; these will also allow to properly describe the initial static equilibrium. In a following step, a plastic model will be implemented to take off-fault rupture into account.

References

[1] Y. Ida. Cohesive force across the tip of a longitudinal-shear crack and Griffiths specific surface energy. *J. Geophys. Res.*, 77, 3796–3805, 1972.

[2] F. Irzal, J.J.C. Remmers, C.V. Verhoosel, and R. de Borst. An isogeometric analysis Be zier interface element for mechanical and poromechanical fracture problems. *International Journal for Numerical Methods in Engineering*, 97, 608–628, 2014.

[3] J. C. J. Schellekens and R. de Borst. On the numerical integration of interface elements. *Int. J. Numer. Meth. Engng.*, 36, 43–66, 1993.

[4] C.H. Scholz. *The Mechanics of Earthquakes and Faulting*. Cambridge University Press, 2002.

[5] E.L. Templeton and J.R. Rice. Off-fault plasticity and earthquake rupture dynamics: 1. dry materials or neglect of fluid pressure changes. *Journal of Geophysical Research: Solid Earth*, 113, 2008.

[6] C.V. Verhoosel, M.A. Scott, R. de Borst, and T.J.R. Hughes. An isogeometric approach to cohesive zone modeling. *International Journal for Numerical Methods in Engineering*, 87, 336–360, 2011.

Proceedings of the 22nd UK Conference of the
Association for Computational Mechanics in Engineering
2 - 4 April 2014, University of Exeter, Exeter

Multiphysics simulations of smart structures using isogeometric finite elements

***C. Willberg[1] and S. Duzcek[2]**

[1]German Aerospace Center (DLR);Institute of Composite Structures and Adaptive Systems; Structural Mechanics, Lilienthalplatz 7, 38108, Braunschweig
[2]Otto-von-Guericke-University, Institute of Mechanics, Universitätsplatz 2, 39106, Magdeburg

*christian.willberg@dlr.de

ABSTRACT

Active piezoelectric materials are widely used for noise-cancelation devices, to suppress unwanted vibrations, or to control the shape of high precision devices, such as optical instruments and measuring devices. Piezoelectric ceramics, e.g. made of lead-zirconate-titanate (PZT), serve both as actuators and sensors to fulfil the aforementioned goals. Nowadays, another important area of application of piezoelectric materials is the development of structural health monitoring (SHM) systems. One common approach uses a network of piezoelectric ceramics. These ceramics are surface-mounted on or embedded into the structure to excite and to receive ultrasonic guided waves. In thin-walled structures these waves are called Lamb waves and have complex physical properties. In order to gain a deeper insight into the underlying physics efficient and powerful numerical tools are needed. A viable means are finite element schemes based on higher order polynomial shape functions. Consequently, the objective of the paper is the development and the evaluation of isogeometric finite elements (electro-mechanical coupling). They are capable of reducing the computational effort noticeably and at the same time they offer very accurate results. The advantages of this higher order finite element is demonstrated using different numerical examples, highlighting the static as well as dynamic properties of higher order finite element methods. In the case of a wave propagation analysis the authors focus on three different higher order methods. Therefore, the spectral element method (SEM), the p-version of the finite element method (p-FEM) and isogeometric analysis is scrutinized and compared with standard elements.

Key Words: *isogeometric analysis; piezoelectricity; smart structures; structural health monitoring (SHM)*

1. Introduction

One focus of current research activities in aerospace, marine, automotive and civil industry applications is on incorporating networks of (smart/intelligent) components (actuators, sensors) into new lightweight designs [4]. These transducer networks typically made of piezoelectric ceramics can be either surface-mounted on or embedded into the structure. In doing so, one is given the chance to actively alter the structural response of a system.
Another important research area investigates concepts of SHM systems. The idea is to receive precise information about the structural health by analyzing measured signals. Therefore, a robust SHM system can provide life cycle health monitoring to avoid extended periods of inspections, reduce maintenance costs and avoid unexpected catastrophic failures. A widely used SHM approach applies ultrasonic waves, in thin-walled structures so called Lamb waves, as basis of damage detection devices. Lamb waves are mainly excited and sensed by surface-bonded piezoelectric actuators and sensors, respectively. Furthermore, the simulations of Lamb waves need a fine spatial and temporal resolution. These examples show the wide range of branches, where smart systems can be applied. In conjunction with the mentioned application new questions arise, such as finding the optimal placement of actuators/sensors in a network and ensuring an efficient energy supply.

In order to cease the opportunities presented by utilizing smart structures a powerful numerical tool to predict their behaviour is needed. In engineering applications, the finite element method (FEM) provides an efficient means for the numerical analysis wide range of "real life" problems.

Normally about 80% of the overall process time to solve an engineering problem is required to generate a good quality mesh [1]. Consequently, the efficiency can be drastically increased when the geometrical description given by a CAD-software can be directly imported to a FEM-software and used to generate an optimal mesh. The isogeometric approach presented in this article is very flexible and is applicable to a vast class of problems arising in engineering practice.
In the following, the theoretical background for the creating isogeometric piezoelectric finite elements is presented. First, the isogeometric NURBS shape functions are introduced, and the finite element equations of the piezoelectric element are presented. Then, the constitutive equations of an electromechanically coupled piezoelectric material in the low-voltage range are given.

2. Isogeometric analysis for piezomechanical material

A B-spline basis is comprised of piece-wise polynomials joined with prescribed continuity conditions. To define a B-spline of polynomial order p in one dimension one needs to understand the notion of a knot vector $\mathbf{V}$. A knot vector is a set of coordinates in a parametric space, written as

$$\mathbf{V} = [\beta_0, \beta_1, \beta_2, .., \beta_{n_{\text{cont}}+p}, \beta_{n_{\text{cont}}+p+1}] \quad \text{with} \quad \beta_i \leq \beta_{i+1}\,, \tag{1}$$

where i is the knot index, $i = 0,\ 1,\ ...,\ n_{\text{cont}} + p + 1, \beta_i$ is the i^{th} knot and n_{cont} is the total number of control points [3]. There are various ways to define B-spline basis functions, but for computer implementation the application of a recurrence formula is the most common way [3]. The first order basis functions $N(\beta)_{i,0}$ of polynomial degree $p = 0$ are

$$N_{i,0}(\beta) = \begin{cases} 1, & \text{if} \quad \beta \in [\beta_i, \beta_{i+1}) \\ 0, & \text{otherwise.} \end{cases} \tag{2}$$

The basis functions $N_{i,p}(\beta)$ of higher order $p > 0$ are defined as

$$N_{i,p}(\beta) = \frac{\beta - \beta_i}{\beta_{i+p} - \beta_i} N_{i,p-1}(\beta) + \frac{\beta_{i+p+1} - \beta}{\beta_{i+p+1} - \beta_{i+1}} N_{i+1,p-1}(\beta)\,, \tag{3}$$

where the indices i and p denote the ith basis function of polynomial order p. Utilizing the B-spline basis functions $N_{i,p}(\beta)$, the NURBS basis function $R_i^p(\beta)$ and the position vector $\mathbf{X}$ of the position vector of the described curve are defined as

$$R_i^p(\beta) = \frac{N_{i,p}(\beta) w_i}{\sum_{j=1}^{n_{\text{cont}}} N_{j,p}(\beta) w_j} \quad \text{and} \quad \mathbf{X}(\beta) = \sum_{i=1}^{n_{\text{cont}}} R_i^p(\beta) \mathbf{P}_i\,, \tag{4}$$

where w_i are weights corresponding to each function $N_{i,p}$. An arbitrary NURBS curve can be described as shown in [3] with control points in global cartesian coordinates $[x_1, x_2, x_3]$ and weight parameters w_i. The derivatives of the NURBS basis functions as well as the formulation in 2D or 3D are given as [3].
Based on Ikeda [2] the equation of motion easily can be derived. For the development of a finite element the displacements $\mathbf{u}$ and the electrical potential Φ in a local domain (element) can be expressed in terms of the nodal displacements and the nodal electrical potentials ($\mathbf{U}_{\text{cont}}$, $\boldsymbol{\Phi}_{\text{cont}}$) and the matrices of the mechanical and electrical interpolation functions ($\mathbf{H}_u$, $\mathbf{H}_\phi$) as [8]

$$\mathbf{u} = \mathbf{H}_u \mathbf{U}_{\text{cont}} \quad \text{and} \quad \Phi = \mathbf{H}_\phi \boldsymbol{\Phi}_{\text{cont}}. \tag{5}$$

This formula is similar to the geometrical description of NURBS shown in Eq. (4). In isogeometric finite elements the nodal displacements and the nodal electrical potentials correspond to those at the control points. The deflections and the electrical potentials at any point of the finite element of the structure can be obtained using Eq. (5). Substituting Eq. (5) into the variational formulation [2], results in the discretized form of the equations of motion of a piezoelectric continuum [7]

$$\mathbf{M}_{uu} \ddot{\mathbf{U}}_{\text{cont}} + \mathbf{K}_{uu} \mathbf{U}_{\text{cont}} + \mathbf{K}_{u\phi} \boldsymbol{\Phi}_{\text{cont}} = \mathbf{f}_{ext} \tag{6a}$$

$$\mathbf{K}_{\phi u} \mathbf{U}_{\text{cont}} - \mathbf{K}_{\phi\phi} \boldsymbol{\Phi}_{\text{cont}} = \mathbf{q}_{ext}\,. \tag{6b}$$

The indices uu, $\phi\phi$ and $u\phi$ denote the coupling between displacement - displacement, electrical potential - electrical potential and displacement - electrical potential, and $\mathbf{M}$, $\mathbf{K}$ are the mass matrix and the stiffness or coupling matrices. The vectors $\mathbf{f}_{ext}$, $\mathbf{q}_{ext}$, $\ddot{\mathbf{U}}_{\text{cont}}$, $\mathbf{U}_{\text{cont}}$ and $\boldsymbol{\Phi}_{\text{cont}}$ are the mechanical forces, the electrical charges, the accelerations of the control points, the displacements of the control points and electrical potentials of the control points, respectively.

3. Numerical examples

In the following two models are presented to illustrate the performance of isogeometric finite elements. First, a clamped piezoelectric bimorph beam with a simple geometry is studied and second the convergence of Lamb wave propagation problem is investigated.

3.1. Bimorph ring actuator

The clamped bimorph ring actuator consists of two piezoelectric layers [7]. The material of both layers is PIC 151 [7]. The height of the layers is $h/2 = 0.254\,mm$. Both layers are poled in opposite directions and an electrical potential difference of $\Delta\Phi = 200\,V$ between the top and the bottom surface is applied, which activates both actuators. The opposite polarization introduces a bending moment. Due to the symmetry of the problem only a quarter of the ring is modelled with NURBS elements as well as with standard finite elements (C3D20E). This simplifies the application of the boundary conditions in comparison to any smaller segment, which could also be used. Results calculated with ABAQUS by applying a very fine mesh (C3D20E, dof=676404) are taken as reference values.
In Fig. 1 the evolution of the relative error of the maximum u_3-displacements with respect to the degrees-of-freedom is illustrated. The simulations utilizing the isogeometric piezoelectrical element concept are performed with three different polynomial degree templates. The polynomial degree is changed only in x_1- and x_2-direction ($p_1 = p_2 = p$). In x_3-direction for all isogeometric NURBS elements a quadratic polynomial ($p = 2$) has been prescribed.

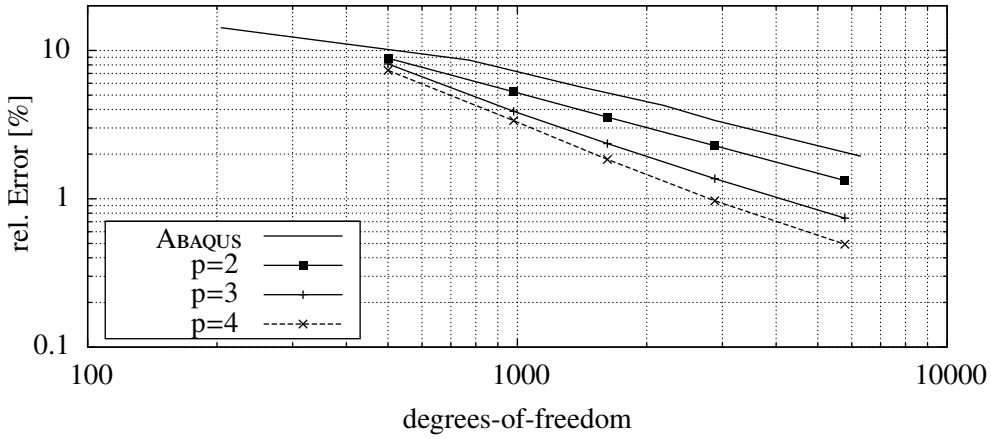

Figure 1: Convergence of three NURBS ($p_1 = p_2 = p$, $p_3 = 2$) and one ABAQUS solution (p=2).

Increasing the number of degrees of freedom results in a decreasing error for both numerical models. As expected, the accuracy increases using higher polynomial degrees. The convergence rate of the quadratic ABAQUS elements and the quadratic NURBS elements are identical, because an equal polynomial order of the shape functions is used. The convergence rate only depends on the polynomial degree [7] and not on the polynomial type. NURBS elements are nevertheless better due to the exact approximation of the geometry. This can also be seen in Fig. 1, where the NURBS curve ($p = 2$) and the ABAQUS solution have the same convergence rate, but the NURBS solution is more accurate due to the exact description of the geometry. The solution with isogeometric NURBS elements needs only one half of the degrees-of-freedom to get the same accuracy as the ABAQUS solution.

3.2. Lamb wave propagation problem

In this section the convergence of a wave propagation problem is studied. A two-dimensional model is used as illustrated in [6]. The polynomial degree in thickness direction is $p = 4$ for all higher order

approaches. The isogeometric approach is compared to a p-FEM and a spectral finite element (SEM) approach [6, 5].
The Figures 2 display the results of the convergence study for the A_0-mode with respect to a varying polynomial degree in global x_1-direction. The polynomial degree in thickness direction is chosen as $p_{x_2} = 4$. To obtain a converged solution the finite element mesh is refined in x_1-direction. χ_{A_0} is the number of "nodes" per wavelength.
The curves are steady except for small peaks experienced in the convergence curves of SEM and p-FEM. This behavior can be attributed to local element eigenfrequencies. All curves converge faster for higher polynomial orders.
It has to be noted that the convergence rate of the N-FEM elements is significantly higher than for SEM and p-FEM ones. The latter two approaches show a very similar convergence behavior. Additional studies concerning the convergence rate of C^1- and C^0-continuous isogeometric finite elements are conducted in [5].

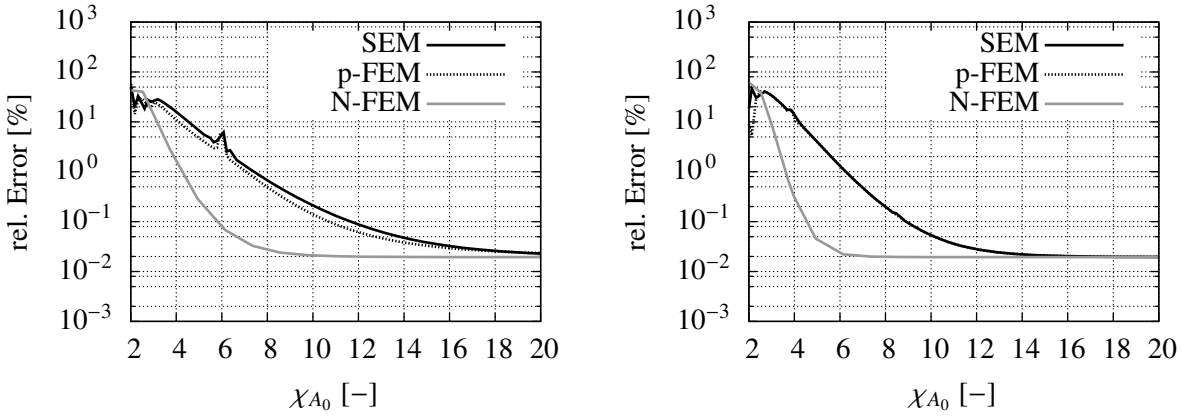

Figure 2: Convergence curve for the A_0-mode.

4. Conclusions

In the paper the development of a new isogeometric piezoelectric finite element is presented. For the simulation of complex structures the isogeometric analysis has great advantages.
The illustrated tests have demonstrated that the use of higher order polynomial degrees in isogeometric elements results in a reduction of the required total number of degrees-of-freedom in static as well as dynamic simulations. Furthermore, it is shown that a better geometrical approximation with isogeometric elements, e.g. if circular piezoelectric patches are used, results in more accurate solutions in comparison to standard isoparametric finite elements.

References

[1] T. J. R. Hughes, J. A. Cottrell, and Y. Bazilevs. Isogeometric analysis: CAD, finite elements, NURBS, exact geometry and mesh refinement. *Comp. Meth. in App. Mech. Eng.*, 194:4135–4195, 2005.

[2] T. Ikeda. *Fundamentals of piezoelectricity*. Oxford science publications. Oxford University Press, 1996.

[3] L. Piegl and W. Tiller. *The NURBS Book*. Springer, ISBN: 3-540-55069-0, 1995.

[4] A. Raghavan and C. E. S. Cesnik. Review of guided-wave structural health monitoring. *The Shock and Vibration Digest*, 39:91–114, 2007.

[5] C. Willberg. *Development of a new isogeometric finite element and its application for Lamb wave based structural health*. PhD thesis, Fortschritt-Berichte VDI Verlag, ISBN: 978-3-18-344620-9, 2013.

[6] C. Willberg, S. Duczek, J. M. Vivar-Perez, D. Schmicker, and U. Gabbert. Comparison of different higher order finite element schemes for the simulation of Lamb waves. *Comp. Meth. in App. Mech. Eng.*, 241-244:246–261, 2012.

[7] C. Willberg and U. Gabbert. Development of a three-dimensional piezoelectric isogeometric finite element for smart structure applications. *Acta Mech.*, 223(8):1837–1850, 2012.

[8] O. C. Zienkiewicz and R. Taylor. *The Finite Element Method; Volume 1: Basis*. Butterworth-Heinemann, ISBN: 0 7506 5049 4, 2000.

Proceedings of the 22nd UK Conference of the
Association for Computational Mechanics in Engineering
2 - 4 April 2014, University of Exeter, Exeter

3D EXTENDED ISOGEOMETRIC BOUNDARY ELEMENT METHOD (XIBEM) FOR ACOUSTIC WAVE SCATTERING

***Michael J. Peake, Jon Trevelyan and Graham Coates**

Durham University, School of Engineering and Computing Sciences, South Road, Durham, DH1 3LE

*m.j.peake@dur.ac.uk

ABSTRACT

An isogeometric boundary element method based on NURBS is used to find solutions to the Helmholtz equation. The method is extended in a partition-of-unity sense, multiplying the NURBS functions with families of plane waves; this new method is called the eXtended Isogeometric Boundary Element Method (XIBEM). When compared to non-enriched boundary element simulations, using XIBEM significantly reduces the number of degrees of freedom required to obtain a solution with a given error.

The extension used here (and in similar Trefftz methods) requires a set of wave directions to be specified. Ideally, these directions are uniformly spaced points over the unit-sphere. Simple schemes (e.g. latitude/longitude and discretised cube methods) have been proposed previously. However, while these schemes provide adequate spacing of wave directions, they do not allow an arbitrary number of wave directions to the be chosen. The authors use a novel algorithm, based on a physical analogy of charged particles held in static equilibrium on a spherical surface.

The XIBEM formulation will be described, including a focus on the novel method of choosing a uniformly spaced set of plane wave directions for the enrichment. Numerical results show the reduction in degrees of freedom required to obtain approximations of engineering accuracy.

Key Words: *acoustics; Helmholtz; boundary elements; isogeometric; wave scattering*

1. Introduction

The *boundary element method* (BEM) is an effective tool for analysing homogeneous acoustic scattering problems: it inherently includes the conditions of infinite domains and only requires the boundary of a scatterer to be meshed.

Recently, in general BEM research, various authors have explored the possibility of taking the basis functions used to describe a geometry in CAD and using them directly in a numerical analysis [1, 2, 6]. This concept is known as *isogeometric analysis* (IGA).

The papers above have shown that an IGA-BEM approach is viable and produces accurate results. However, simulations in acoustics are still limited by an old heuristic rule that dictates that 10 degrees of freedom per wavelength per coordinate direction are required to obtain approximations of engineering accuracy. A number of enriched (or Trefftz) methods have been developed to overcome this. In particular, the authors are interested in the partition-of-unity BEM (PU-BEM) [5]. In this, the approximation basis of the boundary elements is enriched by a family of plane waves. This greatly reduces the numbers of degrees of freedom that are required to solve a problem of a given wavelength.

When using the PU-BEM, it has been found important to use an analytical description of the geometry. This has only been available a few geometries, thus far. However, by using the basis functions used in CAD, this requirement is automatically fulfilled. This paper shows how the combination of IGA-BEM and partition-of-unity enrichment provides for an accurate and computationally efficient algorithm that can interface well with a CAD environment.

The authors have successfully used a partition-of-unity enrichment with 2D isogeometric BEM simulations—a combination termed the eXtended Isogeometric Boundary Element Method (XIBEM)

[3]. This conference paper considers the advance to 3D simulations. The authors focus on a novel approach to determine the directions of propagation of the enriching waves. Some initial results of 3D XIBEM simulations are given.

2. XIBEM

2.1. Analytical formulation

$\Omega \subset \mathbb{R}^3$ is an unbounded, homogeneous domain containing a smooth scatterer of boundary $\Gamma := \partial\Omega$. Acoustic waves, considered in the frequency domain with $\exp(-\iota\omega t)$ time dependence, are governed by the Helmholtz equation:

$$\nabla^2\phi(\mathbf{p}) + k^2\phi(\mathbf{p}) = 0, \quad \phi \in \mathbb{C}, \mathbf{q} \in \Omega, \tag{1}$$

where $\nabla^2(\cdot)$ is the Laplacian operator, ϕ is a complex wave potential, and k the is wavenumber—directly related to the wavelength $\lambda = 2\pi/k$. ι is used to denote the imaginary number, to avoid confusion with subscripts i and j later. The scatterer is impinged by an incident plane wave,

$$\phi^{\text{inc}}(\mathbf{p}) = A^{\text{inc}} \exp\left(\iota k \mathbf{d}^{\text{inc}} \cdot \mathbf{p}\right), \quad \left|\mathbf{d}^{\text{inc}}\right| = 1, \tag{2}$$

where A^{inc} is the incident wave amplitude and the unit vector, $\mathbf{d}^{\text{inc}}$, is the direction of propagation.

To solve this problem using boundary elements, a boundary integral equation is required. The derivation of the conventional BIE is well-known and yields:

$$\frac{1}{2}\phi(\mathbf{p}) = \int_\Gamma \left[\frac{\partial\phi(\mathbf{q})}{\partial n(\mathbf{q})} G(\mathbf{p},\mathbf{q}) - \phi(\mathbf{q})\frac{\partial G(\mathbf{p},\mathbf{q})}{\partial n(\mathbf{q})}\right] \mathrm{d}\Gamma(\mathbf{q}) + \phi^{\text{inc}}(\mathbf{p}), \quad \mathbf{p},\mathbf{q} \in \Gamma, \tag{3}$$

where $\mathbf{p}$ is an evaluation point, $\mathbf{q}$ is an integration point, and n is an outward-pointing, unit normal. Further, $G(\mathbf{p},\mathbf{q})$ is the fundamental solution or *Green's function*, representing the field effect experienced at $\mathbf{q}$ due to a source radiating at $\mathbf{p}$. The potential at any point $\mathbf{p}$ can be evaluated with (3) if $\phi(\mathbf{q})$ and $\partial\phi(\mathbf{q})/\partial n(\mathbf{q})$ over the entire the boundary is found.

2.2. Numerical implementation

Non-uniform rational B-splines (NURBS) are ubiquitous in CAD software and so it is NURBS basis functions that the authors use to discretise the scatter boundary, Γ. Another current development in IGA is T-splines, a superset of NURBS. Regardless of using NURBS or T-splines, both can be decomposed into their constituent Bézier patches. It is this decomposed mesh that the current authors use in the simulations of this work.

The boundary, Γ, is discretised into $E+1$ boundary elements which provide the analytical geometry of the scatterer. On each element, Γ_e, the variation in ϕ is expressed in terms of the rational Bézier basis functions, R^e_{ij},

$$\phi^e(\mathbf{q}(\xi_1,\xi_2)) = \sum_{i=0}^{p}\sum_{j=0}^{q} R^e_{ij}(\xi_1,\xi_2)\phi^e_{ij}, \tag{4}$$

where ϕ^e_{ij} is the potential associated with each NURBS basis function. A partition-of-unity enrichment is introduced, multiplying each basis function by a linear expansion of plane waves; (4) is rewritten

$$\phi^e(\mathbf{q}(\xi_1,\xi_2)) = \sum_{i=0}^{p}\sum_{j=0}^{q} R^e_{ij}(\xi_1,\xi_2)\sum_{m=0}^{M} A^e_{ijm}\exp\left(\iota k \mathbf{d}^e_{ijm}\cdot\mathbf{q}\right), \quad \left|\mathbf{d}^e_{ijm}\right| = 1, \tag{5}$$

where there are $M+1$ plane waves expanded on each basis function; each wave has a prescribed direction of propagation, $\mathbf{d}^e_{ijm} \in \mathbb{R}^3$, and unknown amplitude, $A^e_{ijm} \in \mathbb{C}$.

Substituting (5) into (3) and, for compact presentation, applying the *sound hard* boundary condition, $\partial\phi(\mathbf{q})/\partial n(\mathbf{q}) = 0$, gives

$$\frac{1}{2}\phi(\mathbf{p}) + \sum_{e=0}^{E}\sum_{i=0}^{p}\sum_{j=0}^{q}\sum_{m=0}^{M}\int_{-1}^{1}\frac{\partial G(\mathbf{p},\mathbf{q}(\xi_1,\xi_2))}{\partial n(\mathbf{q}(\xi_1,\xi_2))} R^e_{ij}(\xi_1,\xi_2)\exp\left(\iota k\,\mathbf{d}^e_{ijm}\cdot\mathbf{q}(\xi_1,\xi_2)\right)|J|\,\mathrm{d}\xi\, A^e_{ijm} = \phi^{\text{inc}}(\mathbf{p}) \tag{6}$$

where $|J|$ is the Jacobian of transformation of the mapping from global coordinates to local (ξ_1,ξ_2) coordinates.

(6) is collocated at a sufficient number of points to yield a linear system of equations can can be solved to find the unknown values of A^e_{ijm}.

3. Equal spacing of $\mathbf{d}^e_{ijm}$ about the unit sphere

Works in plane-wave enriched FEM and BEM approaches most commonly involve a uniformly spaced set of directions $\mathbf{d}^e_{ijm}$. In 2D, it is a simple procedure to take equally spaced points about the unit circle. In 3D, the same process for the unit sphere is more complex.

The authors have developed an algorithm based upon the physical analogy of an arbitrary number of charged particles held in static equilibrium on a spherical surface [4]. $M + 1$ particles of unit mass and electrical charge lie on the surface S of a unit radius sphere at locations described by vectors $\mathbf{u}_i$. At time t, the Coulomb force vector acting on each particle is given by

$$\mathbf{F}_i^t = A \sum_{j=0}^{M} \frac{(1-\delta_{ij}) \times \mathbf{r}}{|\mathbf{r}|^3}, \tag{7}$$

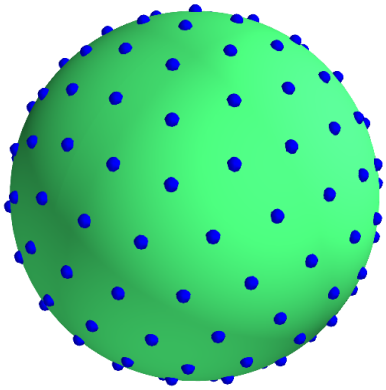

Figure 1: Converged solution of Coulomb force algorithm [4]; $M = 151$.

where where A is a scalar multiplier, δ_{ij} is the Kronecker delta, and $\mathbf{r} = \mathbf{u}_i - \mathbf{u}_j$. $\mathbf{F}_i^t$ will be oriented away from S, so the vector $\mathbf{f}_i^t$ is defined as the projection of $\mathbf{F}_i^t$ on S, given by

$$\mathbf{f}_i^t = (\mathbf{F}_i^t \times \mathbf{u}_i^t) \times \mathbf{u}_i^t. \tag{8}$$

The acceleration, $\ddot{\mathbf{u}}_i$, of each particle is

$$\ddot{\mathbf{u}}_i^t = \mathbf{f}_i^t - c\dot{\mathbf{u}}_i^t, \tag{9}$$

where c is a viscous damping coefficient and $\dot{\mathbf{u}}_i$ is the velocity of the particle. The velocity and position at the subsequent time, $t + \Delta t$, are given by

$$\dot{\mathbf{u}}_i^{t+\Delta t} = \dot{\mathbf{u}}_i^t + \ddot{\mathbf{u}}_i^t \Delta t, \tag{10}$$

$$\mathbf{u}_i^{t+\Delta t} = \frac{\mathbf{u}_i^t + \dot{\mathbf{u}}_i^t \Delta t}{\left|\mathbf{u}_i^t + \dot{\mathbf{u}}_i^t \Delta t\right|}, \tag{11}$$

where (11) normalises the position vectors to relocate the particles back onto S. Equations (7) to (11) are repeated in a time-stepping scheme to reach a converged solution, such as the one seen in Figure 1. Suitable values of A, c and Δt can be found in [4].

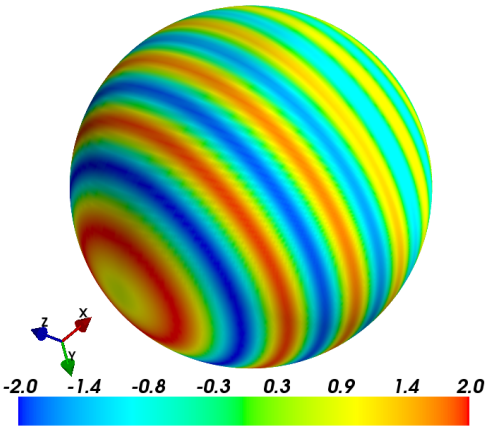

Figure 2: Scattering by a sphere at $k = 20$. Real-part of acoustic potential are shown.

4. Numerical results

Here, numerical results from simulations of a plane wave scattering on the surface of a sound hard sphere (radius $a = 1$) are presented. The incident wave has unit amplitude and propagates in the direction $\mathbf{d}^{\text{inc}} = [1, 0, 0]$. An analytical solution exists such that the scattered acoustic potential ϕ^{scat} can be found at any point $x(r, \theta)$ by

$$\phi^{\text{scat}}(r,\theta) = \sum_{n=0}^{\infty} -\frac{i^n(2n+1)j_n'(ka)}{h_n'(ka)} P_n(\cos\theta) h_n(kr) \tag{12}$$

where j_n is the spherical Bessel function of the first kind, h_n is the spherical Hankel function of the first kind, and P_n is the Legendre function of the first kind. A visual representation of the real part of the potential over the surface of the sphere can be seen in Figure 2.

Figure 3 shows a comparison of the number of degrees of freedom required to obtain an L^2 error of engineering accuracy (1%) using a conventional BEM scheme and the proposed XIBEM scheme. It shows that far fewer degrees of freedom are required with XIBEM simulations. With a conventional BEM scheme, approximately 10 degrees of freedom per wavelength in each coordinate direction are required on each element. With the XIBEM, only 3 degrees of freedom per wavelength are required.

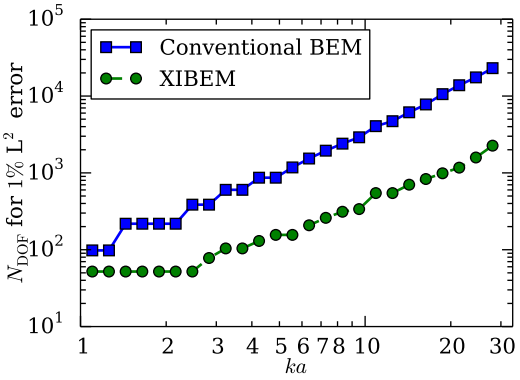

Figure 3: Comparison of N_{dof} required to obtain 1% error with conventional BEM and XIBEM.

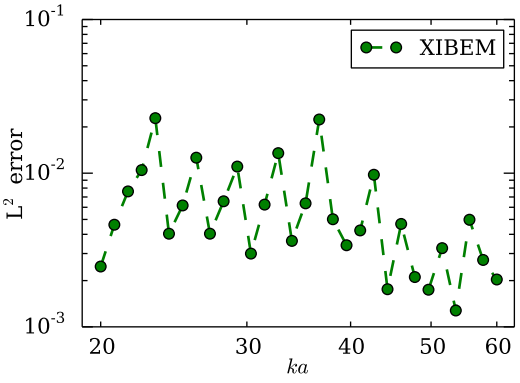

Figure 4: L^2 errors of XIBEM of medium wavelength simulations of unit sphere problem.

Figure 4 shows the errors of XIBEM simulations using 3 degrees of freedom per wavelength in each coordinate direction for shorter wavelengths than Figure 3. All simulations exhibit reasonable levels of accuracy, with all but two achieving the 1% target accuracy. A small increase in the number of degrees of freedom used would guarantee that all simulations were below this threshold. The last simulation on the figure, for $ka = 60$, uses 10,322 degrees of freedom; a similar conventional BEM simulation would require $N_{\mathrm{dof}} = 114,608$.

5. Conclusions

The PU-BEM reduces the number of degrees of freedom required to solve a Helmholtz problem such as the example in this paper. However, until now, only a few geometries have been considered due to the requirement of an analytically described geometry.

Using the functions used to describe geometry in CAD directly in a BEM simulation and enriching this basis in a partition-of-unity fashion—a combination termed XIBEM—has dramatically reduced the number of degrees of freedom required, per wavelength per coordinate direction, to solve a problem to engineering accuracy.

Using only 3 degrees of freedom per wavelength means that XIBEM needs approximately 9% of the number of equations that conventional BEM schemes need and the resulting matrix is < 1% of the size of the conventional BEM system matrix. This means, for a fixed computational resource, problems of much shorter wavelengths can now be solved.

References

[1] K.A. Belibassakisa, K.V. Gerostathisb, Th.P. Kostasb, C.G. Politis, P.D. Kakisa, A.I. Ginnisa and C. Feurera. A BEM-isogeometric method for the ship wave-resistance problem. *Ocean Engineering*, 60, 53–67, 2013.

[2] L. Heltai, M. Arroyo, and A. DeSimone. Nonsingular isogeometric boundary element method for Stokes flows in 3D. *Computer Methods in Appield Mechanics and Engineering*, 268, 514–539, 2014.

[3] M.J. Peake, J. Trevelyan, and G. Coates. Extended isogeometric boundary element method (XIBEM) for two-dimensional Helmholtz problems. *Computer Methods in Appield Mechanics and Engineering*, 259, 93–102, 2013.

[4] M.J. Peake, J. Trevelyan, and G. Coates. The equal spacing of N points on a sphere with application to partition-of-unity wave diffraction problems. *Engineering Analysis with Boundary Elements*, 40, 114-122, 2014.

[5] E. Perrey-Debain, J. Trevelyan, and P. Bettes. Plane wave interpolation in direct collocation boudary element method for radiation and wave scattering: numerical aspects and applications. *Journal of Sound and Vibration*, 261(5), 839–858, 2003.

[6] R.N. Simpson, M.A. Scott, M. Taus, D.C. Thomas, and H. Lian. Acoustic isogeometric boundary element analysis. *Computer Methods in Appield Mechanics and Engineering*, 269, 265–290, 2014.

Proceedings of the 22nd UK Conference of the
Association for Computational Mechanics in Engineering
2 – 4April 2014, University of Exeter, Exeter

Computational thermal conductivity in porous materials: numerical and statistical approaches

***A. El Moumen, T. Kanit and A. Imad**

Mechanics laboratory of Lille. Lille1 University, cite scientifique, 59655 Villeneuve d'ascq, Frensh.

*aelmoumen@gmail.com

ABSTRACT

In this paper, the numerical homogenization technique and morphological analysis are used in order to compute the thermal conductivity in microscale of porous materials. The objective is to quantify the difference between microstructures with overlapping and non-overlapping pores. The relationships between their morphological parameters and their macroscopic effective thermal conductivities are proposed. Statistical parameters such as, covariance and integral range are introduced for morphological characterization. The microstructure volume is related with all microstructure parameters. The equivalent morphology concept for thermal conductivity is introduced after development of some relationships between morphological parameters.

Keywords: *Numerical and statistical homogenization; porous materials; morphological analysis; effective thermal conductivity; equivalent morphology concept.*

1. Introduction

Heat transport through porous media is of great interest in chemical, mechanical, geological, environmental and petroleum applications. For these reasons, the determination of the effective linear thermal conductivity (ELTC) for various porous media is of great practical interest in the efficient design of industrial equipment. Generally, two techniques of homogenization are available in this topic, existing analytical estimates or computational numerical methods. The homogenization refers to the process of considering a statistically homogeneous representation of the heterogeneous material, called deterministic representative volume element (RVE).

To study the real effect of the morphology porous media, it is necessary to develop other techniques based on microstructure morphology analysis by statistical methods. The numerical results are coupled with statistical parameters in order to obtain some morphological and thermal properties. This is the case of El Moumen et al. [1] and Torquato [2] for composite structures.

In this study, the computation of effective thermal conductivity in porous materials is proposed using numerical and statistical approaches. The first microstructure containing spherical pores without any contact between neighbouring pores, and the second morphology with overlapping spherical pores. The covariance notion and the integral range are used for morphological characterization. The equivalence between porous microstructures with overlapping and non-overlapping spherical pores is proposed for different morphological parameters. The obtained relationships between two used microstructures are introduced to define the concept of equivalent morphology.

2. Microstructures and meshing

In this investigation, thermal numerical computations of porous materials, containing a random distribution of identical spherical or ellipsoidal pores are presented. Two types of microstructures are considered: microstructure 1 with non-overlapping spherical or ellipsoidal pores and microstructures 2 with overlapping pores, based on the Boolean model of spheres. The microstructure is generated by using the Poisson process, see figure 1.a. The regular finite element (FE) mesh is superimposed on the image (figure 1.b) of the porous microstructure using the so-called multi-phase element technique. Indeed, an image of the microstructure is used to attribute the phase property to each integration point of a regular mesh, according to the color of the underlying voxel. Figure 1.c gives an example of the

used FE mesh in this study.

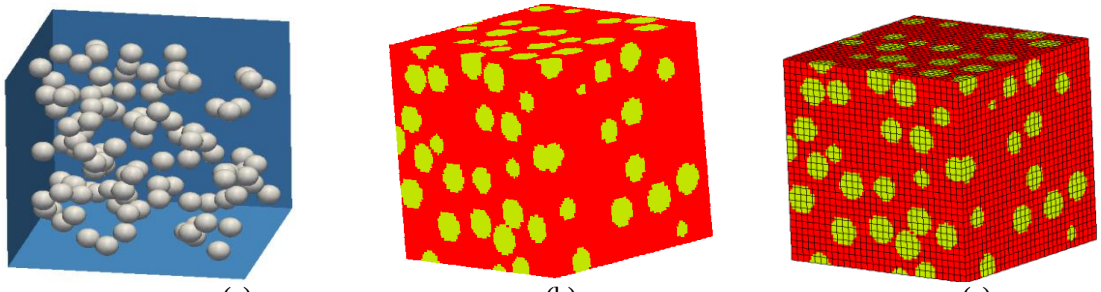

(a) (b) (c)

Figure 1: Microstructures meshing: (a) implantation of particles, (b) initial image and (c) mesh of the image.

Both phases are considered as linear thermal conducting. The considered thermal conductivities for matrix phase λ_m and pores λ_i are:

- Case 1: $\lambda_m = 0.3W/m.K$ and $\lambda_i = 0.024W/m.K$ with contrast $c = \lambda_m / \lambda_i = 12.5$.
- Case 2: $\lambda_m = 0.5W/m.K$ and $\lambda_i = 0.024W/m.K$ with contrast $c = \lambda_m / \lambda_i = 20.8$.
- Case 3: $\lambda_m = 0.6W/m.K$ and $\lambda_i = 0.024W/m.K$ with contrast $c = \lambda_m / \lambda_i = 25$.

3. Computational thermal simulations

3.1 Realizations generation

Apparent properties were defined as the FE calculation macroscopic results of volumes smaller than RVE. For each elementary volume V of considered porous material, containing N pores, n different realizations were created and Periodic boundary conditions were applied. The number of realizations n, considered for each fixed volume V containing N pores is given in table 1. As a result, an increasing volume V means an increasing the number N.

Table 1: Number of realizations *n* used for each fixed number of pores *N*.

N	2	5	20	50	100	200	250
n	216	40	20	15	9	3	2

3.2 Fluctuations of pores volume fraction and thermal conductivity.

The objective of this part is to determine the relationship, an equivalence, between apparent volume fractions f^a of non-overlapping pores obtained by N particles and real volume fractions f obtained by the same N but in overlapping case. In the case of non-overlapping spheres, the apparent pore volume fraction is evaluated by: $f^a = NV_{sphere} / V_{total}$. It is noted that, in the case of non-overlapping spheres $f = f^a$ and $f \leq f^a$ for overlapping spheres case. Figure 2.a shows the variation of the relative pores volume fraction f / f^a versus N in an example of porous material containing N pores. The objective here is to obtain a relationship between f and f^a for larger volumes. This figure shows an asymptotic value equals to 0.28. One can write for larger volumes:

$$f \simeq 0.28 f^a \quad (1)$$

For thermal conducting homogenization of porous materials, an example of the obtained numerical results is presented in figure 2.b for different realizations. The same results are obtained in other cases. This figure shows the average values and its intervals of confidence as a function of the volume size. It shows that the dispersion of results decreases when the size of the domain increases. The error

which means standard deviation of the ELTC is represented with vertical bars. This error decreases when the volume size increases, and tends to zero for RVE.

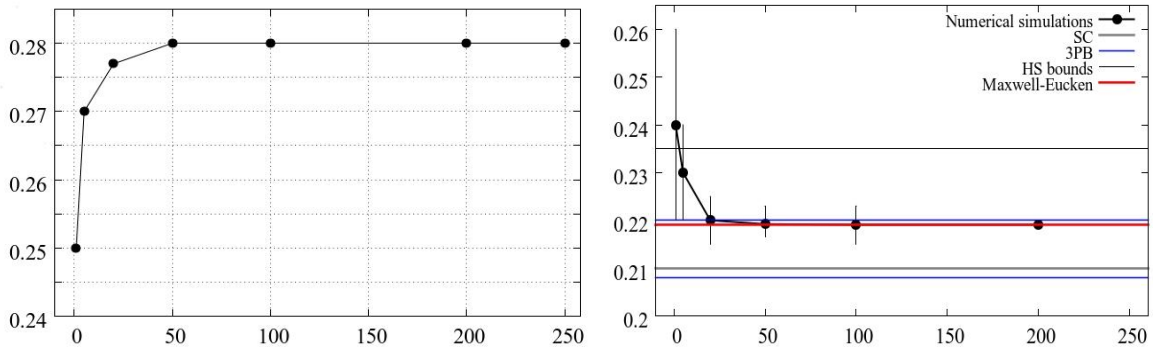

(a) (b)

Figure 2: Fluctuation of macroscopic properties: (a) pores volume fraction and (b) example of estimated thermal conductivities versus volume size for *f=0.23*.

4. Benefits of identifying and using statistical parameters

Identification of the statistical parameters by using mathematical morphology yields a number of benefits relevant for porous microstructures. The mathematical morphology methods combined with numerical results are used to study the representativity and the anisotropy of porous microstructures. The statistical laws of the mathematical morphology can be used to relate between morphological, statistical and thermal parameters of random microstructures. In geostatics, it is well known that for thermal properties, this relation can be written versus V or N as:

$$D_\lambda^2(V) = f(1-f)(\lambda_i - \lambda_m)^2 \frac{A}{V} \qquad \text{Or} \qquad D_\lambda^2(N) = f(1-f)(\lambda_i - \lambda_m)^2 \frac{A}{N} \tag{2}$$

Where $D_\lambda^2(V)$ is the variance of the volume V and A is the integral range.

The obtained numerical results by set realizations, presented in table 1, of each volume size $V = N$, are used to determine the numerical variance $D_\lambda^2(N)$ for each N. The fitting methods according to Eq.(2) between volume size N and its numerical variance $D_\lambda^2(N)$, obtained by set n different realizations, give us the value of integral range noted A_F. The obtained values of A_F for each microstructure are compared to f / N_{RVE} (the volume of one pore in RVE). Table 3 gives the different obtained values of A_F for microstructures 1 and 2 and for each studied case.

Table 2: Comparison between integral ranges of two microstructures for *f*=0.23.

	Microstructure 1: non-overlapping pores			Microstructure 2: overlapping pores		
cases	Case 1	Case 2	Case 3	Case 1	Case 2	Case 3
N_{RVE}	15	20	20	15	15	15
$A^* = f / N_{RVE}$	0.015	0.012	0.012	0.016	0.016	0.016
A_F	0.015	0.012	0.013	0.13	0.135	0.145
A_F / A^*	1	1	1	8	8	9

The relationship between volume fractions of two used porous microstructures, is given by Eq.(1). It is possible to make other relationships between morphological parameters of two microstructures, such as pores number N and radius R of spherical pores. From results of table 3, the relationship between integral ranges of two microstructures is:

$$A^o = 8A^h \tag{3}$$

Where A^o is the integral range defined as the volume of one pore in overlapping spherical pores N^o and A^h for non overlapping pores N^h case. The Eq.(3) can be written as following :

$$\frac{f}{N^o_{RVE}} = 8\frac{f^a}{N^h_{RVE}} \tag{4}$$

The combination between Eq.(1) and Eq.(4) gives the relation between pore number N :

$$\frac{N^h_{RVE}}{N^o_{RVE}} \simeq 28 \tag{5}$$

According to Eq.(5), it appears that the RVE of the porous microstructures with non-overlapping spheres is larger 28 times than RVE of its equivalent in porous microstructures with overlapping spheres. Defining as A the volume of one pore in two microstructures, and developing the Eq.(3), it is possible to make a relationship between pore size of two microstructures as following:

$$A = \frac{4}{3}\pi R_o^3 = 8\frac{4}{3}\pi R_h^3 \Rightarrow R_o = 2R_h \tag{6}$$

Where R_o is the radius of overlapping spheres in original morphology and R_h is the radius of non-overlapping spheres in its equivalent morphology. As the pore volume fraction case, it appears that the number N and radii of overlapping pores accept an equivalent one in non-overlapping case. Therefore, in the equivalent morphology, the radius of one pore is 2 times the radius of one pore in overlapping spheres case (original morphology). Using these conditions, the equivalent morphology concept can be proposed for thermal conductivity of porous media as shown in figure 3.

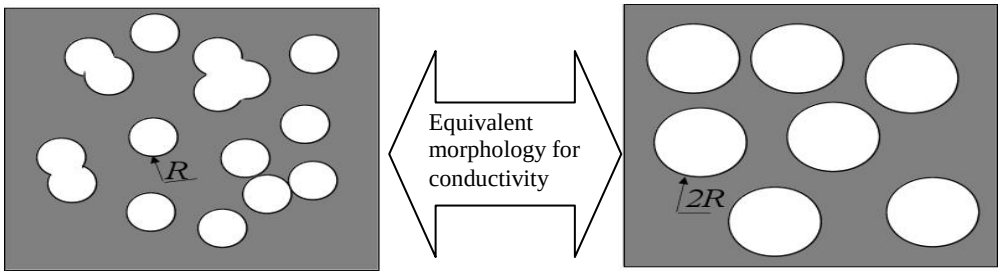

Figure 3: Equivalent morphology concept in porous media.

5. Conclusion

The principal objective of this study is to quantify the difference between porous microstructures with overlapping pores and porous microstructures with non-overlapping pores. The FEM coupled with statistical laws is used for morphological and numerical characterizations. Some relationships between morphological parameters of two microstructures, like pores number N , porosity f and radii, were determined. It appears for conductive properties, any isotropic mixture of overlapping pores is equivalent to certain pores volume fraction, radius, and pores number in non-overlapping case. These results suggest us to define the concept of equivalent morphology.

6. References

[1] A. El Moumen, T. Kanit, A. Imad, H. El Minor, Effect of overlapping inclusions on effective elastic properties of composites. Mechanics Research Communication, 53, 24-30, 2013.

[2] S. Torquato, Morphology and effective properties of disordered heterogeneous media. International Journal of Solids and Structures 35, 2385–2406, 1997.

Proceedings of the 22nd UK Conference of the
Association for Computational Mechanics in Engineering
2 – 4April 2014, University of Exeter, Exeter

STOCHASTIC THERMOMECHANICAL ANALYSIS OF NUCLEAR GRAPHITE USING PARAFEM

***Jose David Arregui-Mena[1], Lee Margetts[2,3], Louise Lever[3], Graham Hall[1] and Paul Mummery[1]**

[1]School of Mechanical, Aerospace and Civil Engineering, University of Manchester,
Oxford Road, Manchester, M13 9PL
[2]School of Earth, Atmospheric and Environmental Sciences, University of Manchester,
Oxford Road, Manchester, M13 9PL
[3]Research Computing, University of Manchester, University of Manchester,
Oxford Road, Manchester, M13 9PL

*jose.arreguimena@postgrad.manchester.ac.uk

ABSTRACT

A Stochastic Thermoelastic Finite Element Method with a Direct Monte Carlo procedure is proposed to predict the mechanical behavior of Gilsocarbon nuclear graphite. The spatial variability of material properties of different types of nuclear graphite has been studied between billets, between lots and in some cases within a billet. However, the influence of these random fluctuations on the mechanical behavior of nuclear graphite is limited. For this study in particular the coefficient of thermal expansion was selected as a random variable. In order to test the influence of spatial variability on nuclear graphite, the open source software ParaFEM is being extended to interface with third party software libraries that can generate spatially variable 3D random fields for any particular material property.

Keywords: *Probabilistic Analysis, Finite Element Method, Nuclear Graphite*

1. Introduction

Nuclear energy is one of the main sources of electricity for members of the OCDE [1]. There are several types of technologies to produce nuclear energy, several historical, geographical and political factors created very different types of nuclear reactors. All reactors share the same physical principles. However, the main differences between reactors are the materials that are used to moderate the nuclear reactions. In the United Kingdom nuclear graphite was selected as the moderator and carbon dioxide as the coolant for the first and second generation of nuclear reactors; Magnox and Advanced Gas-Cooled Reactors (AGR) respectively. Thousands of stacked graphite bricks form the graphite core of the reactor. The graphite bricks are configured to form several pathways and round channels to place the fuel and other instruments. The graphite components produced for nuclear applications require a high purity and density, and isotropic material behavior to assure a long lifetime and good performance of graphite subjected to neutron irradiation. Nevertheless, the processes of neutron irradiation and radiolytic oxidation, a reaction between the carbon dioxide and graphite, constantly damage the nuclear graphite core. Weight loss, strains and cracking can produce distortions on the channels impeding the loading and unloading of fuel and also reduce the capacity of the reactor to produce electricity. Moreover, the nuclear graphite core cannot be replaced, so the graphite core is considered to be one of the limiting components of the usable lifetime of the reactor.

Periodical inspections track the ageing effects on graphite caused by nuclear irradiation. A device explores the surface of the graphite core to measure the ovality and dimensions of the core channels. In addition to these tests, samples can be taken from the graphite core [2]. However, this type of inspection cannot predict the ageing effects at the exterior of the bricks. The state of the graphite bricks is estimated using finite element models that predict the strain produced by the thermal loading, nuclear irradiation and radiolytic oxidation.

A new approach is being investigated by the authors that may help engineers better understand the behaviour of nuclear graphite subjected to the conditions of an operating reactor. This approach is the inclusion of random material properties in the finite element models. To test the influence of the variability of material properties on nuclear graphite behaviour, a hypothesis is proposed: *that tiny spatial variations in "initial" material property values have a significant effect on the mechanical performance of nuclear graphite during its in-service lifetime.*

This hypothesis is proposed because the structure of graphite can widely vary depending on the process of manufacture [3]. The spatial variability of material properties of different types of nuclear graphite has been studied between billets, between lots and in some cases within a billet [4,5]. However, research into the influence of these fluctuations on the mechanical behaviour of nuclear graphite is limited. Here, the initial variability in graphite properties of manufactured bricks is represented in the finite element models using random fields. In this paper the coefficient of thermal expansion (CTE) was selected as the random variable.

To test our hypothesis, the open source software for parallel finite element analysis, ParaFEM, is being extended to interface with third party software libraries that can generate spatially variable 3D random fields for any particular material property. These random fields are used to characterize and distribute the random fluctuations of a material in each finite element. However, a single realization is not capable of representing the whole nature of a random system, thus several realizations of a random field are created following a Monte Carlo Simulation scheme. The cost of analysing multiple realizations and the inclusion of the random fields highly increases the computational power required to analyse a system. To overcome this, the software ParaFEM employs several techniques that distribute the useful computations on parallel platforms to reduce solution time. ParaFEM is written in modern Fortran and is based on the book by I.M. Smith, D.V. Griffiths and L. Margetts [6].

2. Methodology

The Monte Carlo Simulation methodology was chosen to characterize and study the random fluctuations of material properties of nuclear graphite. This approach merges the simulation technique of Monte Carlo and the deterministic finite element analysis. The Monte Carlo Simulations are considered to be the most general approach for probabilistic finite element modelling. Moreover, the Monte Carlo Simulation strategy does not require major modifications to existing deterministic software and is very suitable for parallel computation. The general procedure of this method follows: (1) Determine the set of random and deterministic variables; (2) characterize the density function and correlation parameters of the random variables; (3) use a random field generator to produce a set of random fields; (4) calculate the solution of each realization with the deterministic finite element program; (5) gather and analyse the information of the simulations; (6) verify the accuracy of the procedure (Figure 1) [7].

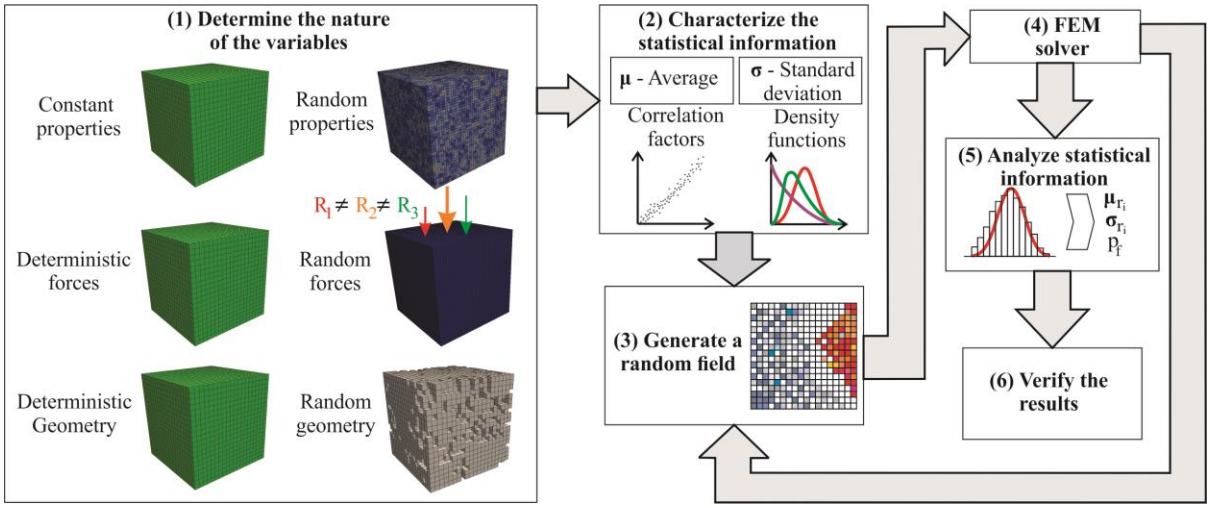

Figure 1: Description of the general procedure of the Direct Monte Carlo Simulation

3. Random field – Local Average Subdivision Method

The random field generator chosen to distribute the values of the coefficient of thermal expansion (CTE) is the Local Average Subdivision (LAS) Method [8,9]. The procedure for a one-dimensional implementation employs a top-down recursive method. To start the procedure, a general average value is obtained from experimental data. In the first stage, the region is subdivided into two equal subdomains; the subdomains are assigned with new values that have to fulfil a condition, the values of each subdomain have to be the average of the global value or parent. This process is repeated over and over until the desired refinement of the mesh is achieved.

The input values to calibrate the random are the mean, standard deviation and the correlation length of the variable of interest. The mean and standard deviation are obtained from experimental values and the correlation length is a variable that relates the values of the variable in a given length. In this length the average values returns the mean value of the chosen variable. Examples of different correlation lengths for the CTE are given in Figure 3.

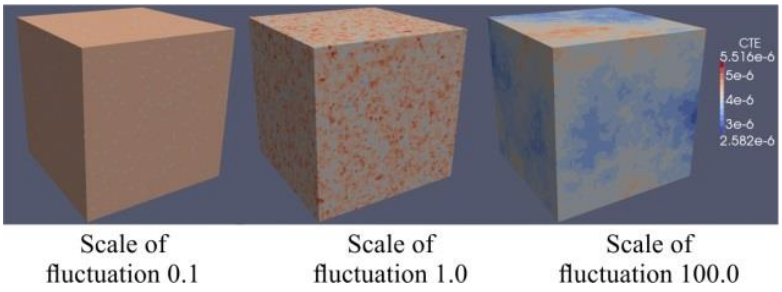

Figure 2: Comparison of 3 different scales of fluctuation

4. Finite Element Analysis

Thermal stresses are generated when a temperature change together with certain conditions are present. Several factors can cause thermal stresses such as temperature gradients, when the object of study is constrained in some way that the free expansion cannot occur, and also when there are material incompatibilities [10]. The latter is the one that is of interest to this study. In order to represent these material incompatibilities the random field generator described in Section 3 was selected to generate random fields for the CTE of graphite. A brick of an AGR reactor was chosen as the geometry to perform the analysis. The values of the material properties of Gilsocarbon a semi-isotropic graphite used for the simulations and for the random fields are given in Table 1.

Table 1: Common values for virgin isotropic graphite Gilsocarbon

Material properties of isotropic graphite	Mean Values	Standard Deviation
Mean coefficient of thermal expansion	4.35×10^{-6} $(°C)^{-1}$	8.7×10^{-7} $(°C)^{-1}$
Poisson's ratio	0.2	
Dynamic Young's modulus	10 GPa	

Free expansion was allowed in all the regions of the brick. Two sets of temperature fields were chosen as an example. In Case 1, the first temperature field is a homogenous increment of temperature of 100 °C. In Case 2, the temperature field takes the form of a linear gradient, where the temperature outside of the brick is 20 °C rising to 120 °C in the bore. The temperature distribution for a typical realization for Case 1, its corresponding random field for the CTE, and results of a typical analysis are shown in Figure 3.

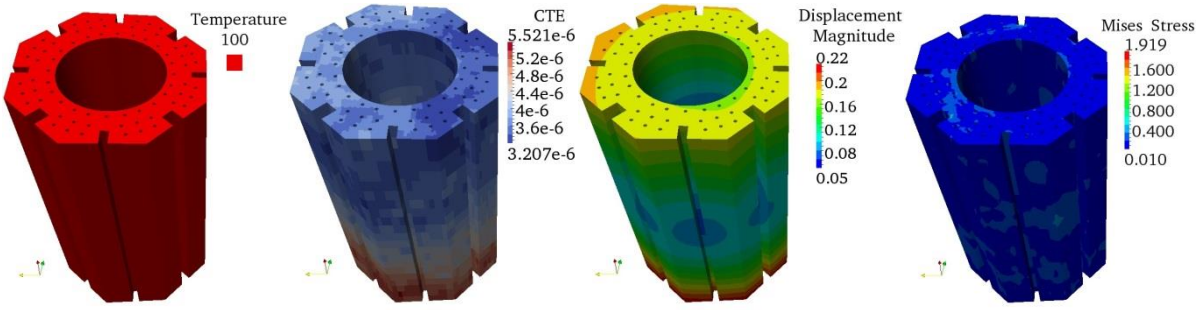

Figure 3: Case 1 (homogenous temperature distribution), material properties of a random field of the CTE, displacement field and stress analysis of a typical realization for the first analysis (from left to right)

The corresponding images for Case 2, the temperature distribution for the linear gradient, random field, displacements and stress analysis are presented in Figure 4.

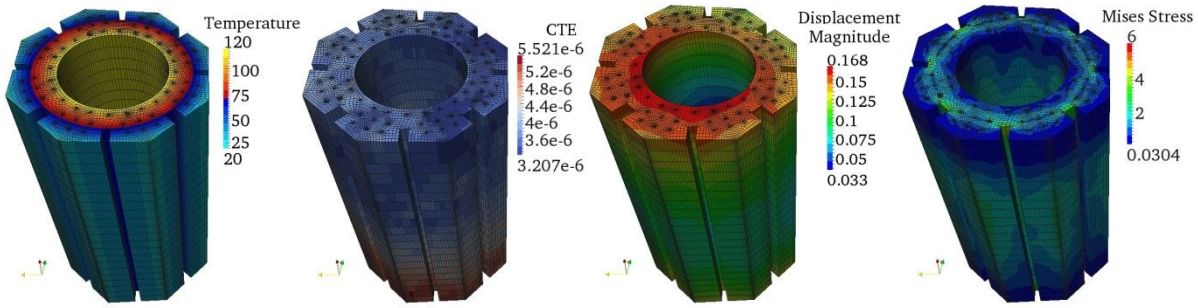

Figure 4: Case 2 (linear gradient for the temperature distribution), material properties of a random field of the CTE, displacement field and stress analysis of a typical realization for the second analysis (from left to right)

5. Conclusions

The analyses show that even in the early life of a graphite core, some unexpected stresses can be generated by the inhomogeneity of the material properties of graphite, even with a homogenous temperature gradient. These initial stresses are usually neglected (set to zero) and may years later contribute to the early cracking of a brick. To more accurately account for material inhomogeneity and its influence on the thermo-mechanical behaviour of nuclear graphite, it is necessary to consider the relationship between Young's Modulus and the CTE. The relationship between these two material properties is going to be considered in future work.

A methodology is proposed to incorporate random material variation into nuclear graphite. These random variations are represented by random fields that can be incorporated into open source deterministic finite element software. In this paper only single realizations are given to illustrate the concept. In the conference presentation, the speaker will present results from a full Monte Carlo Simulation and show how this can be used to obtain an accurate estimation of the response variables.

Acknowledgements

The authors wish to thank the support and resources provided by the Mexican National Science and Technology Council (CONACYT). This work made use of the facilities of N8 HPC provided and funded by the N8 consortium and EPSRC (Grant No.EP/K000225/1). The Centre is co-ordinated by the Universities of Leeds and Manchester.

References

[1] International Energy, A., *Technology Roadmap: Nuclear Energy [electronic resource]*. IEA Technology Roadmaps,2218-2837. 2010, Paris: OECD Publishing.

[2] Yang, E., et al. *Model-based estimation and filtering for condition monitoring of AGR nuclear graphite cores*. 2010.

[3] Yoda, S. and K. Fujisaki, *An approximate relation between Young's modulus and thermal expansion coefficient for nuclear-grade graphite*. Journal of Nuclear Materials, 1983. **113**(2–3): p. 263-267.

[4] Preston, S.D. *The effect of material property variations on the failure probability of an AGR moderator brick subject to irradiation induced self stress. [electronic resource]*. 1989.

[5] Strizak, J.P., *Spatial variability in the tensile strength of an extruded nuclear-grade graphite.* . 1991, Technical Information Center Oak Ridge Tennessee

[6] Smith, I.M., et al., *Programming the finite element method*. Fifth edition / I. M. Smith, D. V. Griffiths, L. Margetts. ed. 2014, Chichester, West Sussex, United Kingdom: John Wiley & Sons Inc. xiv, 664 pages.

[7] Haldar, A. and S. Mahadevan, *Reliability assessment using stochastic finite element analysis*. 2000, New York ; Chichester: John Wiley & Sons. xvi, 328.

[8] Fenton, G.A. and D.V. Griffiths, *Risk assessment in geotechnical engineering*. 2008, Hoboken, N.J.: Chichester : John Wiley & Sons. xvii, 461.

[9] Fenton, G.A. and E.H. Vanmarcke, *Simulation of Random-Fields Via Local Average Subdivision.* Journal of Engineering Mechanics-Asce, 1990. **116**(8): p. 1733-1749.

[10] Manson, S.S., *Thermal stress and low-cycle fatigue*. 1966, New York,: McGraw-Hill. xi, 404 p.

Proceedings of the 22nd UK Conference of the
Association for Computational Mechanics in Engineering
2 – 4April 2014, University of Exeter, Exeter

TEMPERATURE DATA ANALYSIS FROM FIELD SCALE THERMAL MONITORING

***Majid Sedighi[1], Daniel P. Bennett[1], Shakil A. Masum[1], Hywel R. Thomas[1], Erik Johansson[2] and Topias Siren[3]**

[1]Geoenvironmental Research Centre, School of Engineering, Cardiff University, The Queen's Buildings, Newport Road, Cardiff, CF24 3AA, UK
[2]Saanio & Riekkola Oy, 4 Laulukuja, Helsinki, FI-00420, Finland
[3]Posiva Oy, Olkiluoto, Eurajoki, FI-27160, Finland

*SedighiM@cf.ac.uk

ABSTRACT

This paper presents the results of an investigation into the thermal behaviour of a site proposed for the deep geological disposal of high level radioactive waste in Finland. Temperature data have been collected through a monitoring programme carried out at the site and the ONKALO Underground Rock Characterisation Facility (URCF). Various computational methods and approaches have been adopted to provide an insight into the ground's thermal behaviour at the site and facilities constructed in the ONKALO. A Non-uniform Discrete Fourier Transform (NDFT) analysis has been carried out on the data collected from the access ramp and surface datasets. The methodology adopted for the NDFT analysis and results obtained are described in this paper. The results achieved provide an improved understanding of the thermal evolution in the rock, the repository facility and the subsurface soil at the site.

Keywords: *ONKALO; Olkiluoto; thermal monitoring; data analysis*

1. Introduction

This paper presents the results of a thermal monitoring programme carried out at a site in Finland, where a geological repository for the disposal of high level nuclear waste is being considered. The site, which is located in the Gulf of Bothnia, has been selected for the possible disposal of the spent fuel produced by two nuclear power plants on the Olkiluoto Island.

An Underground Rock Characterisation Facility (URCF), named ONKALO, has been constructed at the site, which comprises approximately 5km of access tunnel to the 420m disposal depth[1]. Figure 2 presents the ONKALO. The ONKALO URCF allows for the testing of the design concept as the construction is developed and provides on-site information of rock conditions [1].

As part of a multidisciplinary monitoring programme, data related to geological, thermal, rock mechanics, hydrogeological and hydrogeochemical processes have been collected by Posiva Oy [2,3,4]. Temperature data collected at the Olkiluoto site and ONKALO at various locations have been studied and analysed including the three categories of temperature datasets as follows: i) data collected from the 57 deep boreholes, ii) measurements in the ONKALO, iii) surface data obtained from four weather stations and four measurement ditches [5].

This paper presents a description of the investigation and analysis undertaken on temperature datasets relate to the ONKALO measurements which include temperature data recorded at 11 tunnel stations/chainages [4,5]. The methodology adopted for analysing the temperature time series from the monitoring programme at these locations is discussed. Temperature evolutions with time at 11 chainage points along the ONKALO access ramp, i.e. CH0 to CH4580, have been collated during the monitoring programme. The time series data of the outside temperature and three stations located close to the entrance of the ONKALO ramp are presented in Figure 2.

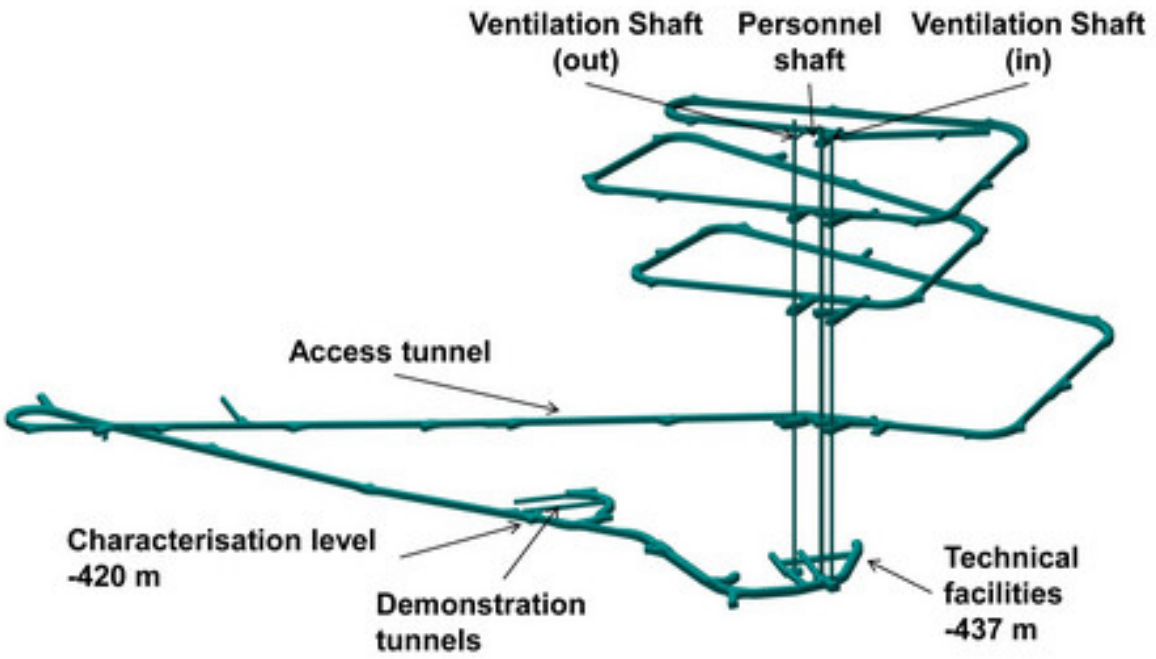

Figure 1: The ONKALO Underground Rock Characterization Facility [1].

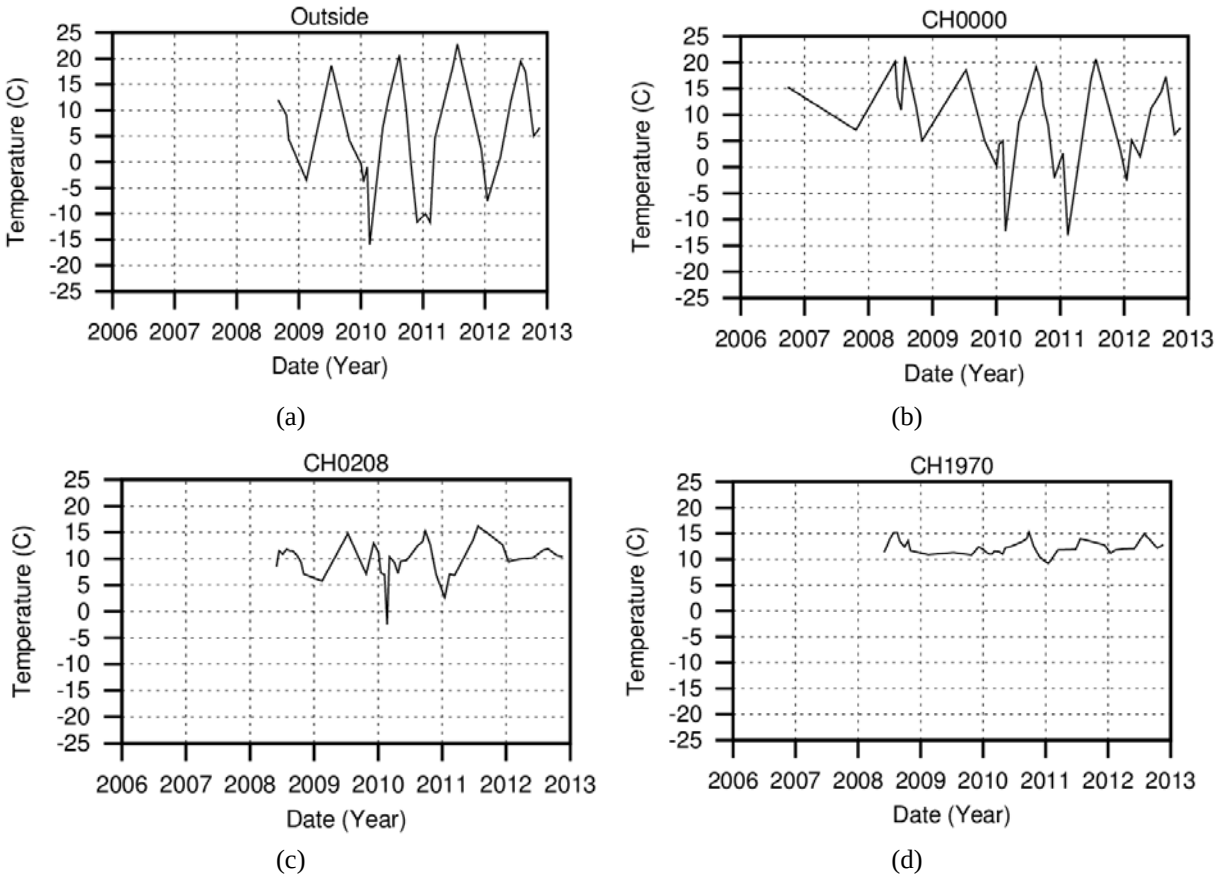

Figure 2: Time series data related to the station outside of the ONKALO ramp (a) and chainges CH0000 (b), CH0208 (c) and CH1970(d) which are the first three chainages along the ONKALO ramp [4,5].

2. Analysis of time series of the ONKALO ramp

In order to obtain the characteristics of the time series data from 11 chainages in ONKALO ramp, a Fourier Transform analysis has been carried out for each data point/series. The analysis was carried out using the toolkit developed at the Geoenvironmental Research Centre, i.e. NUDAT [5,6]. The main data analysis features incorporated into the NUDAT include: i) Frequency domain analysis, ii) Long-term trend determination, iii) Aberrant point identification (spike detection), iv) Smoothing/averaging/down-sampling functions and v) Second order event candidate detection [5]. The quantitative identification of the frequency content of a time series is calculated by applying a Non Uniform Discrete Fourier Transform (NDFT). The implementation of the NDFT capability in NUDAT provides the option to automatically remove the zero frequency component from the input time series.

The frequency content and amplitude of the time series have been obtained by the application of the NUDAT toolkit. Example results of the NDFT analysis of data related to the ONKALO ramp are presented in Figure 3.

The annual cycle (365-day wavelength) has been found to contain the largest amplitude of temperature recorded at most tunnel chainage locations.

The temperature amplitude for a 365 day cycle calculated at different chainage locations is shown in Figure 4. As shown in Figure 4, the largest variations of the temperature amplitude correspond to the two locations nearest to the surface. The variations in temperature for these two locations were found to be approximately 14 ^{o}C and 10.5^{o}C. The variations in the temperature amplitude for the other stations are approximately 3^{o}C or less and associated with 365 days cycle.

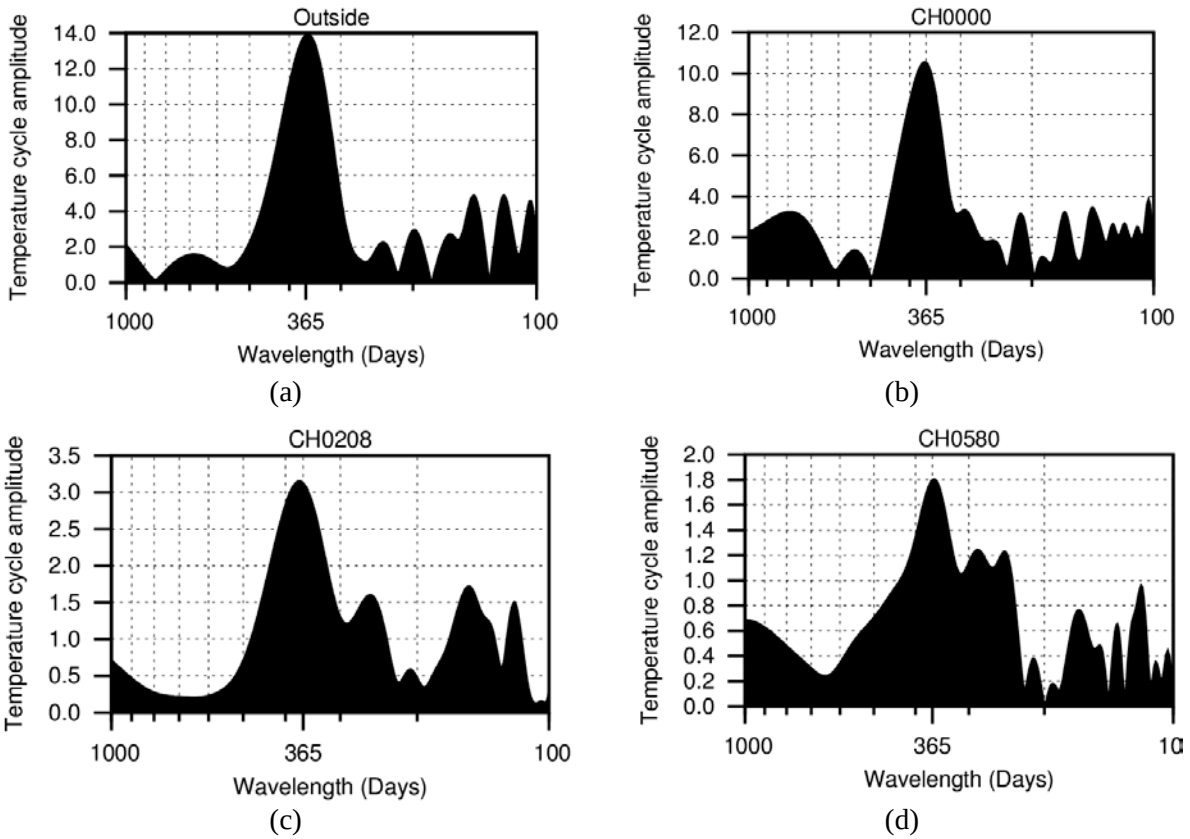

Figure 3: Temperature cycle amplitude versus wavelength calculated from the NDFT analysis of time series related to the station outside of the ONKALO ramp (a) and chainges CH0000 (b), CH0208 (c) and CH1970(d).

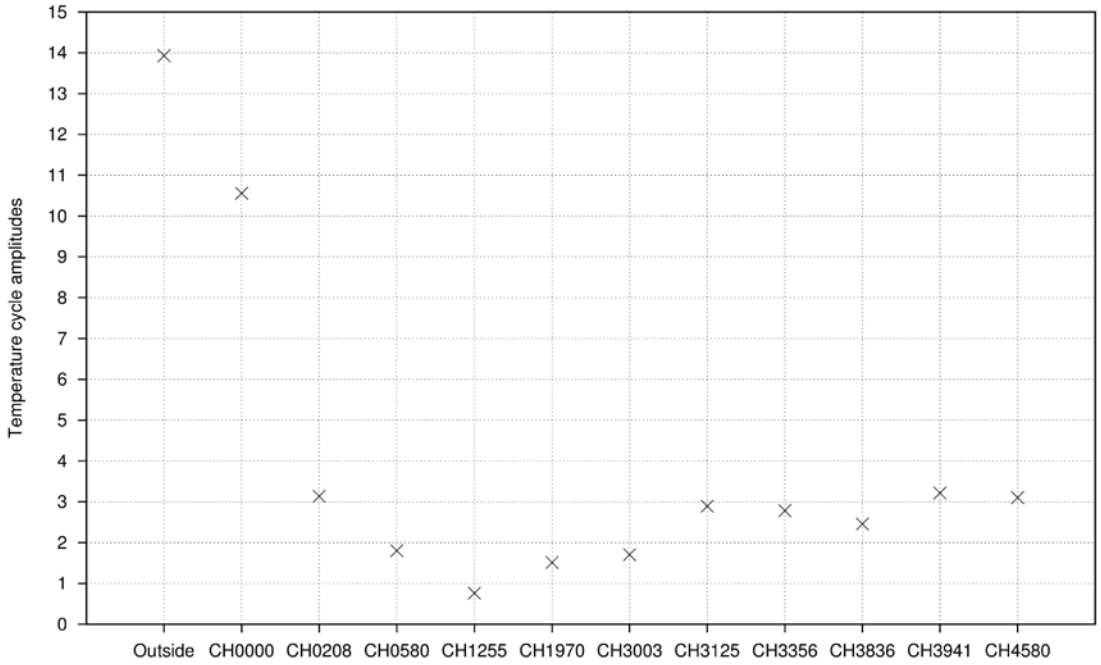

Figure 4: Temperature cycle amplitude versus wavelength calculated from the NDFT analysis related to chainges CH0000 to CH0208.

3. Conclusions

The results of an investigation into the thermal behaviour of an Underground Rock Characterisation Facility, i.e. ONKALO, for a site proposed for the deep geological disposal of high level radioactive waste in Finland have been presented. Non Uniform Discrete Fourier Transform (NDFT) have been successfully applied to provide an improved understanding of the thermal regime of the ONKALO and access ramp.

Acknowledgements

The work presented was performed by the Geoenvironmental Research Centre, Cardiff University under contract to Posiva Oy. The financial support received is acknowledged.

References

[1] Posiva. *ONKALO – Main Drawings in 2007*. Working Report, Posiva, OY, 2008.

[2] Posiva. *Programme of Monitoring at Olkiluoto during Construction and Operation of the ONKALO*. Report POSIVA 2003-5, Posiva Oy, 2003.

[3] Posiva. *Monitoring at Olkiluoto–A Programme for the Period before Repository Operation*. Report POSIVA 2012-01, Posiva Oy, 2012.

[4] E. Johansson and T. Siren. *Results of monitoring at Olkiluoto in 2012, Rock mechanics*. Working Report, 2013-47, Posiva Oy, 2014.

[5] M. Sedighi, D.P. Bennett, S.A. Masum, H.R. Thomas and E. Johansson. *Analysis of temperature data at the Olkiluoto*. Working Report 2013-58, Posiva Oy, 2014.

[6] D.P. Bennett, R.J. Cuss, P.J. Vardon, J.F. Harrington and H.R. Thomas. Data analysis toolkit for long-term, large-scale experiments. *Mineralogical Magazine*, 76(8), 3355-3364, 2012.

[7] D.P. Bennett, R.J. Cuss, P.J. Vardon, J.F. Harrington, M. Sedighi, and H.R. Thomas. Second order exploratory data analysis of the Large Scale Gas Injection Test (Lasgit) dataset, *Special Publication in Geological Society of London on Gas Generation and Migration in Radioactive Waste Repositories* (under review), 2014.

Proceedings of the 22nd UK Conference of the
Association for Computational Mechanics in Engineering
2 – 4April 2014, University of Exeter, Exeter

FINITE ELEMENT BASED CONTACT SOLUTION FOR TRACTIVE ROLLING CONTACT OF GRADED COTING

***R. Yazdanparast[1], A. Moradi and M. Safajuy**

[1]Department of Aerospace Engineering, Sharif University of Technology, Azadi Ave., Tehran
*yazdanparast.reza110@gmail.com

ABSTRACT

This study presents the finite element based solution for tractive rolling contact between a rolling rigid cylinder and a fixed graded coating foundation which has been attached on the elastic plane body. The graded coated roles as load transmitter in contact surface, causes significant enhancement in the contact surface properties and consequently the fatigue life, so has undeniable extension in industrial applications. As In this paper, the rigid cylinder rolls with constant velocity on the graded coating foundation, so the proposed solution implemented in steady state case. At results this paper investigates the effects of the coating thickness and the coefficient of friction on the surface contact tractions and the stick zone length which are performed analytically by some researchers at recently.

Key words: *Graded coating, rolling contact, steady state rolling contact*

1. Introduction

Todays Rolling contact problem has wide extention the in fabrication of rollers in printing machines, ball bearings present in rotating machines, railway and etc. In this application in order to achieve an optimum tribological system, one may use one of the three lubrication, design and materials options to significant enhancement in the contact surface properties and consequently increasement in the fatigue life. The new materiel Graded coating is one of the best choice for these purposes. In the contact applications the graded coating play roles as load transfer components. The elastics properties of this material may vary continuously and gradually in some directions which results the reduction in the elastic mismatch at coating and substrate interfaces. The recent analytical research on graded coating focus on the behaviour of the FGM coatings under various loading conditions (i.e. under normal, sliding and rolling loading conditions) by the some assumption in elastic properties variation such as exponentially or power law functionally and etc.[7]. the rolling contact problems have been invesigeted experimantaly in details, however the modeling of this phonomena in analitical and numerical done by some reachers. Numerical methods which are introduced in this field may be classfy as local analysis contact domain based on half space assumptions which numerically discretized which are solved by boundary element methods and global methods based on the general continuum mechanics approach which are solved by a finite element method [9]. local analysis contact domain due to the use of half space assumptions encountered with restirictions in general applications. the Finite element method for the rolling contact based on some assumptions have been extendened three decade. At First in 1986 J.T. Oden et all [5] Published solution for rolling contact problem for finite deformations of a viscoelastic cylinder and R. Kennedy [8] extended the Finite element analysis for the steady and transiently moving/rolling nonlinear visceoelastic structures. At 1987 the formulation and computational results for Three-dimensional finite deformation, rolling contact of a hyperelastic cylinder implemented by J.M. Bass [4] and along this thay modeled the three-dimensional rolling contact for a reinforced rubber tire[6]. J.J. Kalker [3] introduced the rolling contact based on the hertzian assumption in the Three-dimensional for Elastic Bodies and at following this approach was modeled numerically with non hertzian assumption by K.P. singh and B.paul [2]. G. Hu and P. Wriggers [1] in order to imporove the numerical solution via an itrative solution procedure end finite element mesh refinement, published an addaptive Finite element of steady-state rolling contact for hyperelastic in finite deformation based on residual based a posterior error estimator for rolling contact problem with coulomb friction. Due to nature of rolling contact in some problem, some reasercher [1,2,3], solved and simlify the the rolling contact in stationary point and steady state case. Along this an arbitrary Lagrangian Eulerian (ALE) formulation of bodies in rolling

contact based on the Theoretical foundations and finite element approach have been introduced by U. Nackenhorst[9] in 2004. in the ALE discretization the motion of body are decompose in two purely rigid body motion by χ mapping and deformation by ϕ mapping which described separately by Eulerain and Lagrangian framework respectively. Rolling contact problems in nature are dynamic problems. Each particale that enter in the Contact patch and leave it, may experiment various state such as sliding or sticking case in an instant. This process is in different stages for different parts of the contact area. If the overall motion of the bodies be constant at all time, then an overall steady state may be attained. Here the state of each surface particle is varying in time, but the overall distribution can be constant. This is formalised by using a coordinate system that is moving along with the contact patch. The solution of rolling contact depends on the history of the contact. In the rolling contact of two deformable bodies by 1 and 2 attachment with velocity of v_1 and v_2 respectly there are two possibilities: if two body have an equal velocites, its called rolling, else if we faced with reletive velocity in contact zone which has been called sliding or rolling with sliding. In general The dynamic contact problems have transeint nature where the overall motion of bodies in contact varies with time. However the steady-state case is rarely true in reality, especially in acceleration and braking phase of motion for moving vehicles. While the transient case are approperiate for modeling of dynamic contact problems under time-varying velocity conditions. In the result section in order to show the robustness of presented numerical model, an example have been solve. In this example the tractive rigid cylinder which is rolling on deformable coated FGM foundations have been modelled and validated with analytical solutions recently done by M. A. Gulera and et all [7]. In order to verification, the effects of the coating thickness and the coefficient of friction on the surface contact tractions and the stick zone length have been investigated and compared with analytically results.

2. Formulation

2.1 contact conditions

In this section we will drive the contact conditions and finite element discretization of boundary value problem for rigid rolling cylinder on the deformable coated FGM foundation. We denote Γ_c^2 for rigid rolling cylinder as current mortar (or master) surface which penetrate in to the coated foundation as current non-mortar (or salve) surface Γ_c^1 and use averaged non-mortar side normal for contact discretization.

2.1.1 Normal contact condition

We introduce *e* as normal distance between two adjacent particles on mortar (master) and non-mortar (slave) contact surfaces. Now the conditions for normal contacts with respect to *e* may be defined as:

$$\begin{aligned}
&\{if \ \ (e=0)\\
&\ conctact\ occur \rightarrow in\ the\ contac\ zone(C) \Rightarrow p_n \geq 0\\
&eles\ if\ \ (e>0)\\
&\ dont\ conctact\ accur\ and\ in\ the\ exterior\ zone(E) \Rightarrow p_n = 0\ \}\\
&where\ (C \cup E = A_c\ (potential\ contact\ \ area)\ \ \&\ C \cap E = \varnothing)
\end{aligned} \tag{1}$$

2.1.2 tangential contact condition

suppuse that x^1 and x^2 are vector position (with reference to global coordinate system) of two adjacent particles on non-mortar(slave) and mortar (master) surfaces respectively. For these particles in rolling contact we introduce some definitions as:

$$
\begin{aligned}
&c = \dot{x}^1 - \dot{x}^2 \quad creep \\
&v = -\dot{x} = (\frac{\dot{x}^1 + \dot{x}^2}{2}) \quad rolling\ velocity\ (for\ small\ displacements) \\
&u = u^1 - u^2 \quad displacement\ difference \\
&\Rightarrow s = c - (\frac{\partial u}{\partial x})v + \frac{\partial u}{\partial t} \quad slip(relative\ velocity\ of\ two\ particle\ in\ contact)
\end{aligned} \tag{2}
$$

Now if *c*, *u* and *v* are independent of the time t, the steady state rolling will be occur, eles the non-steady state rolling will be dominant as follows:

$$
\begin{aligned}
&s = c - (\frac{\partial u}{\partial x})v \quad steady\ state\ rolling \\
&s = c - (\frac{\partial u}{\partial x})v + \frac{\partial u}{\partial t} \quad non-steady\ state\ (or\ transient)\ rolling
\end{aligned} \tag{3}
$$

Finally the local tangential components of traction p_t at the position of contact particles will be defined as following:

$$
\begin{aligned}
&\{if \quad (|s_t| \neq 0) \\
&\Rightarrow \quad p_t = -\frac{(\mu f_n)s_t}{|s_t|} \rightarrow in\ slip\ zone(H) \\
&eles \\
&\quad p_t \leq -\mu f_n \quad \rightarrow in\ stick\ zone(T)\} \\
&where\ (T \cup H = C(contact\ zone)\ \&\ T \cap H = \varnothing)
\end{aligned} \tag{4}
$$

Where s_t and f_n are tangential slip and total normal force components respectively and μ is coulomb's friction.

2.2 Finite element discretization

In this section the discretized finite element formulation of the contact problem will be implemented. We define the discrete initial displacement and velocity vector as follows:

$$U_0 = (u_0(x_1)^T, u_0(x_2)^T, ..., u_0(x_n)^T)^T \tag{5}$$

And

$$\dot{U}_0 = (v_0(x_1)^T, v_0(x_2)^T, ..., v_0(x_n)^T)^T \tag{6}$$

And the matrix form of Lagrange multipliers in normal and tangential directions will be writing as following matrix notation:

$$\Lambda_n(t) = (\Lambda_{n_1}(t), , ..., \Lambda_{n_N}(t))^T \quad \forall i = 1:N \in \mathrm{I}_c \ \forall t \in T\ (total\ time) \tag{7}$$

$$\Lambda_t(t) = (\Lambda_{t_1}(t), , ..., \Lambda_{t_N}(t))^T \quad \forall i = 1:N \in \mathrm{I}_c \ \forall t \in T \tag{8}$$

Now the general equation of motion for two bodies in contact can be difined as follows:

$$
\begin{aligned}
&find\ U(t), \lambda_n(t), \lambda_t(t)\ such\ that\ \forall t \in T \\
&M\ddot{U}(t) + KU(t) = L(t) + B_n^T \lambda_n(t) + B_t^T \lambda_t(t) \\
&U(0) = U_0, \dot{U}(0) = \dot{U}_0
\end{aligned} \tag{9}
$$

Where K is the total tangential stiffness matrix without contact, M is total math matrix, B is addetive sitffness due to the contact presense and L is the extenal force matrix in each time step.

2.2.1 steady state condition

in the steady state condition, The all time derivatives of the displacement are zero and the overall motion of the bodies is constant at all times. so it is sufficeint to solve steady state problem just at any arbitrary time t_0. On the other hand no need to perform any time discretization process in dynamic modeling of rolling contact. However the momentom equatiom of motion at any arbitrary time t_0 may be simplified as:

$$\begin{aligned} &find\ U(t_0)\ ,\lambda_n(t_0),\ \lambda_t(t_0)\ such\ that\ \forall t_0 \in T \\ &K\,U(t_0) = L(t_0) + B_n^T\,\lambda_n(t_0) + B_t^T\,\lambda_t(t_0) \\ &U(0) = U(t_0) = U_0,\ \dot{U}(0) = \dot{U}(t_0) = \dot{U}_0 \end{aligned} \tag{10}$$

and by linearization of qu(10) in space dicription, we have:

$$\begin{bmatrix} R_u(U(t_0),\Lambda_n(t_0),\Lambda_t(t_0)) \\ R_{\lambda_n}(U(t_0),\Lambda_n(t_0)) \\ R_{\lambda_t}(U(t_0),\Lambda_t(t_0)) \end{bmatrix} + \begin{bmatrix} K_{UU} & K_{U\lambda_n} & K_{\lambda_n\lambda_t} \\ K_{\lambda_n U} & K_{\lambda_n\lambda_n} & 0 \\ K_{\lambda_t\lambda_n} & 0 & K_{\lambda_t\lambda_t} \end{bmatrix} \begin{Bmatrix} \Delta U(t_0) \\ \Delta\Lambda_n(t_0) \\ \Delta\Lambda_t(t_0) \end{Bmatrix} = 0 \tag{11}$$

Where R_u, R_{λ_n} *and* R_{λ_t} are residual forces will drive form the variation of total energy with respect to the U, λ_n and λ_t respectively.

3. Results

Example:regid Cylinder rolling on deformable graded coating plane foundation

This section presents a numerical solution of tractive rolling contact between a rigid cylinder and a deformable graded coating plane foundation in the steady state case. This study investigates the effects of the coating thickness and the coefficient of friction on the surface contact tractions and the stick zone length. In this example the external force (*P* and Q), surface contact tractions and the stick zone length are estimated based on the predetermined *H/R*, μ and t values. Where the *H* is distance from cylinder to the surface of foundation without any deformation, R is the radius of cylinder, μ frictional coefficient and *t* is the thickness of coated foundation.

References

[1] G. Hu, P.Wriggers. on adaptive finite element method of steady-state rolling contact for hyperelastic in finite deformations. *Comput. Methods Appl. Mech. Engrg*, 191,1333-1348, 2002.

[2] K.P. Singh, B. Poul. Numerical solution of non-Hertzian elastic contact problems. J. Appl. Mech,24,484-490, 1974.

[3] J.J. Kaller. Three-dimensional elastic bodies in rolling contract. *Kluwer Academic Pablishers,Dordrecht*, 1990.

[4] J.M. Bass. Three-dimensional finite deformation rolling contact of a hyperelastic cylinder: formulation of problem and computational results. *Comput struct*, 26,991-1004, 1987.

[5] J.T. Oden, T.L. Lin. On the general rolling contact problem for finite deformations of a viscoelastic cylinder, *Comput. MethodsAppl. Mech. Engrg*, 57,297–376, 1986.

[6] L.O. Faria, J.M. Bass, J.T. Oden, E.B. Becker. A three-dimensional rolling contact model for a reinforced rubber tire.*Tire Sci.Technol*, 17 (1), 217–233, 1989.

[7] M. A. Gulera, S. Adibnazari, Y. Alinia. Tractive rolling contact mechanics of graded coatings. *International Journal of Solids and Structures*, 49,929-945, 2012.

[8] R. Kennedy, J. Padovan. Finite element analysis of steady and transiently moving/rolling nonlinear viscoelastic structure–II. *Shell and three-dimensional simulations, Comp. Struct*, 27 (2) , 259–273, 1987.

[9] U. Nackenhorst.The ALE-formulation of bodies in rolling contact Theoretical foundations and finite element approach. *Comput. Methods Appl. Mech. Engrg*, 193,4299-4322, 2004.

Proceedings of the 22nd UK Conference of the
Association for Computational Mechanics in Engineering
2 – 4April 2014, University of Exeter, Exeter

NON-LINEAR MODELS OF FRICTIONAL HEATING DURING BRAKING

***Piotr Grzes**

Faculty of Mechanical Engineering, Bialystok University of Technology (BUT),
45C Wiejska Street, Bialystok 15-351, Poland

*p.grzes@pb.edu.pl

ABSTRACT

The coupling between the temperature dependence of the coefficient of friction and the angular speed of the disc during braking was studied. The numerical calculations using the finite element method (COMSOL Multiphysics 4.4) were performed based on the equation of motion and the thermal problem of friction. Both axisymmetric (2D) and spatial (3D) FE models were developed, assuming that the corresponding temperatures on the working surfaces of the pad and the disc are equal. In order to compare the results obtained for different values of the contact pressure it was established that kinetic energy transferred into heat in the form of the heat flux densities is also equal. A single braking process was simulated for two cermet materials of the pad with noticeably different thermal conductivities combining with cast-iron brake disc. The results were determined for the temperature dependent-coefficient of friction as well as its constant value at the room temperature. The comparative analysis revealed that even the slight change in the coefficient of friction at the studied contact pressures and the materials affects significantly the braking time (12÷40%), speed and slightly the maximum temperature of the sliding components of the brake (1÷4%).

Keywords: *temperature; disc brake; temperature-dependent coefficient of friction; finite element method*

1. Introduction

The heating of the friction elements of the disc brake being in sliding contact may lead to the change in the coefficient of friction, contact pressure, thermophysical and mechanical properties of the materials, cause excessive wear, brake fluid vaporization, deformations/cracks of the disc, degradation of the pad material, etc. [1]. Numerical calculations of temperature in disc brake employs either axisymmetric [2, 3] or three-dimensional models [3, 4]. The first arrangement is used when the sliding speed is high (uniform temperature distribution in the circumferential direction) or the coefficient of mutual overlap of the pad and disc is close to the unit. The three-dimensional model reveals possible to occur non-uniformities on the rubbing path of the disc due to relative motion of the sliding components.

In this paper both 2D and 3D non-linear models of frictional heating in disc brakes were developed to study the influence of the fluctuations of the coefficient of friction on the braking time, angular speed of the disc and the temperature distribution in the pad and the disc.

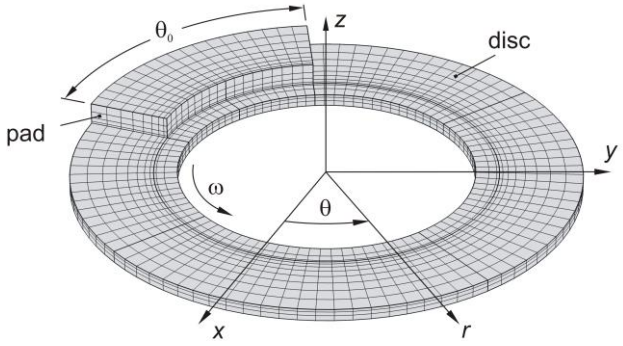

Figure 1: 3D finite element mesh of the pad-disc brake system

2. Basic equations

Consider a braking process of a vehicle from initial speed V_0 to standstill. A deceleration of the vehicle is performed using four disc brake systems, assuming equal distribution of the braking force. In calculations the disc is restricted to the half of its thickness due to geometrical symmetry about the mid-plane (Fig. 1). At this assumptions, the equation of motion at braking has the form [5]:

$$\frac{d}{dt}\left[\frac{mV^2(t)}{2}\right] = 8 f(T) p_0 \omega(t) \iint_{A_{pad}} r dr d\theta, \tag{1}$$

where m is the mass, V and ω are the forward and angular speed of the vehicle, accordingly, f is the coefficient of friction, T is the temperature, $p_0 = \text{const}$ is the contact pressure, A_{pad} is surface area of the pad, t is the time. Approximation of the integral in Eq. (1) with the pad's area leads to:

$$\frac{dV(t)}{dt} = \frac{8 f(T) p_0 r_m A_{pad}}{m r_w}, \tag{2}$$

where r_w is the average radius of the wheel, r_m is the equivalent radius of the pad. After integration of the ordinary differential equation (2), we find the rule change of the speed during braking:

$$V(t) = \frac{8 p_0 r_m A_{pad}}{m r_w} \int_0^t f(T) dt. \tag{3}$$

The time of braking t_s (time of a stop) is found from the equation (3) as $V(t_s) = 0$.

On the other hand, the specific capacity of friction during braking, and hence, the total intensity of the heat fluxes directed to the pad and the disc is given by [5]:

$$q(r,t) = p_0 f(T) r r_w^{-1} V(t). \tag{4}$$

The separation of heat between the pad and the disc during braking is governed by the condition of equal temperatures on the contact surfaces of the sliding bodies. Thus, the proposed mathematical model of the frictional heating during braking takes into account the relationship between the speed and the temperature.

3. Numerical analysis

A single braking process from initial vehicle speed V_0 = 100 km/h (wheel radius r_w = 0.314 m, initial angular speed of the disc ω_0 = 88.464 s^{-1}) to standstill is analysed using the finite element method (COMSOL Multiphysics 4.4). The two FE models of the disc brake were developed: 2D (axisymmetric) and 3D (three-dimensional) based on the same dimensions (Tab. 1) apart from the pad arc length θ_0 (Fig. 1) [4]. In the 2D axisymmetric model the pad arc length was θ_0 = 360°, whereas in the three-dimensional model the pad covered the rubbing path partly θ_0 = 64.5°. In order to obtain equal braking times for these two computational cases (at the constant coefficient of friction), different values of kinetic energy proportional to the surface areas of the pads were considered (E_k = 2.213 MJ for 2D and E_k = 396.5 kJ for 3D model). Those values corresponded with the vehicle mass of 5736.7 kg and 1027.8 kg, respectively. The properties of materials are shown in Tab. 2.

The 2D FE model consisted of 3423 axisymmetric quadrilateral elements (1998 for the pad and 1425 for the disc). Fixed number of 95 of elements in the disc was used in radial direction giving the dimension of about 0.0005 m. In the axial direction the dimension of an element both in the pad and the disc increased with the distance from the contact surface, approximately from 0.000025 m to 0.0005 m, respectively. The grid was consistent (the dimensions of elements) with the mesh developed in article [3]. The total overall number of the hexahedral elements of the 3D model of the pad-disc system was equal 3678 (576 for the pad and 3102 for the disc). The disc area in axial

direction was divided into 3 elements with the element ratio of 0.5, whereas the pad into 4 elements with the element ratio of 0.25, due to lower thermal conductivity in relation to the disc material. In the radial direction 8 elements for the pad and 11 elements for the disc were established, which gave 94 elements in the circumference of the disc. The numerical calculations of the temperature fields in the pad and the disc were performed at constant f(20°C) and temperature-dependent coefficient of friction (Fig. 2).

Table 1: Dimensions of the pad and the disc [4]

	Pad	Disc
Inner radius, $r_{p,d}$ [m]	0.0765	0.066
Outer radius, $R_{p,d}$ [m]	0.1135	
Thickness [m]	0.01	0.0055

Table 2: Thermophysical properties of materials of the pad and the disc [4]

	Cermet FC-16L (pad)	Cermet FMC-16 (pad)	Cast iron ChNMKh (disc)
Thermal conductivity, K [W/(mK)]	0.79	34.3	51
Specific heat, c [J/(kgK)]	961	500	500
Density, ρ [kg/m^3]	2500	4700	7100

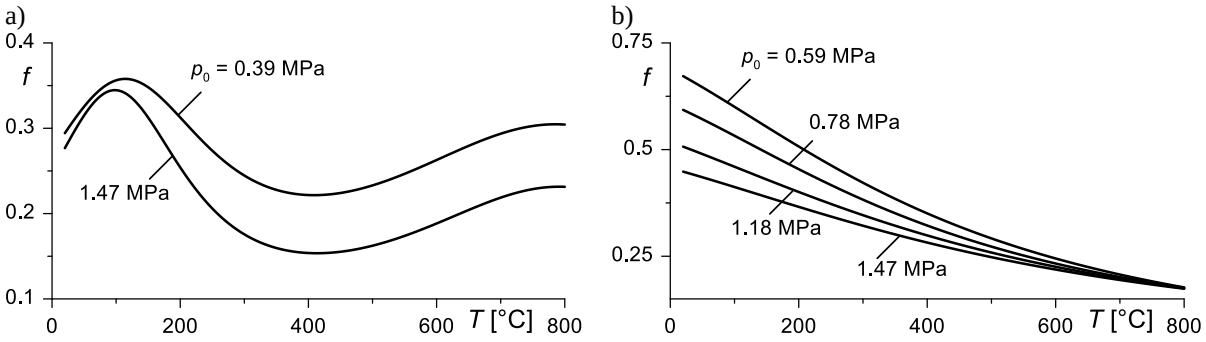

Figure 2: Temperature dependencies of the coefficient of friction for: a) FC-16L/ChNMKh; b) FMC-11/ChNMKh [4]

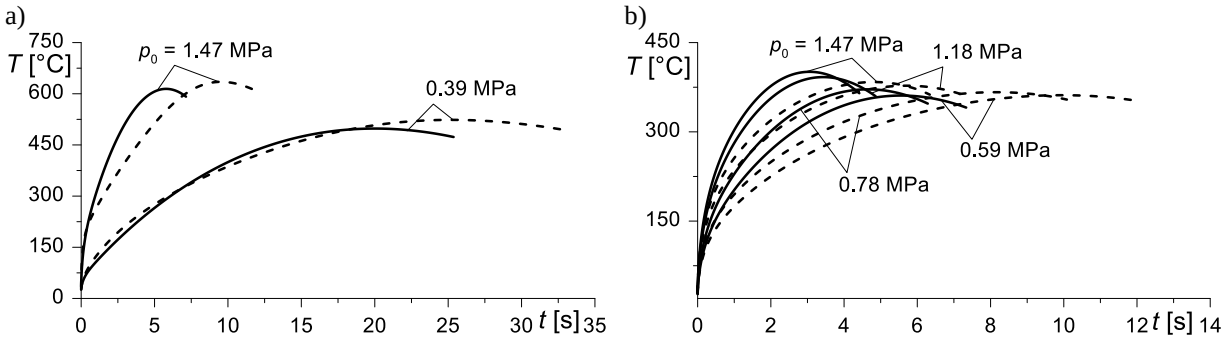

Figure 3: Temperature evolutions at the pad-disc interface (maximum radius $R_d = R_p = 0.1135$ m) obtained using 2D model a) FC-16L/ChNMKh; b) FMC-11/ChNMKh; $f(T)$ dashed lines; f(20°C) solid lines

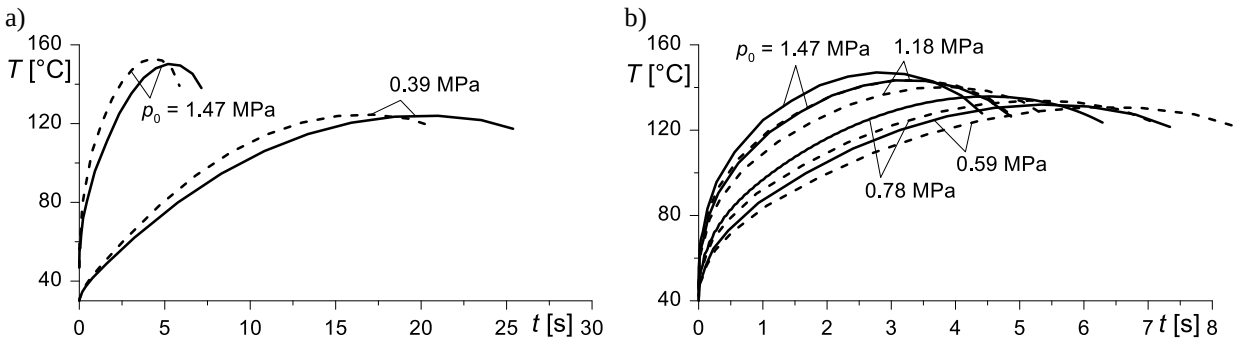

Figure 4: Temperature evolutions at the pad-disc interface (maximum radius $R_d = R_p = 0.1135$ m) obtained using 3D model: a) FC-16L/ChNMKh b) FMC-11/ChNMKh; $f(T)$ dashed lines; $f(20°C)$ solid lines

The evolutions of temperature at the pad-disc interface calculated at the constant (solid line) and the temperature-dependent (dashed line) coefficient of friction using 2D and 3D models are shown in Fig. 3 and Fig. 4, respectively. The braking time for the friction pair FC-16L/ChNMKh at the constant coefficient of friction is either shorter or longer depending on the maximum temperature achieved (Fig. 3, 4), which stems from the temperature dependencies of the coefficient of friction (Fig. 2a). For the pad made of FMC-11 and cast-iron brake disc, the braking time is underestimated at every studied contact pressure due to almost linear decrease in the coefficient of friction with the increase in temperature (Fig. 2b). As can be seen the maximum attained temperature from 3D model is several times lower than the temperature calculated using axisymmetric model (2D) due to different values of the kinetic energy ($E_k = 2.213$ MJ for 2D and 396.5 kJ for 3D model).

4. Conclusions

In this paper FEA of temperature distributions in the disc brake using 2D and 3D numerical models was carried out. Based on the obtained results it was concluded that neglecting the temperature dependence of the coefficient of friction may lead to significant change in the braking time (up to 40%), whereas the maximum temperature was almost unchanged. The direct comparison of the results calculated using 2D and 3D models at the condition of equal temperature on the contact surfaces of the pad and the disc was not possible, since the geometries were different (in 3D model the pad covers the rubbing path of the disc partly). The three-dimensional model allowed to identify the distribution of the coefficient of friction at the pad-disc interface, however the computational time was about 1000 times longer than using the axisymmetric model.

Acknowledgements

The present article is financially supported by the National Science Centre in Poland (research project No 2011/01/B/ST8/07446).

References

[1] A.A. Yevtushenko and P. Grzes. The FEM-modeling of the frictional heating phenomenon in the pad/disc tribosystem (a review). N*umerical Heat Transfer Part A-Applications*, 58, 207-226, 2010.

[2] A. Adamowicz, P. Grzes. Analysis of disc brake temperature distribution during single braking under non-axisymmetric load. *Applied Thermal Engineering*, 31, 6-7, 1003-1012, 2011.

[3] A.A. Yevtushenko and P. Grzes. Axisymmetric FEA of temperature in a pad/disc brake system at temperature-dependent coefficients of friction and wear. *International Communications in Heat and Mass Transfer*, 39, 1045-1053, 2012.

[4] A.A. Yevtushenko, A. Adamowicz and P. Grzes. Three-dimensional FE model for the calculation of temperature of a disc brake at temperature-dependent coefficients of friction. *International Communications in Heat and Mass Transfer*, 42, 18-24, 2013.

[5] COMSOL Multiphysics 3.5, Heat Generation in a Disc Brake, 2008.

Proceedings of the 22nd UK Conference of the
Association for Computational Mechanics in Engineering
2 - 4 April 2014, University of Exeter, Exeter

Quasi-Static Analysis of Self-Cleaning Surface Mechanisms

***Muhammad Osman[1] and Roger A. Sauer[1]**

[1] Aachen Institute for Advanced Study in Computational Engineering Science (AICES), RWTH Aachen University, Templergraben 55, 52056 Aachen, Germany

*osman@aices.rwth-aachen.de

ABSTRACT

Based on a finite element (FE) model, we study the self-cleaning effect, also known as the lotus effect, which is observed on hydrophobic surfaces. The interaction between these surfaces, liquid droplets, and pollutant particles is investigated through a force analysis. Some forces such as the capillary force and the contact line force, require the computation of the liquid droplet membrane deformation, governed by the Young-Laplace equation. Based on this analysis, we compute the net force governing the behaviour of a particle in contact with a 2D liquid droplet. This work provides answers to the following questions: In a quasi-static framework, does the self-cleaning mechanism work for given surface and droplet parameters? I.e: would a particle be lifted off by the water droplet or not? How do the model parameters affect the net force acting on the particle? The parameters considered in this study are: volume and density of the liquid droplet, and size, density and contact angle of the pollutant particle.

Key Words: *Self-cleaning mechanism, contact angle, static wetting, nonlinear finite element analysis, droplet membranes*

1. Introduction

The self-cleaning phenomenon, also called the lotus effect, is observed in some natural and artificial surfaces. These are hydrophobic surfaces which minimize the surface contact with water, thus splitting it into small spherical droplets. This allows a smooth rolling/sliding over the surface while sweeping away pollutant particles. The mechanical principles behind this mechanism are complex as they involve the coupling of several problems; contact on multi-scale rough surfaces, fluid flow inside the droplets, droplet membrane deformation, wettability and contact angle, and the interaction between droplet and pollutant particles. In this work, we discuss some aspects of the last three problems, and provide solutions based on FE computations.

Liquid droplets can be treated computationally as a structural membrane governed by the Young-Laplace equation, and an internal liquid flow governed by the Stokes equation. Different approaches can be used to solve the two problems. A simple approach is solving the two problems in a decoupled manner, where each problem is solved separately [1]. For quasi-static droplets, an internal bulk pressure substitutes the flow, as in Sauer et al. [2] and Sauer [3], where stabilized formulations are presented for modelling of liquid membranes in static contact, based on the finite element method (FEM). Osman et al. [1] studies dynamic contact of droplets on rough surfaces, considering Stokes model for the internal liquid flow. The interaction between solid particles and air bubbles inside liquids is investigated by Schulze [4]. Osman et al. [5] and Kralchevsky et al. [6] discuss the force analysis involved in attachment/detachment of small pollutant particles to/from large liquid droplets under the assumption of a pre-defined location of the contact line as a boundary condition, and flat non-deformable liquid surface. Here we extend this study to provide solutions for arbitrary sizes of droplets and particles. Furthermore, the contact line is obtained from the numerical solution of the deformed liquid membrane.

2. FE Model

2.1. Governing equations

A system of a quasi-static liquid droplet, a flat rigid surface and a spherical pollutant particle is considered. The difference between the internal and the external pressure on the liquid membrane interface $\triangle p$ is balanced by the surface curvature $2H$, through the Young-Laplace equation,

$$2H\gamma_{LG} = \triangle p \qquad [N/m^2], \tag{1}$$

where γ_{LG} is the surface tension at the gas-liquid interface. The pressure difference across the interface can be expressed as

$$\triangle p = p_f - p_c, \qquad p_f = p_0 + \rho_w g y, \tag{2}$$

where p_f is the fluid bulk pressure comprising the capillary pressure p_0 and the hydrostatic pressure in terms of the liquid density ρ_w, gravity g and the surface height y. A contact pressure p_c appears where interactions between the membrane and other surfaces take place. For normalization, we multiply Eq.(1) by L/γ_{LG} to obtain the dimensionless quantities marked with tilde,

$$2\tilde{H} = \tilde{p}_f - \tilde{p}_c, \qquad \tilde{p}_f = \lambda + B\,\tilde{y}, \qquad B = \frac{\rho_w g L^2}{\gamma_{LG}}, \tag{3}$$

where λ is the Lagrange multiplier accounting for the capillary pressure, B is the so called Bond number, and L is the characteristic length, usually taken as the droplet diameter. The contact line $\mathcal{L}_c$ is the location where the three phases co-exist, forming a specific contact angle θ with the particle surface, denoted as θ_p (θ_s in case of contact with the substrate surface). The force equilibrium at the contact line is expressed in terms of the interfacial tractions $\boldsymbol{t}_{SG}$, $\boldsymbol{t}_{LG}$ and $\boldsymbol{t}_{SL}$ at the solid-gas, liquid-gas and solid-liquid interfaces, respectively, as,

$$\boldsymbol{t}_{SG} + \boldsymbol{t}_{LG} + \boldsymbol{t}_{SL} + \boldsymbol{q}_n = \mathbf{0}, \tag{4}$$

where $\boldsymbol{q}_n$ is the force which counterbalances the normal projection of $\boldsymbol{t}_{LG}$ w.r.t the substrate surface (particle). The normal and tangential components of Eq.(4), respectively read,

$$\gamma_{SG} - \gamma_{LG}\cos\theta - \gamma_{SL} = 0, \tag{5}$$

$$q_n - \gamma_{LG}\sin\theta = 0, \tag{6}$$

where γ_{SL} , γ_{SG} and γ_{LG} denote the surface tension at the three interfaces. Eq.(5) is known as Young's equation. The FE implementation of the above equations can be found in [3].

2.2. Force balance

The considered spherical pollutant particle of radius r_p and density ρ_p, is subjected to four forces shown in Fig.(1): particle weight $\mathbf{F}_G$, contact line force $\mathbf{F}_{CL}$, hydrostatic force $\mathbf{F}_H$, and buoyancy force $\mathbf{F}_B$, defined as follows:

$$\mathbf{F}_G = \frac{4}{3}\pi r_p^3 \rho_p \mathbf{g}, \tag{7}$$

$$\mathbf{F}_{CL} = \oint_{\mathcal{L}_c} \boldsymbol{t}_{LG}\,\mathrm{d}\mathcal{L}_c, \tag{8}$$

$$\mathbf{F}_H = \int_{a_w} p_f\,\mathbf{n}\,\mathrm{d}a_w \approx p_0 A_w \mathbf{N}, \tag{9}$$

$$\mathbf{F}_B = \rho_w g \mathcal{V}_w \mathbf{N}, \quad \mathcal{V}_w = \frac{\pi b}{6}(3a^2 + b^2), \tag{10}$$

where $\mathbf{n}$ is the normal to the wetted area A_w, while $\mathcal{V}_w$ is the wetted volume of the particle, $\mathbf{N}$ is the normal to the contact line along the particle axis, and a & b are distances defined in Fig.(1). The effective force $\mathbf{F}_e$ is the summation of all forces. Among the above parameters, the location of the contact line $\mathcal{L}_c$, the traction along the liquid-gas interface $\mathbf{t}_{LG}$, and the internal pressure p_f require computation of the membrane deformation. Friction and surface adhesion between the particle and the substrate are not considered in this work.

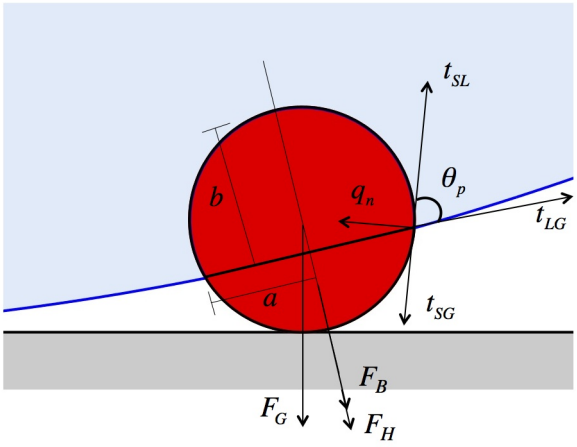

Figure 1: Schematic of the forces acting on a particle in contact with a liquid droplet.

3. Results and Discussion

Computations here are based on the stabilized FE formulation for liquid membranes [3]. In the following examples, we consider quasi-static droplets in contact with a super-hydrophobic flat surface ($\theta_s = 180°$) and a spherical pollutant particle with various contact angle ($\theta_p = 30° - 180°$). The particle is considered fixed to the substrate surface at different locations, and the membrane deformation is computed for different parameters such as the volume and density of the droplet and the particle, as well as θ_p. Knowing the location of the contact line and the associated membrane surface tangents, the force balance can be obtained, and thus the effective force $\mathbf{F}_e$. The vertical component of $\mathbf{F}_e$ determines whether the particle is lifted to the droplet or not.

3.1. Example 1

We consider a weightless spherical droplet ($B = 0$), of radius $R = 2L$, with Dirichlet boundary conditions at the upper half, in contact with a spherical rigid pollutant particle fixed at three different locations along the vertical axis of symmetry of the droplet. These locations are distinguished by the vertical distance y_p, measured from the centre of the particle to the horizontal level (marked with dotted line in Fig.(2)), which is tangent to the undeformed droplet from the bottom. Although the contact angle of the particle is fixed to $\theta_p = 120°$, the direction of the effective force $\mathbf{F}_e$ alters as the particle penetrates into the droplet (i.e y_p increases), as shown in Fig.(2). This is due to the membrane deformation, which causes a change in the direction of the contact line force, which is dominant in the case of relatively light particles ($\rho_p = \rho_w$).

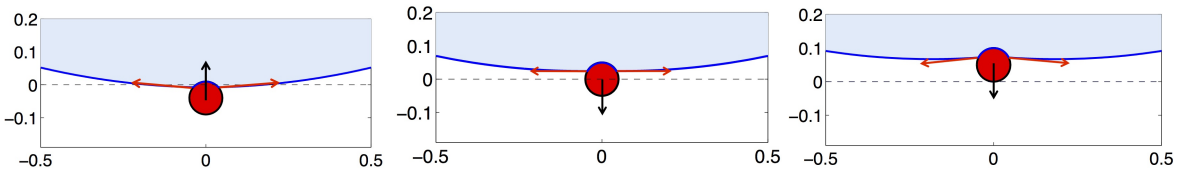

Figure 2: FE solution of a weightless droplet (B=0) in contact with a pollutant particle of contact angle $\theta_p = 120°$ and radius $r_p = 0.05L$, fixed at a distance $y_p = -0.025, 0$, and $0.05L$ (left to right). Black arrows show the direction of the effective force $\mathbf{F}_e$.

3.2. Example 2

In the second example we consider an axisymmetric water droplet ($B = 0.1316$, $R = 2L$) on a flat surface with $\theta_s = 180°$, and in contact with a spherical rigid pollutant particle ($\rho_p = \rho_w$, $r_p = 0.05L$) fixed at a point on the substrate surface where the droplet membrane is just touching the particle at $\theta_p = 180°$ (see Fig.(3)). Dirichlet boundary conditions in the horizontal direction are applied to the droplet membrane at the axis of symmetry. The droplet deformation is shown for the range of $\theta_p = 30° - 180°$ in Fig.(5). The particle is lifted towards the droplet when the sign of $\mathbf{F}_e \cdot \mathbf{g}$ is negative, which means $\mathbf{F}_e$ points upwards, at a critical θ_p. A smaller particle is lifted to the droplet at a higher contact angle, as observed in Fig.(4).

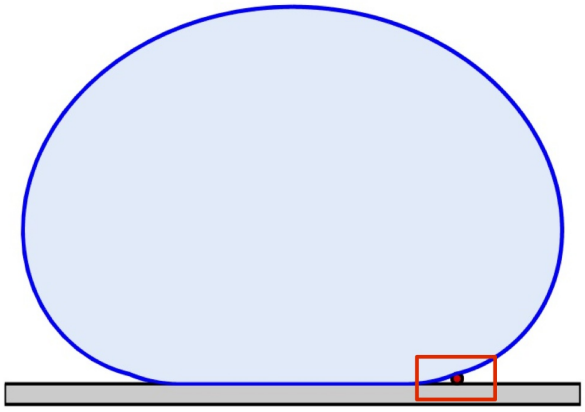

Figure 3: FE solution for a droplet in contact with a flat surface ($\theta_s = 180°$) and a spherical rigid particle with $\theta_p = 180°$.

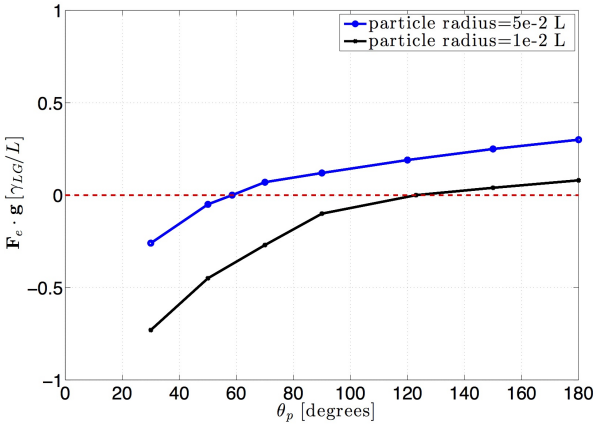

Figure 4: Equilibrium force at various contact angles θ_p of the pollutant particle.

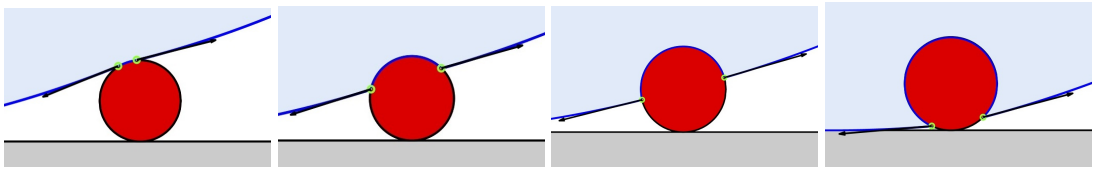

Figure 5: FE solution of a deformed water droplet (B=0.1316) in contact with a flat surface, and a pollutant particle ($r_p = 0.05L$) of contact angle $\theta_p = 180°, 120°, 90°$ and $30°$ (left to right). Black arrows show the direction of the tangential contact line force.

4. Conclusions

A force analysis for the interaction of pollutant particles with quasi-static liquid droplets is presented. A numerical treatment of the droplet deformation is required to determine the contact line force. A particle is lifted up to the droplet if the contact line force is large enough to overcome the other forces. The direction of the contact line force depends on the contact angle and size of the particle, membrane deformation at the contact line, the droplet volume, and the penetration of the particle into the droplet. The first example showed that a detachment is possible if the particle is further penetrated, for example by other forces, into the droplet. The second example showed that smaller particles are lifted at higher contact angles, compared to larger particles.

Acknowledgements

The authors are grateful to the German Research Foundation (DFG) for the financial support, under grant numbers SA 1822/ 3-2 & GSC 111.

References

[1] M. Osman, R. Rasool and R.A. Sauer. Computational Aspects of Self-Cleaning Surface Mechanisms, in: *Advances in Contact Angle, Wettability and Adhesion*. Edited by K.L.Mittal, chapter 7. Scrivener, 2013.

[2] R.A. Sauer, X. T. Duong and C.J. Corbett. A computational formulation for constrained solid and liquid membranes considering isogeometric finite elements. *Comput. Method Appl. Mech. Engrg.*, 271, pp. 48-68, 2014.

[3] R.A. Sauer. Stabilized finite element formulations for liquid membranes and their application to droplet contact. *Int. J. Numer. Math. Fluids*, submitted, 2013.

[4] H.J. Schulze. *Physico-chemical Elementary Processes in Flotation*, Elsevier, 1984.

[5] M. Osman and R.A. Sauer. Mechanical modeling of particle-droplet interaction motivated by the study of self-cleaning mechanisms. *Proc. Appl. Math. Mech.*, 10, pp. 85-86, 2010.

[6] P.A. Kralchevsky and K. Nagayama. *Particles at Fluids Interfaces and Membranes: Attachment of Colloid Particles and Proteins to Interfaces and Formation of Two-Dimensional Arrays*. Elsevier, Vol. 10, 2001.

Proceedings of the 22nd UK Conference of the
Association for Computational Mechanics in Engineering
2 – 4April 2014, University of Exeter, Exeter

SPACE-TIME DISCETIZETION OF FRICTIONAL ROLLING CONTACT IN DEFORMABLE BODEIS

***R. Yazdanparast[1], A. Moradi and M. Safajuy**

[1]Department of Aerospace Engineering, Sharif University of Technology, Azadi Ave., Tehran
*yazdanparast.reza110@gmail.com

ABSTRACT

This paper presents the space-time discretization for frictional rolling contact of deformable bodies based on finite element and finite difference methods. Due to the some difficulties in convergency and dissipate in kinetic energy at the contact nodes the dynamic modelling of contacts encounter with some restrictions. In this paper in order to overcome of these restrictions, the space-time discretization implemented based on Roth's method. At results based on recent works two examples have been investigated for deformable cylinder which rolls on the deformable foundation based on steady state and transient assumptions. Results show that this method has good convergency for modelling of dynamic rolling contact problems.

Keywords: *rolling contact; transient and steady state contact; dynamic contact*

1. Introduction

Rolling contact problem has wide extention in industrial applications such as rollers in printing machines, ball bearings present in rotating machines, railway and etc. fatigue problem in railways and ball bearings and dynamic instability in rolling printing causes some problems in practics for material design of these components. the rolling contact problems have been invesigeted experimantaly in details, however the modeling of this phonomena in analitical and numerical done by some reachers. Numerical methods which are introduced in this field may be classfy as local analysis contact domain based on half space assumptions which numerically discretized and solved by boundary element methods and global methods based on the general continuum mechanics approach which are solved by finite element method [8]. local analysis contact domain due to the use of half space assumptions encountered with restirictions in general applications. the Finite element method for the rolling contact based on some assumptions have been extendened in three decades. At First in 1986 J.T. Oden et all [5] Published the solution for rolling viscoelastic cylinder with finite deformations and R. Kennedy [7] extended the Finite element analysis for the steady and transiently moving/rolling nonlinear visceoelastic structures. At 1987 the formulation and computational results for Three-dimensional finite deformation, rolling contact of a hyperelastic cylinder implemented by J.M. Bass [4] and along this thay modeled the three-dimensional rolling contact for a reinforced rubber tire[6]. J.J. Kalker [3] introduced the rolling contact based on the hertzian assumption in the Three-dimensional for Elastic Bodies and at following this approach was modeled numerically with non hertzian assumption by K.P. singh and B.paul [2]. G. Hu and P. Wriggers [1] in order to imporove the numerical solution via an itrative solution procedure and finite element mesh refinement, published an addaptive Finite element for hyperelastic in finite deformation based on residual based posterior error estimator for rolling contact problem with coulomb friction. Due to nature of rolling contact in some problem, some reasercher [1,2,3], solved and simplified this in the stationary point and the steady state case. Along this an arbitrary Lagrangian Eulerian (ALE) formulation of bodies in rolling contact based on the Theoretical foundations and finite element approach have been introduced by U. Nackenhorst[8] in 2004. In the ALE discretization the motion of body are decompose in two mapping. the purely rigid body motion by χ and the deformation by ϕ which described separately by Eulerain and Lagrangian framework respectively. Rolling contact problems in nature are dynamic problems. Each particale that enter in the Contact patch and leave it, may experiments various state such as sliding or sticking case instantaneously. If the overall motion of the bodies will be constant at all time, then the overall steady state assumption may be acceptable. The solution of rolling contact depends

on the history of the contact. In general, The dynamic contact problems have transeint nature i.e. the overall motion of bodies in contact varies with time. However steady-state case is rarely true in reality, especially in acceleration and braking phase of motion for moving vehicles. While the transient case are approperiate for modeling of dynamic contact problems under time-varying velocity conditions. In this section in order to model the general dynamic contact problems in numerical framwork, the weak formulations have been presented. The time derivative of the displacement is replaced by its finite difference and the initial boundary value problem is converted to a sequence of static problems which have been solve by finite element method. In the numerical modleing of dynamic contact there are two difficulties which causes failure in ruslts. First there is may not uniquness in sulotion of contact dynamic for two bodies and second the dissipation in kinetic energy at contact nodes causes oscillations of the energy on the contact boundary. In this paper in order to overcome of these difficulties the Rothe's method have been used in time and space discritization. In the result section in order to show the robustness of presented numerical model, two examples have been solved and the dynamic contact of two deformable bodies with transient and steady state motions investigated numerically.

2. Formulation

In this section the formulation we will drived in spatial discretization based on semi-discrete Galerkin method. By 'semi-discrete the time dimension remains continuous at this moment. in the Galerkin Method, the arbirary functions such as displacment and its time varients combinations over the two bodies express as a linear combination of the basis function:

$$\tilde{u}(x,t)=\sum_{i=1}^{n}U_i(t)\varphi_i(x), \qquad \tilde{v}(x,t)=\sum_{i=1}^{n}V_i(t)\varphi_i(x) \tag{1}$$

Where $\{\varphi_1(x),\varphi_2(x),...,\varphi_n(x)\}$ are the set of Courant basis functions for bodeis in contact over Ω where $\{\Omega_1\cup\Omega_2=\Omega\in R^2\}$ while the matrix form of coefficients on eq (1) can be written as:

$$U(t)=(U_1(t),V_1(t),...,U_n(t),V_n(t))^T \tag{2}$$

2.1 Discretization of the contact forces

Let $\mathrm{I}_c=\{i\,|x_i\in\Gamma_c\,(\textit{contact area})\}$ be the set of indexes of the contact nodes. select the $\{\psi_i\}_{i\in\mathrm{I}_c}$ and $\{\zeta_i\}_{i\in\mathrm{I}_c}$ such that $\psi_i(x_j)=\zeta_i(x_j)=\delta_{ij}$ as basic functions for the approximation of the normal and tangential displacements and stress respectively. So we can write:

$$\begin{aligned}\int_{\Gamma_c}\tilde{\lambda}_n(x,t)\varphi_i(x)n_{i1}ds &= n_{i1}\int_{\Gamma_c}\tilde{\lambda}_n(x,t)\psi_i(x)ds\\ \int_{\Gamma_c}\tilde{\lambda}_n(x,t)\varphi_i(x)n_{i2}ds &= n_{i2}\int_{\Gamma_c}\tilde{\lambda}_n(x,t)\psi_i(x)ds\end{aligned} \tag{3}$$

Where $\tilde{\lambda}_n$ is the approximation of the normal contact stress and $n_i=(n_{i1},n_{i2})^T$ is the normal vectors at the contact nodes. At following the matix form of eqation (3) with contact conditions will be drive. over domain of contact we can write:

$$\tilde{u}_n=(x_i,t)=\tilde{u}(x_i,t).n_i=U(t)^T.N_i \quad \forall i\in\mathrm{I}_c \ \forall t\in T \tag{4}$$

where N_i contains on appropriate positions the coordinates of the unit outward normal vector n_i at $x_i, i\in I_c$ and zeros elsewhere. By this discritzation the contact for non-penetration condition will be written as follows:

$$U(t)^T.\ N_i\le 0 \quad \forall i\in\mathrm{I}_c \ \forall t\in T\,(\textit{overall time}) \tag{5}$$

And

$$\int_{\Gamma_c}\tilde{\lambda}_n(x,t)\psi_i(x)ds=\Lambda_{ni}(t)\le 0 \quad \forall i\in I_c \ \forall t\in T \tag{6}$$

Finally, since the condition $\int_{\Gamma_c} \tilde{\lambda}_n \tilde{u}_i ds = 0$ one can write:

$$\int_{\Gamma_c} \tilde{\lambda}_n \tilde{u}_i ds = \int_{\Gamma_c} \tilde{\lambda}_n \sum_{i \in I_c} U(t)^T . N_i \psi_i(x) ds = \sum_i U(t) . N_i \int_{\Gamma_c} \tilde{\lambda}_n \psi_i(x) ds = 0 \tag{7}$$

its matrix form is given by:

$$\Lambda_{n_i}(t)(U(t)^T . N_i) = 0 \quad \forall i \in \mathrm{I}_c \ \forall t \in T \tag{8}$$

Similarly, in the tangential direction we may define $\Lambda_{ni}(t) \int_{\Gamma_c} \tilde{}_t(x,t)\zeta_i(x) ds$ and the vectors T_i such that:

$$\tilde{u_t}(x_i,t) = U(t)^T . T_i, \quad \forall i \in \mathrm{I}_c \ \forall t \in T \tag{9}$$

By using $\tilde{w_t} = \sum_{i \in \mathrm{I}_c} w_t(x_i)\zeta_i$ as test funtion and by assuming positive and constant value for coefficient of friction μ over the whole contact boundary and denote $\dot{U}_t(t) = \dot{U}_t(t^T) . T_i$ the contact candition in tangential diriection will be write as follwing:

$$\int_{\Gamma_c} \tilde{\lambda}_t (w_t(x_i) - \dot{U}_t(t))\zeta_i ds - \mu \int_{\Gamma} \tilde{\lambda}_n (|w_t(x_i)| - |\dot{U}_{t_i}(t)|)\zeta_i ds \geq 0 \quad \forall i \in \mathrm{I}_c \ \forall t \in T \tag{10}$$

Finally equation (10) is equivalent to:

$$\begin{cases} \dot{U}_{t_i}(t) = 0 \ \Rightarrow \ |\Lambda_{t_i}| \leq -\mu \Lambda_{n_i}(t) & \forall i \in \mathrm{I}_c \ \forall t \in T \\ \dot{U}_{t_i}(t) \neq 0 \ \Rightarrow \ \Lambda_{t_i}(t) = \mu \Lambda_{n_i}(t) \operatorname{sgn} \dot{U}_{t_i}(t) & \forall i \in \mathrm{I}_c \ \forall t \in T \end{cases} \tag{11}$$

2.2 finite element discretization

In this section the semi-discrete matrix formulation of the contact problem will be implemented. We define the discrete initial displacement and velocity vector as follows:

$$U_0 = (u_0(x_1)^T, u_0(x_2)^T, ..., u_0(x_n)^T)^T \tag{12}$$

And

$$\dot{U}_0 = (v_0(x_1)^T, v_0(x_2)^T, ..., v_0(x_n)^T)^T \tag{13}$$

And the matrix form for Lagrange multipliers in normal and tangential direction write as following matrix notation:

$$\Lambda_n(t) = (\Lambda_{n_1}(t), , ..., \Lambda_{n_N}(t))^T \quad \forall i = 1{:}N \in \mathrm{I}_c \ \forall t \in T \tag{14}$$

$$\Lambda_t(t) = (\Lambda_{t_1}(t), , ..., \Lambda_{t_N}(t))^T \quad \forall i = 1{:}N \in \mathrm{I}_c \ \forall t \in T \tag{15}$$

the matrix notation of the momentom equation for two bodies in contact can be difined as follows:

$$\begin{aligned} &find \ U(t), \lambda(t), \lambda_t(t) \ such \ that \ \forall t \in T \\ &M\ddot{U}(t) + K U(t) = L(t) + B_n \lambda_n(t) + B_t^T \lambda_t(t) \\ &U(0) = U_0, \dot{U}(0) = \dot{U}_0 \end{aligned} \tag{16}$$

Where K is the total tangential stiffness matrix without contact, M is total math matrix, B is addetive sitffness matrix due to the contact presense and L is the extenal force matrix in each time step. by linearization of equation(16) in space dicription, we have:

$$\begin{bmatrix} M_{UU} & 0 & 0 \\ 0 & 0 & 0 \\ 0 & 0 & 0 \end{bmatrix} \begin{Bmatrix} \Delta\ddot{U}(t) \\ 0 \\ 0 \end{Bmatrix} + \begin{bmatrix} R_u(U(t), \Lambda_n(t), \Lambda_t(t)) \\ R_{\lambda_n}(U(t), \Lambda_n(t)) \\ R_{\lambda_t}(U(t), \Lambda_t(t)) \end{bmatrix} + \begin{bmatrix} K_{UU} & K_{U\lambda_n} & K_{\lambda_n\lambda_t} \\ K_{\lambda_n U} & K_{\lambda_n\lambda_n} & 0 \\ K_{\lambda_t\lambda_n} & 0 & K_{\lambda_t\lambda_t} \end{bmatrix} \begin{Bmatrix} \Delta U(t) \\ \Delta\Lambda_n(t) \\ \Delta\Lambda_t(t) \end{Bmatrix} = 0 \tag{17}$$

2.3 Time-stepping algorithms

in the section 2.2 we have drived the spatially discretized form of the problem while the time dimension kept continuously at all time. So at following via the timestepping procedures the total time discretization will be accomplished. So we divide the time interval T into subintervals with non-overlapping and equal lengths as following:

$$T = \bigcup_{k=0}^{L-1} [t_k, t_{k+1}] \tag{18}$$

Where $t_0 = 0, t_L = T$. and $k < t_{k+1}$ and $\Delta t = t_{k+1} - t_k$. for simplicity one can may use the of these notations $u^k = U(t_k)$, $v^k = \dot{U}(t_k)$, $a^k = \ddot{U}(t_k)$. At this process the solution satisfying equation (16) only in a finite number of time-steps defined by t_k. Thus in order to find the other solutions the totally discretized problem defines as follows:

$$\begin{aligned} &\forall k \in \{0,1,...,L-1\} \ \textit{find} \ a^{k+1}, \lambda_n^{k+1}, \lambda_t^{k+1} \ \textit{such that} \ \forall t \in T \\ &Ma^{k+1} + K u^{k+1} = L^{k+1} + B_n^T \lambda_n^{k+1} + B_t^T \lambda_t^{k+1} \\ &u^0 = U_0, \ v^0 = \dot{U}_0 \end{aligned} \tag{19}$$

For the solution of this problem the direct integration algorithms have been proposed which may be derived from Taylor's expansion of the displacement U and the velocity $\dot{U}$ at t_k With respect to time.

References

[1] G. Hu, P.Wriggers. on adaptive finite element method of steady-state rolling contact for hyperelastic in finite deformations. *Comput. Methods Appl. Mech. Engrg*, 191,1333-1348, 2002.

[2] K.P. Singh, B. Poul. Numerical solution of non-Hertzian elastic contact problems. J. Appl. Mech,24,484-490, 1974.

[3] J.J. Kaller. Three-dimensional elastic bodies in rolling contract. *Kluwer Academic Pablishers,Dordrecht*, 1990.

[4] J.M. Bass. Three-dimensional finite deformation rolling contact of a hyperelastic cylinder: formulation of problem and computational results. *Comput struct*, 26,991-1004, 1987.

[5] J.T. Oden, T.L. Lin. On the general rolling contact problem for finite deformations of a viscoelastic cylinder, *Comput. MethodsAppl. Mech. Engrg*, 57,297–376, 1986.

[6] L.O. Faria, J.M. Bass, J.T. Oden, E.B. Becker. A three-dimensional rolling contact model for a reinforced rubber tire.*Tire Sci.Technol*, 17 (1), 217–233, 1989.

[7] R. Kennedy, J. Padovan. Finite element analysis of steady and transiently moving/rolling nonlinear viscoelastic structure–II. *Shell and three-dimensional simulations, Comp. Struct*, 27 (2) , 259–273, 1987.

[8] U. Nackenhorst.The ALE-formulation of bodies in rolling contact Theoretical foundations and finite element approach. *Comput. Methods Appl. Mech. Engrg*, 193,4299-4322, 2004.

Electronic Version Only
ISBN 978-0-902746-30-5